NASA TECHNICAL
MEMORANDUM

NASA TM X-64894
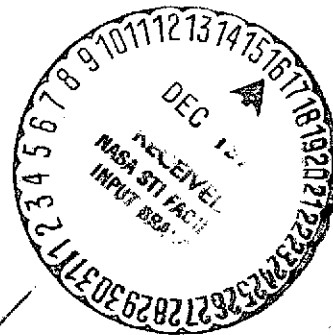
AIRBORNE VISIBLE LASER OPTICAL
COMMUNICATIONS (AVLOC) EXPERIMENT

Electronics and Control Laboratory

November 1974

NASA

George C. Marshall Space Flight Center
Marshall Space Flight Center, Alabama

1. REPORT NO. NASA TM X-64894	2. GOVERNMENT ACCESSION NO.	3. RECIPIENT'S CATALOG NO.
4. TITLE AND SUBTITLE Airborne Visible Laser Optical Communications (AVLOC) Experiment		5. REPORT DATE November 1974
		6. PERFORMING ORGANIZATION CODE
7. AUTHOR(S) Electronics and Control Laboratory		8. PERFORMING ORGANIZATION REPORT #
9. PERFORMING ORGANIZATION NAME AND ADDRESS George C. Marshall Space Flight Center Marshall Space Flight Center, Alabama 35812		10. WORK UNIT NO.
		11. CONTRACT OR GRANT NO.
		13. TYPE OF REPORT & PERIOD COVERED
12. SPONSORING AGENCY NAME AND ADDRESS National Aeronautics and Space Administration Washington, D.C. 20546		Technical Memorandum
		14. SPONSORING AGENCY CODE

15. SUPPLEMENTARY NOTES
Prepared by Electronics and Control Laboratory

16. ABSTRACT

A series of optical communication experiments between a high altitude aircraft at 18.3 km (60,000 ft) and a ground station were conducted by NASA from summer 1972 through winter 1973. The basic system was an optical tracker and transmitter located in each terminal. The aircraft transceiver consisted of a 5-mW HeNe laser transmitter with a 30-megabit modulator. The ground station beacon was an argon laser operating at 488 nm. A separate pulsed laser radar was used for initial acquisition. The objective of the experiment was to obtain engineering data on the precision tracking and communication system performance at both terminals. Atmospheric effects on the system performance was also an experiment objective. The system description, engineering analysis, testing, and flight results are discussed.

EDITOR'S NOTE

17. KEY WORDS	18. DISTRIBUTION STATEMENT Unclassified-unlimited *James D. Fedd Little*

19. SECURITY CLASSIF. (of this report) Unclassified	20. SECURITY CLASSIF. (of this page) Unclassified	21. NO. OF PAGES 481	22. PRICE NTIS

ACKNOWLEDGMENT

The AVLOC program combined an in-house MSFC effort with the contracted work of ITT-Gilfillan in San Fernando, California, and the Chrysler Corporation's Space Division in New Orleans, Louisiana. The overall program was managed by NASA's Office of Aeronautics and Space Technology. Those assisting from the OAST were Jack Levine, Ed Buckley, and John Meson.

MSFC personnel, with Sperry-Rand Corp. support contractor personnel, were responsible for the design, construction, and operation of the ground station. This included the design, fabrication, and integration of the telescope/ computer control and servo system, pulse code modulation communications electronics, tracking and uplink command electronics, telemetry and data acquisition instrumentation, dome control servo system, video acquisition aid, display and recording system, and computer systems software. MSFC personnel contributing to this work were St. John Courtenay, Daryl Craig, Ron George, Truman Moore, Don Griner, Derryl Evans, Jim Zurasky, Charles Hawkins, William Robinson, Joseph Pour, John Gould, Clyde Jones, Paul White, Harry Reid, Ron McIntosh, Fred Roe, Ralph Grubb, Dr. George Doane, Dennis Thomas, Mike Robinson, Dick Tuggle, Charles Wyman, J. Patterson, Frank Nola, Truman McClard, Danny Coleman, John Frazier, Pete Marrero, Ed Braknis, Thelma Robbe, and Martha McCartney. Sperry-Rand Corp. personnel contributing were Bill Hurd, Glenn Shelton, Lee O'Neal, Claude Neely, Charles Childers, Gary Hunt, Fred Walters, Jim McGee, and O. B. Williams. Hayes International Corp. personnel contributing were Bill Stisher and Reese Eidson.

The meteorological data and weather forecasts were provided by Joe Sloan and Dale Johnson of MSFC and Luke Gilchrist of Northrop Corp.

ITT-Gilfillan was responsible for the Aircraft Optical Communications Package (AOCP) and associated remote electronics, Ground Checkout Equipment (GCE), the Ground Based Acquisition Aid (GBAA), the design analysis and acquisition of the retroreflectors, and flight support. The ITT-Gilfillan personnel who contributed to this work were Virgil Hammock, L. Marcusen, Jerry Redmann, Jack Priebe, Bob Yancey, Leo Cordone, Bill Wilson, Tom Dixon, Fanning Oakley, and Mary Castro.

Chrysler, as integration contractor, was responsible for integration of the airborne equipment into the aircraft, including the AOCP and its physical mounting, power and cabling, data acquisition and telemetry, environmental control of the aircraft package, onboard computer command and control, gimbal mirror platform, and cockpit controls. Additional areas of

TABLE OF CONTENTS

TABLE OF CONTENTS (Continued)

TABLE OF CONTENTS (Concluded)

LIST OF ILLUSTRATIONS

LIST OF ILLUSTRATIONS (Continued)

LIST OF ILLUSTRATIONS (Continued)

LIST OF ILLUSTRATIONS (Continued)

LIST OF ILLUSTRATIONS (Continued)

LIST OF ILLUSTRATIONS (Continued)

LIST OF ILLUSTRATIONS (Continued)

LIST OF ILLUSTRATIONS (Continued)

LIST OF ILLUSTRATIONS (Continued)

LIST OF ILLUSTRATIONS (Continued)

LIST OF ILLUSTRATIONS (Continued)

LIST OF ILLUSTRATIONS (Continued)

LIST OF ILLUSTRATIONS (Continued)

LIST OF ILLUSTRATIONS (Concluded)

LIST OF TABLES

LIST OF TABLES (Continued)

LIST OF TABLES (Concluded)

LIST OF ACRONYMS

A/D   Analog to Digital

AGC   Automatic Gain Control

AOCP   Airborne Optical Communications Package

AVLOC   Airborne Visible Laser Optical Communications

BAPE   Balloon Atmospheric Propagation Experiment

BED   Bit Error Detector

BER   Bit Error Rate

BS   Beam Steerer   --ON FIGURES ONLY--

CCSD   Chrysler Corporation Space Division

CW   Continuous Wave

D/A   Digital to Analog

DEMOD   Demodulator

ECS   Environmental Control System

EFL   Effective Focal Length

El   Elevation

FFT   Fast Fourier Transform

FOV   Field-of-View

GBAA   Ground Based Acquisition Aid

GCE   Ground Checkout Equipment

GFE   Government Furnished Equipment

GSE	Ground Support Equipment
GSFC	Goddard Space Flight Center
HVPS	High Voltage Power Supply
ID	Image Dissector
IFOV	Instantaneous Field-of-View
I/O	Input/Output
JSC	Johnson Spacecraft Center
KD* P	Potassium Dihydrogen Phosphate
MGC	Manual Gain Control
MSFC	Marshall Space Flight Center
MSMV	Monostable Multivibrator
MUX	Multiplexer
NB	Narrow Band
ND	Neutral Density
NRZ	Nonreturn to Zero
OAST	Office of Aeronautics and Space Technology
OOK	On-Off Keying
PAM	Pulse Amplitude Modulation
PCM	Pulse Code Modulation
PDF	Probability Density Function

LIST OF ACRONYMS (Continued)

PDI   Pilot Directional Indicator

PMT   Photomultiplier Tube

PN   Pseudorandom Word

PSD   Power Spectral Density

QMP   Quadrant Multiplier Phototube

RCVR   Receiver

REC   Remote Equipment Cannister

RER   Remote Equipment Rack

ROM   Read Only Memory

R/L   Root Locus

SD   Standard Deviation

SEO   Scientific Equipment Operator

S/N   Signal to Noise

SRM   Short Range Missle

TAR PRES   Target Presence

TEM   transverse electro-magnetic

TQ   Torquer -- ON FIGURES ONLY

VCO   Voltage controlled oscillator

VCXO   Voltage-controlled crystal oscillator

VID PRES   Video Presence

AIRBORNE VISIBLE LASER OPTICAL COMMUNICATIONS (AVLOC) EXPERIMENT

INTRODUCTION

Background

ADVANTAGES OF OPTICAL COMMUNICATIONS SYSTEMS

The historical trend in communications has been to higher and higher frequencies. Hence, the attractiveness of the laser in communication systems was immediately obvious upon its discovery in 1960.

Interest in this application of the laser stems largely from the promise of greater information capacities and communication distances than have been realized heretofore. The properties of laser radiation which make these improvements possible are its short wavelength and its relatively high degree of coherence, as compared with other sources of optical radiation. However, the real advantage in communications at optical frequencies lies in the ability to form narrow beamwidths with small "antennas." For the first time, a source of optical radiation is available which approaches a carrier in spectral purity, suggesting the use of many of the coherent detection techniques that have been developed to a high degree of sophistication in the RF spectral region. Unfortunately, the performance of a coherent detection system at optical frequencies, particularly at the visible wavelengths, is severely limited by a turbulent transmission medium such as the atmosphere through which any ground-based system must operate. Under these conditions, the simpler photon-counting receiver can still be used to exploit many of the laser properties in communications.

When comparisons between approaches are made, the performance of the overall communications system must be considered. A comparison of laser efficiency alone, for example, is inadequate for judging the performance of optical communications systems. A photon-counting system is considerably simpler and less critical of mechanical alignment than a heterodyne or homodyne system and is potentially more reliable. Further, the use of visible or near-visible wavelengths, which exhibit impractically small coherence apertures in a turbulent medium, is very desirable from the detector standpoint. High-detectivity, large-gain bandwidth product detectors are

available in this spectral region. Many of these detectors can be "electronically gimballed" to provide a large search/acquisition field of view and a small, low-noise field of view for tracking and communicating. The high degree of background spatial filtering offered by these devices, when combined with currently available narrow bandpass optical filters, virtually eliminates the optical background problem. These acquisition and tracking techniques make the handling of extremely narrow (fractional arc second) transmitted beamwidths practical.

The basic justification for communications at optical frequencies lies either in the need for extremely wide information bandwidth or in the need for the very high "antenna" gains available. The latter provides a number of useful advantages, including extreme link privacy and efficient utilization of transmitted power for the very long range (interplanetary) communications. Specifically, some applications which promise great benefit to NASA would be high data rate and tracking systems for the Shuttle, Synchronous Data Relay Satellites, deep space probes, and earth orbital scientific satellites.

The significant benefit stemming from laser technology as regards these applications is its inherent capabilities for providing precision tracking simultaneously with high data rate communications. At the same time, these systems can be implemented at a savings of weight and power.

FACTORS LIMITING PRESENT DAY OPTICAL COMMUNICATIONS SYSTEMS PERFORMANCE

For the full potential of laser communications systems to be realized, considerable research must be performed in attacking certain existing problem areas. The most pressing areas requiring research are discussed in the following paragraphs.

ATMOSPHERIC PROBLEM

Cloud covers degrade optical communication, making certain ground station locations impractical. However, the degree of cloud penetration by various wavelengths and beamwidths has not been determined. Furthermore, even in a clear atmosphere, clear air turbulence will cause scintillation on an optical beam. This scintillation is, in effect, a variation in instantaneous signal strength at the receiver. The statistics of this scintillation as a function of meteorological conditions, beamwidth, wavelength and receiver telescope aperture are not known at this time. One means of improving the received signal-to-noise ratio is to communicate with very short pulses and to blank

2

the receiver between pulses. The limit to this technique is the extent that a pulse is widened or stretched in time because of scattering in the atmosphere. This pulse stretching is also a measure of the ultimate bandwidth of the atmosphere as a transmission medium. Atmospheric attenuation of a light beam, which is a function of the wavelength and beamwidth, is not known.

TRACKING AND ACQUISITION

Because of the extremely narrow transmitted beamwidths and the small fields of view of optical detectors, sophisticated and highly developed techniques of acquisition and tracking are demanded. The fractional arc-second pointing and tracking accuracies required place severe restraints on the system optical tolerances and electronic circuit design.

SPACE QUALIFICATION/SYSTEMS ENGINEERING PROBLEMS

Optical communications systems pose unique problems in the space qualification of certain components and subsystems. Not only is the space qualification of the individual components complex, but also the interfacing of certain components, such as the laser and modulator, further complicates space qualification of the overall system. In general, the launch environment and required reliable sustained operation in space will place severe demands on the design of system components to assure the maintenance of boresight and other critical optical alignments.

Atmospheric Propagation Research

THEORY

The study of wave propagation through the atmosphere was spurred by the advent of the laser. This vigorous effort to mathematically model the atmosphere and its effects upon laser propagation became the essential groundwork for determining the theoretical performance of laser communications systems operating in atmospheric media. Significant work in this field was initially performed by Kolmogorov and Tatarski and more recently by Fried. It was demonstrated that the effects of the turbulent atmosphere on the laser beam result in random amplitude and phase variations, giving rise to scintillation, angle-of-arrival fluctuations, and wavefront phase distortions. The value of this work is in predicting the performance limitations of optical communications systems operating through the atmosphere.

EXPERIMENTAL STUDIES

It is mandatory to verify these theoretical studies in order to establish their credibility for use in the design of optical communications systems. In an effort to confirm theory, numerous laser atmospheric propagation experiments have been conducted. Because of the difficulty involved in implementing vertical propagation studies, virtually all of the work performed previously has been necessarily limited to horizontal paths. These ground-based studies have generally verified and substantiated the existing theoretical models. However, the equivalent experimental confirmation over a vertical path has until recently been lacking. Because of the important potential application of satellite-earth optical communications systems, the present studies were addressed to determining experimentally the effects of laser propagation through the atmosphere over vertical paths.

To obtain the previously lacking vertical propagation data, programs were initiated by NASA's Goddard Space Flight Center (GSFC) and Marshall Space Flight Center (MSFC) under the sponsorship of NASA's Office of Aeronautics and Space Technology (OAST). The GSFC program is entitled Balloon Atmospheric Propagation Experiment (BAPE), and the MSFC program, with which this report deals, is entitled Airborne Visible Laser Optical Communications (AVLOC).

Goddard's BAPE program was the first in which vertical propagation data were obtained. The program involved a balloon-borne receiver and a ground station which housed the lasers. The primary objectives were to obtain uplink scintillation data at wavelengths of 514.5 nm and 10.6 μm, and correlate these data with microthermal measurements made with an instrument attached to the balloon-borne package.

AVLOC Program

TECHNICAL

The AVLOC program was designed to provide a controlled test bed at high altitudes near the zenith of a ground tracking station. The ground station was located atop Madkin Mountain on Redstone Arsenal, and the airborne test bed was installed in a WB-57F aircraft.

The basic experimental procedure was to obtain initial acquisition on the target aircraft with a pulsed argon laser radar which tracked retroreflectors mounted on the underside of the aircraft. The coarse tracking system provided

aiming of the telescope so that the beacon laser beam illuminated the aircraft transceiver. The beacon laser was then automatically tracked by the airborne transceiver, which simultaneously transmitted a boresighted helium-neon (He-Ne) laser beam down to the ground station. After cooperative, two-way pointing and tracking was established, the optical communications systems performance could be evaluated while atmospheric propagation data were collected simultaneously. This link provided a means of directly evaluating the vertical atmosphere as a two-way optical communications medium and to test contemporary optical communication design techniques in an aerospace environment.

Installation of the test bed in an aircraft provided a means of evaluating acquisition and tracking techniques and communication systems performance, as well as vertical atmospheric propagation effects in a dynamic operating environment with its characteristic vibration modes and thermal/vacuum conditions.

MANAGEMENT

The AVLOC program combined an in-house MSFC effort with the contracted work of ITT-Gilfillan in San Fernando, California, and Chrysler Corporation Space Division in New Orleans, Louisiana. The overall program was managed by Henry Anderton of OAST. The MSFC program manager was Wayne Wagnon, with Dr. J. L. Randall the principal investigator. Co-principal investigators were Dr. Estil Hoversten of the Massachusetts Institute of Technology, Dr. William Webb of the University of Alabama, and Dr. Sherman Karp of the Department of Transportation.

ITT-Gilfillan was responsible for the Aircraft Optical Communications Package (AOCP) and associated remote electronics, Ground Checkout Equipment (GCE), the Ground Based Acquisition Aid (GBAA), the design analysis and acquisition of the retroreflectors, and flight support. The ITT program manager was John Ward.

Chrysler, as integration contractor, was responsible for integration of the airborne equipment into the aircraft, including the AOCP and its physical mounting, power and cabling, data acquisition and telemetry (TM), environmental control of the aircraft package, onboard computer command and control, gimbal mirror platform, and cockpit controls. Additional areas of responsibility were systems analysis for flight operations and flight support. The Chrysler program manager was John Riles.

MSFC personnel, along with Sperry-Rand Corp. support contractor personnel, were responsible for the design, construction, and operation of the ground station. This included the design, fabrication, and integration of the telescope/computer control and servo system, pulse code modulation (PCM) communications electronics, tracking and uplink command electronics, TM and data acquisition instrumentation, dome control servo system, video acquisition aid, display and recording system, and computer systems software.

PROGRAM OBJECTIVES

Overall OAST Optical Communications Program Objectives

The primary objective of the Optical Communications Program is to develop laser technology for operational uses in the 1970 decade. In particular, large manned earth-orbiting space stations, multi-satellite utility programs, manned lunar orbiters and lunar bases, and eventually manned bases and orbiters on the planets will require increased performance in data links, as well as noninterfering frequency allocation or new communication modes for such links. A favorable means of achieving this objective is through the use of directed narrow beam laser communications systems.

Because of the wide range of applications in which laser communications may be used, the feasibility of various optical communications techniques will be established. This will be accomplished through laboratory research and development, field tests, aircraft and balloon test flights, and spaceborne experiment flights which have been formulated as a result of previous Optical Communications Experiment Program studies.

Recent efforts of the Optical Communications Program have been conducted through BAPE and AVLOC. In addition, advanced and supporting technology tasks have been studied to support these programs and proposed satellite experiments.

The BAPE test flights performed by GSFC [1] and the AVLOC tests performed by MSFC have complemented each other. The objectives of the BAPE test flights were to determine the effects of propagating a laser up through the atmosphere and to obtain data on the atmospheric turbulence effects of laser communications. The AVLOC tests have been beneficial in determining the degree that a light beam is affected by vertical transmission through the atmosphere using controlled, repeatable programs of altitude and zenith angle changes.

6

AVLOC Program Objectives

The primary objective of this project has been to obtain test data on a laser communication link propagating vertically through the atmosphere. Specifically, the following objectives were to be achieved:

1. Obtain atmosphere-produced scintillation statistics for both the uplink and downlink beams.

2. Determine angle-of-arrival fluctuation for both uplink and downlink beams.

3. Measure directly the bit error rate (BER) on the downlink beam caused by scintillation.

4. Determine the atmospheric transmission for both uplinks and downlinks.

5. Evaluate objectives 1, 2, and 3 as a function of receiving aperture size, range, zenith angle, and beamwidth, as appropriate.

6. Evaluate critical electro-optical components and their restraints imposed by and upon their operating environment.

7. Evaluate a two-way optical communications system in a dynamic operating environment, resulting in a qualitative evaluation of acquisition, tracking, pointing, and boresighting design techniques.

SYSTEM DESCRIPTION

Functional Description and Basic Acquisition Sequence

The basic experimental system consists of a two-way optical link between the ground station located on Madkin Mountain at Redstone Arsenal and the high-altitude WB-57F aircraft, circling over the ground station. A sketch of the setup is given in Figure 1. The aircraft circles over the ground station at a radius of 12.2 km (40 000 ft) and an altitude of 18.3 km (60 000 ft). The ground station transmits two beams up to the aircraft: a green laser radar beam at 514.5 nm and a blue beam at 488.0 nm. The green beam is transmitted by the GBAA that is physically strapped to the telescope and is reflected by optical retroreflectors on the aircraft back down on the GBAA receiver. Thus, the GBAA continuously tracks the aircraft, allowing the blue beam (which is boresighted to the green beam) to continuously floodlight the aircraft. With the

blue beam floodlighting the aircraft, the gimbal platform aboard the aircraft directs the field of view of the coarse tracker onboard the aircraft to the ground station, thereby allowing this tracker to "acquire" the blue beam. Once the blue beam is acquired, the gimbal platform, making use of the coarse tracker error signals, brings the blue beam within the field of view of the fine tracker and maintains it there. Once the fine tracker acquires the blue beam, the AOCP pointing system is activated, which directs the outgoing red beam (632.8 nm) along the received line of sight. Thus, the ground tracking system locks onto the red beam and turns control of the telescope from the GBAA to the line tracker. The precision boresight of the transmit/receive channels keeps the upgoing blue beam precisely aligned with the received red beam. Thus, acquisition is completed when the two systems are locked together in a two-way link, and commands may be sent up over the blue beam for real-time control of the experiment package by the principal investigator, while TM is simultaneously received over the red beam on the ground.

ARGON LASER
UPLINK BEAM (BLUE)
0.488 MICROMETERS

GROUND BASED ACQUISITION
AID/LASER RADAR (GREEN)
0.51 MICROMETERS

HELIUM-NEON LASER
DOWNLINK BEAM (RED)
0.633 MICROMETERS
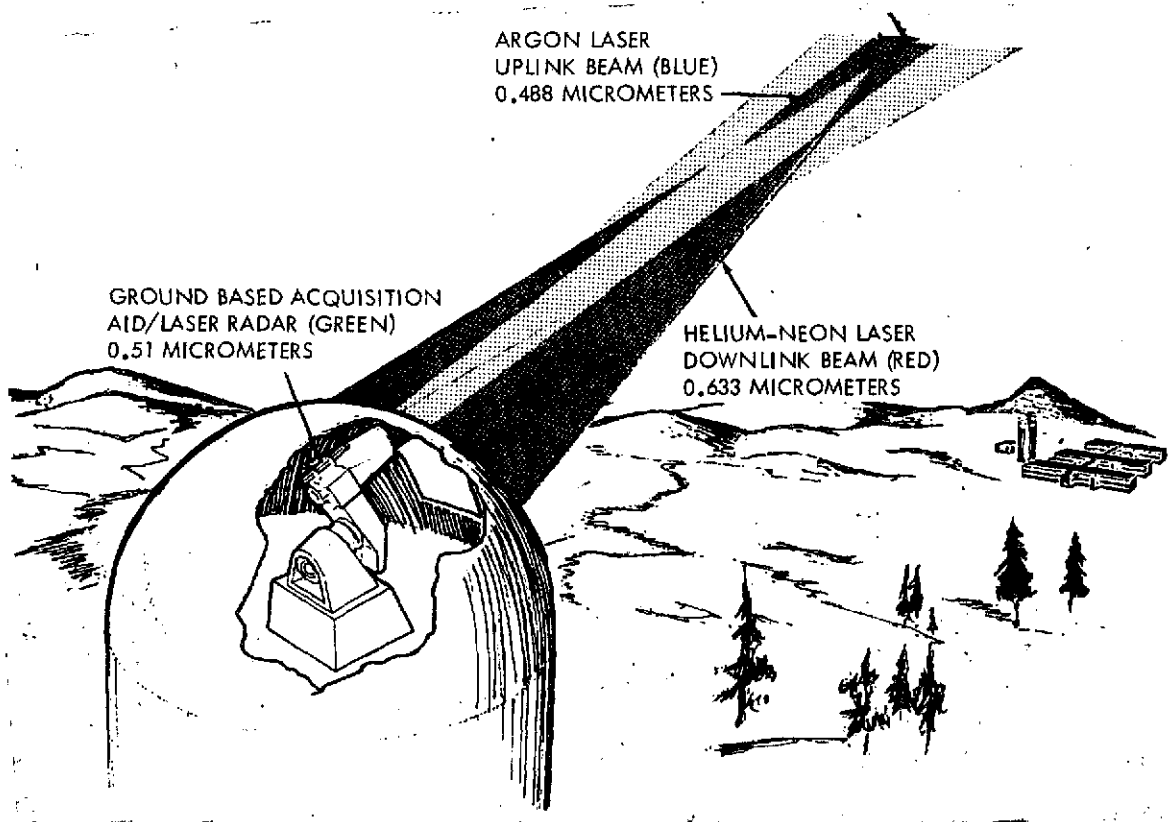
Figure 1. Madkin Mountain ground station.

The aircraft and airborne equipment are sketched in Figure 2 and illustrated in Figure 3. The aircraft is a WB-57F NASA Earth Observation aircraft, SN No. 926. Originally, a USAF U-2 "spy plane" was to be used, but because of marginal weight and volume capabilities of the U-2 to meet requirements and because of schedule conflicts with ongoing U-2 scientific programs, the decision was made early in the program to shift to the WB-57F aircraft. This aircraft has an altitude capability greater than 18 km (60 000 ft) and weight volume capabilities greatly in excess of program requirements.
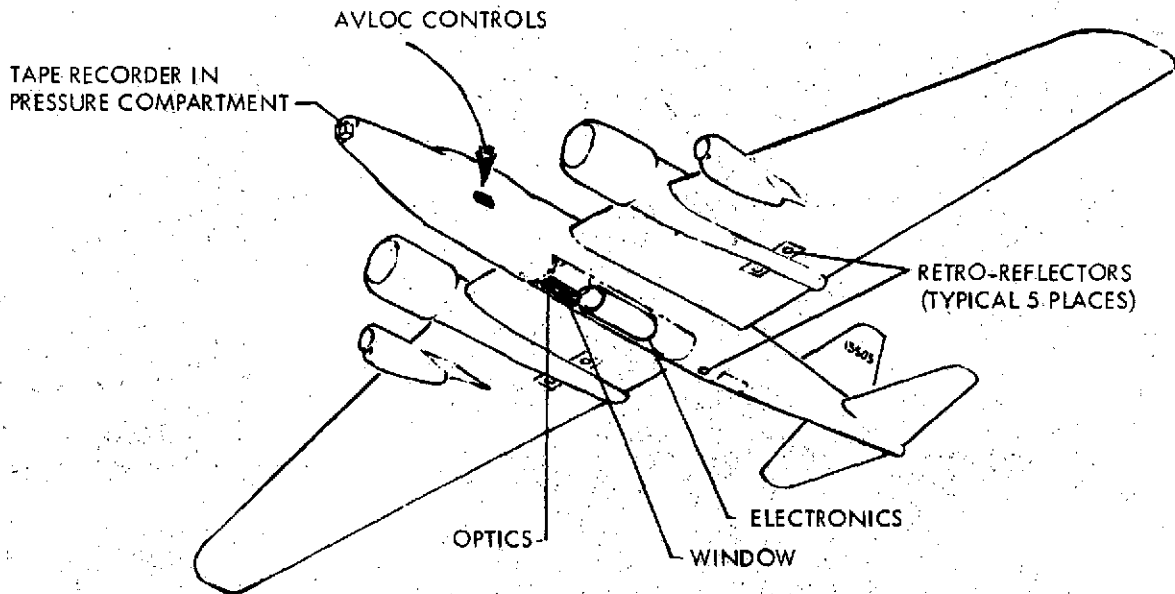
Figure 2. Sketch of aircraft and airborne equipment.

The basic airborne equipment consists of an experiment assembly which is suspended over an optical window in the bomb bay, a remote equipment canister also in the bomb bay, operator controls in the navigator compartment, and a tape recorder mounted in the nose compartment. The experiment assembly contains the AOCP and the gimbal mirror. The remote equipment canister houses the support electronics. Environmental control is provided for both the support electronics and the AOCP, whereas the tape recorder and the operator controls are located in compartments that were already pressurized. The gimbal platform operates in the ambient environment.
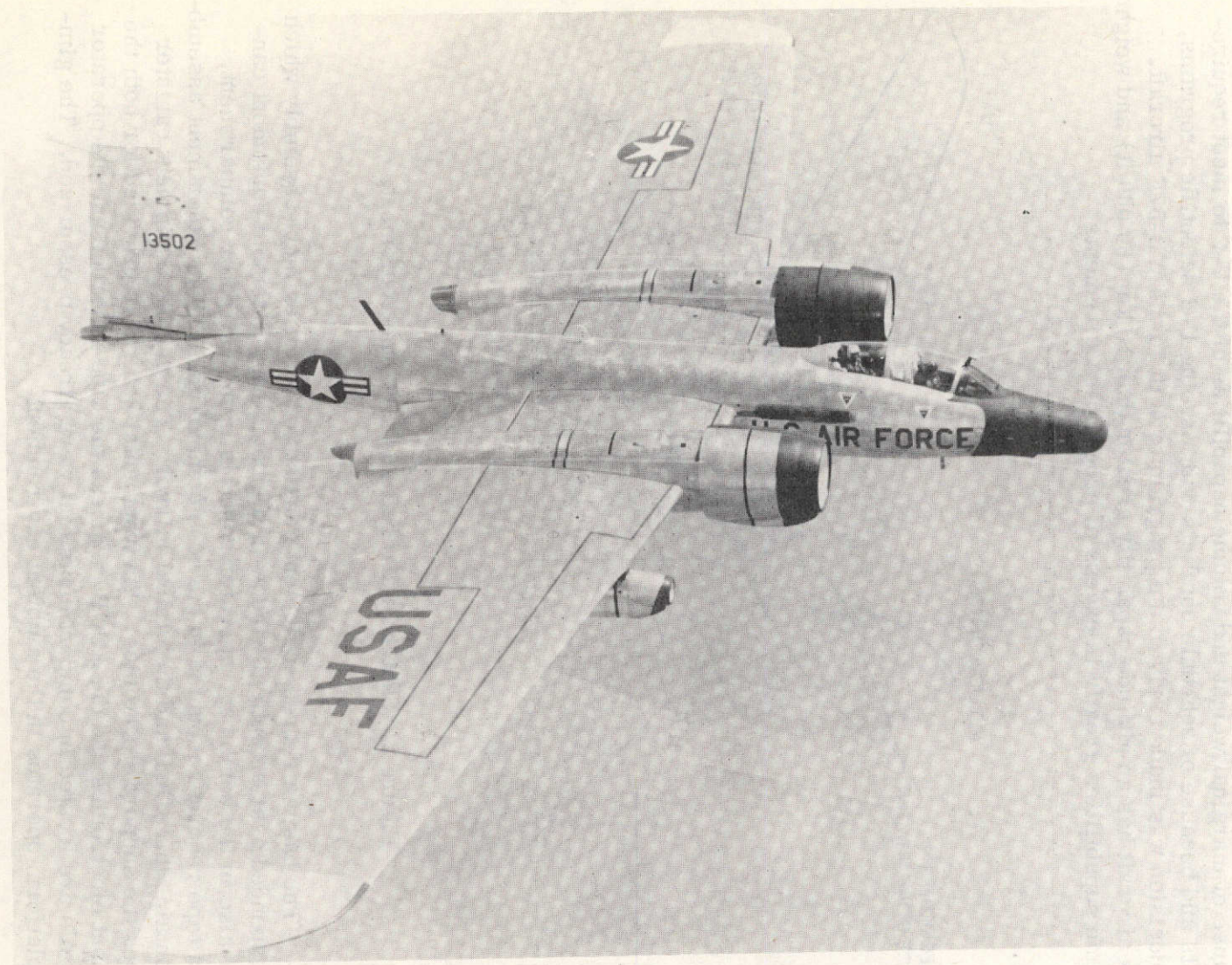
Figure 3. Photograph of WB-57F aircraft.

Major Subsystems

AIRCRAFT SYSTEM

The major airborne equipment consists of the AOCP, the Remote Equipment Canister (REC), the gimbal platform, cockpit controls, and the items required to install this hardware in the aircraft (e.g., platform and cable harnesses). The tape recorder flown in the aircraft will be discussed in the following pages. A block diagram of the primary airborne equipment is given in Figure 4.
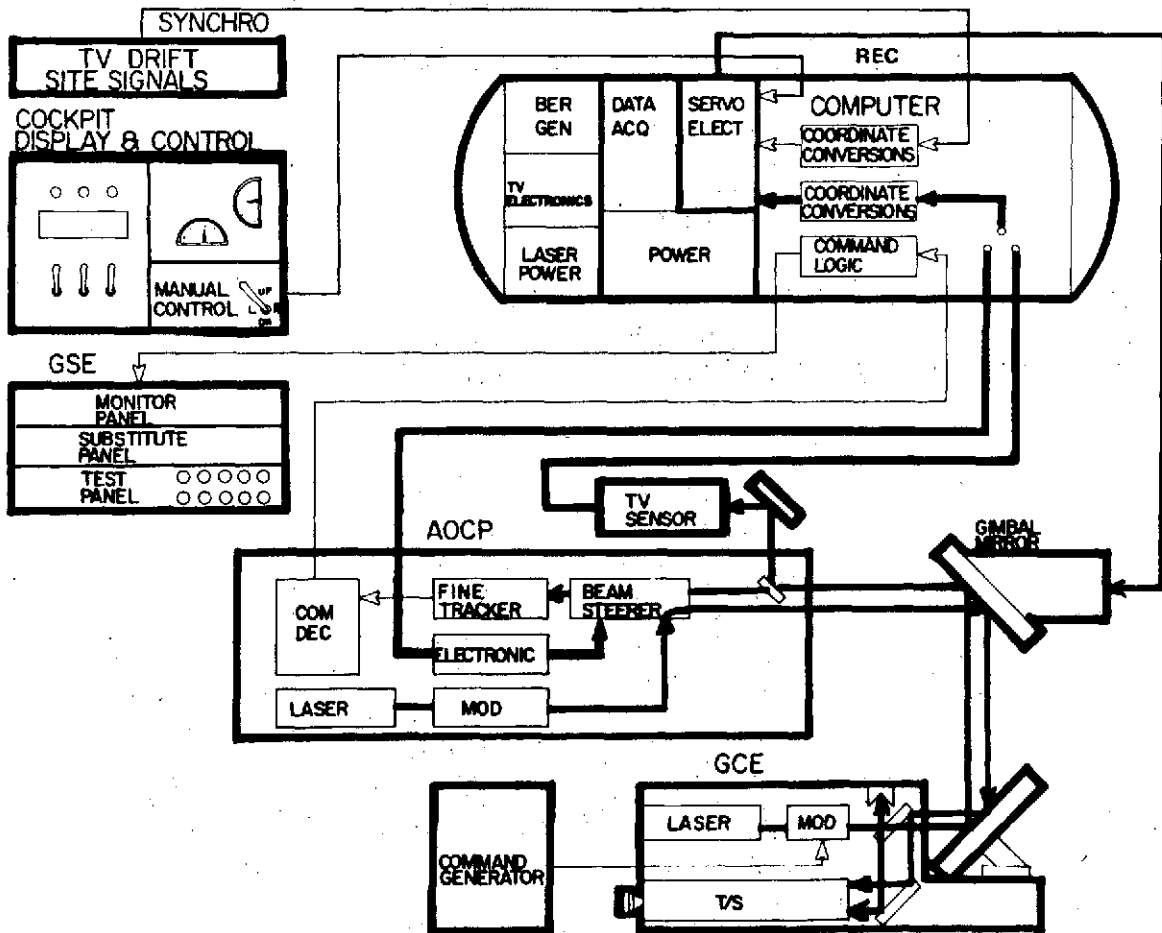
Figure 4. AVLOC simplified block diagram.

AIRBORNE OPTICAL COMMUNICATIONS PACKAGE (AOCP)

General

The AOCP is a laser transceiver system providing the capability of duplex communications and includes acquisition, tracking, pointing, and atmospheric scintillation monitoring subsystems. Figure 5 is the AOCP hardware tree showing the various system elements and their relationships.

The AOCP design specifications were determined early in the program as a result of several planning meetings held at NASA/MSFC between ITT-Gilfillan technical personnel and the AVLOC principal investigator team. Figure 6 shows the AOCP unit and lists some of the significant parameter values. Table 1 gives a more complete list of the AOCP specifications. These final system specifications did not vary appreciably from those set forth initially, although some were made more complete or more stringent as the operational environment became better defined.

Figure 7 shows the AOCP unit mounted in its test fixture. This equipment view shows the receiver collection aperture and the concentric folding mirror and periscope path to the TV acquisition aid. The coordinate reference frame is defined in this view. The X-axis is directed along the line of sight and the position sensing is in the orthogonal YZ-plane. It should be noted the transmitter aperture is offset from the center of the Cassegrainian receiver collector and located in the center of the annulus. The reason for this is to avoid a central obscuration in the transmitted beam. A more thorough analysis of this effect is given later in this report.

The operation of the AOCP can be understood by Figure 8, which shows the system functional block diagram. Since in the operational acquisition sequence the ground beacon first illuminates the aircraft terminal, the AOCP receiver section will be described first. A modulated (10.7-MHz subcarrier) argon laser beam (488 nm) from the ground station (or GCE) is guided by the coarse gimballed mirror onto the relatively wide field-of-view TV acquisition aid. The TV acquisition aid subsystem detects and tracks the position of the ground beacon within its 87.2- by 122-mrad (5- by 7-deg) field of view and provides pointing commands in two axes to control the gimballed mirror to within the fine acquisition field of view of the AOCP equipment. The fine acquisition and tracking function is illustrated in Figure 9. The fine acquisition is accomplished by an all electronically scanned image dissector (ID) detector searching sequentially a 128- by 128-element raster with a frame time of 1 sec. Each raster is approximately 68 μrad on a side, and the instantaneous field of view is 86 μrad, which provides

12
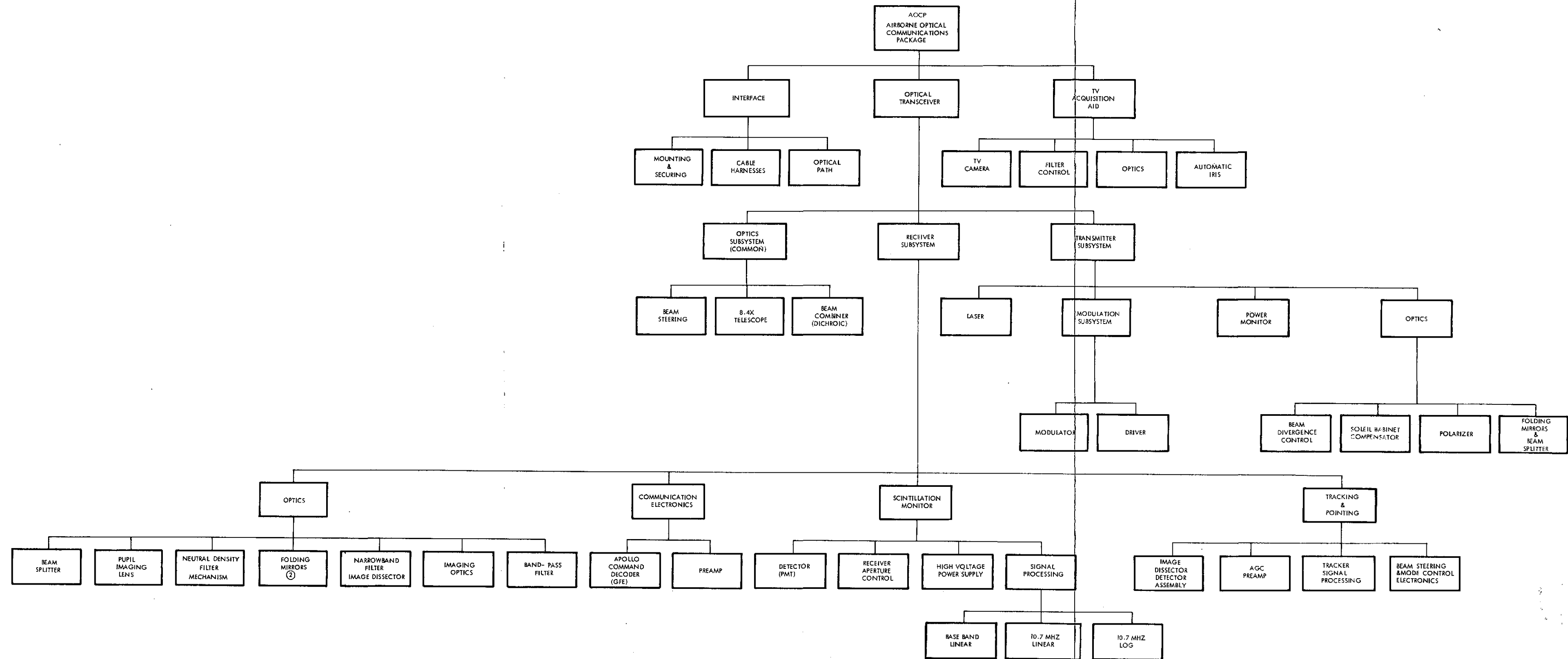
Figure 5. AOCP hardware tree.

a better than 20 percent scan overlap. For the fine tracking system to acquire, the optical signal must exceed a threshold level of 1×10^{-10} W/cm² and be modulated with a 10.7-MHz signal. This latter condition prohibits false lockon to bright objects in the background.
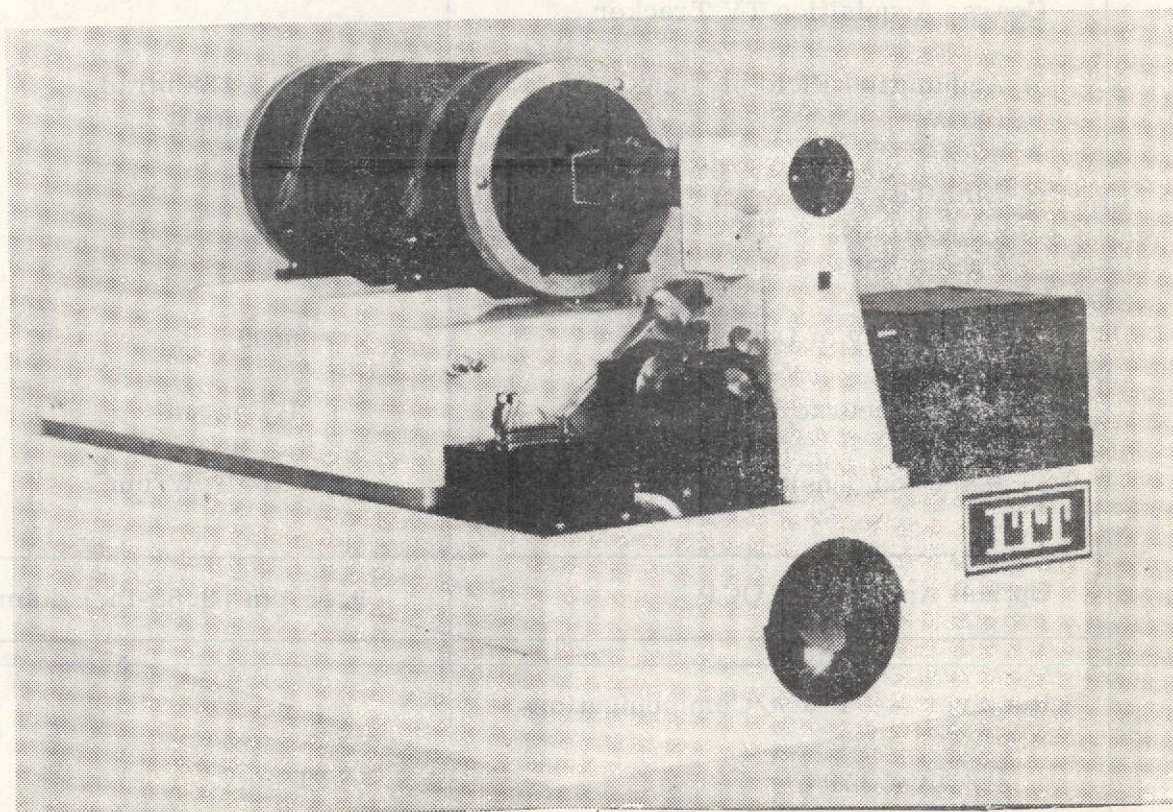
Specifications		Acquisitions FOV	7 x 10 deg
Size	27.18 x 39.37 x 57.15 cm (10.7 x 15.5 x 22.5 in.)	Fine Track FOV	0.5 x 0.5 deg
		Track Bandwidth	1 kHz
Weight	36.3 kg (30 lb.)	Track AGC B.W. Dynamic Range	300 Hz, 60 dB
Power Input	150 W	Track/Point Accuracy	1 μrad rms
Aperture Size	9.16 cm (4 in.)	Mean Acquisition Time	1 sec
Transmit Wavelength	632.8 nm	Point Ahead Range	± 500 μrad
Receive Wavelength	488 nm	Transmitted Beamwidth	20 to 500 μrad
Data Rate	30 Mbit/sec		

Figure 6. AOCP unit.

TABLE 1. AOCP SUMMARY SPECIFICATIONS

Coarse Acquisition TV Tracker	
Acquisition Field of View (FOV)	87.2 × 122 mrad (5 × 7 deg)
Linearity	< 10 %
Frame Rate	60/sec
Probability of Detection	> 0.99
Track Accuracy	< 1.5 mrad
Detection Sensitivity	1×10^{-10} W/cm^2
Optical Aperture, AOCP	9.85-cm (3.88-in.) diam
Receiver — Track/Communications	
Detector Type	ITT 4012
Spectral Response	S-20
Detection Sensitivity	1×10^{-10} W/cm^2
Fine Acquisition FOV	8.7 × 8.7 mrad (0.5 × 0.5 deg)
Instantaneous FOV	87.3 × 87.3 μrad (18 × 18 arc sec)
Effective Focal Length	1.13 m
Acquisition Frame Rate	1 frame/sec
Scan Format	128 × 128 element digital raster

TABLE 1. (Continued)

Track Scan Type	Partial scan — cruciform
Track Scan Rate	16 kHz
Track Bandwidth	Up to 1000 Hz
Tracking Accuracy	0.2 arc sec rms
Receiver Attenuation	30/1 variable
Communications Bandwidth	50 kHz
Modulation Type	10.7 MHz subcarrier FM
Optical Wavelength	488 nm
Optical Bandpass	± 1.0 nm
Tracker Signal Dynamic Range	60 dB
Tracker AGC Bandwidth	300 Hz
Optical Transmission	0.15
Receiver — Scintillation Monitor	
Detector Type	Photomultiplier RCA 8644
FOV	8.7 × 8.7 mrad (0.5 × 0.5 deg)
Dynamic Range	60 dB
Bandwidth	5 kHZ

TABLE 1. (Continued)

Outputs	Baseband linear 10. 7 MHz linear 10. 7 MHz log
Effective Aperture	9. 85–cm diam (3. 8 in)
Ratio of Aperture Variation	100/1 in area
Optical Bandwidth	$\pm$ 1 nm
Optical Wavelength	488 nm
Optical Transmission	0. 2
Pointing Subsystem	
Beam Steerer Type	Torque driven mirror, flex pivot mounted
Bandwidth	240 Hz
Steering Angle Range	$\pm$ 8. 7 mrad (0. 5 deg) two axes
Closed Loop Pointing	$\leq$ 5 μrad (1 arc sec) peak to peak
Transmitter	
Laser Type	He–Ne
Laser Power	5 mW, TEM_{00}
Wavelength	633 nm
Beam Divergence	25 to 600 μrad (5 to 120 arc sec) variable

TABLE 1. (Concluded)

Modulator Type	Transverse field electro-optical deuterated potassium dihydrogen phosphate (KD*P)
Modulation Format	On-off keying (OOK)
Modulation Index	75%, variable operating point
Data Rate	30 megabits/sec
Weight	76 kg (167 lb) excluding Remote Equipment Rack (RER)
Power Consumption	200 W

LASER/MODULATOR COMPARTMENT

TV CAMERA

TV CAMERA PERISCOPE, AUTOMATIC IRIS CONTROL AND FILTER SELECTOR

VARIABLE WAVE PLATE

POLARIZER

TV CAMERA FOLDING MIRROR

RECEIVE/COLLECTION APERTURE

ITT
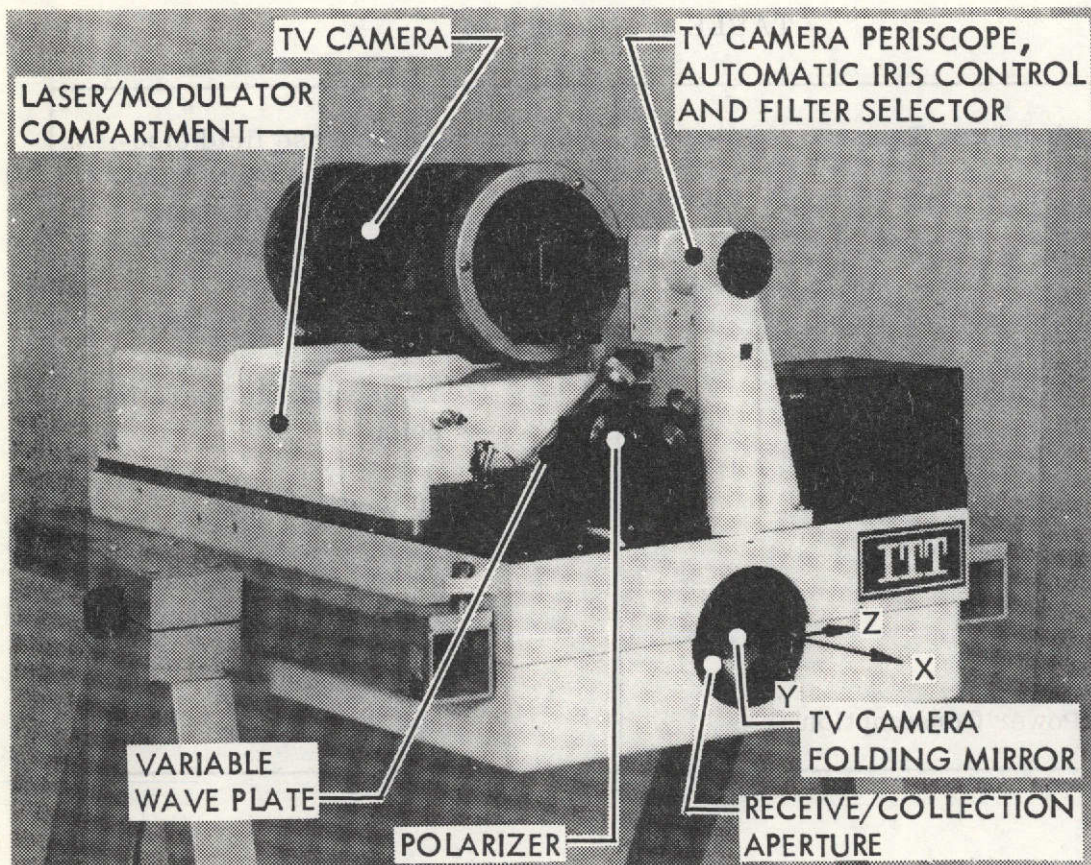
Figure 7. AOCP flight package.

Upon identification of the beacon, the receiver tracker switches into a Track scan mode (the mode control functions and circuitry are described in the beam-steering section of this report). The Track scan is of the cruciform type which effectively displaces the optical image of the beacon back and forth in two axes alternately about the detection aperture, as illustrated in the lower half of Figure 9. This action places a scan modulation on the detected signal which, when synchronously demodulated with the sweep drive signal, provides a measure of the optical image position in the sampling aperture. A more complete design discussion of this technique is given in the tracker section of this report.

The tracker output is a measure of the position of the optical beacon image on the detector photocathode relative to the detector's null axis. The output signals are in rectilinear coordinates in the YZ-plane.

Figure 8. AOCP functional block diagram.

POWER SUB–SYSTEMS

110V 60 Hz
+ 28 VDC REGULATED
+ 28 VDC UNREGULATED

–1000 VDC
–1500 VDC
–2000 VDC
110V 60 Hz
+ 5 VDC
+ 15 VDC
–15 VDC
+28 VDC REG
+28 VDC UNREG
+ 45 VDC

B1
B2
B3
B4
B5
B6

LASER
MODULATOR
DRIVER

SOLEIL BABINET
WINDOW
POLARIZER

CONVERTER IF AMPL & DETECTOR
10.7 MHz LOG OUTPUT

AGC AMPLIFIER
AGC CONTROL OSCILLATOR

CONVERTER IF LINEAR AMPL
LASER POWER MONITOR ELECTRONICS
POWER MONITOR
PMT
HVPS
10.7 MHz LINEAR OUTPUT
LASER POWER OUTPUT

STEPPER METER

BEAM DIVERGENCE TELESCOPE
BEAM SPLITTER
LASER SHUTTER

BASEBAND OUTPUT
BASEBAND AMPLIFIER
PREAMP
MGC AMPLIFIER

HVPS
8645 SCINTILLATION MONITOR
PMT

BEACON PRESENCE

ACQUISITION SCAN GENERATOR

TRACK DEFEAT
BEACON PRESENCE

DEFLECTION AMPLIFIER
TRACK CIRCUITRY

APERTURE STOP

BEAM SPLITTER
NB FILTER
BEAM COMBINER
BEAM STEERER
BEAM STEERER Z
COLLI-MATING LENS
CASSEGRAIN OBJECTIVE

633 nm
514 nm

SIGNAL SEPARATION FILTER
10.7 MHz
IMAGE DISSECTOR DETECTOR
N.B. FILTER
N.D. FILTER WHEEL
STEPPER MOTOR

MODULATION OUTPUT TO APOLLO COMMAND DECODER

TV CAMERA
FILTER

TRACKING ERROR FILTER
E_X, E_Y
TRACK ERROR SIGNALS TO RECORDER

B.S. ELECTRONICS
TO Y AND Z BS

÷ 2
Σ_Y, Σ_Z
OUTPUT TO CCSD

OUTPUTS
1 BEAM DIVERGENCE POSITION
2 TV TRACKER FILTER POSITION
3 RECEIVER ATTENUATION POSITION
4 SCINTILLATION MONITOR APERTURE POSITION
5 LASER SHUTTER POSITION
6 TV CAMERA VIDEO
7 E_Y, E_Z TRACKER SIGNALS TO RECORDER
8 E_Y, E_Z TRACKER SIGNALS TO CCSD GIMBAL DRIVE

9 BEACON PRESENCE SIGNAL
10 BEAM STEERER HOLD SIGNAL
11 SCINTILLATION MONITOR BASEBAND SIGNAL
12 SCINTILLATION MONITOR 10.7 MHz LOG SIGNAL
13 SCINTILLATION MONITOR 10.7 MHz LINEAR SIGNAL
14 LASER POWER MONITOR SIGNAL

COMMAND INPUTS
A DIGITALLY CODED MODULATION
B BEAM DIVERGENCE COMMAND (1–6)
C LASER SHUTTER OPEN/CLOSE
D TV TRACKER FILTER IN/OUT
E RECEIVER ATTENUATION (1–4)
F SCINTILLATION MONITOR APERTURE STOP IN/OUT
G TRACK DEFEAT
H BEAM STEERER ON/OFF
I BORESIGHT ADJUST Σ_Y, Σ_Z

21

Figure 9. AOCP search and track mode illustration.

Referring to the block diagram of Figure 8 and the photograph of Figure 10, the receiver optical path can be traced and the physical components identified. Laser radiation from the ground beacon is collected by the 9.85-cm diameter catadioptric objective and passes through the collimating lens, reflects from the Z-axis beam steerer onto the Y-axis beam steerer and through the dichroic beam combiner. From the beam combiner, the received radiation passes through a bandpass filter centered about 488 nm and is divided into two paths by a neutral beam splitter, providing 80 percent of the energy into the tracking receiver path and 20 percent (less absorption losses) into the scintillation monitor path. Considering the tracking receiver first, the received radiation is reflected from the splitter, passes through the imaging lens and receiver attenuator neutral density (ND) filter, and is folded onto the receiver narrow band optical filter and focused at the image dissector detector photocathode. The path to the scintillation monitor detector is from the splitter through a lens which forms an image of the system entrance pupil through an aperture stop located in the pupil image plane, and folded onto the scintillation monitor photomultiplier detector. A detailed discussion and analysis of the receiver optical system is presented under the optical discussion heading.

The transmitter path can be traced by referring to Figure 11. Beginning with the laser, the 633-nm laser beam is folded twice and directed through the electro-optical modulator and out of the laser compartment through the cover seal window. From the window, the polarization modulated beam is passed through a variable phase retardation plate (Soleil-Babinet compensator), through a polarizer, reflected from a folding mirror, and directed into the lower level. Referring again to Figure 10, the transmitter path enters the lower level and is directed past a cutoff shutter and through the beam divergence control telescope. The transmitted beam emerges from the divergence control telescope and impinges onto a beam sampling splitter, which reflects less than 1 percent of the power in the transmitted beam onto a power and modulation monitor photomultiplier detector. The primary beam passes through the beam sampling splitter and is reflected from a path folding mirror onto the dichroic beam combiner, where the transmitter and receiver optical paths combine. The transmitter and receiver paths are made parallel, i.e., boresighted mechanically at the beam combiner. The transmitted beam then reflects at the beam combiner and exits through the same path followed by the received beam and is offset to avoid the central obscuration of the Cassegrainian telescope.

The AOCP mechanical structure is formed from a hogged-out ribbed aluminum block to maximize strength and alignment stability. All optical elements are mounted directly to the main plate on either the top or bottom levels. The laser compartment was designed so that a 1.01×10^5 - N/m^2 (14.7-psi) pressure loading would not deform the laser/modulator mounting

LASER POWER MONITOR
DETECTOR

FOLDING MIRROR

BEAM SPLITTER,
TRANSMITTER

BEAM
DIVERGENCE
TELESCOPE

SCINTILLATION
MONITOR
DETECTOR

Z-AXIS
BEAM STEERER

DICHROIC
BEAM COMBINER

ENTRANCE PUPIL
IMAGING LENS

AFOCAL
TELESCOPE

NARROW BAND
OPTICAL FILTER

Y-AXIS
BEAM STEERER

RECEIVER
BEAM SPLITTER

TRACKER IMAGING
LENS

IMAGE DISSECTOR

RECEIVER ATTENUATOR

NARROW BAND OPTICAL FILTER

Figure 10. AOCP optical path.

FOLDING MIRROR
MODULATOR, ADJUSTABLE

LASER MODULATOR

GLAN-THOMSON
POLARIZER

SOLEIL-BABINET
COMPENSATOR

FOLDING MIRROR
LASER, ADJUSTABLE

He-Ne LASER

▪▪▪▪▪▪▪▪▪▪▪ TRANSMITTER
OPTICAL PATH

Figure 11.   AOCP transmitter optical path.

plate and cause a boresight error between the transmitter and receiver. Figure 12 shows a view of the AOCP top level with the laser compartment cover removed and indicates the location of the various system components and assemblies. A more detailed description of the mechanical design of the transmitter compartment will be given in a later section of this report. Figure 13 is a view of the underside of the AOCP showing locations of the various components and assemblies.

System Design

Mechanical

The AOCP is subjected to operation in an environment that is hostile to precision electro-optical devices. The altitude, which causes wide pressure variations, temperature variations, and vibration, are the three main enemies of any precision electro-optical device. All three of these factors are present in the AOCP operating environment and have been used to establish the packaging rationale. The two basic assemblies most affected by the operating environment are the laser—modulator package and the basic optical package. The package rationale for each of these will be discussed in turn.

The laser itself is a commercial unit adapted to the AOCP, and as such is not designed to withstand any of the deformations caused by pressure variations. These pressure variations introduce misalignment in the laser itself and severely degrade performance. To eliminate these deformations, an approach was necessary that would maintain a stable environment for the laser.

The approach taken in the laser—modulator package was to have the laser, the laser modulator, and associated optics all mounted on a rigid baseplate. This baseplate has large openings machined through it, and the bottom of the package is closed via a steel diaphragm. The remainder of the package is enclosed in an aluminum container which is ribbed to preserve its structural shape and to insure that the O-ring sealing surfaces are not distorted. In operation, the entire package is constantly pressurized at 1.01×10^5 N/m^2 (1 atm). Any pressure variations are compensated for by the diaphragm. Thus, the volume of the laser—modulator package is constantly changing as a function of external pressure changes, causing the diaphragm to flex. The net result is a constant pressure environment for these critical components. Since temperature variations also cause pressure changes, these temperature-induced pressure variations are also compensated for by the diaphragm technique. This entire package has been tested in a vacuum environment (10^{-5} T), and the soundness of the approach has been demonstrated.

CONNECTOR PLATE

APOLLO
COMMAND
RECEIVER

TEST POINT
BOARDS

REMOTE BORESIGHT
CONTROL
ELECTRONICS

EL ERROR GEN

TARGET PRES GEN
& FOCUS REQ

BEAM STEERER
ON/OFF/AUTO
SWITCH

10.7 MHz AMPL
+ 32 KHz AMPL

AZ ERROR GEN

CLOCK & TRACKER
TIMING

AZ/EL RAMP/STEP
GENERATOR

FOLDING MIRROR,
MODULATOR, ADJ

LASER MODULATOR

FOLDING MIRROR,
LASER, ADJUSTABLE

He Ne LASER

POWER SUPPLY

TV ACQ AID AUTO
IRIS & NB FILTER
ASSEMBLY

PERISCOPE, TV
ACQ AID

GLAN-THOMSON
POLARIZER

SOLEIL - BABINET
COMPENSATOR

MODULATOR
DRIVER

BEAM
DIVERGENCE
POSITION
CONTROL

27

Figure 12.   AOCP flight package top view (cover removed).
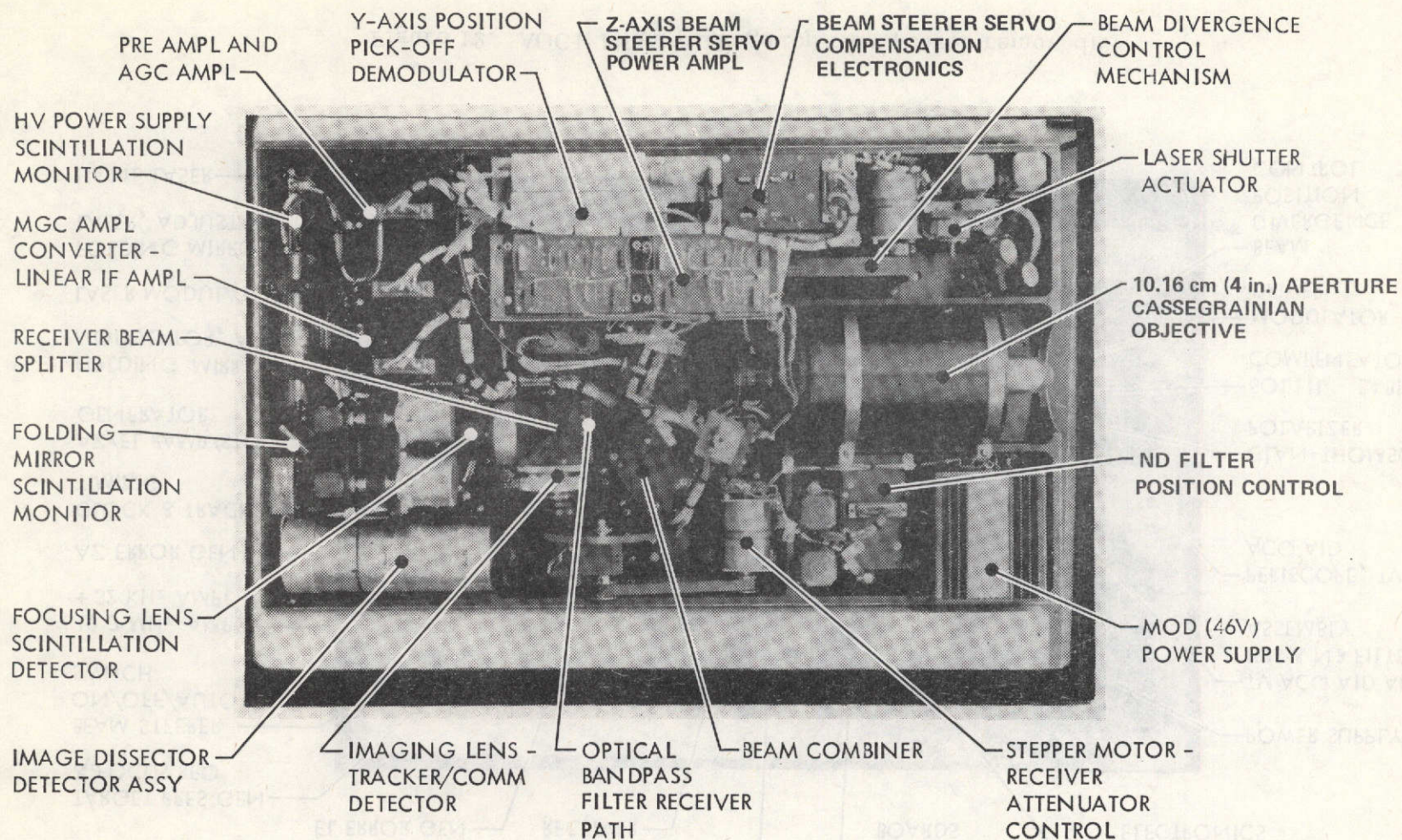
Figure 13. AOCP flight package bottom view (cover removed).

Y-AXIS BEAM STEERER
SERVO POWER
AMPLIFIER

Z-AXIS POSITION
PICK-OFF
DEMODULATOR

Z-AXIS BEAM
STEERER
ASSEMBLY

COLLIMATING
LENS

STEPPER MOTOR
BEAM
DIVERGENCE
CONTROL

CONVERTER AND
DET., AGC
CONTROL,
15.2 MHz OSC

TRANSMIT PATH
FOLDING/
ALIGNMENT
MIRROR

SCINTILLATION
MONITOR
DETECTOR

TV ACQUISITION
AID FOLDING
MIRROR

RECEIVED
APERTURE CONTROL
MECHANISM

PREAMPLIFIER

ELECTRICAL
BORESIGHT
ADJUSTMENT
MECHANISM

Y-AXIS BEAM
STEERER
ASSEMBLY

NARROW BAND
OPTICAL FILTER,
IMAGE DISSECTOR

FOLDING MIRROR,
FIXED, RECEIVER
TRACK/COMM

RECEIVER
ATTENUATOR
FILTER WHEEL

Figure 13. (Concluded).

The optical package itself, to which the laser—modulator package is affixed, is a complex and densely packaged unit. The constraints of the program in terms of time and costs predicated a "building block" approach to the design. Rather than fabricate an intricately machined housing with a multiplicity of integrated optical devices, a baseplate design was utilized which permitted all other devices to be fastened to it as discrete components. This is a very cost-and time-effective method of packaging an engineering type of unit, as it permits concurrent discrete parts fabrication and also lends itself well to the myriad modifications necessary on an engineering unit. It was possible to modify an individual element without completely disassembling the entire unit.

The basic concept required a rigid, reasonably light baseplate or "optical bench," to which all other components were to be attached. A wrought aluminum billet was procured for the baseplate and was extensively machined on both top an bottom. The net result was a light yet rigid baseplate surrounded by high webbed walls around its periphery, and with considerable internal webbing. This yielded a light, rigid structure that was not too difficult to fabricate and yet had the high degree of torsional rigidity so vital in any optical system. The billet was rough machined, stress relieved, and then finish machined. This insured the long-term stability required. The baseplate could have been fabricated out of a weldment or brazement, but the fabrication of the weldment pieces, welding, heat-treating and subsequent finish machining and stress relieving would have constituted a longer fabrication cycle, without producing the dimensional stability inherent in a homogeneous billet. Once the baseplate was fabricated, all of the other elements of the electro-optical train, which had been fabricated concurrently, were then fastened to it as completed subassemblies. These subassemblies mount by precision interface and have sufficient adjustment capability to facilitate accurate system alignment. The entire optical baseplate was then enclosed top and bottom. Mounting ears were provided to interface with the carrying vehicle. These ears provide a three-point suspension in the vehicle.

Figure 14 shows the AOCP mechanical package configuration with the outline dimensions and approximate center-of-gravity location.

Optical

The common optics sybsystem includes the Cassegrainian-catadioptric objective lens, the collimating lens, the beam-steerer mirror, and the dichroic beam combiner. Figure 13 shows the location of these elements in the system.
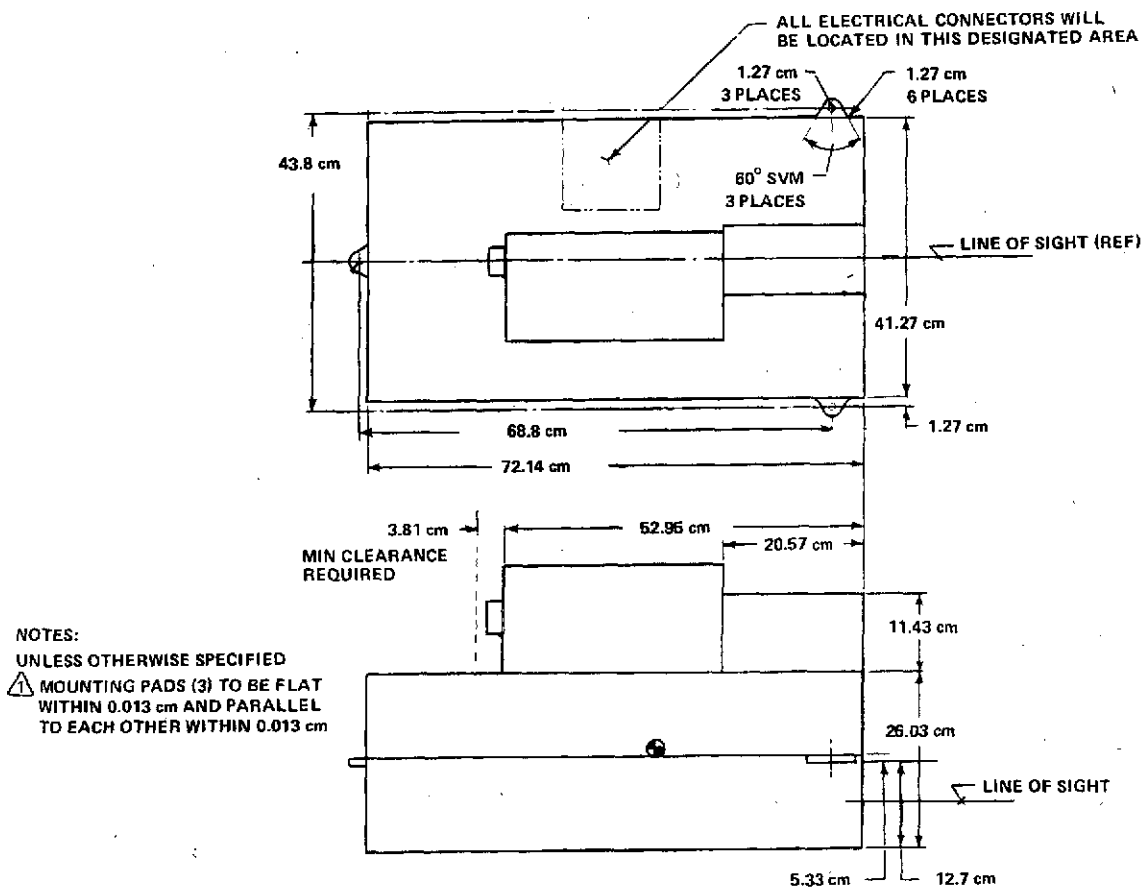
Figure 14. AOCP mechanical outline.

The catadioptric objective lens serves as the system "antenna." This lens system was manufactured by Willey Optical Co. from a design for NASA/GSFC. The initial design specifications were for a compact (short length) 0.035-rad (0.2-deg) field of view with the resolution defined by the Rayleigh criterion of better than 10×10^{-6} rad (2 arc sec). The objective lens focal length is nominally 63.5 cm (25 in.), and the clear aperture is 9.85 cm (3.88 in.), giving a numerical aperture ratio of f/6. The objective lens is a modified Schmidt design shown schematically in Figure 15. The total system length of 15.24 cm (6 in.) resulted in an unusually compact design. The focal length is variable over a considerable range by adjustment of the secondary mirror. Another feature is the prime focus location inside the primary mirror which permits the collimating lens to be mounted directly into the objective housing. This provides a substantial reduction in the size of the AOCP common optics section over an earlier unit designed around a Questar objective.
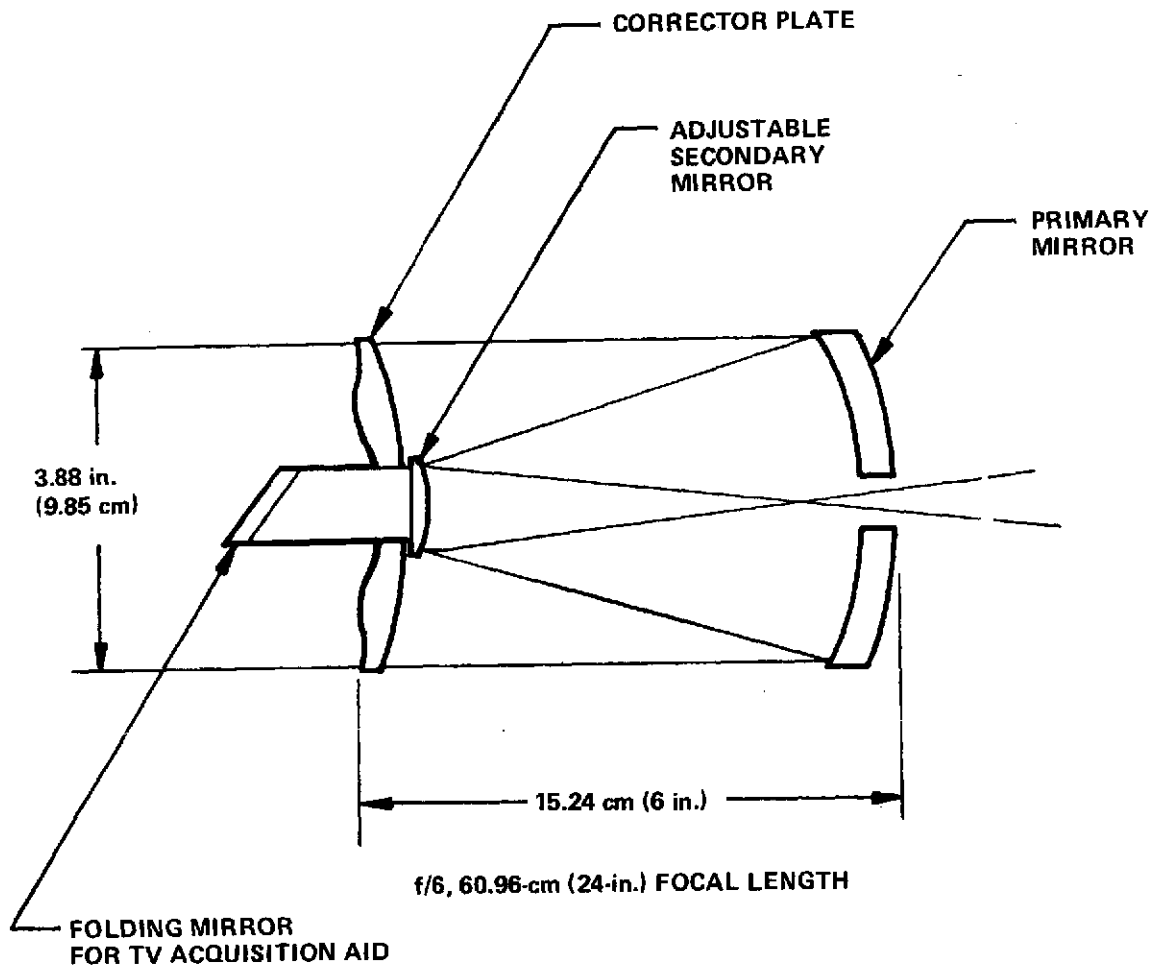
Figure 15. Catadioptric objective lens.

The first lens was manufactured to ITT wavefront deformation tolerances of better than $\lambda/20$ but it was broken in shipment. In the interest of schedules, the lens was replaced by Willey from stock with a rework of the corrector plate. The second unit proved to be unacceptable in a Foucoult test because of a cusp peak in the corrector plate in the center of the entrance pupil annulus. The objective lens was reworked a second time, and the performance was greatly improved. This latter lens system was installed in the field after the system had been delivered to NASA/MSFC.

The collimating lens is a multielement Nikon objective having a focal length of 75 mm. An adapter plate was made to interface the collimating lens to the catadioptric objective and form an afocal telescope as shown schematically in Figure 16. The afocal telescope power was determined by a careful measurement of the system entrance and exit pupils and determined to be 8.398. The exit pupil is located approximately 11.4 cm (4.5 in.) from the vertex of the collimating lens rear element. This permits the pupil to be located between the beam-steerer mirror to minimize vignetting due to mirror motion.

The beam-steerer mirror size is determined by the size of the exit ray bundle and the field of view divergence, as illustrated in Figure 17. The distance of the beam-steerer mirror from the system exit pupil is made as short as possible to reduce the mirror size and improve its dynamic characteristics. The beam-steerer mirror diameter D_M normal to the optical axis is given by

$$D_M \cong D_e + 2X_M \tan \frac{\theta'}{2}$$

where θ is the system field of view $\times$ afocal magnification, X_M is the distance from exit pupil to mirror, and D_e is the diameter of a focal system exit pupil.

For a 10.5-mrad (0.6-deg) field of view, a magnification of 8.4, an exit pupil diameter of 1.17 cm (0.462 in.) and a mirror separation of 3.81 cm (1.5 in.) from the pupil, the mirror diameter projected onto the normal to the optical axis is 1.42 cm (0.56 in.). To allow for a 45-deg mirror tilt and a ±2-deg mirror rotation, the mirror size was set at 2.54 cm (1 in.).

The last element in the common optics train is the dichroic beam combiner, which was designed for a nominal 40-deg incidence angle. The 633-nm reflectance is 0.8 or greater, and the 488-nm transmission is 0.95 or greater. The beam combiner is gimbal mounted with spring-loaded retention to permit coarse mechanical boresighting of the transmitted and received paths. The precision boresight is achieved electronically by offset tracking bias. The location of the common optical system elements is shown in Figure 13.

Receiver Subsystem

The AOCP receiver section comprises the receiver optics, tracking/communications sensor, tracking electronics, communications electronics, scintillation monitor, and the beam steering subsystem. Although beam steering is a common element with the transmitter, it is controlled by the receiver

tracker and will be described as a receiver subsystem. The location of the various receiver elements to be discussed in this section can be determined by referring to Figures 12 and 13.

COLLIMATING LENS

ENTRANCE
PUPIL

9.85 cm

(3.88 in.)

OBJECTIVE LENS

EXIT PUPIL

1.17 cm
(0.462 in.)

$$M = \text{POWER OF TELESCOPE} = \frac{3.88}{0.462} = 8.398$$
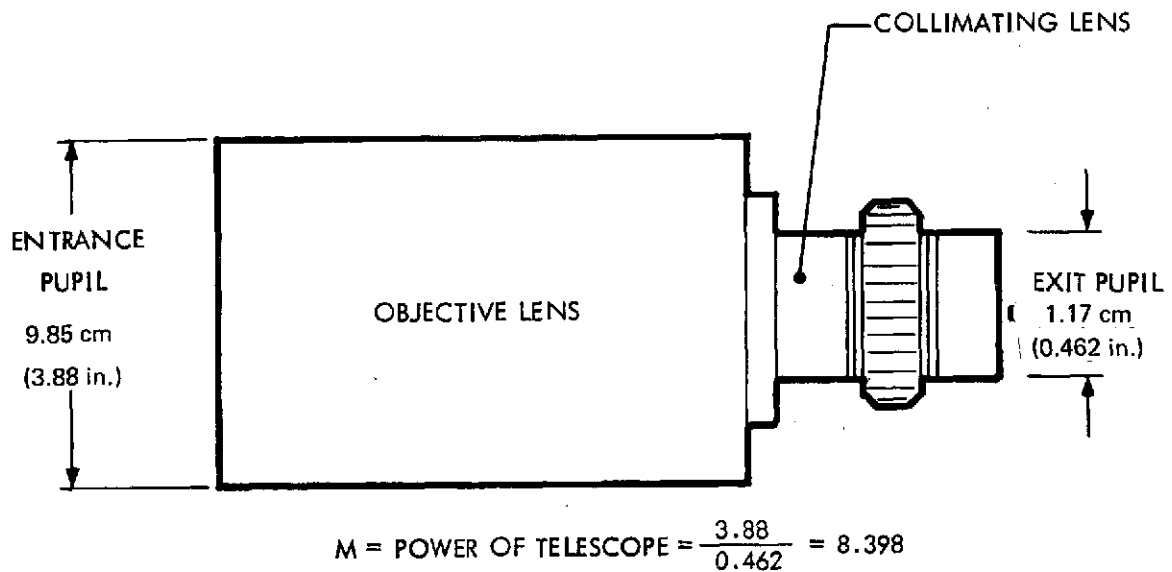
Figure 16. Afocal telescope system.

BEAM STEERER
MIRROR LOCATION

D_M MIRROR DIAMETER PROJECTED NORMAL TO
THE OPTICAL AXIS

θ'

OPTICAL AXIS

$\theta' = MX$ FIELD OF VIEW OF TELESCOPE

EXIT PUPIL

X_{M_2} X_{M_1}
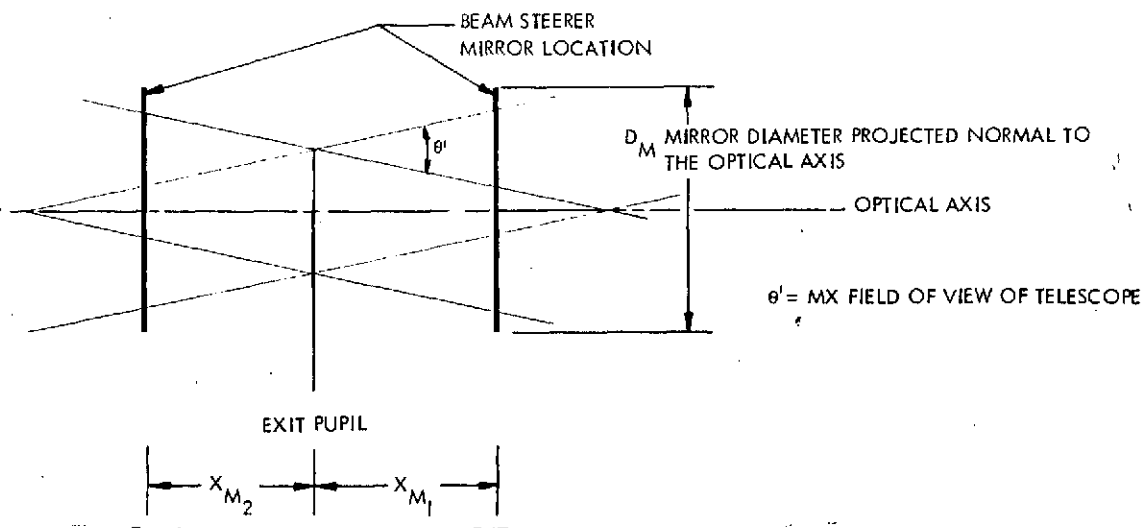
Figure 17. Beam-steerer size determination.

The primary functions of the AOCP receiver subsystem are

1. Search, identification, and acquisition of a 488-nm laser beacon within an 8.7- by 8.7-mrad (0.5- by 0.5-deg) field of view.

2. Lockon and auto track of the laser beacon with the precision of a few microradians with a 1-kHz tracking bandwidth, providing two-axis output signals proportional to the position of the beacon relative to the sensor electrical null position.

3. Closed-loop pointing of the transmitter laser beam through the beam steering elements to a precision of a few microradians rms in a 200-Hz bandwidth.

4. Monitoring atmospherically induced signal fading over a wide dynamic range, both at baseband and at a 10.7-MHz subcarrier frequency with a bandwidth of 5 kHz.

5. Detecting modulation on the uplink laser beam for command of the AOCP status.

6. Providing electronic boresight correction between the transmitter and receiver subsystems.

Acquisition and Tracking

The key element of the acquisition and tracking receiver is the ID detector. This device has the capability of effectively scanning a large search field of view with a smaller instantaneous field of view (IFOV), thereby providing a large measure of spatial filtering of the background scene. The ID detector construction is shown in Figure 18. An optical scene imaged on the photocathode produces an equivalent photoelectron image that is relayed onto the aperture plate by electromagnetic focus coils surrounding the electron drift tube section. When a deflection field is applied through a second set of coils, the electron image corresponding to the optical scene can be swept about the small aperture. Only the photoelectrons passing through the sampling aperture enter the multiplier section of the detector and produce an output. Consequently, the ID detector effectively scans a large scene with a small sensing element, all electronically.

For acquisition, the AOCP ID detector searches a square field in a TV raster-type scan, "looking" for the position of the laser beacon. The linear two-dimensional scan in the image plane photocathode becomes a solid angle in the space when viewed through the receiver imaging optical system.
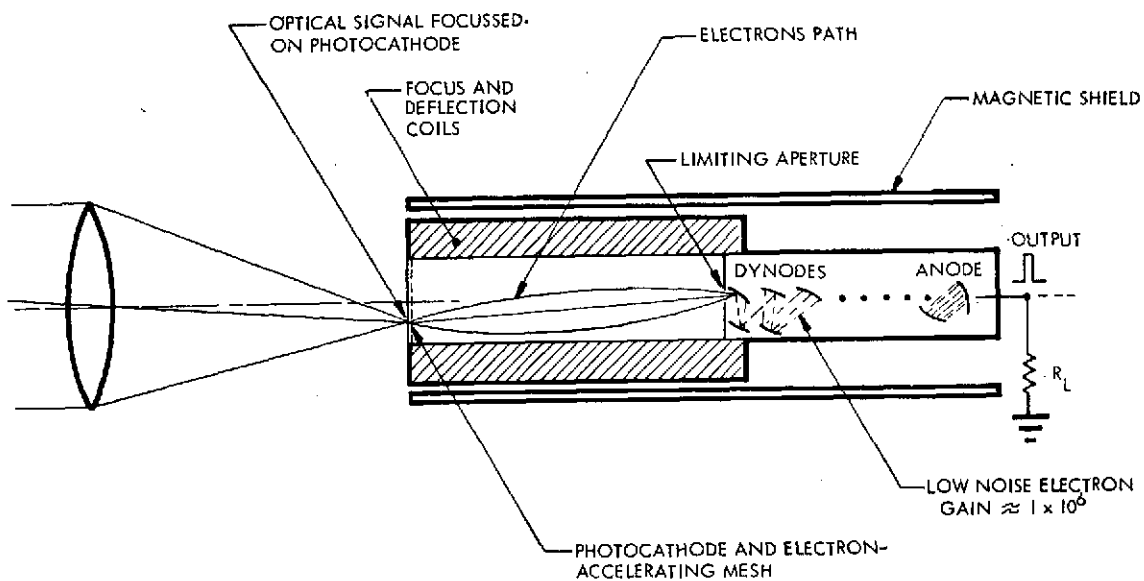
Figure 18. Image dissector assembly.

Figure 19 defines the effective focal length of the AOCP receiver imaging system. The optical system comprises the 8.398-power afocal telescope and a 135-mm focal length Schneider lens, resulting in an effective total system focal length of 1133.73 mm. Figure 20 illustrates the total search field of view obtained by the 12.7-mm square search area on the ID photocathode. Similarly, Figure 21 defines the angular size of the scan aperture corresponding to the 0.1-mm square ID aperture.
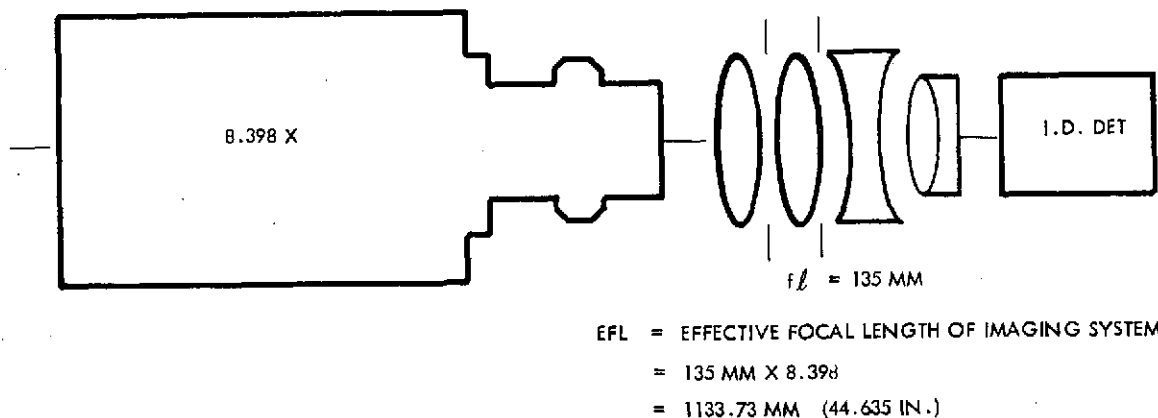
Figure 19. Imaging system.
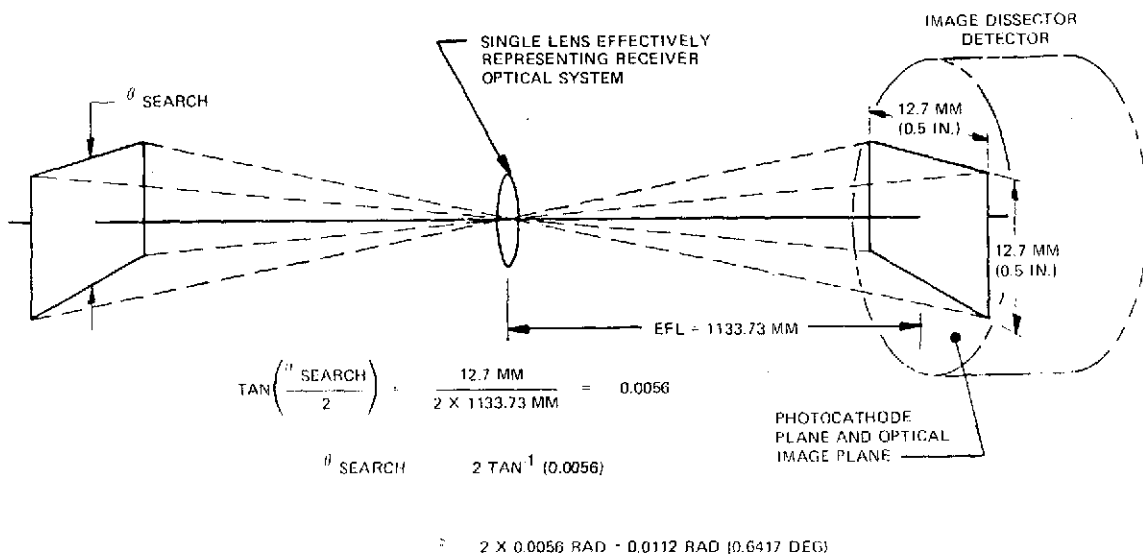
Figure 20. Fine track search field of view.
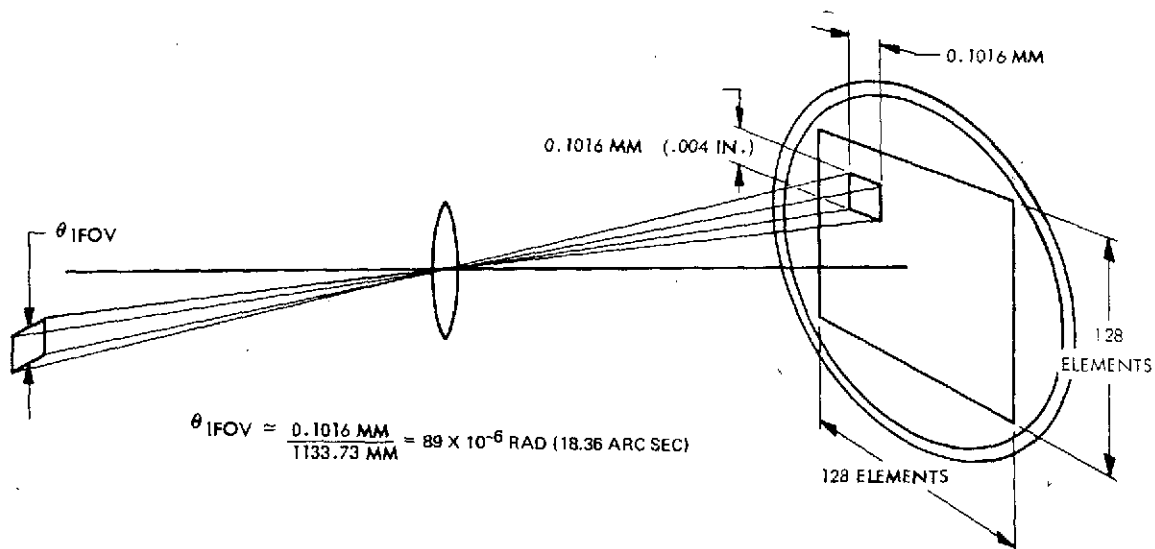
Figure 21. Fine track instantaneous field of view.

Tracker Operation

In the initiate mode, the ID tracker is made to scan the search field of view in a sequentially stepped raster format covering 128 by 128 elements with a 24-percent area overlap to insure complete field coverage. This mode provides considerable spatial filtering of the uniform background level. Additional background suppression is obtained by narrow-band optical filtering centered around the 488-nm beacon wavelength.

Figure 22 illustrates the narrow-band optical filter characteristics. Further background suppression is achieved by looking for the beacon modulation or signals exceeding the detection threshold. If a signal should exceed the detection threshold, the tracker would pause for a time at that element and determine whether it was due to the beacon by sensing the 10.7-MHz subcarrier modulation presence. If the modulation was not present, the acquisition search would continue. It should be noted here that the switching between Search and Track modes is completely automatic. Whenever track lockon is lost, the system automatically reverts to a Search mode.
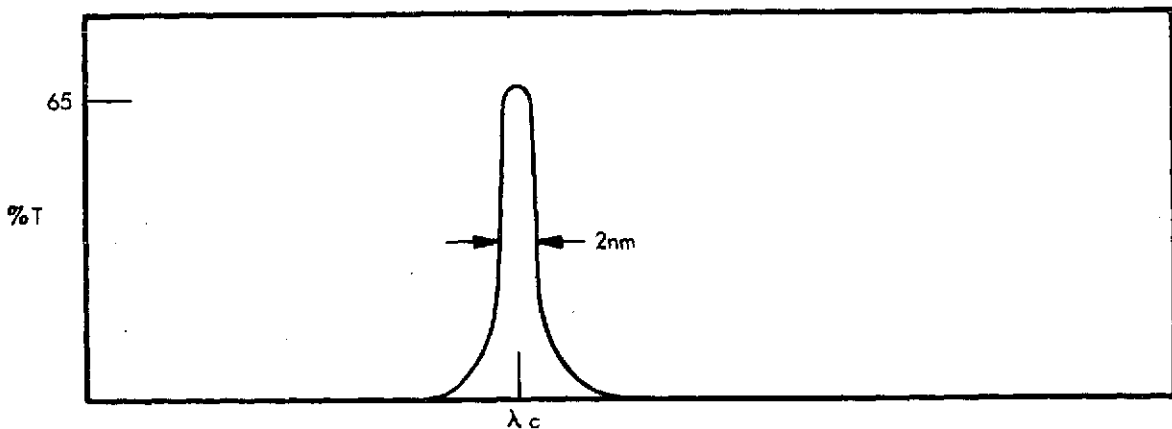
Figure 22. Transmission profile.

Figure 23 is a functional block diagram of the AOCP optical tracker. When a beacon image has been acquired and identified by the Search mode, the circuitry automatically switches to the Track scan mode. Sweep waveforms are

generated by converting the outputs of a 14-stage synchronous counter to analog current. The first seven bits (highest frequency) are converted to generate the Y-axis staircase sweep, and the last seven bits are converted to generate the Z-axis staircase sweep. The waveforms are shown in Figure 24.

The step rate is 16 kHz, giving a dwell time of 62.5 μsec per element and a frame time of 1 sec.

A step size of 68 μrad (14.1 arc sec) covers the 87-mrad (0.5-deg) dimension in 128 steps. With an IFOV of 89 μrad (18.5 arc sec), a 24 percent overlap of elemental areas results throughout the scan.

In the Acquisition mode, the ID tracker is essentially in an open-loop configuration, as compared with the Track mode in which the video information is processed for position. Offsets and/or drifts that might affect the acquisition sweep are prevented by use of solid-state switches on the track loop and track sweep circuits.

Video from targets will be pulses of 62.5-msec duration, with amplitude dependent upon source brightness. Selection of the uplink beam target is accomplished by detection of the 10.7-MHz modulation on the beam. As shown in the block diagram of Figure 23, the image dissector output is amplified in an amplifier tuned to 10.7 MHz, rectified, and level detected. Within one step time, a digital level hereafter referred to as video presence (VID PRES) is generated, indicating that acquisition of the uplink beam has been completed and fine tracking can be commenced.

In this Track mode, a modulation is placed on the optical signal (henceforth called the video) by partially deflecting a photoelectron image out of the detection aperture in two axes. A partial deflection scan implies that the photoelectron image is not completely swept out of the aperture. The partial scan is employed to insure that some photoelectrons from the beacon image always enter the detector so that continuous communication is maintained. The amplitude modulation thus produced is demodulated synchronously with the deflection sweeps to determine the precise location of the photoelectron image centroid. A bias current is supplied to the deflection coils to exactly center the deflection sweep about the photoelectron image centroid. The bias current supplied to the deflection coils to effect the aperture scan centering is a measure of the beacon image position relative to the sensors null axis, i.e., zero bias position.

Figure 23. AOCP image dissector tracker.

Figure 24. Search scan waveforms.

40

The VID PRES logic level controls the Acquisition/Track mode status. When VID PRES is in a "1" state:

1.   The clock input is removed from the acquisition sweep counter, stopping the Search scan.

2.   The track sweep switches are enabled, thereby commencing a cruciform scan at the immediate dc position.

3.   The demodulator steering gates are enabled, thereby providing for closed-loop tracking of the target image.

The track sweep is an analog cruciform of 8 kHz with individual Y- and Z-axis waveforms as shown in Figure 25. The scan amplitude is set so that the target electron is never completely deflected off the aperture. Although the sweep amplitude depends on the optical image size, it is nominally less than ±1 IFOV for the AOCP ID tracker. The scan causes a pulse duration modulation of the video signal

The track video signal shown typically in Figure 25 has a frequency of 32 kHz (four times the track scan frequency). The video signal is amplified and limited, thereby providing a position and duration pulse train to the demodulator. A three-stage AGC is employed by the stages preceding limiting to minimize delays (phase shift) which result in an unstable track lock caused by cross talk at the demodulator output. The AGC accommodates a 70-dB input dynamic range in a 120-Hz bandwidth, which is typical of signal characteristics caused by scintillation.

The video pulse train is synchronously demodulated with the output being an analog error signal proportional to the distance (the angle) between the center of the cross scan and the center of the target. It is noted that the transition from acquisition to track takes place when a target presence (TAR PRES) is generated. The target image can be anywhere within the square 89-μrad (18.5-arc sec) IFOV; however, it probably will not be at the center.

The demodulator error signals are summed with the initial cross scan position to move the cross scan so that it becomes contered on the target image, and the demodulator error voltage approaches zero. The centered video waveform is shown in Figure 25. The Track mode is characterized by a type-O control loop, where any movement within the acquisition field of view results in an automatic correction to the deflection coil current so that the cruciform remains centered on the target image. The track loop bandwidth is nominally 1 kHz.
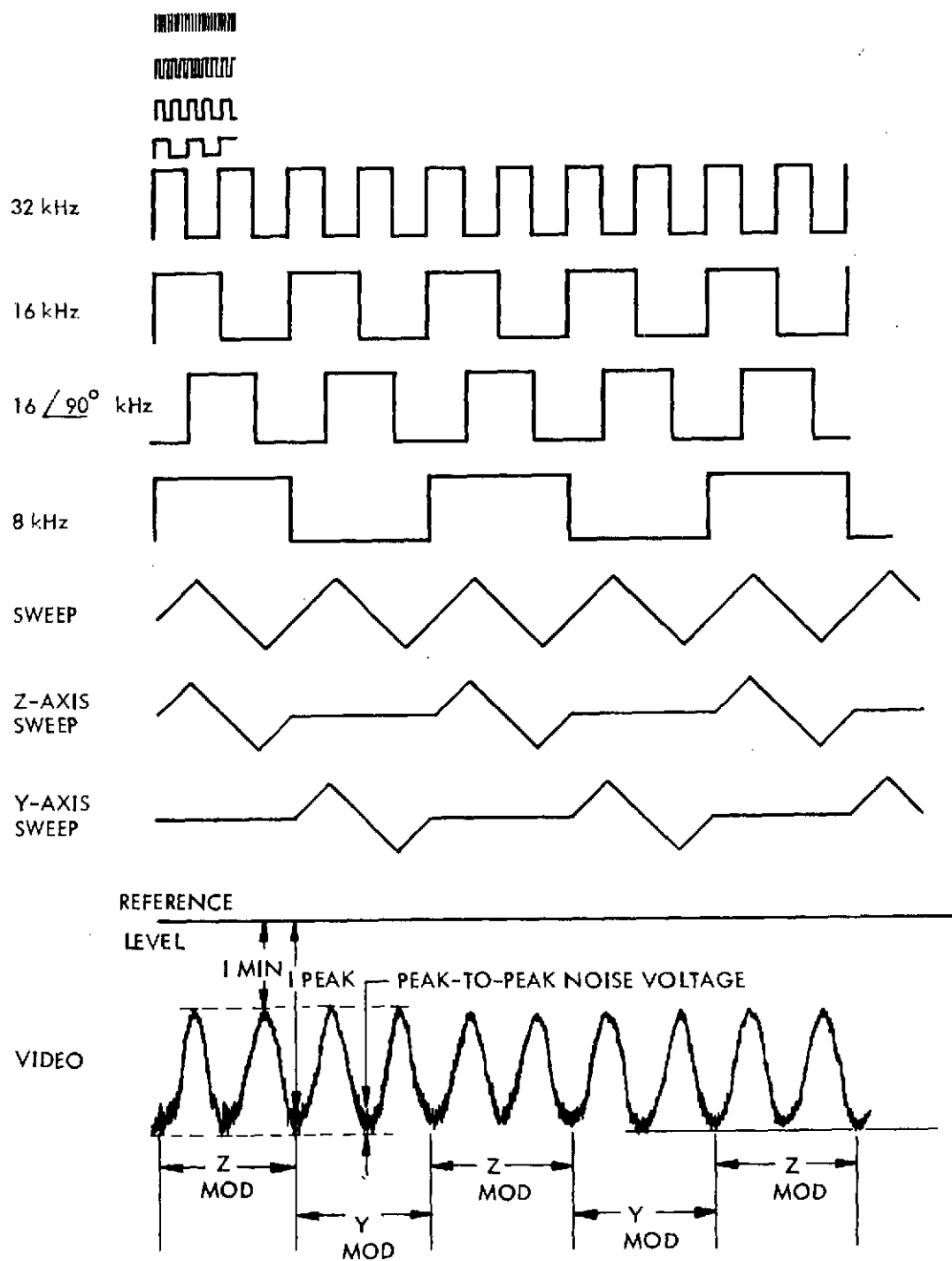
Figure 25.   Track mode timing diagram.

While tracking, valid target position signals are generated by sampling the deflection coil currents. The target position signals, having a transfer function of 1.13 V/mrad (0.33 V/arc min), are applied to the beam steerers. The beam steerers position the uplink target image to a reference position and fine point the downlink beam based on this reference.

Tracking is maintained as long as VID PRES is "1." The VID PRES status is relatively high bandwidth in that the status change occurs within tens of microseconds of applying or removing a 10.7-MHz signal at the preamp. Because of scintillation, signal fades of 100-msec duration are common. Therefore, the VID PRES changes states during these fades. Even with intervals of no signal, the Track scan position is maintained within an IFOV. To prevent breaking lock during fades, the VID PRES loss is delayed approximately 180 msec. The resultant digital level is referred to as TAR PRES and is the digital level used by the ID tracker to sequence between acquisition and track. The return to acquisition occurs, therefore, only if the 10.7-MHz signal is lost for greater than 180 msec.

Loss of TAR PRES returns the ID tracker to the Acquisition mode. The transition is also used to place a 50-msec short on the tracking loop error demodulators. As noted previously, the tracking functions are disabled during acquisition. However, the error demodulator outputs which have a 2-sec time constant can become high during tracking, since they effect the closed-loop operation. The outputs are shorted momentarily upon return to acquisition to prevent offset and drift of the acquisition scan.

It is evident from Figure 23 that the VID PRES signal is the primary AOCP mode control. A timing diagram of the various control signals derived from the VID PRES signal is shown in Figure 26. Two of the control levels, TAR PRES and DEMOD SHORT, are used internal to the ID tracker and were discussed in the previous section. The BEAM STEERER RELAY level is delayed 120 msec from the VID PRES signal. The BEAM STEERER RELAY "1" level represents the time during which the pointing is under control of the ID Tracker. The SPEED LIMITED level is derived from the TAR PRES signal and provides a 600-msec delay during which the beam-steerer drive voltage is limited.

Beam Steerers

Operational Description. One loop (or channel) of the beam-steerer subsystem is shown in Figure 27, which describes the basic elements from a functional viewpoint. The incoming laser beam is collected by a 10.16-cm (4-in.) aperture afocal telescope. The beam emerging from the telescope is routed to beam-steering mirrors, one for each channel (Y and Z), then to another set of optics, the function of which is to focus the beam on the face of the ID tracker.
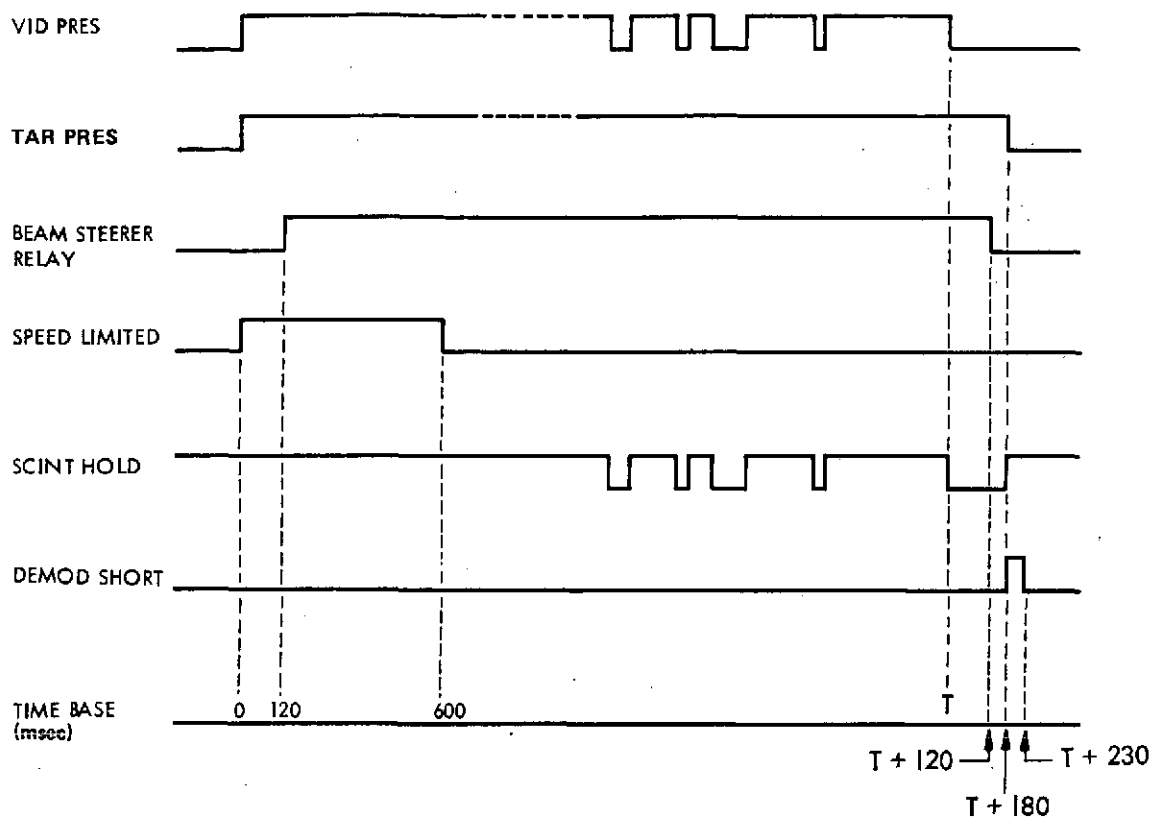
Figure 26. Control signal timing.
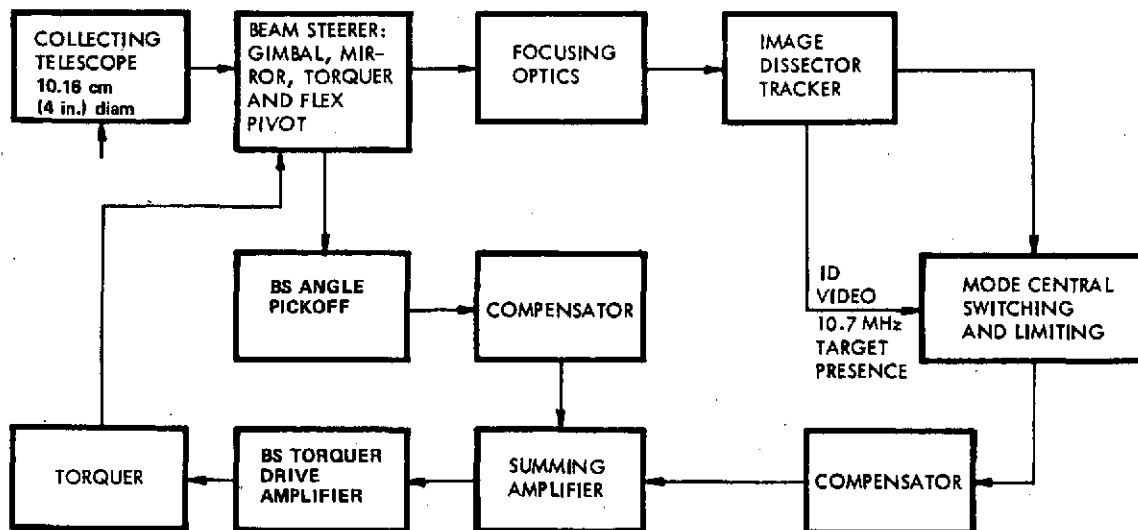
Figure 27. Function configuration of the beam-steering subsystem.

44

The tracker develops three sets of outputs that are of further use to the beam-steerer subsystem:

1. Y and Z error signals

2. Video from the image dissector

3. 10.7-MHz target present signal

Image dissector video output and the 10.7-MHz target present signal control the mode of the beam-steerer subsystem. The error signals are appropriately routed to the remainder of the subsystem as called for in each mode.

Beam—Steering Gimbal, Mirror, Torquer, and Flex Pivot. A summary of the characteristics of these devices and associated equipment follows:

1. Mirror

    a. Flatness — $\lambda/20$

    b. Size — 25-mm diameter

    c. Angular gain — 2 rad/rad

2. Kaman Science Corp. Pickoff

    a. Gain 24.8 V/cm (63 V/in.), (calibration curves on file)

    b. Moment arm [effective 1.65 cm (0.65 in.)]

3. Bendix Flex Pivot

    a. 0.63-cm (1/4-in.) pivot 5008-600

    b. 9.25×10^{-2} N m/rad (13.1 oz in./rad) torque gradient

4. Aeroflex Torquer TQ-10Y-35P

    a. Torque gradient — 6.25×10^{-3} N m/a (0.885 oz in./A)

    b. Resistance — $4.35 \ \Omega$

    c. Inductance — 0.966×10^{-3} H

    d. Back emf — 5.53×10^{-3} V/rad/sec

5. Rotating Assembly

    a. Components

        (1) Mirror

        (2) Gimbal cell

        (3) Rotor of torquer

        (4) Outer shell of flex pivot

    b. Total Polar Moment of Inertia

        (1) Y loop: 1.34×10^{-6} N-m sec^2 (19×10^{-5} oz in. sec^2)

        (2) Z loop: 1.34×10^{-6} N-m sec^2 (19×10^{-5} oz in. sec^2)

A photograph of the fine beam-steering assembly is shown in Figure 28.

Image Dissector Tracker. The ID tracker was designed and fabricated by ITT-Gilfillan and is described in detail elsewhere in this report. For the purposes of this discussion, its principal functional characteristics are sufficient. The output of the tracker is expressed as volts per centimeter of displacement of the focused image from the electrical center of the tracker at the photocathode. In addition, the tracker has a nominal 1-kHz bandwidth. Summarizing the characteristics of the ID tracker, the tracker output gradient is 10 V/cm (25.6 V/in.), and the tracker bandwidth is 1000 Hz.

FLEX PIVOT

MIRROR

POSITION PICK-OFF

TORQUER
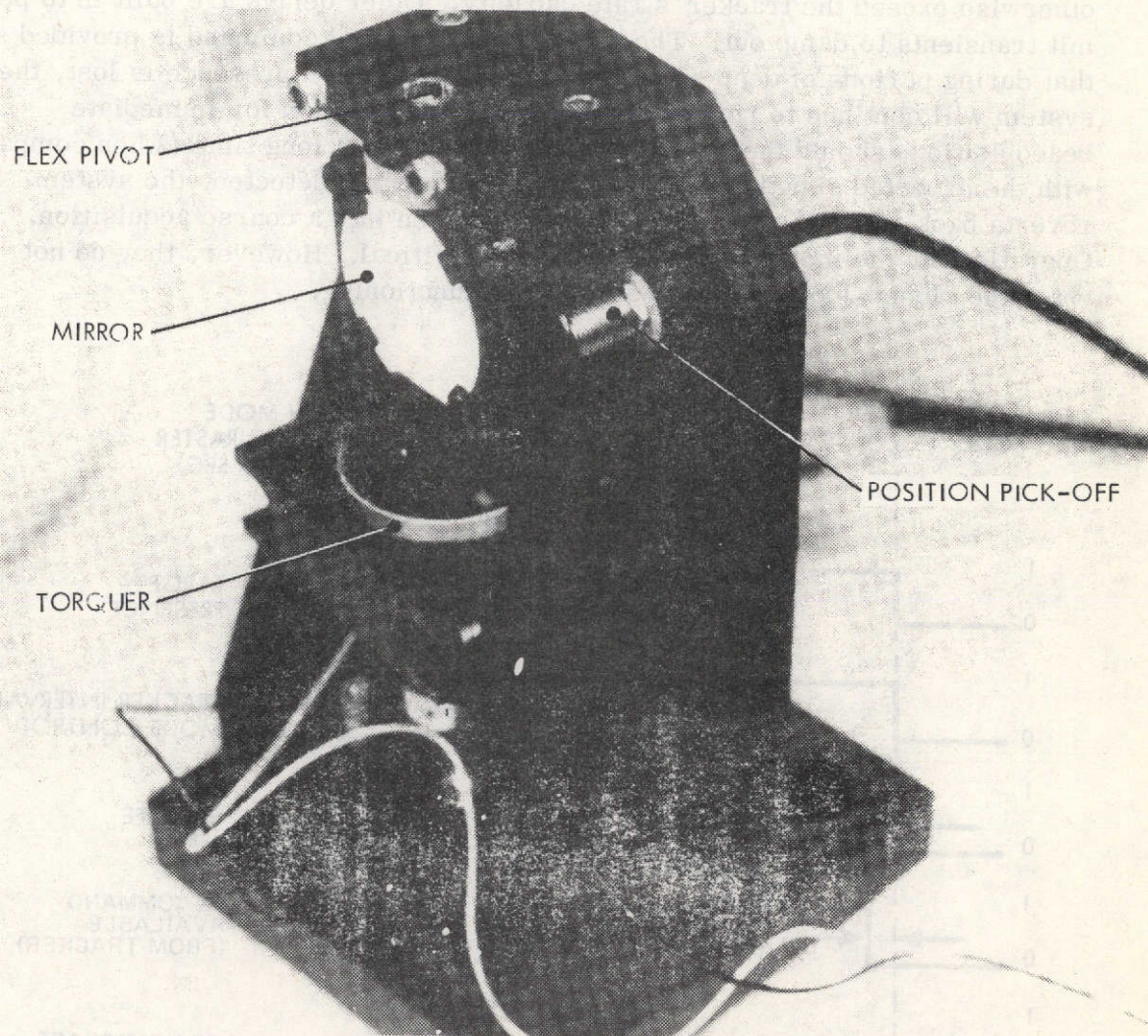
Figure 28. Beam-steerer assembly.

Mode Control. The operating mode control is an important part of the acquisition process if operation in a signal fade environment is required. The function of the mode control subsystem is to provide switching signals to select the appropriate sensor controlling the system operation. For example, the mode control logic determines when the system should be in coarse or fine track, search or track, pointing system angular rate limit, pointing angle hold, or fine track search raster reset. Figure 29 indicates the logic level condition for the control of the various modes indicated and the time associated with the delay intervals. The rate limit, for instance, limits the velocity of the optical image at the ID detector. This is necessary because acquisition near the edge of the field of view would cause the tracker to apply immediately a large rate command

to zero the image position to the beam-steerer subsystem. Such a rate would otherwise exceed the tracker's rate capacity. Other delays are built in to permit transients to damp out. The beam-steerer's hold command is provided so that during periods of deep signal fades when the beacon presence is lost, the system will continue to remember the last target position for immediate reacquisition, should the signal reappear. If, after a long time (when compared with the expected signal fade period) the signal is not detected, the system reverts back to a fine acquisition search and then into a coarse acquisition. Operationally the mode control aspects are ciritical. However, they do not enter the closed-loop dynamics of ordinary functioning.
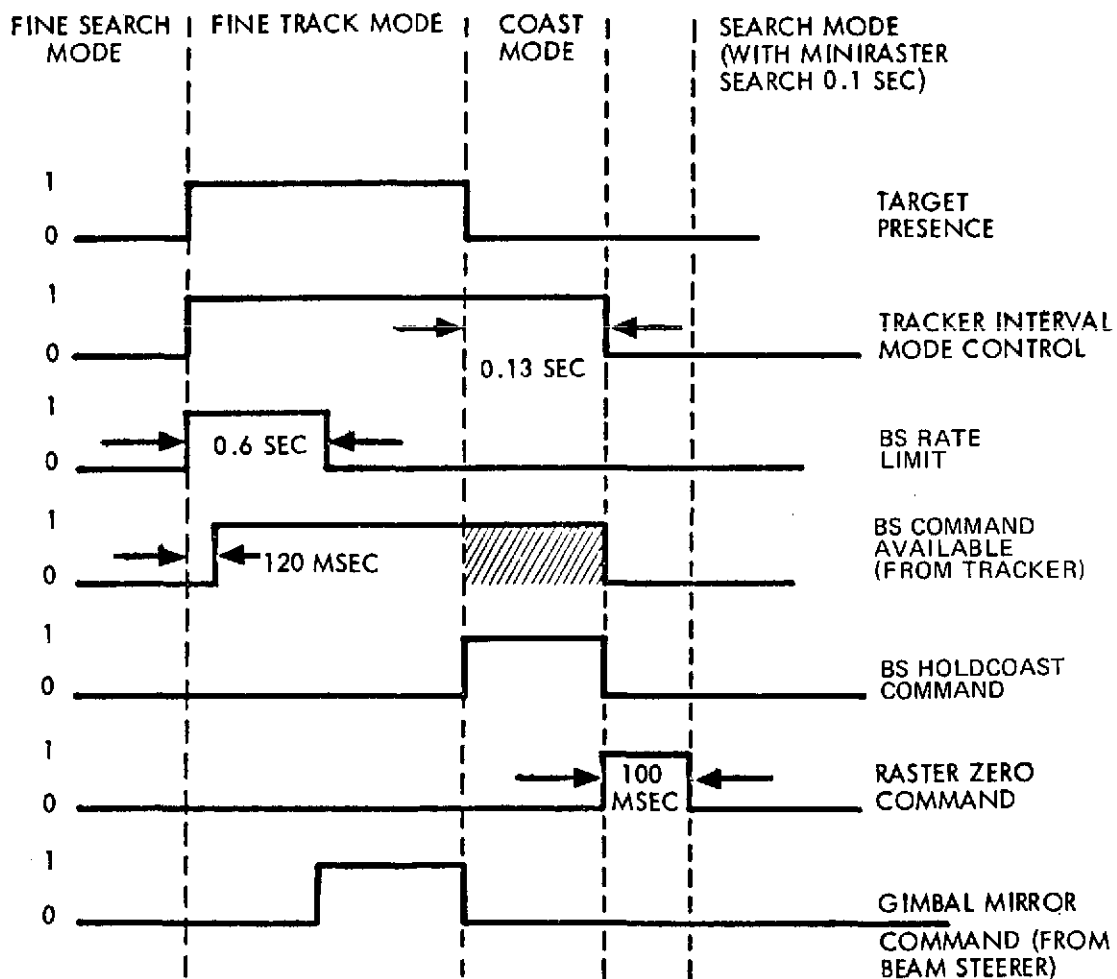
Figure 29. Mode control logic.

Forward Path Compensation. Figure 30 is the appropriate timing diagram for the modes. Thes various modes of operation are necessary to allow the

48

COIL CURRENT

NO COIL CURRENT } RELAYS 1, 2, 3, 5-1

VIDEO | NO VIDEO

TARGET PRESENCE | ACT MODE

BS FOLLOW TRACKER | BS TO ZERO | RELAY 1

SPEED | NO SPEED LIMITING | RELAY 2
LIMITED | | RELAY 3

NORMAL

NORMAL | RELAY 5-1

0 120   600   0 120
                         180
                         0 50

TIME-msec

BS Y-Z CONTROL

RELAY 1

O RELAY 3

RELAY 2

Figure 30. Mode timing diagram.

49

subsystem to handle transient conditions associated with target lockon and loss and deep fades of the incoming laser signal.

When the beam-steerer subsystem is operating in its tracking mode, the tracker error signal is supplied to the forward loop compensation circuits. The output on this circuit is summed with the compensated output of the beam-steerer mirror angle pickoff properly phased for negative feedback. The resultant signal is utilized to drive the torquer which acts on the gimbal, mirror, and flex pivot.

Scintillation Monitor

The scintillation monitor subsystem was added to the receiver later in the program as a result of a principal investigator meeting held at NASA/MSFC. The purpose of the scintillation monitor is to measure atmospherically induced intensity fades in the received signal. A functional block diagram of the scintillation monitor is given in Figure 31.
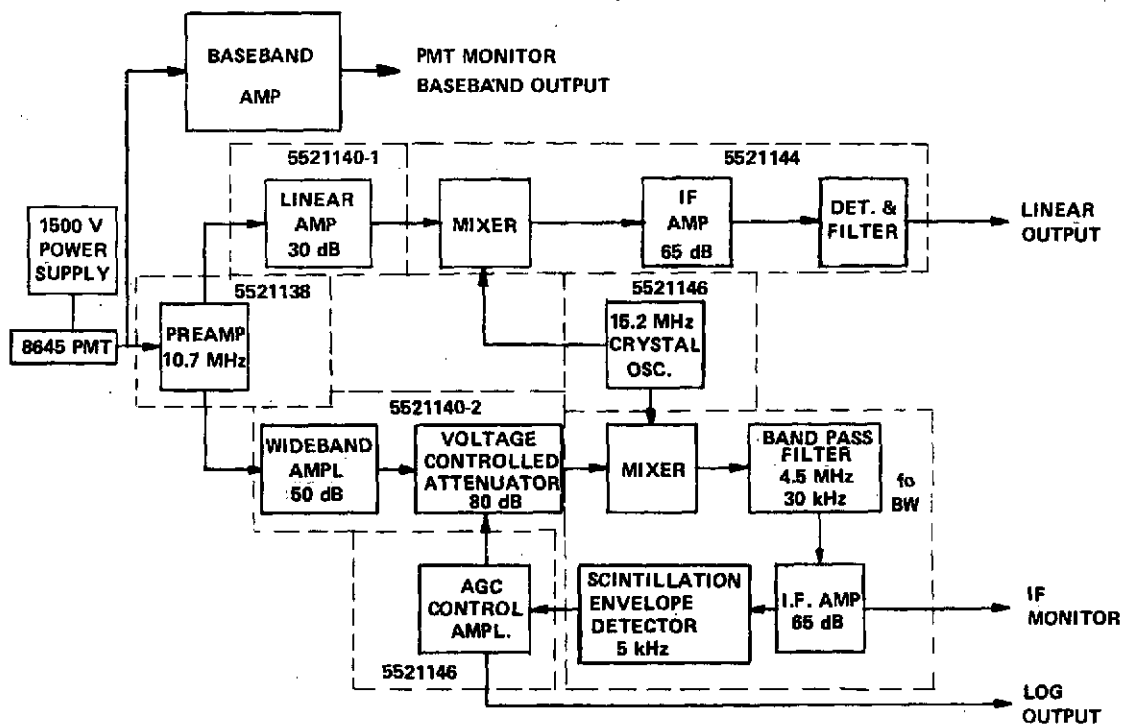
Figure 31. Scintillation monitor functional block diagram.

The scintillation monitor is located in the AOCP receiver section and receives energy split from the tracking and communications channel by the beam splitter shown in Figure 10. The lens that follows the beam splitter images the entrance pupil of the AOCP afocal telescope onto an aperture stop and also serves as a field lens to converge the received radiation onto the scintillation monitor photomultiplier detector. The field of view of the scintillation monitor detector is approximately 10.4 mrad (0.6 deg) in diameter, which assures that there is no vignetting edge modulation induced by the beam-steerer pointing noise.

The radiation detected by the scintillation monitor photomultiplier is modulated by a 10.7-MHz subcarrier, which is amplitude modulated by variations in atmospheric transmission of the uplink path. The output of the photomultiplier passes through a matching network (bandpass filter) to a 10.7-MHz AGC controlled amplifier. The amplifier output is rectified, filtered to 10 MHz, and used as the AGC control for the amplifier. A dc control voltage varying from +0.5 to +4.5 V supplies 80 dB of control range to the amplifier. The circuit sensitivity is therefore 10 dB/0.5 V linear in dB/V throughout the range. Since the AGC control loop bandwidth is 10 kHz, the AGC voltage is a direct logarithmic indication of the uplink optical scintillation.

A linear amplifier coupled out of the matching network also operates in the 10.7-MHz range. A manual gain control allows selection of a portion of the log amplifier range and will be especially useful for selecting high level signals that are compressed in the logarithmic output. A detector, filter, and amplifier after the linear amplifier permit utilization of the maximum dynamic range for a 10-kHz scintillation monitor bandwidth.

A third output is derived directly from the photomultiplier detector and is linear with received optical power over a baseboard range (dc coupled) to 5 kHz.

Three calibratable signal outputs are provided in the scintillation monitor as follows:

1. A signal linearly proportional to the total power incident on the detector at a baseboard range of 0 to 5 kHz

2. A signal linearly proportional to the fluctuations in power of the 10.7-MHz subcarrier modulated onto the ground station beacon

3. A signal proportional to the log of the power in the 10.7-MHz subcarrier on the received beam

Transmitter Subsystem

The transmitter subsystem consists of the helium-neon laser, optical modulator, modulator driver, optical compensator and polarizer, beam divergence control telescope, and laser power monitor.

The laser, modulator, and modulator driver are housed in a hermetically sealed compartment under 1.01×10^{-5} N/m^2 (1 atm) of dry nitrogen. The construction of the laser compartment is illustrated in Figure 32. The laser, folding mirrors, and optical modulator are mounted on a 1.27-cm (0.5-in.) thick aluminum plate hermetically sealed to the AOCP main frame. This mounting plate is pressure released to avoid flexing in reduced pressure environments. The compartment pressure seal is formed by a thin steel plate recessed into the AOCP main frame, with hermetic feedthroughs for electrical power and modulator driver signals.
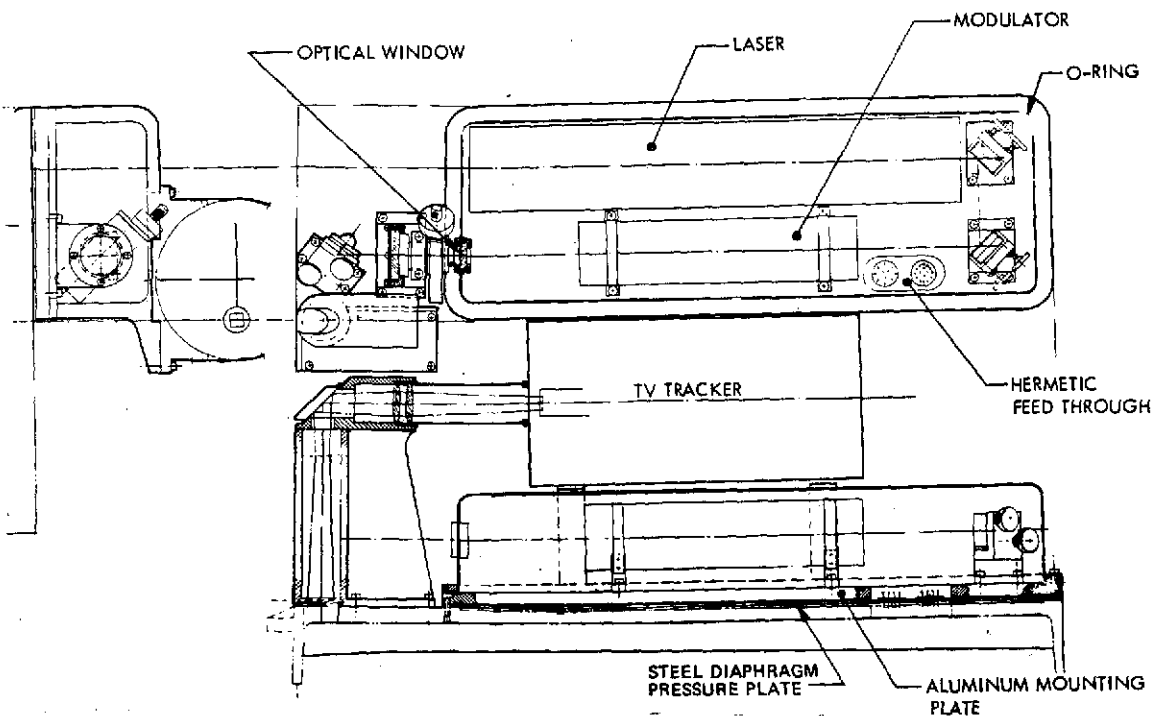
Figure 32. Laser transmitter optical layout.

Laser

The source of optical radiation is a Spectra-Physics Model 120 continuous wave (CW) helium-neon laser, operating in a single mode (TEM_{00}) at a 633-nm wavelength with an output power of approximately 5 mW. The laser beam is directed through the optical modulator by finely adjustable folding mirrors, providing both lateral and angular positioning of the beam in the modulator aperture.

It has been necessary to replace the laser plasma tube several times during the course of the system operation because of difficulty in startup. At least one flight was made during which the laser failed to start. The specific problem identified with this characteristic was low voltage from the 110-V power system on the aircraft.

Modulator

The electro-optical modulator consists of four 90-percent deuterated KD*P crystals having the dimensions of 3.5 by 3.5 by 50.8 mm, producing a polarization modulation over an approximately 100-MHz electrical bandwidth. The modulator package is illustrated in Figure 33. The modulation system in includes a Soleil-Babinet compensator which converts the polarization modulated light into the on—off amplitude-modulated format.
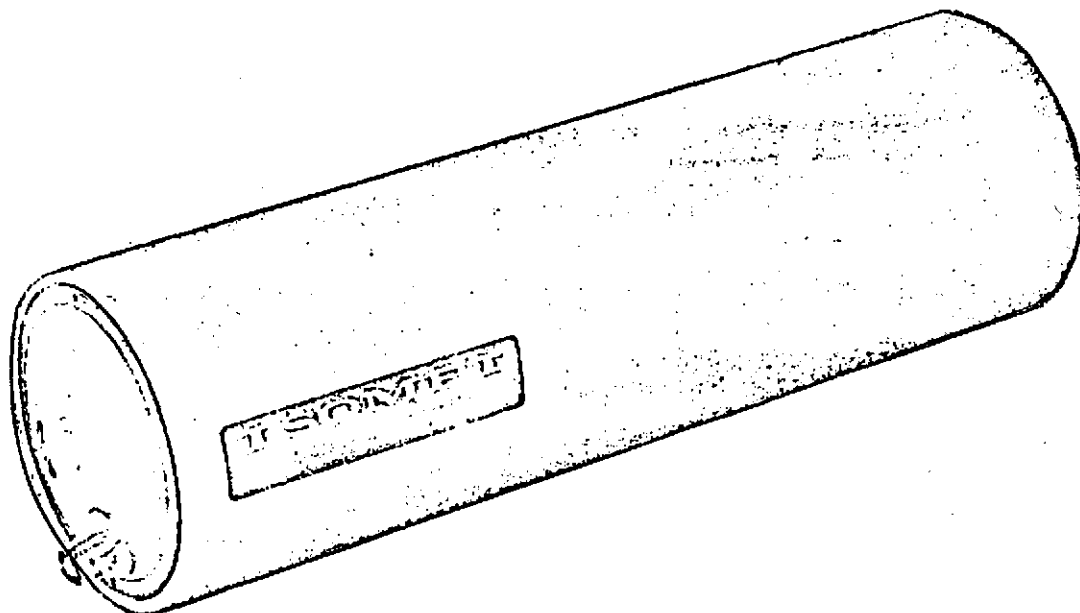
Figure 33. Optical modulator.

Modulator Driver

The modulator driver interfaces the analog/digital (A/D) converter with the optical modulator. The driver accepts a nominal 0-and 1-V digital signal from a 75-Ω source and provides a 0-and 50-V output at the necessary impedance match to drive the optical modulator. The driver employs an all solid-state design and consists of three pulse amplifiers, two emitter followers, and a modified push-pull output stage.

Information Coding. The video A/D converter uses a form of the delta modulation process which transmits, one bit at a time, the changes in the video analog signal. The changes in the analog input signal are determined by comparing the input level with the level of a previously sampled portion of the input by means of a digital feedback loop. The difference between the levels of the reconstructed analog and the input video appears as an error signal from the comparator which feeds a binary decision circuit. In a conventional linear integration delta coder, positive or negative pulses are generated at the clock rate, depending upon wether the reconstructed output is greater or less than the input analog. The pulses generated are either positive or negative at each clock period, and their amplitudes are constant, regardless of the magnitude of the error. The analog signal is reconstructed from the pulse train by an integrator whose output decreases or increases a fixed amount, depending upon the polarity of the pulse and its input. The feedback from the integrator to the comparator is degenerative, so that the reconstructed signal approaches the input signal, as shown in Figure 34. The digital signal coupled out of the A/D converter is the pulse train from the binary decision circuit. The analog signal can be reconstructed at the receiver by using an integrator identical to the converter.

The A/D conversion employed in this equipment is a slight modification of the conventional process in that a pulse train of only one polarity is used to drive the integrator. A pulse either exists or does not exist at each clock period. The integrator circuit consists of an integrating capacitor and a resistor. The capacitor charges one step of voltage when there is an input pulse and discharges through the resistor in the absence of a pulse. The integrator is nonlinear, since the leakage current is proportional to the voltage across the integrating capacitor, as shown in Figure 35.

Figure 36 is a block diagram of the A/D converter. The input analog video is amplified and compared with the reconstructed analog at the summing junction. The difference voltage is fed to the first binary decision circuit, which samples the error signal at a rate determined by the system's

LINEAR INTEGRATION

INPUT
ANALOG

SIGNAL RECONSTRUCTED FROM
DIGITAL PULSE TRAIN

DIGITAL SIGNAL FROM BINARY DECISION CIRCUIT

CLOCKING SIGNAL
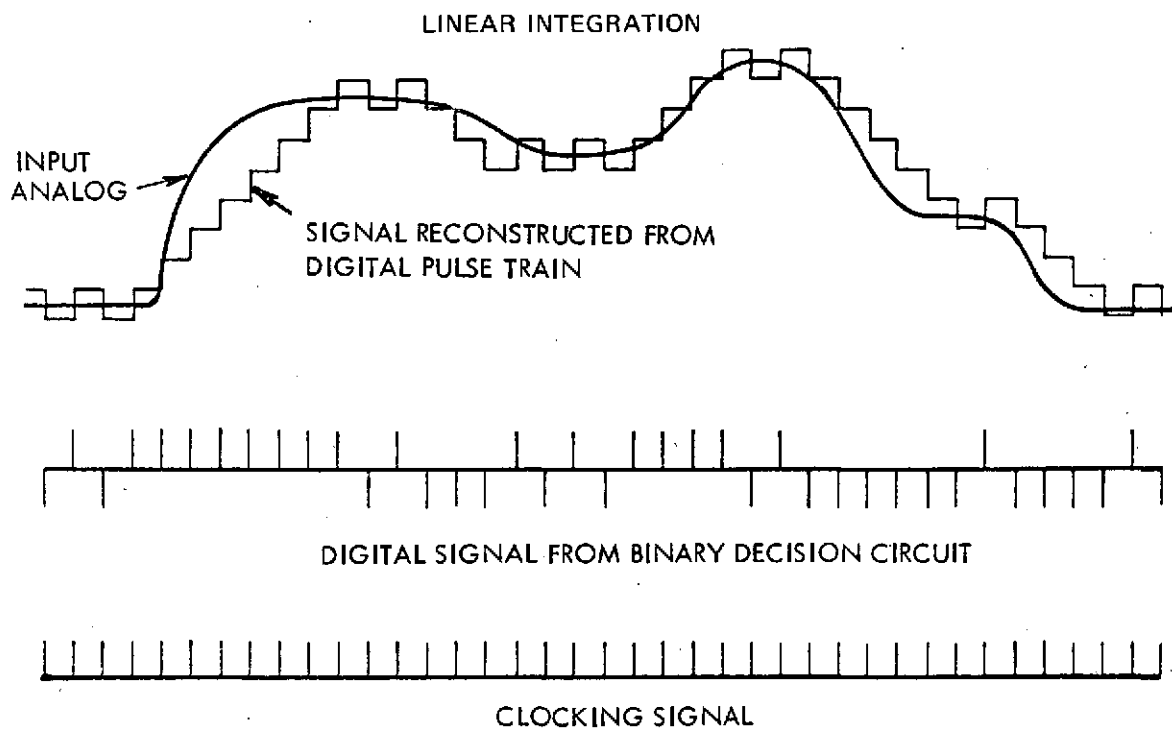
Figure 34. Delta modulation process.

NONLINEAR INTEGRATION

INPUT ANALOG

SIGNAL RECONSTRUCTED FROM
DIGITAL PULSE TRAIN

DIGITAL SIGNAL FROM BINARY DECISION CIRCUIT

CLOCK SIGNAL
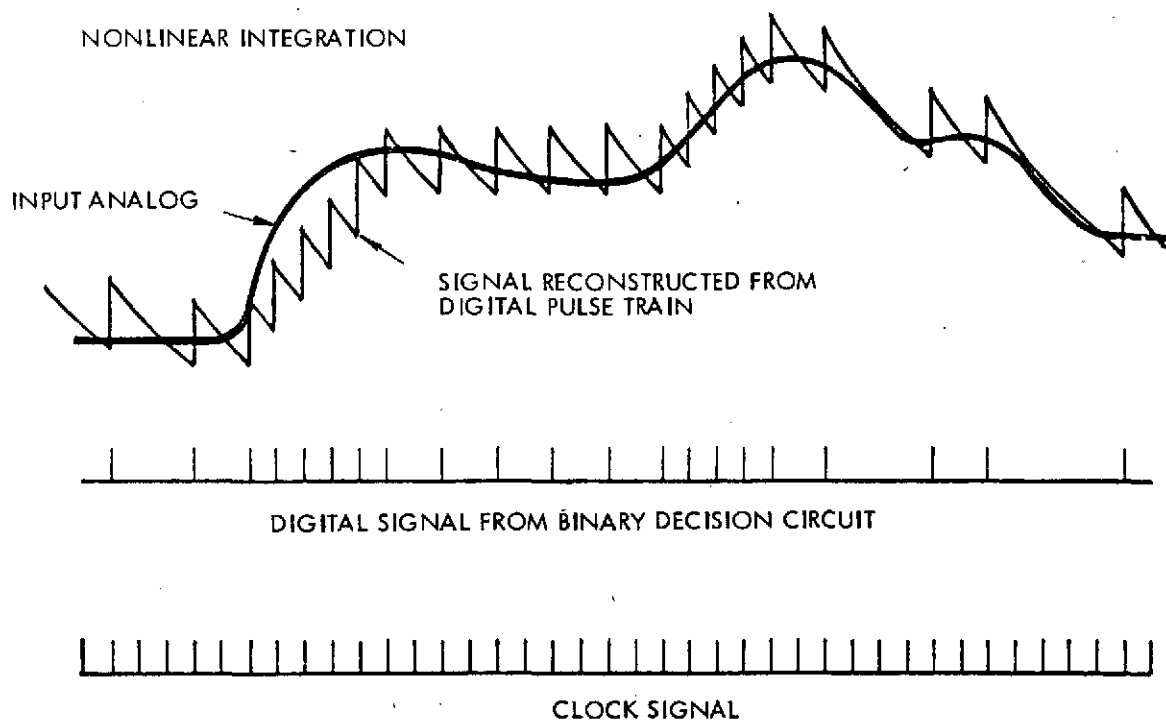
Figure 35. Delta modulation process, nonlinear.

clock generator. If the error voltage exceeds a prescribed threshold, a pulse appears at the output of the first decision circuit. The pulses appearing at the output of the first decision circuit have some leading and trailing edge jitter, which is proportional to the magnitude of the error signal. To remove this signal, a second decision circuit is used. The clock signal gating the second decision circuit is delayed slightly so that it does not respond to the jittering edges on the pulses from the first decision circuit. The pulse train from the second decision circuit is fed to the integrator, which reconstructs an analog video signal from the pulses. The reconstructed analog is fed to the summing junction and to an output which permits monitoring of the A/D conversion performance. The digital signal from the second decision circuit, which contains the video information, is of the return-to-zero form. The reclocker circuit converts the output to a nonreturn-to-zero (NRZ) signal at a nominal 0-and 1-V level, which is accepted by the optical modulator's driver circuit.

Pseudorandom Generator. A relatively short, 31-bit pseudorandom pattern length has been utilized in the communication experiment equipment for BER measurement. This length is adequate for measuring error rate on the present wideband laser link and at the same time permits scintillation measurement by use of convenient low center frequency filters at the ground station.

For some communication channels, longer pattern lengths (on the order of 2^{11} to 2^{13}) are required to adequately measure error probability. These channels are characterized by intersymbol interference extending over many adjacent bit intervals. A noise band telephone channel is an example. Here the interference is caused by phase distortion due to one or more sharp cutoff filters in tandem. In these cases, the error probability at a particular bit time depends on the particular combination of a number of the adjacent bits. Measurement of average error probability requires a sufficiently long pattern to be sure all possible bit combinations are used during the measurement.

In the AVLOC system, however, the inherent channel bandwidth (optical carrier) is much broader than the signal bandwidth, even at the highest bit rate (30 Mbs). The intersymbol interference caused by the channel is thus negligible. The pattern length only has to be sufficiently large so as to insure that all combinations of the two bits immediately adjacent to the current bit are exercised. This could be insured by a pattern as short as 15 bits. The reason for considering the immediately adjacent bits is to insure that any intersymbol interference caused by imperfectly matched filtering in the communication detector is properly measured.
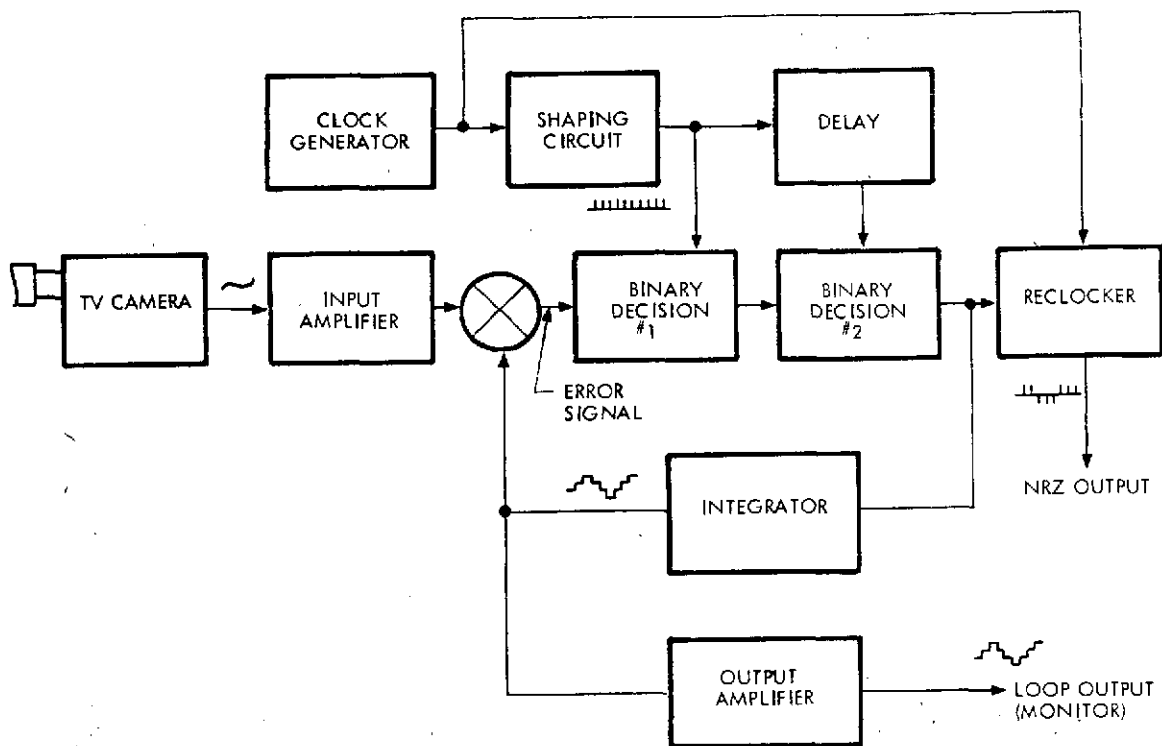
Figure 36. Analog-to-digital converter block diagram.

Since the pattern is periodic, its spectrum consists of a number of discrete spectral lines, as shown in Figure 37 for the 30-MHz bit rate. The scintillation measurement made with data modulation can be achieved by filtering out one of the spectral lines (greatest amplitude component) and measuring its fluctuating amplitude. If the pattern is too long, the spacing between spectral lines will be too close to separate with simple filters. The selected length, 31 bits, permits this filtering with convenient values of center frequency. For example, extraction of the fundamental spectral line requires the following nominal center frequencies:

Bit Rate	Fundamental Frequency
30 kbs	970 Hz
1 Mbs	32 kHz
5 Mbs	160 kHz
30 Mbs	970 kHz
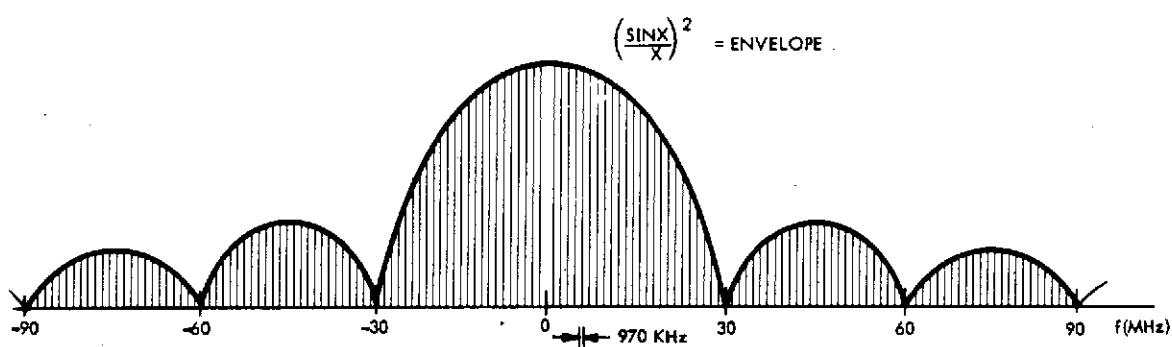
Figure 37. Spectrum—30-MHz rate.

For bit rates above 30 kbs, extraction of the fundamental code frequency component readily enables measurement of scintillation within the entire 0- to 5-kHz band. At the 30-kbs rate, the first five code components fall within the 5-kHz band. Consequently, extraction of only the 970-Hz component would limit the scintillation band to nominally 0 to 500 Hz. The pseudorandom word (PN) spectrum, or any intensity modulation, poses potential problems to the optical tracker. If the code components fall in the spectral region of the scan modulation or tracker bandwidth, erratic tracking or loss of track can result.

Laser Power Monitor

The function of the laser power monitor is to measure the average modulated laser power and to monitor the noise on the output laser beam within a 5-kHz bandwidth. The noise measurement is made so that any noise existing within this bandwidth will not be interpreted as atmospherically induced. The laser power monitor is an RCA type 8644 photomultiplier, which samples less

than 1 percent of the transmitted laser power. Narrow band and neutral density filters are located in the power monitor path to reduce the laser power and background power on the detector to an acceptable level ($\sim10^{-10}$ W). Calibration data on the power monitor are listed in another section of this report.

Beam Divergence Control

The beam divergence control subsystem provides a continuously variable transmitted beam divergence control, i.e., without interruption of the transmitted beam. The divergence is made in six discrete steps by displacement of one lens of a small telescope. The range of adjustment is from near-diffraction limit for the 3.81-cm (1.5-in.) output beam diameter to approximately 1.0 mrad. The calibration data for this device are presented in a later section. This beam decollimation is achieved without loss caused by vignetting and without substantial output beam diameter change in the design selected.

The divergence subsystem comprises a movable positive focal length lens L_1 and a fixed positive focal length relay lens L_2. Lens L_1 provides a twofold function: (1) it produces a point image of the laser input beam which is movable relative to lens L_2 and (2) it permits a selection of the appropriate telescope power to control the exit beam diameter to insure proper location and size of the transmitted beam in the primary optical system exit pupil. Figure 38 shows the optical schematic for the beam divergence telescope. The basic equation describing the beam divergence subsystem operation is

$$\tan \frac{\theta}{2} = \frac{y(a-f_2)}{Mf_1f_2} \tag{2}$$

or for small angles,

$$\theta \simeq \frac{2y(a-f_2)}{Mf_1f_2} \tag{3}$$

where

θ = the beamwidth in object space from the system primary afocal telescope,

59

y = the radius of the beam at the input of the beam divergence telescope (at L_1),

a = the distance between lens L_2 and the point image formed by L_1,

f_1 = the focal length of lens L_1,

f_2 = the focal length of lens L_2, and

M = the magnification of the primary afocal telescope.
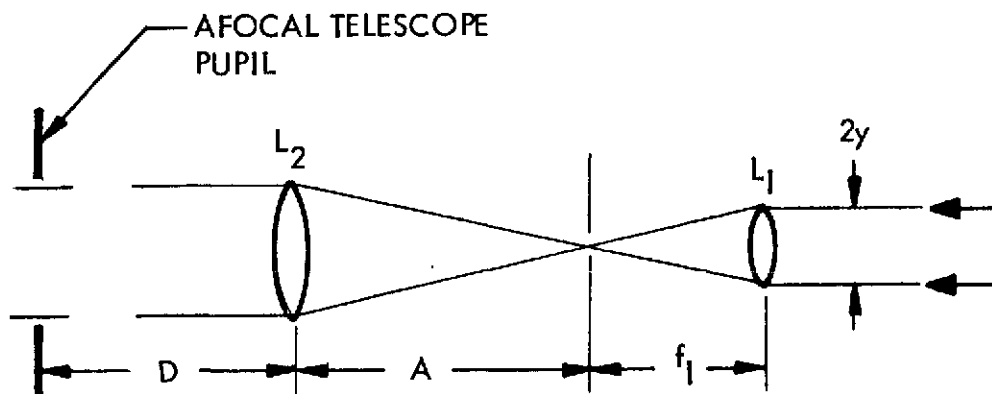
Figure 38.   Beam divergence telescope optical schematic.

Figure 39 shows the mechanism that controls the beam divergence. The actuator is a six-position stepper motor controlled by an electronic logic circuit.   Lens L_1 is mounted in a honed piston/cylinder for precise axial motion.   The spring-loaded piston assembly is driven by a precision cam and follower.   The cam shape and position on the stepper motor shaft determine the range of the beam divergence adjustment.   Calibration of the beam divergence control is described in another section of this report.
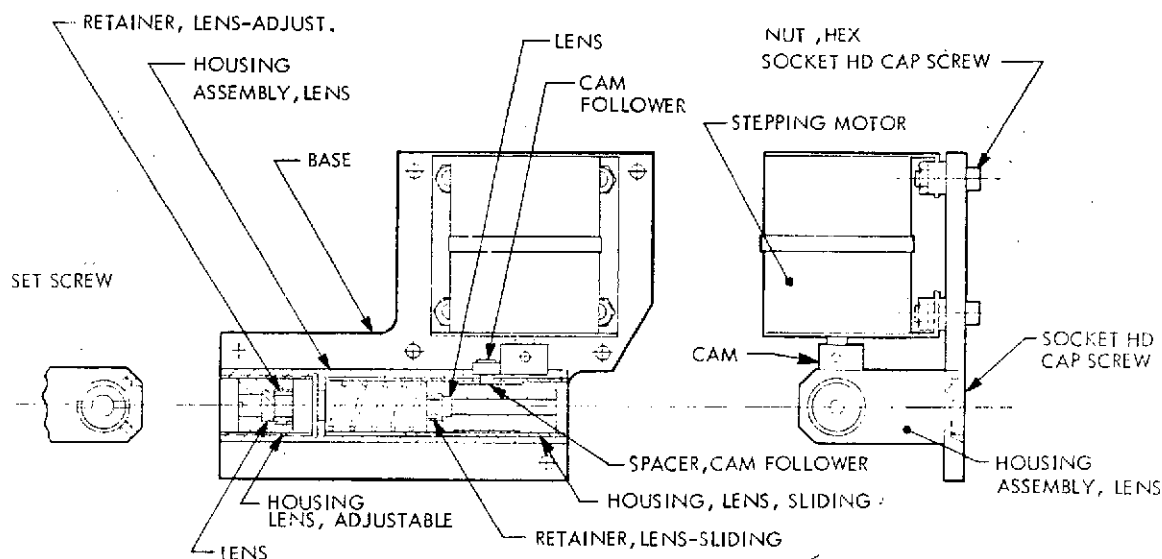
Figure 39. Telescope, adjustable (AOCP).

TV Acquisition Aid

The TV coarse acquisition aid was adapted from an ITT electro-optical sensor designed for the Short Range Missile (SRM) application. The system consists of a 525-line TV camera and associated adaptive threshold electronics. The system provides error signal outputs over an operating field of 87 by 122 mrad (5 by 7 deg). The camera's optical system consists of a periscope imaging system with an entrance aperture which is coaxial with the AOCP prime optical system. Also contained in the optical system is a narrow band optical filter centered at 488 mm to aid in background discrimination for detection of the argon beacon laser. The camera operates at a standard 60-Hz field rate, which allows for the update of the coarse error signals at a 30-Hz rate. This coarse error signal is then fed to the computer for control of the gimbal mirror during the coarse track mode of the acquisition sequence.

Command Receiver and Decoder

The command receiver consists of a modified AN/DRW-13 command signal receiver decoder. This receiver is used to decode an audio subcarrier modulation transmitted on the 10.7-MHz modulated 488-nm laser beam. The decoded signals are sent to the computer for experiment control and command operation. During the AVLOC experiment, parameters variable by command were the beam divergence, receiver attenuation, and communications modes. The detailed table of commands is given elsewhere in this report.

GIMBAL MIRROR SUBSYSTEM

The gimbal mirror platform (Figure 40) is used to acquire the uplink laser beam and direct it into the AOCP optics. A roll-pitch configuration is used in which the roll (outer) gimbal axis is aligned with the aircraft longitudinal axis (X-axis), which is constructed as a yoke (half gimbal) so it will not interfere with the laser beams. The pitch axis is aligned with the aircraft vertical axis (Y-axis). This arrangement causes the deflection of the laser beam to be doubled in the pitch axis relative to the roll axis; that is, for 1 deg of mirror travel in the pitch axis, the laser beam moves 2 deg, whereas in the roll axis there is a one-to-one relationship between mirror travel and beam deflection. To compensate for this effect, inertia wheels are used in the pitch axis (for inertial stability), and the mirror is driven from the wheels through a two-to-one reduction. Therefore, if the aircraft moves (in pitch, for example), but the inertial wheels remain fixed, then the mirror will move half the angle of the aircraft movement, thereby causing the laser beam to move through the same angle as the aircraft (twice the mirror angle) to compensate for this aircraft movement.
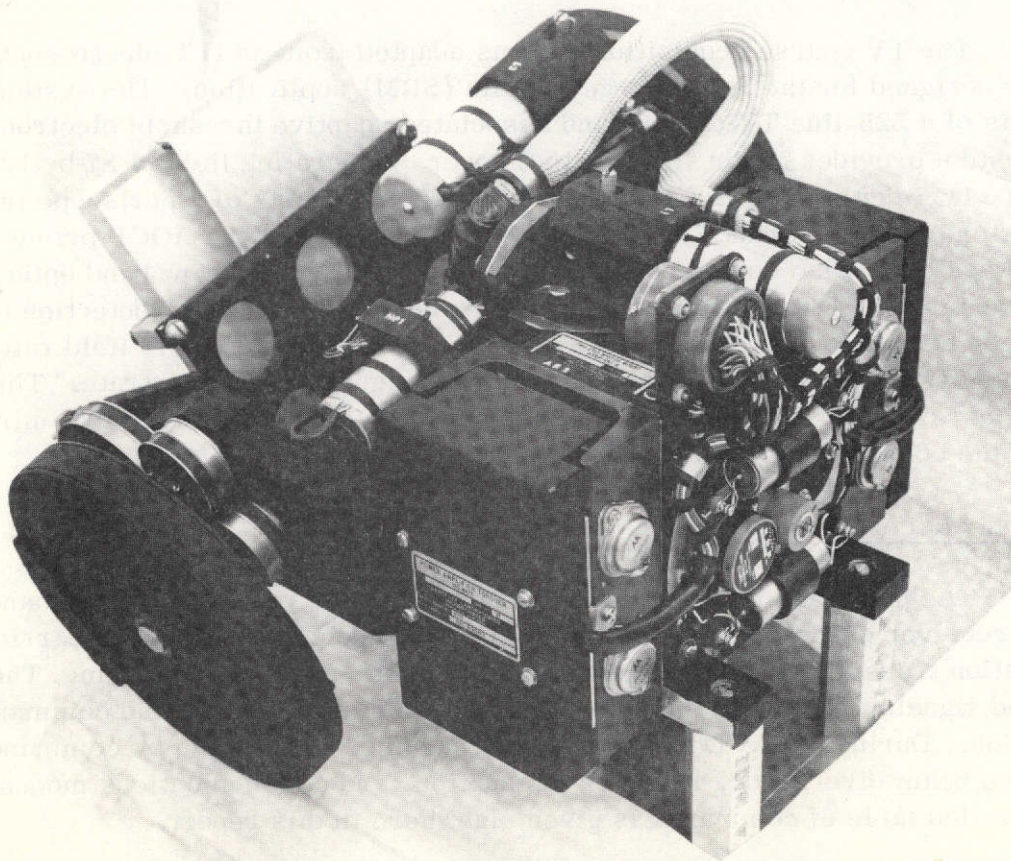
Figure 40. Gimbal mirror platform.

Because of the preceding considerations, all quantities in the pitch axis are referred to the inertial wheels axis rather than the mirror axis. The rate gyro is on the inertia wheel shaft, and the angle readout potentiometer is driven from this shaft. The inertia wheel shaft is driven, of course, by the pitch torquer.

A block diagram of the gimbal platform subsystem is shown in Figure 41. The first block is the gimbal electronics chassis, and the second block is the platform itself. Even though the overall control system has several operational modes, the platform itself has only one input line from the computer. The various modes are switched inside the computer.

The first amplifier inside the gimbal electronics is an isolation amplifier which was added to the purchased platform system. The amplifier isolates the computer from the gimbal electronics. The next amplifier sums the rate gyro output with the input from the computer. Thus, it can be seen that the gimbal platform loop is a rate loop, and inputs from the computer represent rate commands. The summing amplifier is followed by a unity gain inverter and then the driver stage.

The driver, which is located in the gimbal electronics, is connected in a feedback arrangement with the power amplifier, which is located on the gimbal platform. The power amplifier drives the brushless dc torquer, which is directly coupled to the gimbal shaft, which contains the rate gyro and drives the angle readout potentiometer. Up to this point the two axes are identical except for electronics gain, which is larger in the roll axis to compensate for the larger inertia in that axis. Otherwise, the axes differ only in that the mirror is driven off the pitch inertia shaft through a 2:1 reduction, as was explained previously. The potentiometer outputs are used both in the computer and for the display meters in the cockpit.

REMOTE EQUIPMENT CANISTER

In addition to the basic AOCP and gimbal platform hardware, considerable supporting electronics was required. These chassis and black boxes were housed in an environmentally controlled canister 213 by 81 cm (84 by 32 in.). The principal units contained in the REC were the control system computer, electrical power distribution system, TM measurement system, and communications and tracking electronics. The REC is pictured in Figure 42.
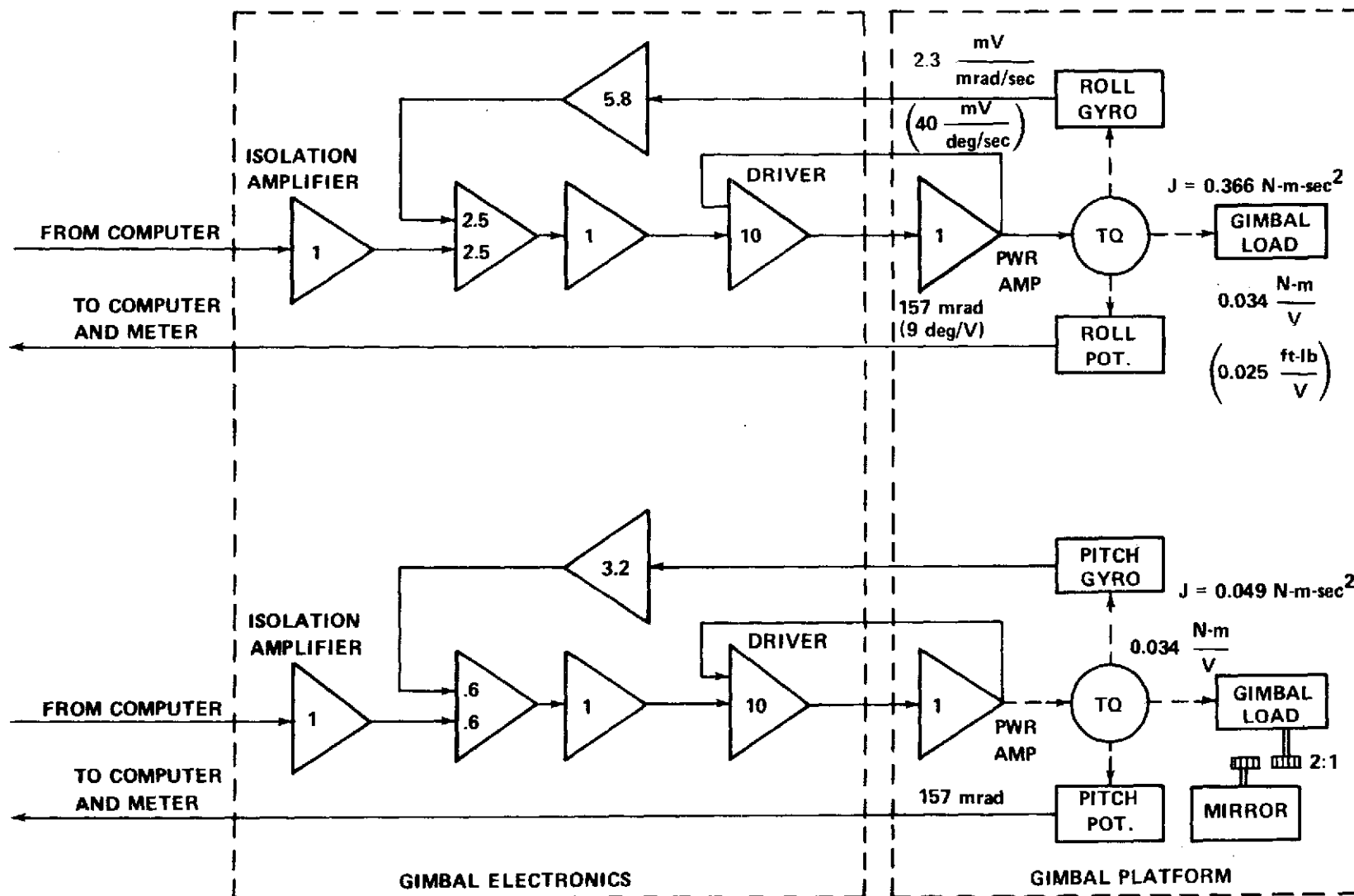
Figure 41. Block diagram of gimbal control system.
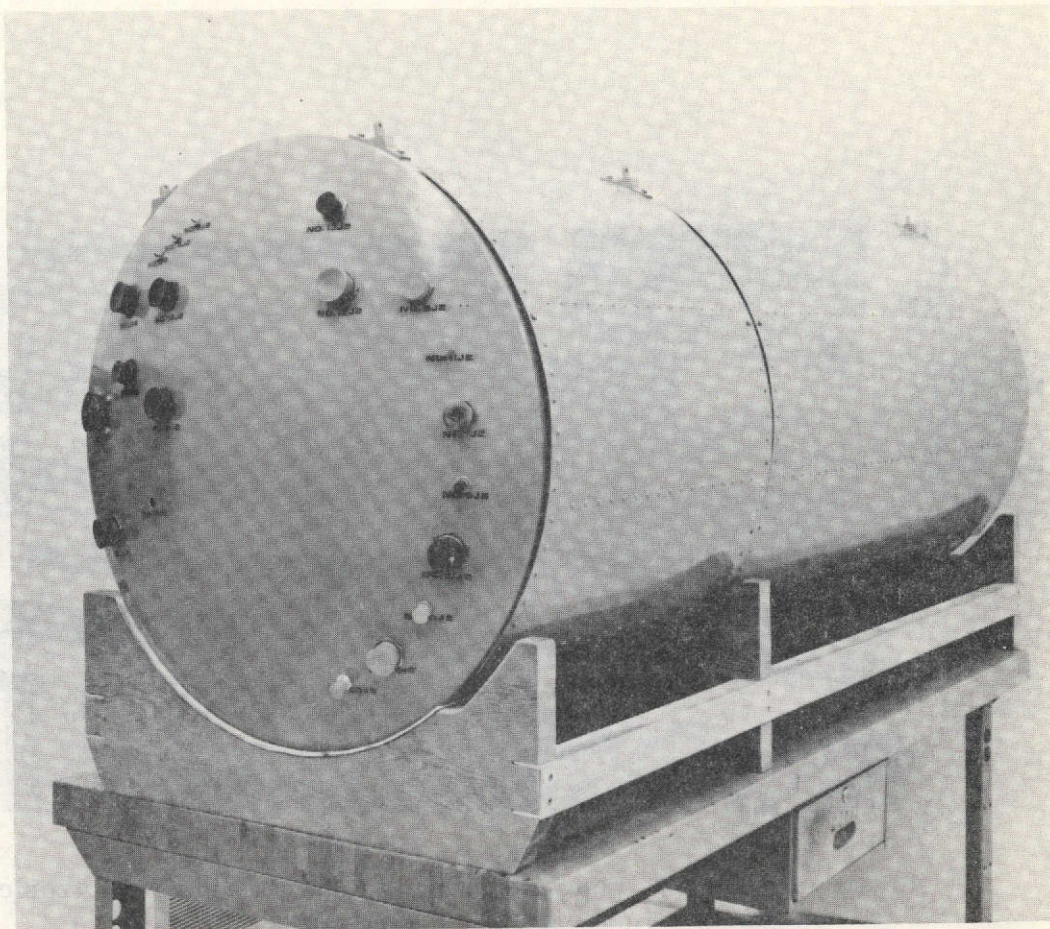
Figure 42. Remote Equipment Canister.

General Description

Figure 43 shows the REC with the sliding electronic rack partially extended. Visible on the extreme right is the General Automation SPC-16 general-purpose computer. The computer interface unit with exposed wire wrap terminals is shown directly above the computer. The iridite-coated box directly to the left of the computer interface is the power distributor box. The small yellow components on the top shelf are the voltage controlled oscillator (VCO) assemblies, and the black box directly to their left is the 28-Vdc regulated supply. Also on the top shelf, but not visible, are the pulse amplitude modulation (PAM) multiplexer and the gimbal servo electronics. The space below the shelf contains the measurement distributor box which is placed on the right, where the cables attach, and the four 60-Hz inverters, which are on the left. The computer power supply is mounted behind the computer interface unit. Figure 44 shows the detail hardware attachments for the components on the sliding rack. Located in the left canister bay are the remote electronics required for the TV tracking system, PCM electronics (30-megabit A/D system and PN generator) and the laser power supply. This equipment was described previously but is shown in Figure 45.

65
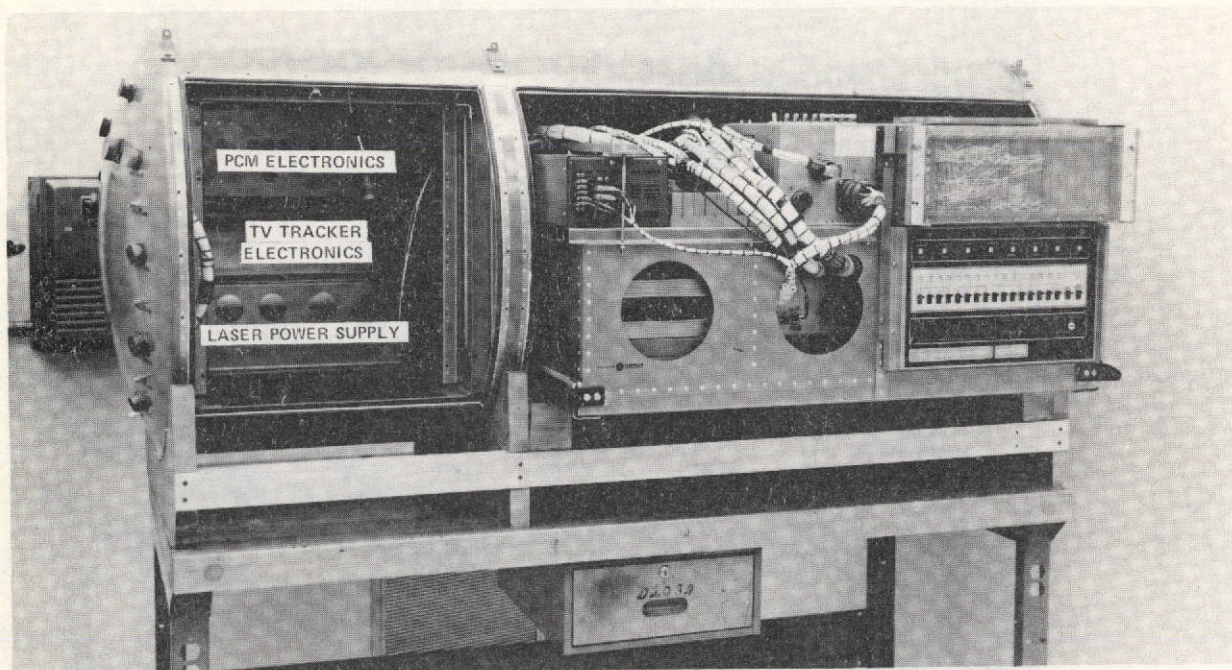
Figure 43. Remote Equipment Canister (with sliding electronic rack partially extended).
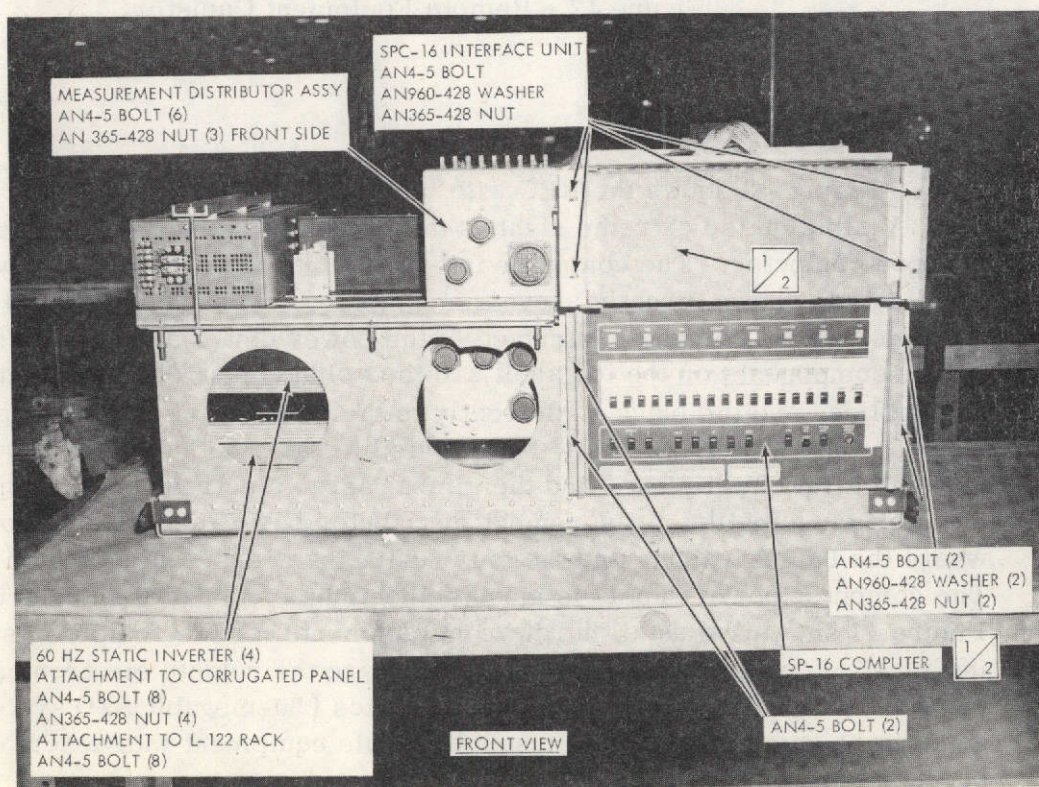
Figure 44. Front view, rack assembly.

AD CONVERTER

J15

J14 ➤ BIT ERROR RATE CLOCK
(TO GCE)

J421

TV TRACKER PROCESSOR

J412

J13 ◄— TV VIDEO
(FROM AOCP TV CAMERA)

J10 ➤ VIDEO OUTPUT TV TRACKER
(TO TV MONITOR)

J2 ➤ TV TRACKER ERROR & BEACON
PRESENCE (TO CCSD)

J3 ➤ VIDEO OUTPUT
(TO CCSD)

J413

DISTRIBUTION
&
He-Ne LASER POWER

J12 ◄— TV CAMERA SYNC & BLANKING
(TO TV TRACKER PROCESSOR)

J8 ◄— DOWNLINK MODULATION
(FROM CCSD)

J18 ➤ DIGITAL MODULATION
(TO AOCP LASER MOD DRIVER)

J1 ➤ He-Ne LASER POWER
(TO AOCP LASER)

Figure 45. Remote Equipment Rack (RER) block diagram.

67

Electrical Power and Network Subsystem

The requirements on the electrical power and networks subsystems are as follows:

1. Provide components, wiring and cabling necessary to control, convert, regulate, and distribute electrical power to the various AVLOC subsystems.

2. Provide the controls, switching, and calibration functions required for both ground and flight operations. A block diagram of the system is depicted in Figure 46. The nomenclature used in the blocks, such as 1A11 for the power distributor, identifies the box and location area (box No. 11 in the REC). All the circuitry designed and built by Chrysler for this project is contained within the power distributor, the measuring distributor, and the two control boxes.
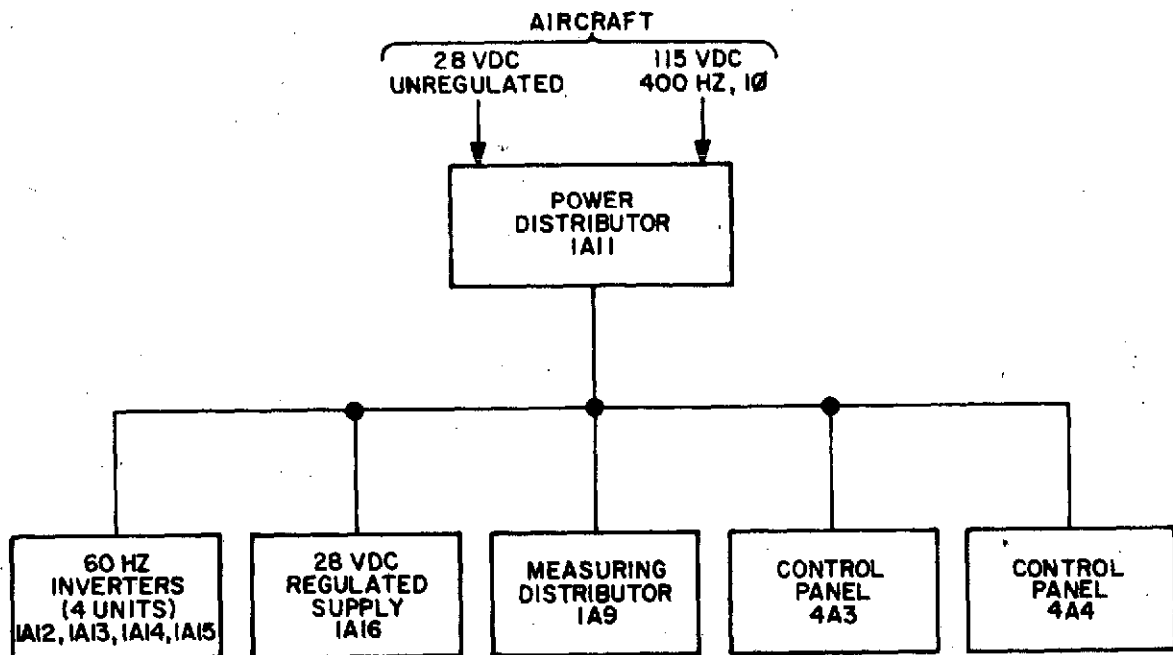
Figure 46. Power and networks control systems block diagram.

68

Power

All electrical power for the system is derived from the WB-57F aircraft electrical power system, consisting of 28-Vdc unregulated and 110-Vac, 400-Hz, single-phase electrical power. The simplified schematic of Figure 47 shows the derivation of each bus. The main power is controlled by a relay K1 located in the power distributor. Contacts A1 and A2 of this relay control the 28 Vdc and contacts B1 and B2 control the 400-Hz ac. The relay is operated either from Control Panel A (located at the operator's position) or from the ground support equipment (GSE), described later in this report. Each of the main power distribution circuits is protected by a circuit breaker. The breakers are located on the side of the power distributor and are accessible external to this box. Four of the circuit breakers (CB1 through CB4) are physically interconnected so that they are always turned on together. This is necessary since the four 60-Hz inverters are connected in parallel, and all four units must be operational to obtain the proper output.

Several small regulated supplies are provided, as shown in Figure 47. A +5-V supply is in Control Panel A and a +15-V supply in Control Panel B. In addition, the power distributor contains a small supply for the gimbal readout potentiometers. The -15 V buses from the computer represent the external loads for switching and electrical measurements placed on this supply, which are internal to the computer.

The system load distribution is shown in Figure 48. Most of the load is imposed on the 28 Vdc from the aircraft, which in addition to supplying the 60-Hz inverters, also powers the gimbal platform, the unregulated power to the AOCP, and various small loads as indicated. The 400-Hz power from the aircraft supplies all the regulated supplies and also the rate gyro electronics in the gimbal platform.

A simplified schematic of the 28-V unregulated distribution is shown in Figure 49. The circuit breaker CB8 protects the coil of the main contactor K1 and also the panel illumination lights. The 28-V power to the GSE does not pass through a breaker or a switch and is therefore always available when the aircraft power is on. The power to the coarse and fine beacon lights is switched on in the computer, in response to logical discretes, as is the power to the coax relay which selects the signal to be transmitted on the optical downlink.

A simplified schematic of the 28-Vdc regulated supply is shown in Figure 50. This supply, which is powered from the 400-Hz aircraft power through the main contactor K1 and circuit breaker CB5, is provided solely to the AOCP for use in the beam-steerer drive electronics and to the measuring distributor for TM.
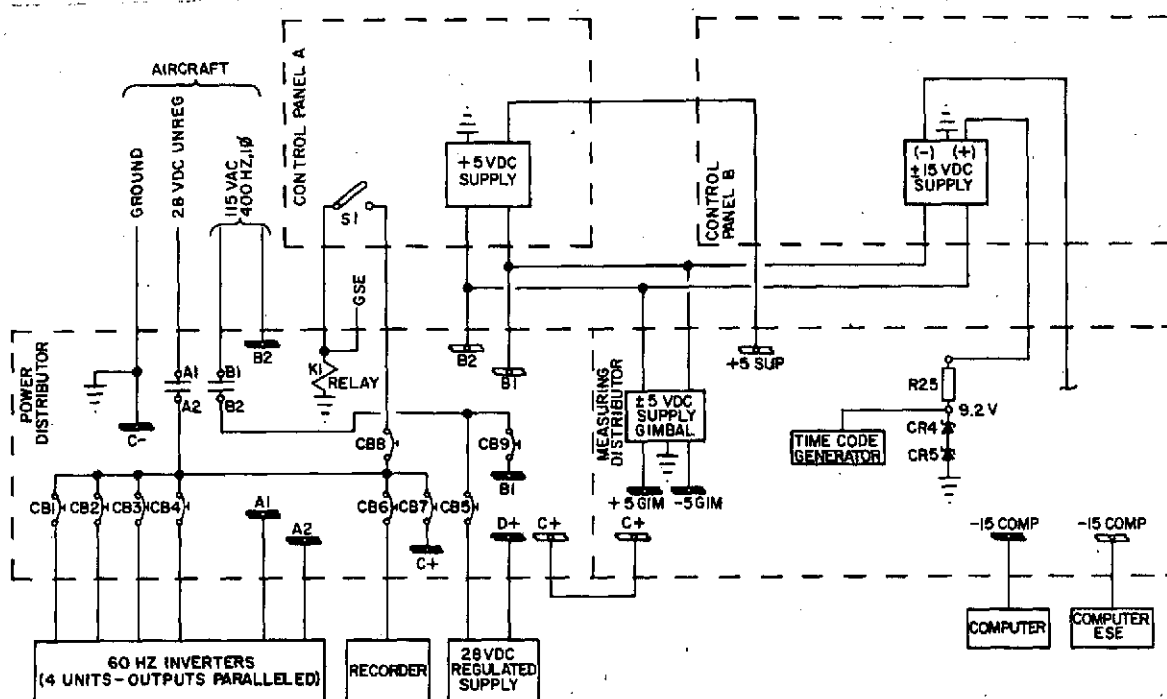
Figure 47. Power system simplified schematic.
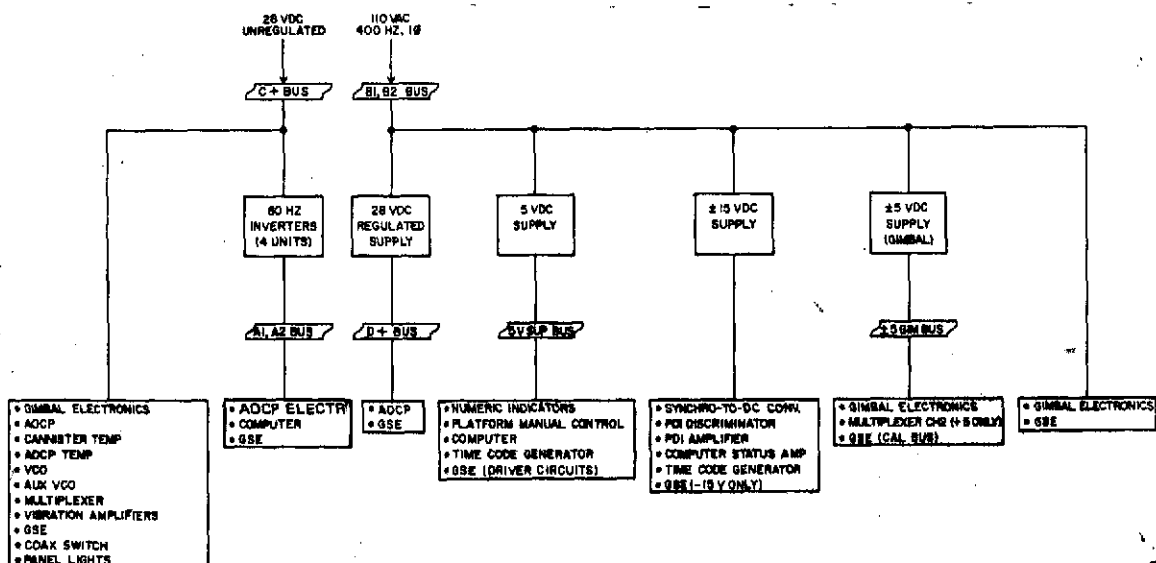
Figure 48. Bus load distribution.

70
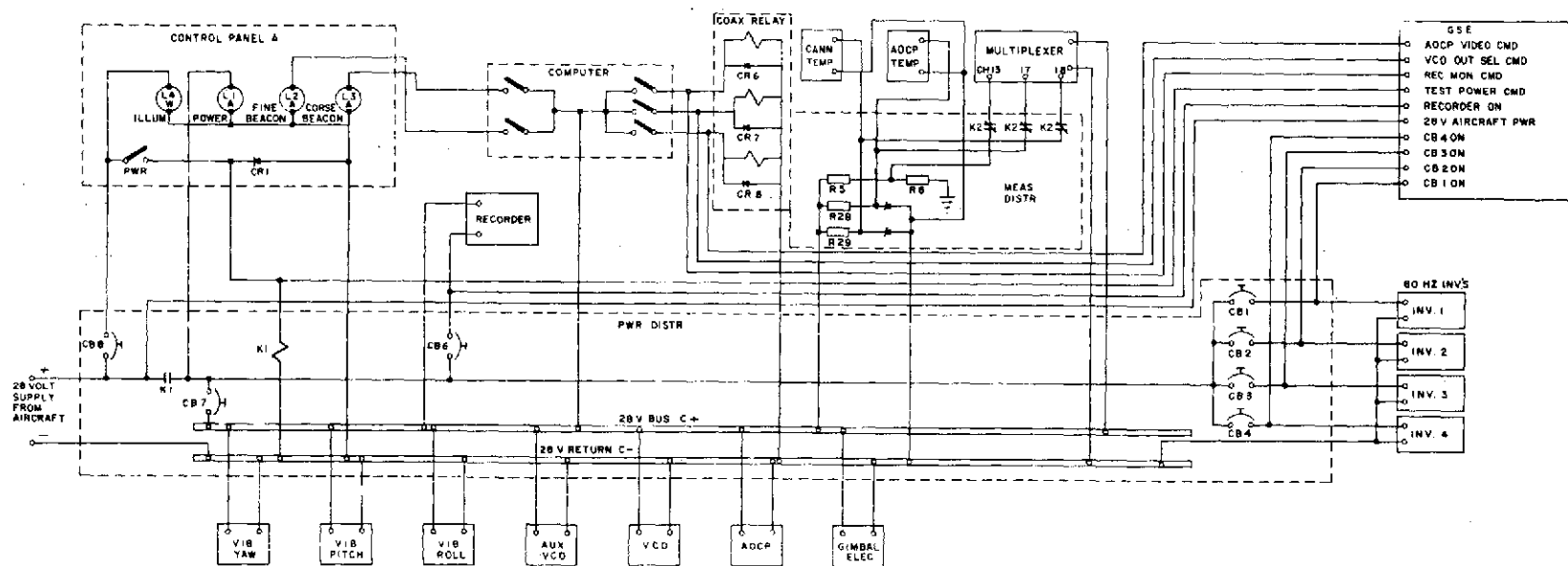
Figure 49. 28-V unregulated power distribution simplified schematic.
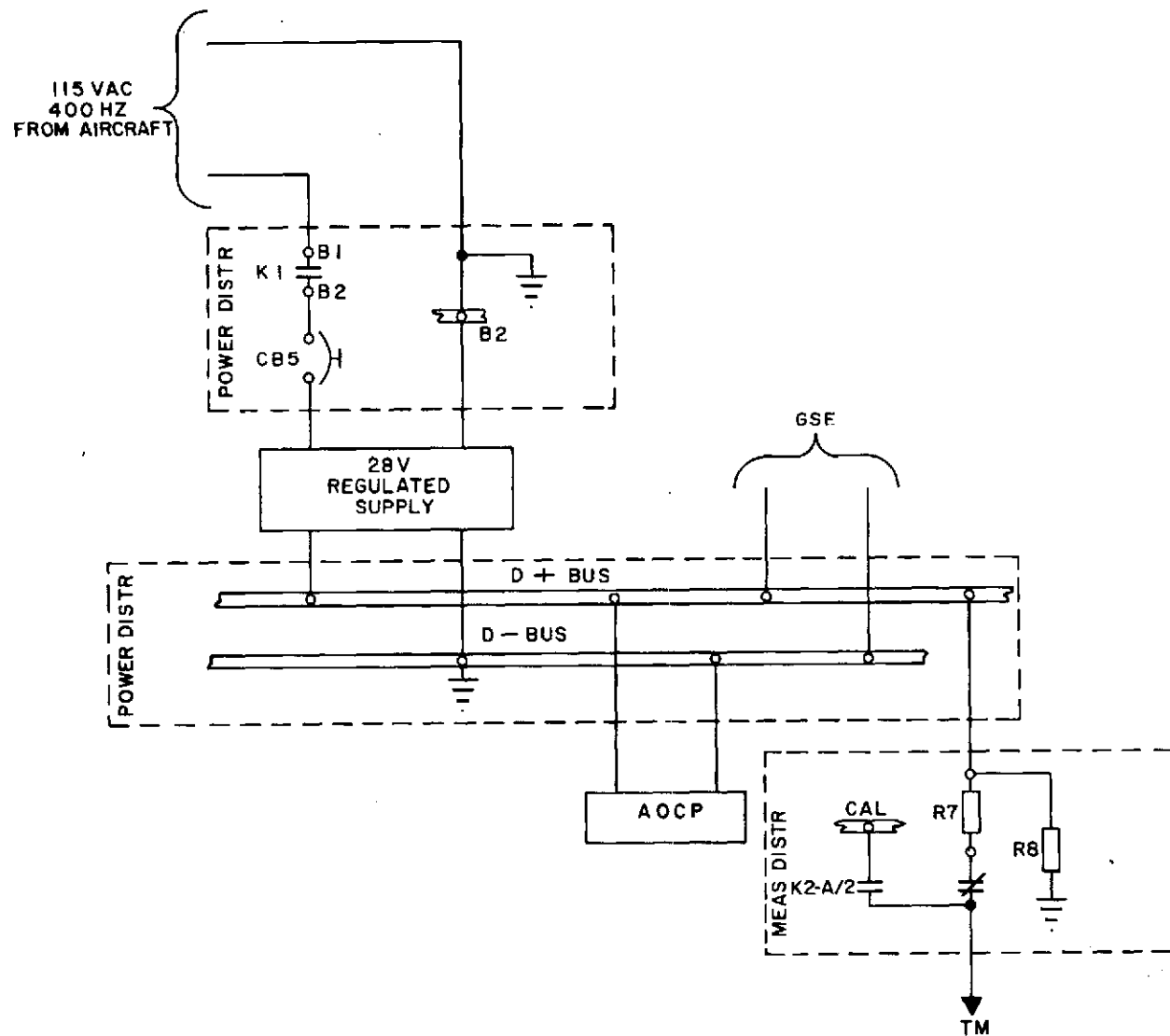
Figure 50. 28-Vdc regulated power distribution simplified schematic.

The 400-Hz simplified schematic is shown in Figure 51 and the 60-Hz distributor in Figure 52. The main load on the 60-Hz power is the computer, followed by the airborne laser supply and the TV tracker electronics.

Networks and Operator Controls

Networks and controls are contained in the measuring distributor and the two control panels. The measuring distributor contains the calibration circuitry, the coax relay, the time code generator, and terminal boards for signal processing. In addition, the measurements distributor serves as a distribution center for all signals to and from the AOCP and AOCP remote electronics (located in the REC).

A schematic of the coax relay and typical calibration channels is given in Figure 53. The coax relay, under command of the computer or GSE, selects any one of three different downlink signals: (1) channel 1 input to the recorder which is a composite VCO telemetry, used to verify on the ground that the recorder is functioning and also to establish a common time base between the ground and flight operations, (2) auxiliary VCO output which contains, in addition to the VCO signal, other signals such as uplink scintillation, and (3) the TV video from the coarse tracker. A spare channel for future growth is also provided. All four channels of the relay are independently selectable so that the computer must be programmed to select only one at a time.

Two T-bar calibration relays, k_1 and k_2, are provided for calibration of the TM signals. Typical circuits for both the bipolar and single-ended channels are shown in Figure 53. The GSE provides five step calibration signals during preflight operations.

Digital Computer Subsystem

Requirements

The Digital Computer System consists of a General Automation SPC-16 computer, associated interface chassis, and regulated power supplies, which are housed in three separate modules. A picture of the computer module and a discription of the front panel control functions are given in Figure 54. The functions are implemented on a series of plug-in cards (boards) in the interface chassis. A description of these boards is given in Table 2.
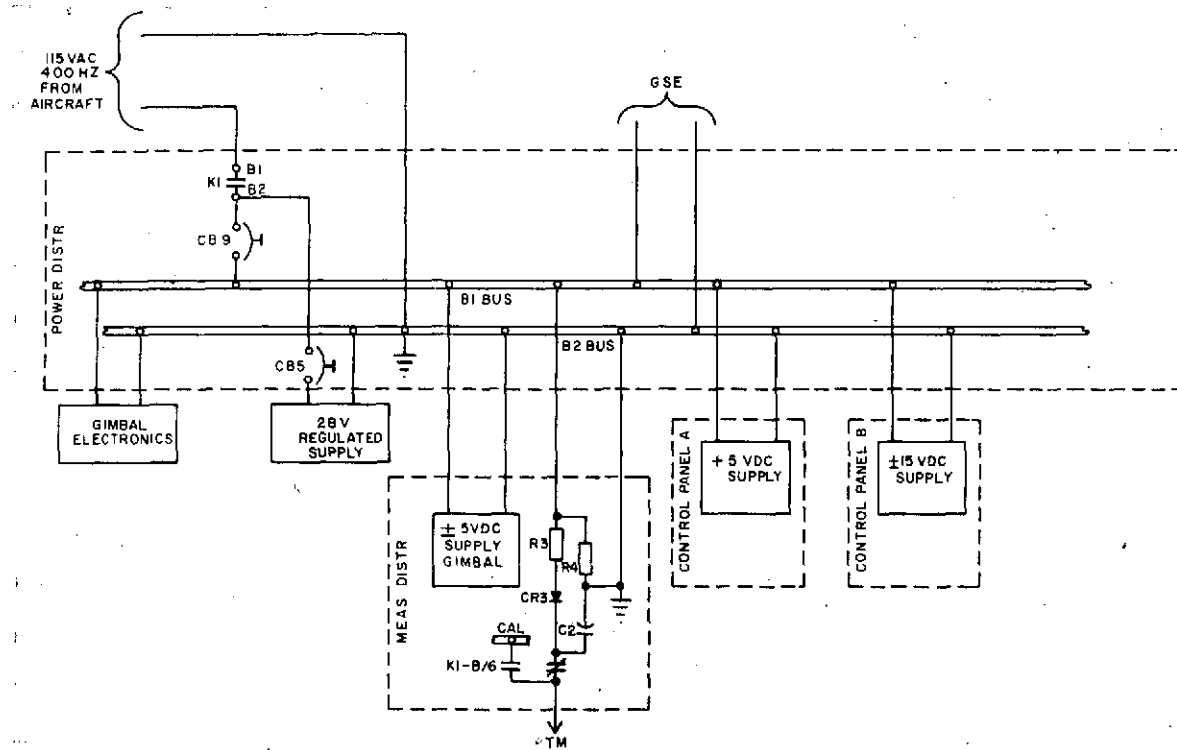
Figure 51. 400-Hz distribution simplified schematic.
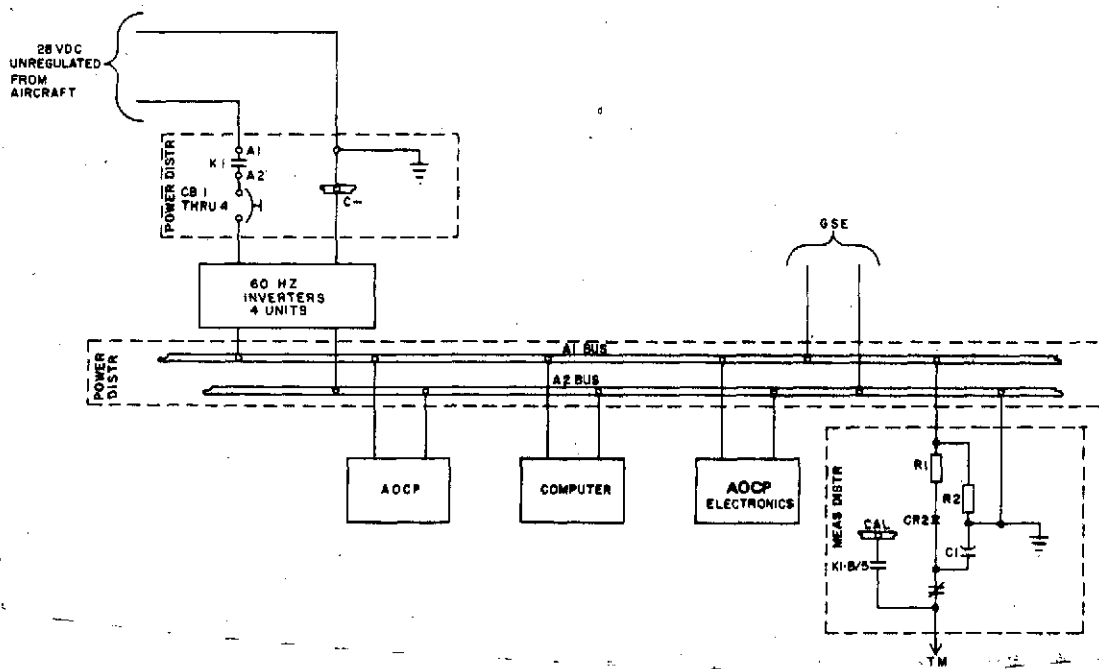
Figure 52. 60-Hz distribution simplified schematic.

This section covers the software program. Detailed information on the computer itself is given in the General Automation SPC-16 computer reference manual.
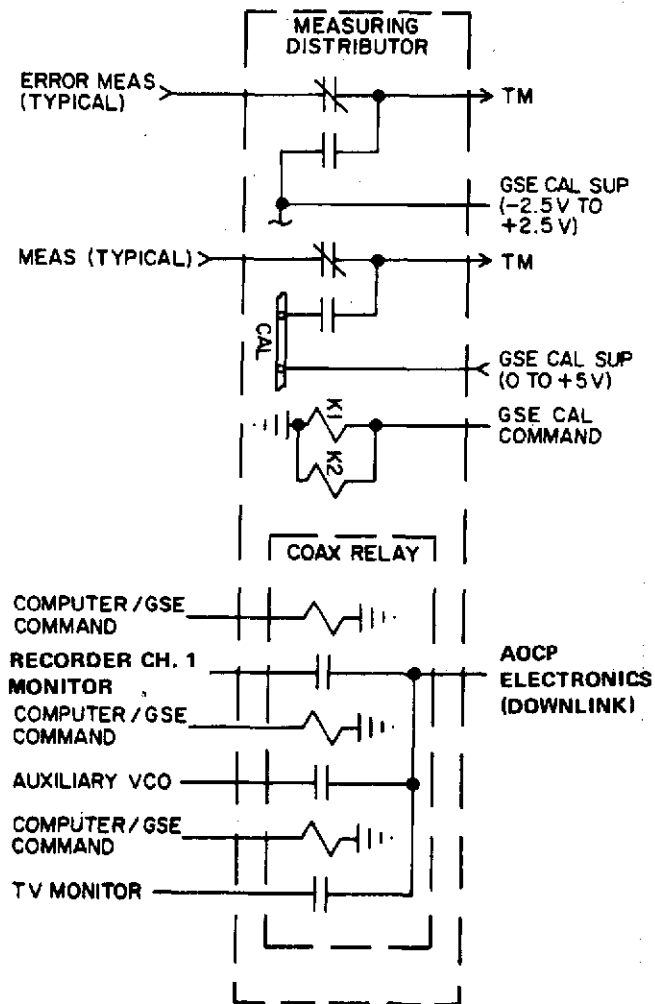
Figure 53. Typical networks control circuits.

The computer performs the following general functions: (1) systems ground test, (2) operational mode selection, (3) coordinate conversions for autotrack and slave modes and gimbal platform control in all modes, (4) time code generator synchronization, (5) uplink command decoding and experiment
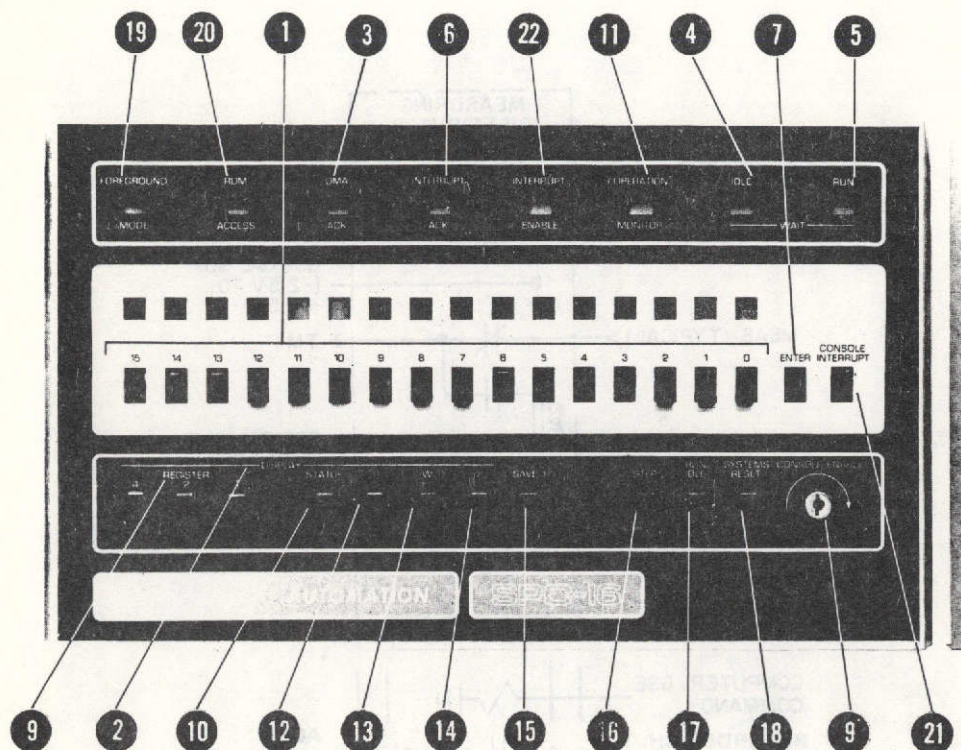
1. Sixteen Console Data switches used to enter data or instructions into the console display register and the select registers. These switches may be tested as sense switches or used as data input switches during program execution.
2. Register Display indicators indicates contents of the console display register. The register is loaded under program control in the run mode and by the selected register in the idle mode.
3. Direct Memory Access/Automatic Data Channel Acknowledge indicator.
4. Idle Indicator. When both Run and Idle indicators are lit, the computer is in the wait mode.
5. Run Indicator. When both Run and Idle indicators are lit, the computer is in the wait mode.
6. Interrupt Acknowledge indicator indicates when an interrupt is being serviced.
7. Enter switch, in the idle mode, replaces the contents of the selected register with the contents of the console data switches.
8. Console Key Lock used to disable all console switches when in the locked position. Console can also be locked in the idle mode.
9. Three Register Address switches used to select one of the eight operational registers to receive data from the console data switches. The selected registers value will be displayed on the console indicator lights in the idle mode.
10. Status switch used to place the computer status indicators and shift counter into the System Console Display register.
11. Operations Monitor Alarm indicates when the alarm has been activated.
12. "P" switch displays the contents of the program counter on the console display indicators. The program counter may be changed by the console data switches.
13. "W" switch displays the contents of the Working register.
14. "I" switch displays the contents of the instruction register.
15. Save "I" switch used to preserve the contents of the instruction register for repeated execution in the idle mode.
16. Step switch used to execute the instruction currently in the "I" register and increment the program counter to the next instruction. This switch starts program execution after the computer is placed in the run mode.
17. Run/Idle switch used to place the computer in either the idle or run mode.
18. System Reset switch used to initialize the computer and the input/output system.
19. Foreground/Processing indicator indicates which set of 8 programmable registers is being used.
20. ROM Access indicator indicates when a Read Only Memory is being accessed for instructions or data.
21. Console Interrupt switch requests an interrupt.
22. Interrupt Enable indicator indicates interrupt system is enabled.

Figure 54. SPC–16 computer console.

TABLE 2. PLUG-IN COMPUTER LOADS

Board Type	Description
Power Board	Printed circuit board to provide interconnection — the interface cables and the interface mother-board (wire wrap interconnection).
Device Drive Adapter (DDA)	Logic to decode input/output addresses and control pulses.
Differential Data Input (DDI)	Logic to accept either 0 or 5 V or open or -15 V as a discrete input.
Buffered Contact Output (BCO)	Logic + relays closed under computer control. Normally open contacts rated at 0.5 A.
Output Holding Amplifiers	Eight sample and hold amplifiers. 12 bit. 0.0025 V per bit scale factor. Full-scale range is +5.117 to -5.117 Vdc.
High Level Multiplexer (HLM)	Eight differential input -5.117 to +5.117-V channels. Maximum input voltage is 7 V.
Analog—Digital Card (ADC)	12-bit ladder network. Logic and comparator for both A/D and D/A conversion.

control, (6) in-flight testing, mode sensing and control, and (7) autostart and equipment initialization. The autostart and power-fail computer provide in-flight startup capability as well as automatic recovery when a power failure occurs during flight or on the ground.

Interface Chassis

The interface chassis contains the computer input and output (I/O) interface electronics. The I/O functions are given in Table 3.

Status Display and Tone Sequences

Located on Control Panel A is a two-digit experiment status display, which is used to indicate specific experiment status to the test operator during the test, acquisition, and tracking phases of operation. Special phases and codes are given in the following list:

Test Phase	Code	Meaning or Comments
Test	23	Software is in ground test mode.
All Phases	22	Gimbal mirror is being driven to the caged position under computer control.
	97	Beam divergence indication not operational.
	XO	RX attenuation indication not operational.
	99	Power upauto restart.
In-Flight-Test	14	Laser Power Monitor checks out OK.
	15	Laser Power Monitor not indicating "Laser ON"
	06	I/O command RX attenuation operable.

Test Phase	Code	Meaning or Comments
	07	I/O command RX attenuation not operable.
	33	In-Flight test software subroutine being executed.

All other status indications are listed in Table 4.

The uplink commands are generated in the laser ground station by modulating the uplink laser beam with a sequential set of frequencies. These discrete frequencies, when demodulated and detected by the onboard receiver, are presented to the computer system as uplink tone closures. The tone closures, their sequence, and the command to be executed by the computer for each tone sequence are given in Table 5.

Ground Test Codes

The ground test panel (GSE module) is designed for use with the computer to execute certain computer-controlled systems tests. The GSE switch settings and associated computer routines are given in Table 6.

System Control Modes

A primary function of the digital computer is to control the gimbal mirror platform in response to one or more of three input signals, depending on the operational mode that is being used. The input signals are manual input, drift-site TV, and AOCP track signals. The AOCP error sensor is fixed in the XYZ coordinates of the aircraft, whereas the gimbal mirror can move through large angles relative to these axes. Thus, in the autotrack mode, the computer must perform a coordinate conversion between the two coordinate systems. Similarly, in the slave mode another coordinate conversion must be performed between the drift-site TV (which is also movable, but about other axes) and the gimbal platform. In the manual mode, on the other hand, no coordinate conversions are required.

The operational mode is determined by the settings of the acquire and auto/manual control switches and by whether beacon presence signals are received. The inputs to the computer and the mathematical computations required are given for each mode in Table 7.

TABLE 3. INPUT/OUTPUT FUNCTIONS

Item		No.
Discrete Inputs	Ground Test Indications	6
	Uplink Tone Command Signals	12
	Experiment Status Indications	7
	Control Panel Status Indications	5
	Spare	2
	TOTAL	32
Discrete Outputs	Ground Test Indications	6
	Time Code Generator Controls	2
	Control Panel Display Indications	8
	Control Panel Status Indications	2
	Experiment Control Closures	15
	Spare	3
	TOTAL	36
Analog Outputs	Mirror Control Analog Drives	2
	Ground Test Analog Output	1
	Computer System Status Measurement	1
	Spare	4
	TOTAL	8
Analog Inputs	Gimbal Mirror Position Measurements	2
	Experiment Status Indications	3
	Experiment Positioning Measurements	6
	Control Panel Manual Positioning	1
	Drift Site TV Positioning Measurements	2
	Spare	2
	TOTAL	16

TABLE 4. ONBOARD DISPLAY CODES

Display		Command Status Indications		
Tens Digit	Units Digit	Collect Aperture Position (2 Pos.)	Beam Divergence (6 Pos.)	Receiver Attenuation (6 Pos.)
0	0	0	0	0^a
0	1	0	0	1
0	2	0	0	2
0	3	0	0	3
0	4	0	0	4
0	5	0	0	5
0	6	← I/O Command/Read/OK →		
0	7	← I/O Command/Read/Error →		
0	8	0	1	0^a
0	9	0	1	1
1	0	0	1	2
1	1	0	1	3
1	2	0	1	4
1	3	0	1	5
1	4	Laser Power OK and I/O Command Read OK		
1	5	Laser Power Output Failure		
1	6	0	2	0^a
1	7	0	2	1
1	8	0	2	2
1	9	0	2	3
2	0	0	2	4
2	1	0	2	5
2	2	← System to Caged Position →		
2	3	← Ground Test in Execution →		
2	4	0	3	0^a
2	5	0	3	1
2	6	0	3	2
2	7	0	3	3
2	8	0	3	4
2	9	0	3	5
3	0	← Inflight Test →		
3	1	—	—	—
3	2	0	4	0^a
3	3	0	4	1
3	4	0	4	2
3	5	0	4	3
3	6	0	4	4
3	7	0	4	5
3	8	—	—	—
3	9	—	—	—
4	0	0	5	0^a
4	1	0	5	1
4	2	0	5	2
4	3	0	5	3
4	4	0	5	4
4	5	0	5	5
4	6	—	—	—
4	7	—	—	—
4	8	—	—	—
4	9	—	—	—

TABLE 4. (Concluded)

Display		Command Status Indications		
Tens Digit	Units Digit	Collect Aperture Position (2 Pos.)	Beam Divergence (6 Pos.)	Receiver Attenuation (6 Pos.)
5	0	1	0	0^a
5	1	1	0	1
5	2	1	0	2
5	3	1	0	3
5	4	1	0	4
5	5	1	0	5
5	6	—	—	—
5	7	—	—	—
5	8	1	1	0^a
5	9	1	1	1
6	0	1	1	2
6	1	1	1	3
6	2	1	1	4
6	3	1	1	5
6	4	—	—	—
6	5	—	—	0^a
6	6	1	2	1
6	7	1	2	2
6	8	1	2	3
6	9	1	2	4
7	0	1	2	5
7	1	1	2	—
7	2	—	—	—
7	3	—	—	0^a
7	4	1	3	1
7	5	1	3	2
7	6	1	3	3
7	7	1	3	4
7	8	1	3	5
7	9	1	3	—
8	0	—	—	—
8	1	—	—	0^a
8	2	1	4	1
8	3	1	4	2
8	4	1	4	3
8	5	1	4	4
8	6	1	4	5
8	7	1	4	—
8	8	—	—	—
8	9	—	—	0^a
9	0	1	5	1
9	1	1	5	2
9	2	1	5	3
9	3	1	5	4
9	4	1	5	5
9	5	1	5	
9	6			
9	7	Beam Divergence Not Operational		
9	8			
9	9	Start After Power Down (all discretes reset)		

a. Least significant digit. 0 = Rx attenuation measurement not operational.

TABLE 5. UPLINK COMMANDS AND CODING OF TONES

Command	Tone Master	Sequence Tone 'X'	Sequence Tone 'Y'	Remarks
Track Mode Defeat	6	1	2	Hold Type
Increase/Decrease Aperture	1	1	3	On = Decrease (hold type)
Increase Receiver Attenuation	6	1	4	Momentary ≅ 20 msec
Decrease Receiver Attenuation	6	1	5	Momentary ≅ 20 msec
Increase Beam Divergence	6	2	3	Momentary ≅ 20 msec
Decrease Beam Divergence	6	2	4	Momentary ≅ 20 msec
Remove/Install TV Filter	6	2	5	On = Remove (hold type)
Laser Shutter Open Override	6	3	4	On = Close ≅ 3 sec
Select Video for Downlink	6	3	5	On = Select (hold type)
Select Telemetry for Downlink	6	4	5	On = Select (hold type)
Select Recorder Monitor Downlink	6	2	1	On = Select (hold type)
Select Bit Error Downlink	6	3	1	On = Select (hold type)
Enable/Disable Beam Deflector	6	4	1	On = Select (hold type)
Remove/Install ND Filter	6	5	1	On = Select (hold type)
Spare	6	3	2	
Spare	6	4	2	
Spare	6	5	2	
Spare	6	4	3	
Spare	6	5	4	

Notes on Command Coding

1. Tone 6 is the master tone which initiates action in computer software.

2. The first tone 6 received will generate a time sync pulse (5 Vdc, 20 msec) to be placed on the computer status channel of magnetic tape, and the IRIG 'B' time code generator hours will be set to 10 hr.

3. Tone or Uplink Command Sequence:

   A — Tone 6 on for 1 sec.   D — All tones off for 0.5 sec.
   B — All tones off for 0.5 sec. E — Tone 'Y' on for 1 sec.
   C — Tone 'X' on for 1 sec.   F — All tones off for 0.5 sec.

4. Maximum time for Tone Sequence 6, 'X,' and 'Y' will be 4.5 sec.

TABLE 6. GROUND TEST CODES

Switch Positions					Test Subroutine
16	8	4	2	1	
0	0	0	0	0	Analog Output Channel 1
0	0	0	0	1	Analog Output Channel 2
0	0	0	1	0	Analog Output Channel 3
0	0	0	1	1	Analog Output Channel 4
0	0	1	0	0	Analog Output Channel 5
0	0	1	0	1	Analog Output Channel 6
0	0	1	1	0	Analog Output Channel 7
0	0	1	1	1	Analog Output Channel 8
0	1	0	0	0	Discrete Output
0	1	0	0	1	Discrete Input
0	1	0	1	0	Analog Input
0	1	0	1	1	Go to Utility Subroutine
0	1	1	0	0	Analog Input Teletype
0	1	1	0	1	Zero Data Start
0	1	1	1	0	Discrete Output Teletype
0	1	1	1	1	Return Main Program

TABLE 7. MATHEMATICAL COMPUTATIONS

Operational Mode	Inputs	Range of Inputs	Computation	Computation Time (msec)	Remarks
Manual	$M\theta\varphi$	1, 2, 3, and 4 V	$M\theta\varphi = 1\ V = \max + \theta$ –drive	10 Total	No coordinate conversion; θ and φ are checked for limits.
	θ	+10 to –75 deg	$M\theta\varphi = 2\ V = \max - \theta$ –drive		
	φ	+20 to +60 deg	$M\theta\varphi = 3\ V = \max + \varphi$ –drive		
			$\theta\varphi = 4\ V = \max - \varphi$ –drive		
Slave	α_r	–20 to +20 deg	$\theta_{cp} = \tan^{-1}\left(\sin\alpha_r \tan\delta_r\right)$	12 Total	θ – input in volts
	θ_r	+10 to –75 deg	$\theta_c = \theta_r - \theta_{cp}$		θ_r – conversion in radians
	δ_r	0 to +5 deg	$\varphi_{cp} = 90\ \deg - \tan^{-1}\left(\dfrac{\tan\alpha}{\sin\theta_{cp}}\right)\begin{matrix}\alpha\neq 0\\ \alpha\cong 0\end{matrix}$		θ_{cp} – θ correction present
	φ_r	+20 to +60 deg	$\varphi_{cp} = \alpha$		θ_{CL} – θ correction last
			$\varphi_c = \varphi_{cp}/2$		θ_c – output drive
					α_r – input in radians
					δ_r – input in radians
Coarse Auto-Track (TV)	V_Y	–3 to ±5 deg	$\theta_{cp} = \dfrac{-Z\sin\theta_r - Y\cos\theta_r}{\sin 2\varphi_A}$	17 Total	$Z = V_Z$
	V_Z	–3 to +3 deg			$Y = V_Y$
	θ_r	+10 to –75 deg	$\varphi_{cp} = \dfrac{Z\cos\theta_r - Y\sin\theta_r}{2}$		
	φ_r	+20 to +60 deg			
Fine Auto-Track	E_Y	–0.3 to +0.3 deg		20 Total	
	E_Z	–0.3 to +0.3 deg	$\varphi_A = -\dfrac{\pi}{4} - \varphi_r/2$		$Z = E_Z + B_Z$
	B_Y	–0.3 to +0.3 deg			$Y = E_Y + B_Y$
	B_Z	–0.3 to +0.3 deg	$\theta_c = \theta_{cp}$		
	θ_r	+10 to –75 deg	$\varphi_c = \varphi_{cp}$		
	φ_r	+20 to +60 deg			

A digital flow diagram is given in Figure 55. From both the aircraft and the AOCP package, the digital system receives both discrete commands and analog inputs. The computer outputs commands (relay closures) to the experiment and analog output drives to the gimbal platform.
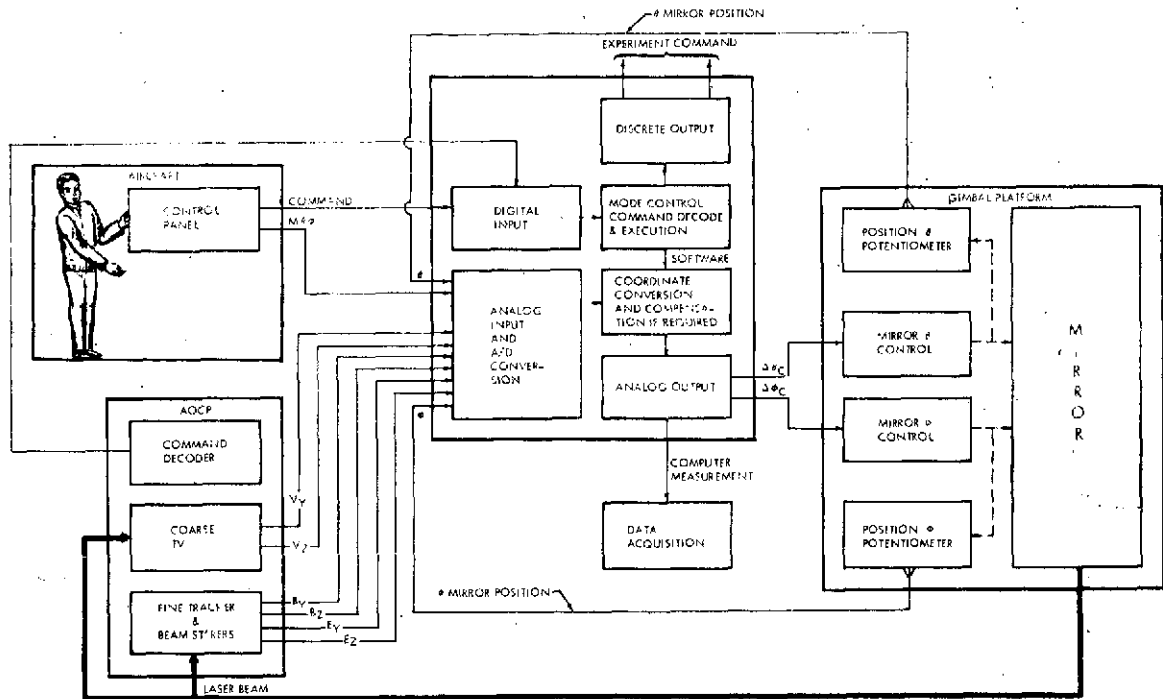
Figure 55. Digital control flow diagram.

Software Description

The flight program must perform the following functions:

1. Automatically initialize all software and controlled hardware to the desired uplink acquisition status upon application of power.

2. Determine the operational mode based on control panel switches and input discrete and select corresponding experiment control subroutines.

3.   Decode the serial uplink commands and execute the correct stimulus to the experiment.

4.   Synchronize onboard time code generator with ground recorded data for subsequent data reduction.

5.   Provide a means of in-flight experiment test and status display.

6.   Provide a means of ground test and verification.

7.   Provide a means of verification, listing, loading, punching, and modification of the flight program outline.

8.   Determine automatically which mode of gimbal mirror tracking is to be executed and perform the correct drive signal application to the mirror gimbal electronics.

For the utility program use, refer to the General Automation SPC-16 utility program reference manual.

COCKPIT PANELS

Two control panels, designated Control Panel A and Control Panel B, are provided as shown in Figure 56. Control Panel A, which is the main control and display panel, provides the main power switch, the mode selection switches, and display of equipment status. Operational modes are selected on the basis of the acquire switch and the auto/manual switch, giving a total of four operational modes: (1) manual, (2) auto-track, (3) slave, and (4) cage. In the auto-track mode, the system can be in either coarse auto-track and/or fine auto-track, as indicated by the "TV beacon" and "fine track" lights. A more detailed discussion of the operating modes is given in a later section of this report.

Control Panel B provides control and display for the gimbal platform. These include meters for readout of gimbal position and a four-position thumb switch for gimbal rate commands.

POWER ON TV BEACON FINE TRACK

TEST POWER EXPERIMENT STATUS ACQUIRE AUTO

OFF OFF MANUAL

U P
L R
DN
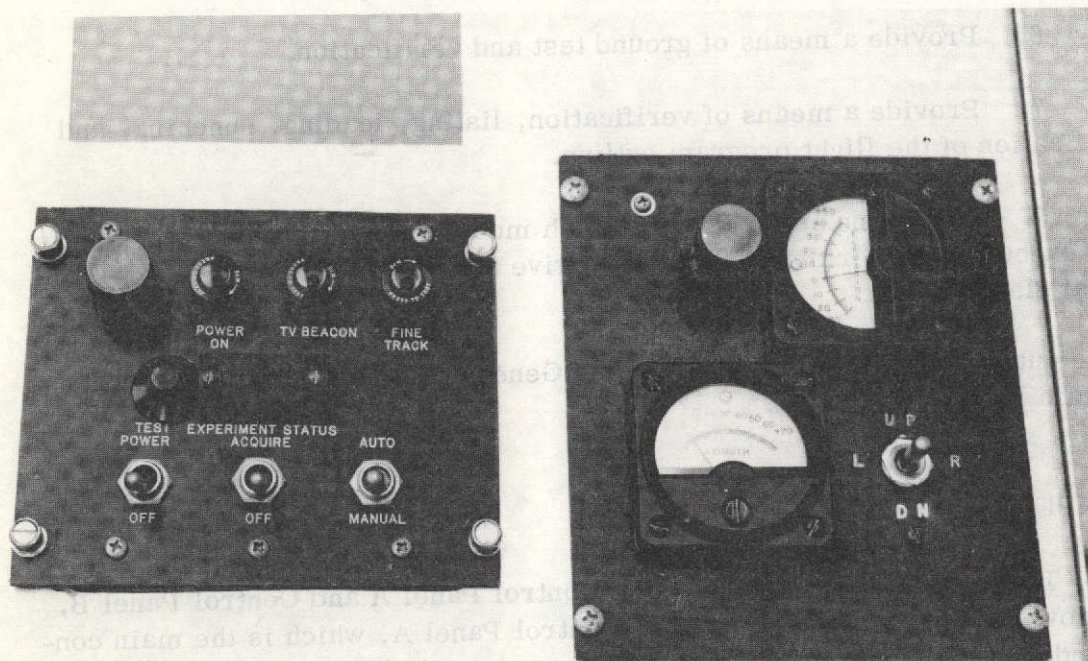
Figure 56. Control Panels A (left) and B.

AIRCRAFT INSTALLATION

General

The aircraft installation requirements are summarized as follows:

1. Experiment assembly containing AOCP and gimbal platform in bomb bay

2. A 68.6-cm (27-in.) diameter optical window in fairing

3. An aerodynamic fairing around window to reduce turbulence

4. REC in bomb bay

5. Experiment control panels in rear cockpit

6. A pilot directional indicator (PDI) in the front cockpit

7. The AR-1700 tape recorder in nose compartment

8. Five arrays of retroreflectors on the aircraft wings and fuselage

9. Electrical harness for interconnecting the system

10. An environmental control system for maintaining required pressure and temperature for the AOCP and REC

The weight breakdown of the airborne AVLOC equipment is listed in Table 8. The location of the equipment, except for the retroreflectors, is illustrated in Figure 57.
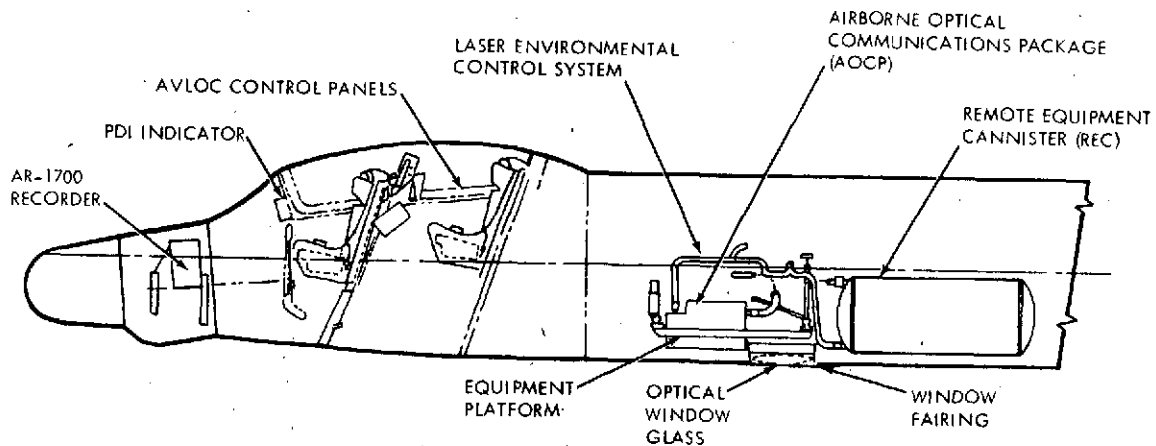
Figure 57. Profile of equipment installation.

Experiment Assembly

The experiment assembly served as a kind of optical bench for establishing the alignment of the AOCP and gimbal mirror to the aircraft coordinate system. The experiment assembly (as flown) is illustrated in Figure 58.

89

TABLE 8. AVLOC WEIGHT BREAKDOWN

Equipment	Weight (kg)
Experiment Platform	208
Platform Structure	80
Gimbal Mirror Platform	21.8
Isolation System	13.6
Environmental Enclosure	21.3
Experiment Package (AOCP)	71.7
Remote Electronic Equipment	212.3
Canister and Racks	40.8
Isolation System	2.27
Gimbal Control	3.63
Electrical Power	64
60-Hz Static Inverter	29
Power Relay Assembly	4.54
28-Vdc Converter	16.8
Measurement Distributor	4.54
Cables and Connectors	9.08
Onboard Computer System (SPC-16)	39.5
Data Management	31.7
Tape Recorder (Ampex AR-1700)	29.5
VCO Assembly	1.6
VCO Assembly Auxiliary	0.68
AUX Electronics	30.4
Experiment Ancillary Equipment	121.6
Electronic Canister Support	6.8
Experiment Truss	20.4
Window Glass	27.2
Window Structure and Fairing	29.5
Retroreflectors	6.8
Environmental Controls (Ducts)	11.3
Cables and Connectors	15.9
Control Panel	3.6
Total Weight	542
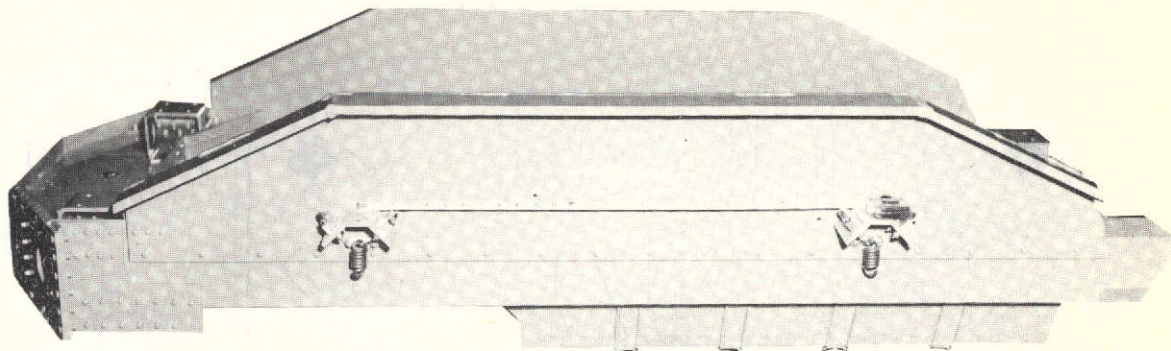
Figure 58. Experiment platform.

Figure 59 is a sketch of the experiment assembly isolation system. The experiment assembly installed in the aircraft is illustrated in Figure 60.

Optical Window

A 68-cm (26.75-in.) diameter by 4.23-cm (1.66-in.) thick optical window was installed in a removable fairing in the belly of the aircraft in a slightly side-looking manner, as illustrated in Figure 61. The window had a flatness figure of $\lambda/2$ with a parallelism of 9.6 μrad (2 arc sec) and weighed 36.7 kg (81 lb).

Remote Equipment Canister

The REC was suspended from the fuselage longerons in the aircraft by especially designed brackets, as illustrated in Figure 62.

Experiment Control Panels

The experiment control panels (described earlier in this report) were located in the rear cockpit compartment on the right-hand side, as shown in Figure 57.

Pilot Directional Indicator (PDI)

A block diagram of the PDI subsystem is shown in Figure 63. The PDI indicates to the pilot when he is flying the desired flight circle about the ground station. Slant range and angular coordinates to the aircraft are available from the GBAA and telescope to which it is mounted. The ground computer computes the position of the aircraft relative to its desired position and outputs a 0 to 5-V analog voltage proportional to the error.
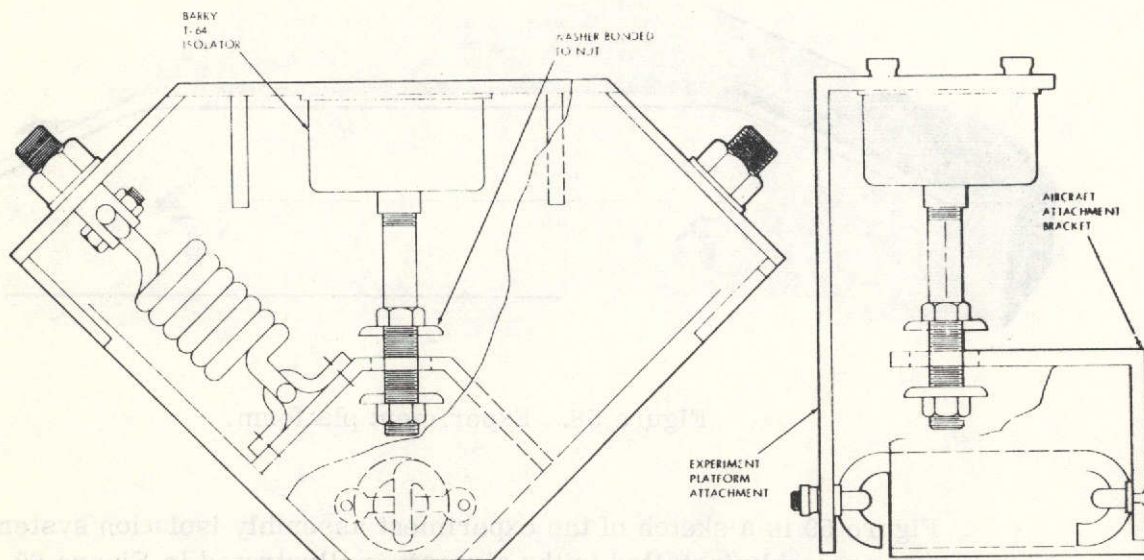
Figure 59. Isolation system.
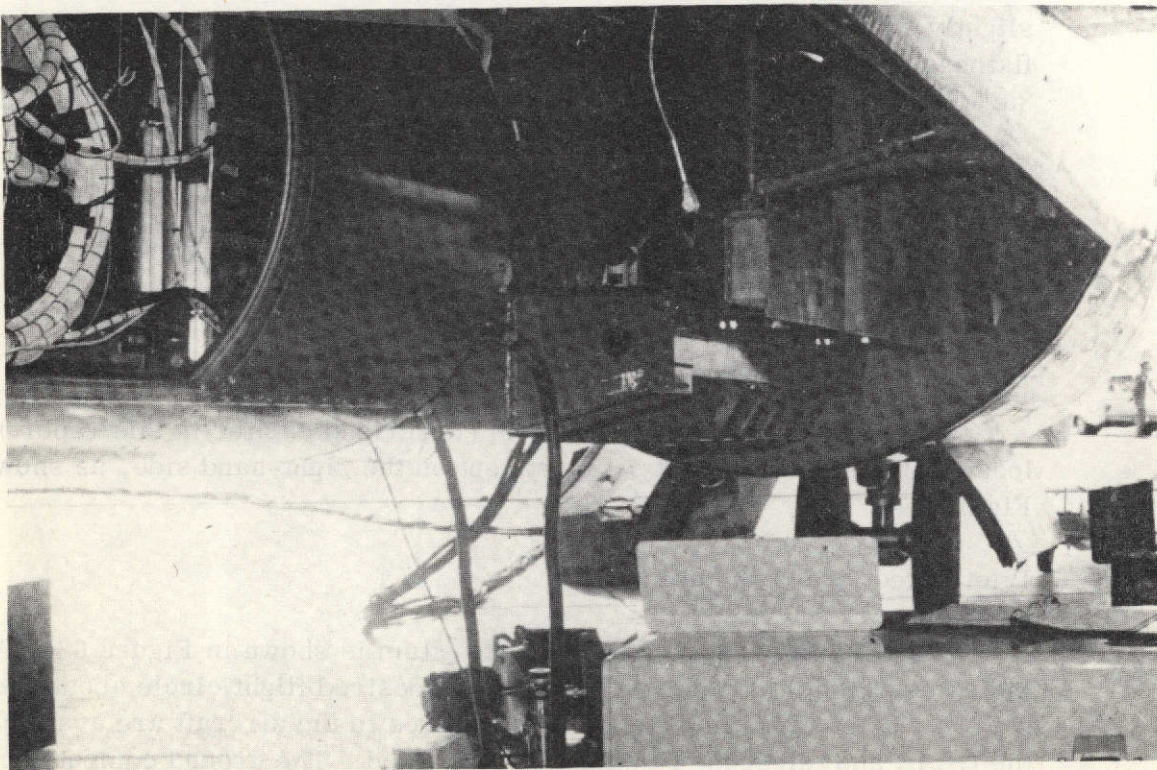
Figure 60. Experiment assembly installed in aircraft.
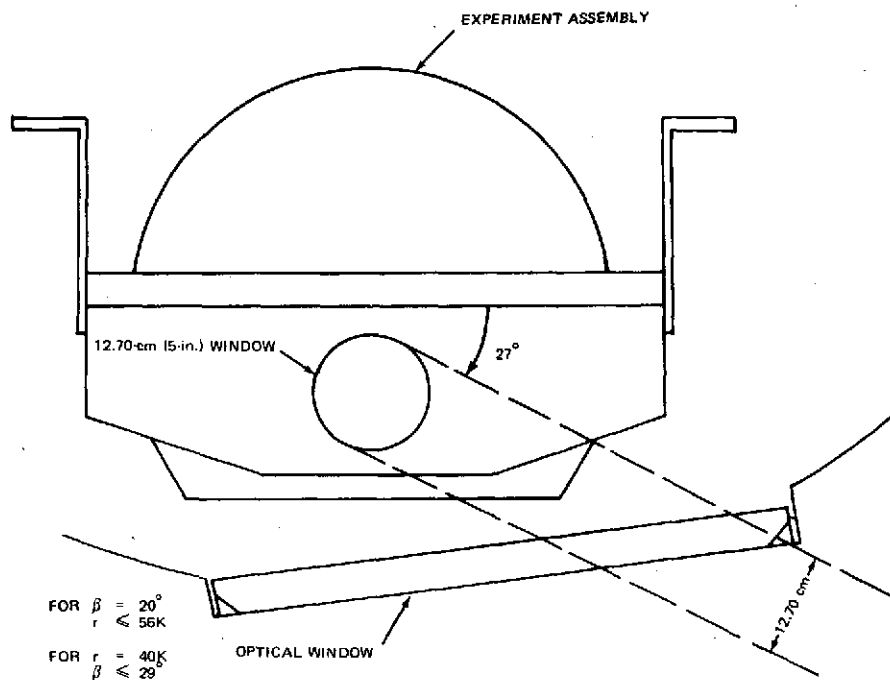
Figure 61. Experiment window.

The PDI is a +50 to 0 to -50-μA ruggedized meter movement supplied with a 50 multiplier resistor to make it into a +2.5 to 0 to -2.5 voltmeter. It is also supplied with a low-series resistance and shunting zener diode to protect the movement in the absence of an acquired signal. Consequently, the pilot display is a zero-center meter that points to the left for too-near distances and to the right for too-far distances. The pilot files "into" the needle, an operation which tends to keep the meter centered. The display scale in meters per volt is determined by the ground computation, as is the nominal range that gives a zero reading. With sufficient flexibility in the ground computer programming, the desired circle diameter can be varied as the ground operator desires.

Tape Recorder

The AR-1700 instrumentation recorder was installed on shock mounts in the pressurized area foward of the cockpit, as shown in Figure 57.
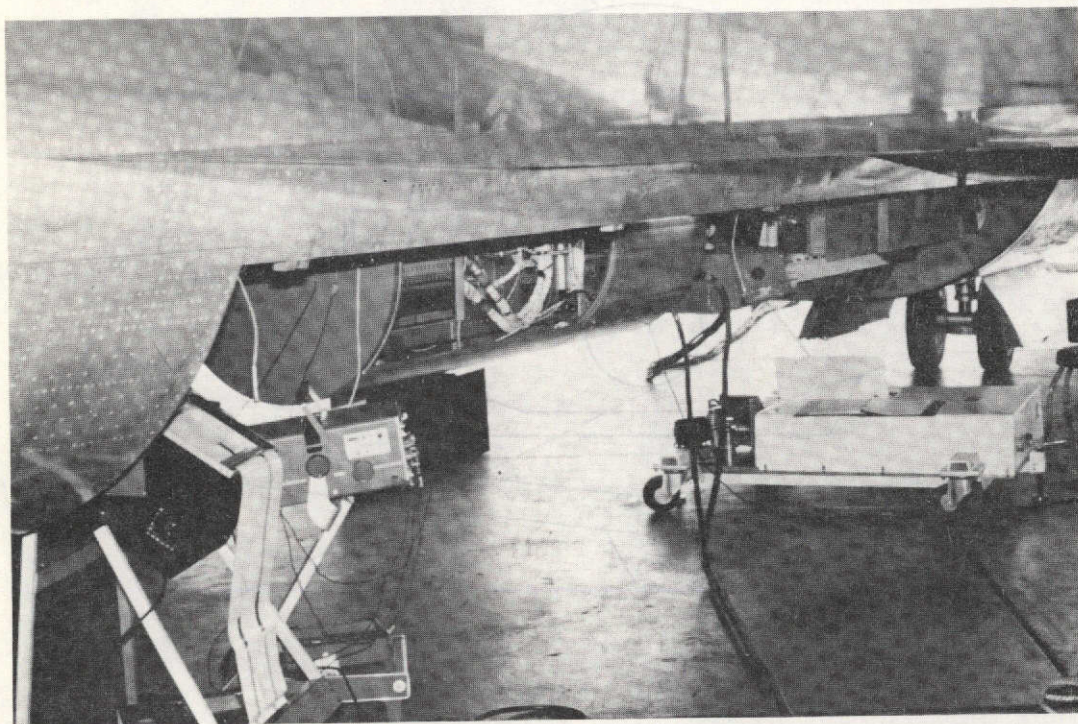
Figure 62. Canister installed in aircraft.

Retroreflectors

Five retroreflector arrays were installed on the aircraft wings and fuselage, as shown in Figure 2. One of the arrays is shown in Figure 64. Each individual retro has a diameter of 7.62 cm (3 in.). The retros are tilted from the horizontal at approximately 0.73 rad (42 deg) and the wing-mounted units are rotatable about the vertical through 6.28 rad (360 deg). For these angles the nacelle and fuselage do not obscure the GBAA laser beam for the range of parameter variations encountered during flight.

Environmental Control System

The environmental control system (ECS) is required to maintain a temperature of both the AOCP and the REC at 24° C ± 8.3° C (75° F ± 15° F) and to maintain a pressure equivalent to 7.62-km (25 000-ft) altitude or lower.

A sketch of the ECS is given in Figure 65. This system takes cold air from the cockpit cold-air duct, downstream of the refrigeration package in the left inboard wing, and routes it into the bomb bay for mixing with hot air. The hot air is taken from the engine bleed air supply and routed through a hot-air modulation valve before combining with the cold air. It is this valve, which is controlled by the temperature control unit, that determines the temperature of the mix. Past the modulating valve, the mixed air is split up, part of it passing through the AOCP and the remainder through the REC, before being recombined and dumped into the pressurized equipment bay.

The temperature control unit operates from either the inlet temperature sensor or the exit sensor, depending on whether the AVLOC system is on or off. With the system on, the inlet temperature is held to 24°C (75°F), whereas with the equipment off the exit temperature is held to 32° C (90° F). The reason for the latter provision is to assure against moisture condensation during descent from maximum altitude into a hot, humid atmosphere.
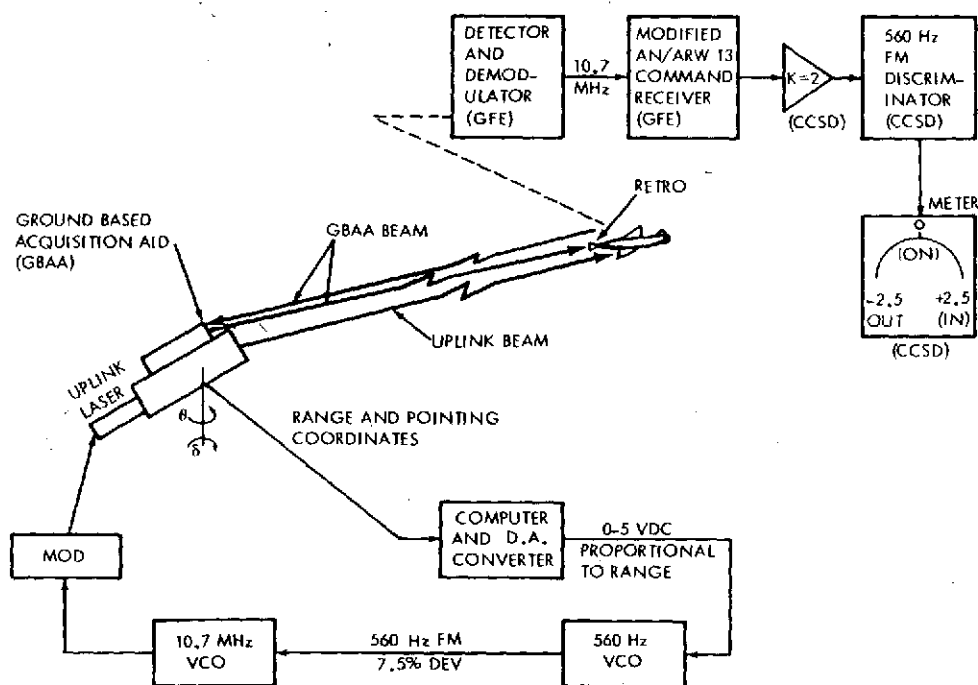
Figure 63. Block diagram of the PDI subsystem.
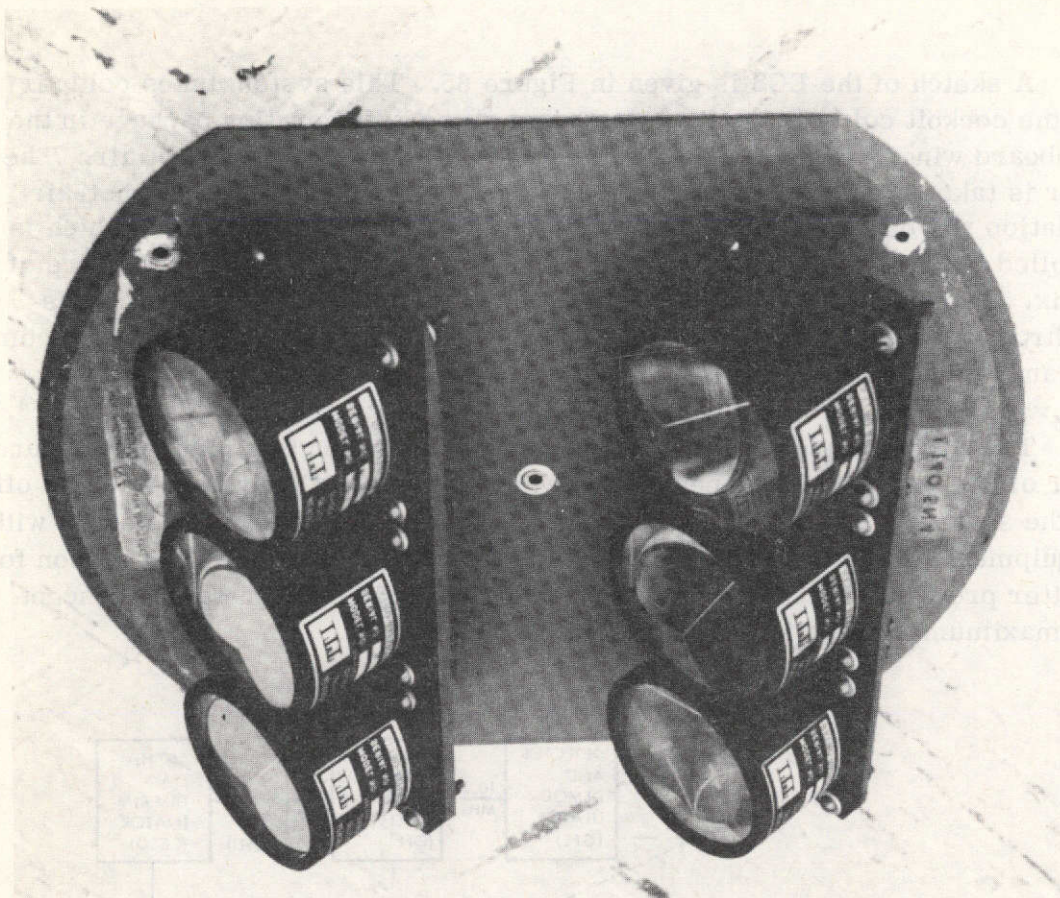
Figure 64. Retroreflector array.

A temperature control panel with temperature display meters is provided in the rear cockpit. This panel allows the selection of either manual or automatic operation. In the manual mode, the hot-air modulating valve can be controlled directly.

GROUND STATION

GENERAL DESCRIPTION

The AVLOC ground station is housed in a three-story observatory located on Madkin Mountain at Redstone Arsenal, Alabama, as illustrated in Figure 66. On the upper level of the observatory is a 61-cm
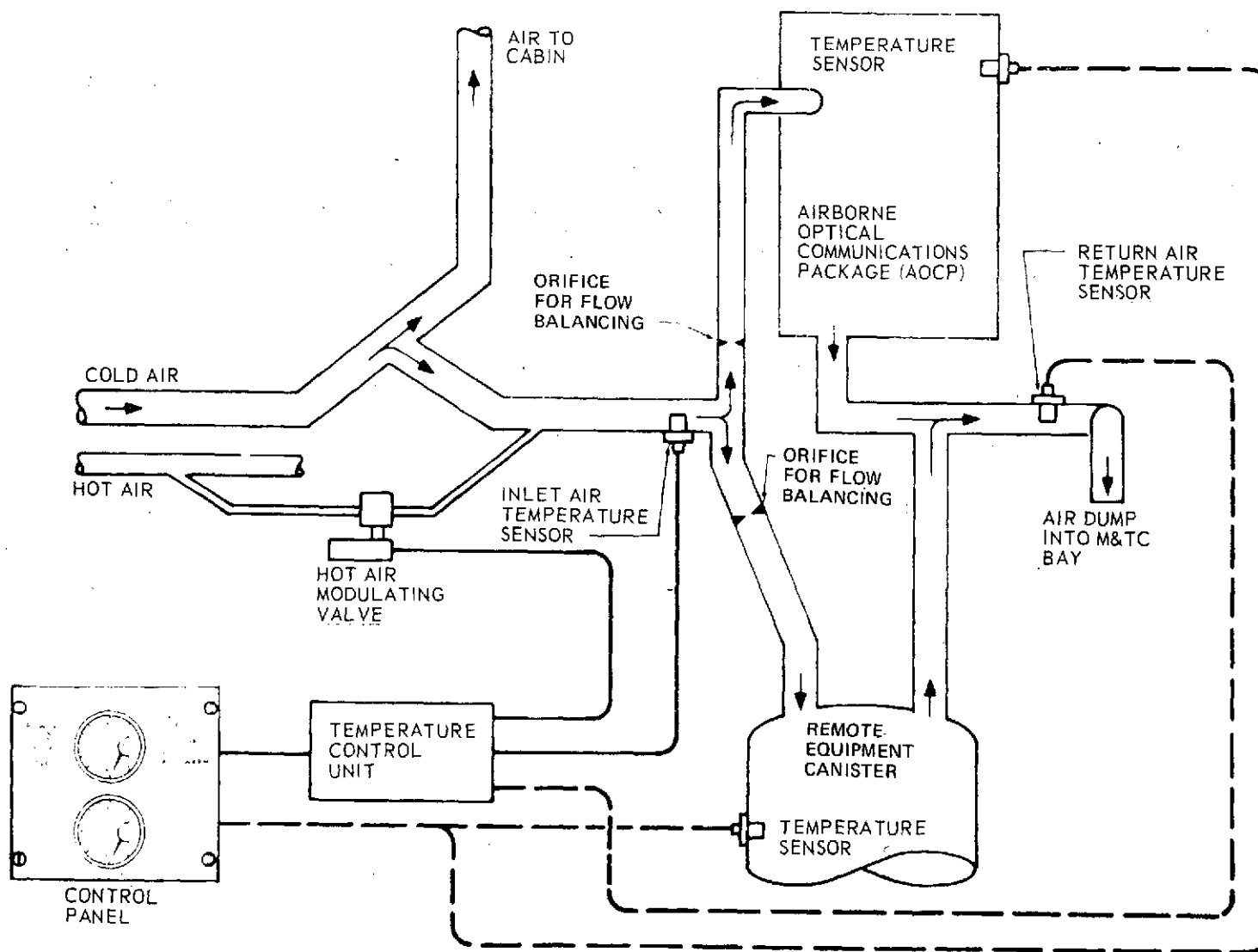
Figure 65. Environmental control system.
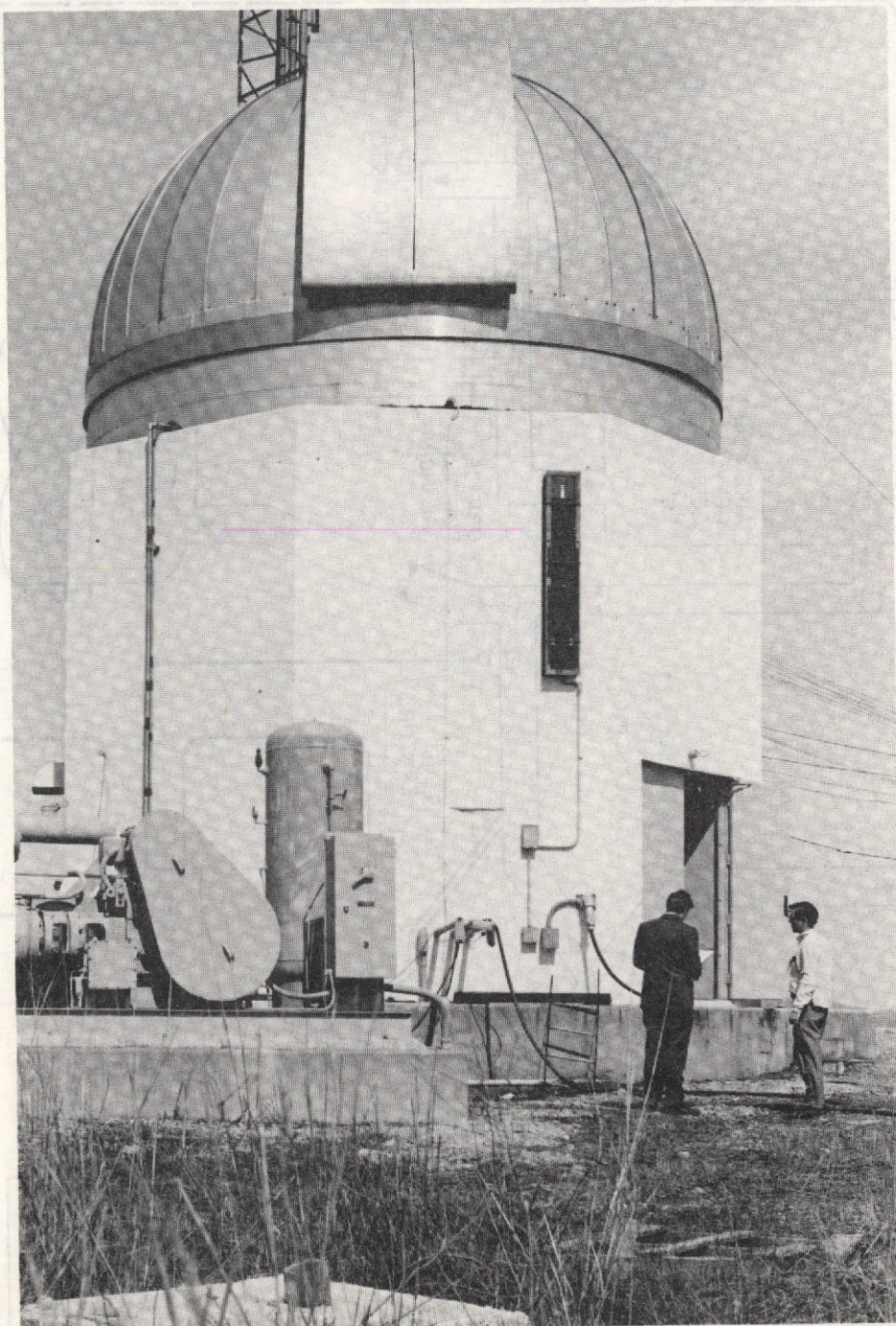
Figure 66. AVLOC ground station.

Cassegrainian telescope, with a Coudé focus, attached to a polar-equatorial telescope mount. The ground station laser transceiver is located at the Coudé focus of the telescope so that it transmits the 488-nm blue beacon laser and receives the 633-nm red AOCP laser beam through the telescope optics. Attached externally to the telescope tube and aligned parallel to the telescope optical axis is the GBAA 514.5-nm pulsed green laser acquisition radar transceiver. Also similarly attached are three television cameras, which are a part of a backup visual acquisition system. The second floor of the ground station houses the control computer, control consoles, the experiment monitoring and recording equipment, and most of the associated rack-mounted electronics. The VHF and UHF communications equipment, the laser cooling heat exchanger, and other housekeeping equipment are located on the ground floor. An observation trailer, for use by the principal investigators, is located adjacent to the ground station. Figure 67 is a simplified block diagram of the ground station.

MAJOR CAPABILITIES

Laser Beam Pointing

The telescope is capable of pointing the laser transceiver and GBAA laser beams with arc-second accuracy.

Target Acquisition

The GBAA pulsed laser radar is capable of acquiring a cooperative target entering a 10-deg radar fence propagated toward a prearranged acquisition point. When the GBAA receives returns from the retroreflectors attached to the underside of the target aircraft, it enters the track mode and furnishes pointing error information to the telescope drive. When pointing errors have been reduced sufficiently, mutual tracking between the ground station laser transceiver and the AOCP laser transceiver will be established. A backup visual acquisition system utilizes a 522-mrad (30-deg), a 174-mrad (10-deg), and a 17.4-mrad (1-deg) FOV TV camera system and a joystick controller to position the telescope for laser acquisition.

Target Tracking

Unlike the GBAA, which tracks reflections of its transmitted beam, the laser transceiver is designed to track the red laser transmitted from the target aircraft AOCP. Similarly, the AOCP is designed to track the blue beacon laser from the ground station. This mutual tracking capability is essential for conducting the AVLOC experiments.
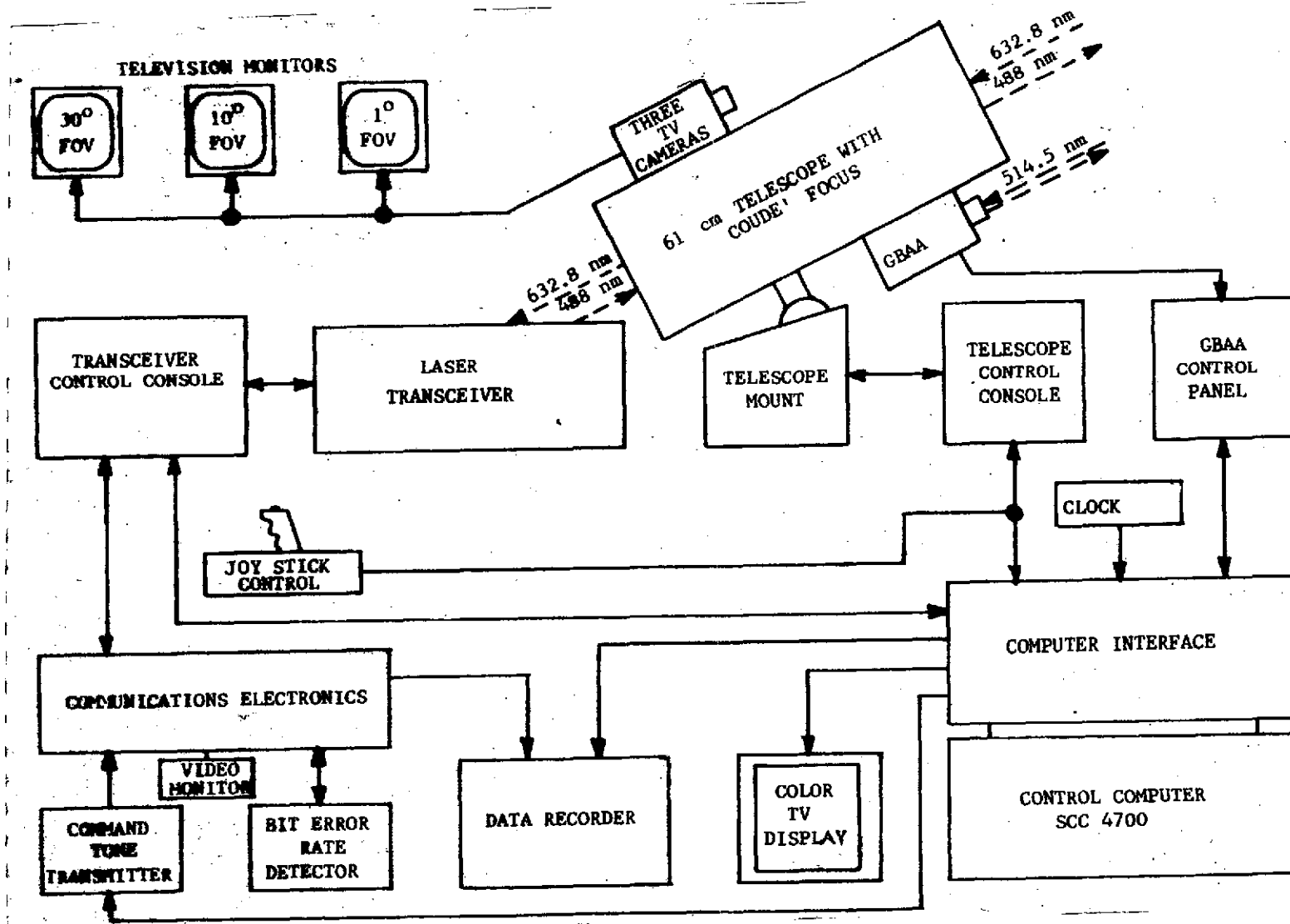
Figure 67. Ground terminal block diagram.

Laser Communications

After mutual tracking has been established, the ground station is capable of transmitting data on the blue beacon laser and receiving data transmitted from the AOCP on the red laser. Uplink communications consist of audio tone sequences, which are recognized as operation commands by the AOCP, and a variable frequency tone which is used to drive a PDI. Downlink communications are commanded from the ground station by tone sequences and can be either a 31-bit pseudorandom sequence, telemetry data, airborne recorder playback, or video from an airborne television camera.

Data Handling

All potentially useful data generated during experiments are recorded for future data reduction and analysis. PAM and frequency multiplexing are incorporated for maximum utilization of available recorder channels. Selected data are displayed graphically and alphanumerically at strategic locations over a closed-circuit TV system. Video recorders are utilized for recording these data for future reference. Decommutators and discriminators enable real-time monitoring of multiplexed telemetry data received over the downlink beam from the aircraft.

TELESCOPE

General

The telescope is a 61-cm Cassegrainian Coudé type manufactured by the Goerz Optical Company. It is sketched in Figure 68 and pictured in Figure 69. The f/3.5-paraboloidal primary mirror is 61 cm in diameter with a focal length of 2.13 m. The telescope is presently set up as a Coudé telescope. The hyperboloidal Coudé secondary produces an amplification factor of 8.57 to yield a system effective focal length of 13.29 m and a system f ratio of 30.

When the telescope was first installed, the wobble of the declination axis was 125 μrad (25 arc sec) peak to peak. After the telescope was disassembled and the declination axis bearing assembly was reworked, this wobble, which was caused by improper bearing preload and alignment, was much improved. The adjusting mechanism of the first folding flat (located at the intersection of the primary optical axis and the declination axis) was reworked to provide more accurate adjustment. The second folding flat (located at the intersection of the

FINDER SCOPE

SECONDARY ASSY.

TUBE

1st FOLDING
FLAT ASSY.

CUBE

PRIMARY MIRROR

DECLINATION SHAFT &
ELECTRICS

MIRROR CELL

TORQUE MOTOR

DECLINATION HOUSING

SHAFT &
ELECTRICS

DECLINATION
AXIS

POLAR AXIS

BASE

COUNTERWTS.

COUDÉ FOCUS
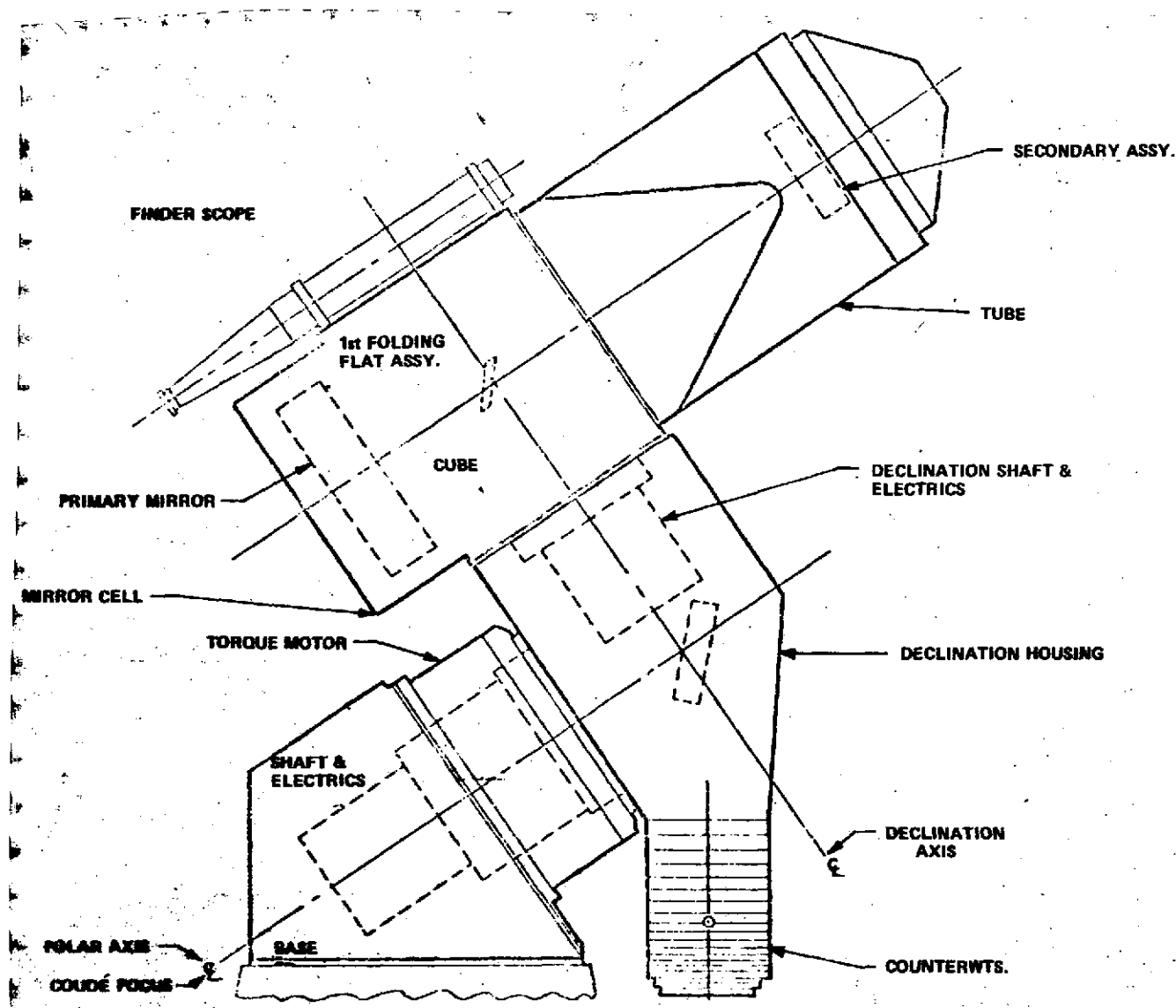
Figure 68. Sketch of 61-cm Cassegrainian/Coudé telescope.
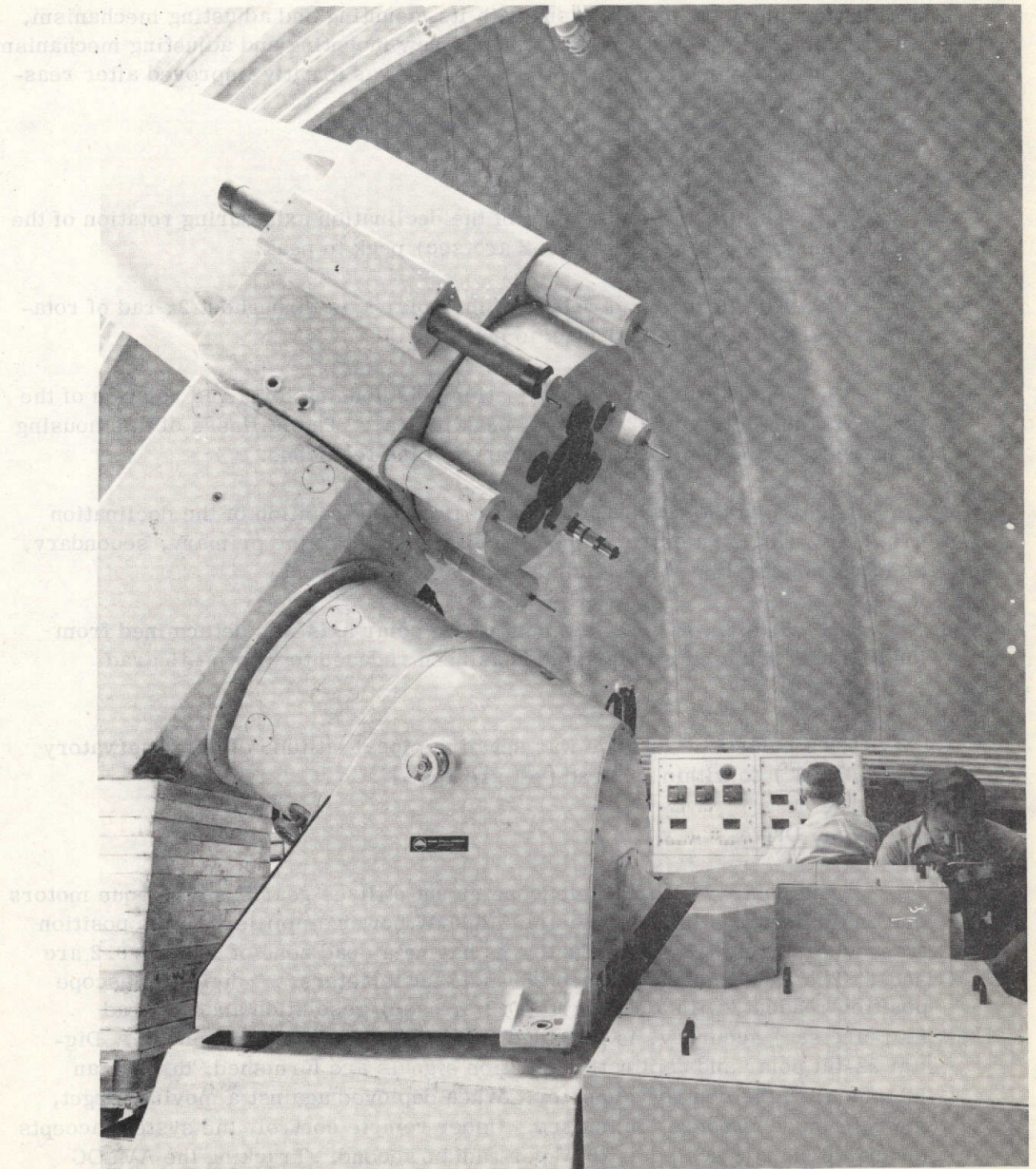
Figure 69. Photograph of 61-cm Cassegrainian/Coude telescope.

declination and polar axes), along with its mounting and adjusting mechanism, was replaced with a more rigid flat and a new mounting and adjusting mechanism. The mechanical performance of the telescope was greatly improved after reassembly and alignment.

The existing errors are as follows:

1.   The flexure and wobble of the declination axis during rotation of the declination axis only is 6 μrad (1.2 arc sec) peak to peak.

2.   The flexure and wobble of the polar axis throughout 2π rad of rotation is 4 μrad (0.8 arc sec) peak to peak.

3.   The flexure of the declination axis housing for π rad rotation of the polar axis is 160 μrad (32 arc sec) peak to peak. The stiffness of this housing is inadequate and limits the performance of the telescope.

4.   With the declination axis vertical, the rotation of the declination axis only reveals an error in the optical alignment of the primary, secondary, and first folding flat of 25 μrad (5 arc sec) peak to peak.

5.   The error in the azimuth of the polar axis was determined from the azimuth of the star Polaris and has been reduced to within $\pm$45 μrad ($\pm$9 arc sec).

[The polar axis latitude was set to the local latitude of the observatory (34° 40' 1.8") to within $\pm$5 μrad ($\pm$1 arc sec).]

Telescope Drive

The polar equatorial telescope mount utilizes gearless dc torque motors driven by linear, silicon transistor, 1600-W power amplifiers. The position transducers are 2048-pole Inductosyns having a dead zone of 1 μrad (0.2 arc sec). The rate transducers are 260-pole tachometers. A digital telescope position readout, with a 1.5-μrad (0.3-arc sec) resolution and $\pm$5-μrad ($\pm$1-arc sec) accuracy, is provided on the telescope control console. Digital 22-bit polar and declination position signals are furnished, through an interface, to the control computer. When deployed against a moving target, the rate mode of operation is used. Under remote control, the system accepts dc analog signals scaled at 20-V per radian/second. Tracking the AVLOC aircraft in a circular flight path over the ground station involves continuously changing telescope polar and declination drive rates from signals originating

104

in the GBAA or laser transceiver as X and Y coordinate analog position signals. The coordinate transformation and rate scaling are performed in the control computer, with necessary A/D and D/A conversions being performed in the computer interface rack. Figure 70 is a diagram of the telescope control circuits.

LASER TRANSCEIVER

The laser transceiver, shown in Figure 71, is described in this section according to the four principal functions it performs of providing:

1.   A tracking channel for 633-nm light and starlight

2.   A communications receiver for 633-nm light

3.   An argon laser transmitter channel

4.   A starlight observation channel

Tracking System

The laser tracker is capable of acquiring and tracking either an He-Ne laser beam or starlight over the central 0.87-mrad (3-arc min) field of the Coudé telescope. The remainder of the 8.7-mrad (30-arc min) field is folded into a star observation channel by a large folding flat having a central aperture which passes the 0.87-mrad (3-arc min) field to the tracking and communication system. Referring to Figure 72, the central 0.87-mrad (3-arc min) field is collimated by an off-axis parabolic mirror (M_1), which is tilted by 70 mrad (4 deg) to the telescope axis. This mirror produces a convenient diameter-collimated beam of 1.9 cm (0.75 in.), but more importantly it provides a relay pupil (image of the primary mirror) at a convenient position. The mirror M_1 lies beneath the main baseplate and reflects the light up to a flat mirror (M_2), which folds the collimated light into the horizontal plane of the main baseplate. The parabola produces an image of the primary mirror at the transfer mirror (M_3), and is arranged that way so that motion of this transfer mirror is analogous to moving the primary mirror. The amount of angular motion required of the transfer mirror is equal to one-half the field of view (0.44 mrad) multiplied by the ratio of the primary mirror diameter to the beam diameter at the transfer mirror.
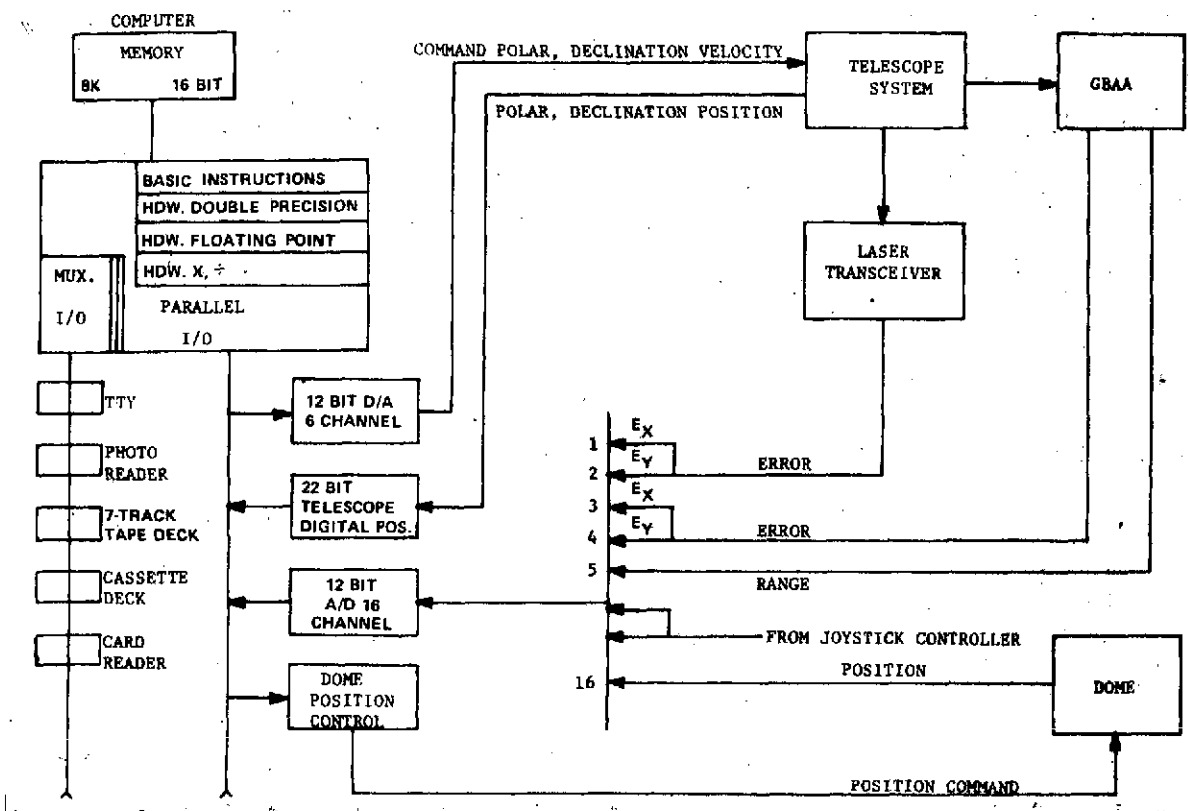
Figure 70. Telescope control block diagram.

Transfer Mirror Design

The transfer mirror assembly, shown in Figure 73, consists of a small mirror pivoted piezoelectrically about two orthogonal axes and maintains the incoming laser-beam image (or star image) in the center of the tracking field. The mirror is attached by thin metal hinges of two pairs of piezoelectric actuators situated across orthogonal diameters of the support structure.

The angular response of the mirror is essentially linear with applied voltage to each pair of drive elements. The calibration curve of Figure 74 shows that a voltage of approximately 100 V can provide an equivalent primary mirror angular range of 0.44 mrad (1.5 arc min). The control signals for the drive elements are derived from the up-down, left-right outputs of the four-quadrant photomultiplier tube used in the tracking system.
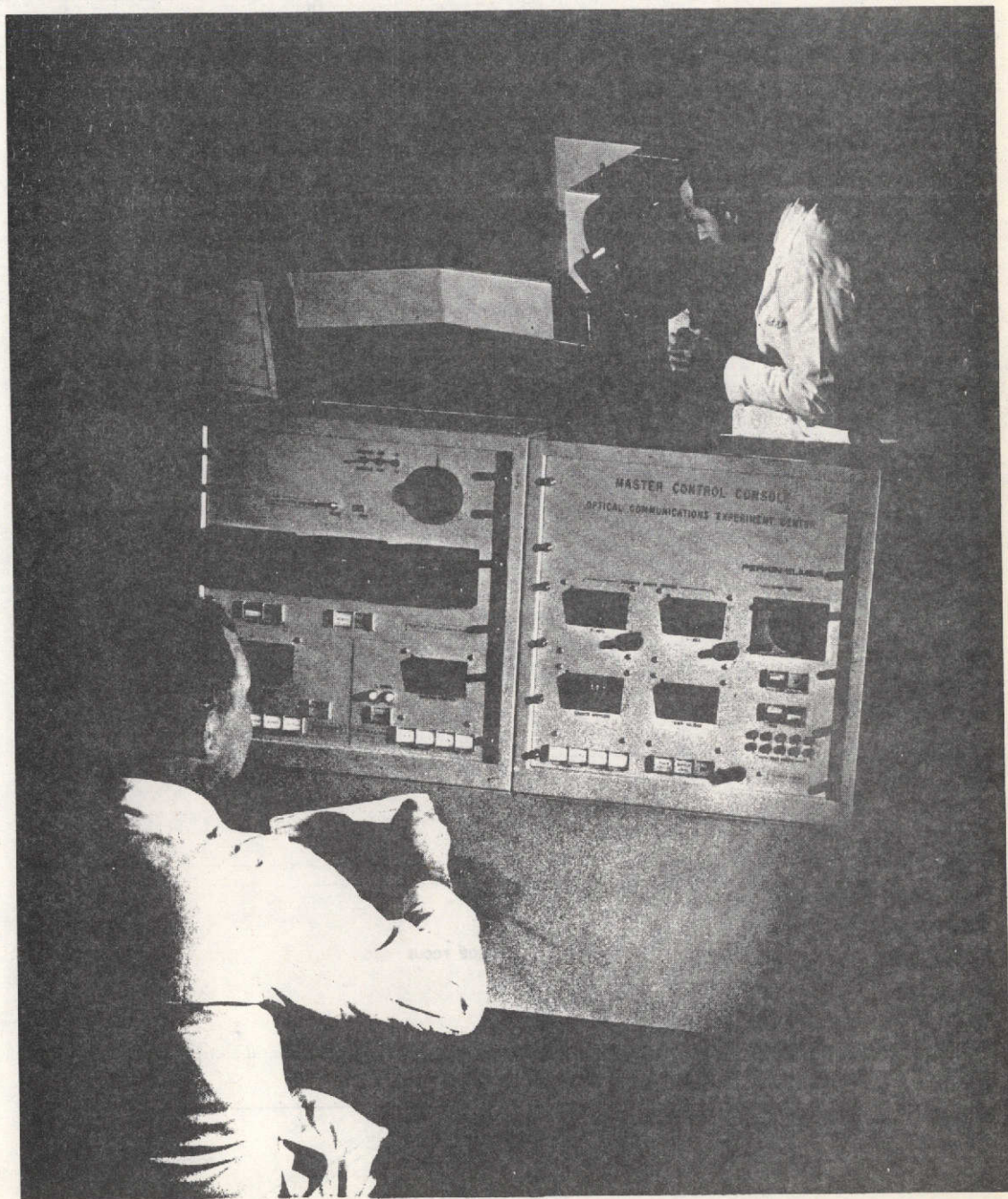
Figure 71.   Laser transceiver and control console.
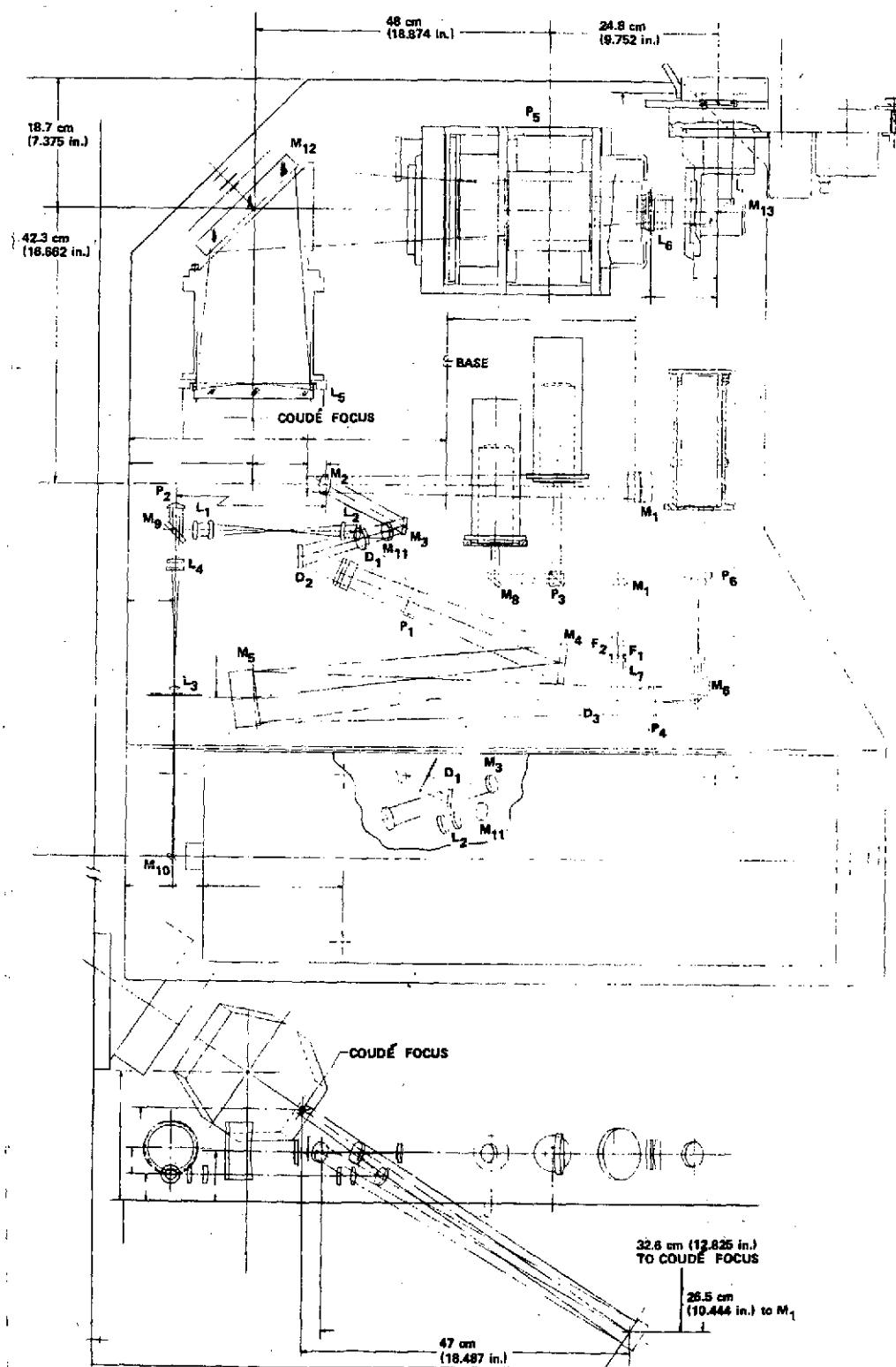
Figure 72. Optical layout of laser transceiver.

Angular Displacement (Arc Minutes)

1.5

1.0

0.5

50   100

Voltage (Volts)
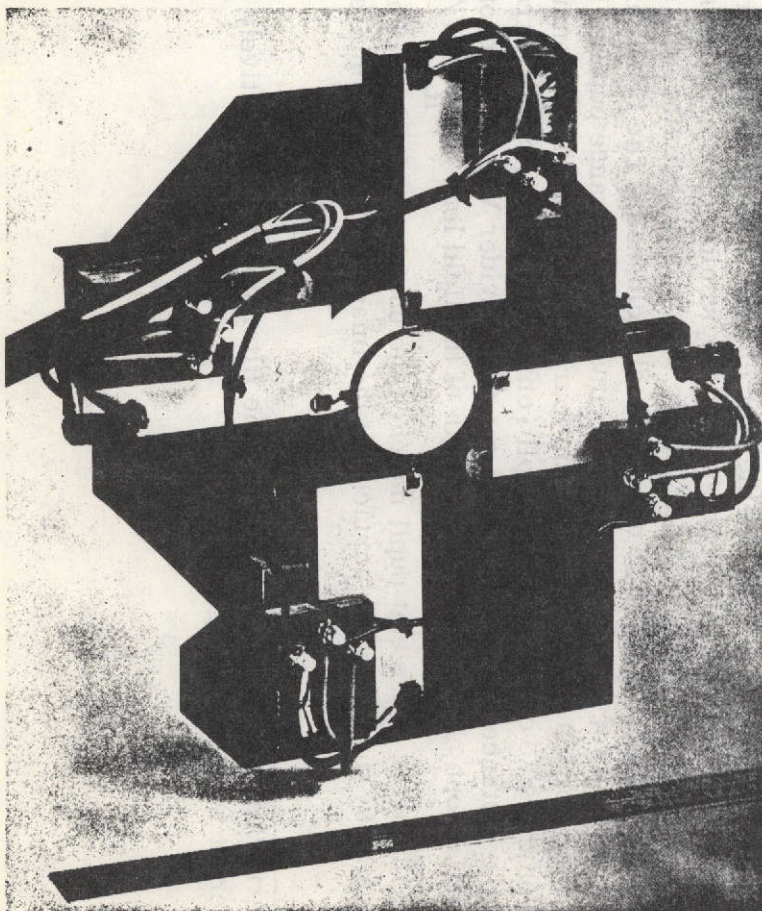
Figure 73. Transfer mirror servo drive assembly.
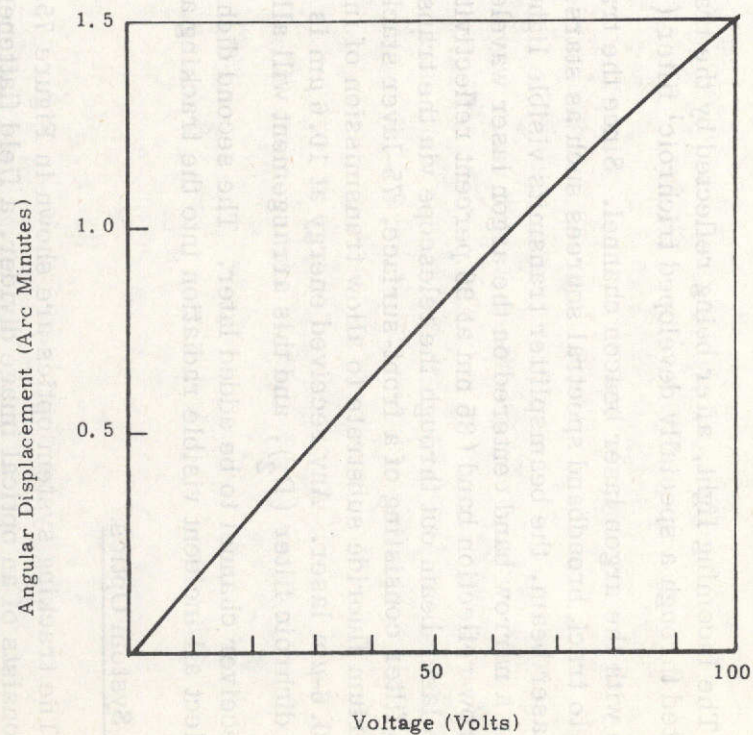
Figure 74. Transfer mirror calibration chart.

Beam Combining Dichroics

The incoming light, after being reflected by the transfer mirror, is transmitted through a specially developed trichroic[1] filter (D_1) which forms the interface with the argon laser beacon channel. Since the tracking system is designed to track broadband spectral sources such as stars, in addition to a 633-nm laser beam, the beamsplitter transmits visible light (75 percent) except for a narrow band centered on the argon laser wavelength (488 nm). This narrow reflection band (35 nm at 99 percent reflectivity) serves to route the argon laser beam out through the telescope via the transfer mirror. The trichroic filter consisting of a front-surface, 75-layer stack is vacuum coated onto a barium fluoride substrate to allow transmission of infrared radiation from a 10.6-μm laser. Any received energy at 10.6 μm is transmitted through a second dichroic filter (D_2), and this arrangement will allow a 10.6-μm tracker and receiver channel to be added later. The second dichroic filter is designed to reflect all incident visible radiation into the tracking and receiving system.

Tracking System Optics

The tracking system optics are shown in Figure 75. This fine guidance system consists of an optical image divider, a field flattener, and a four-quadrant photomultiplier tube. The optical schematic (Fig. 76) shows an on-axis diffraction image focused between the two elements of the field divider. The image is divided into four parts, and the four emerging cones of light are brought back parallel to the optical axis by the use of a pyramid-shaped field corrector. This allows the use of a narrow-band filter in the optical path since the energy is now passed through the filter at near-normal incidence. The two-element image divider also serves as a field lens to image the entrance pupil of the optical system (primary mirror) onto the four quadrants of the photomultiplier tube. Given the size of the entrance pupil (or relayed image of the entrance pupil) D, the distance of this pupil from the field divider V, and the photocathode size d, one chooses the focal length of the field lens as $f_R = dV/(d+D)$ so that the diameter of the exit pupil matches the photocathode size. The field lens is formed by the two outer surfaces of the image divider in combination,

---

1. The term "trichroic" is used because the filter operates selectively upon three different wavelength regions.

110
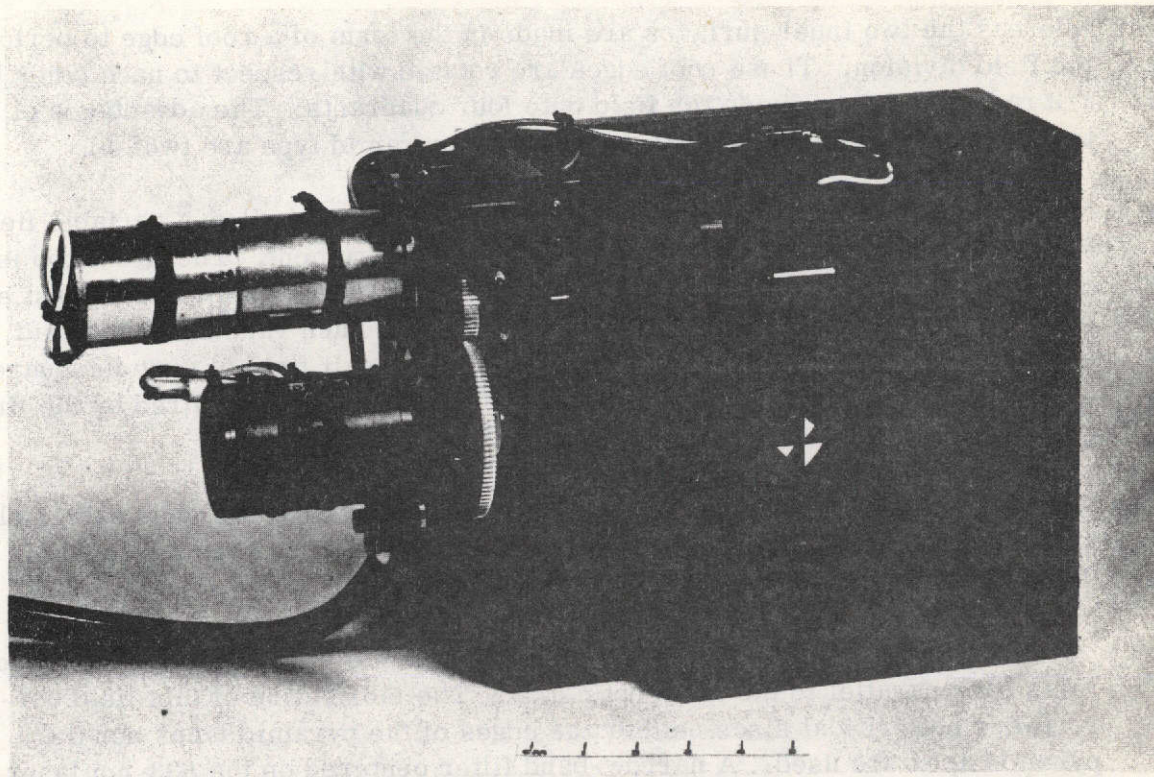
Figure 75. Tracker channel image divider
and variable field stop assembly.
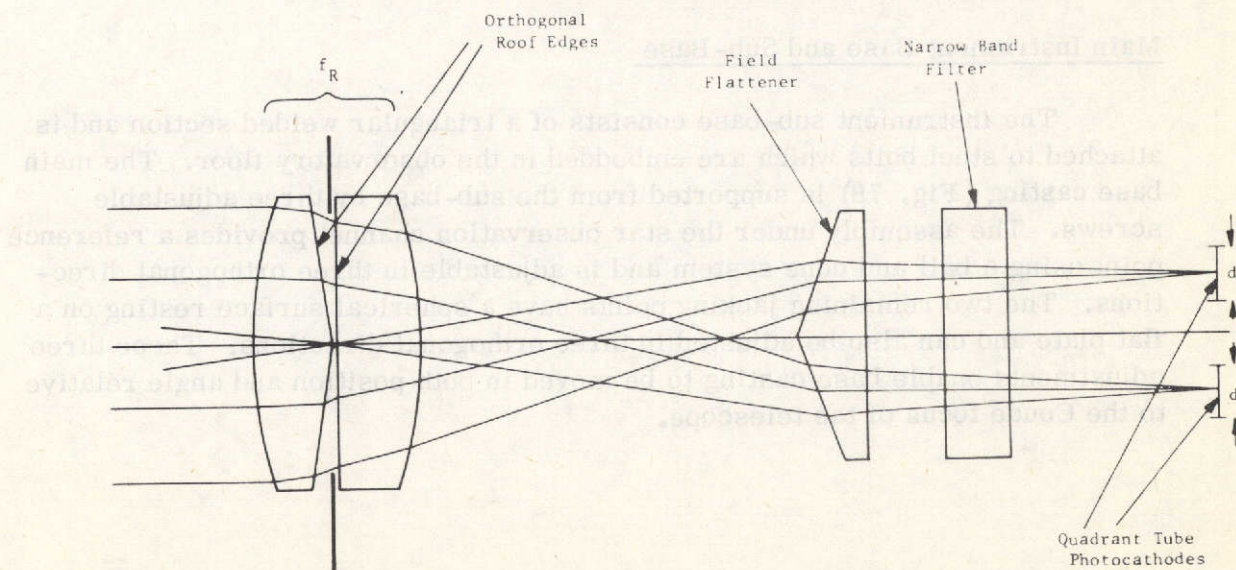
Figure 76. Optical field splitter and field corrector.

whereas the two inner surfaces are made in the form of a roof edge to perform the field division. These roof edges are rotated with respect to each other by $\pi/2$ rad (90 deg) to divide the field onto four quadrants. The advantages of this type of field divider over a conventional pyramid type are twofold:

1. The two elements are separated slightly and allow a variable field stop to be placed at the final focal plane of the instrument. The field stop is constructed as two thin metal vanes (0.0076-cm thick) which slide against each other and are driven by a common screw thread. Each vane has a $\pi/2$-rad (90-deg) slot cut in its end, and therefore the overall field of view is square but continuously variable from zero to the maximum field required by the fine guidance system [0.87 mrad (3 arc min)].

2. The edge where the image division occurs can be made extremely sharp since it consists of the intersection of two planes. Then the image is divided into four parts with negligible loss of light.

An optical field corrector is used to bend the light from the four quadrants back parallel to the main optic axis. The fabrication of this field corrector is not critical since neither the edges of the pyramid faces nor the pyramid apex are used. A narrow-band filter centered on the 633-nm laser line is placed between the prismatic field flattener and the quadrant multiplier phototube (QMP) and the filter can be removed for star-tracking purposes. This type of tracking system provides four partial images of the entrance pupil (Fig. 77). The varying states of illumination of these four images are used to electronically sense the image position. After acquisition and tracking have been accomplished, the instrument can be used to demodulate a 633-nm received beam in the communication channel.

Main Instrument Base and Sub-Base

The instrument sub-base consists of a triangular welded section and is attached to steel bolts which are embedded in the observatory floor. The main base casting (Fig. 78) is supported from the sub-base by three adjustable screws. The assembly under the star observation channel provides a reference point using a ball and cone system and is adjustable in three orthogonal directions. The two remaining jacking points have a spherical surface resting on a flat plate and can also be adjusted in three orthogonal directions. These three adjustments enable base casting to be moved in both position and angle relative to the Coudé focus of the telescope.

112
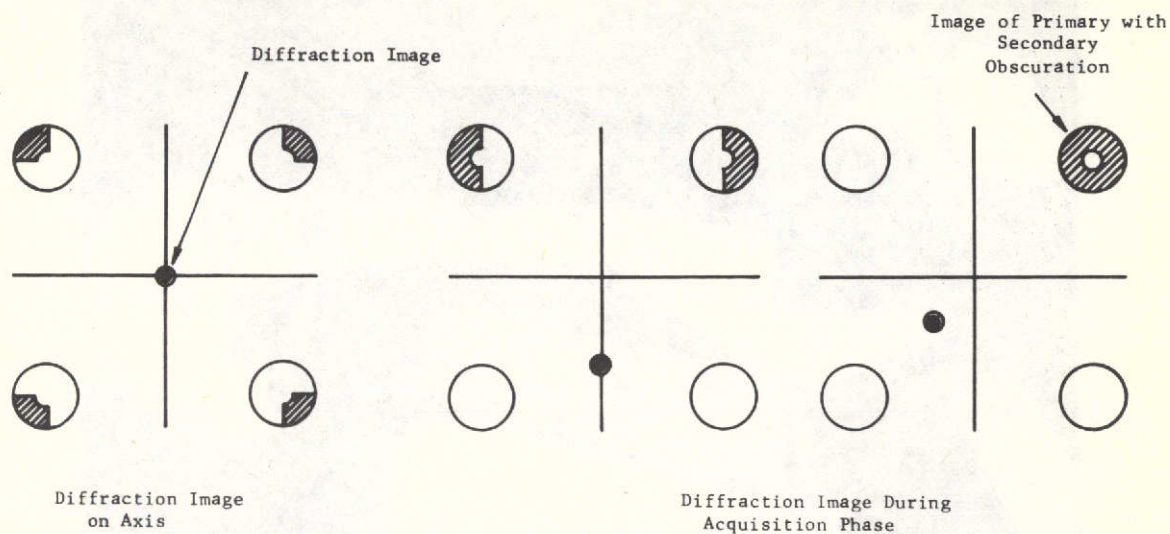
Figure 77. QMP illumination conditions during acquisition and tracking.

Experiment Master Console

The master console shown in Figure 79 remotely controls all tracking, receiving, and laser beacon functions with the exception of the power of the GFE argon laser.

GROUND BASED ACQUISITION AID

System Functional Description

The GBAA system hardware is pictured in Figure 80. Figure 81 is a block diagram of the system. The GBAA has the capability of acquiring a cooperative target consisting of a high-flying aircraft carrying a cube corner retro-reflector array. The target is acquired at a slant range of from 9.15 km (30 000 ft) to 30.5 km (100 000 ft) while traveling at an angular velocity $\leqq 8.7$ mrad/sec (0.5 deg/sec). Target acquisition is accomplished by the interception of the aircraft's retroreflectors by the GBAA Search scan. As illustrated in Figure 82, the Search or Fence scan is one in which a 174-by 1.6-mrad (10-by 0.09-deg) solid angle is scanned in the far field simultaneously by both transmitter and receiver. The 174-mrad (10-deg) fence is scanned in 128 overlapping steps. As the aircraft passes through the Search scan, a transmitter beam reflection from the cube corner's retroreflectors is
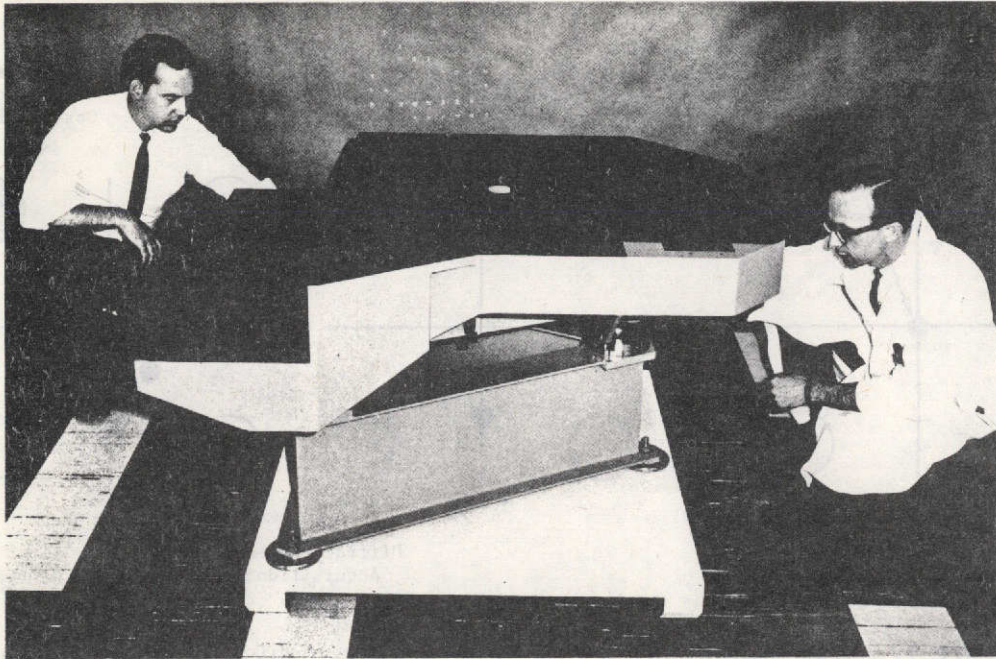
Figure 78. Main base casting and instrument sub–base assembly.
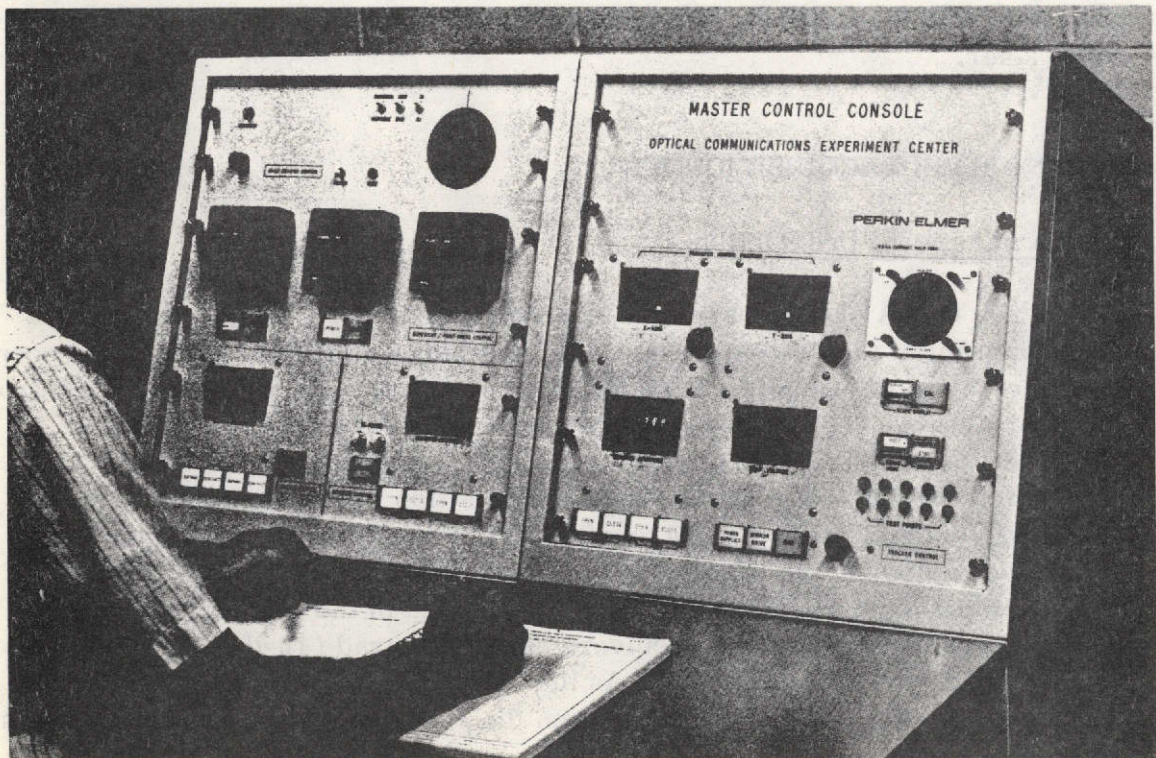
Figure 79. Master control console, advanced laser tracker,
and transmitter.
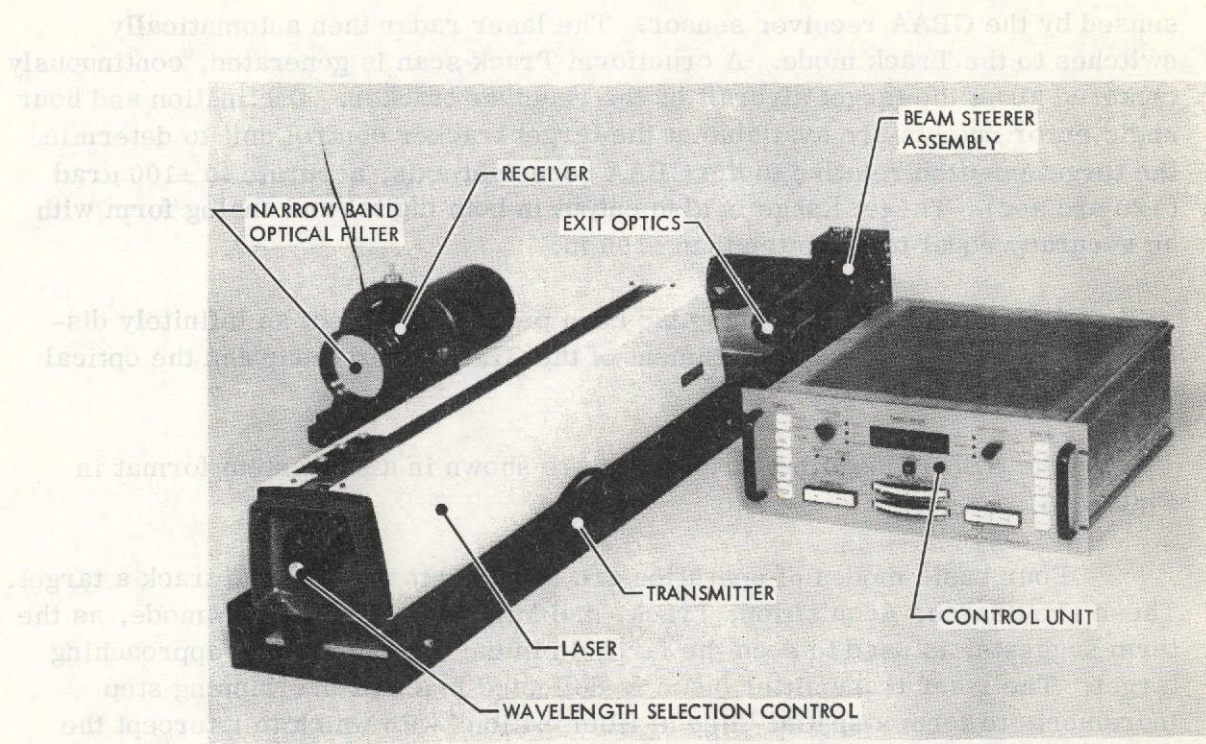
Figure 80. Photograph of GBAA.
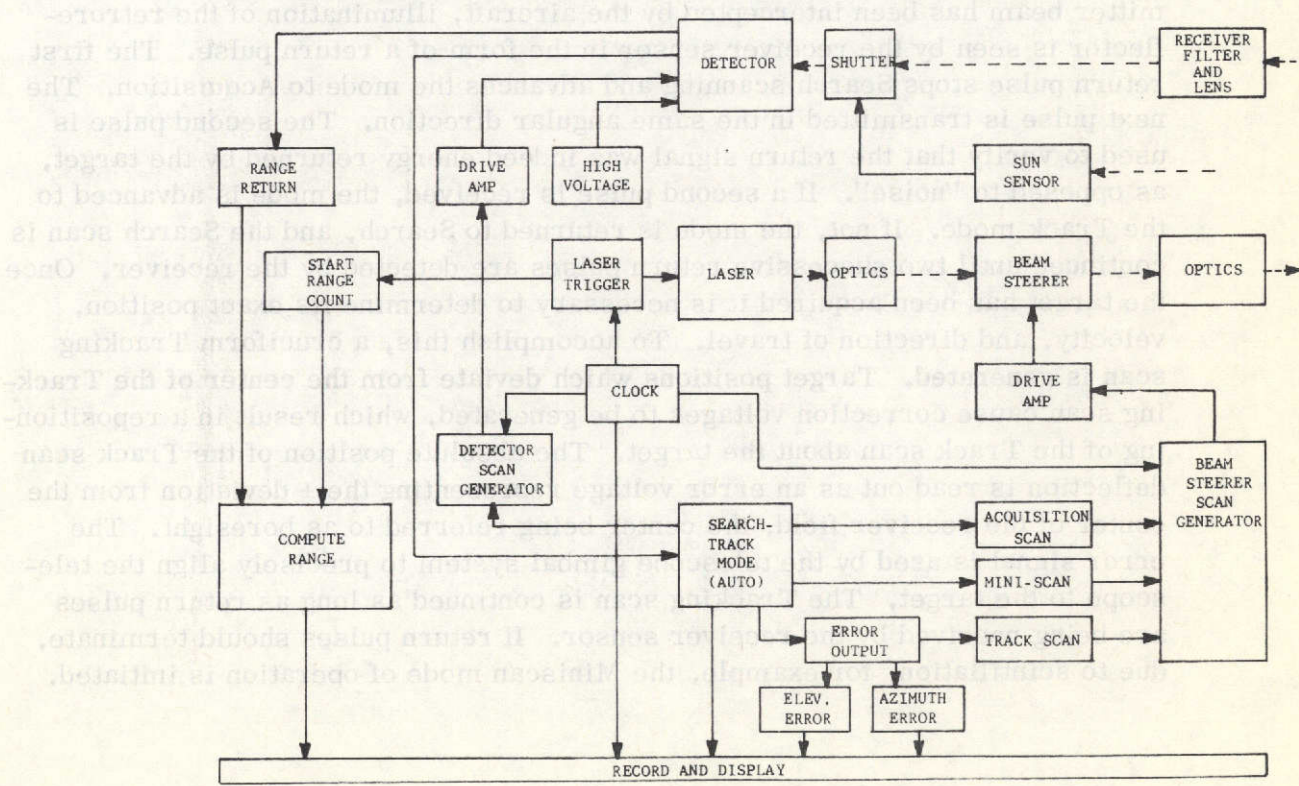
Figure 81. Block diagram of GBAA.

sensed by the GBAA receiver sensor. The laser radar then automatically switches to the Track mode. A cruciform Track scan is generated, continuously centered about the target aircraft by the receiver tracker. Declination and hour angle error outputs are available at the target tracker control unit to determine the target position relative to the GBAA boresight axis, accurate to ±100 μrad (±20 arc sec). Target Range is also output in both digital and analog form with an accuracy equal to or better than ±100 m.

A Star tracking mode has also been provided to affect an infinitely distant point source for mutual alignment of the GBAA laser radar and the optical communications telescope.

The GBAA operating parameters are shown in a subsystem format in Figure 83.

Four basic modes of operation are required to acquire and track a target. These are Search, Acquisition, Track, and Miniscan. The Search mode, as the term suggests, is used to scan the far field in the direction of the approaching target. The laser transmitter beam is deflected in small overlapping step increments to form a spatial "line of illumination" with which to intercept the approaching aircraft. In a similar fashion, the receiver sensor's IFOV is scanned across the sensor photocathode in overlapping steps such as to be surrounded by the line being scanned by the transmitter in the far field. Once the transmitter beam has been intercepted by the aircraft, illumination of the retroreflector is seen by the receiver sensor in the form of a return pulse. The first return pulse stops Search scanning and advances the mode to Acquisition. The next pulse is transmitted in the same angular direction. The second pulse is used to verify that the return signal was indeed energy returned by the target, as opposed to "noise". If a second pulse is received, the mode is advanced to the Track mode. If not, the mode is returned to Search, and the Search scan is continued until two successive return pulses are detected by the receiver. Once the target has been acquired it is necessary to determine its exact position, velocity, and direction of travel. To accomplish this, a cruciform Tracking scan is generated. Target positions which deviate from the center of the Tracking scan cause correction voltages to be generated, which result in a repositioning of the Track scan about the target. The absolute position of the Track scan deflection is read out as an error voltage representing the ± deviation from the center of the receiver field, the center being referred to as boresight. The error signal is used by the telescope gimbal system to precisely align the telescope to the target. The Tracking scan is continued as long as return pulses are being received by the receiver sensor. If return pulses should terminate, due to scintillation, for example, the Miniscan mode of operation is initiated.

116

Figure 82. GBAA aid.

RECEIVER OPTICS ASSEMBLY
- LENS – 65 mm f/0.75, 365-mrad (21 deg) FOV
- FILTER – 514.5 nm BANDPASS
- PROTECTIVE SHUTTER – INTERFERENCE

RECEIVER SENSOR
- IMAGE DISSECTOR – F4012 – S-20
- HV POWER SUPPLY – -2.4 kV
- FOCUS CURRENT REGULATOR – 230 mA
- PREAMPLIFIER – 50 kHz BANDPASS

TARGET TRACKER
- ACQUISITION SCAN – 128 STEP, ± 87-mrad (± 5 deg)
- TRACK SCAN – ± 16 STEP ELEV./AZIM.
- DEFLECTION GENERATOR – 150 mA/in.
- LASER TRIGGER – 2.5 V PEAK 2 μs PULSE WIDTH
- ERROR O.P. – ± 5.0 V INTO 100 Ω LOAD
- BEAM STEERER SCAN GEN. – 1 kHz LOW-PASS
- TIMING CONTROL – DIGITAL

READOUT & CONTROL
- ELEVATION ERROR – ± 87 mrad (± 5 deg)
- AZIMUTH ERROR – ± 87 mrad (± 5 deg)
- SEARCH-TRACK MODE – AUTOMATIC SWITCH
- TEST – STATIC
- SWEEP POSITION SELECT
- ON-OFF – POWER

BEAM STEERER
- POWER DRIVE AMPLIFIER – ± 5.0 V FULL DEFLECTION
- TRANSMIT/RECEIVER TRACK – POT. ADJUSTMENT (DEFLECTION/ADJUSTMENT)

BEAM STEERER
- PIEZOELECTRIC DEFLECTOR – ± 11.6 mrad (± 40 min.)
- TRANSMITTER OPTICS – 174 x 174 mrad (10 x 10 deg) FAR FIELD DEFLECTION

TRANSMITTER
- ARGON ION LASER – TEM_{00} 514.5 nm
- PULSED DRIVER – 1 kHz PULSE REPETITION RATE 15 μm PULSE WIDTH

RANGING SYSTEM
- OUTPUTS – ANALOG, DIGITAL
- RANGE 30.5 km (100 000 ft)
- RANGE MONITOR – VISUAL

Figure 83. GBAA system parameters.

117

In Miniscan, a small raster-type field is scanned to relocate the target. It consists of a search pattern covering a field of approximately 11.3-mrad (0.65-deg) square. The first return pulse received while in Miniscan resets the mode control to the Track mode, and target tracking continues. If no return is received within 12 Minifield scans, the mode control is recycled to the Search mode, where the field is once again searched in the original 174-mrad (10-deg) line scan, or a 174- by 174-mrad (10- by 10-deg) raster-type scan, as selected by the operator. The Acquisition scan sequence is depicted in Figure 84.

Fence Scan

In the Search mode, the transmitter and receiver search the far field using a line scan consisting of 128 overlapping steps covering a 174-mrad (10-deg) angle. The Fence scan can be positioned anywhere in a 174- by 174 mrad (10- by 10-deg) FOV.

The control unit provides selectable search scan options that will

1. Search the total 174- by 174-mrad FOV — Raster scan

2. Search a single 174-mrad line — Fence scan

3. Search a specific 174-mrad — Offset

4. Search a 174-mrad fence at elevation boresight — Center scan

All scans — Acquisition, Track, and Miniscan, are digitally generated using TTL logic components. The Acquisition scan generator is seven-bit binary up-on counter which counts from 0 to a maximum count of 128 and back to 0. This produces a 128-step sawtooth waveform Fence scan with a cycle rate of approximately 8 Hz. The Fence scan searches the field from left to right at a stepping rate of 1 kHz. At the end of each search line the scan is rapidly retraced at a rate of 8 kHz. The Fence scan is positioned at a zero elevation angle by momentary depression of the Center scan button on the control unit. It may also be positioned to an elevation angle of 65.45 mrad (-3.75 deg) by selection of Offset. These two conditions are attained as the elevation acquisition counter is set to either logic No. 64 or logic No. 16, respectively. When in the Fence mode, the elevation acquisition counter is held static subsequent to position selection.

118
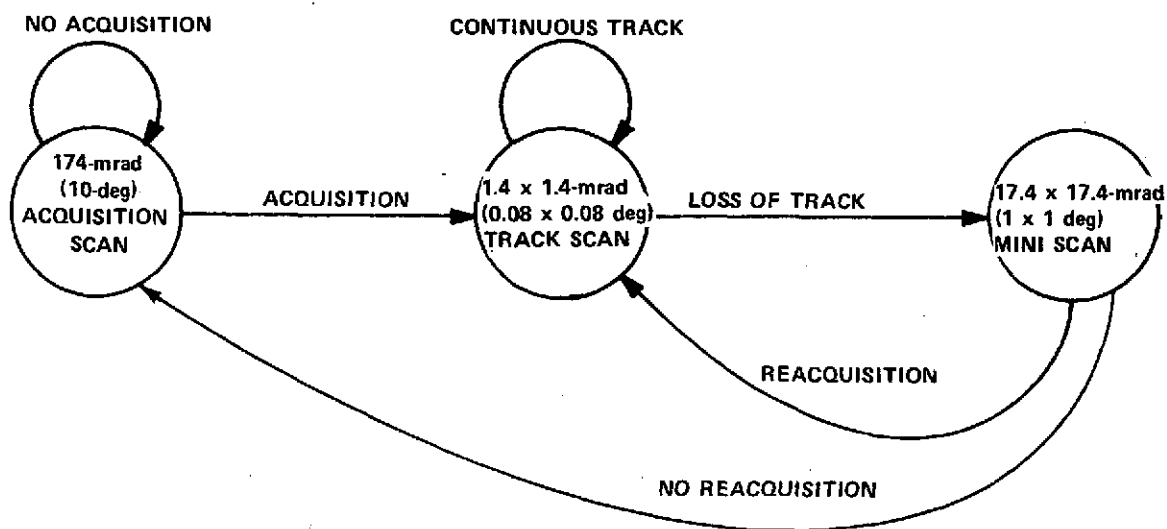
Figure 84. GBAA automatic scan sequence.

Raster Scan

When Raster is selected, the azimuth counter continues generating the 128-step Fence scan. At the end of each azimuth line, the elevation acquisition counter is advanced one count, resulting in an elevation deflection of 1.4 mrad (0.08 deg). This generates a raster-type scan which searches the total 174-mrad (10- by 10-deg) FOV. At the end of each field scan the elevation counter is rapidly down counted to count No. 0. This produces an elevation sawtooth scan waveform of 128 steps which repeats at a rate of 16 Hz.

If at any time during the Raster scan the Fence mode is selected, the elevation drive will cease, and the scan will continue in azimuth at that point in the FOV. In this manner, the Fence scan can be positioned anywhere in the 174- by 174-mrad FOV by selection at the control unit.

Track Scan

When the first target return pulse is detected, the operating mode switches from Search to Acquisition. In the Acquisition mode, the clock pulse drive to all deflection scan generators is inhibited, and a second pulse is transmitted. If the initial pulse was a false alarm (noise pulse), the mode automatically returns to Search, and the Fence scan continues. When two successive return pulses are detected, the mode switches from Acquisition to Track.

119

In the Track mode, elevation and azimuth sawtooth scans are generated as pictured in Figure 85. The instantaneous field of view is deflected about the target by a Track scan consisting of ±16 steps; each step equals 0.09 mrad (0.005 deg). The track scan alternately deflects in elevation and azimuth to produce the ±1.4-mrad (0.08-deg) cruciform pattern. The Track waveform initially positions the transmitter and receiver on the target and scans off the target. In this manner, the on-target time (above and below and to the right and left) is weighed to determine the actual target position.

As previously mentioned, there are ±16 track steps of 0.09 mrad (0.005 deg) each, which result in a total deflection equivalent to ±1 acquisition step. This deflection is obtained by preceding each acquisition counter with a four-bit track counter. Sixteen track step increments are therefore necessary to advance the acquisition counters one step. The step rate remains at 1 kHz, producing a complete cruciform scan at 15 Hz. Subsequent to Track scanning off the target, the Track scan is rapidly retraced in 250 μsec as it is driven with a 64-kHz retrace clock pulse.

Track scanning continues, provided that the target ramains in the FOV and an appropriate signal-to-noise level is maintained. If the signal is interrupted for a period of two complete cruciform Track scans, the mode switches from Track to Miniscan.

Minisearch Scan

The Minisearch scan generator produces the pattern shown in Figure 85. It covers a far field area of 11.1 by 11.1 mrad (0.64 by 0.64 deg). Typical elevation and azimuth miniscan waveforms are shown in Figure 85. The azimuth eight-step scan and retrace sawtooth waveform has a cycle rate of 120 Hz. The elevation scan cycles at 15 Hz. The 8 by 8 Acquisition step Miniscan is generated as the four-bit track counters are driven with 16 clock pulses per each acquisition step. Each acquisition step, for both transmitter beam deflector and receiver, is generated in 16 0.09-mrad (0.005-deg) increments. The finer stepping granularity reduces the beam deflector's tendency toward overshoot and ringing, which might be encountered when using larger step increments.

The elevation and azimuth step sequencing is controlled by a flip-flop with control counter synchronization. The first target return pulse received when in Miniscan mode switches the mode to Track. If no target is sensed within 12 minifields, the mode returns to Search. When reverting to the Search mode, the scan is either Fence or Raster, as determined by selection at the control unit.

120
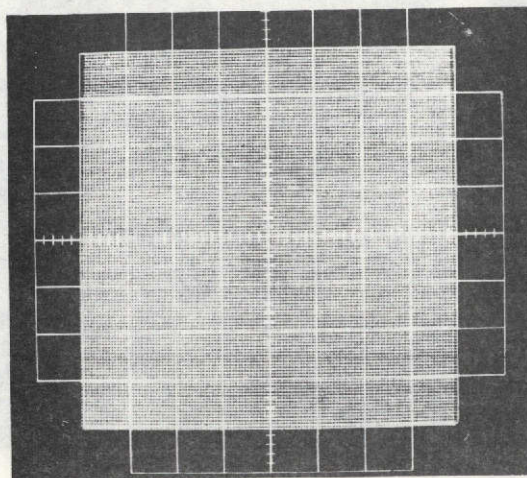
a. Search Scan
128-Step/174-mrad Fence–with 174- x 174-mrad Field Option
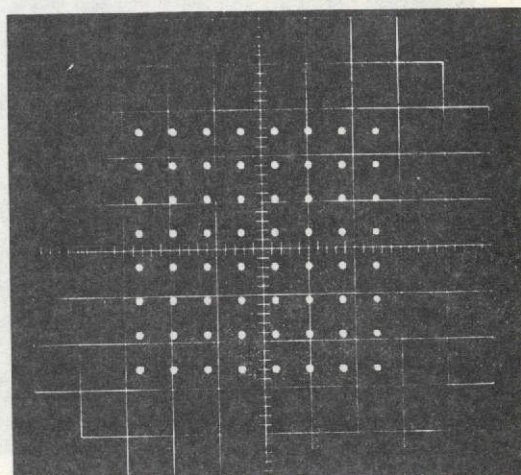
b. Mini-Search Scan
8 x 8 Steps/Field – 1.4 mrad/Step
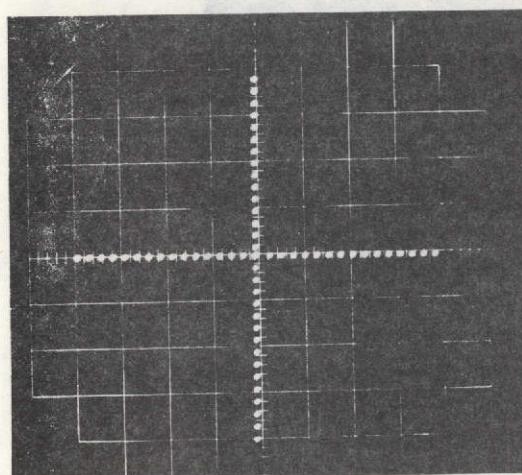
c. Tracking Scan
± 16 Step = ± 1.4 mrad
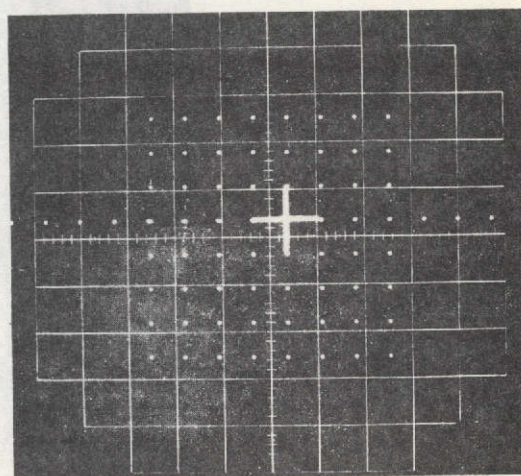
d. Fence – Minifield and Track Scans
(Superimposed)

(Signals applied to oscilloscope inputs: vertical – voltage at elevation coil current sampling resistor; horizontal – voltage at azimuth coil current sampling resistor.)

Figure 85. GBAA target tracker scan waveforms.
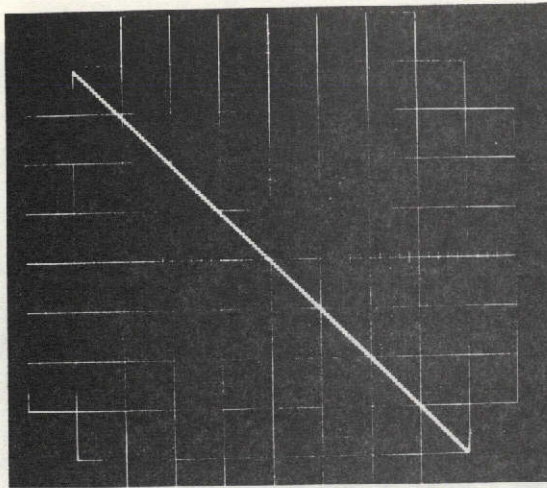
e. Search Fence
128-Step – 74-mrad Azimuth Scan
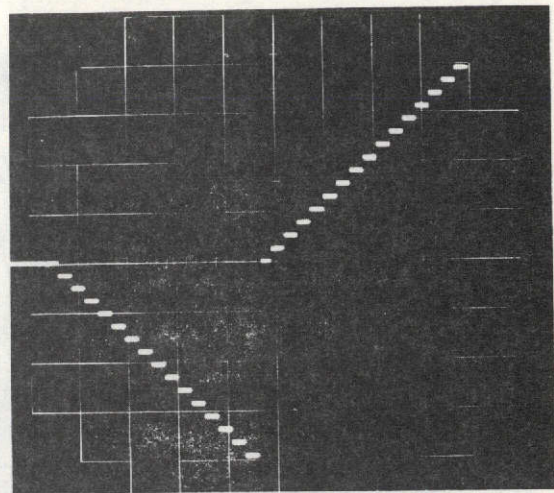
f. Track Scan
± 16 Step – 0.09-mrad/Step
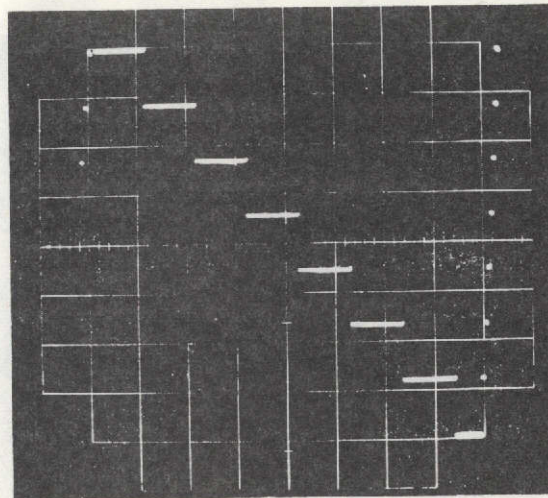
g. Mini-Search
8-Step Elevation and Azimuth – 1.4-mrad/Step

(Signals applied to oscilloscope inputs: vertical – voltage at coil current sampling resistor; horizontal – internal sweep.)

Figure 85. (Concluded).

COMPUTER

The computer used for control of the AVLOC experiment was an SCC-4700 computer with teletype input. This equipment is located on the second floor of the optical tracking station facility, as shown in Figure 86. Immediately to the left of the computer is a rack of computer interface hardware.

The computer is a 16-bit, 920-nsec, general-purpose machine featuring 48-bit floating point, double-precision, multiply/divide hardware.

For the AVLOC experiment, the computer had 16-channel, 12-bit A/D inputs and 8-channel, 12-bit D/A outputs for accepting tracking error inputs and providing tracking and pointing command data to the telescope.
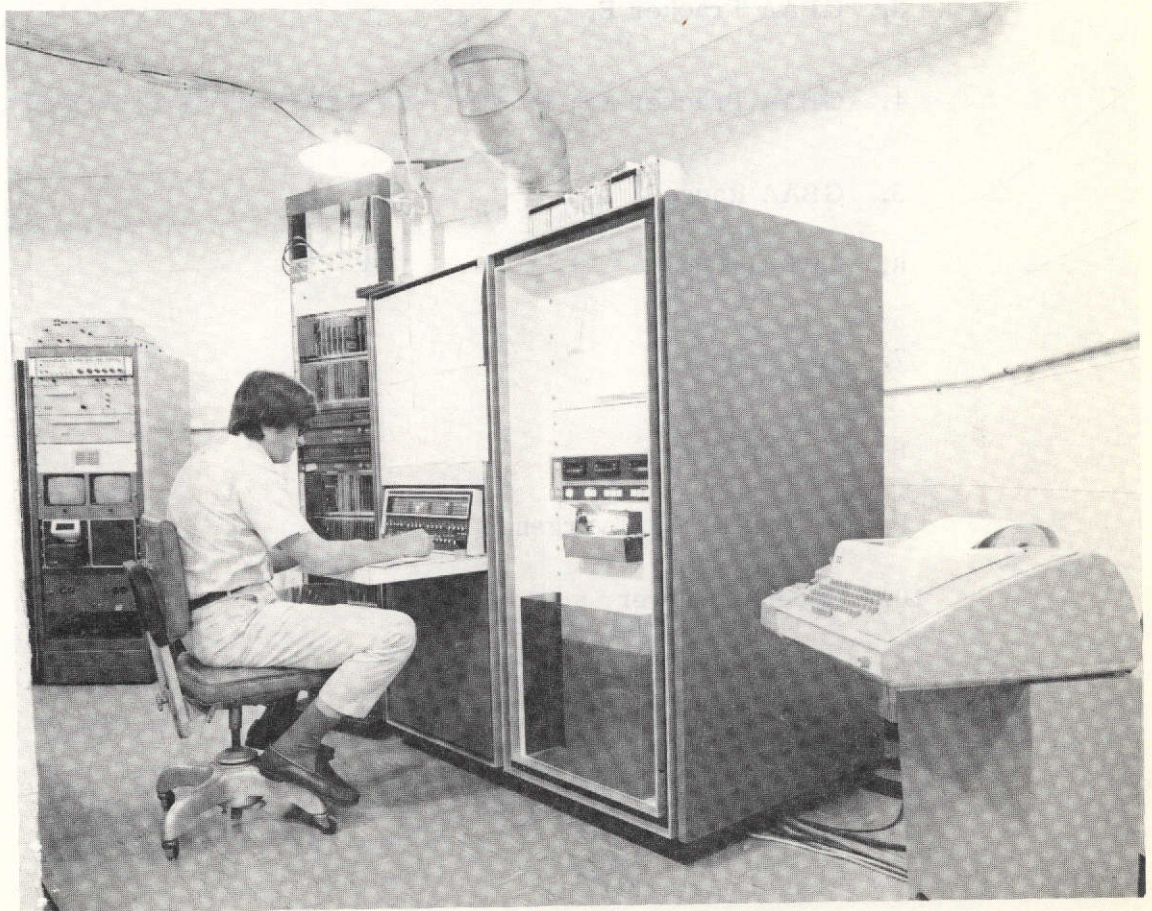
Figure 86. Tracking station computer.

DATA HANDLING

Computer Interface Rack

Data to and from the control computer are routed through the computer interface rack (Fig. 86) for A/D conversion, digital to digital interfacing, or D/A conversion. In addition, data to be displayed alphanumerically are routed through the computer interface rack for conversion to the digital format required by the character generators. The A/D channel assignments are:

1. Fine Tracker E_X

2. Fine Tracker E_Y

3. GBAA Tracker E_X

4. GBAA Tracker E_Y

5. GBAA Range

6. Joy stick E_X

7. Joy stick E_Y

8. Beacon Power

9. Beacon Beam Divergence

10. Receiver Power

11. Background Power

12. Receiver Attenuation

13. Receiver Aperture

14. Fine Tracker FOV

15. Receiver FOV

16. Dome Position

The D/A channel assignments are:

1. Polar Velocity

2. Declination Velocity

3. Ground Track Circle X

4. Ground Track Circle Y

5. Polar Error

6. Declination Error

7. Open

8. PDI to Tone Generator

The telescope position and clock digital interfaces are described in Appendix A. Two clocks located in this rack furnish experiment time and time-of-day data.

Telemetry Data Rack

The telemetry data rack contains discriminators for monitoring downlink VCO telemetry data, a decommutator for monitoring downlink PAM telemetry data on the 22-kHz VCO channel, a PAM multiplexer and VCO channels for multiplexing data to be recorded and four patch panels to facilitate routing of data. The ground station data recording system and the aircraft telemetry and data recording system are described in the following paragraphs.

TV Monitor Rack

The TV monitor rack contains the three monitors associated with the joystick controller acquisition system. It also contains four alphanumeric display monitors, character generators, and electronics. The items displayed alphanumerically are as follows:

1. GBAA Data

   a. Slant Range

   b. Vertical Altitude (desired, delta)

   c. Horizontal Radius (desired, delta)

125

d.   Target

c.   X Error

f.   Y Error

g.   Experiment Time

2.   AOCP Status

   a.   Scintillation Aperture

   b.   Receiver Power Attenuation

   c.   Beam Divergence

   d.   Experiment Time

3.   Fine Tracker Data

   a.   Target

   b.   Beacon Power

   c.   Beacon Divergence

   d.   X Error

   e.   Y Error

   f.   Receiver Power

   g.   Background Power

   h.   Receiver Filter

   i.   Receiver Aperture

   j.   Tracker FOV

   k.   Receiver FOV

   l.   Experiment Time

4. Master Experiment Status (color)

    a. GBAA Track

    b. Fine Tracker Track

    c. Polar Error

    d. Declination Error

    e. Aircraft Azimuth

    f. Aircraft Zenith

    g. Experiment Time

TV Control Rack

The TV control rack contains 2 general-purpose monitors, a waveform monitor, camera control electronics, a camera control panel, a TV pulse generator, 10 video distribution amplifiers, and 8 pulse distribution amplifiers. Routing of data is through a patch panel installed in the rack. Figure 87 shows the ground station television distribution system.

Observation Trailer

The observation trailer TV distribution system is an extension of the ground station system and is intended to allow the principal investigators to monitor many of the same data and parameters being displayed in the ground station. Displays may be recorded on videotape for future reference. The observation TV system is described in Appendix A.

TARGET ACQUISITION

Prior to acquisition, the telescope is pointed toward the prearranged acquisition point, and the GBAA and laser transceiver are activated. In the acquisition mode, the GBAA laser beam is scanned 174 mrad (10 deg) to form a radar fence in the acquisition area. Referring to Figure 81, pulses from the clock trigger the beam steerer, the detector scan generator, and the laser trigger. The laser trigger excites the 514.5-nm green laser into pulsed operation. The laser beam passes through optical elements to the piezoelectrically actuated beam steerer. The beam steerer and following
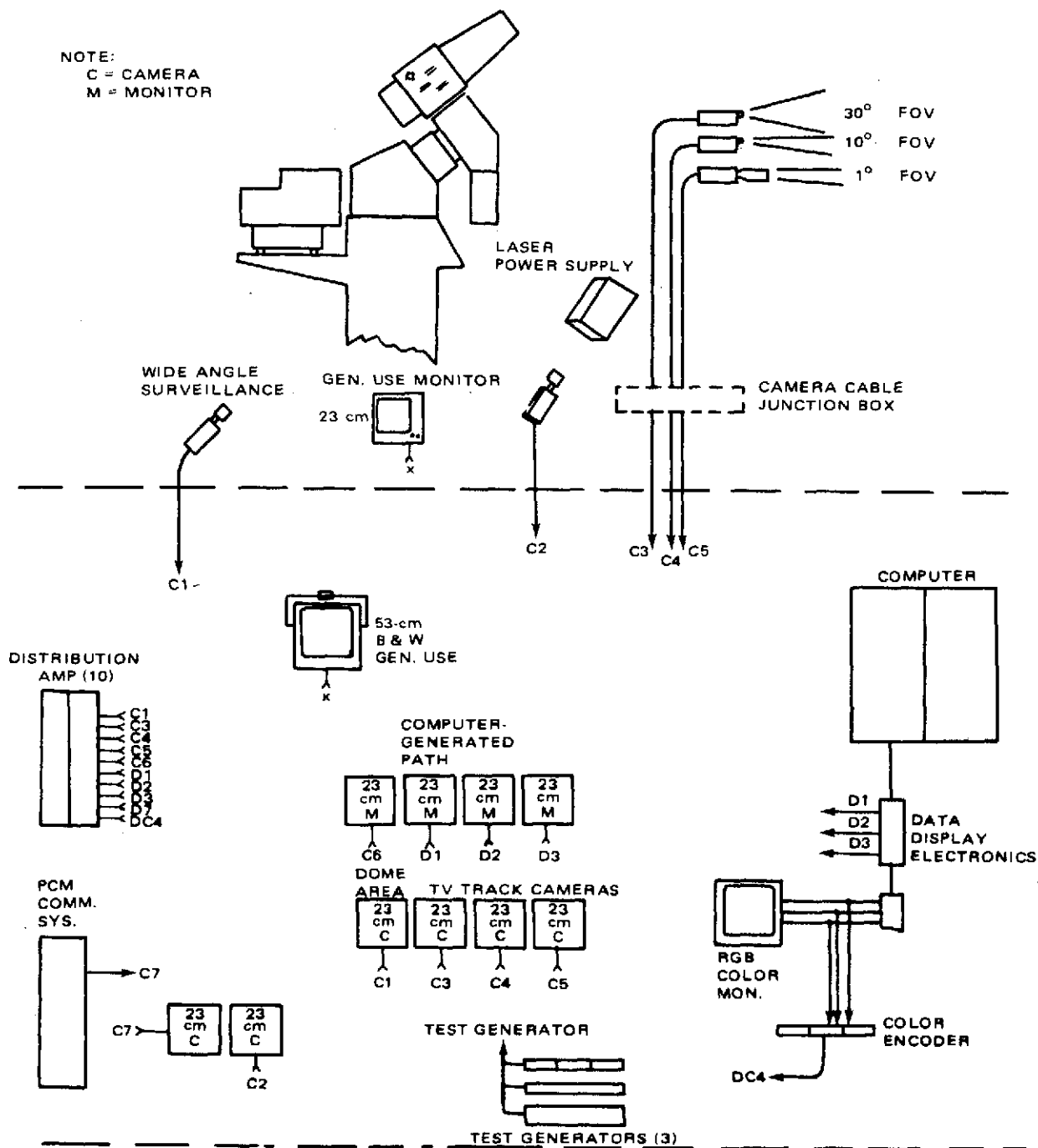
Figure 87. Ground station TV system.

optical elements produce the 174-mrad fan-shaped beam scan, or radar fence. When the target aircraft enters the radar fence, returns from retroreflectors attached to the underside of the aircraft pass through the receiver lens and sun-protect shutter to the detector. Two successive returns cause the GBAA to automatically enter track, producing a 1.4- by 1.4-mrad (0.08- by 0.08-deg) cruciform scan centered on the target. The GBAA detector is an image dissector whose face is electromagnetically scanned in synchronism with the transmitted beam so that return beam X and Y position errors are detected. In the Track mode, these error signals are applied to the beam steerer and, through an A/D interface, to the computer. The computer commands polar and declination telescope velocities which tend to null out the pointing error. When the pointing error becomes small, the beacon laser, which is amplitude modulated at 10.7 MHz, illuminates the aircraft. When illuminated by the beacon laser, a detector in the AOCP initiates a beacon presence signal which activates the red downlink laser, and the AOCP enters the Track mode, pointing the red laser toward the ground station. When the red laser beam falls within the ±0.436-mrad (± 90-arc sec) FOV of the laser transceiver tracking detector, the laser transceiver also enters the Track mode, and acquisition is complete.

TARGET TRACKING

Referring to Figure 88, the incoming red beam passes through a telescope to the transfer mirror, where it is deflected to a dichroic beam splitter. It passes through an ND filter and an FOV aperture to the quadrant multiplier tracking detector. Before reaching the detector, the beam is split into four parts by an image divider so that a partial image falls on each of the four quadrants of the QMP. The varying states of illumination of these four partial images are used to electronically sense the location of the total image. Referring to Figures 89 and 90, a gate generator gates the four cathodes of the QMP so that, at any instant, two cathodes are conducting. The resulting QMP output is amplified, inverted, and gated to sum the direct outputs of quadrants I and II with the inverted outputs of quadrants III and IV to derive the X-axis signal. The Y-axis is derived by summing the direct outputs of quadrants I and IV with the inverted outputs of quadrants II and III. After smoothing in the drive amplifier, these signals are applied to the transfer mirror piezoelectric actuators and, through buffers and interfaces, to the computer, as indicated in Figure 91. The computer adjusts telescope polar and declination drive rates in a direction to reduce detected pointing errors. The transfer mirror, having a quicker response than the telescope, insures tracking continuity and smooth drive.
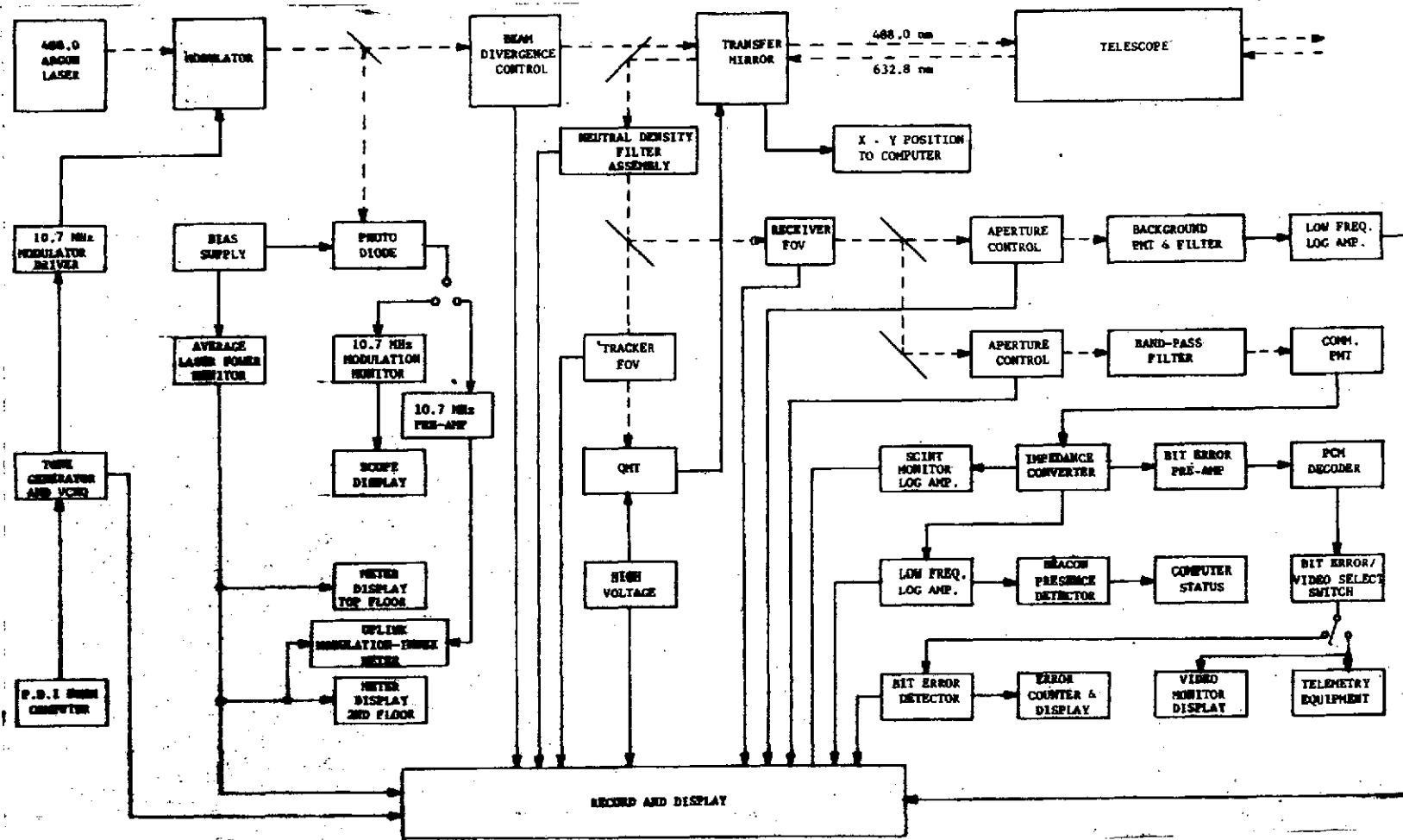
Figure 88. Laser transmit and receive channels block diagram.
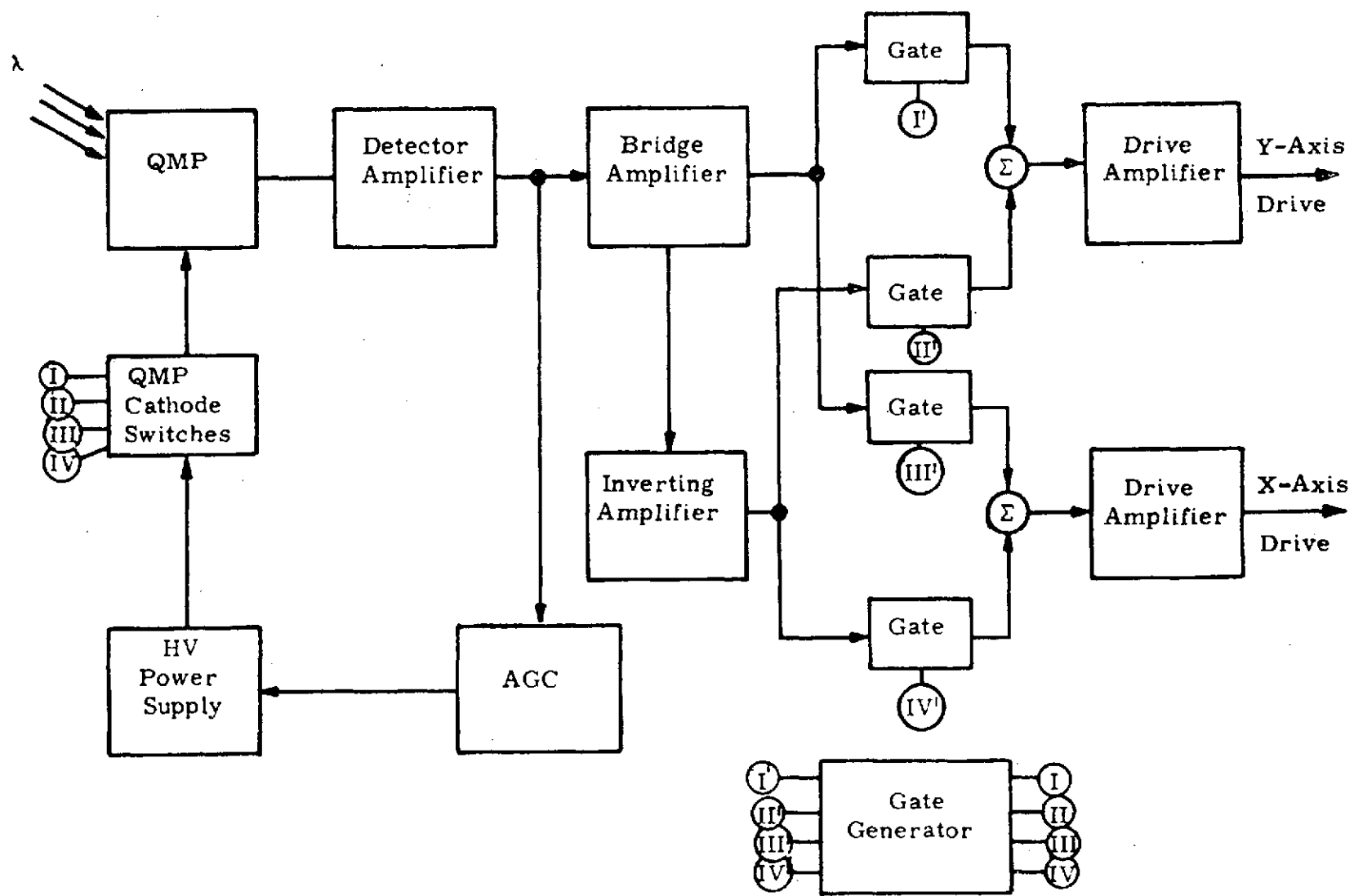
Figure 89. Fine tracker electronics block diagram.
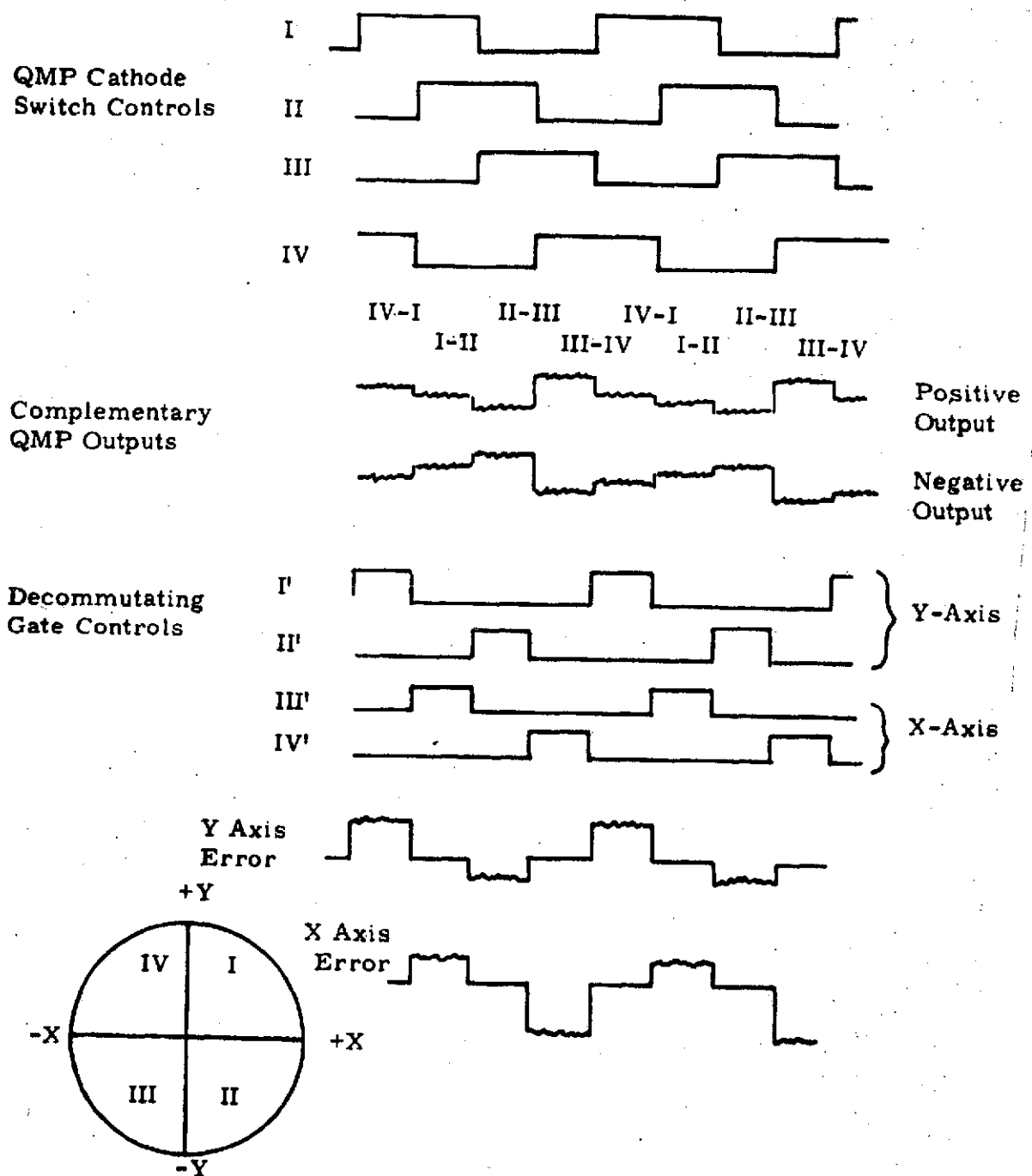
Figure 90. Fine tracker logic.
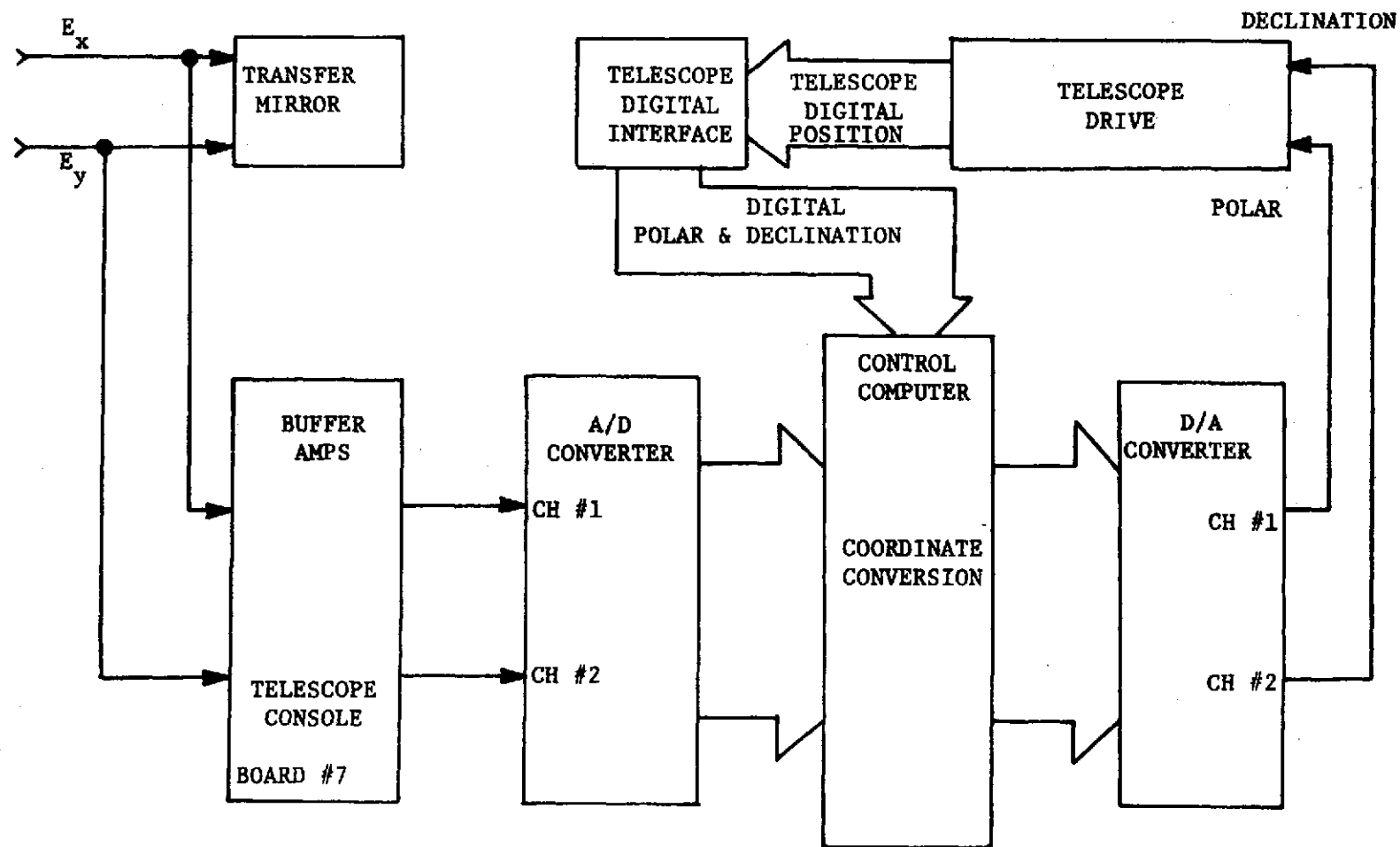
Figure 91. Pointing command signal flow diagram.

LASER COMMUNICATIONS

Transmit Channel

Referring to the left side of Figure 88, audio tones generated in the tone generator are applied to frequency modulate the 10.7-MHz VCXO subcarrier generator. The modulated subcarrier is applied to a 10.7-MHz modulator driver whose output drives an optical modulator located in the path of the 488-nm blue laser. The amplitude-modulated blue laser passes through other optical elements and out through the telescope. The tone generators and VCXO are part of the command tone transmitter shown in Figure 92. Boards A-2 through A-7 are keyed fixed-frequency oscillators, while A-12 is a free-running 10.7-MHz VCXO. The control panel allows the selection of three-tone sequences and has a transmit button to initiate the sequence. The logic and timing board, A-1, contains the circuitry for keying the tones in the sequence selected. When the transmit button is depressed, the selected tones sequentially frequency modulate the 10.7-MHz subcarrier. Board A-10 is a VCO operating continuously at a center frequency of 560 Hz. Its instantaneous frequency is determined by the magnitude of a dc voltage from the computer, which is derived by comparing the horizontal component of the GBAA range signal with a desired range signal stored in the computer. The output of board A-10 is applied continuously to the VCXO, which is applied continuously to the optical modulator. When detected at the aircraft, the signal drives a PDI, informing the pilot of the amplitude and direction of his deviation from the desired circular flight path.

A portion of the transmitted beam is deflected to a vacuum photodiode, whose amplitude detects the 10.7-MHz subcarrier for display on an oscilloscope. The photodiode bias supply is a 44-V battery pack. Because diode bias current is a function of incident light, transmitter power is a function of bias current. Meters displaying average laser power on a zero to five scale, derived from diode bias current, are located on the second and third floors. Circuit configurations allow the percent of modulation to be calculated by

$$\text{Percent modulation} = 1.33 \times \frac{\text{Peak-to-peak narrow band voltage out}}{\text{Power monitor meter reading}}. \quad (4)$$

Receive Channel

Referring again to Figure 88, after passing through the ND filter, a portion of the incoming red laser is deflected through the receiver FOV aperture to two aperture controls. One portion of the beam is directed through a 700-nm

bandpass filter to the background PMT detector. The output of the detector is amplified in a low-frequency log amplifier and recorded as background scintillation. The other portion of the beam passes through a 1.3-nm-wide bandpass filter to the communications detector. The detector output is a 30 megabits-per-second downlink PCM, which is routed to an impedance converter. This unit furnishes a high-impedance output to a low-frequency log amplifier, which activates the beacon presence detector, and a low-impedance output to the scintillation monitor log amplifier, which is tuned to respond to a strong 2-MHz component in the 31-bit pseudorandom sequence downlink modulation. Another low-impedance output is furnished the bit error preamplifier. This and the PCM decoder (Fig. 93) perform signal conditioning and relocking functions to restore the signal to pure binary form. Depending on the modulation present, the signal will be routed either to the bit error detector or to the telemetry equipment. If the 31-bit pseudorandom sequence downlink modulation has been selected the signal will be routed to the bit error detector, where it will be compared bit by bit with an identical sequence generated on the ground. The error rate will be displayed on a counter, and an analog voltage representing BER will be recorded. If telemetry is on the downlink beam, it will be recorded and also demultiplexed and displayed. Video downlink modulation will be displayed on a TV monitor.

DATA ACQUISITION SYSTEM

AIRBORNE TELEMETRY SUBSYSTEM

A block diagram of the data acquisition subsystem is shown in Figure 94. Engineering data are received at the input of the PAM multiplexer (MUX), where they are time-division multiplexed and transmitted to the IRIG channel 14 of the VCO assembly. There, they are frequency-division multiplexed with 10 channels of other data. The output of the VCO assembly is routed to channel 2 of the Ampex Model AR-1700 tape recorder, where it is direct recorded at a speed of 7 1/2 ips. The output of the VCO assembly is also sent to the auxiliary VCO assembly, where it is mixed with the signals from two constant-bandwidth VCO's and a proportional VCO to form a frequency-multiplexed output data signal. This signal is then sent through a four-position coaxial switch to modulate the helium-neon laser downlink. The coax switch is used to select one of three downlink signals: the output data signal, a TV video signal, or channel 1 of the tape recorder pickup head. The recorder signal gives a positive indication of onboard recording. Coaxial switch positions are selected through commands on the laser uplink. Not shown in this diagram is the

provision made to select for the downlink either the output of the coaxial switch or of a BER generator, which provides a reference for determining atmospheric effects on the optical downlink. The PAM MUX data inputs and VOC channel assignments are listed in Figure 95.
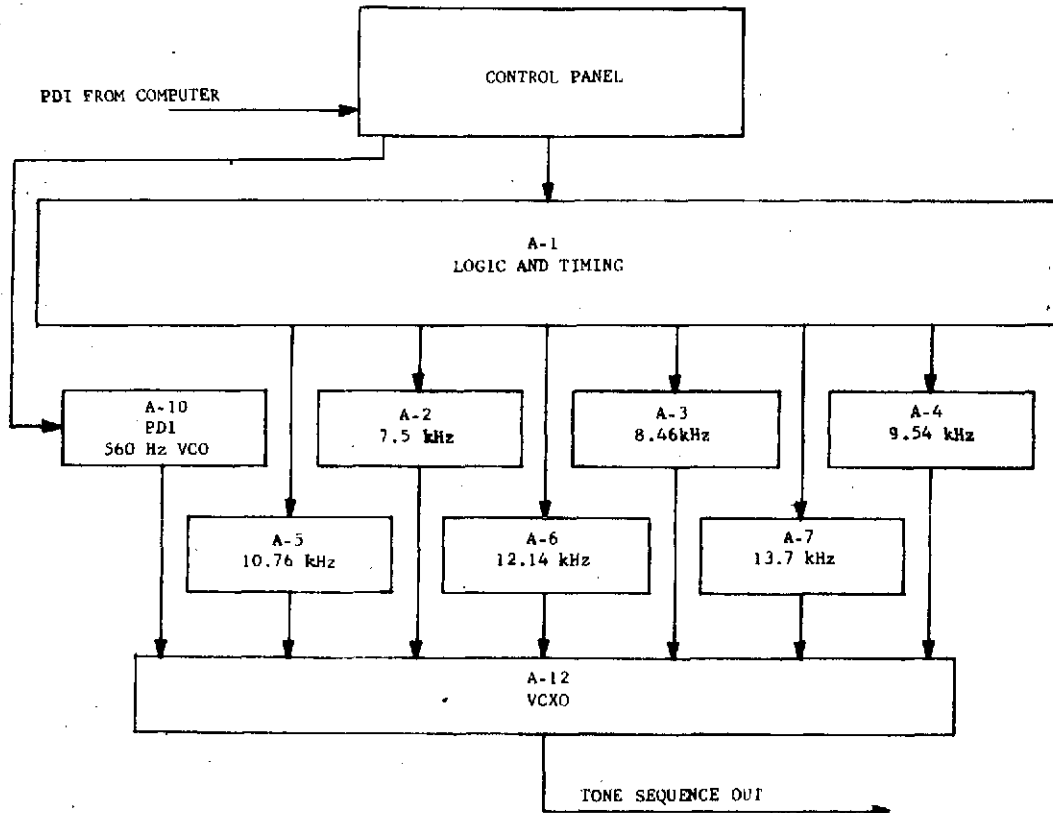
Figure 92. Command tone transmitter block diagram.

The measurement program, containing 32 measurements, is given in Table 9. Eighteen of these are static engineering measurements, PAM multiplexed at five samples per second.

The PAM Multiplexer Teledyne Model 306A2K1V3(150D10) is a high-level (0 — 5 Vdc) MOS FET commutator with one pole operating on a 30-channel format.

136
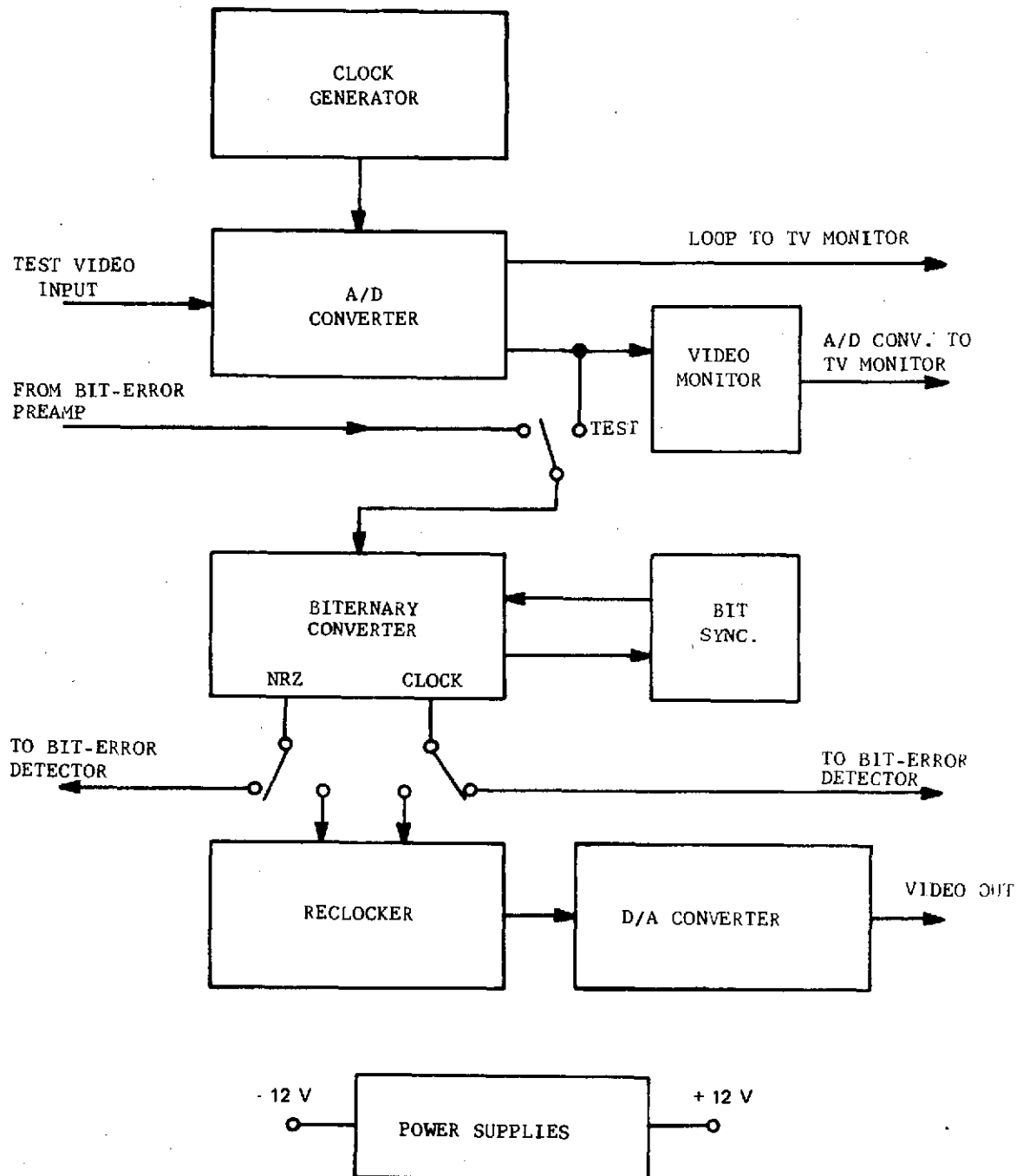
Figure 93. PCM equipment block diagram.
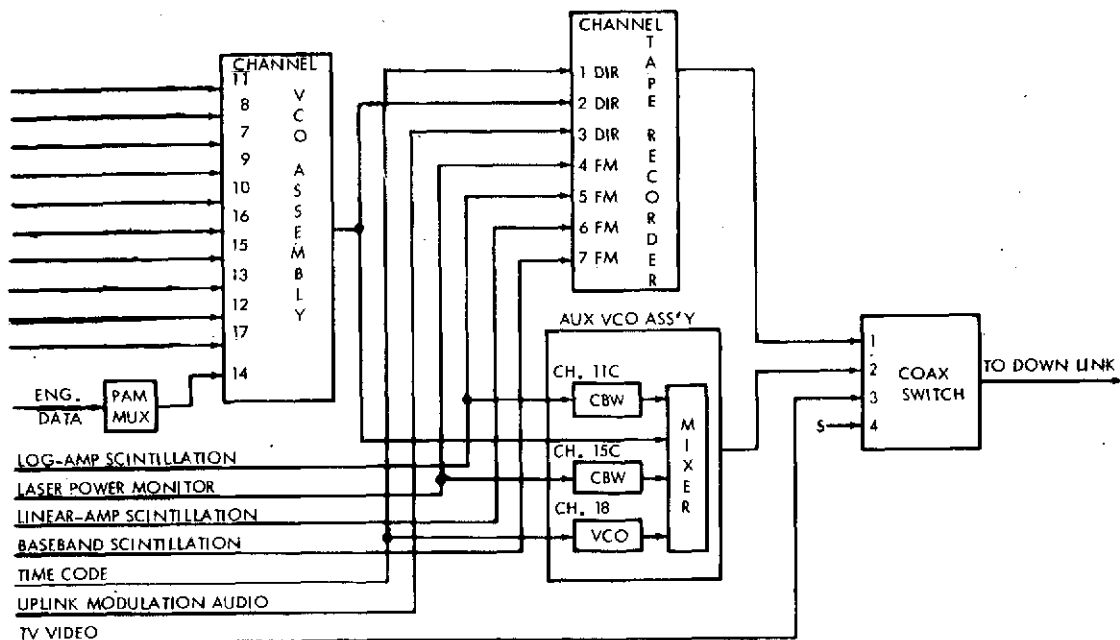
Figure 94. Block diagram of the data acquisition subsystem.
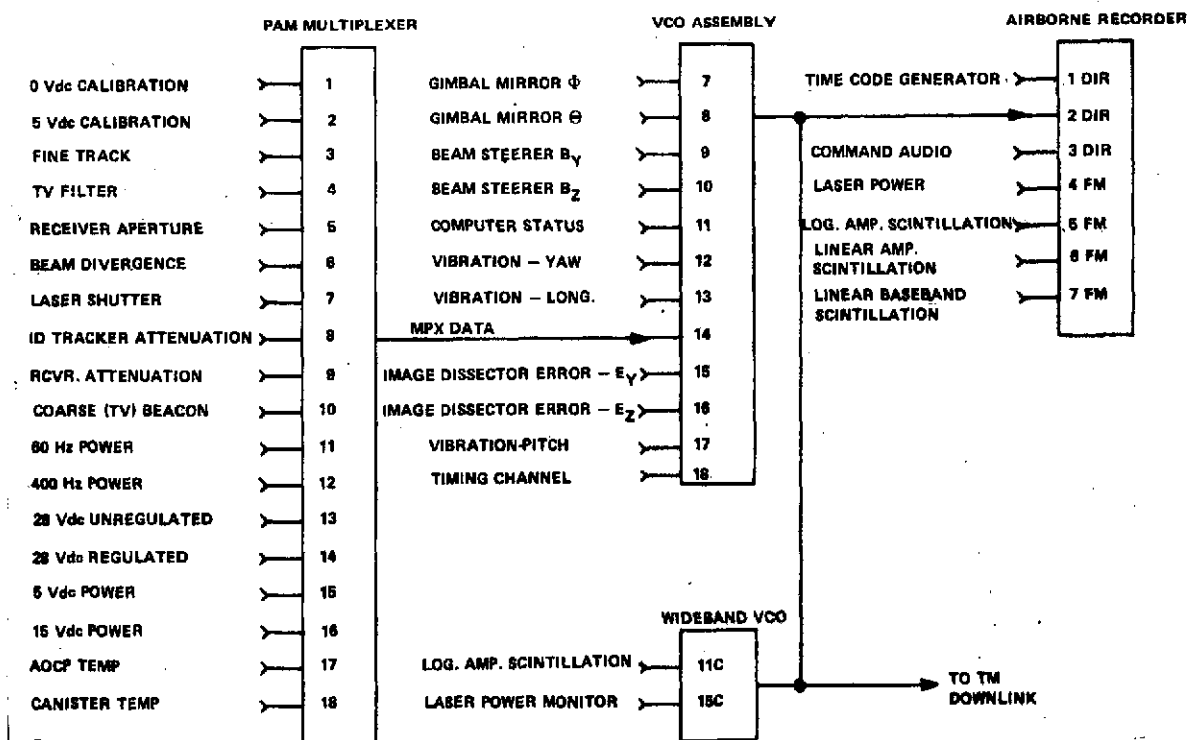
Figure 95. Aircraft telemetry data system.

138

TABLE 9. AVLOC MEASUREMENTS PROGRAM

Measurement Number	Measurement Description	Range	Channel	Response
M-1-1	Fine Track Bit	0 or 3.5 V	Commutated[a] Ch. 3	5 sps[b]
M-2-1	I.D. Error, E_Y	±0.1 deg (±5 V)	VCO Ch. 15	1050[c]
M-2-2	I.D. Error, E_Z	±0.1 deg (±5 V)	VCO Ch. 16	1050[c]
M-3-1	Linear Scintillation	0 to 5 Vdc	FM Record Ch. 6	5000
M-3-2	Log Scintillation	0 to 5 Vdc	FM Record Ch. 5	(d)
M-4-1	He-Ne Laser Power	0 to 5 Vdc	FM Record Ch. 4	(e)
M-5-1	Beam Divergence	0 to 5 Vdc	Commutated Ch. 6	5 sps
M-7-1	Uplink Audio	5 V Peak to Peak	Direct Record Ch. 3	400 Hz, 125 Hz
M-8-1	Receiver Attenuation	0 to 5 Vdc	Commutated Ch. 9	5 sps
M-9-1	Aperture Size	0 to 5 Vdc	Commutated Ch. 5	5 sps
M-10-1	Beam Steerer, B_Z	±200 arc sec (±5 V)	VCO Ch. 10	220[c]
M-10-2	Beam Steerer, B_Y	±0.1 deg (±5 V)	VCO Ch. 9	160[c]
M-11-1	Timing Signal		Direct Record Ch. 2	
M-12-1	TV Filter	0 V to 5 V	Commutated Ch. 4	5 sps
M-13-1	Gimbal Angle ϕ	±5 V	VCO Ch. 7	35 Hz
M-13-2	Gimbal Angle θ	±5 V	VCO Ch. 8	45 Hz
M-14-1	Vibration, Pitch	±0.1 g	VCO Ch. 17	1050[c]
M-15-1	Vibration, Yaw	±0.1 g	VCO Ch. 12	330[c]
M-16-1	Vibration, Longitude	±0.1 g	VCO Ch. 13	450[c] Hz
M-17-1	Computer Status	0 to 5 Vdc	VCO Ch. 11	110
M-18-1	Coarse Track Bit	0 to 3.5 Vdc	Commutated Ch. 10	5 sps
M-19-1	60-Hz Power	0 to 130 Vac	Commutated Ch. 11	5 sps
M-20-1	400-Hz Power	0 to 130 Vac	Commutated Ch. 12	5 sps
M-21-1	28-V Unreg. dc	0 to 32 Vdc	Commutated Ch. 13	5 sps
M-22-1	28-V Reg. dc	0 to 32 Vdc	Commutated Ch. 14	5 sps
M-23-1	5-V Indicator Supply	0 to 6 Vdc	Commutated Ch. 15	5 sps
M-24-1	15-V Control Supply	0 to 16 Vdc	Commutated Ch. 16	5 sps
M-25-1	Laser Shutter Position	0 to 5 Vdc	Commutated Ch. 7	5 sps
M-27-1	AOCP Temperature	0 to 50° C	Commutated Ch. 17	5 sps
M-28-1	Canister Temp	0 to 50° C	Ch. 18	5 sps
M-29-1	Baseband Scintillation	0 to 5 Vdc	FM Record Ch. 7	
M-30-1	Linear Scintillation	0 to 5 Vdc	Commutated Ch. 8	5 sps

a. Commutator IRIG Channel 14.
b. Samples per second.
c. Assumes special discriminator output filters to allow for subcarrier deviation ratio of approximately two. Nearest standard filter is assumed to be used.
d. Constant bandwidth VCO to ground link 96 kHz.
e. Constant bandwidth VCO to ground link 128 kHz.

139

As seen from the waveform diagram of Figure 96, the channel format
is as follows: Positions 1 and 2 are occupied by the frame synchronization
pulse. Positions 3 through 30 are PAM data channels 1 through 28, respec-
tively.
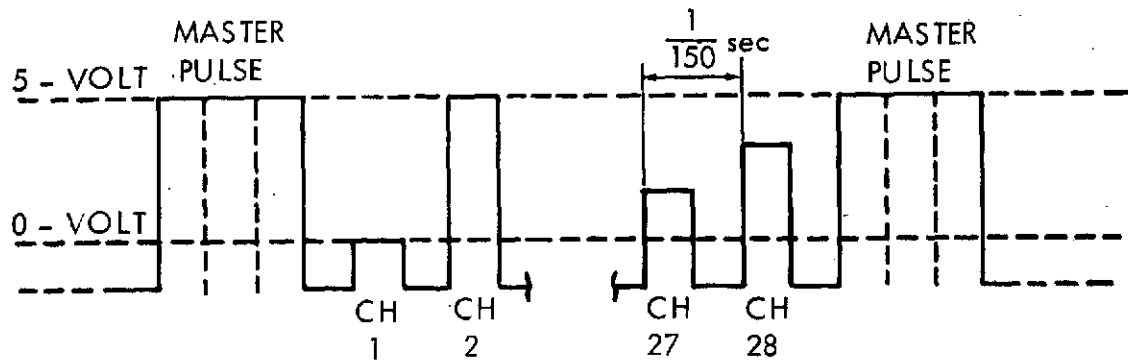
Figure 96. PAM multiplexer waveform.

The format is in accordance with IRIG-STD 106-66 and is classified as a PAM
wavetrain at 50 percent duty cycle having a channel positive pedestal of 1 1/4 V.
The PAM gain is 0.745. The total sampling rate is 150 samples per second,
giving a channel sample rate of 5 samples per second. The input signal level
is 0 to 5 Vdc. The input impedance, each channel, is 15 MΩ minimum. The out-
put impedance is 500 Ω maximum. Channel 1 is programmed for a 0-V cali-
bration level as an input, whereas channel 2 is programmed for 5 V. The PAM
MUX signal characteristics are listed in Table 10.

The VCO assembly consists of three types of functional subassemblies:
(1) a mount assembly that accepts up to 12 plug-in modules; (2) 11 propor-
tional-bandwidth, VCO assemblies which have been selected to cover IRIG
channels 7 through 17, and (3) a mixer amplifier that mixes the output of the
VCO's. The VCO's for channels 7, 8, 9, 10, 15, and 16 are adjusted for a
0 to 5-V input range. The VCO's are IRIG standard telemetering voltage-
controlled, frequency-modulated subcarrier oscillators. The VCO signal
characteristics are listed in Table 11. Component specifications are given in
Table 12.

TABLE 10. SIGNAL CHARACTERISTICS FOR AIRCRAFT MPX COVERING DATA FOR 30 CHANNEL–MAXIMUM FRAME–SAMPLE RATE 50 Hz

Data	Channel Number	Analog Range (V)	Parameter Range
Beacon Presence	3	0 to 5	Off, On — Discrete
TV Filter	4		In/Out — Discrete
Receiver Aperture	5		In/Out — Discrete
Beam Divergence	6		5 Steps, mrad
Laser Shutter	7		In/Out — Discrete
Tracker Attenuation	8		4 Steps — ND
Receiver Attenuation	9		In/Out — Discrete
Fine Beacon Presence	10		On/Off — Discrete
60 Hz Power	11		0 to 30 V — Linear
400 Hz Power	12		0 to 130 V — Linear
28 Vdc Unregulated	13		0 to 32 V — Linear
28 Vdc Regulated	14		0 to 32 V — Linear
5 Vdc Power	15		0 to 6 V — Linear
15 Vdc Power	16		0 to 16 V — Linear
AOCP Temperature	17		0 to 50° C — Linear
Canister Temperature	18		0 to 50° C — Linear

TABLE 11. SIGNAL CHARACTERISTICS — AIRCRAFT VCO CHANNEL DATA

Data	VCO Channel No.	Analog Range (V)	Parameter	Carrier Frequency (kHz)	Bandwidth (Hz)
Gimbal Mirror Angle ϕ	7	± 2.5	+0.87 to −0.52 rad	2.3 ± 7.5 % Deviation	35
Gimbal Mirror Angle θ	8	± 2.5	+1.22 to −0.17 rad	3.0 ± 7.5 % Deviation	45
Beam Steerer Angle B_Y	9	± 2.5	± 4.35 mrad	3.9 ± 7.5 % Deviation	160[a]
Beam Steerer Angle B_Z	10	± 2.5	± 4.35 mrad	5.4 ± 7.5 % Deviation	220[a]
Computer Status	11	0 to 5		7.35 ± 7.5 % Deviation	110
Vibration — Yaw	12	± 2.5	± 1 g	10.5 ± 7.5 % Deviation	330[a]
Vibration — Longitude	13	± 2.5	± 1 g	14.5 ± 7.5 % Deviation	450[a]
PAM Data	14	0 to 5		22.0 ± 7.5 % Deviation	330
Image Dissector Error E_Y	15	± 2.5	± 121 μrad	30.0 ± 7.5 % Deviation	1050[a]
Image Dissector Error E_Z	16	± 2.5	± 121 μrad	40.0 ± 7.5 % Deviation	1050[a]
Vibration — Pitch	17	± 2.5	± 1 g	52.5 ± 7.5 % Deviation	1050[a]
Timing Channel	18	1.5 to 3.5	IRIG B, 1 kHz	70.0 ± 7.5 % Deviation	1050
Log Scintillation	11C	0 to 5	0 to 5	96.0 ± 8.0 kHz Deviation	8000
Laser Power Monitor	15C	0 to 5	0 to 5	128.0 ± 8.0 kHz Deviation	8000

a. Wider than standard bandwidth.

TABLE 12. VCO ASSEMBLY COMPONENT SPECIFICATIONS

Voltage Controlled Oscillator
(Vector An Aydin Company, MT 541-5 Series)

Input Voltage Level	0 to 5 V or ± 2. 5 V
Input Impedance	500 kΩ min
Frequency	IRIG proportional-bandwidth, channels 7 through 17
Output Voltage Level	0. 85 V peak to peak; 0 to 2 V rms at test point
Output Impedance	47 kΩ Nominal
Frequency Deviation	± 7. 5 %
Power Requirements	28 Vdc ± 15 % at 6. 5 mA nominal, 11 mA max

Mixer Amplifier
(Vector An Aydin Company, Series MTA-48-2,
Wired with Series B Pin Functions)

Gain	Variable up to 20
Frequency Response	± 0. 25 dB from 300 Hz to 200 kHz
Input Impedance	100 ± 10 %
Output Impedance	Less than 100 Ω
Input Signal	100 mV min
Output Signal	Set at 2 V rms for this application
Power Requirements	28 Vdc ± 15 % 6 mA nominal, 9 mA max

Mount

Vector An Aydin Company, Model M-172 MA, 12-Position Mount

Connector J2 Position is wired for MTA-Series B Mixer Amplifier

Connector	VOC IRIG Channel	Connector	VCO IRIG Channel
J-3	17	J-9	11
J-4	16	J-10	10
J-5	15	J-11	9
J-6	14	J-12	8
J-7	13	J-13	7
J-8	12		

The output of the VCO assembly, after mixing in the linear mixer amplifier, is a frequency-division multiplex wavetrain, which is available for recording and for transmission on the optical downlink.

The auxiliary VCO assembly consists of a mount assembly, two constant bandwidth VOC's, one proportional bandwidth VCO, and a mixer amplifier. This assembly has been installed to provide sufficiently high frequency response to accommodate the log-amplitude scintillation, laser power monitor, and time code signals and to mix the wavetrain from the other VCO assembly into a common frequency-multiplex signal for transmission on the optical downlink. Its output waveform bandwidth is too large for direct-record on a tape recorder track at 19-cm/seo (7.5-ips) tape speed. However, the component signals are separately recorded before mixing. The component specifications are given in Table 13.

The three accelerometers are of the piezoelectric type. They are used with a Gulton Model ES 6044B charge amplifier-type signal conditioner, which is rated at maximum gain to give 120-mV output per picocoulomb. The output is biased at 2.5 Vdc, giving a minimum range after amplification of 0.1 g. The specifications for the charge amplifier are as follows:

Gain Range	20:1 (continuously variable): maximum gain, 120 mV/pc
Frequency Response	5 % 5 Hz to 10 kHz
Linearity	2 % up to 4.9 V peak to peak
Load Impedance	50 kΩ to 1 MΩ shunted with 2000 pF max
Output Impedance	500 Ω (nominal)
Quiescent Noise Level	50 mV peak to peak (2 Hz to 7000 Hz) at max gain with 330 pF across input
Power Input	25 mA max at 28.0, 4, and -8 Vdc
Limiting	0.0 (+0.1, -0.0) V and 5.6 V max

Bias	2.5 V ± 5 % dc
Harmonic Distortion	Less than 2 % from 3 Hz to 5 KHz for output voltages up to 4.9 V peak to peak
Overload Recovery	
Signal Transient	5 msec for transient; 3 times normal input level
Pulse Transient	50 msec after application of 1 msec; –1 V pulse input
Supply Transient	5 mV max output for 1 V change in dc
Output Protection	No damage ± 5 Vdc or less applied to output wire
Case Isolation	Greater than 50 MΩ at 50 Vdc (for proper performance, case ground and circuit ground should be connected at end of output cable).

The airborne tape recorder is an Ampex AR-1700 model. It is set up to record at 19 cm/sec (7.5 ips) with a 2.54-cm (1-in.) recording tape using only seven tracks arranged as follows:

Track 1   Direct record of time code waveform

Track 2   Direct record of PAM/FM and FM multiplexed data, which is played back over the data link to indicate recorder operation.

Track 3   Direct record of uplink audio modulation from the command receiver

Track 4   FM record of experiment laser power monitor signal

TABLE 13. AUXILIARY VCO ASSEMBLY COMPONENT SPECIFICATIONS

Voltage Controlled Oscillator (Vector An Aydin Company, MTS 47-1 Series)	
Input Voltage	Between -2.5 V and + 5.0 Vdc, set for 0 to 5 Vdc
Input Impedance	50 kΩ min
Frequency	IRIG constant bandwidth channels 11C and 15C at 96 kHz and 128 kHz center frequency, respectively, and proportional channel 18 at 70 kHz.
Frequency Deviation	± 8 kHz
Output Voltage	0.85 V peak to peak min with 10 kΩ load, 0 to 2 V rms at test point
Output Impedance	47 kΩ nominal
Power Requirements	28 ± 4 Vdc at 6.5 mA nominal, 11 mA max

Mixer Amplifier
Same as listed under VCO assembly above.
Output level is set at 1 V peak to peak into 75 Ω as required by modulation requirements of the laser modulator.

Mount
Similar to the VCO assembly mount, except that only four inputs are provided for. The channel input connectors are given below:

Connector	Channel
J3	15C
J4	11C
J5	IRIG 18

146

Track 5   FM record of experiment data signal log amplitude scintillation

Track 6   FM record of experiment data signal linear amplitude scintillation.

Track 7   FM record of experiment data signal linear baseband scintillation.

The tape recorder specifications are given in Table 14 and the signal characteristics are listed in Table 15.

Calibration data for the temperature probes are given in Figure 97. The thermistor-type sensor, which has a negative temperature coefficient, puts out 5.7 V at 0° C and 0.95 V at 50° C.

GROUND STATION TELEMETRY SYSTEM

The format, PAM MUX data inputs, and VCO channel assignments of the ground station telemetry system are shown in Figure 98. Engineering data are received at the input of the PAM MUX, where they are time-division multiplexed and transmitted to IRIG channel 17 of the VCO assembly. There the data are frequency multiplexed with 13 channels of other data. The output of the VCO assembly is routed to channel 4 of the tape recorder, where it is direct recorded at a speed of 19 cm/sec (7.5 ips).

The PAM MUX signal characteristics are listed in Table 16 and the VCO signal characteristics in Table 17.

The ground station tape recorder is a 14-track Ampex FR 1900, recording 10 channels of input data at 19 cm/sec in the following format:

Track 1   Direct record of downlink TM composite

Track 2   Direct record of command audio and servo

Track 3   Direct record of time code IRIG composite

Track 4   Direct record of VCO composite

TABLE 14. AIRBORNE TAPE-RECORDER SPECIFICATIONS

Direct Record	
(All measurements per IRIG 106-69)	
Input Level	0.25 to 2.5 V rms.
Input Impedance	Modified to provide 10 kΩ, unbalanced to ground.
Output Impedance	75 Ω ± 10 % for all frequencies.
Response	Wideband II at tape speed of 19 cm/sec (7 1/2 ips), bandwidth 400 Hz to 120 kHz, S/N 20 dB.

FM Record	
(All measurements per IRIG 106-69)	
Input Impedance	1000 Ω ± 10 % in parallel with 150-pF maximum, unbalanced to ground.
Input Sensitivity	+0.25-V peak to 2.50-V peak adjustable.
Output (Reproduce)	Reproduce preamps have a 40-dB gain. These units have a 75-Ω output impedance and plug into a preamp housing built into the standard transport enclosure.
dc Center Frequency Drift	Less than ± 0.75 % of deviation over a 273° F temperature range (-50° C to 80° C).
Linearity	0.25 % of total deviation measured per IRIG 106-69 over a 273° F temperature range (-50° to 80° C) after 15-min warmup.
Second Harmonic Distortion	Less than 50 dB for all speeds over a 273° F temperature range (-50° C to 80° C) measured at center frequency after 15-min warmup.
Bandwidth	Wideband group II at tape speed 7 1/2 ips, center frequency 56.25 kHz input frequency dc to 35.25 kHz.
General Specifications	Power 28 V at 305 W max at 120 ips in record mode less heater. If heater required, 225 W additional required below 13° C (55° F).

TABLE 15. SIGNAL CHARACTERISTICS — AIRCRAFT RECORDER 19 cm/sec (7.5 ips)

Data	Channel Number	Mode	Analog Range (V)	Parameter Range (V)	Bandwidth (kHz)	Center Frequency FM Carrier (kHz)
Time Code	1	Direct	≈ 2.5 peak to peak	IRIG Code "B" on 1-kHz Carrier		
VCO Carriers	2	Direct	≈ 2.5 peak to peak	See VCO Sheet for Data and Carriers	125	
Uplink Audio Commands	3	Direct	≈ 2 peak to peak		Data ≤ 2.0	
Laser Power Monitor	4	FM	0 to 5	0 to 20[a]	5	56.25 Wideband II
Log Amplitude Scintillation	5	FM	0 to 5	0 to 20[a]	5	56.25 Wideband II
Linear Amplitude Scintillation	6	FM	0 to 5	0 to 20[a]	5	56.25 Wideband II
Linear Baseband Scintillation	7	FM	0 to 5	0 to 20[a]	5	56.25 Wideband II

a. See calibration data

Track 5   Spare

Track 6   Spare

Track 7   Spare

Track 8   Spare

Track 9   FM record of BER

Track 10   FM record of intercom audio

Track 11   FM record of background power

Track 12   FM record of (2 MHz) scintillation

Track 13   FM record of baseband scintillation

Track 14   FM record of argon beacon laser power.

The tape recorder signal characteristics are listed in Table 18.

AUXILIARY EQUIPMENT

GROUND CHECKOUT EQUIPMENT

The function of the GCE is to test the AOCP, permit accurate optical alignment, and simulate the ground-based portion of the optical communications link. The GCE also is capable of exercising the gimbal mirror, computer, and other components in the integrated airborne system. The GCE capabilities include:

1.   Self-checks alignment, focusing, and optical modulator operation.

2.   Tests static and dynamic alignment of AOCP with visual and electronic readout of alignment/tracking performance.

3.   Checks tracking capabilities of the ID tracker, beam steerers, and gimbal mirror.

4. Checks operation of helium-neon laser and modulator on AOCP.

5. Checks command decoder and command execution.

Figure 99 is the GCE hardware tree showing the various subsystem relationships.
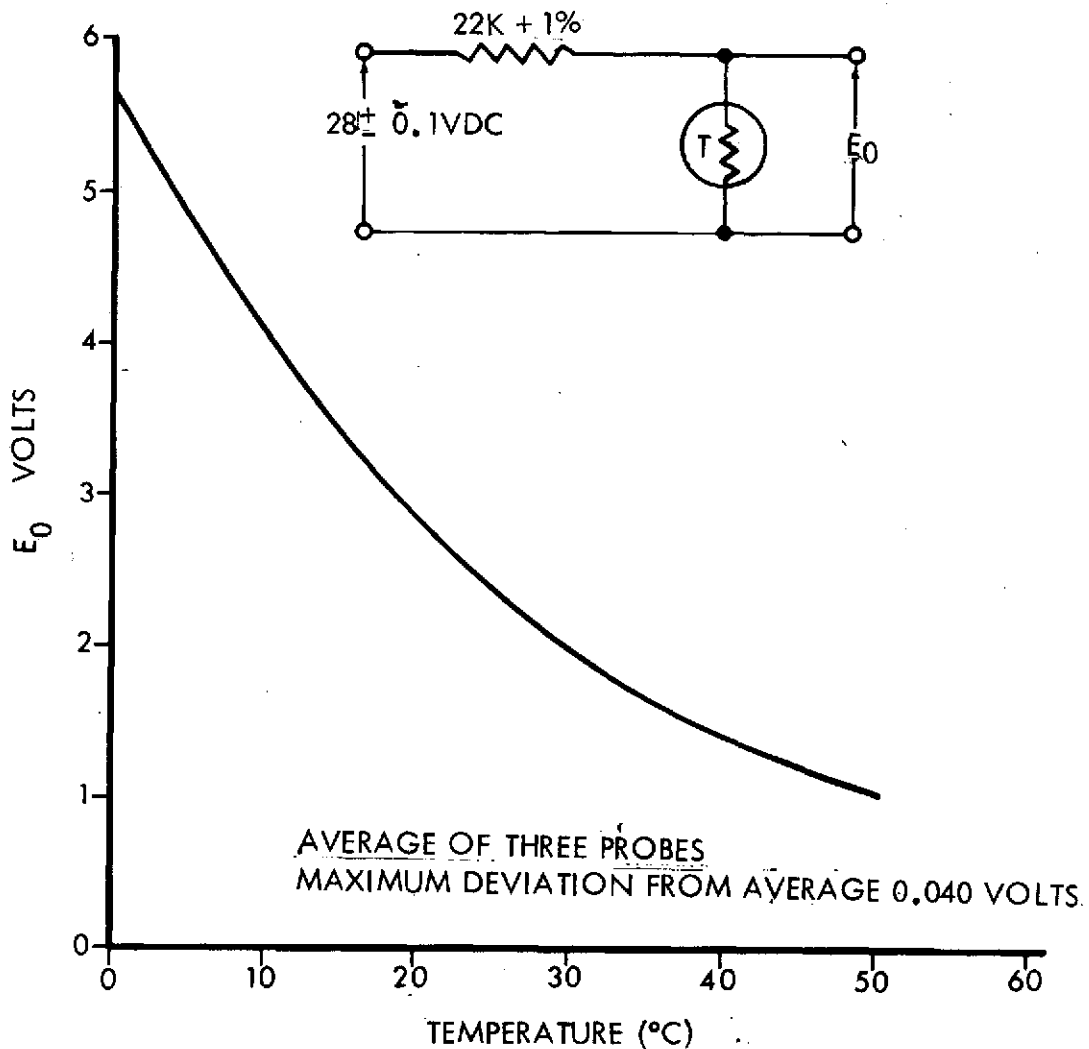
Figure 97. Temperature calibration curve.

TABLE 16. SIGNAL CHARACTERISTICS — GROUND STATION PAM DATA,
0- TO 60-CHANNEL 60-Hz SAMPLE RATE

Data	Channel Number	Analog Range (V)	Parameter Range
Beam Divergence	2	0 to 5	
Receiver FOV	3		
Tracker FOV	4		
Receiver Aperture	5		
Receiver Attenuation	6		
Tracker QMP High Voltage	7		
Dome Position	8		0 to 10 V; 0 to 2π rad (360°)
Fine Tracker Target Presence	10		On/Off Discrete
GBAA Target Presence	11		On/Off Discrete
GBAA Search Mode	12		On/Off Discrete
GBAA Miniscan Mode	13		On/Off Discrete

TABLE 17. SIGNAL CHARACTERISTICS — GROUND STATION VCO CHANNEL DATA

Data	VCO Channel Number	Analog Range (V)	Parameter Range	Carrier Frequency	Bandwidth (Hz)
Ground Track Circle X	2	± 10		560 Hz ± 7.5% Deviation	8
Ground Track Circle Y	3	± 10		730 Hz ± 7.5% Deviation	11
Telescope Polar Velocity	5	± 10	± 87 mrad/sec (5 deg/sec)	1.3 kHz ± 7.5% Deviation	20
Telescope Declination Velocity	6	± 10	± 87 mrad/sec	1.7 kHz ± 7.5% Deviation	25
GBAA Range	8	0 to 4	0 to 40 km	3.0 kHz ± 7.5% Deviation	45
GBAA Error X	9	± 5	± 87 mrad	3.9 kHz ± 7.5% Deviation	60
GBAA Error Y	10	± 5	± 87 mrad	5.4 kHz ± 7.5% Deviation	80
Telescope Error Polar	11	± 10	± 2.42 mrad (± 500 arc sec)	7.35 kHz ± 7.5% Deviation	110
Telescope Error Declination	12	± 10	± 2.42 mrad	10.5 kHz ± 7.5% Deviation	160
Fine Tracker System Error X	13	± 10	± 0 to 436 μrad (± 90 arc sec)	14.5 kHz ± 7.5% Deviation	220
Fine Tracker System Error Y	14	± 10	± 0 to 436 μrad	22.0 kHz ± 7.5% Deviation	330
PAM Data	16	0 to 5		40.0 kHz ± 7.5% Deviation	600

TABLE 18. SIGNAL CHARACTERISTICS — GROUND STATION RECORDER CHANNELS
AT 19 cm/sec (7.5 ips)

Data	Channel Number	Mode	Analog Range (V)	Parameter Range	Bandwidth (kHz)	Center Frequency FM (kHz)
Aircraft Composite TM Data	1	Direct	≈ 1 peak to peak		125	
Command Audio and Servo Ref. Carrier	2	Direct	≈ 1 peak to peak		125	
Time Code	3	Direct	≈ 1 peak to peak	IRIG & Amr. Composite Time Codes	125	
VCO Carriers	4	Direct	≈ 2 peak to peak	See VCO Data Sheet	125	
Bit Error Rate	9	FM	0 to 10	Variable	32	56.25 Wideband II
Intercom Audio	10	FM	2 peak to peak		32	56.25 Wideband II
Background Power	11	FM			32	56.25 Wideband II
2 kHz Scintillation	12	FM			32	56.25 Wideband II
Average Received Power (Baseband Scintillation)	12	FM			32	56.25 Wideband II
Beacon Power	14	FM			32	56.25 Wideband II
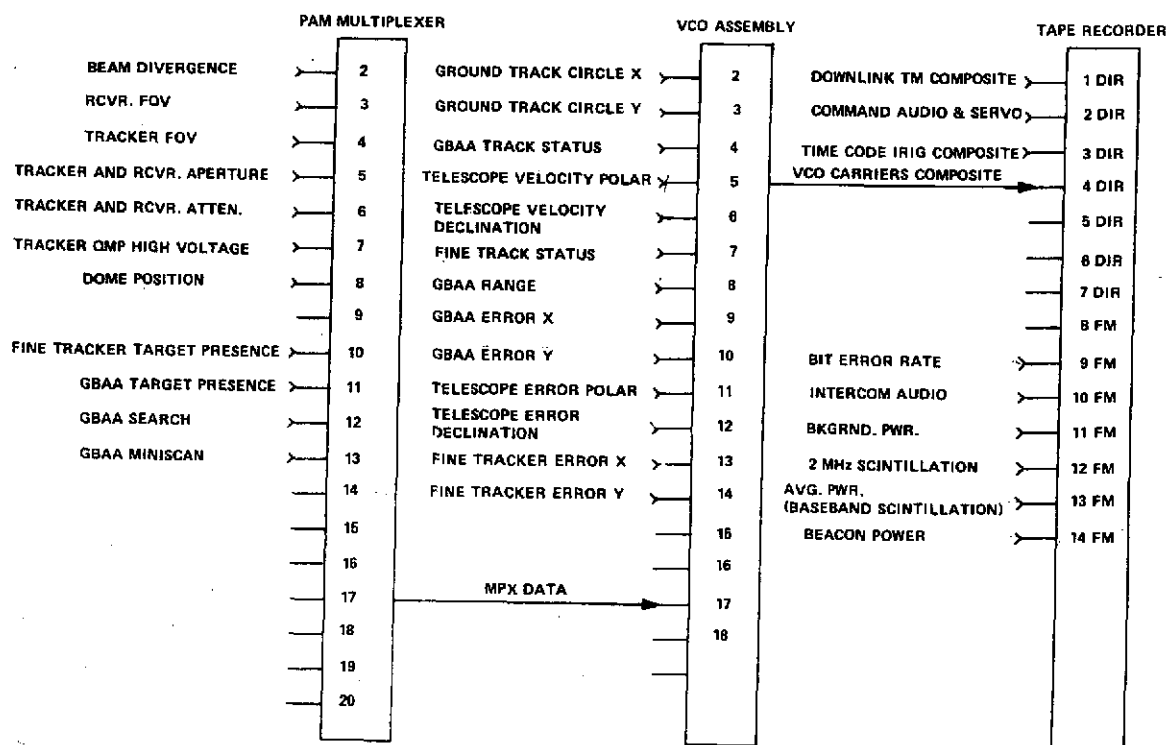
Figure 98. Ground station telemetry data system.

The GCE consists of two units, the control panel and the optical unit, which are linked by cables (not shown in the figure). The optical unit is mounted on a low-profile dolly so that it can be positioned under the fuselage of the WB-57F aircraft in which the AOCP is installed. Figure 100 is a photograph of the GCE equipment with the cover open. The GCE control console (Fig. 101) is a rack of electronic equipment mounted on a four-wheel dolly and consists of the following items:

1. Tone generator for controlling the modulation impressed on the laser modulator in the GCE optical unit.

2. High frequency oscilloscope (Tektronix R454) for observing the modulation from the GCE and AOCP lasers, the outputs of the Y-Z position sensor, and for general utility.

155
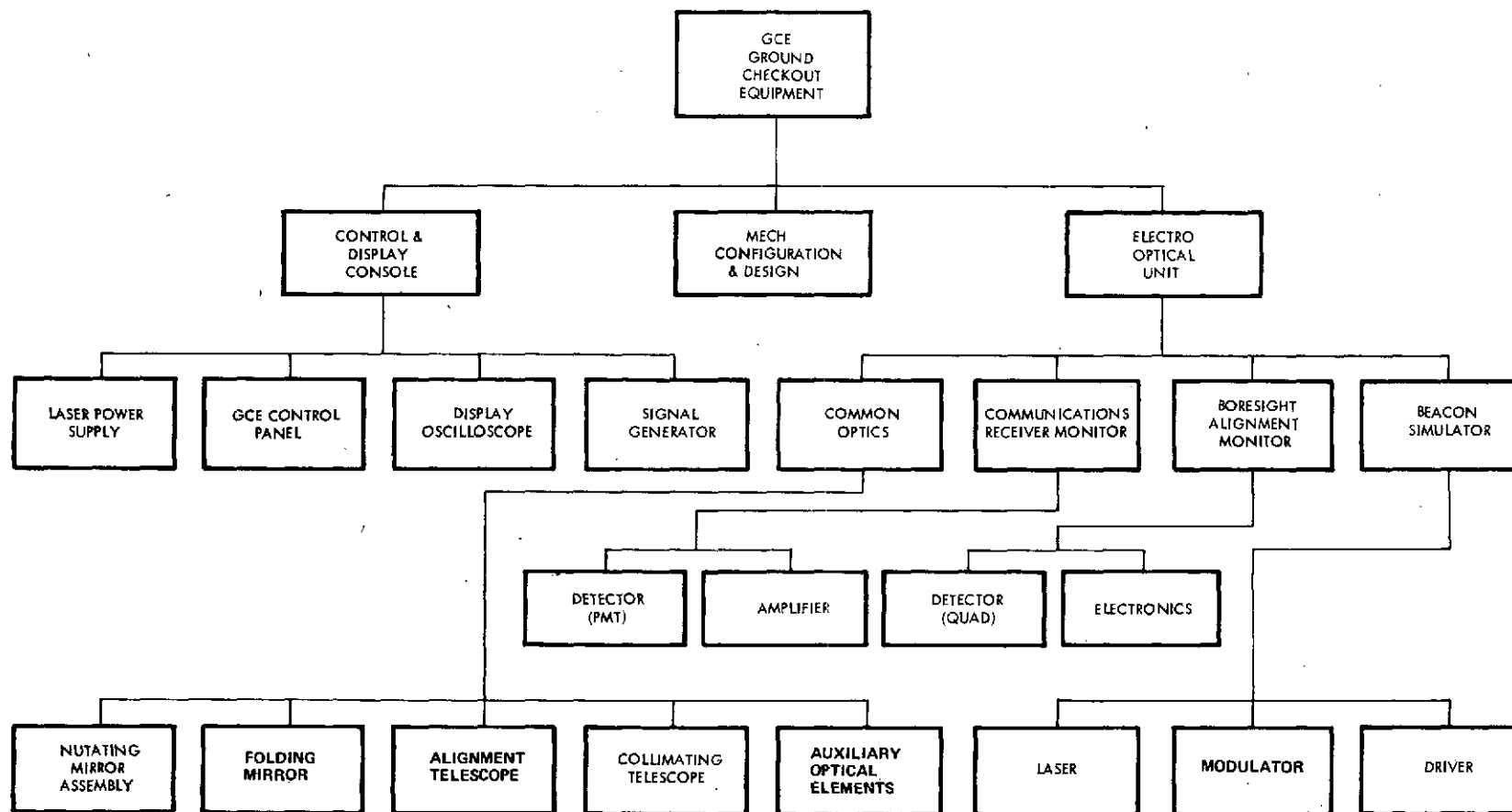
Figure 99. GCE hardware tree.
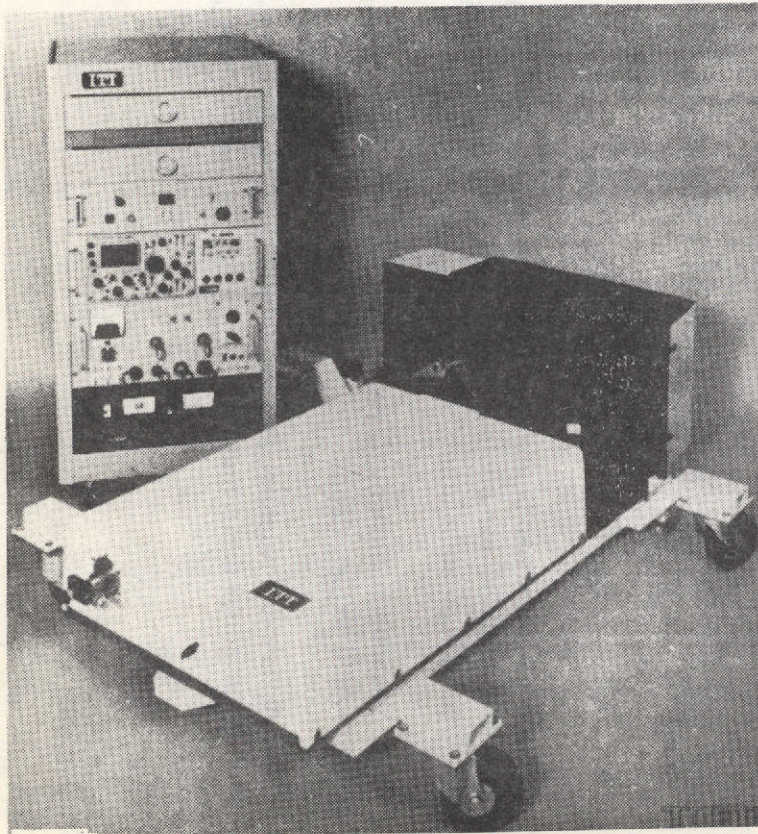
Figure 100.   AVLOC system GCE.
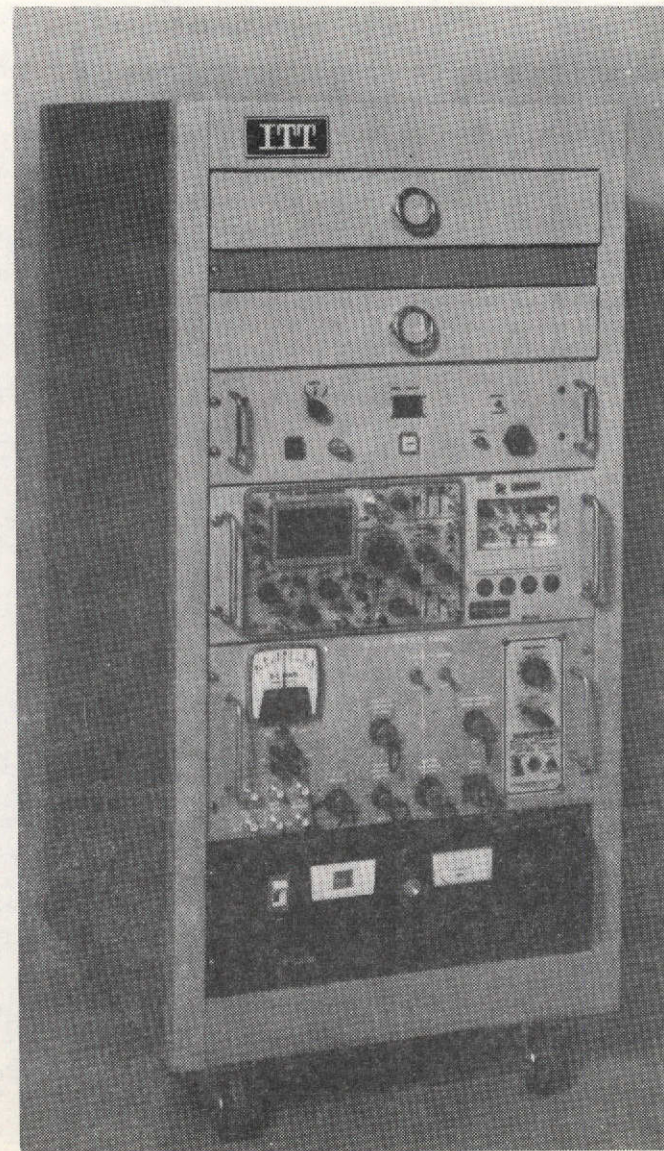
Figure 101.   GCE control and display console.

3. Control panel, which controls the variable-speed nutating mirror motor and dc power on the GCE optical head, provides meter readout of the Y-Z position sensors, controls the flip mirror and shutter solenoids, and accepts BER clock and video signals from the aircraft-mounted equipment.

4. Power supply for RCA LD 2108 argon laser (later replaced by Spectra-Physics Model 162 laser), which is mounted on the GCE optical head.

Also included in the rack are two drawers for storing cables.

A small remote-control box, which connects by cable to the control panel, is provided to permit actuation of the motorized potentiometers in the AOCP for adjustment of the electronic boresight.

The GCE optical unit is an assembly of optical and electronic components and subsystems on an aluminum baseplate, mounted on a low-slung, four-wheel dolly. The following items are included:

1. An argon laser with an output power of several milliwatts at 488 nm to simulate the uplink beam to the opcom receiver on the AOCP.

2. A set of optical attenuators (density: zero, three, five and infinity), mounted on a rotary holder and controlled by a knob on the bulkhead adjacent to the optical viewer. These attenuators control the laser beam power.

3. An electro-optical modulator (Lasermetrics EOM-704) and a modulator driver.

4. A 28-power laser beam expander (Spectra Physics).

5. An 8.3-power beam expander (10.16-cm diameter exit beam), with three folding mirrors, for projecting the collimated argon laser beam and receiving the helium-neon laser beam from the AOCP.

6. Various beam splitters, mirrors, and a cube corner for directing the beams to desired locations.

7. A viewer (telescope) for visually observing the argon and helium-neon laser beams and their mutual alignment, as well as for testing optical collimation.

8. A two-axis position sensor with associated optics and nulling mirror for electronic readout of boresight and tracking misalignment.

9. A photomultiplier detector and amplifier for detecting the modulation on each of the laser beams and providing signals for display on the oscilloscope in the GCE control panel.

10. A 15.24-cm-diameter flat mirror, mounted in an adjustable holder on the shaft of a variable-speed motor for providing a nutation of the projected laser beam through various angles [nominally 0 to 140 mrad (6 deg)] and at various rates.

11. A rectangular mirror, mounted in an adjustable holder which rides on a track, for directing the projected beam upward into the aircraft window at a variety of angles.

Figure 102 is a functional block diagram of the optical unit, and Figure 103 shows the physical layout of this unit for easier identification of the components.

The beacon section includes an argon laser operating at 488 nm followed by an ND filter wheel for controlling the beacon power. The initial design used a laser which proved to be unreliable and unstable in output beam direction. The laser plasma tube was short lived and replaced three times under warranty. The argon laser was then replaced with a newly developed Spectra-Physics Model 162, which has demonstrated excellent stability and life characteristics and greatly improved the performance of the system. The laser is followed by an electro-optical modulator, which places a 10.7-MHz RF subcarrier on the optical beam simulating the communications channel of the operational ground station. The 10.7-MHz subcarrier is FM modulated with the uplink command information to exercise the AOCP receiver system. A beam expander telescope (28X) expands the laser beam to fill the entrance pupil (1.2-cm diameter) of the output telescope. Most of the laser energy reflects from the beam splitter, shown in the functional block diagram, and exits the system through the afocal telescope (8.3X), the rotating mirror, and the adjustable folding mirror. The rotating mirror is included to conically scan the output beam direction through an adjustable cone angle at an adjustable angular rate. This is accomplished by a dual-wedge mirror mounting assembly, which can be differentially rotated to provide deflection angle magnitudes from 0 to approximately 174 mrad (10 deg). The larger scan angles, which are beyond the field of view of the AOCP, are used to exercise the coarse acquisition system and the gimballed mirror. The folding mirror permits the GCE exit beam to be directed up into the aircraft window from various directions simulating different acquisition approach flight paths.
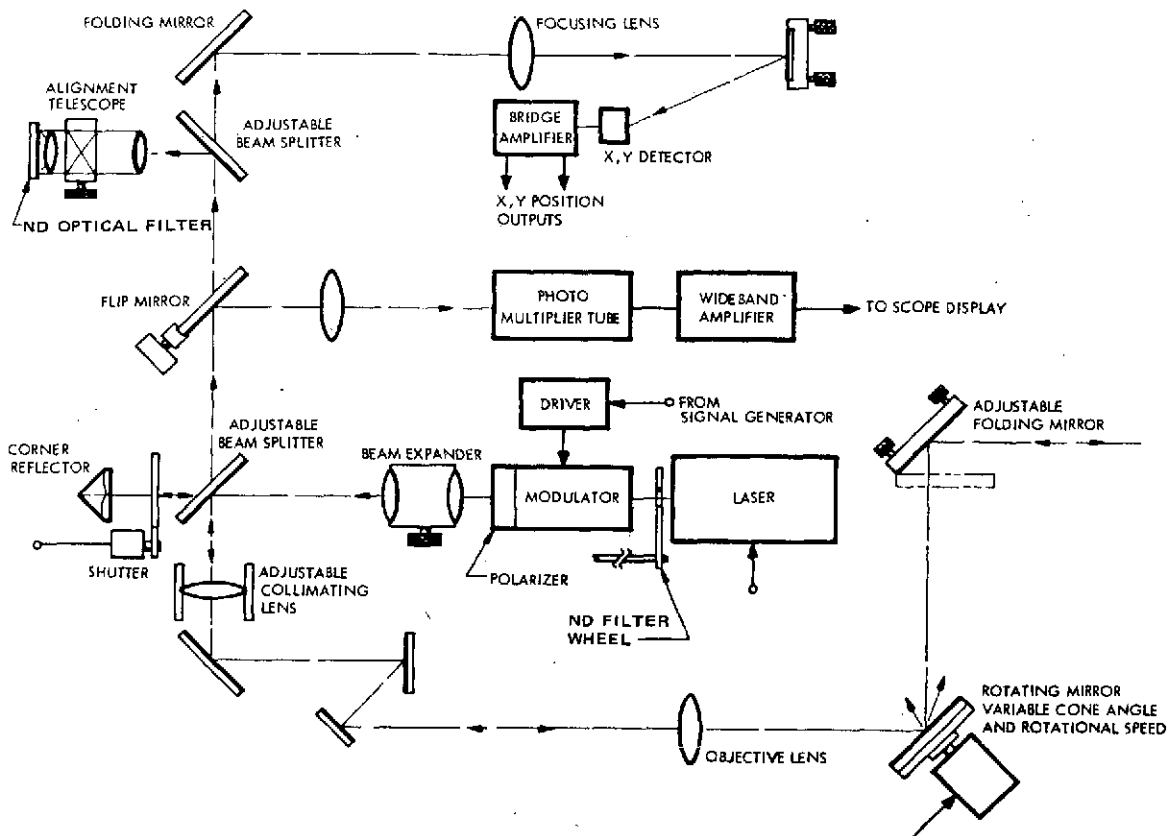
Figure 102. GCE electro-optical unit functional
block diagram.

Figure 104 shows the orientation of the GCE beneath the WB-57F air-
craft for checkout in two different ground station approaches. In addition to
the beam coarse direction control, the adjustable folding mirror provides a
fine adjustment of the beam direction for quantitative calibration of the AOCP
acquisition field and error signal gains. This mirror can also be positioned
so as to autocollimate the GCE afocal telescope in its self-alignment and cal-
ibration mode.

A portion of the GCE laser energy passes through the adjustable beam
splitter (coated to reflect 488-nm radiation and transmit 633-nm radiation) and
impinges on the corner reflector when the shutter is opened. The reflector
returns the energy from the 488-nm laser to the beam splitter, where it is
reflected into the receiver portion of the optical unit for pointing direction refer-
ence and 10.7-MHz modulation index monitoring purposes. When the flip-mir-
ror is in position, the GCE laser is deflected onto the photomultiplier detector,
and the 10.7-MHz subcarrier is detected and dc coupled through a wideband

160

MODULATOR — X-Y SENSOR

MODULATION DETECTOR —

BEAM EXPANDER —

IMAGING LENS —

FIELD LENS —

ADJUSTABLE NULLING MIRROR

BEAM SPLITTER —

FOLDING MIRROR SLIDING GUIDE RAIL

ALIGNMENT TELESCOPE —

FLIP MIRROR —

SHUTTER —

ARGON LASER

FOLDING MIRROR

RETRO – REFLECTOR —

ROTATING MIRROR

COLLIMATING LENS —

AFOCAL TELESCOPE OBJECTIVE LENS 100 MM DIA. I METER FOCAL LENGTH
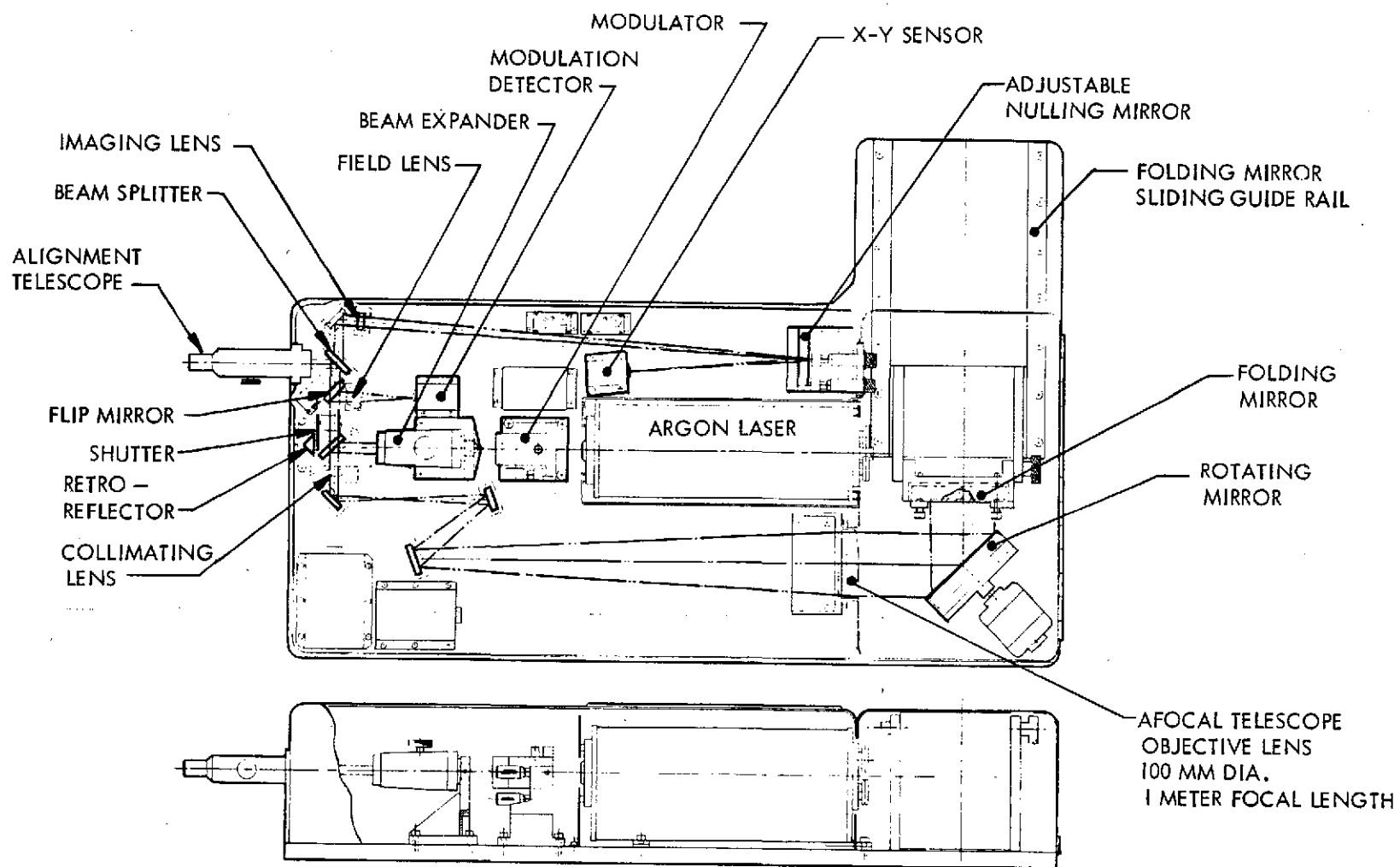
Figure 103. Ground Checkout-Equipment.

amplifier for display on the control console oscilloscope. This permits monitoring and control of the modulation depth of the laser subcarrier.

When the flip-mirror (controlled from the console) is removed from the optical path, the beam from the retroreflector continues onto the beam splitter element, which reflects a portion of the energy into the alignment telescope to obtain a visual reference of the beam position and quality. The main part of the beam passes through the beam splitter and is imaged onto an X-Y position detector. The X-Y sensor provides an output in two orthogonal axes, indicating the beam position on the detector. An adjustable folding mirror is used to precisely center the 488-nm image on the X-Y sensor's null axis to establish the transmitted beam reference direction for later comparison with the received beam's position from the AOCP. This then determines the magnitude and direction of any boresight error within the AOCP system. The AOCP boresight correction is accomplished by commanding an offset track to the ID tracker from the GCE while nulling the receiver AOCP beam on the GCE X-Y sensor.

In operation, the collimated 10.16-cm-diameter, 488-nm beam is directed into the AOCP and acquired and tracked. The AOCP then points its 633-nm beam back toward the GCE unit. The AOCP transmitted beam enters the GCE afocal telescope after reflection from the folding and rotating mirrors and passes through the beam splitter into the GCE receiver section. When the flip-mirror is in position, the incoming beam is folded onto the photomultiplier detector for AOCP modulation index measurement. Removal of the flip-mirror permits the AOCP laser beam to be imaged onto the X-Y position sensor. Since the X-Y position sensor has previously been nulled with the GCE laser, the position read from the X-Y sensor from the AOCP beam is a measure of boresight error between the AOCP receiver and transmitter. When the rotating mirror is operated, causing the GCE beam to be deflected dynamically, the AOCP tracker will detect the input angle change and correct for this deflection by closed-loop pointing of the beam steerer mirrors. Consequently, the AOCP transmitted beam direction exactly compensates for the GCE rotating mirror's deflection, and the image on the X-Y sensor remains still. As the rotational rate of the GCE mirror is increased, the AOCP control system lag can be observed at the X-Y sensor output. The nulling sensitivity existing in the X-Y position sensor is better than 1 μrad.

Figure 105 is the electrical block diagram for the GCE. The dashed line represents the interface between the optical unit and the control console. The interface cabling and optical unit operation and mode selection occurs at the GCE control panel (Fig. 101).

162

A. ACQUISITION
SIMULATION

B. CIRCULAR FLIGHT
PATH SIMULATION
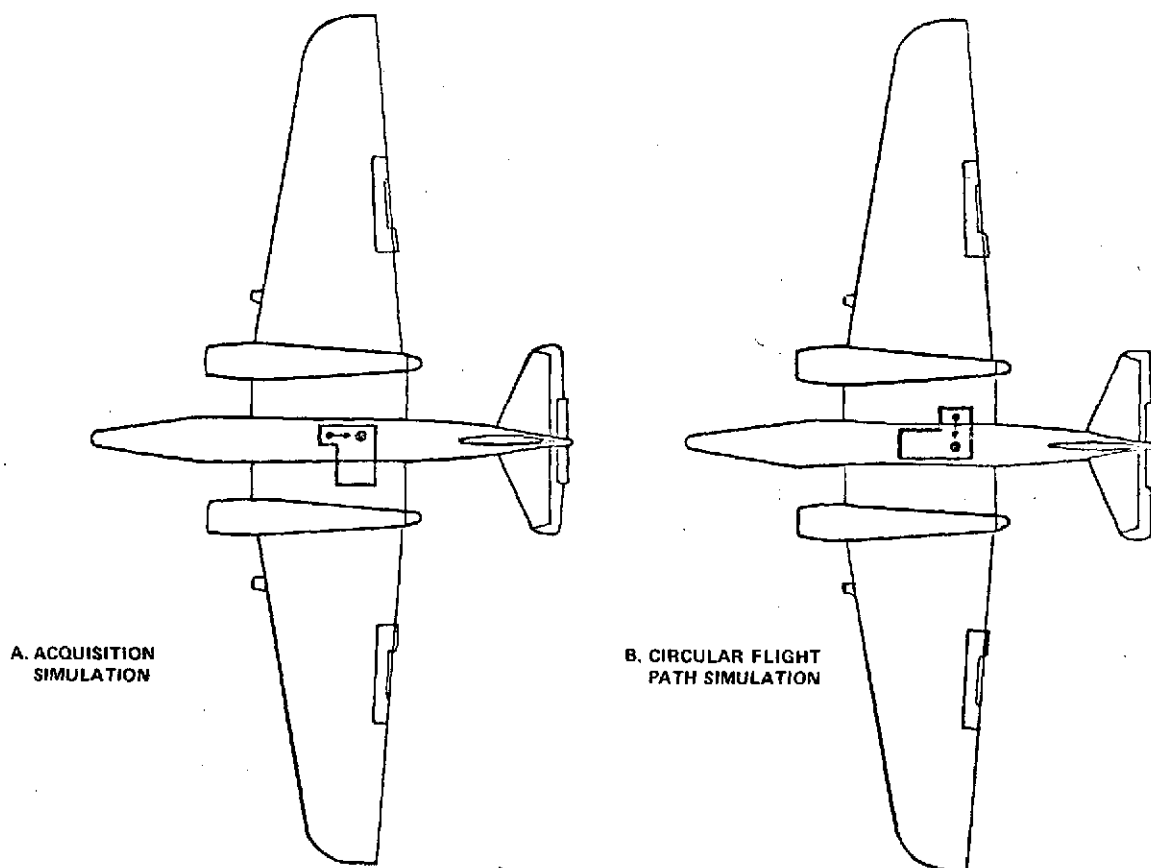
Figure 104. GCE orientations.

ELECTRICAL GROUND SUPPORT EQUIPMENT (GSE)

The electrical GSE consists of a module and associated cabling for perform-
ing electrical tests on the AVLOC system. Figure 106 is a photograph of the
module. Consisting of a 122-cm-high by 48.3-cm-wide rack, the module con-
tains three major panels plus a bottom storage drawer. Access to the rack is
through a hinged rear door.

The GSE is used primarily for electrical and functional tests of the entire
AVLOC system during laboratory and preflight operations. However, the unit
is also used to check out the airborne system when the AOCP is removed, such
as preparing for the system integration tests.
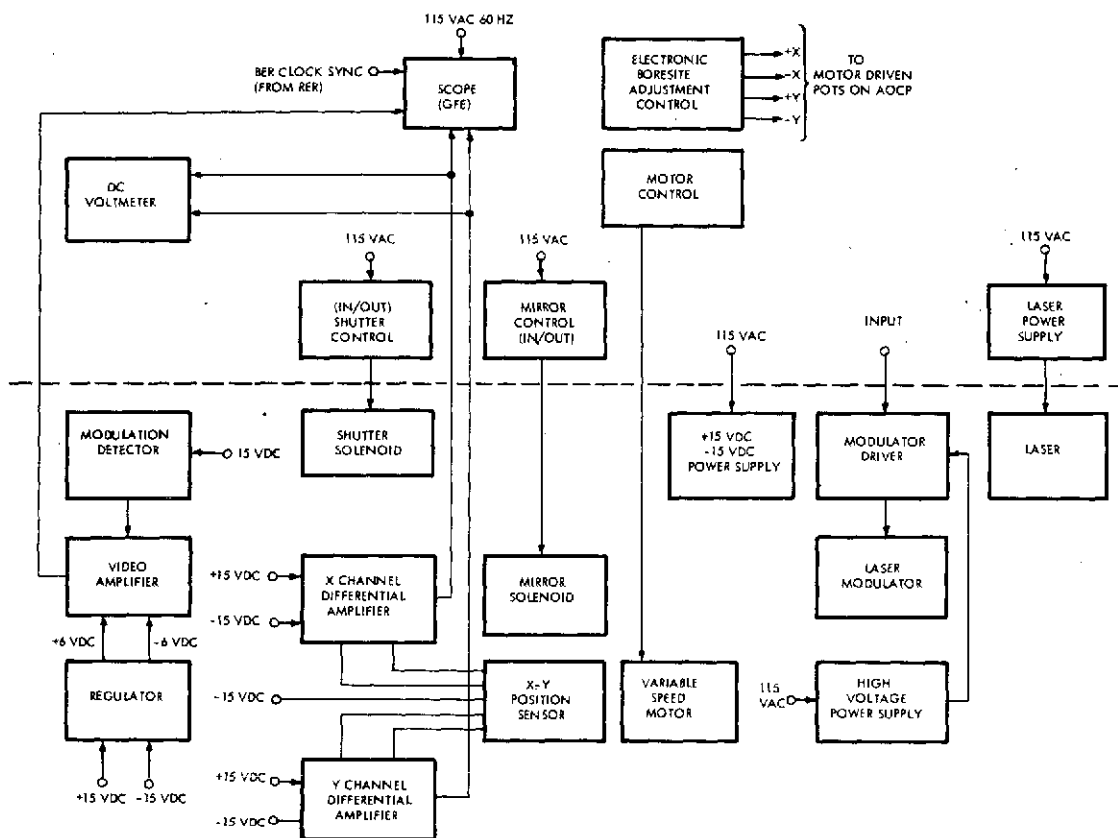
Figure 105. Electrical block diagram of GCE.

The monitor panel contains the primary controls and displays used in system checkout and also distributes power and measurements to the other two panels. The functions of the monitor panel are described in Table 19.

The substitute panel is used for testing the auxiliary equipment when the AOCP equipment is disconnected. It does this by simulating inputs to the auxiliary equipment and measuring the resultant responses. The substitute panel functions are given in Table 20.

The test-point access panel provides selected test points for monitoring system operation and making measurements with external test equipment. These functions are given in Table 21.

164
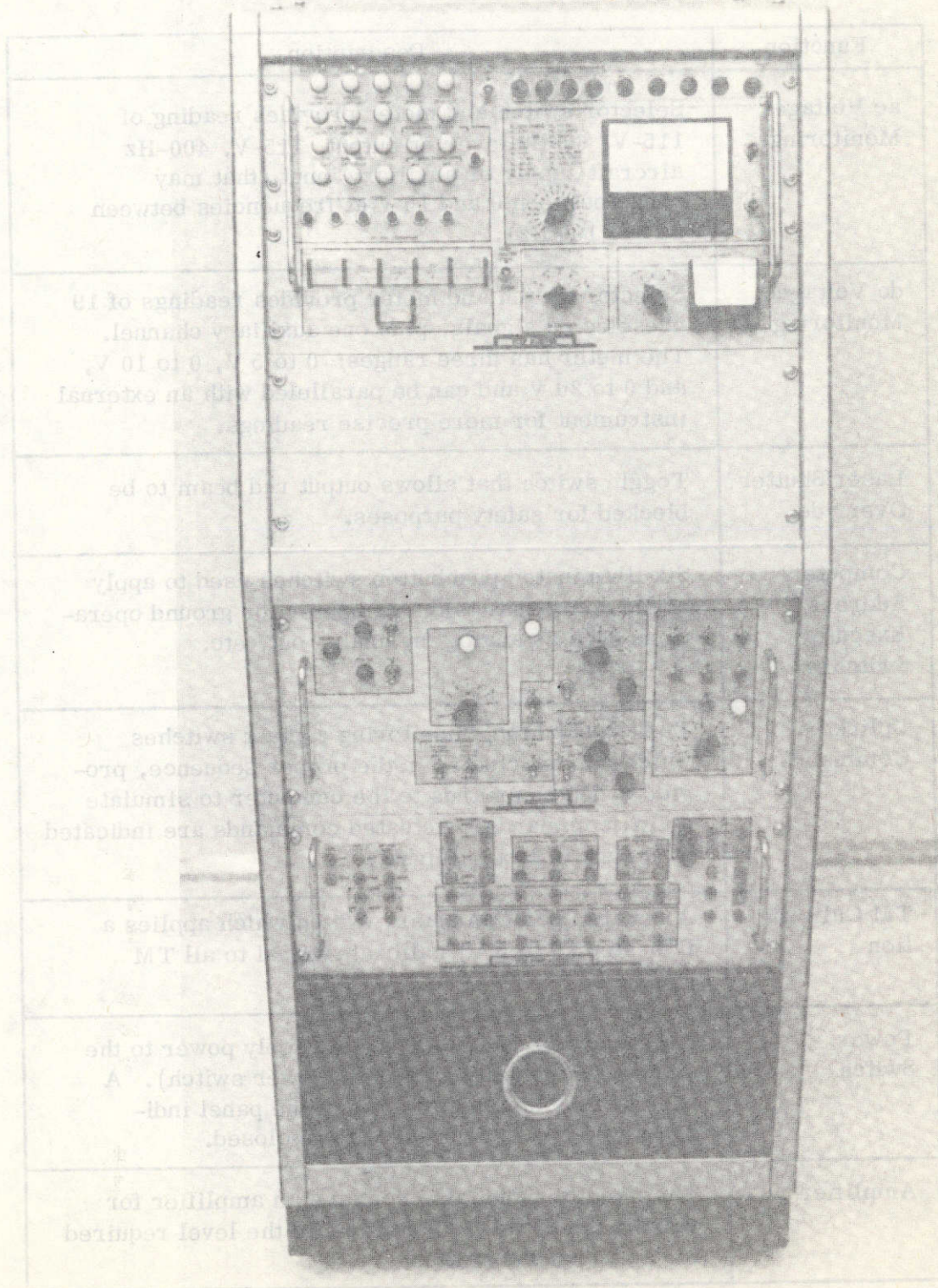
Figure 106. GSE module.

TABLE 19. MONITOR PANEL FUNCTIONS

Function	Description
ac Voltage Monitoring	Selector switch and meter provides reading of 115-V, 60-Hz inverter output, 115-V, 400-Hz aircraft supply or auxiliary input (that may range between 0 and 15 V at frequencies between 25 and 100 Hz).
dc Voltage Monitoring	Selector switch and meter provides readings of 19 preselected signals, plus one auxiliary channel. The meter has three ranges: 0 to 5 V, 0 to 10 V, and 0 to 30 V and can be paralleled with an external instrument for more precise readings.
Laser Shutter Override	Toggle switch that allows output red beam to be blocked for safety purposes.
Computer Address/ Execute Switches	Six illuminated pushbutton switches used to apply coded commands to the computer for ground operations such as analog in, analog out, etc.
Uplink Commands	Eight pushbutton, monitoring contact switches which, when actuated in the proper sequence, provide coded commands to the computer to simulate uplink commands. Actuated commands are indicated by a bank of labeled lights.
TM Calibration	A reverse position rotary switch which applies a five-step (0 to 5 V) calibrate signal to all TM channels.
Power Switch	Toggle switch used to remotely apply power to the system (in parallel with main power switch). A bank of nine lamps at the top of the panel indicates which circuit breakers are closed.
Amplifier	The monitor panel also contains an amplifier for raising the downlink TM signal to the level required for a ground TM station.

166

TABLE 20. SUBSTITUTE PANEL FUNCTIONS

Function	Description
Analog Substitute	Two rotary switches and associated pots are used to apply 0 to 5 Vdc and 0 to ± 5 Vdc, respectively, as simulated inputs from the AOCP. Ten functions for the 0 to 5 V input and seven functions for the bipolar input are accommodated. The selected voltage can be read on the dc monitor panel meter.
Discrete Substitute	Three toggle switches provide on/off logic signals as simulated inputs from the AOCP.
Power Monitoring	Illuminated lamps indicate when power is supplied during subsystem testing.
Continuity Monitoring	An eight-position rotary switch and indicator lamp check the shield connections returned to common on the REC end.
Uplink Commands	Momentary contact pushbutton switches, when actuated in the proper coded sequence, send command codes to the computer over any one of 17 lines. A lamp indicates when the command is received

GROUND HANDLING EQUIPMENT

Experiment Assembly Transporter

The Experiment Assembly Transporter dolly (Fig. 107) is used to transport the Experiment Platform Assembly and to install it into the aircraft. The transporter jacks allow adjusting the height over a range of more than 30 cm for installation of the experiment platform into the aircraft.

Experiment Test Support (Yellow Frame)

The Experiment Test Support frame is used to support the Experiment Platform Assembly during laboratory testing and checkout. The support height, which is adjustable over a 50-cm range, is nominally the same as the aircraft support height. The Experiment Test Support is also shown in Figure 107.

TABLE 21. TEST-POINT PANEL FUNCTIONS

Function	Description
Drift-Site TV Signal Substitution	Test points are provided to accommodate a synchro—simulator for testing the drift-site TV when the system is removed from the aircraft.
Tape-Recorder Channels	Test points are provided for monitoring the tape-recorder channels.
Auxiliary Meter Inputs	Test points are provided for using the monitor panel meter to read any of the signals monitored on the test panel.
dc Power	Test points provide both regulated and unregulated 28-V power for external use.
Signal Monitoring	All other test points on the panel are for monitoring specific signals.

Canister Cradle Transporter

The Canister Cradle Transporter is used to support the REC during laboratory tests, to transport it, and to support it during installation into the aircraft. For installing the canister into the aircraft, manual bomb hoists (USAF Aero 14C or equivalent) are used in conjunction with the cradle transporter, as shown in Figure 108.

RADAR VECTORING OF TARGET AIRCRAFT

The Army Missile Command's assistance was obtained in order to place the WB-57F aircraft into the proper flight path. A modified Nike-Hercules radar system was used for this purpose. The system included both an acquisition and a tracking radar. In a typical flight, the aircraft would be acquired by radar in the Birmingham area (approximately 160 km south of Huntsville), vectored north so as to enter the tracking station area on a tangential path to the desired circular flight pattern, and then continually vectored in the desired circular path (approximately an 11.2-km radius). This was done by means of a VHF link

168
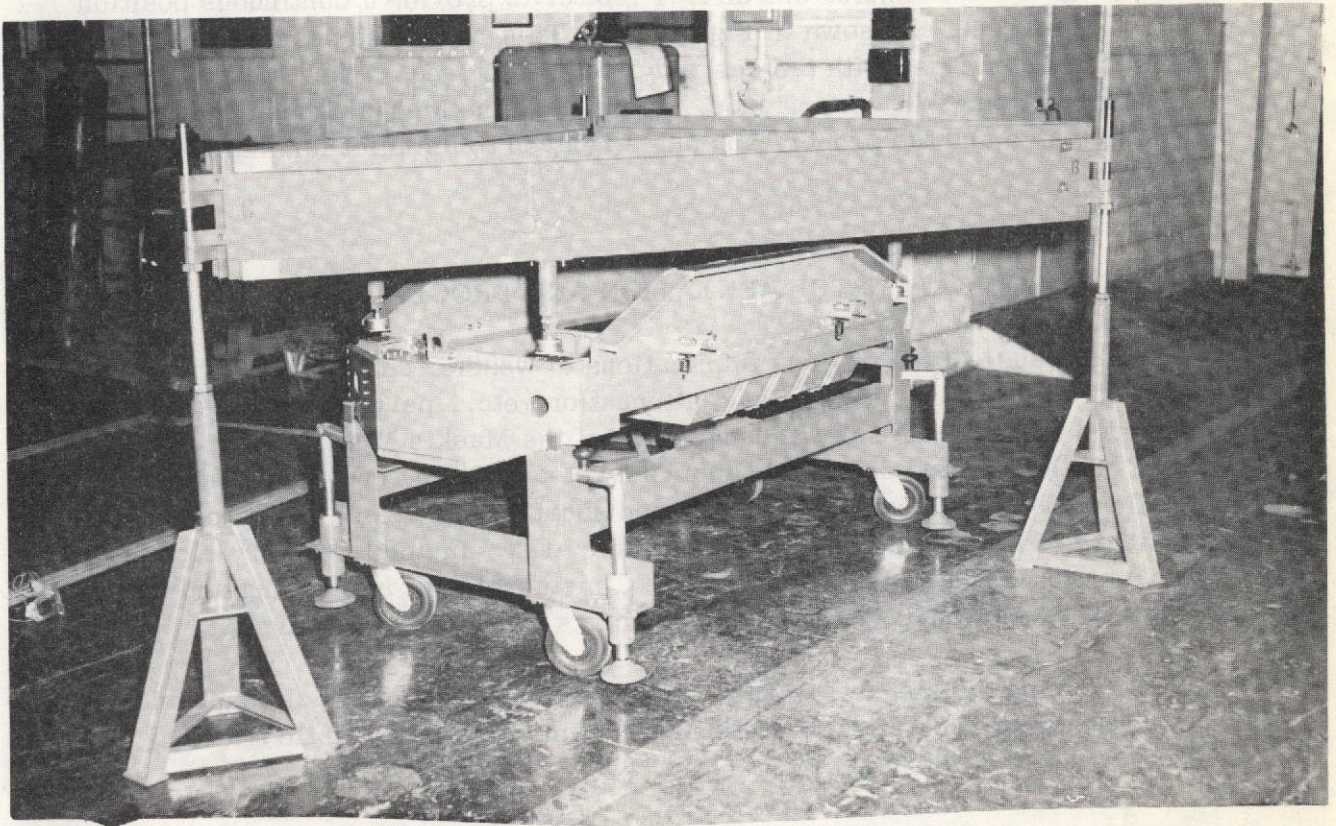
Figure 107. Experiment Assembly Transporter.
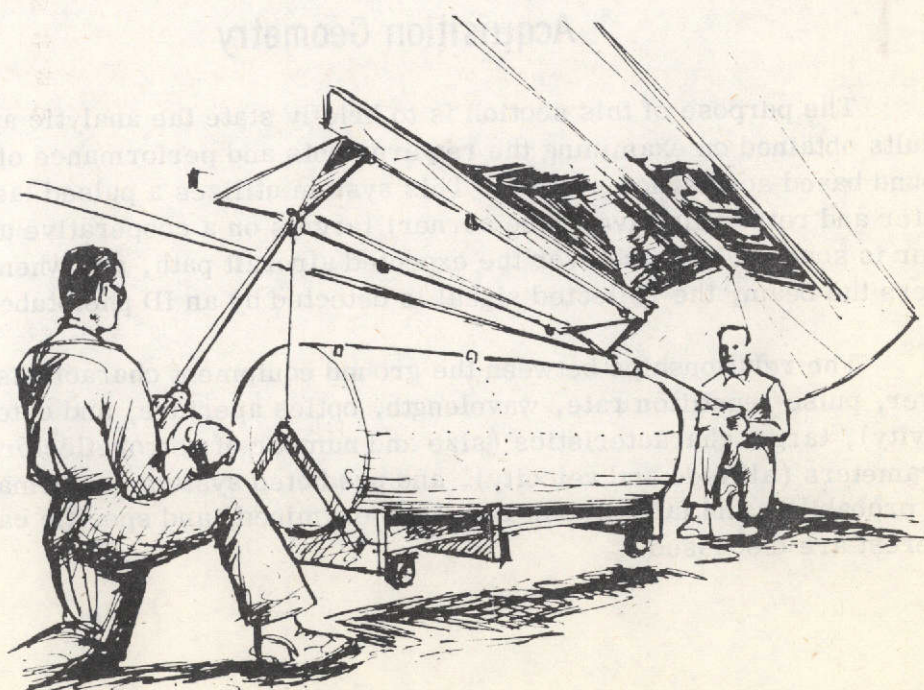
Figure 108. Canister installation.

between the radar site and the aircraft pilot. The tracking radar was interfaced with an HP-9800 computer and an X-Y plotter to provide a continuous position plot of the target, as shown in Figure 109. This real-time position plot was continually compared with the desired circle, centered on the Madkin Mountain tracking station. With experience, the effect of the high-altitude winds could be anticipated and the proper bank angle relayed to the pilot for maintaining the circle.

METEOROLOGICAL INSTRUMENTATION AND PROCEDURES

Because of the obvious implications of weather conditions on the measurement of scintillation, atmospheric attenuation, etc., pertinent weather data were recorded during each experiment flight. At the Madkin Mountain site, temperature, humidity, wind direction, and wind velocity were recorded. Additionally, a balloon-borne radiosonde was launched shortly before each flight to obtain a vertical profile of weather conditions in the area. In addition, very close coordination was required with the MSFC meteorologist in planning and executing each flight. National Weather Service charts were used extensively.

During the last few flights, a relative measurement of atmospheric transmission was obtained by taking a photometric reading while tracking Polaris with the telescope.

ENGINEERING ANALYSIS

Acquisition Geometry

The purpose of this section is to briefly state the analytic approach and results obtained on examining the requirements and performance of an active ground based acquisition system. This system utilizes a pulsed laser transmitter and retroreflective (cube corner) targets on a cooperative aircraft. The laser is scanned in space over the expected aircraft path, and when the aircraft enters the beam, the reflected signal is detected by an ID phototube camera.

The relationships between the ground equipment characteristics (laser power, pulse repetition rate, wavelength, optics aperture, and detector sensitivity), target characteristics (size and number of retroreflectors), aircraft parameters (altitude and velocity), and predicted system performance (detection probability and false alarm rate) are examined, and specific cases of interest are discussed.

170

TARGET TRACKING RADAR

ACQUISITION RADAR

CONSOLE

X-Y PLOTTER

H-P-9800
CALCULATOR

MADKIN MOUNTAIN
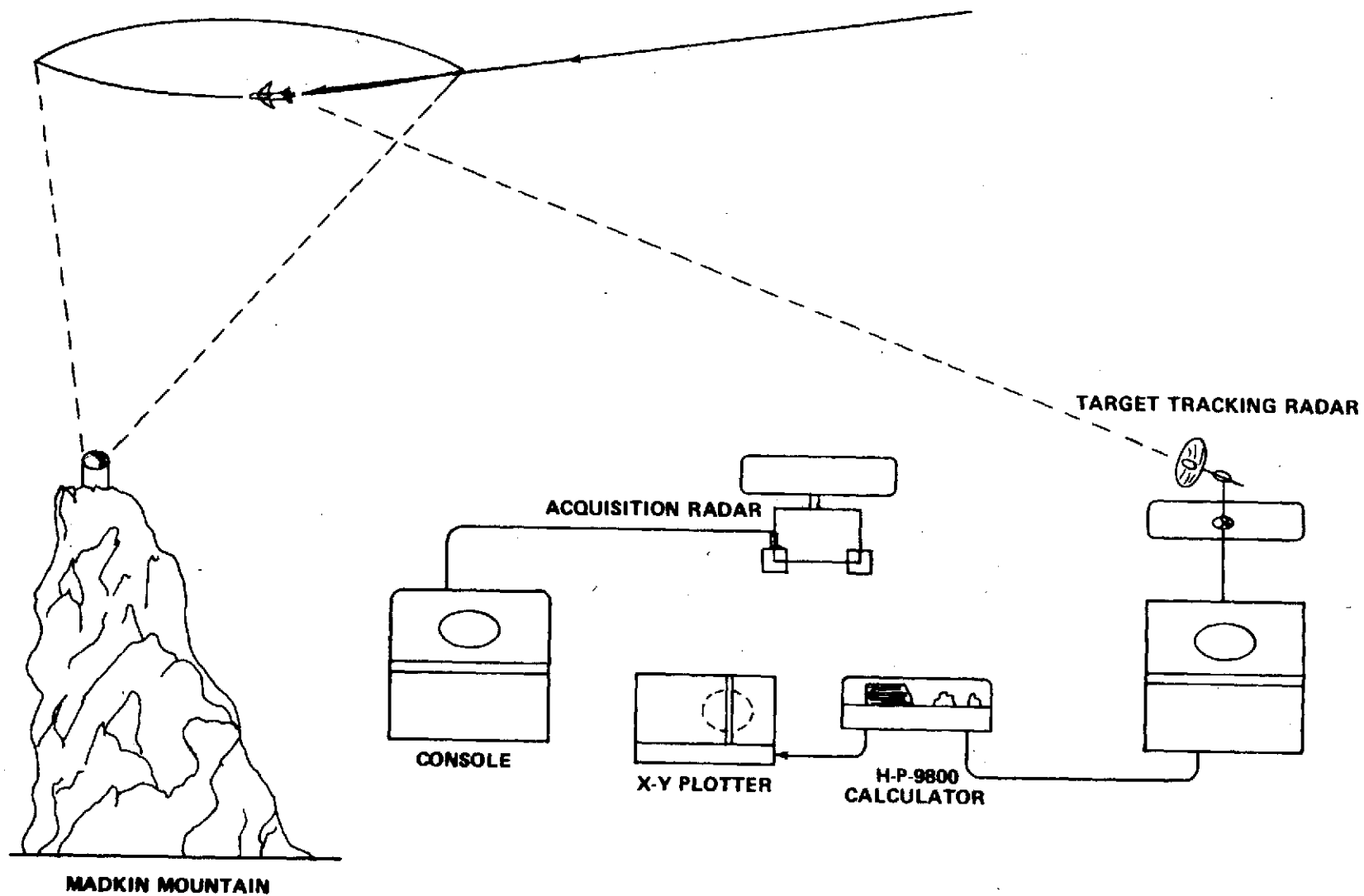
Figure 109. Radar tracking instrumentation.

GEOMETRICAL CONSIDERATIONS

GENERAL RELATIONSHIPS

Developed in the following paragraphs are the relationships between the scan geometry of the laser transmitter, the aircraft velocity and altitude, the pulse repetition rate of the laser, and the beam divergence of the laser transmitter (i.e., the scan element angular size).

The geometry of the system is shown in Figure 110. The aircraft is flying at velocity v and altitude H and is at range R from the ground based acquisition system. The line of sight from the ground station to the aircraft is at an angle θ with the local vertical, and the angular velocity of the aircraft with respect to the ground station is $\dot{\theta}$. The acquisition system transmits laser pulses of angular width $\Delta\phi$, using n such pulses to sweep out the search scan angle ψ. Successive pulses overlap by the fraction ρ_x.

The image dissector camera is effectively inactive during its retrace, which requires some fraction ϵ of the trace scan period.

In order to allow some time, T_{acq}, to change the mode of operation of the ID camera from Search to Acquisition and Track, an effective overlap in the scheme is provided in the direction of the aircraft velocity. The overlap factor is ρ_y.

The target aircraft is known to be flying a course that will pass within the search scan angle ψ and is traveling with an angular velocity $\dot{\theta}$; therefore, its possible position sweeps out a solid angle at a time rate of

$$\Omega_a = \psi\dot{\theta} \quad . \tag{5}$$

(The subscript a refers to aircraft.)

The ground acquisition system operating in the Search mode must sweep out or scan its search field of view at a somewhat faster rate because of the overlap factors and the ID tube retrace factor previously mentioned. The search rate of the system is

$$\Omega_s = \Omega_a (1 + \epsilon) (1 + \rho_x) (1 + \rho_y) , \qquad (6)$$

or, from equations (5) and (6),

$$\Omega_s = \psi\theta (1 + \epsilon) (1 + \rho_x) (1 + \rho_y) . \qquad (7)$$

A diagram illustrating the above relationship is shown in Figure 111.

Let the laser pulse repetition rate be f pulses per second, the time between pulses be t seconds, and the laser beam have a square cross section of angular dimension $\Delta\phi$.

The pulse repetition rate is reciprocal of the time between pulses, i.e.,

$$f = \frac{1}{\tau} . \qquad (8)$$

The solid angle of the laser beam must be

$$(\Delta\phi)^2 = \frac{\Omega_s}{f} = \Omega_s \tau . \qquad (9)$$

The number of elements per search scan line n is then

$$n = \frac{\psi(1 + \rho_x)}{\Delta\phi} . \qquad (10)$$
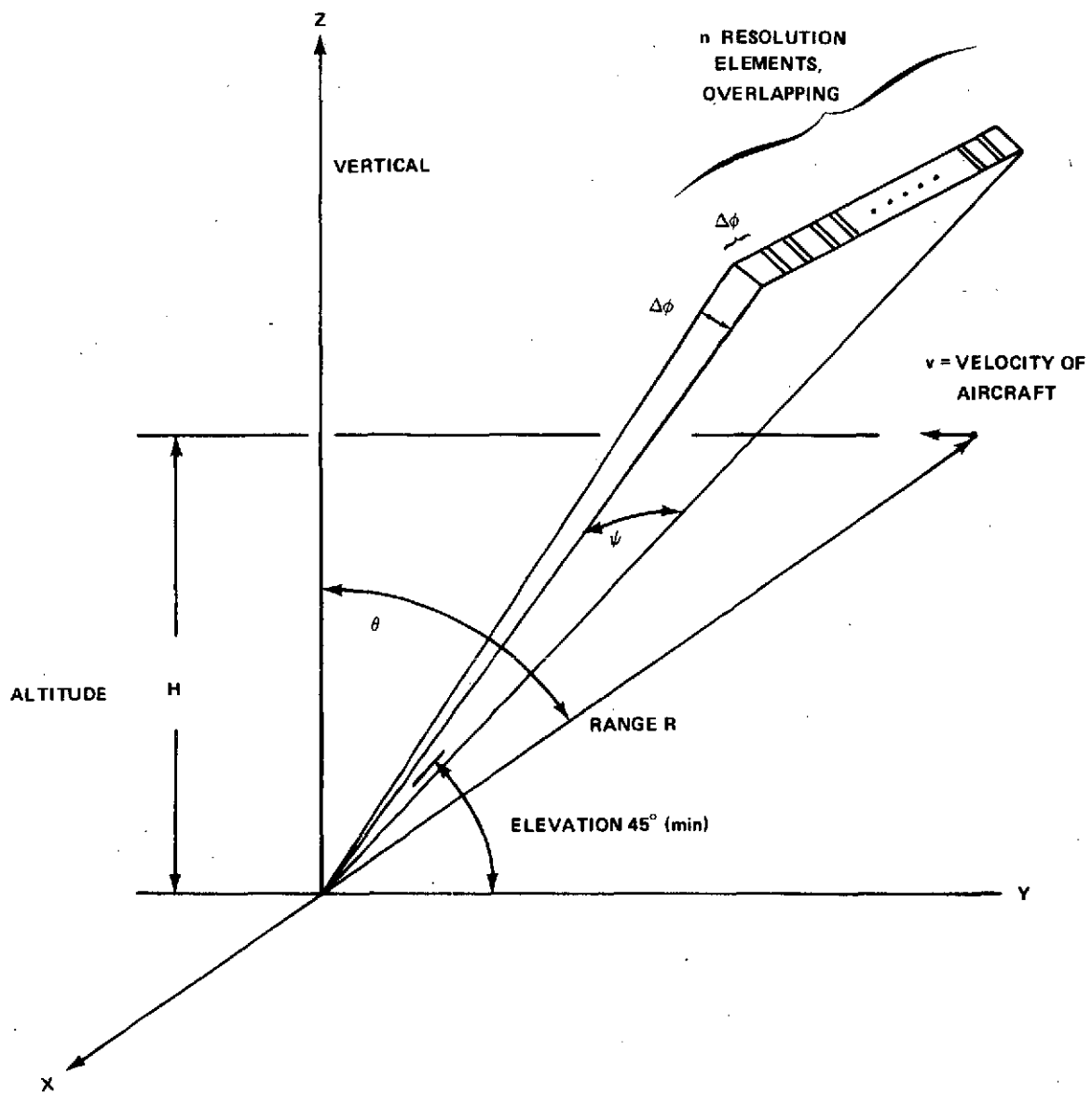
Figure 110. System geometry.
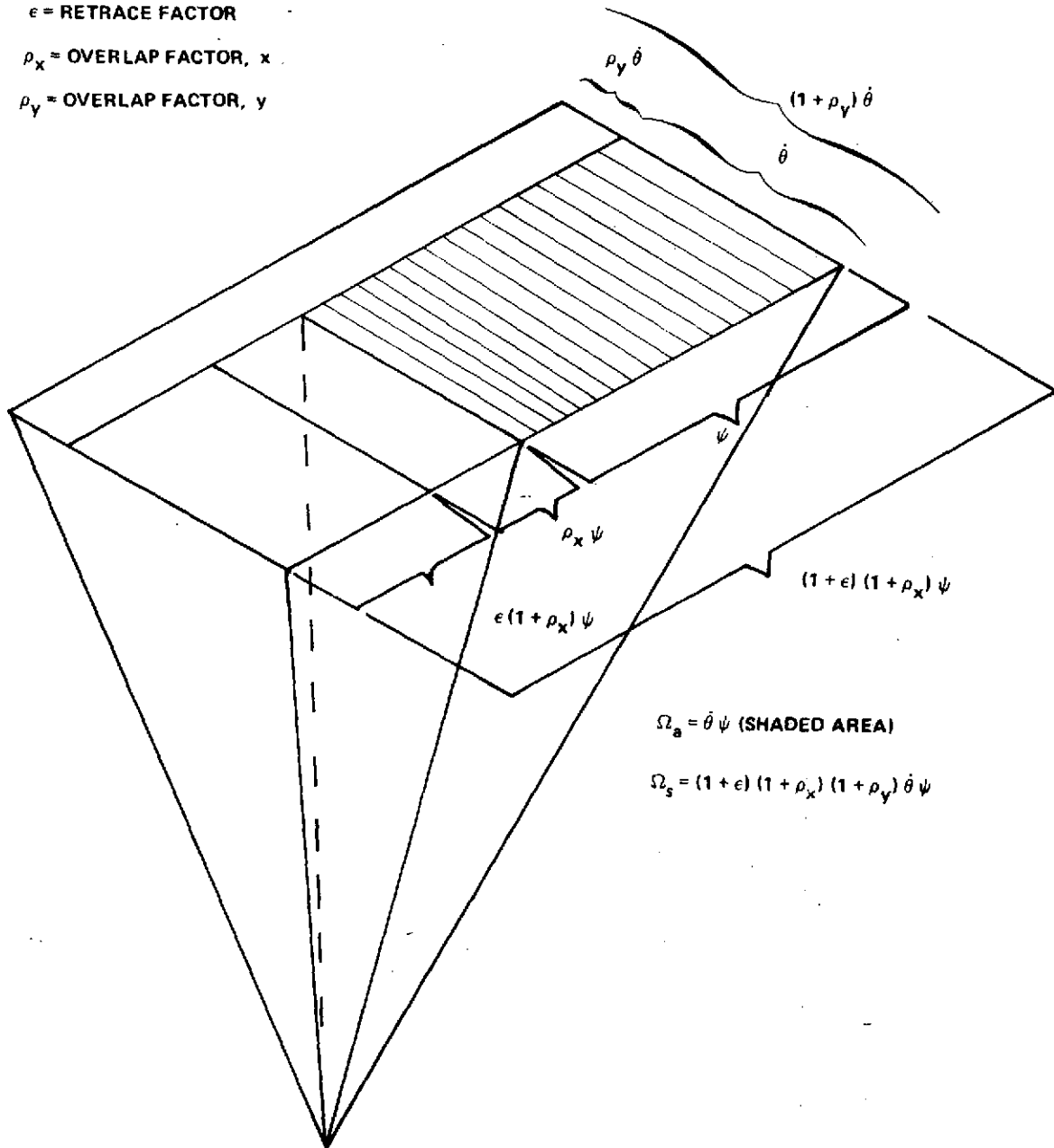
Figure 111. Representation of solid angle scan rate (steradians/sec) for aircraft (Ω_a) and search system (Ω_s).

Taking the square root of equation (9) and substituting in equation (10), one obtains

$$n = \frac{\psi(1 + \rho_x)}{(\Omega_s \tau)^{1/2}} \quad .$$

(11)

Substituting equation (7) into equation (11),

$$n = \frac{\psi(1 + \rho_x)}{[\psi \theta (1 + \epsilon)(1 + \rho_x)(1 + \rho_y)]^{1/2}} \quad .$$

(12)

This simplifies to

$$n = \left[\frac{\psi(1 + \rho_x)}{\theta(1 + \epsilon)(1 + \rho_y)\tau} \right]^{1/2} \quad .$$

(13)

The time T_ϕ for the aircraft to pass through the beamwidth $\Delta\phi$ is

$$T_\phi = \frac{\Delta\phi}{\theta} \quad .$$

(14)

The minimum (worst case) time the system will have to perform the mode range from Search to Acquisition and Track is

$$T_{acq} = \rho_y T_\phi = \frac{\rho_y \Delta\phi}{\theta} \quad .$$

(15)

176

The search line scan period τ_ψ is

$$T_\psi = n \ \tau \ (1 + \epsilon) \tag{16}$$

Also,

$$T_\psi = T_\phi \ (1 - \rho_y) \ . \tag{17}$$

It should be noted that

$$T_\phi = T_\psi + T_{acq} \ . \tag{18}$$

APPLICATION TO SPECIFIC CASES

The relationships derived previously are now applied to specific cases of interest, and the results are presented in tabular form. These results are used later in radiometric calculations.

The following values are assumed:

$$\psi \ = \ 0.175 \ \text{rad} \ (10 \ \text{deg}),$$

$$\phi \ = \ 8.7 \ \text{mrad/sec} \ (0.5 \ \text{deg/sec}),$$

$$\epsilon \ = \ 0.2,$$

$$\rho_x \ = \ 0.1,$$

$$\rho_y \ = \ 0.2.$$

It is noted that θ, in radians/seconds is

$$\theta = \frac{v}{H} \cos^2 \theta \qquad\qquad (19)$$

where v is the aircraft velocity and H its altitude. The assumed value of 0.5 deg/sec is appropriate for acquisition at $\theta = 45$ deg for an aircraft of velocity 0.206 m/sec (400 n. mi./hr) at an altitude of 12.2 km (40 000 ft) or greater.

Several pulse repetition rates were of interest, corresponding to the ranges available from gallium arsenide semiconductor diode lasers and pulsed argon ion gas lasers.

The specific values chosen for f were 200, 400, 1000, 2000, and 4750.

Using the above assumed values in equations (8) and (13), one can calculate n, the number of laser pulses (or resolution elements) per scan. This result is substituted into equation (10), which is solved for $\Delta\phi$. Also, T_ϕ, T_{acq}, and T_ψ are calculated from equations (14), (15), and (16).

The results are given in Table 22.

TABLE 22. SCAN PARAMETERS AS A FUNCTION
OF LASER PULSE REPETITION RATES

f (sec^{-1})	τ (sec)	n	$\Delta\phi$ (rad)	T_ϕ (sec)	T_ψ (sec)	T_{acq} (sec)
200	0.0050	58	0.0002	0.3793	0.3161	0.063
400	0.0025	82	0.0023	0.26832	0.2236	0.045
1000	0.0010	129	0.00015	0.1705	0.1421	0.028
2000	0.0005	183	0.00105	0.1202	0.1002	0.020
4750	0.00021	281	0.00068	0.0783	0.0652	0.013

Aircraft Beam — Steerer Loop

The keynote of the beam-steerer design philosphy at the onset of the AOCP was flexibility. Fundamental to the selection of this course of design was the fact that little was known of the dynamics of the atmosphere for which the beam-steerers were to correct. Much has been learned during the course of the AVLOC program regarding beam steering that could and would be factored into later such designs. Notwithstanding the evolution of the beam-steering subsystem during the program, the final iteration showed marked similarties to the original system. The major differences are manifest in the very portions of the subsystem set aside to absorb those anticipated evolutionary changes, namely, the loop compensation circuits. Figures 112 and 113 are presented to give an indication of those changes that ultimately took place during the life of the program. The final configuration shown in Figure 113 is that used in the final successful test flights.

The design analysis presented herein will accomplish the following purposes:

1. Present the final beam-steering subsystem configuration and brief operational description.

2. Define the characteristics and sources (when appropriate) of the elements making up the beam-steerer subsystem.

3. Present a complete servo block diagram of the subsystem (Y-loop).

4. Simplify the loop consistent with the bandwidth of the subsystem.

5. Develop a root locus of the simplified system, identifying the location of the closed loop poles and zeros (p-z) for the appropriate loop gain.

6. Present the results of a freqaency response taken from the p-z configuration and compare the analytical results with test measurements.
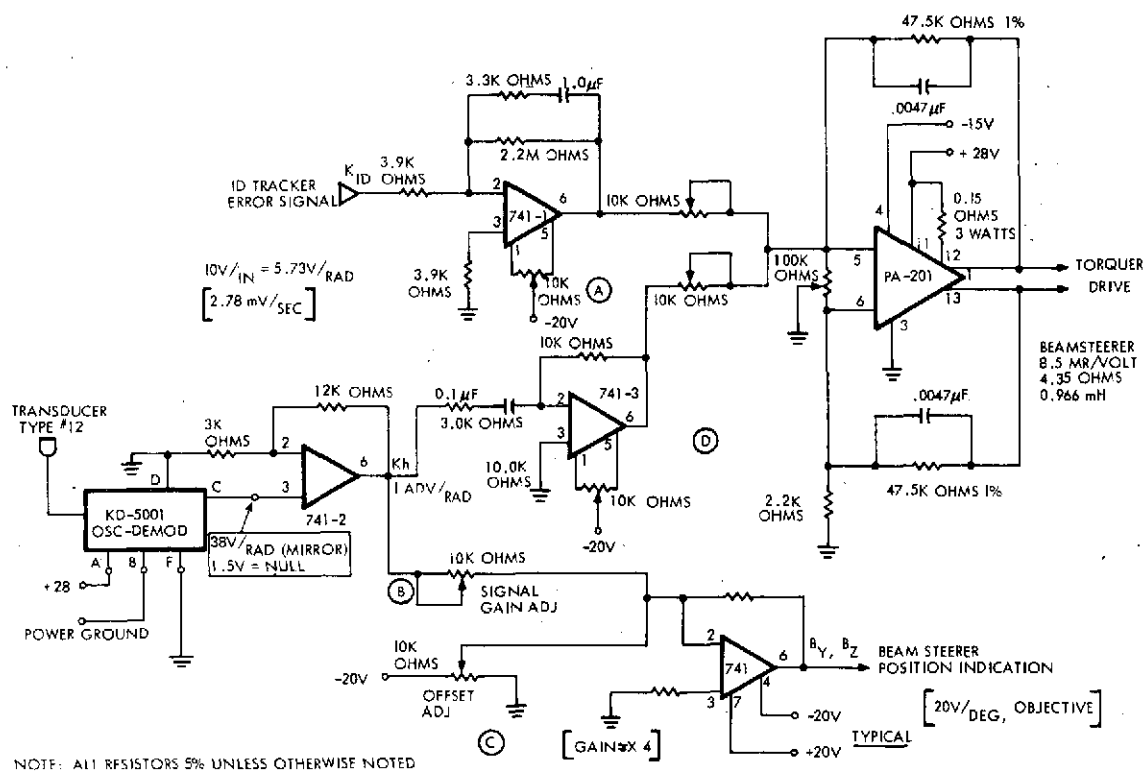
Figure 112. Original subsystem compensation.
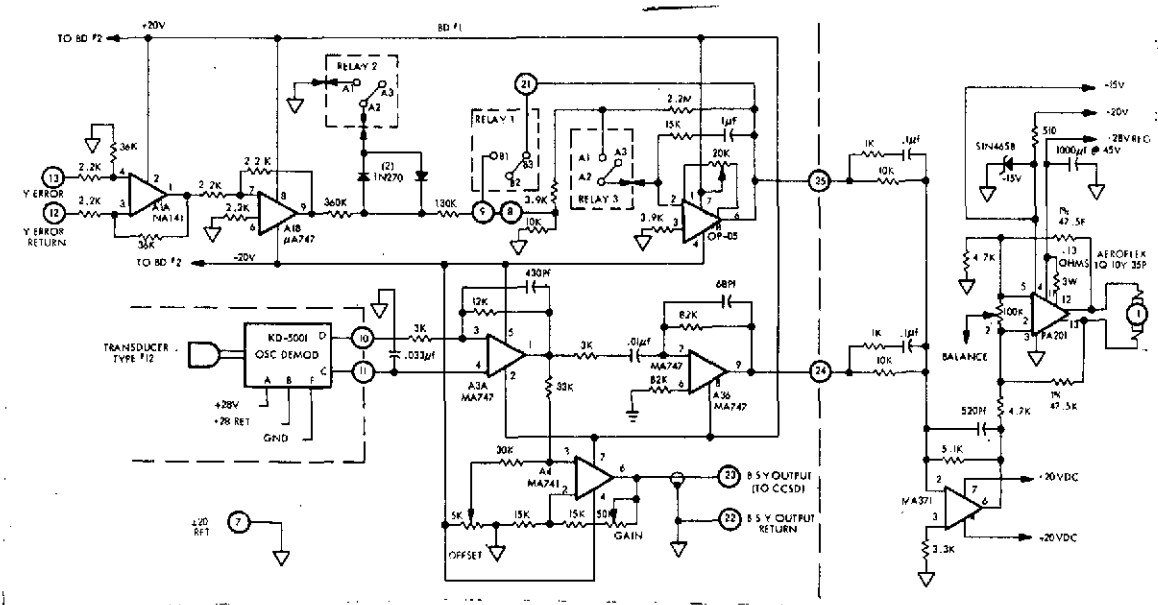
Figure 113. Final compensation configuration.

OPERATIONAL DESCRIPTION

One loop (or channel) of the beam-steerer subsystem was shown in Figure 27. This figure describes the basic elements from a functional viewpoint. The incoming laser beam is collected by a 10-cm aperture afocal telescope. The beam emerging from the telescope is routed to beam-steering mirrors, one for each channel (Y and Z), then to another set of optics whose purpose is to focus the beam on the face of the ID tracker.

The tracker develops three sets of outputs that are of further use to the beam-steerer subsystem:

1. Y and Z error signals

2. Video from the image dissector

3. 10.7-mHz TAR PRES signal

The ID video output and the 10.7-mHz TAR PRES signal control the mode of the beam-steerer subsystem. The error signals are appropriately routed to the remainder of the subsystem as called for in each mode.

FOWARD PATH COMPENSATION

From Figure 113 the circuits shown in Figure 114 are extracted. Some simplification is also accomplished in that switching is not included. The circuit shown makes up the compensation block of Figure 27. The characteristics of each stage of the circuit are developed below and shown adjacent to the appropriate part of the circuit in Figure 114.
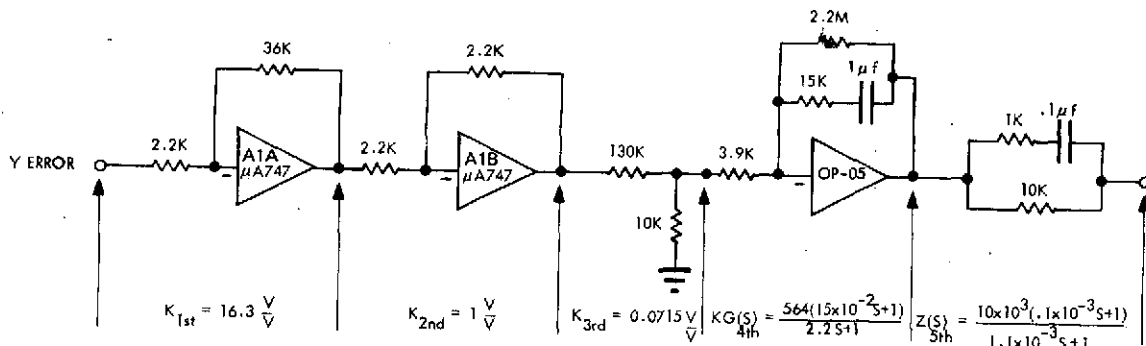
Figure 114. Foward path compensation circuits.

When the beam-steerer subsystem is operating in its tracking mode, the tracker error signal is supplied to the forward loop compensation circuits. The output on this circuit is summed with the compensated output of the beam-steerer mirror angle pickoff properly phased for negative feedback. The resultant signal is used to drive the torquer which acts on the gimbal, mirror, and flex pivot. Refer to Figure 114 for the following development.

First Stage (A1A)

The first stage is a simple feedback amplifier arrangement with the error supplied to the inverting input. The gain of this stage is

$$G = \frac{R_{fb}}{R_{in}} = \frac{36K}{2.2K} = 16.3 \quad . \tag{20}$$

Second Stage (A1B)

The second stage is a configuration similar to the first stage that has a gain of unity:

$$G = \frac{R_{fb}}{R_{in}} = \frac{2.2K}{2.2K} = 1 \quad . \tag{21}$$

Third Stage

The third stage is merely a resistor divider that splits the signal in the ratio $10/140 = 0.0715$.

Fourth Stage

The fourth stage represents the first stage with frequency-dependent terms that help shape the response of the subsystem. The transfer function for this stage is found in the usual manner: i.e., Z_{fb}/Z_{in}.

$$GH = \frac{564 \left(15 \times 10^{-3} S + 1 \right)}{2.25 + 1} \, VV$$

Fifth Stage

This circuit is the summing impedance which interfaces with the summing impedance from the feedback path compensation circuits. The circuit impedance will be necessary when the summation is made. It is therefore shown below:

$$Z_5 = \frac{10 \times 10^3 \left(0.1 \times 10^{-3} S + 1\right)}{1.1 \times 10^{-3} S + 1} \qquad . \qquad (23)$$

Clearly, this circuit provides additional frequency dependency and hence contributes to the compensation.

FEEDBACK PATH COMPENSATION

This block will be considered next because it contributes in a similar way to the beam-steerer torquer drive amplifier as does the forward path compensation. Figure 115 extracts from Figure 27 the portion of the subsystem concerned with feedback path compensation. This will be handled as was the forward path.
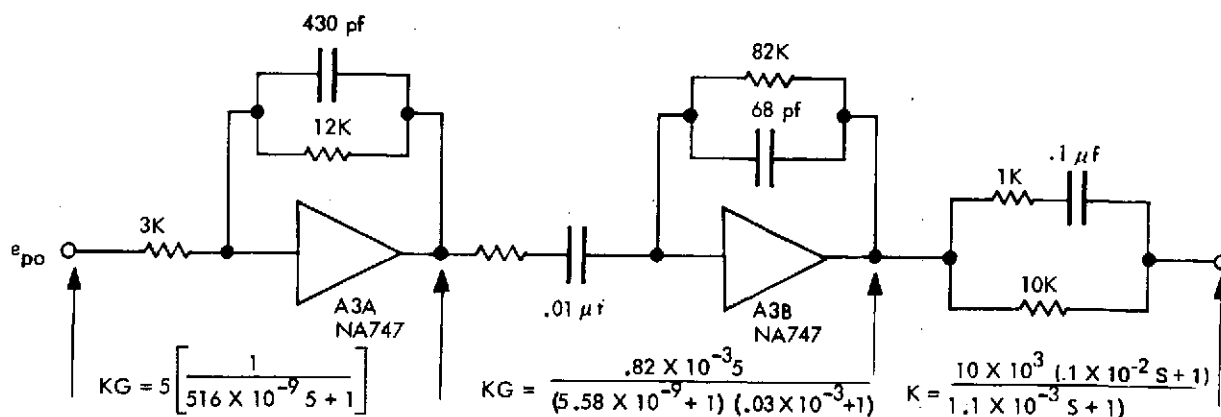
Figure 115. Feedback path compensation circuits.

First Stage (A3A)

This stage acts as an amplifier for the signal emanating from the Kaman position pickoff. It should be noted that the signal is into the noninverting input of the amplifier. As a result, the expression for the gain of the first stage is slightly different. Note also that while the transfer function developed has a frequency-dependent term, its influence is not felt in the region of interest to the beam-steerer subsystem. A simple gain is used when applying this stage to latter uses. The transfer function is

$$KG = \frac{Z_{fb} + Z_{in}}{Z_{in}} = 5\left[\frac{1}{5.16 \times 10^{-9}S+1}\right] \text{ V/V} \text{ .} \tag{24}$$

Second Stage

The second stage provides a portion of the feedback path compensation by virtue of its input resistor/capacitor combination that is effective in the beam-steerer frequency range. Its transfer functions are

$$KG = \frac{0.82 \times 10^{-3}S}{(5.58 \times 10^{-9}S+1)(0.03 \times 10^{-3}S+1)} \frac{\text{V sec}}{\text{V}} \text{ .} \tag{25}$$

Third Stage

The third stage of the feedback compensation is the summing impedance that interfaces with the forward path. Its electrical characteristics are identical, i.e.,

$$Z = \frac{10 \times 10^{3} (0.1 \times 10^{-3} S + 1)}{1.1 \times 10^{-3} S + 1} \text{ V/V} \text{ .} \tag{26}$$

184

SUMMING AMPLIFIER

The first point to deal with is the character of the summing process. For this the model shown in Figure 116 is used.
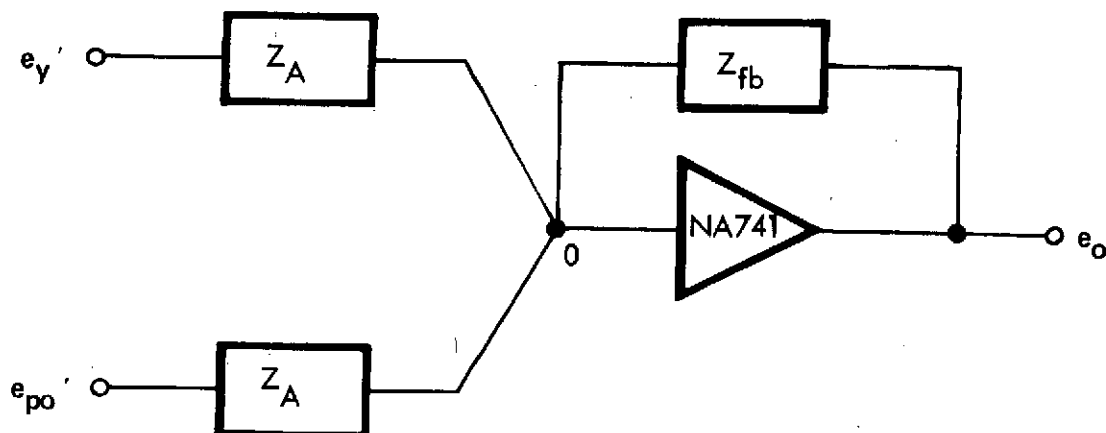
Figure 116. Model of summing amplifier.

The conditioned signals from the tracker and the pickoff are represented by e' and $e_{po'}$. Z_A is the summing impedances previously derived. Using the current summing at Node 0, $I_{ey'} + I_{po'} + I_{fb} = 0$.

$$\frac{e_{y'}}{Z_A} + \frac{e_{po'}}{Z_A} + \frac{e_o}{Z_{fb}} = 0,$$

(27)

yielding

$$e_o = \frac{Z_{fb}}{Z_A} \left(e_{y'} + e_{po'} \right) .$$

(28)

On this basis we then obtain

$$\frac{Z_{fb}}{Z_A} = \frac{0.51 \left(1.1 \times 10^{-3} S + 1\right)}{0.1 \times 10^{-3} S + 1} \; . \tag{29}$$

In this case the high-frequency influence of the 520 pf capacitor has already been removed from the expression.

BEAM-STEERER TORQUER DRIVE AMPLIFIER

The Torque Systems, Inc. PA201 is used for torquer drive purposes. This amplifier has a bridge output configuration, and as a result, even with the signal being delivered to the apparently noninverting input, the gain for the device in the voltage mode is

$$K = \frac{R_{fb}}{R_{in}} = \frac{47.5K}{4.7K} = 10 \; V/V \; . \tag{30}$$

This completes the subsystem description which is necessary before discussing the performance analysis.

PERFORMANCE ANALYSIS

All of the information (except for high-frequency terms) developed above is shown in the block diagram of Figure 117. In addition, the figure is laid out in a fashion to facilitate analysis, i.e., each block has the transfer characteristic associated with it. This analysis will start with the innermost loop — the gimbal and flex pivot loop — and continue expanding until an expression for the complete system is developed. Since earlier analyses have dealt with the relation θ_e/θ_i, that approach will be continued. This means that the effect of the collecting telescope never enters the analysis.

Figure 117. AOCP beam-steerer servo diagram.

FLEX PIVOT/GIMBAL CELL LOOP

Using the notation shown in Figure 117, we have

$$\frac{\theta_o}{T} = \frac{6.089}{7.25 \times 10^{-6}S^2 + 1} \text{ rad/Nm} \quad . \tag{31}$$

As expected, this is a marginally unstable loop because of the undamped nature of the mass/springs of the flex pivot/gimbal cell.

TORQUER/GIMBAL CELL BACK emf LOOP

No significant amount of damping is provided by the back emf of the torquer, but this loop is included since earlier analyses have considered it. The analysis yields

$$\frac{\theta_o}{V_T} = \frac{0.00883 \text{ rad/V}}{1.61 \times 10^{-9}S^3 + 7.2 \times 10^{-6}S^2 + 0.271 \times 10^{-3}S + 1} \quad . \tag{32}$$

When the denominator of this expression is investigated for roots, the following is obtained:

$$(S = 4.5 \times 10^3)(S^2 + 7S + 138 \times 10^3) \quad . \tag{33}$$

The very small coefficient of the S term in the quadratics indicates that some damping, although small, is afforded by the back emf of the torquer.

GIMBAL ANGLE PICKOFF/COMPENSATION/TORQUE DRIVE AMPLIFIER LOOP

The characteristic equation of the beam-steerer subsystem becomes more involved as more and more of the mechanism is encompassed by the expression. Applying the proper rule of combination,

$$\frac{\theta_o}{V_c} = \frac{0.0883\ (0.1 \times 10^{-3}S+1)(0.03 \times 10^{-3}S+1) \text{ rad/V}}{4.85 \times 10^{-18}S^5 + 0.232 \times 10^{-12}S^4 + 2.56 \times 10^{-9}S^3 + 15.7 \times 10^{-6}S^2 + 0.41 \times 10^{-3}S + 1} \quad . \tag{34}$$

We note at this point that the dc gain is precisely 10 times that of the previous loop. This is due to two factors: (1) The troque drive amplifier has a gain of 10 and (2) the dc gain of the feedback path is zero as a result of the free S in the numerator of the compensation that comes from the series capacitor in the feedback path. Clearly then, the feedback loop of concern at this point of the analysis is effective only so long as dynamics are in existence, i.e., when θ is not constant. Considering the very undamped nature of the gimbal/flex pivot situation, the kind of feedback provided is quite to the point, having its greatest effect in dynamic conditions.

188

TOTAL OPEN LOOP EXPRESSION θ_B/θ_e

At this point we are ready to look at the complete beam-steerer sub-system. First, the total open-loop expression for θ_B/θ_e will be written in the form of the previous relations to expose the dc gain of the open-loop expression. Following this, the expression will be converted to the form used in root locus (R/L) work, and the analyses will be carried on from that point. The significant steps in the following will be to

1. Obtain the total open-loop expression.

2. Convert the expression to the R/L form.

3. Simplify the expression on the basis of the pole and zeros in the open loop.

4. Draw an R/L, locating the pole locations at the point called for by the existing loop gain values.

5. Using the pole locations from the R/L, develop the closed-loop expression for the ratio θ_e/θ_i and plot the poles and zeros of this relationship.

6. Perform a frequency response of the θ_e/θ_i and compare it with the measurements taken on the system.

$$\frac{\theta_B}{\theta_e} = \frac{7907(15\times10^{-3}s+1)(1.1\times10^{-3}s+1)(0.1\times10^{-3}s+1)(0.03\times10^{-3}s+1)}{(0.159\times10^{-3}s+1)(2.2s+1)(0.1\times10^{-3}s+1)(4.85\times10^{-18}s^5+0.232\times10^{-12}s^4+2.56\times10^{-9}s^3+15.7\times10^{-6}s^2+0.410\times10^{-3}s+1)} \text{ rad/rad}$$

$$(35)$$

From this we see that (1) the dc gain of the open loop is 7907 rad/rad and (2) a pole and zero at $S = -10 \times 10^3$ rad/sec exist and hence cancel each other.

To continue, the expression is now converted to the R/L format:

$$\frac{\theta_B}{\theta_e} = \frac{2.32\times10^{12}(s+33.3\times10^3)\,(s+66.6)\,(s+910)}{(s+0.455)\,(s+6.4\times10^3)\,(s^5+47.8\times10^3s^4+528\times10^6s^3+3234\times10^9s^2+1658\times10^{12}s+206\times10^{15})} \qquad (36)$$

Synthetic division is used to factor the fifth-order term, giving

$$\frac{\theta_B}{\theta_e} = \frac{2.32 \times 10^{12} \, (S+33.3 \times 10^3) \, (S+66.6) \, (S+910)}{(S+0.455) \, (S+6.4 \times 10^3) \, (S+202) \, (S+348) \, (S+35.5 \times 10^3) \, (S+5.9 \times 10^3 + 7 \times 10^3) \, (S+5.9 \times 10^3 -_j 7 \times 10^3)} \cdot (37)$$

Note that two more simplifications are in order at this point: (1) The pole at $S = -35.5 \times 10^3$ rad/sec is very close to the zero at $S = -33.3 \times 10^3$; we shall consider these as cancelling each other; (2) three poles are so far out from the area of interest that their deletion would make only a small change in the continuing analysis. Figure 118 shows the root locations for total θ_B/θ_e. Since our concern focuses in the region of $0 \rightarrow 3000$ rad/sec, a good representation of the system can be achieved by eliminating the complex poles at $S = 5.9 \times 10^3 \pm_j 7 \times 10^3$ rad/sec and the real pole at $S = 6.4 \times 10^3$ rad/sec. The "gain" value must also be modified to properly eliminate these poles. Carrying out the proper operations results in

$$\frac{\theta_B}{\theta_c} = \frac{4090 \, (S + 910) \, (S + 66.6)}{(S = 0.455) \, (S + 202) \, (S + 348)} = \frac{N}{D} \cdot \quad (38)$$

This set of poles and zeros is shown in Figure 119 along with the locus of the poles of the closed-loop expression for θ_e/θ_i as the open-loop gain goes from 0   4090. The final location of the poles is that of the closed-loop for gain 4090.

On the basis of the root locations and the fact that

$$\frac{\theta_e}{\theta_i} = \frac{1}{1 + \dfrac{\theta_B}{\theta_e}} = \frac{1}{1 + \dfrac{N}{D}} ,$$

$$\frac{\theta_e}{\theta_i} = \frac{D}{\text{poles location from root locus}}$$

$$= \frac{(S + 0.455)(S + 202)(S + 348)}{(S + 66.6)(S + 1020)(S + 3540)} \; ,$$

(40)

for which the dc value is 1/7887, close to the reciprocal of the dc gain of 7907 developed earlier.

The pole/zero configuration of θ_e/θ_i is shown in Figure 120. From this arrangement a frequency response was generated. The results of this are shown in Figure 121 along with test data.

Inspection of Figure 121 shows that the test data and analysis of the Y-loop agree quite well to the vicinity of 100 rad/sec. The results diverge in the neighborhood of 100 rad/sec and pick up a somewhat parallel response after that point which seems to differ from the analytical results by a factor of two. This difference is unexplained at this time.

GROUND STATION FINE TRACKER

Tracking System Optics

The fine guidance system consists of an optical image divider, a field flattener, and a four-quadrant PMT. The optical schematic, which is shown in Figure 76, shows an on-axis diffraction image focused between the two elements of the field divider. The image is divided into four parts, and the four emerging cones of light are brought back parallel to the optical axis by the use of a pyramid-shaped field corrector. This allows the use of a narrow-band filter in the optical path since the energy is now passed through the filter at near normal incidence. The two-element image divider also serves as a field lens to image the entrance pupil of the optical system (primary mirror) onto the four quadrants of the PMT. Given the size of the entrance pupil (or relayed image of the entrance pupil) D, the distance of this pupil from the field divider V, and the photocathode size d, one choses the focal length of the field lens as $f_R = d\,V/(d + D)$ so that the diameter of the exit pupil matches

the photocathode size. The field lens is formed by the two outer surfaces of the image divider in combination, whereas the two inner surfaces are made in the form of a roof edge to perform the field division. These roof edges are rotated with respect to each other by 90 deg to divide the field into four quadrants. The advantages of this type of field divider over a conventional pyramid type are twofold:

1. The two elements are separated slightly and allow a variable field stop to be placed at the final focal plane of the instrument. This stop is constructed as two thin metal vanes (0.076-mm thick), which slide against each other and are driven by a common screw thread. Each vane has a 90-deg slot cut in its end and therefore the overall field of view is square but continuously variable from zero to the maximum field required by the fine guidance system 873 μrad (3 arc-min).

2. The edge where the image division occurs can be made extremely sharp since it consists of the intersection of two planes. Then the image is divided into four parts with negligible loss of light.

An optical field corrector is used to bend the light from the four quadrants back parallel to the main optic axis. The fabrication of this field corrector is not critical since neither the edges of the pyramid faces nor the pyramid apex are used. A narrow-band filter centered on the 632.8 — nm laser line is placed between the prismatic field flattener and the QMP and the filter can be removed for star tracking purposes. This type of tracking system provides four partial images (Figure 77) of the entrance pupil, and the varying states of illumination of these four images are used to electronically sense the image position. After acquisition and tracking have been accomplished, the instrument can be used to demodulate a 632.8 — nm received beam in the communication channel.

Fine Track Electronics

This section includes a description of the fine guidance electronics, i.e., the pointing error sensor (QMP) transfer mirror drive, and the switching logic.

Transfer Mirror Drive

The transfer mirror drive forms the electronic portion of the closed-loop precision tracking function of the ground station fine tracker. An optical path from the transfer mirror, through the image dividing prisms, to the QMP closes the loop to provide a null balanced servo system. A block diagram of the fine guidance electronic system was shown in Figure 89, and the schematic is shown in Figure 122.

192
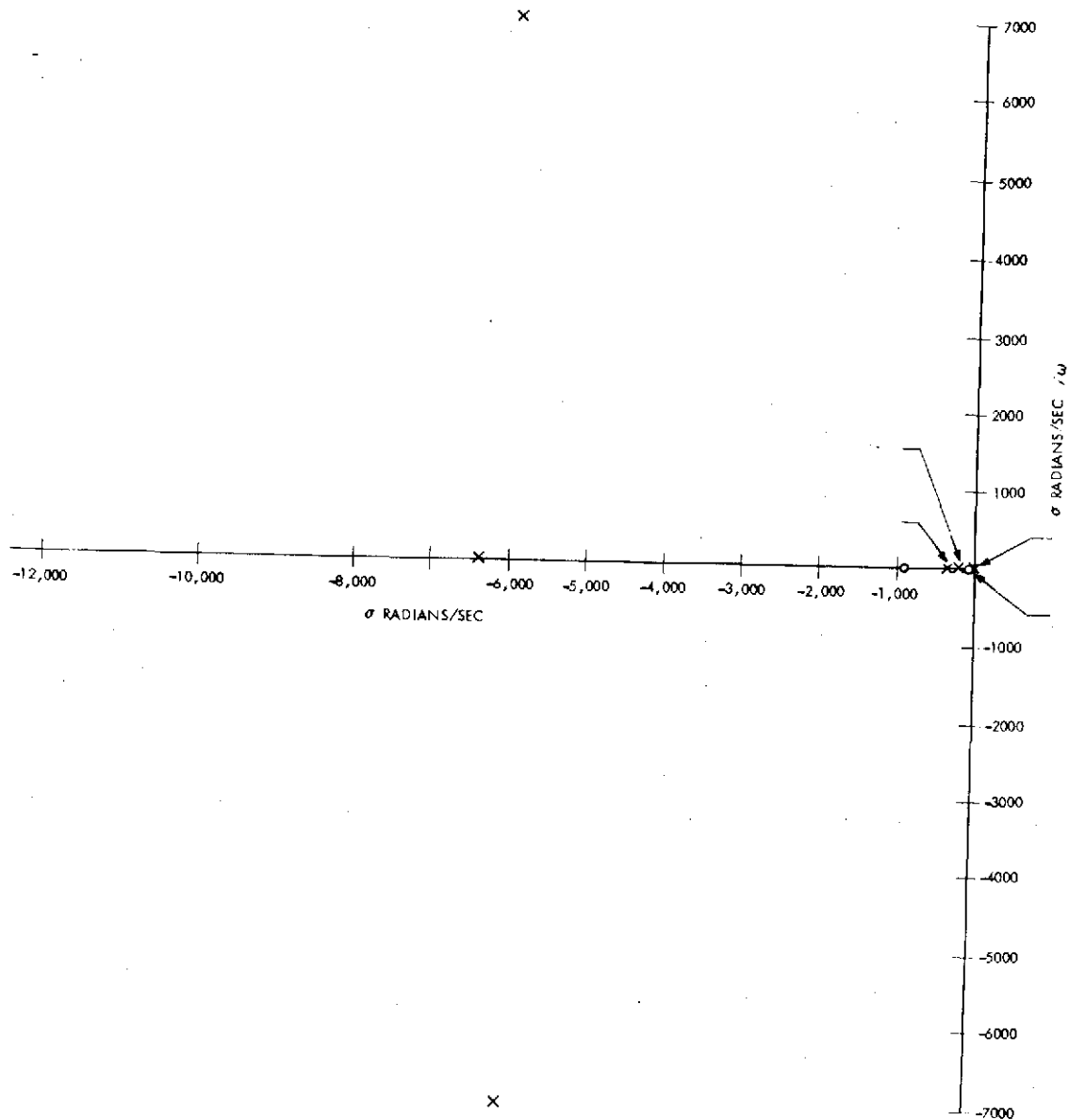
Figure 118. Root locations of total open-loop expression (cancelling pole and zero near $S = -33.5 \times 10^3$ not shown).

193
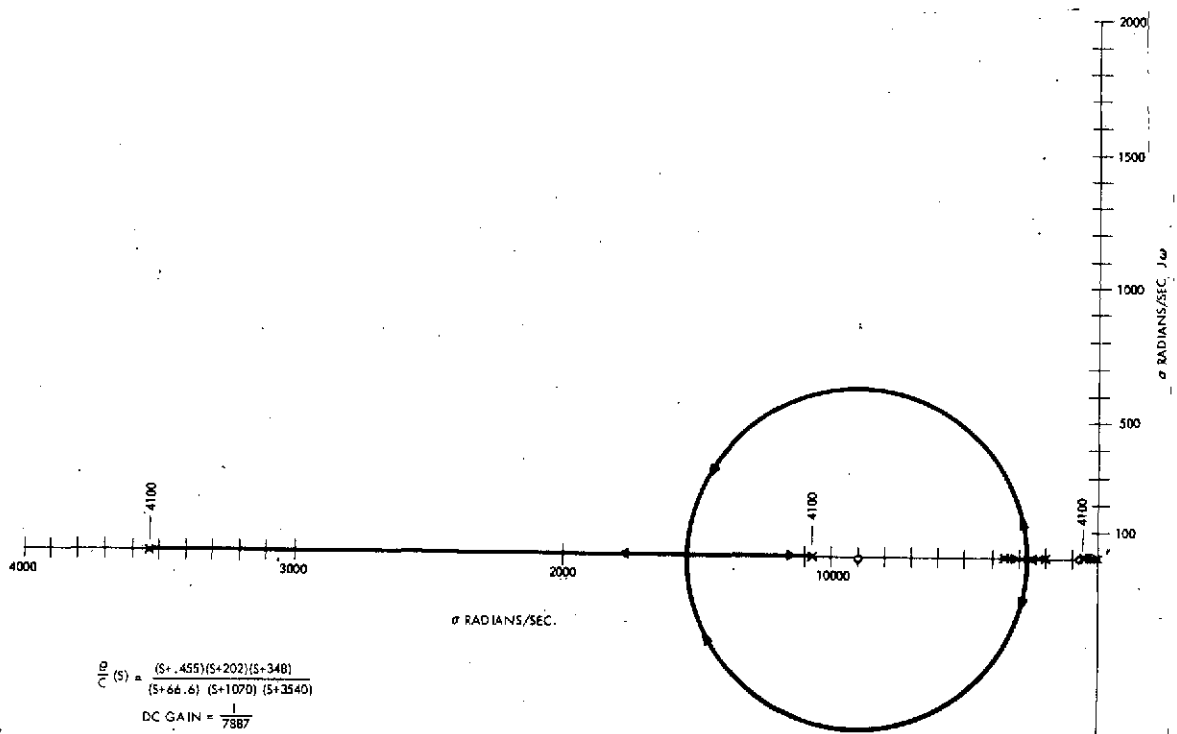
Figure 119. Open-loop root location/root locus/closed-loop root location for simplified θ_B/θ_c with "gain" of 4090.

The gate generator provides two outputs. One is used to switch the QMP cathodes on. The four cathodes are turned on, two at a time, in sequence. The error information is generated by gating the summing amplifier in sychronism with the QMP cathodes using the second output from the gate generator. This process was illustrated in Figure 90. The four cathodes are illustrated and identified on the left of the figure. The cathode switching waveforms are illustrated at the top right of the figure. Note that at any instant of time, two cathodes are on and two cathodes are off. The resulting output from the QMP is illustrated below the cathode switching waveforms along with the inverted output. The "on cathodes" are identified above the output waveforms. Below the QMP outputs, the decommutating waveforms are illustrated. I' and III' gate the positive output, while II' and IV' gate the inverted output as indicated in the block diagram. Finally, the error signals are indicated at the bottom of the figure. The Y-axis error signal is generated by gate I' operating on the positive output and gate II' operating on the inverted output. The complete Y-axis error signal

194

waveform is composed of the output from cathodes number IV and I minus the output from cathodes II and III. After smoothing, this Y-axis error signal is amplified to drive the Y-axis of the transfer mirror. Similarly gates III' and IV' are used to generate the X-axis error signal (consisting of the output from quadrants I and II minus the output from quadrants III and IV), which in turn drives the X-axis of the transfer mirror. Note that the magnitude and sign of the error signal is a function of the illumination of the position of the beacon image with respect to the apex of the image divider.

Fine Tracker Control Loop

The fine tracker control loop is a Type O servomechanism consisting of the QMP, the transfer mirror, and the associated circuitry. Figure 123 is a block diagram of the major loop components. θ_i, θ_b, and θ_c are angles referred to the object space of the telescope. $H(s)$ is the transfer function of all frequency-dependent circuits lumped together.

$$H(s) = 59 \frac{(0.015s + 1)}{(0.165 + 1)(0.165 + 1)(0.0025 + 1)} , \qquad (41)$$

$$K_1 = 9.36 \times 10^5 \text{ V/rad} , \qquad (42)$$

$$K_2 = 6.30 \times 10^{-6} \text{ rad/V} . \qquad (43)$$

The QMP and the decommutation circuitry combined produce the gain constant K_1. The transfer mirror has a gain constant K_2. Combining these factors with $H(s)$ yields the open-loop gain $C(s)$.

$$C(s) = K_1 K_2 H(s)$$

$$= 348 \frac{(0.015s + 1)}{(0.165 + 1)(0.165 + 1)(0.0025 + 1)} . \qquad (44)$$
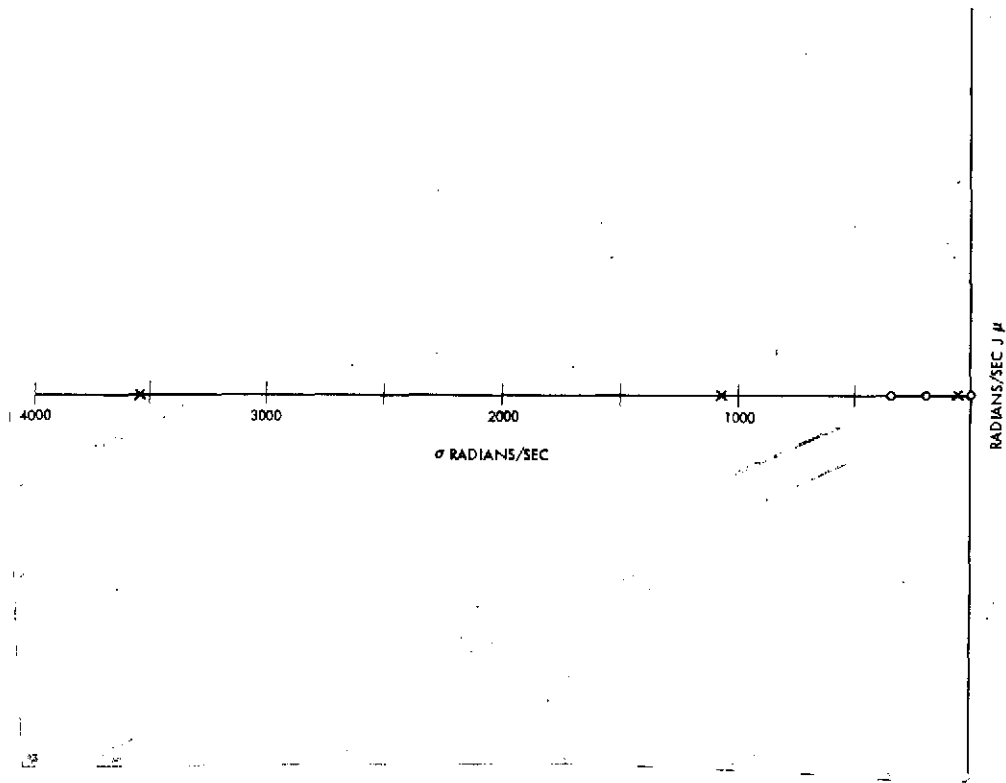
Figure 120. Pole/zero configuration of θ_e/θ_i for beam-steering subsystem.
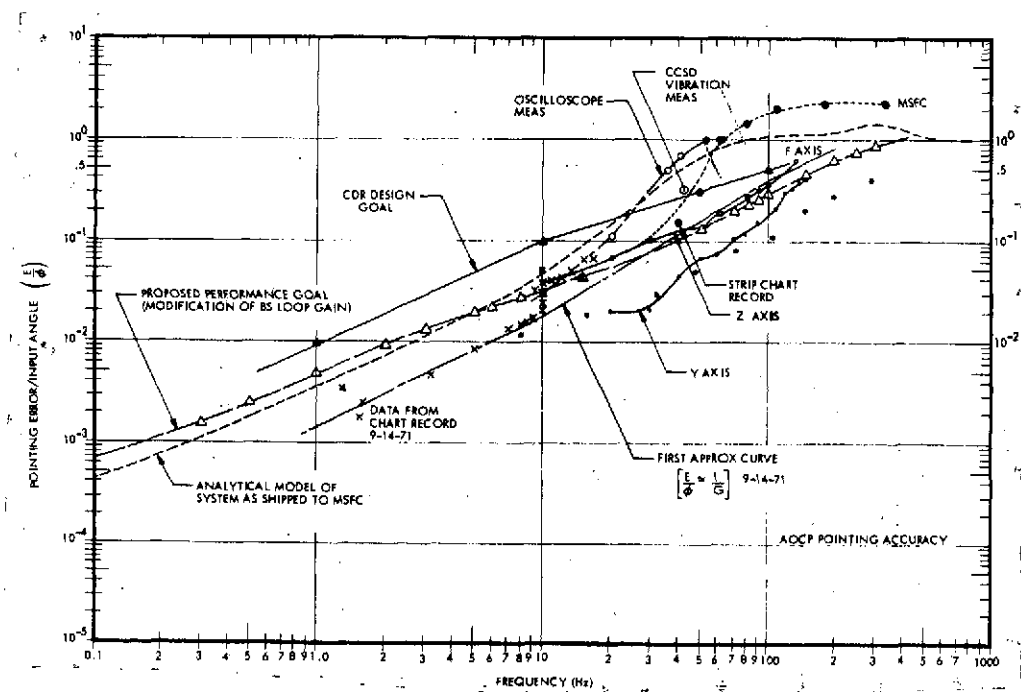
Figure 121. Results of frequency response analysis of pole/zero location shown with test results.
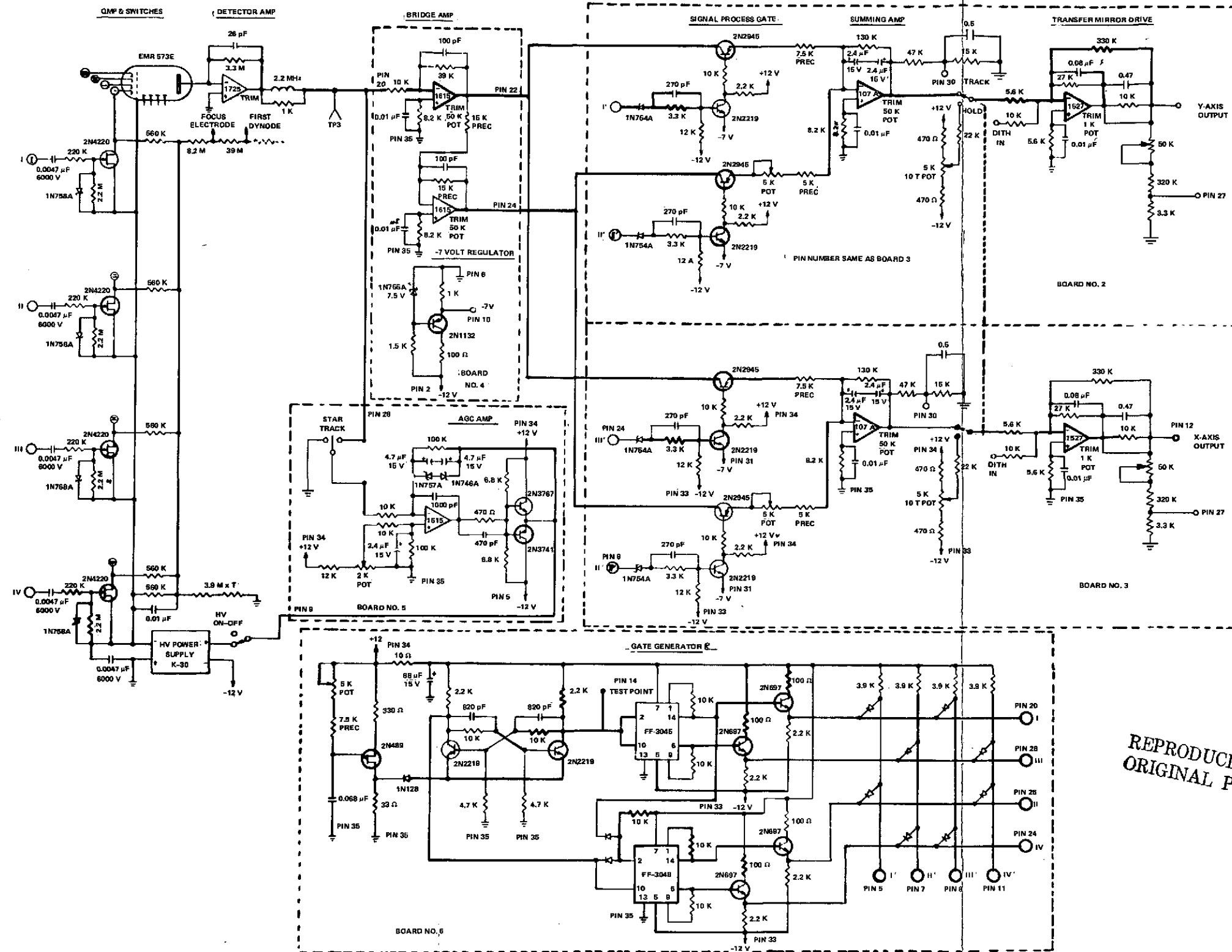
Figure 122. Fine guidance circuit schematic.

FOLDOUT FRAME

FOLDOUT FRAME

$$\frac{59\,(0.015\,S+1)}{(0.16\,S+1)\,(0.16\,S+1)\,(0.002\,S+1)}$$

INPUT — θ_i + θ_e → QMP-DEMOD $K_1 = 9.36 \times 10^5$ V/rad → H(S) → TRANSFER MIRROR POSITION

$-\ \theta_b$

TRANSFER MIRROR $K_2 = 6.30 \times 10^{-6}$ rad/V
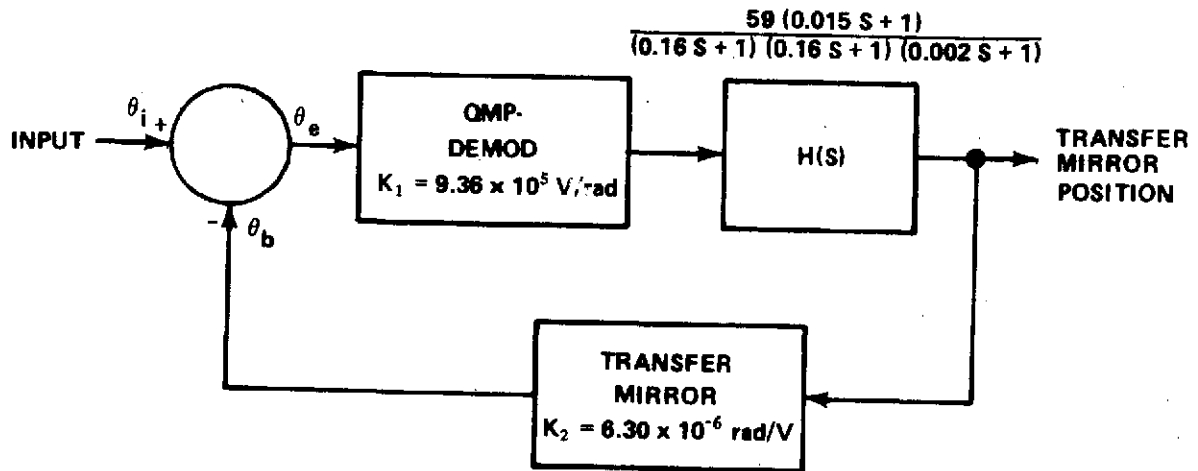
Figure 123. Block diagram of major loop components.

The open-loop gain is 51 db at zero frequency and has a unity gain cross-over frequency of 30 Hz. With this type of servomechanism, the closed-loop pointing error is proportional to θ_i, the input angle, and is a maximum of 1.45 μrad at the edge of the 873-μrad tracking field.

Figure 124 shows the results of a frequency response analysis performed on the fine track control loop. The ordinate is pointing error θ_e divided by the input angle θ_i, and the abscissa is the frequency associated with the input angle θ_i. These angles are referred to the object space of the telescope. At zero frequency the function becomes 0.029, and at higher frequencies where the transfer mirror has little effect, it approaches unity.

Fine Tracker Sensitivity

Tracking channel sensitivity may be investigated by calculating the QMP anode current that is expected during acquisition. Using the same radiometric approach that was used for the communication channel with only tracker channel transmittance, cathode radiant sensitivity and electron multiplier gain parameter changes, i.e., the anode current is

$$i_a = \frac{4 P_T\, T_T\, T_A\, A_C\, T_{TC}\, S_D\, G}{\pi R^2\, \phi^2}$$

where

$$T_{TC} = \text{the transmittance of the tracking channel} - 9.8 \times 10^{-3},$$

$$S_D = \text{the QMP cathode radiant sensitivity} - 0.025 \text{ N/W}$$

and

$$G = \text{the QMP electron multiplier gain} - 10^6$$

Substituting these values and those from Table 27 of the Downlink Radiometric Analysis subsection, given later in this report

$$i_a = \frac{4(1.5 \times 10^{-3})(0.125)(0.1)(2.64 \times 10^3)(9.8 \times 10^{-3})(2.5 \times 10^{-2})(10^6)}{\pi(2.19 \times 10^6)^2(8.39 \times 10^{-4})^2}$$

$$i_a = 4.57 \times 10^{-6} \text{ amperes} \quad .$$

This current level is considered a strong signal for the QMP. Under different experimental conditions where the downlink beam divergence is reduced, a neutral density filter is required in the tracking channel to prevent saturation of the QMP and its electronics.

GBAA OPTICS AND PARAMETERS

This section deals with the radiometry and optics of the GBAA. The pertinent parameters are listed in Table 23. The transmitter optics are shown in Figure 125.
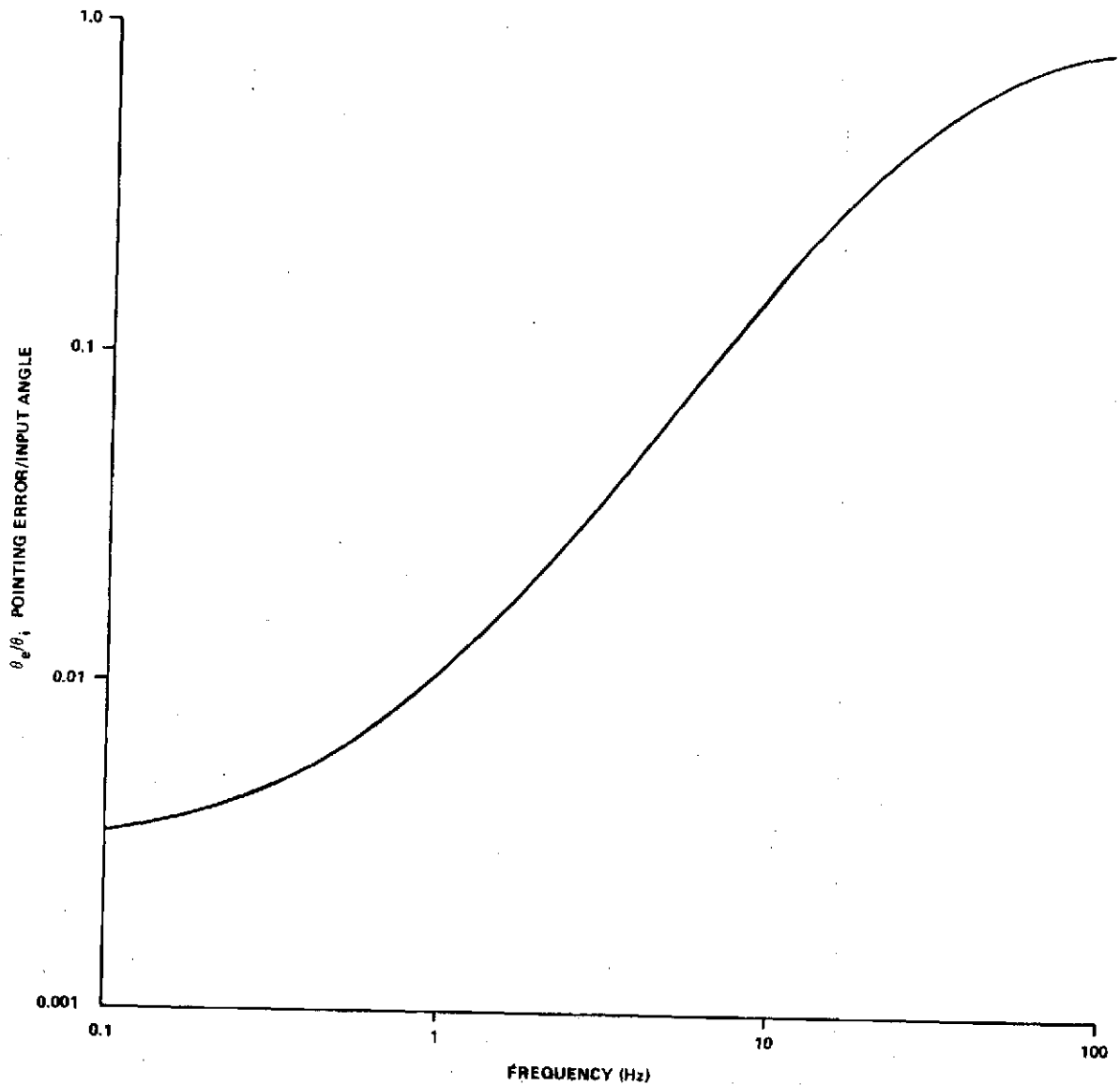
Figure 124.   Frequency response of fine tracker.

TRANSMITTER OPTICAL DESIGN

Transmitter Output Beam Divergence

In the TEM_{00} mode, the distribution of laser beam power across the beam follows the Gaussian curve, and the beam diameter is defined as the diameter at which the power density fails to $1/e^2$ or 13. 5 percent of the maximum power density in the beam, as shown in Figure 126.

TABLE 23. GBAA SYSTEM PARAMETERS

Transmitter
Laser, Britt Model 2000A Burst Argon Laser TEM_{00} 514.5-nm wavelength Pulse width: 15 μsec Repetition rate: 1000 Hz Minimum peak power: 1.7 W Beam diameter at $1/e^2$ intensity points: 2 mm Beam divergence (before deflector optics): 0.75 mrad

Receiver
ITT F 4012 Vidissector Tube with S-20 photocathode Cathode minimum sensitivity (selected) at 514.5 mm, $\qquad K_{\Delta\lambda}$ = 0.065 A/W Tube scanning aperture, square, 0.1 mm Lens, DeOude Delft Rayxar E 65/0.75, Serial No. L09172, EFL 65 $\qquad$ mm, f/0.75, measured entrance pupil 7.9 cm diameter System bandwidth, $\Delta f = 5 \times 10^4$ Hz Optical filter bandpass at 514.5 nM, $\Delta\lambda$ = 2.0 μm

Retroreflector Array
Glass "corner reflectors," mounted on aircraft Total effective area, A_{cr} = 307 cm^2 Beam spread after retroreflection, ϕ_{cr} = 20 μrad included angle, $\qquad$ or 2.95 $\times$ 10^{-10} sr solid angle

Operating Parameters
Acquisition and tracking total field of view, square 174 $\times$ 174 mrad Scan lines per raster: 128 Scan steps per scan line: 128 Scan flyback time: 12.5 percent of line time Distance, transmitter and receiver to aircraft, 9.1 <R <30.5 km
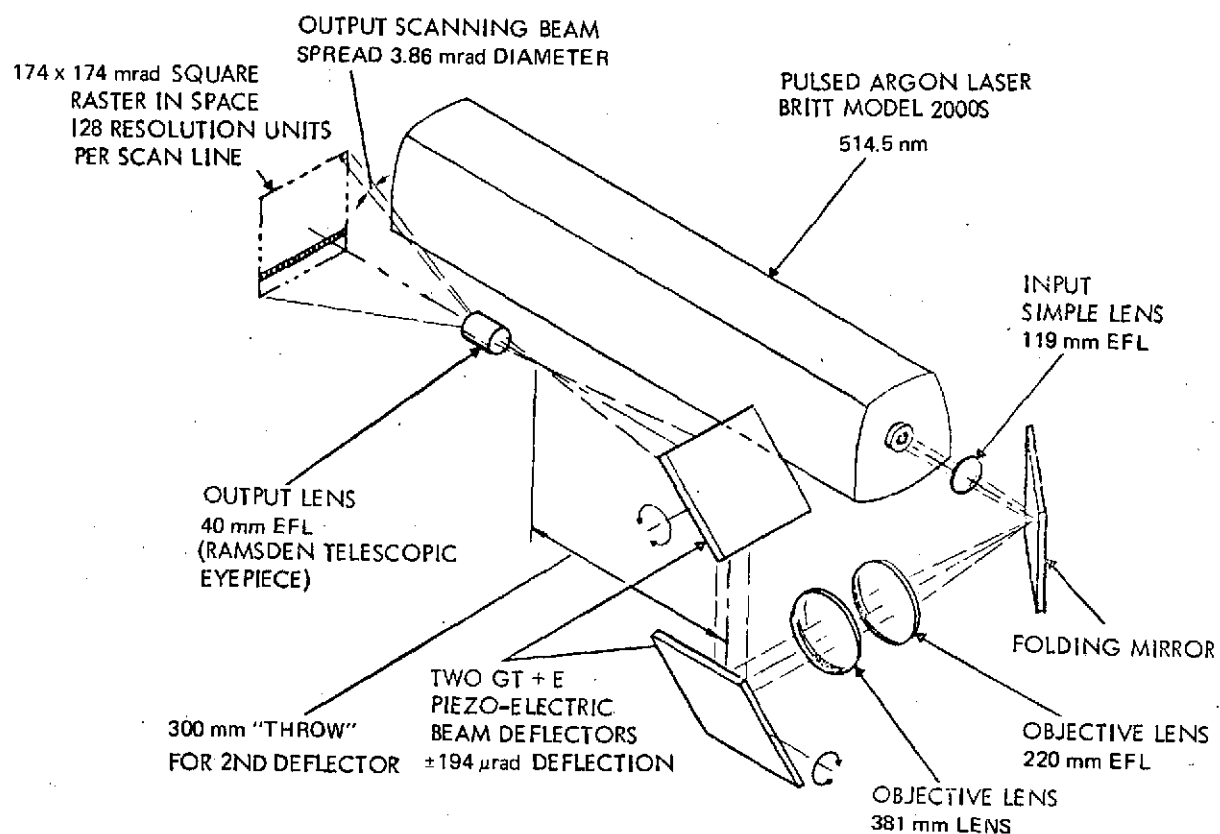
Figure 125. GBAA transmitter optics.
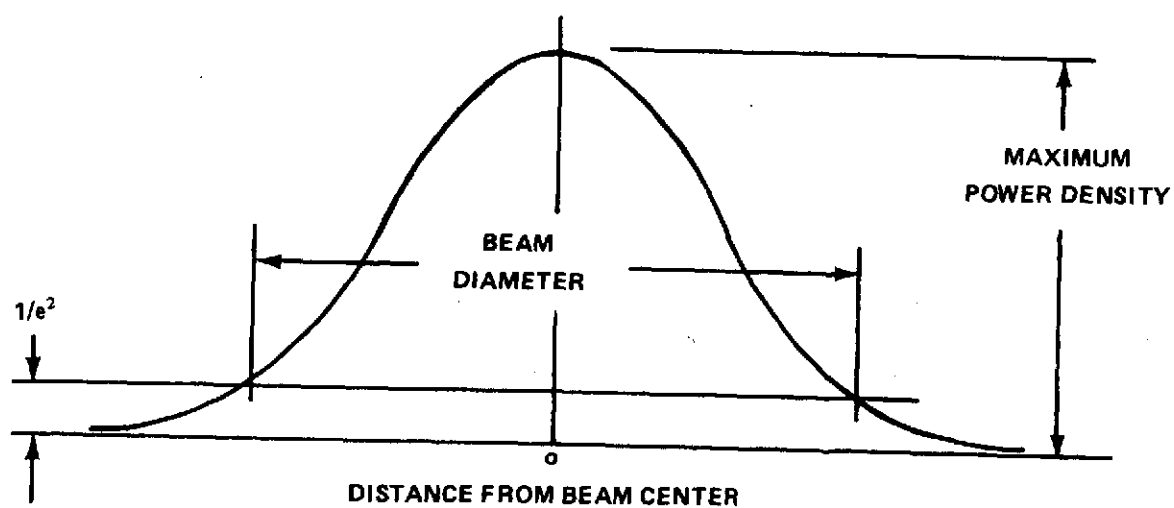
Figure 126. Gaussian beam.

203

Note that the beam diameter at the half-power-density points is approximately 0.6 of that at the $1/e^2$ points and that the power density corresponding to a diameter of one-half that at the $1/e^2$ points is approximately 0.6 of the maximum power density. These two approximations are used later in this discussion. If atmospheric turbulence is absent, the Gaussian distribution of beam power holds at any appreciable distance from the transmitter. Turbulence effects will be discussed later.

Since the 174-by-174-mrad (10-by-10-deg) raster contains 128 lines of 128 scan spots each, each scan spot will be a square 1.364 mrad on a side. (Note that both the transmitter beam and the receiver IFOV are larger than this.) The diagonal of each individual scan spot is 1.928 mrad. In the worst case, the corner reflector will be located at one corner of the square scan spot. Since the transmitter beam is nonuniform over its cross section, it is reasonable (but arbitrary) to decide that the power density at the spot corner must be not less than 0.7 of the power density of the control maximum. As shown above, this diameter is one-half the beam diameter at the $1/e^2$ points. Therefore, the transmitter beam diameter will be

$$\phi_t = 2 \times 1.928 = 3.856 \text{ mrad included angle}$$

or

$$\psi_t = \frac{\pi}{4} (3.856 \times 10^{-3})^2 = 1.168 \times 10^{-5} \text{ sr solid angle.}$$

Beam Deflector Optics

The piezoelectric-driven beam deflector, with an associated optical system is shown schematically in Figure 127. The output beam deflection is determined by the beam deflector movement and the ratio L/f_o. The beam deflector mirrors move ±5.82 mrad, and the laser beam in the location of L moves ±11.64 mrad. It is required that the output beam deflect ±87.3 mrad. Therefore,

$$\frac{L}{f_o} = \frac{87.3}{11.64} = 7.5 \quad,$$

which determines the focal length of the output lens, f_o, other factors being set. Note that the two deflector mirrors are near each other but at different distances L on the optical axis. Use the shorter L in the calculations. This implies that slightly less drive voltage is required for the deflector having the larger distance, inversely as the ratio of the respective distances.
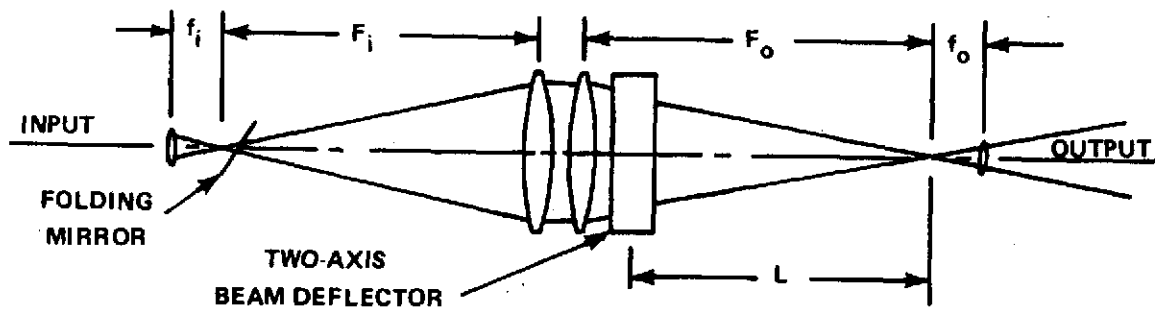
Figure 127. Beam deflector optics.

The optical system is essentially two telescopes, back-to-back, and the output laser beam's divergence, ϕ_o, will be the divergence of the input beam, ϕ_i, multiplied by the magnification of the system:

$$\phi_o = \phi_i \frac{f_1}{F_1} \cdot \frac{F_o}{f_o} \quad . \tag{46}$$

From construction,

$F_1 = 220$ mm, $F_o = 381$ mm, and $L = 312$ mm. Calculating,

$$f_o = \frac{L}{7.5} = \frac{312}{7.5} = 41.6 \text{ mm} \quad . \tag{47}$$

A 40-mm Ramsden telescope eyepiece was used for this lens, because it has less aberrations than a Huygens eyepiece and is readily available. Therefore, $f_o = 40$ mm.

From Table 23, $\phi_i = 0.75$ mrad, and $\phi_o = \phi_t = 3.856$ mrad.

$$f_1 = \frac{3.856 \times 220 \times 40}{0.75 \times 381} = 119 \text{ mm} \quad . \tag{48}$$

This lens is a simple biconvex lens, which has a 114-mm focal length and 29-mm diameter. Only the central 2 or 3 mm of this lens is used. Note that the beam deflection scale factor is set by the output lens, f_o, and that the beam divergence is set by the input lens, f_i, after the output lens has been selected.

RADIOMETRIC CALCULATIONS

The result of these radiometric calculations will be a statement of system performance, expressed as the worst-case atmospheric transmission and scintillation which will allow a system probability of detection, PD = 0.9, with a time between false alarms, TBF = 100 sec.

POWER DISTRIBUTION IN THE GAUSSIAN BEAM

See References 2 and 3 for the development of the following analysis. By inspection of the Gaussian distribution, the beam width at the half-power points is $2.4/4 = 0.6$ of the beam width at $1/e^2$ points. Skolink's derivation for $A(z) = \cos^2 (\pi z/2)$ is applicable to the Gaussian distribution to a close approximation and will be used.

Let

P_t = the total power in the Gaussian beam,

ϕ_t = angular diameter of the laser beam at the $1/e^2$ power density points in radians,

ψ_t = corresponding solid angle of the laser beam = $\pi \phi_t^2 / 4$,

$0.6\,\phi_t$ = angular diameter of the laser beam at the half-power points in radians,

and

$0.36\,\psi_t$ = corresponding solid angle of the half-power laser beam.

Then the peak power density at the center of the Gaussian beam, according to Skolnik, is

$$\frac{0.667 \times P_t}{\frac{\pi}{4}\left(0.6\,\phi_t\right)^2} = \frac{2.358 P_t}{\phi_t^2} \quad \text{W sr}^{-1},$$

or

$$\frac{0.667 \times P_t}{0.36\,\psi_t} = \frac{1.852 P_t}{\psi_t} \quad \text{W sr}^{-1} .$$

Also, by inspection of the Gaussian distribution, at a diameter one-half that at the $1/e^2$ points, the power density is 0.6 of the peak power density, as noted previously. Therefore, the power density at the corners of any individual scan spot is

$$\frac{0.6 \times 1.852 \ P_t}{\psi_t} = \frac{1.111 \ P_t}{\psi_t} \ W \ sr^{-1}$$

Similarly, the peak power density at the center of the beam returned by the corner cube retroreflector array, in watts steradians^{-1}, will be $1.852/\psi_{cr}$ times the total power (watts) in the retroreflected beam. Since the transit time of a laser pulse from transmitter to retroreflector to receiver is much smaller than atmospheric scintillation cycle times, the retroreflected beam may be presumed to travel the same path as its actual energy traveled from the transmitter, and the receiver will be at or near the center of the retroreflected beam.

SCINTILLATION EFFECTS

The total transmission of radiant energy over any relatively long path through the earth's atmosphere fluctuates with time, but the energy received is always less than the energy transmitted. For convenience, the attenuating influences are separated into two concepts: (1) a steady-state transmission factor, T_a, and (2) a fluctuating "efficiency" factor to account for atmospheric scintillation effects over the path, K_{sc}. It is unnecessary here to discuss the mechanisms involved in producing these effects, other than to point out that both factors are pure numbers less than one. The worst-case minimum allowable value of the product of those two factors will be a result of the present calculations.

RADIOMETRIC EQUATIONS

The symbols, definitions, and numerical values of terms used in the radiometric equations are summarized for convenience in Table 24.

The signal current available at the ITT F4012 Vidissector tube photocathode in electrons per second produced in the GBAA system, when the retroreflector array on the aircraft is at the corner of one of the square acquisition scan spots, is   .

$$i_s = \frac{1.111\,P_t\,T_t}{\psi_t} \cdot \frac{T_a\,K_{sc}}{R^2} \cdot \frac{1.852\,N_{cr}\,A_{cr}\,T_{cr}}{\psi_{cr}} \cdot \frac{T_a\,K_{sc}}{R^2} \cdot A_r\,T_f\,T_r\,K_{\Delta\lambda} \times 1.6 \times 10^{19}$$

$$= \frac{3.292 \times 10^{19}\,P_t\,N_{cr}\,A_{cr}\,A_r\,K_{\Delta\lambda}\,T_t\,T_{cr}\,T_f\,T_r\,(T_a\,K_{sc})^2}{\psi_t\,\psi_{cr}\,R^4} \quad \text{electrons sec}^{-1} \quad . \qquad (50)$$

The average photocathode current, in electrons per second, due to blue sky background within the receiver instantaneous field of view is

$$\overline{i_b} = 1.6 \times 10^{19}\,N_b\,A_r\,\psi_r\,\Delta\lambda\,K_{\Delta\lambda}\,T_f\,T_r \quad \text{electrons sec}^{-1} \quad .$$

The threshold photocathode current is

$$i_t = \overline{i_b} + \left[\pi\,K_{PMT}\,\Delta f\,i_b\,\log_e \left(\frac{TFA\,\Delta f}{2} \right) \right] 1/2 \quad \text{electrons sec}^{-1},$$

$$(52)$$

the total photocathode current i is the solution of the following quadratic equation:

$$i^2 + i \left[\pi\,K_{PMT}\,\Delta_f\,\log_e\,4(1-PD) - 2\,i_t \right] + i_t^2 = 0 \quad , \qquad (53)$$

and the minimum signal current, required for system operation with the probability of detection and time between false alarms used in the previous equations, is

$$i_s = i - \overline{i_b} \quad . \qquad (54)$$

This last quanity is to be compared with the available signal current, calculated by means of equation (50).

EVALUATION OF OPTICAL TRANSMISSION AND OTHER FACTORS

The numerical values used in the calculations, as shown in Table 24, are taken generally from data furnished by the suppliers of the respective items. All transmitting glass optical surfaces, except the receiver filter and the Vidissector tube face, are assumed to have the OCLI HEA antireflection coating, optimized for the 514.5-nm wavelength, for which the transmission factor is 0.997 per surface. The transmission of the filter, $T_f = 0.45$, includes surface effects, and the tube face (two surfaces) is assumed uncoated, with 4.4 percent loss per surface. The receiver lens manufacturer quotes its transmission as 81 percent. Folding mirrors will have optimized interference-type reflection coatings, whose reflection factor is 99.5 percent. The beam deflector mirrors are assumed aluminized, with reflection factor of 88 percent each. The efficiency of total reflection, such as in the corner retroflectors, is taken as 99.9 percent reflection. Transmission through glass is taken as 1 percent loss per 10 cm length of path.

The laser output used in the calculations is the minimum of 1.7 W peak, stated by the manufacturer. However, the manufacturer's measurements on the actual laser furnished showed 2.1 W for the 514.5-nm TEM_{00} operation. Its beam divergence was taken from catalog information.

The ITT-published data for cathode sensitivity is conservative, and cathodes are consistently made with considerably higher sensitivities. Published data for S-20 photocathodes show 0.05 A W^{-1}, and no difficulty is experienced in obtaining photocathodes with $K_{\Delta\lambda} = 0.0065 \text{ A W}^{-1}$.

The scan aperture in the ITT FW 4012 Vidissector is 0.1 mm square. In calculating the receiver IFOV, ϕ_r and ψ_r, a 10-percent allowance was made for electronic focusing of this aperture at the photocathode, and a scan spot 0.11 mm square was used.

TABLE 24. DEFINITIONS AND VALUES

Symbol	Definition	Value
A_{cr}	Active area per corner retroreflector	$N_{cr} = A_{cr} = 307 \text{ cm}^2$
A_r	Receiver optical collector area	49.5 cm^2
i	Total photocathode current, electrons sec^{-1}	TBD
$\bar{i}_b$	Background photocathode current, electrons sec^{-1}	TBD
i_s	Signal photocathode current, electrons sec^{-1}	TBD
i_t	Threshold photocathode current, electrons sec^{-1}	TBD
K_{PMT}	Photomultiplier dynode noise factor	1.6
K_{sc}	Efficiency factor to account for atmospheric scintillation effects (one way)	TBD
K_λ	Photocathode response at 514.5 nm	0.065 A W^{-1}
N_b	Radiance of background at filter passband, taken as clear daytime sky	$3 \times 10^{-3} \text{ W cm}^{-2} \text{ sr}^{-1} \text{ nm}^{-1}$
N_{cr}	Number of corner retroreflectors	$N_{cr} A_{cr} = 307 \text{ cm}^2$
PD	Probability of detection	0.9
P_t	Peak power in transmitted laser beam	1.7 W
R	Maximum distance from transmitter and receiver to corner retroreflector	30.5 km
TFA	Time between false alarms	100 sec
T_a	Atmospheric optical transmission (one way)	TBD
T_{cr}	Corner retroreflector optical transmission	0.99
T_f	Receiver optical filter transmission	0.45
T_r	Receiver lens and tube face optical transmission	0.74
T_t	Transmitter optical transmission	0.749
t	Transmitted pulse duration	$15 \times 10^{-6} \text{ sec}$
Δ	Receiver optical filter passband at 514.5 nm	2 nm
Δf	Receiver system bandwidth	$5 \times 10^4 \text{ Hz}$
λ	Laser wavelength (TEM$_{00}$ mode)	514.5 nm
π	Pi	3.14159
ϕ_{cr}	Angular diameter of retroreflected laser beam at $1/e^2$ power density points	0.02 mrad
ϕ_r	Angle of one side of square receiver IFOV	1.7 mrad
ϕ_t	Angular diameter of transmitted laser beam at $1/e^2$ power density points	3.86 mrad
ψ_{cr}	Solid angle subtended by ϕ_{cr}	$2.95 \times 10^{-10} \text{ sr}$
ψ_r	Solid angle of square receiver IFOV	$2.96 \times 10^{-6} \text{ sr}$
ψ_t	Solid angle subtended by ϕ_t	1.17×10^{-5}

The value of N_b, the radiance of a clear daytime sky at 514.5 nm, is cited in Reference 4 as approximately 3×10^{-3} W cm^{-2} sr^{-1} nm^{-1}.

RESULTS OF CALCULATIONS

Substituting the values from Table 24 into equations (50) through (54), the following results are obtained. The available signal photocathode current is

$$i_s = 4.584 \times 10^{10} (T_a K_{sc})^2 \text{ electrons sec}^{-1} . \tag{55}$$

The average background photocathode current is

$$\bar{i}_b = 3.039 \times 10^8 \text{ electrons sec}^{-1} . \tag{56}$$

The threshold photocathode current is

$$i_t = 3.375 \times 10^8 \text{ electrons sec}^{-1} . \tag{57}$$

The total photocathode current is

$$i = 3.468 \times 10^8 \text{ electrons sec}^{-1} . \tag{58}$$

The minimum required signal current is

$$i_s = i - \bar{i}_b = 4.285 \times 10^7 \text{ electrons sec}^{-1} . \tag{59}$$

Setting the available equal to the minimum required signal current,

$$4.285 \times 10^7 = 4.584 \times 10^{10} (T_a K_{sc})^2 , \tag{60}$$

the minimum product of the atmospheric transmission and the atmospheric scintillation efficiency factor is

$$T_a K_{sc} = 0.031. \tag{61}$$

If we assume the minimum $T_a = 0.1$, then the minimum $K_{sc} = 0.31$ for the probability of detection of 0.9 with average time between false alarms of 100 sec.

The calculations show that the system will operate satisfactorily under a worst-case condition as follows:

1. Probability of detection, 0.9.

2. Average time between false alarms, 100 sec.

3. Retroreflector at the extreme corner of an acquisition scan spot.

4. Retroreflector at extreme range of 30.5 km.

5. Atmospheric transmission and scintillation effects combined, $T_a K_{sc} = 0.031$; that is, for an atmospheric transmission, T_a, as low as 0.1, the transmission can be degraded by scintillation effects by an additional factor of $K_{sc} = 0.31$.

RETROREFLECTION EFFICIENCY FACTOR

To study the retroreflection efficiency, a convenient factor is defined:

$$F = \frac{N_{cr} A_{cr} T_{cr}}{\psi_{cr}} \quad . \tag{62}$$

Substituting values from Table 24,

$$F = 1.03 \times 10^{12} \text{ cm}^2 \text{ sr}^{-1} \tag{63}$$

The quantity, ψ_{cr}, is the solid angle of the beam returned by the retro-reflector toward the GBAA. This is affected by two phenomena, the diffraction of the beam by the aperture of each corner reflector and the divergence caused by the pyramidal error (nonorthogonality of the reflecting faces) of each retro-reflector. These will first be discussed separately, then in combination.

DIFFRACTION

Assuming perfect corner cubes, the retroreflected beam's divergence is a function of the shape and size of the effective area of the individual corner-cube retroflectors. The effective area, in turn, is a complicated function of the angle of incidence of the incoming beam from the GBAA transmitter. (The incident angle is measured from the perpendicular to the retroreflector's entrance-exit surface.) A simplifying and "safe" assumption is that the effective area is the equivalent-area circle, with diameter D. The beam angular divergence (diameter) is, then,

$$\phi_{cr} = \frac{2.44\lambda}{D} \text{ rad} \tag{64}$$

For $\lambda = 514.5$ nm and $\phi_{cr} = 19.4$ μrad, $D_{min} = 6.48$ cm. This divergence corresponds to $\psi_{cr} = 2.95 \times 10^{-10}$ sr, used in the previous calculations, referenced above.

PYRAMIDAL ERROR

In the absence (assumed, but impossible) of diffraction effects, a beam from an infinitely distant point source, filling the entrance-exit aperture of the cubecorner retroreflector, will emerge from the retroreflector in six distinct beams of various shapes, depending upon the angle of incidence. If pyramidal error exists, these emerging beams will not be exactly parallel to the entering beam nor to each other. For convenience, pyramidal error is defined as the angle between the incident beam and the worst-case emerging beam. As a consequence of a large enough pyramidal error, it is possible for all six sections of the returning beam to miss the GBAA receiver. The allowable pyramidal error must be specified for the corner cubes.

PYRAMIDAL ERROR AND DIFFRACTION IN COMBINATION

In general, each of the six emerging (reflected) beams resulting from pyramidal error will have its own respective diffraction pattern, its exact form determined by the shape and size of its associated effective aperture, as indicated above. These diffraction patterns, of course, increase the angular "diameter" of their respective beams, and, if the diffraction angular semi-diameter is greater than the pyramidal error, the six retroreflected beams will merge into a single pattern, essentially centered on the incident beam. The resulting pattern will be of more or less uniform intensity, depending upon the amount of pyramidal error and the incident angle at a particular time. The pattern in no case will be absolutely uniform.

PARTIAL SPECIFICATION OF CORNERCUBE RETROFLECTOR

If the diffraction angular diameters of the six retroflected GBAA beams are each to be 19.4 μrad, then a pyramidal error of 9.7 μrad could theoretically result in zero intensity at the center of the composite retroflected beam pattern, and the total beamwidth could be 38.8 μrad. To assure better overlap, retroflectors with 4.85 μrad maximum pyramidal error should be specified; in this case, the total beamwidth could be as large as 29.1 μrad.

RETROREFLECTOR DESIGN

Shape

Two common shapes are used for the cube corner retroreflectors. One is like a cube, cut through on a diagonal between the opposite corners of three adjacent cube sides. The other is additionally cut to remove the three corners of the triangular diagonal face produced in the first shape, so that the diagonal face is then a regular hexagon. (These last three cuts are made perpendicular to the diagonal face.) This hexagonal shape (or circular when the edges are removed) is useful when the angle of incidence is always perpendicular to the entrance-exit face.

Effective Area

The effective area of the cube corner is a rather complicated function of the angle of incidence and the index of refraction of the cube corner material (glass). The graph of Figure 128 shows the relationships for a triangular corner cube, for indices of refraction of 1.000 (trihedral mirror — not glass), 1.517 (Borosilicate glass-BSC2), and 1.798 (Schott Glass SF11 at 514.5 nm wavelength). It is noted that the effective area drops off to 80 percent at an incident angle of about 23 deg for BSC2 glass, and this angle rises to about 26 deg for the SF11 glass. The curves are unsymmetrical about the zero incidence angle, in the plane for which calculations were made. The curve for fused silica (n $\cong$ 1.45) lies intermediate to the curves for n = 1.0 and n = 1.517. There are three planes, at 120-deg intervals, where the same results are obtained. At all intermediate planes, the results are between those shown in the curves.

Transmission Losses

At 514.5-nm wavelength, most optical glasses have from 1-percent to 3-percent loss per inch of optical path length. A nominal 2 percent per inch should be used in this calculation until the exact glass to be used is known.
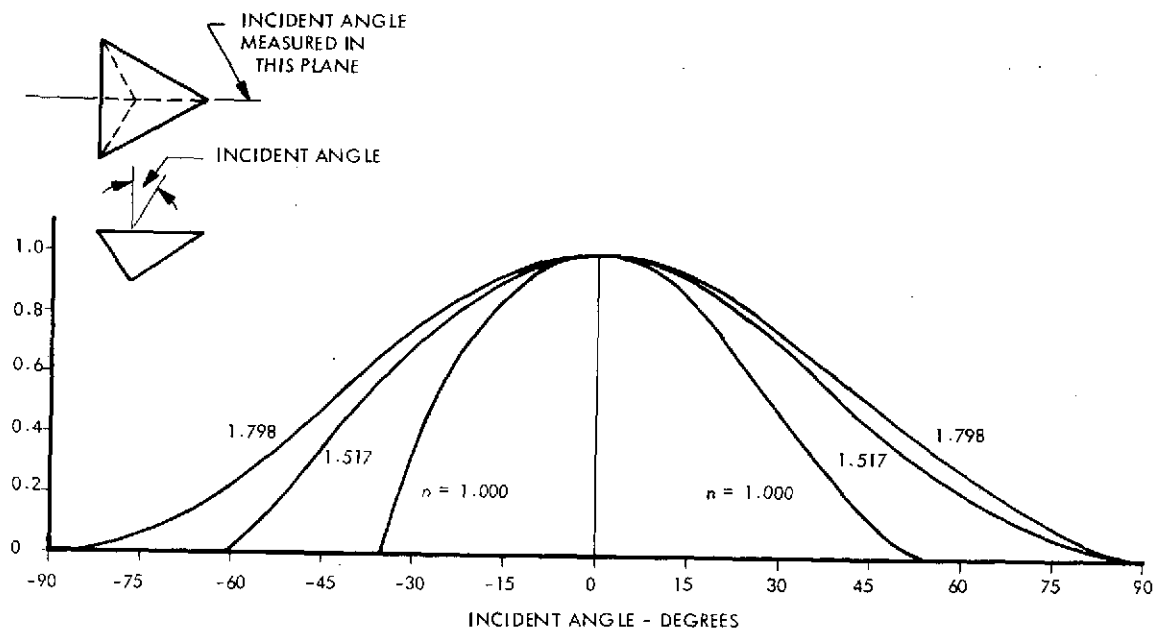
Figure 128. Cube corner retroreflector effective area as function of refractive index η and incident angle.

The Fresnel loss at the entrance-exit surface, with proper antireflection coatings, will be between 0.5 percent and 1 percent per pass through the surface. One percent should be used in this calculation. A good silvered reflective surface, required in corner cube retroflectors when the incidence angle is large enough to preclude the use of total reflection, has a loss of about 10 percent per reflection. There are three such reflections in the corner cube. Thus, for a triangular corner prism, 11 cm on its longest side, whose optical path through the prism is 17.1 cm, the transmission will be

$$T_{cr} = (1 - 0.02)^{17.1} \times (1 - 0.01)^2 \times (1 - 0.1)^3 . \qquad (65)$$

Summary

As shown above, the design criteria are expressed in the equation

$$\frac{N_{cr} \, A_{cr} \, T_{cr}}{\psi_{cr}} = 1.03 \times 10^9 \, cm^2 \, sr^{-1} \; . \tag{66}$$

Any combination of factors which meets this requirement will permit the GBAA to operate in the assumed worst-case radiometric situation.

It can be shown that, where S is the length of a long side of the triangular corner cube in centimeters, the maximum effective area (at normal incidence angle) is

$$A_{cr} = 0.28868 \, S^2 \, cm^2 \tag{67}$$

and that

$$T_{cr} = (1 - 0.02) \; 0.6429S \times (1 - 0.01)^2 \times (1 - 0.1)^3 \; . \tag{68}$$

and

$$\psi_{cr} = \frac{\pi}{4} \left[\left(\frac{20.7056}{S} + 0.9696 \right) \times 10^{-5} \right]^2 \; . \tag{69}$$

Note that A_{cr} must be multiplied by an empirical number derived for this geometry to obtain the effective area for a given case. For the GBAA, this must be correlated with the flight plan of the aircraft to determine the geometry involved. Combining the above factors,

$$N_{cr} \times (\text{area factor}) = 9.41 \frac{(\frac{20.7056}{S} + 0.9696)^2}{S^2 \times (0.98)^{0.6429S}} \qquad (70)$$

The results of this calculation are presented in Figure 129.

Although the triangular-shaped cube corner aperture provides the greater collection area with larger incidence angles, the circular cross section was selected for convenience of mounting. The loss in collection efficiency was offset by the increase in the number of reflectors used in the arrays. The corner reflector arrays are separated on the aircraft to minimize the effects of atmospheric scintillation.

The individual cube corners are aluminized and SiO_2 overcoated to maximize the reflection efficiency over large angles. The technique of assembly of the optical element into the mechanical mount is to secure the glass into the aluminum cylinder with a flexible rolithane potting compound mixed to retain resiliency at the low temperatures so that the optical element is not stressed. The potting is used only in the region indicated in the assembly drawing to avoid abrasion of the coated surfaces that might be produced with expansion and contraction caused by temperature changes. A small airbleed hole is placed in the cover to permit the enclosure to attain the ambient pressure.

The individual cube corner assemblies are mounted in five arrays of six assemblies each for attachment to the aircraft skin. One of the six element arrays is shown mounted on the underside of the WB-57F wing in Figure 130.

After several flights, some coating damage was observed on several of the cube corners as shown in the photographs of Figures 131. This coating flake was determined to have resulted from moisture condensation produced by returning to a very humid environment from the extremely cold high-altitude environment. This moisture collected around the coating surface and probably froze on subsequent flights, causing mechanical abrasions to the coatings. Once a fracture was produced in the hard overcoat, moisture could attack the aluminum

coating, producing the observed defect. The effect of this damage was to reduce the reflection efficiency of the affected unit by an amount proportional to the ratio of the damaged area to the full area of the entrance aperture. The maximum degradation for an affected unit was about 15 percent, which was deemed to be an acceptable amount.
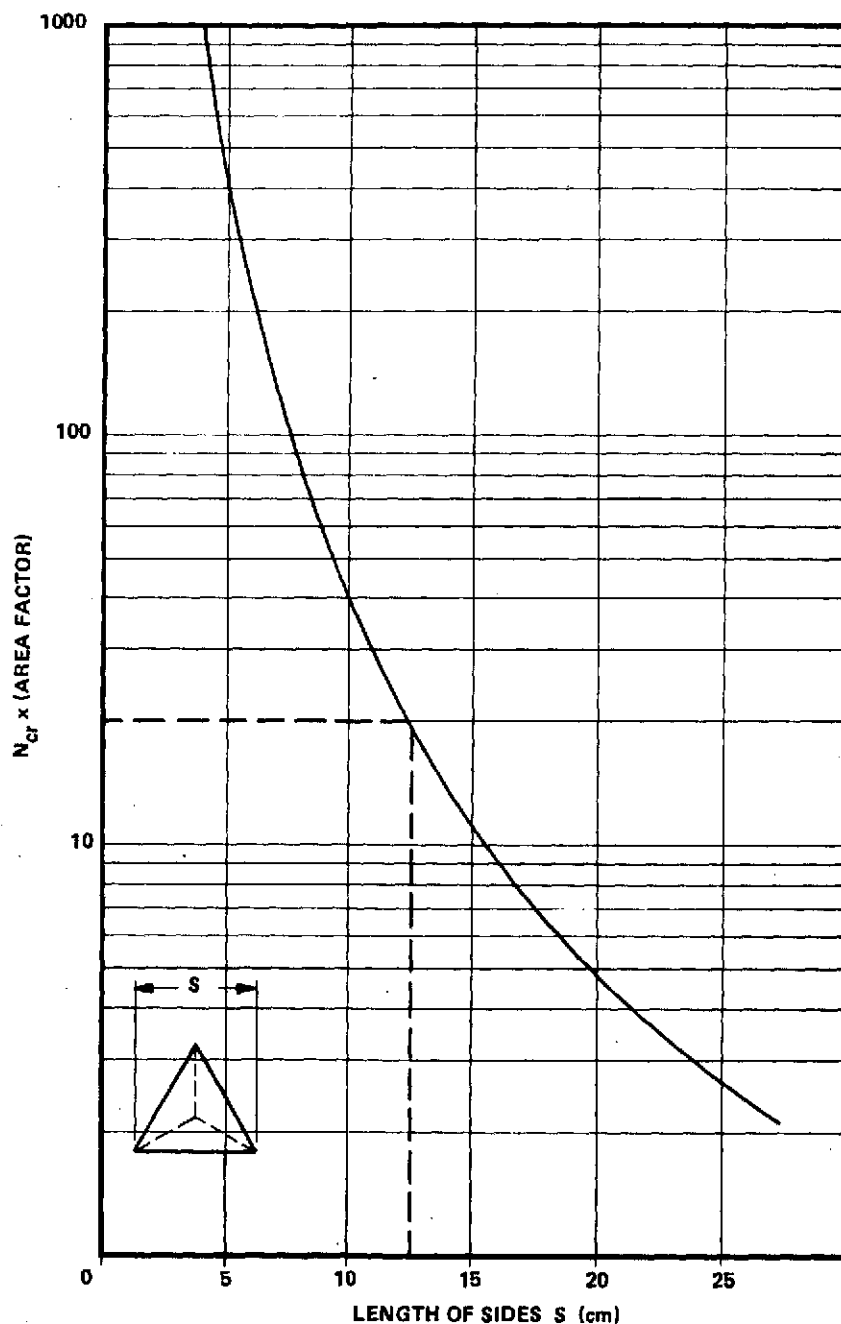
Figure 129. GBAA corner cube retroflectors number required vs. size.
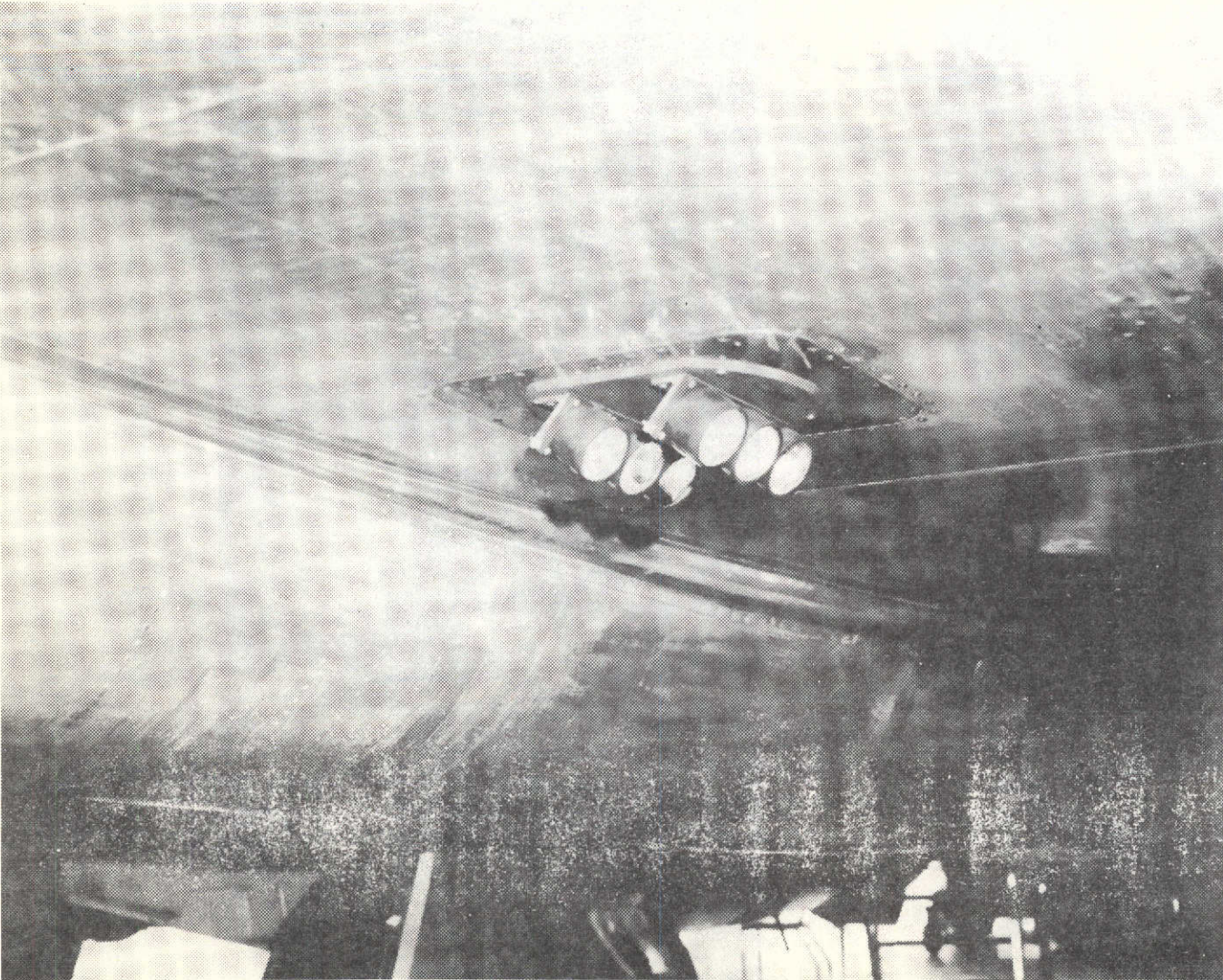
Figure 130. Cube corner assembly array (one of five) installed on WB-57F wing.
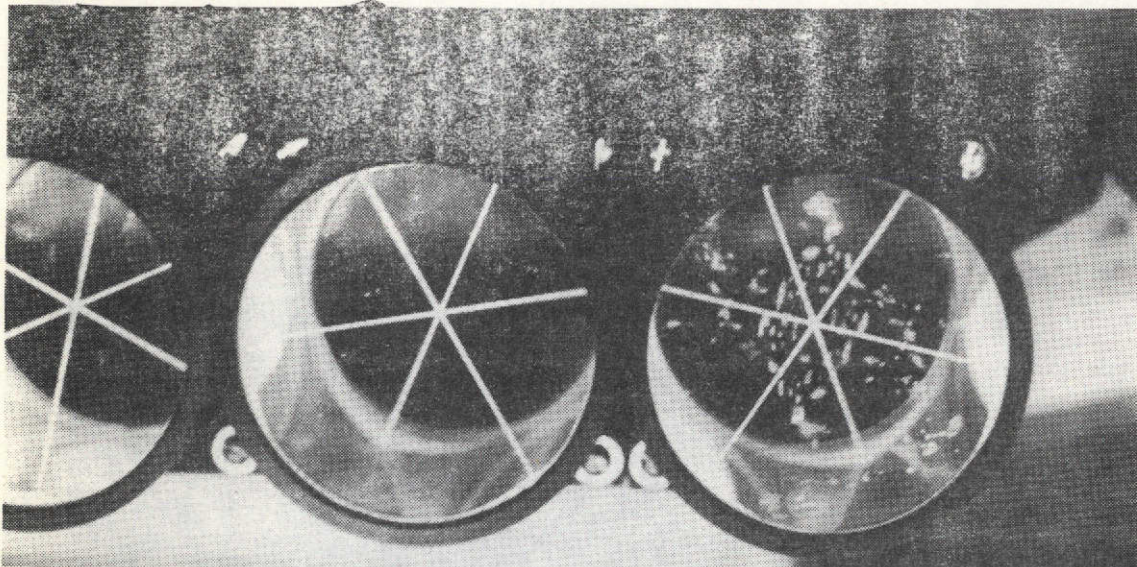
Figure 131. Cube corner assembly showing coating damage.
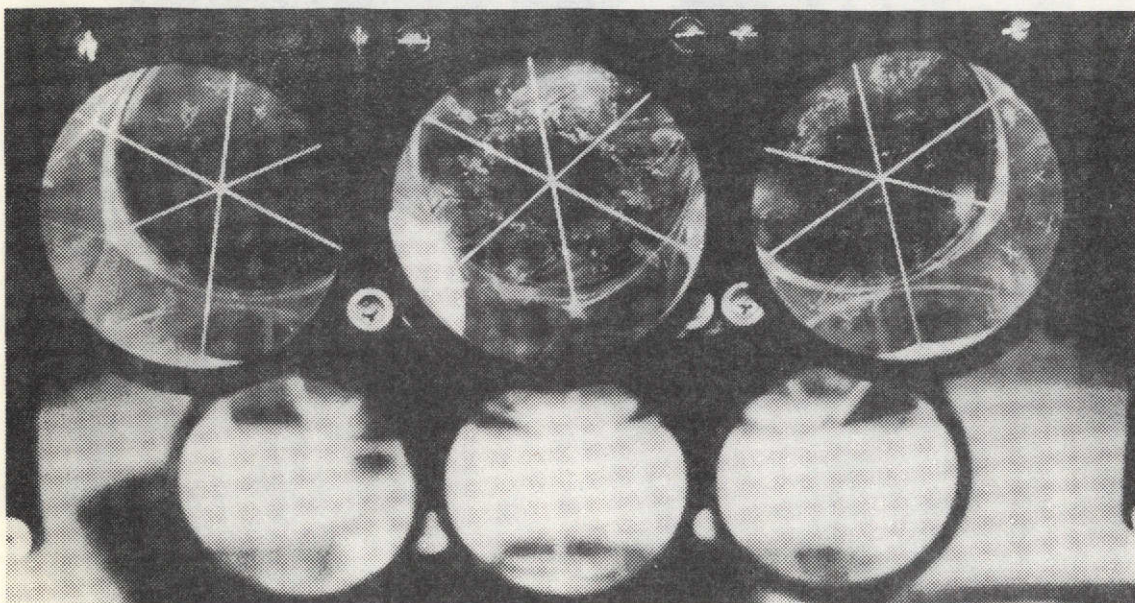
Figure 131. (Concluded).

Uplink Radiometric Analysis

This section presents a system performance analysis for the tracking and communication functions. The uplink analysis implies radiometry from the ground terminal transmitter to the AOCP receiver and includes atmospheric propagation considerations. The transmitted beam widths are assumed to be large compared with the pointing noise; therefore, dynamic pointing error effects are not included. Transmitted beam profiles are assumed to be Gaussian, and the performance is evaluated at the beam half-power point. Also, the beam cross section is assumed to be large compared with the collection aperture.

Results of the analysis presented here are given in Figure 132.

SELECTION OF PARAMETER VALUES

Although the parameters chosen for the several links are printed out on the curves, they are presented in Table 25 with some explanation where required.

The maximum power of 0.2 W is the ground station laser power radiated in the absence of modulation, P_M. The laser average power $\overline{P}$ has been set at $P_M/2$ for Figure 132.

Thus, the power radiated by the intensity-modulated laser is

$$P_R = \overline{P} (1 + \mu \cos \omega_s t) = \frac{P_M}{2} (1 + \mu \cos \omega_s t) \quad , \tag{71}$$

where P_R is the modulated laser power, μ is the modulation index, and ω_s is the subcarrier radian frequency.
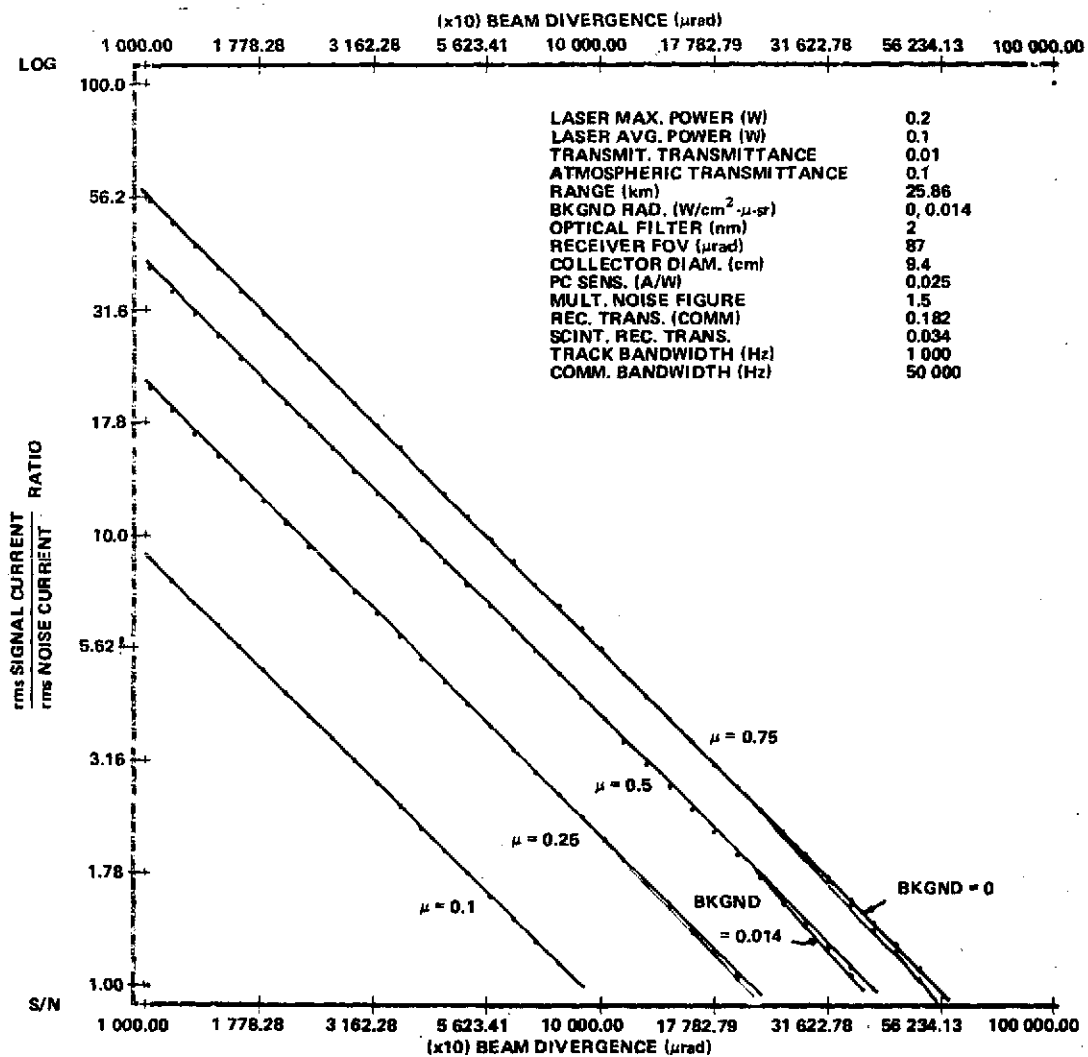
a. Signal-to-noise beam divergence for AVLOC uplink communications detector, $\mu = 0.1$, 0.25, 0.5, and 0.75.

Figure 132. Radiometry.

(x10) BEAM DIVERGENCE (μrad)

| 1 000.00 | 1 778.28 | 3 162.28 | 5 623.41 | 10 000.00 | 17 782.79 | 31 622.78 | 56 234.13 | 100 000.00 |

LOG

10 000.0

3 162.3

1 000.0

RECEIVED POWER (W) × 10^{-12}

316.2

100.0

LASER MAX. POWER (W)	0.2
LASER AVG. POWER (W)	0.1
TRANSMIT. TRANSMITTANCE	0.01
ATMOSPHERIC TRANSMITTANCE	0.1
RANGE (km)	25.86
BKGND RAD. (W/cm^2-μ-sr)	0, 0.014
OPTICAL FILTER (nm)	2
RECEIVER FOV (μrad)	87
COLLECTOR DIAM. (cm)	9.4
PC SENS. (A/W)	0.025
MULT. NOISE FIGURE	1.5
REC. TRANS. (COMM)	0.182
SCINT. REC. TRANS.	0.034
TRACK BANDWIDTH (Hz)	1 000
COMM. BANDWIDTH (Hz)	50 000

31.6

10.0

3.16

BKGND = 0.014

BKGND ≈ 0

1.00

| 1 000.00 | 1 778.28 | 3 162.28 | 5 623.41 | 10 000.00 | 17 782.79 | 31 622.78 | 56 234.13 | 100 000.00 |

(x10) BEAM DIVERGENCE (μrad)

b. Scintillation monitor power vs beam divergence,
AVLOC uplink communications.

Figure 132. Radiometry.

225
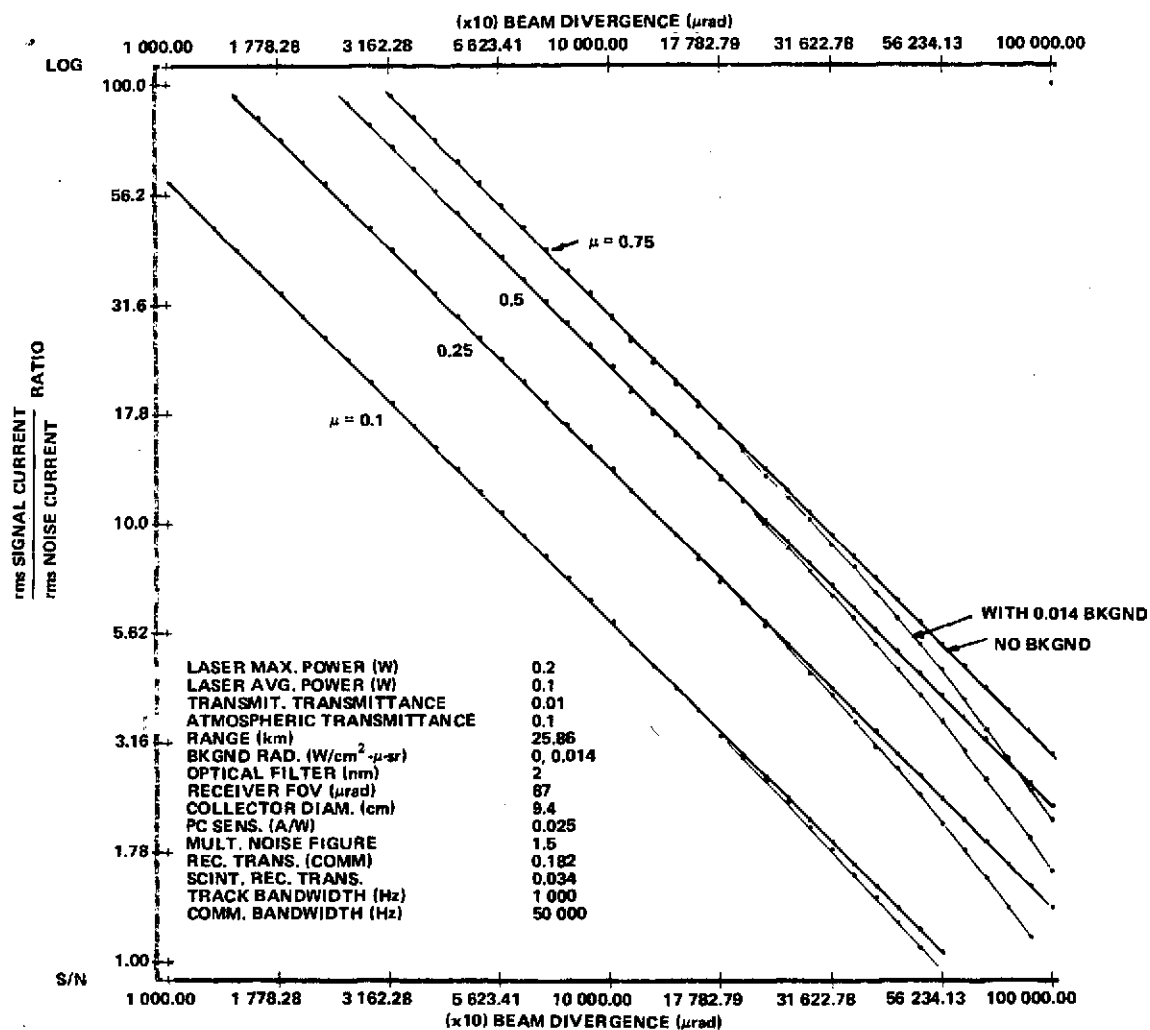
c. Signal-to-noise beam divergence, AVLOC uplink tracking detector,
$\mu = 0.1$, 0.25, 0.5, and 0.75.

Figure 132. Radiometry.

TABLE 25. UPLINK PARAMETERS

Laser maximum power (W)	0.2
Laser average power (W)	0.1
Transmitter transmittance	0.01
Atmospheric transmittance	0.1
Range (km)	25.86
Background radiance (W/cm^2-μ-sr)	0, 0.014
Optical filter width (nm)	2.0
Receiver FOV (μrad)	87.3
Collector diameter (cm)	9.4
Photocathode sensitivity (including mesh) (A/W)	0.025
Multiplier noise figure	1.5
Receiver transmittance (communication)	0.182
Scintillation receiver transmittance	0.034
Track bandwidth (Hz)	1 000.0
Communication bandwidth (Hz)	50 000.0

Background radiances of 0 and 0.014 W/cm^2-μ-sr bracket all the backgrounds to be encountered. The higher value is that for sunlit clouds. As can be seen from the curves, the sunlit background curves are not significantly different from those where no background is used. The optical filter of 2 nm serves only to limit the background power to the receiver. The receiver field of view of 87.3 μrad serves the same purpose, although it is more intimately associated with design considerations of aperture size in the image dissector and the focal length of the telescope.

The collector diameter is the effective unobscured diameter of a collector which is 9.85 cm in diameter with 2.87 cm of central obscuration.

The photocathode sensitivity is taken from the standard S-20 photocathode curve and divided by two to allow for losses in the mesh following the photocathode in the image dissector. The multiplier noise figure of 1.5 is a realistic value based on experience which agrees with analyses.

The communications receiver transmittance of 0.182 is the result of multiplying the transmittances and reflectances of the several elements in the light path of the receiver optics. The value of 0.034 for the scintillation monitor was obtained in the same way. Table 26 lists the elements and the effective transmittances used for both paths.

227

TABLE 26. RECEIVER COMPONENTS TRANSMITTANCES

Elements	Communications Receiver Path	Scintillation Monitor Path
Afocal Telescope	0.60	0.60
Z Steerer	0.96	0.96
Y Steerer	0.96	0.96
Beam Combiner	0.90	0.90
Narrow Band Filter	0.6	0.6
Beam Splitter	0.82	0.14
Lens	0.80	0.85
Neutral Density Filter	0.96	- - -
Mirror	0.97	0.97
	0.182	0.034

The uplink tracker receiver is, of course, common with the communications receiver until the output of the image dissector is reached, where the 10.7—MHz subcarrier tone is separated from the low-frequency components which really contain the tracking information. The tracker scan generates a 32-Hz modulation of the image dissector output current.

Although the tracker modulation index is self imposed by the tracker and is unrelated to the subcarrier modulation index, it will affect the communications signal-to-noise (S/N) ratio. This cross-coupling was not done on the computer simulation because of the many possible combinations.

In fact, the S/N current ratios of the uplink communications channel assume that the tracker modulation is zero. However, during the track modulation the communications S/N will range between the maximum given by Figure 132a and $\sqrt{1 - \mu_T}$ times that value. Thus, if the tracker imposes a 50-percent modulation index on the average incoming power, the S/N current ratio of Figure 132a will vary at a 32-Hz rate from the values given by the curves to $\sqrt{1 - 0.5} = 0.7$ of those values.

The "signal current" used for the track channel is its own modulation signal. The signal current used for the communications receiver is the 10.7 — MHz tone with a noise bandwidth of 50 kHz.

Note also that the S/N ratios given are defined as S/N $\equiv$ rms signal current/rms noise current. (These values must be squared to obtain power S/N.)

In the case of the scintillation monitor, total power to the photomultiplier only is plotted against the transmitted beam divergence.

Downlink Radiometric Analysis

The purpose of this analysis is to show what downlink — received energy levels are required and to determine that the system parameters used during acquisition (the worst case) are adequate for fine tracking at these nominal levels. There was no requirement for downlink communication during acquisition, and it was anticipated that the beam divergence would be decreased before any attempts were made to use the downlink for test purposes. The downlink parameters are given in Table 27, and an estimate of the transmittance of the ground station communication receiver is given in Table 28.

The irradiance at the ground station produced by the downlink laser is

$$H = \frac{4 \, P_t \, T_t \, T_a}{\pi R^2 \phi^2} \tag{72}$$

where

P_t = downlink laser average power output,

T_t = airborne transmitter transmittance,

T_a = atmospheric transmittance,

R = range,

and

ϕ = transmitter beam divergence.

The fine track threshold at the ground station is established when the average anode current of the communication photodetector exceeds 1 μA. Because relatively narrow bandwidths are used for tracking, the tracking photodetector requires much less radiant energy than the wideband communication detector. The receiver light was divided between these two channels, and the tracking sensitivity was adjusted so that both channels had approximately the same signal level threshold. One microampere was chosen empirically to correspond to an incident power level at the tracking tube that was sufficient for reliable fine tracking.

Expanding the radiometry to include receiver parameters yields an expression for the communication detector anode current that is a measure of the combined laser and background irradiances. Dark current is low enough not to appreciably affect these calculations

$$I_a = \frac{4\,P_t\,T_t\,T_a\,A_c\,T_{cr}\,S_d\,G}{\pi\,R^2\,\phi^2} + N_b\,A_c\,T_a\,T_{cr}\,\Delta f\,\frac{\pi}{4}\,\theta^2\,S_d\,G \qquad (73)$$

230

where

A_c = area of collecting aperture,

T_{cr} = transmittance of receiver communication channel,

S_b = photocathode sensitivity,

G = electron multiplier gain,

N_b = background radiance,

Δf = receiver optical bandwidth,

and

θ = receiver FOV.

Using the downlink parameters of Table 27, which correspond to the initial conditions for acquisition, the value of the expected anode current is computed as

$$i_a = \frac{4\ (1.5 \times 10^{-3})\ (0.125)\ (0.1)\ (2.64 \times 10^3)\ (0.083)\ (1.86 \times 10^{-2})\ (4.53 \times 10^4)}{\pi\ (2.19 \times 10^6)^2 (8.39 \times 10^{-4})^2}$$

$$+ (1.4 \times 10^{-2})\ (2.64 \times 10^3)\ (0.083)\ (1.2 \times 10^{-3})\ (\frac{\pi}{4})\ (8.73 \times 10^{-4})^2 (1.86 \times 10^{-2})\ (4.53 \times 10^4)\ (0.1)$$

$$i_a = 1.31 \times 10^{-6} + 1.85 \times 10^{-7}\ \text{amperes}\ .$$

TABLE 27. DOWNLINK PARAMETERS

Laser maximum power (W) 0.005

Laser average power from modulator (P_t, W) 0.0015

Modulation index 0.70

Transmitter transmittance (T_t) 0.125

Atmospheric transmittance (T_a) 0.1

Range (km) (zenith angle, 34 deg; altitude, 18.3 km) 21.9

Background radiance (N_b, W/cm^2-μ-sr) 0.014

Receiver optical bandwidth (Δf, nm). 1.2

Receiver FOV (θ, μrad)   87

Effective collector diameter (cm)   58

Effective collector area (A_c, cm^2) 2640

Photocathode sensitivity (S_d, A/W) . . . . 1.86×10^{-2}

Electron multiplier gain (G) . . . . 4.53×10^4

Communication photodetector dark current (A) . . . . 7.0×10^{-9}

Receiver transmittance, communication channel (T_{cr}). . . .   0.083

Downlink beam divergence (ϕ, μrad)   839

TABLE 28. ESTIMATE OF GROUND STATION COMMUNICATION
RECEIVER TRANSMITTANCE

18 optical surfaces at 0.95. . . . .   0.397

Background monitor beam splitter 0.80

Communication/track beam splitter 0.90

Dichroic beam splitter 0.85

Communication detector bandpass filter 0.53

Telescope primary and secondary mirrors at 0.8 . . . .   0.64

$$T_{cr} = 0.397 \, (0.80) \, (0.90) \, (0.85) \, (0.53) \, (0.64)$$

$$= 0.082 \ .$$

The first term in the expression is the anode current caused by downlink laser radiation. The second term is the background contribution. This background model is for sunlit clouds and is considered to be the worst case. Actual daytime operating conditions are less severe so that background radiation is not troublesome.

In order to consider the statistical nature of the photodetector current and determine how this affects the quality of downlink communications, the radiometry is expanded to yield the quantity $\overline{N}$. This is the average number of photoelectrons emitted from the photocathode during one bit period. Using this expression,

$$\overline{N} = \frac{i_a \tau}{e\,G} \tag{75}$$

where

i_a = anode current of communication photodetector,

τ = integration time or bit duration (33 ns),

e = electronic charge, 1.6×10^{-19} C/electron,

and

G = photomultiplier current gain.

Then, substituting equation (75) for i_a, $\overline{N}$ becomes

$$\overline{N} = \frac{\tau}{e\,G} \left(\frac{4\,P_t\,T_t\,T_a\,A_c\,T_{cr}\,S_d\,G}{\pi\,R^2\,\phi^2} + \frac{T_a\,N_b\,A_c\,T_{cr}\,\Delta f\,\pi\,\theta^2\,S_d\,G}{4} \right)$$

$$= \frac{\tau\,S_d\,T_{cr}\,T_a\,A_c}{e} \left(\frac{4\,P_t\,T_t}{\pi\,R^2\,\phi^2} + \frac{N_b\,\Delta f\,\pi\,\theta^2}{4} \right) . \tag{76}$$

In another section of this report a statistical model of the downlink communications channel is developed. This model uses as input data the average number of photoelectrons emitted per bit, $\overline{N}$.

Downlink Communication System Model

In the following paragraphs a mathematical model is developed for use in predicting the potential performance of the AVLOC communications system. First discussed is the ideal system, one limited by only the most fundamental types of noise. This ideal model is then modified to include the most common sources of noise, encountered in photon-counting communications systems operating in the field.

PERFORMANCE OF AN IDEAL SYSTEM

The performance of an ideal optical communications system is limited by design parameters (such as laser power, modulation index, collection aperture diameter, etc.) and the fundamental fluctuations in the detected signal caused by photocurrent shot noise. This section is concerned with introducing both these system concepts and the analytical techniques that will be expanded later to form a general model.

SENSOR PHOTOCURRENT AND ITS VARIANCE

It is important to clarify first the term "modulation index." Figure 133 depticts a partially modulated binary pulse train. The peak amplitude of this pulse train is A_p, and the minimum amplitude is A_m. The average amplitude is $\overline{A} = (A_p + A_m)/2$, assuming a long random and equally likely series of binary pulses. The modulation index M is defined as

$$M = \frac{A_p}{\overline{A}} - 1 = \frac{A_p - A_m}{A_p + A_m} . \tag{77}$$
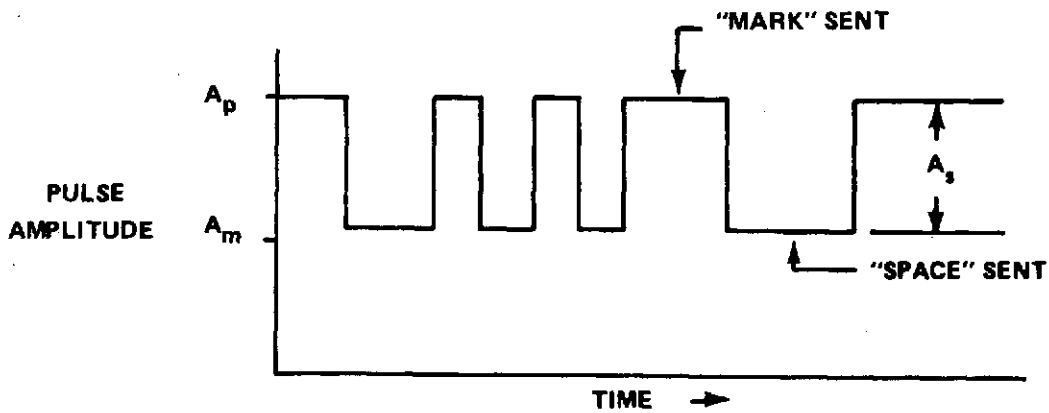
Figure 133. Partially modulated binary pulse train.

In terms of the average amplitude $\overline{A}$, the peak amplitude can be written as $A_p = \overline{A} \, (M + 1)$. In a like manner, the minimum amplitude A_m can be written as $A_m = \overline{A} \, (1 - M)$. The signal amplitude A_s is defined as the difference between the maximum and minimum amplitudes. Consequently, it follows that $A_s = A_p - A_m = 2M \, \overline{A}$.

The amplitudes of Figure 133 may represent any of a number of types of information carriers. For instance, the peak amplitude A_p may represent peak numbers of photons, photoelectrons, photocurrent values, or other like quantities. In an ideal system, the average photoelectron current is directly proportional to the average radiation incident on the photosensor. Consequently, in using the system of subscripts introduced above with an average photoelectron current (electrons/sec) of $\bar{i}$, the resultant expression that represents a mark having been sent is the term $(1 + M) \, \bar{i}$, and likewise, the photocurrent representing a space is $(1 - M) \, \bar{i}$.

The shot noise fluctuations in a photocurrent are well described by a Poisson statistical distribution. Hence, the statistical variance of the number of photoelectrons counted during a time interval Δt is proportional to the product of the photocurrent, i_{pc}, and the sample period, Δt. In equation form,

$$i_p = (1 + M) \, \bar{i}, \quad i_m = (1 - M) \, \bar{i}, \quad \mathrm{var}\,(i_{pc}) = k \, i_{pc} \, \Delta t \quad . \qquad (78)$$

235

The constant of proportionality, $k \geq 1$, is used to describe the noise effects of amplification, such as dynode noise in a multiplier phototube.

BIT ERROR RATE (BER) AND ITS EFFECTS

The product of the sample period, Δt, and the photoelectron current, i_{pc}, is the number N of electrons counted during a sample interval. The decision as to whether a space or mark was sent is made by comparing the number of photoelectrons counted with some threshold value N_t. If the number of electrons counted is greater than N_t, it is decided that a mark was sent. If the number counted is less than N_t, it is decided that a space was sent. Because of the variance in the values of i_{pc}, there is some statistical probability that, although a mark was sent, the product $i_{pc} \Delta t$ in the receiver will be less than N_t. Hence, the receiver logic curcuitry will make an incorrect decision in such cases. The probability of making an incorrect decision during a sample interval is called the bit error rate (BER).

Although other factors such as S/N ratio could be used, BER is more indicative of the quality of a digitally coded communications channel. For channels using nondigital modulation schemes, it is clear that the lower the system's potential BER, the better the information transmission (as measured by fidelity, S/N ratio, or any other method), even though there is no linear relationship between these characteristics. The use of a system's potential BER as a basis to judge its performance provides the advantage of easily considering the adverse effects of many and varied noise factors as a whole. For example, some criteria of performance require that all noise sources, to be combined, must have similar frequency spectra. These analytical techniques would have difficulty in estimating the simultaneous effects of signal current shot-noise and atmospheric turbulence.

It is of value to compare the subjective quality of a closed-circuit video picture as a function of BER in the communications channel. Figure 134 shows the resultant degradation in received picture quality as the BER is increased from 10^{-5} to 0.30, by attenuating the radiation of the transmitted laser beam. These photos were taken during a laboratory test of an Optical Communications System identical to the AOCP and ground station hardware.

236
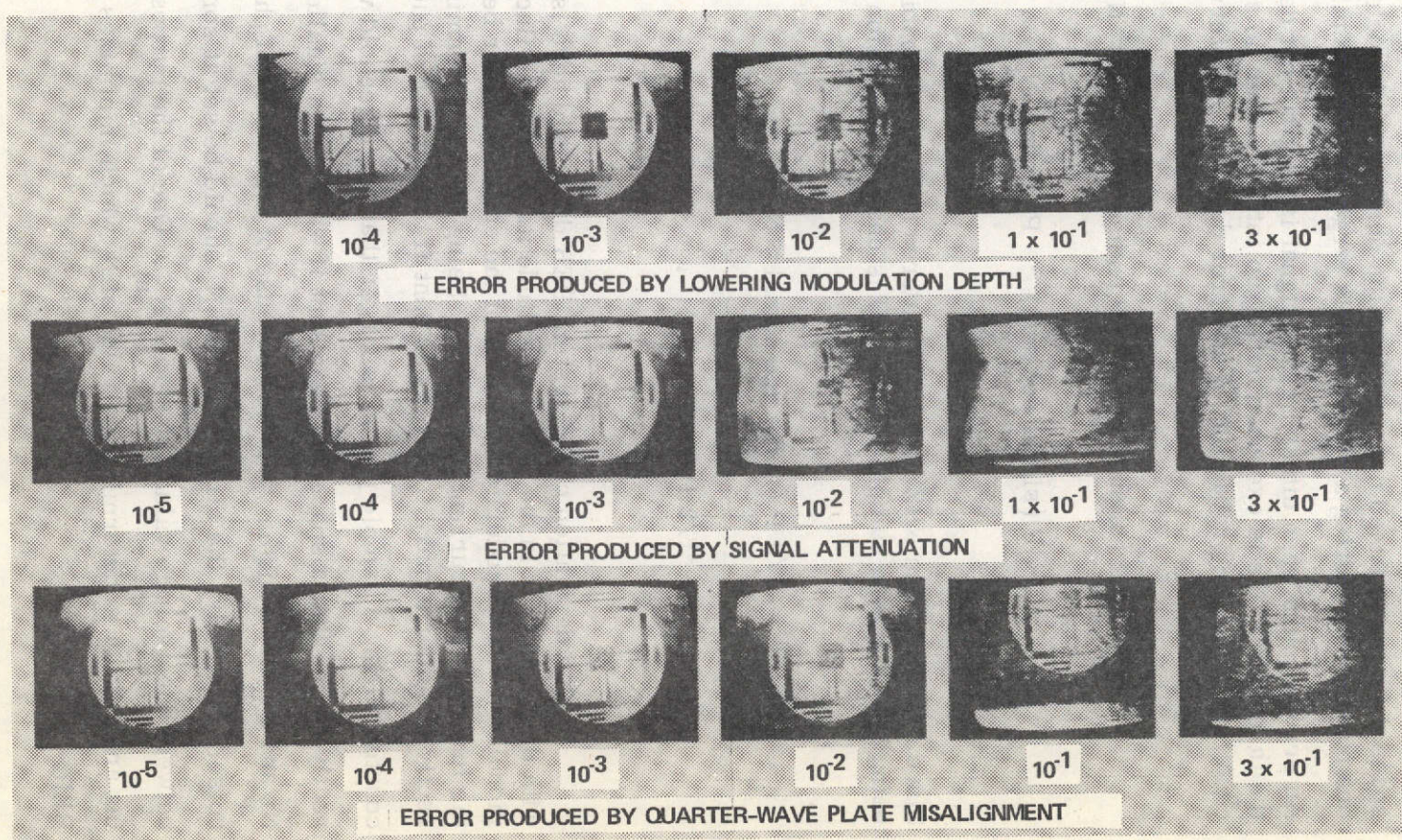
Figure 134. Video picture quality with measured BER for polarization modulation.

ERROR PRODUCED BY LOWERING MODULATION DEPTH

| 10^{-4} | 10^{-3} | 10^{-2} | 1×10^{-1} | 3×10^{-1} |

ERROR PRODUCED BY SIGNAL ATTENUATION

| 10^{-5} | 10^{-4} | 10^{-3} | 10^{-2} | 1×10^{-1} | 3×10^{-1} |

ERROR PRODUCED BY QUARTER-WAVE PLATE MISALIGNMENT

| 10^{-5} | 10^{-4} | 10^{-3} | 10^{-2} | 10^{-1} | 3×10^{-1} |

COMPUTATION OF THE IDEAL SINGLE—CHANNEL BER

In a single-channel, photon-counting type of digital system, a mark or space decision is based upon whether the number of photoelectrons counted in one photosensor during a bit interval is larger than some threshold value, N_t. An error occurs when either: (1) a signal is sent but not detected or, (2) when the threshold value is exceeded during an interval when no signal is sent. In equation form, the probability of an error during a bit interval (the BER) is

$$BER \ = \ P \ (signal \ sent) \ \cdot \ P \ (noise \ and \ signal \leq N_t)$$

$$+ \ P \ (signal \ not \ sent) \ \cdot \ P \ (noise > N_t) \ \ . \tag{79a}$$

Since in the random NRZ coding considered here the probability of a signal being sent during a sample bit interval is one-half, equation (79a) becomes

$$BER \ = \ 1/2 \ P \ (noise \ and \ signal \leq N_t)$$

$$+ \ 1/2 \ P \ (noise > N_t) \ \ . \tag{79b}$$

The derivation of the system BER discussed here is concerned only with the variations in the signal amplitude itself. These fluctuations in the modulated and unmodulated portions of the collected laser beam are caused by the inherent photocurrent shot noise. Using the above terminology, we correctly consider a mark to have been sent if the number of photoelectrons $\tilde{N}_p$ counted during a sample period is larger than the threshold value N_t. We correctly decide that a space has been sent if we detect a smaller value $\tilde{N}_m$. Both $\tilde{N}_p$ and $\tilde{N}_m$ are random variables because of the effects of photocurrent shot noise. Intutively, the threshold value N_t should be set at some number between the average values of $\tilde{N}_p$ and $\tilde{N}_m$. One of the purposes of the following analysis is to determine the value of N_t which minimizes the system's BER.

Equation (79) can be rewritten to include the variables $\tilde{N}_p$ and $\tilde{N}_m$ as

$$\text{BER} = 1/2 \, P \, (\tilde{N}_p \leq N_t) + 1/2 \, P \, (\tilde{N}_m > N_t) \quad . \tag{80}$$

In terms of probability distributions, the components of the last equation are

$$P \, (\tilde{N}_p \leq N_t) = \int_{-\infty}^{N_t} dz \, P \, (\tilde{N}_p = z) \quad , \tag{81a}$$

$$P \, (\tilde{N}_m > N_t) = \int_{N_t}^{\infty} dz \, P \, (\tilde{N}_m = z) \quad . \tag{81b}$$

For large numbers of photoelectrons N, the shot noise (Poisson) distributions are approximately normal.

Hence, keeping in mind that $\overline{N} \, (1 + M) \, \Delta t = i_p$ and $\overline{N} \, (1 - M) \, \Delta t = i_m$, we find that the combination of equations (78) and (81) results in

$$P \, (\tilde{N}_p \leq N_t) = \int_{-\infty}^{N_t} dz \, \frac{e^{-\frac{1}{2}\left(\frac{z - \overline{N} \, (1 + M)}{\sqrt{\overline{N} \, k \, (1 - M)}}\right)^2}}{\sqrt{2\pi} \, \sqrt{\overline{N} \, k \, (1 + M)}} \quad , \tag{82a}$$

and

$$P \, (\tilde{N}_m > N_t) = \int_{N_t}^{\infty} dz \, \frac{e^{-\frac{1}{2}\left(\frac{z - \overline{N} \, (1 - M)}{\sqrt{\overline{N} \, k \, (1 - M)}}\right)^2}}{\sqrt{2\pi} \, \sqrt{\overline{N} \, k \, (1 - M)}} \quad , \quad . \tag{82b}$$

We can use here the tabulated functions P and Q where

$$P(r) = \frac{1}{\sqrt{2\pi}} \int_{-\infty}^{r} e^{-\frac{t^2}{2}} dt, \quad Q(r) = \frac{1}{\sqrt{2\pi}} \int_{r}^{\infty} e^{-\frac{t^2}{2}} dt; \qquad (83)$$

so that equation (80) for the BER simplifies to

$$BER = \frac{1}{2} P\left(\frac{N_t - \overline{N}(1 + M)}{\sqrt{k\overline{N}(1 + M)}} \right) + \frac{1}{2} Q\left(\frac{N_t - \overline{N}(1 - M)}{\sqrt{k\overline{N}(1 - M)}} \right). \qquad (84)$$

In this case, the BER is minimized for a threshold value of

$$N_t = \overline{N}\sqrt{1 - M^2} \left[1 + \frac{k}{2M\overline{N}} \ln\left(\frac{1 + M}{1 - M} \right) \right]^{\frac{1}{2}} \approx \overline{N}\sqrt{(1 - M^2)}, \qquad (85)$$

an approximation easily justified for large values of $\overline{N}$. With this optimum value of N_t, the BER from equation (84) is found to be

$$BER_{\text{Single Channel, Optimum}} = Q\left[\sqrt{\frac{\overline{N}}{k}} \left(\sqrt{1 + M} - \sqrt{1 - M} \right) \right], \qquad (86)$$

240

or approximately

$$Q\left[\frac{\bar{N}}{\sqrt{k}} \left(M + \frac{M^3}{8} + \frac{7 M^5}{128} + + + \right) \right] .$$

Equation (86) is plotted in Figure 135 for two values of modulation index M.

COMPUTATION OF THE IDEAL BINARY CHANNEL BER

Analysis of an ideally balanced binary system is somewhat simpler than that of the single channel, since there is no threshold value N_t to be considered. In this situation, the decision as to whether a mark or space was sent is based on which of two channels has the greater number of photoelectrons. Using subscripts 1 and 2 for the two channels, the expression for the BER can be written analogous to equation (80) as

$$BER = \frac{1}{2} P \left(\tilde{N}_{p_1} < \tilde{N}_{m_2} \right) + \frac{1}{2} P \left(\tilde{N}_{p_2} < \tilde{N}_{m_1} \right) . \qquad (87)$$

For a balanced symmetrical system, the two probabilities are equivalent, and

$$BER = P \left(\tilde{N}_{p_1} < \tilde{N}_{m_2} \right) = P \left(\tilde{N}_{p_1} - \tilde{N}_{m_2} < 0 \right) . \qquad (88)$$

Written in terms of conditional probability distributions, the last equation is

$$BER = \int_{-\infty}^{0} dz \int_{-\infty}^{\infty} dy \ P \left(\tilde{N}_p = z + y \right) . \ P \left(\tilde{N}_m = y \right) . \qquad (89)$$
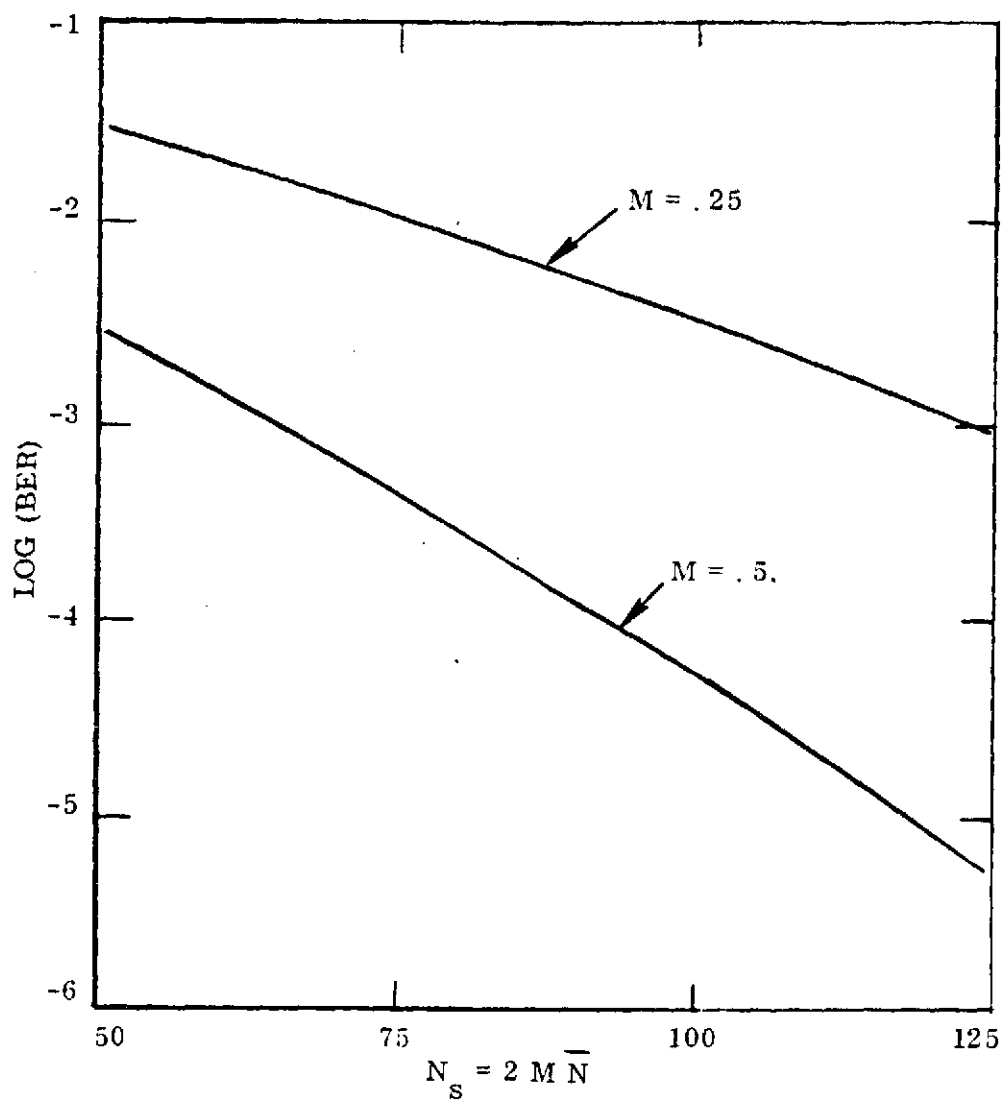
Figure 135. Single-channel BER (factor k is 1.6).

Approximating the probabilities with normal distributions, as was done with equation (82) , the last expression can be arranged in explicit form as

$$BER = \int_{-\infty}^{0} dz \int_{-\infty}^{\infty} dy \frac{e^{-\frac{1}{2}\left[\frac{z + y - N(1 + M)}{\sqrt{k \, \overline{N} \, (1 + M)}}\right]^2}}{\sqrt{2\pi}\sqrt{k \, \overline{N} \, (1 + M)}} \cdot \frac{e^{-\frac{1}{2}\left[\frac{y - N(1 - M)}{\sqrt{k \, \overline{N} \, (1 - M)}}\right]^2}}{\sqrt{2\pi}\sqrt{k \, \overline{N} \, (1 - M)}} .$$

$$(90)$$

This equation, where $\overline{N}$ is the product i_{pc} Δt averaged on one photosensor, can be integrated directly to obtain the simpler form

$$BER_{\substack{Binary \\ Channel, \\ Optimum}} = Q\left(M \, \frac{2\overline{N}}{\sqrt{K}} \right) .$$

$$(91)$$

The last equation is plotted in Figure 136 for modulation indices ranging from 0.3 to 0.8.

COMPARISON OF IDEAL SINGLE-CHANNEL AND BINARY-CHANNEL
SYSTEMS

The practical differences between a single-channel system and a binary-channel system are mainly in the added complexity involved in the binary system's receiver. It is interesting to consider how great an advantage is gained from this additional receiver complexity. Given that the two systems would have the same types of photosensors, modulators, etc., one can calculate the increase in remote terminal laser power required by a single-channel system to equal the performance (BER) of a binary-channel system. By comparing equations (86) and (91), it is seen that the single-channel system's laser power must be increased by the factor

243

$$\text{Required laser power increase} = 1 + \sqrt{1 - M^2} \ . \qquad (92)$$

For example, if the modulator used were capable of a modulation index of 0. 5, the required single-channel laser power increase would be about 87 percent.

Equation (92) implies that both types of systems have about the same performance when used at high-modulation indices and very low noise levels.

CALCULATION OF MODEL SYSTEM'S PERFORMANCE UNDER NOISY CONDITIONS

In the optical communications system under study, there are seven principal sources of noise. For convenience in analysis, all seven may be considered together at the photodetector, even though some noise factors may not actually exist at that point in the signal processing train. Those noise factors not present at the photodetector (such as noise in later amplifiers) can be replaced in analysis with an equivalent noise generator at the photodetector. The seven principal noise factors occurring in the system under study are

1. Laser Generation Noise. A time-varying factor multiplying the average radiative power from the laser. These fluctuations in laser power may be caused by power supply ripple, microphonics, etc.

2. Atmospheric Scintillation Effects. These act in much the same manner as the laser generation noise, above, but, of course, with different frequency and probability distributions.

3. Signal and Background Shot Noise. Variations in the photoelectron current that are proportional to the square root of the current.

4. Background Modulation. A factor usually encountered in scanning systems, in which the background noise may be much greater than that predicted by shot noise calculations.

5. Dark Current. In the system's photodetector, normally of concern only when operating with infrared sensitive sensors at low signal levels.

6. Dynode noise. Significantly increases the fluctuations in photo-electron current during the first stages of amplification. If an electron mul-tiplier-type phototube were not used as the photosensor, the preamplifier would then be an important source of noise of this type.

7. Johnson or Thermal Noise. Usually of concern only if the sensor's load resistor precedes most of the signal amplification.

SENSOR PHOTOCURRENT AND ITS VARIANCE

In a two-level digital signal the seven noise factors discussed above can be combined into multiplicative and additive contributions to the sensor photocurrent, i_{pc}. For the condition of a "mark" being sent, the signal photo-current i_p and its variance are described, as was done with equation (78) by

$$i_p = a(1 + M) \overline{i} + \sum i_n; \hat{N}_p = i_p \Delta t,$$

and

$$var(i_{pc}) = k i_p \Delta t = k \hat{N}_p . \qquad (93a)$$

For the conditions of a "space" being sent, the last equations take the form,

$$i_m = a(1 - M) \overline{i} + \sum i_n , var(i_{pc}) = i_m \Delta t = k \hat{N}_m . \quad (93b)$$

In the last equations, i_{pc} is the instantaneous photocurrent (in electrons/sec), and the term a is the product of factors describing system radiometry, time-varying atmospheric scintillation, and laser generation noise effects. The last term, $\sum i_n$, represents the sum of the dc noise currents, such as background and detector dark current. In the equations for the photocurrent variance, $var(i_{pc})$, the coefficient k describes multiplicative amplifier or dynode noise, and as before, Δt represents the time interval over which the photo-current is sampled.
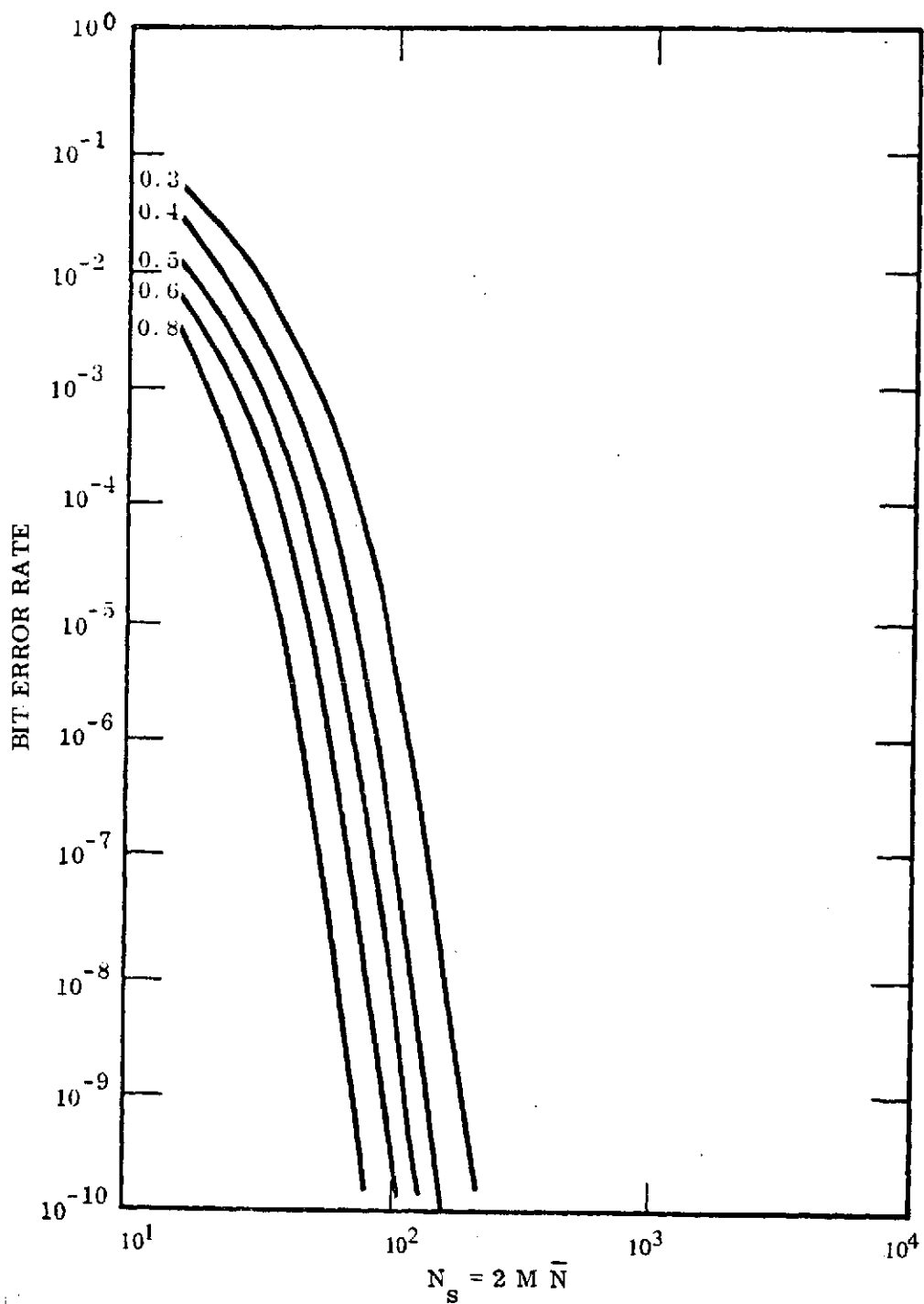
Figure 136. Binary channel BER with modulation index as the parameter (noise factor k is 1.6).

GENERAL FORM FOR THE BER OF A NOISY SYSTEM

Except for an added complexity in the component equations (81), the derivation of the system BER using equations (93) follows that of equation (78). In regard to the previous ideal system, it was assumed that the average signal irradiance on the photosensor was constant. Variations in the photoelectron current were due to shot noise alone. However, in the situation where the system suffers from phenomena such as atmospheric scintillation and its resultant time-varying effects, the major variations in the sensor photocurrent can be due to similar variations in the signal irradiance on the photodetector. Hence, the term $P(\tilde{N}_p = z)$ in equation (81a) must be replaced with a more complex statistical expression. The term $P(\tilde{N}_p = z)$ is the probability that z photoelectrons will be counted during a sample interval if a "mark" is sent, and the long-term average number of photoelectrons counted is $\overline{N}$. However, in the presence of scintillation or fluctuating laser power, $\overline{N}$ is not constant and must be replaced by a random variable $\tilde{N}$. The shot noise in the photocurrent still exists, but a parameter of its distribution, i.e., the population mean, is also a variable. For this reason we have a conditional distribution $P(\tilde{N}_p = z; x)$. This expression represents the probability that the number of photoelectrons counted for a mark sent be z, given that the mean number $\tilde{N}$ is x. It can be seen that the original expression for $P(\tilde{N}_p = z)$ is replaced by

$$P(\tilde{N}_p = z) = \int_{-\infty}^{\infty} dx \, P(\tilde{N}_p = z; x) \cdot P(\tilde{N} = x) \quad . \quad (94)$$

As a consequence, the form of equations (81) for a single-channel BER is changed to

$$P(\tilde{N}_p \leq N_t) = \int_{-\infty}^{\infty} dx \int_{-\infty}^{N_t} dz \, P(\tilde{N}_p = z; x) \cdot P(\tilde{N} = x) \quad (95a)$$

and

$$P(\tilde{N}_m > N_t) = \int_{-\infty}^{\infty} dx \int_{N_t}^{\infty} dz \, P(\tilde{N}_m = z; x) \cdot P(\tilde{N} = x) \quad . (95b)$$

These, combined with equation (80) describe the BER for a single-channel system with additive and multiplicative noise.

To describe the BER for the binary-channel system in a noisy environment, an expression similar to equation (89) can be derived. Hence, written in terms of conditional probability distributions,

$$\text{BER}_{\substack{\text{Binary} \\ \text{Channel}}} = \int_{-\infty}^{0} dz \int_{-\infty}^{\infty} dy \int_{-\infty}^{\infty} dx \; P(\widetilde{N}_p = z + y; \widetilde{N} = x) \cdot P(\widetilde{N}_m = y; \widetilde{N} = x) \cdot P(\widetilde{N} = x).$$

$$(96)$$

Equations (95) and (96) describe the system BER with statistical expressions. To obtain numerical values, these terms must be replaced with algebraic expressions. The most important additional source of noise to be considered here is that caused by atmospheric scintillation. It is well known that these turbulence-induced statistical variations in beam transmittance do not follow the normal probability distribution. For this reason, the next section digresses somewhat to discuss the log-normal distribution, which is more appropriate for use in modeling atmospheric effects.

LOG-NORMAL PROBABILITY DISTRIBUTION

The log-normal probability distribution is applied in situations where a series of independent random impulses c_j have effects on a phenomenon which are dependent on the instantaneous state x_j of the phenomenon. Furthermore, the magnitude of the change in state of the phenomenon, $x_{j+1} - x_j$, is proportional to the magnitude of the impulse c_j and some function $f(x_j)$ of the instantaneous state. Here the state x_j of the phenomenon was produced by c_{j-1}. The equation for the effect of c_j is

$$x_{j+1} - x_j = c_j f(x_j) = \Delta x_j \; .$$

$$(97)$$

248

In the present application, we consider the change (Δx_j) to be a variation in the radiant power transmitted by a turbulent atmosphere and this variation to be equal to the product of the radiant power itself, i.e., $f(x_j) = x_j$, and the magnitude of a number of turbulent impulses c_j. As a consequence, the last equation can be rearranged to obtain the form

$$c_j = \frac{\Delta x_j}{f(x_j)} = \frac{\Delta x_j}{x_j} \quad . \tag{98}$$

The sum $C = \Sigma_j \, c_j$ of a large number of impulses, which are assumed above to be independent, tends to have a normal distribution as implied by the central limit theorem. If each of the impulses c_j has only a very slight effect Δx_j, then the resulting state x_n caused by a very large number of impulses c is

$$C = \sum_{j=0}^{n} c_j = \sum_{j=0}^{n} \frac{\Delta x_j}{x_j} \approx \int_{x_o}^{x_n} \frac{dx}{x} = \ell n \, \frac{x_n}{x_o} \quad , \tag{99}$$

which, in the limit, has a logarithmic relationship to the impulses. Hence, we have a reasonable justification for writing the relationship,

$$\ell n \, x = u \quad , \tag{100}$$

where x is a linear function of the instantaneous radiant flux transmitted through the atmosphere, and u is a normally distributed variable dependent on the characteristics of the atmospheric turbulence. To relate the characteristic parameters of x to those of u, the variate u is assumed to have a mean m and a variance σ^2. The distribution function of u is

$$P\ (u \le U)\ =\ \int_{-\infty}^{U}\ du\ \frac{e^{-\dfrac{(u-m)^2}{2\sigma^2}}}{\sqrt{2\pi\ \sigma^2}}\ \ . \tag{101}$$

The distribution function of x, $\phi\ (x)$, can be determined from equation (101), since from equation (100), x is a function of the random variable u. With the appropriate change of variables,

$$P\ (x \le X)\ =\ \phi\ (X)\ =\ \int_{0}^{X}\ \frac{dx}{x}\ \ \frac{e^{-\dfrac{(\ln x\ -\ m)^2}{2\sigma^2}}}{\sqrt{2\pi\ \sigma^2}}\ \ ;\ X \ge\ 0\ \ . \tag{102}$$

The mean or expected value E(x) of the variable x is given by the Stieltjes integral,

$$E(x)\ =\ \int_{0}^{\infty}\ xd\ \phi\ (x)\ =\ \exp\left(m\ +\ \frac{\sigma^2}{2}\right)\ \ . \tag{103}$$

In a similar manner the expected value of x^2 can be found to be

$$E(x^2)\ =\ \exp\ (2\,m\ +\ 2\sigma^2)\ \ . \tag{104}$$

The variance of x is found from the well-known relationship,

$$var\ (x)\ =\ E(x^2)\ -\ E^2(x)\ =\ e^{2m+\sigma^2}\ (e^{\sigma^2}-1)\ \ . \tag{105}$$

which leads directly to

$$\sigma^2 = \ln\left(1 + \frac{\text{var}(x)}{E^2(x)}\right) = \ln(1 + \rho^2) \quad ,$$

where (106)

$$\text{var}(x) = \rho^2 E^2(x) \quad .$$

It is convenient to work with the normalized variable $x/E(x)$, which also has a log-normal distribution. In terms of the original parameters m and σ, it is found that

$$E\left(\ln\frac{x}{E(x)}\right) = m - \left(m + \frac{\sigma^2}{2}\right) = -\frac{\sigma^2}{2} \quad , \tag{107}$$

and

$$\text{var}\left[\ln\frac{x}{E(x)}\right] = \text{var}\left[\ln(x)\right] = \sigma^2 \quad . \tag{108}$$

The ratio $x/E(x)$ may be considered here to describe the instantaneous transmittance of the atmosphere between the remote and base terminals. Averaged over a sample interval, the photocurrent i and the number of photoelectrons counted, N, are related to the variable x above as

$$\frac{\widetilde{N}}{\overline{N}} = \frac{\widetilde{i}}{\overline{i}} = \frac{x}{E(x)} \quad . \tag{109}$$

The distribution function for $\tilde{N}$ is

$$\phi(x) = P\,(\tilde{N} \le x) = \int_0^x \frac{dx}{x\sqrt{2\pi\,\sigma^2}}\,\exp\,-\left(\frac{\ell n\ x-m}{\sqrt{2\sigma^2}}\right)^2 \quad . \qquad (110)$$

Using equation (104) and the expression $E(\tilde{N}) = \bar{N}$, we find that the probability function for $\tilde{N}$ is

$$\frac{d\phi}{dx} = g(x) = \frac{1}{x\sqrt{\pi}}\,\exp\,-\frac{1}{2}\left(\frac{\sigma}{2} + \frac{1}{\sigma}\,\ell n\,\frac{x}{\bar{N}}\right)^2,\ g(x) = 0,\ x<0 \quad ; \qquad (111)$$

where

$$\sigma^2 = \ell n\left(1 + \frac{\mathrm{var}\,(\tilde{N})}{\bar{N}^2}\right) \quad . \qquad (112)$$

ATMOSPHERIC SCINTILLATION EFFECTS — TYPICAL VALUES

The principal signal fluctuations encountered in a space-to-space optical communications link are those caused by the impressed modulation and fundamental photocurrent shot noise. However, in a satellite-to-ground terminal situation, atmospheric scintillation along the space-to-earth link is expected to influence the system's BER to a great extent, dominating the simpler effects of photocurrent shot noise.

Typical values for the log-amplitude variance, $C_\ell\,(0)$, for an optical path along the zenith angle ψ are estimated to be fairly well represented by the equation $C_\ell\,(0) = 0.73\,(\sec\,\psi)^{11/16}$. The coefficient 0.73, of course, varies from day to day for different locations, and for most astronomical observations, it is probably too large. The variance var $\{P_c\}$, of the detected beam's radiant power P is related to $C_\ell\,(0)$ by the equation

$$\text{var} \left(P_c \right) = P^2 \, \theta \left[\exp \left(4 \, C_\ell \, (0) \right) - 1 \right] = P^2 \, \rho^2 \, , \tag{113}$$

where θ is a complex function of the collector diameter, optical wavelength, and log-amplitude variance. Values of equation (113) for collector diameters of 50, 100, and 150 cm are shown in Figure 137. It is clear that the relative fluctuations represented by the normalized variance ρ^2 in the collected radiant power will affect both the modulated and the unmodulated portions of the beam from the satellite terminal.
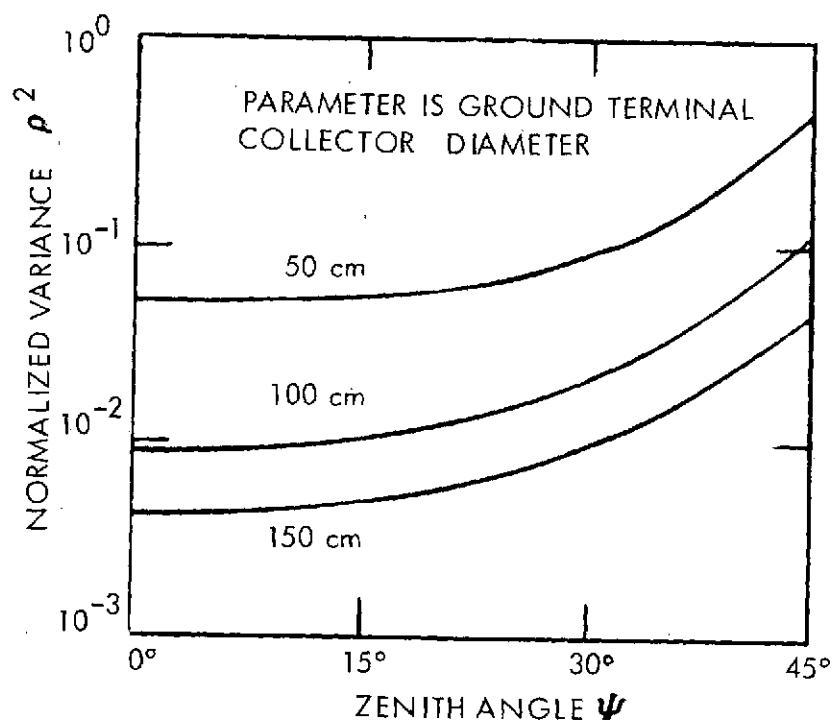
Figure 137. Variation in scintillation normalized variance ρ^2 with zenith angle Ψ.

Figure 138 illustrates the effect of atmospheric scintillation on the transmitted signal. Figure 138a depicts the digitally coded laser beam, with a modulation index of 0.5 and average amplitude $\overline{A}$. The relative fluctuations in the effective transmittance of the atmospheric path are shown in Figure 138b. For purposes of illustration, these fluctuations are pictured as varying at megahertz rates. In an actual system, these atmospheric scintillations would be concentrated below 100 Hz and would vary extremely slowly compared to the data rate. Figure 138c illustrates the resultant signal amplitude as collected by the ground terminal. The modulation index itself is unchanged from that of the transmitted beam in Figure 138a.

NOISY SINGLE- AND BINARY-CHANNEL BER

The variable $x = \overline{ai}\Delta t$ may be used in equation (93) to obtain the definitions,

$$\hat{N}_p = (1 + M)x + \Sigma i_n \Delta t$$

and $\hspace{11cm}$ (114)

$$\hat{N}_m = (1 - M)x + \Sigma i_n \Delta t \ .$$

With these substitutions, equation (111) can be used to rewrite equations (95) in the more general form:

$$P(\tilde{N}_p \leq N_t) = \int_{-\infty}^{N_t} dz \int_0^{+\infty} dx\, g(x)\ \frac{e^{-\frac{1}{2}\left(\frac{z - \hat{N}_p}{\sqrt{k\hat{N}_p}}\right)^2}}{\sqrt{2\pi}\,\sqrt{k\hat{N}_p}}$$

(115a)

and

$$P(\tilde{N}_m > N_t) = \int_{N_t}^{\infty} dz \int_0^{+\infty} dx \, g(x) \frac{e^{-\frac{1}{2}\left(\frac{z - \hat{N}_p}{\sqrt{k\,\hat{N}_p}}\right)^2}}{\sqrt{2\pi}\,\sqrt{k\,\hat{N}_p}} \cdot \qquad (115b)$$

Using the expressions of equation (83), it is found that the noisy single-channel BER is

$$\left. BER \right|_{\substack{\text{Single} \\ \text{Channel}}} = \frac{1}{2} \int_0^{\infty} dx \, g(x) \left[P\left(\frac{N_t - \hat{N}_p}{\sqrt{k\,\hat{N}_p}}\right) + Q\left(\frac{N_t - \hat{N}_m}{\sqrt{k\,\hat{N}_m}}\right) \right] \cdot$$

$$(116)$$

The optimum value for the threshold setting N_t can be found by differentiation to be

$$N_t^2 = \hat{N}_m \hat{N}_p \left[1 + \frac{k \, \ell n \left(\hat{N}_p / \hat{N}_m\right)}{\hat{N}_p - \hat{N}_m} \right] ,$$

or approximately

$$N_t \approx \sqrt{\hat{N}_m \hat{N}_p} \, . \qquad (117)$$
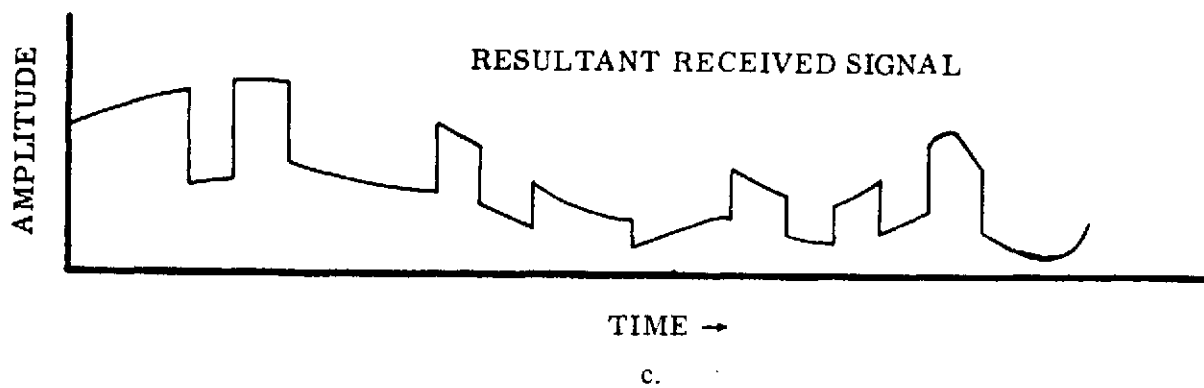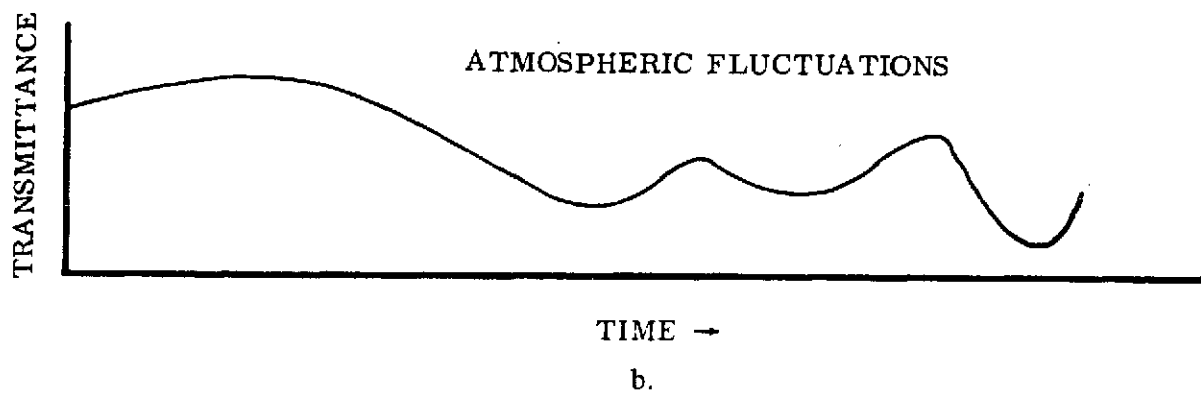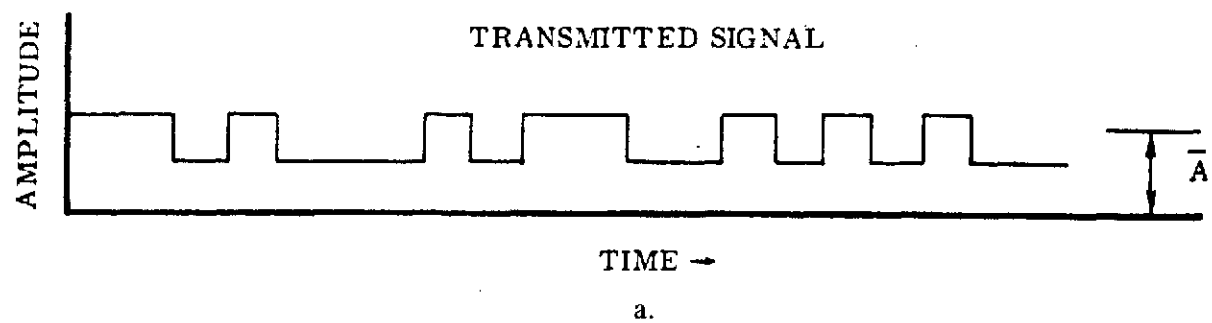
Figure 138. Effects of atmospheric scintillation on a digitally coded beam of average amplitude A.

Hence, by substituting this value for the threshold in equation (116) the simpler form is obtained:

$$\left.\text{BER}\right|_{\substack{\text{Optimum,}\\\text{Single}\\\text{Channel}}} = \int_0^\infty dx\; g(x)\; Q\left(\frac{\sqrt{\hat{N}_p} - \sqrt{\hat{N}_p}}{\sqrt{k}}\right) . \tag{118}$$

In a similar manner, the expression for the balanced binary-channel BER can be written from equation (96) in explicit form as

$$\left.\text{BER}\right|_{\substack{\text{Balanced}\\\text{Binary}\\\text{Channel}}} = \int_{-\infty}^0 dz \int_0^\infty dz \int_0^\infty dx\; g(x)\; \frac{e^{-\frac{1}{2}\left(\frac{z+y-\hat{N}_p}{\sqrt{k\hat{N}_p}}\right)^2}}{\sqrt{2\pi}\sqrt{k\hat{N}_p}} \cdot \frac{e^{-\frac{1}{2}\left(\frac{y-\hat{N}_m}{\sqrt{k\hat{N}_m}}\right)^2}}{\sqrt{2\pi}\sqrt{k\hat{N}_m}} .$$

$$\tag{119}$$

This expression may also be integrated to obtain the simpler form,

$$\left.\text{BER}\right|_{\substack{\text{Balanced}\\\text{Binary}\\\text{Channel}}} = \int_0^\infty dx\; g(x)\; Q\left[\frac{\hat{N}_p - \hat{N}_m}{\sqrt{k\left(\hat{N}_p + \hat{N}_m\right)}}\right] . \tag{120}$$

Equations (118) and (120) describe the performance of single-and binary-channel systems in the presence of additive noise. Measurements on the present optical communications system indicate that, in the laboratory and field tests performed, background noise and photosensor dark current are negligible, i.e., $\Sigma i_n \approx 0$. Representative values of system BER for these test conditions are plotted in Figures 139 and 140 for a dynode noise factor of 1.6.
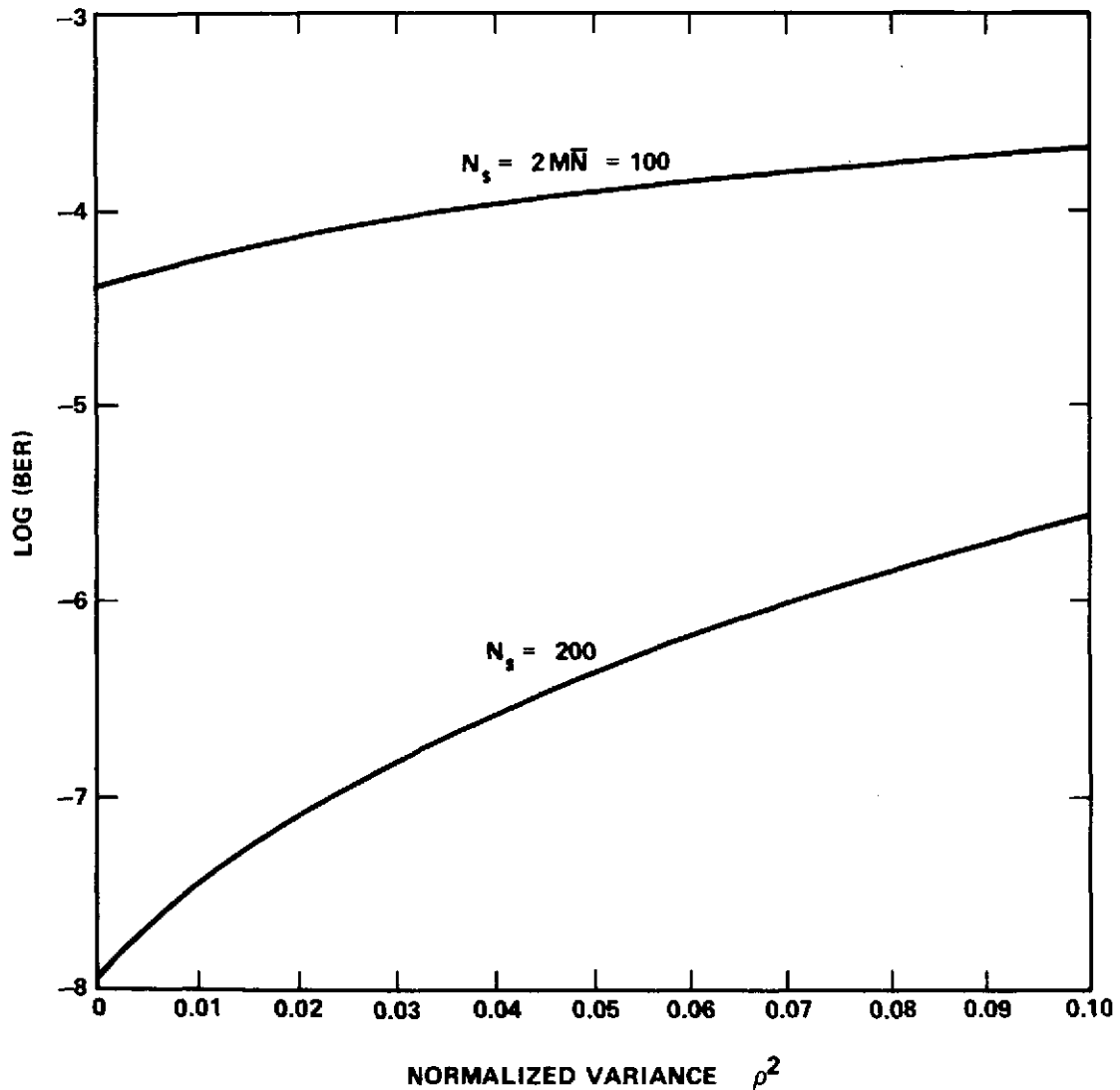
Figure 139. Single-channel BER in the presence of log-normal turbulence for k = 1.6 and M = 5.05.
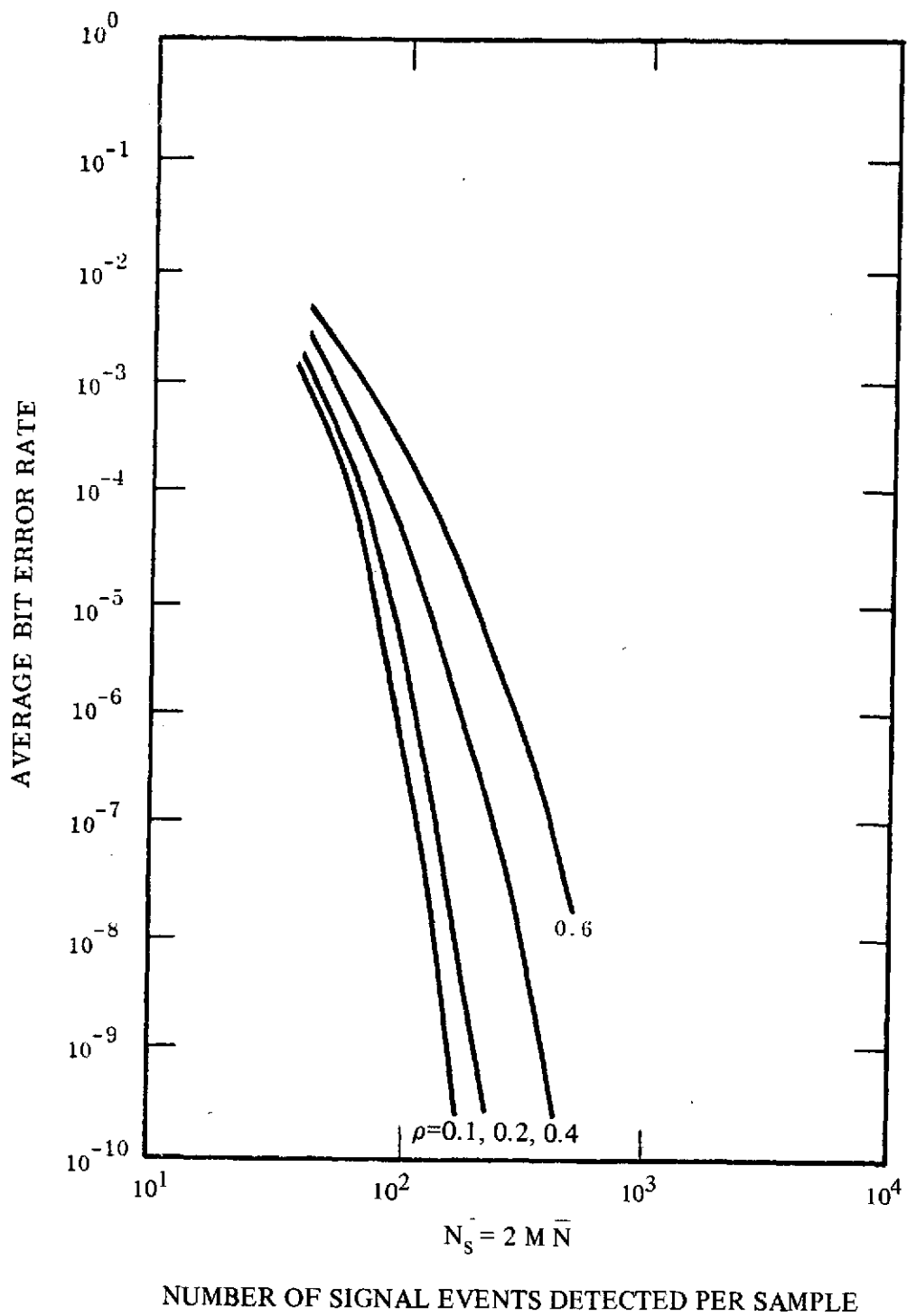
Figure 140. Binary-channel BER in the presence of log-normal atmospheric turbulence for k = 1. 6 and M = 0.4.

DATA, COMMUNICATIONS CHANNEL

Although many complex parameters affect the performance of an optical communications system, four factors are of major concern in the system's evaluation: laser power, signal beam modulation index, atmospheric scintillation, and the resulting BER. Figure 141 is a portion of a recording tape generated with the engineering model during a field experiment. The raw data shown here are the bases for calculations that lead to evaluating system performance.

The two curves in the upper portion of Figure 141 are measurements of the anode current of the system's PMT sensor. The straight line at the top of the figure is the system's zero or dark level. This current measurement is made with all radiation blocked from the photosensor and is an indication of the tube's dark current. The second curve from the top is a record of the tube's output current and shows the noisy effects of atmospheric scintillation. This curve was generated on the 8-km (5-mi) test range at ITT Gilfillan, San Fernado, Calif. The normalized variance determined from this data was $r = 0.31$, the term r being an experimental estimate of the parameter ρ of equation (107). The laser beam was heavily attenuated with neutral density filters during this test run, limiting to 44 the average number of signal events per sample period.

The lowest curve of Figure 141 is a series of 1-sec timing marks, used for setting the horizontal scale. The curve above these timing marks indicates the instantaneous system BER, the output of the bit error detector. Under close inspection, it is seen that error bursts occur as a nonlinear, almost threshold function of the detected signal current. With a digital counter reading the output of the bit error detector, the BER for the sample of Figure 141 was found to be 4.1×10^{-3}.

It was pointed out that the system's BER is a complex function of atmospheric scintillation amplitude r, the ratio of the measured standard deviation to the mean (of any linear function) of the detected signal radiation. The factor r is useful in predicting system performance and as Figure 137 shows, is somewhat under the system designer's control in that scintillation amplitude is greatly affected by receiving aperture diameter. The curve of Figure 142 indicates the strong relationship between aperture diameter and a system's BER. It should be noted that this curve considers the scintillation averaging effects of various aperture size, neglecting the greater radiation collecting ability of larger apertures. The BER curve of Figure 142 would fall at a much greater slope if a constant detected power had not been maintained by attenuating the beam with neutral density filters as the aperture was increased.

260
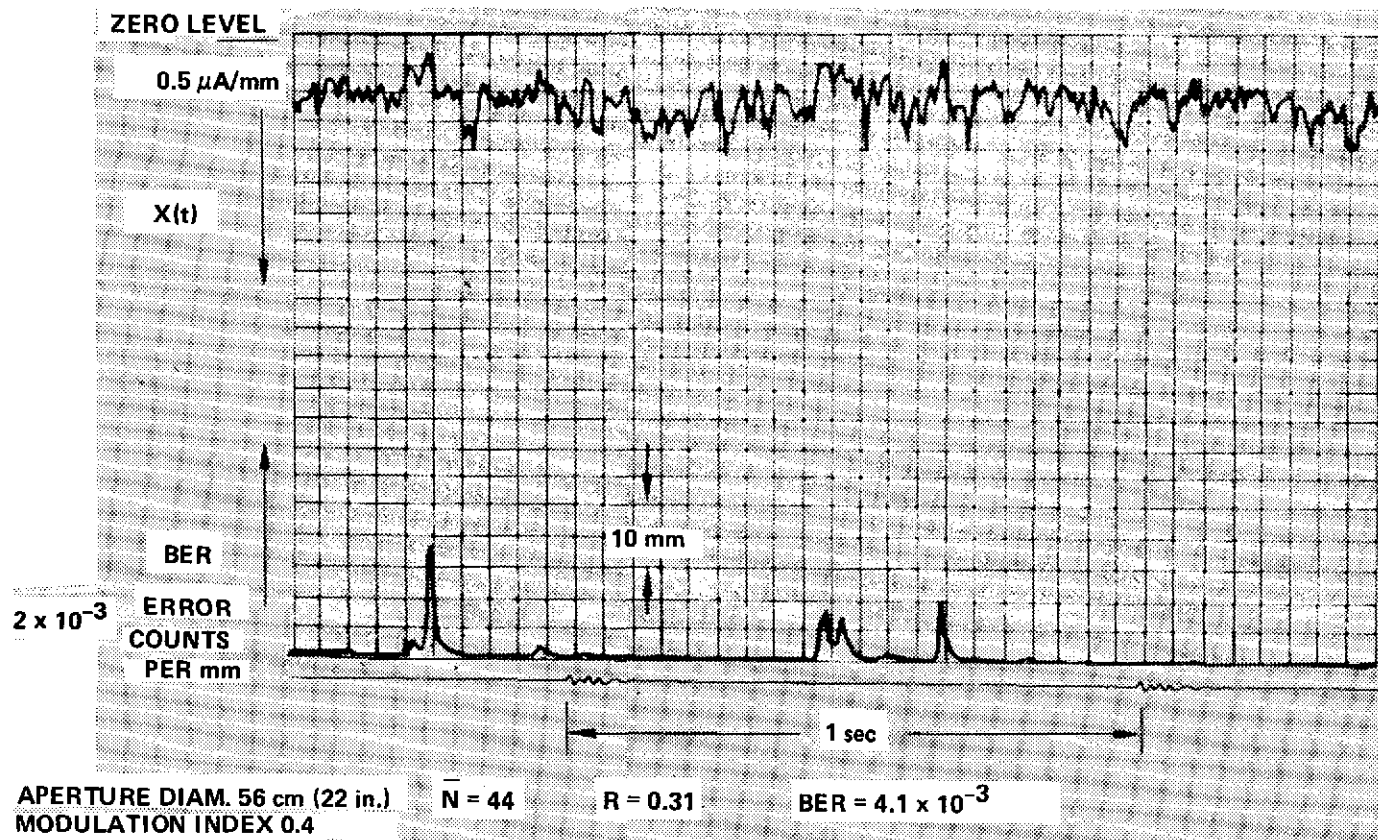
Figure 141. Integrated error output data sample.
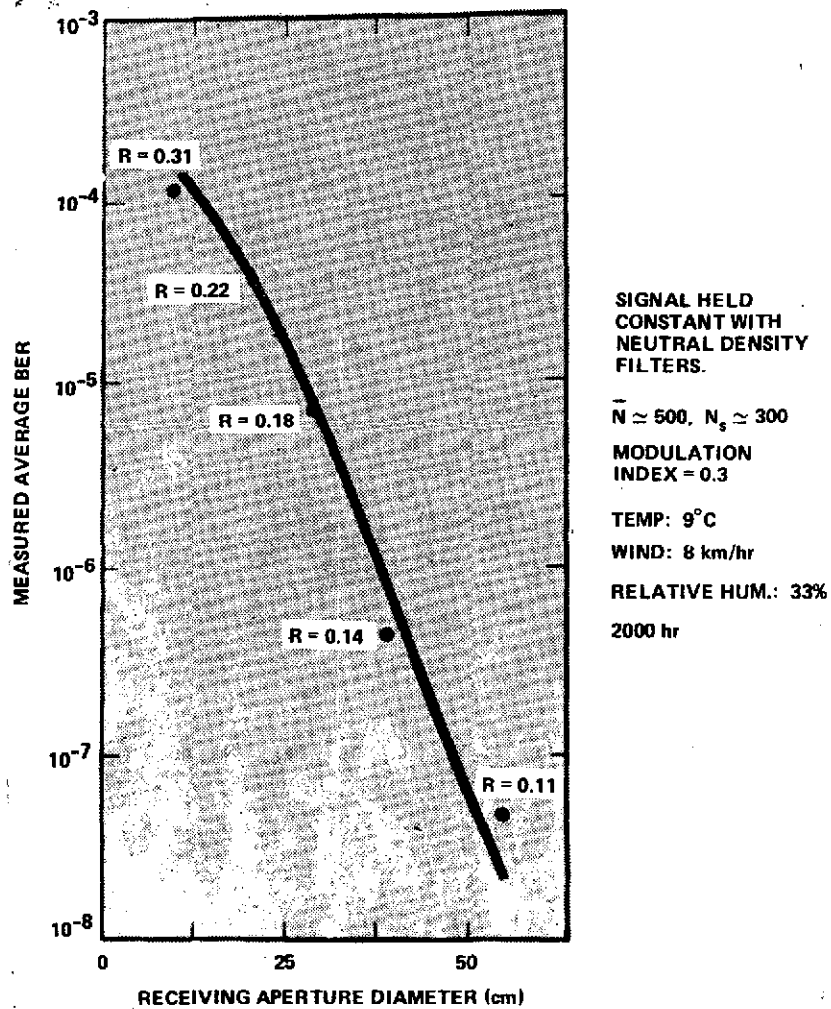
Figure 142. BER vs. receiving aperture.

Figure 142 labels:

R = 0.31
R = 0.22
R = 0.18
R = 0.14
R = 0.11

SIGNAL HELD CONSTANT WITH NEUTRAL DENSITY FILTERS.

$\bar{N} \simeq 500$, $N_s \simeq 300$

MODULATION INDEX = 0.3

TEMP: 9°C

WIND: 8 km/hr

RELATIVE HUM.: 33%

2000 hr

MEASURED AVERAGE BER

RECEIVING APERTURE DIAMETER (cm)
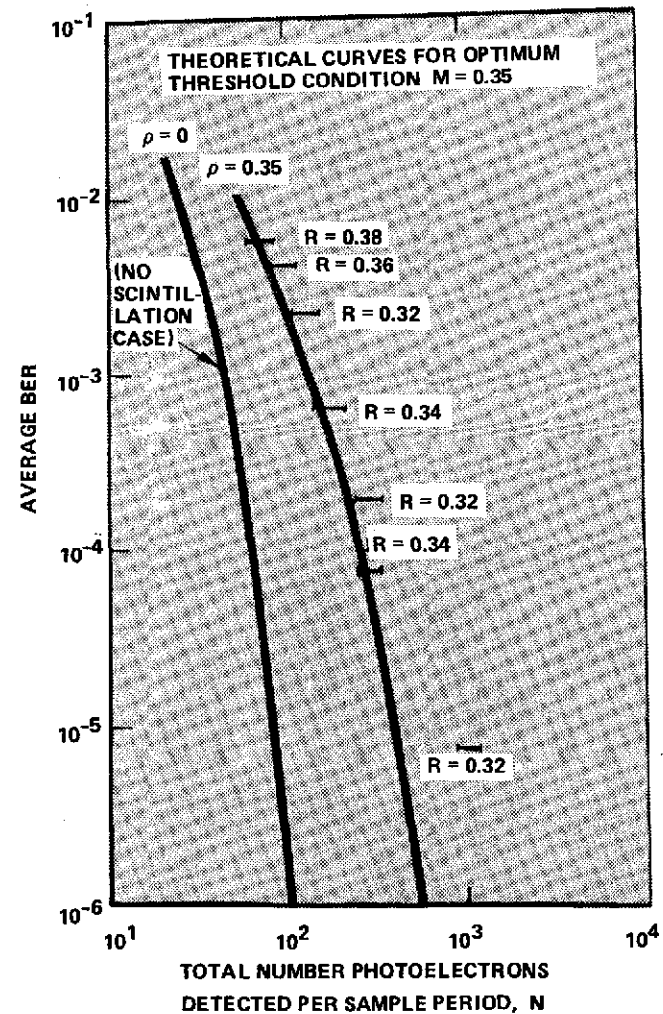
Figure 143. Comparison of experimental data with log-normal atmospheric model for single-channel system.

Figure 143 labels:

THEORETICAL CURVES FOR OPTIMUM THRESHOLD CONDITION M = 0.35

$\rho = 0$

$\rho = 0.35$

(NO SCINTILLATION CASE)

R = 0.38
R = 0.36
R = 0.32
R = 0.34
R = 0.32
R = 0.34
R = 0.32

AVERAGE BER

TOTAL NUMBER PHOTOELECTRONS DETECTED PER SAMPLE PERIOD, N

Figure 143 shows the performance of the communications system in field tests under conditions of heavy turbulence. For comparison the theoretically predicted performance for $\rho = 0.35$ is represented as the solid curve on the right. Data runs with varying laser radiation intensities were recorded, and the results are shown as horizontal bars. The term r is an estimate of the parameter ρ, calculated from experiment data. Since r is a statistic of the nonstationary atmosphere, its value is constantly changing, and the use of the bar interval is appropriate. The fit of theoretical predictions to the tested performance of the system is seen to be quite close.

LASER SAFETY CONSIDERATIONS

Description of Hazard

Laser radiation can be harmful to the body and cause permanent eye damage. In any experiment, such as the AVLOC project, where laser beams are directed through open spaces, there always is a danger of injury due to exposure to excessive levels of laser radiation. Precautions must be taken to assure that project personnel, nonproject personnel, and the general population are adequately protected

For visible laser light, the principal danger is eye damage caused by excessive illumination on the retina. Skin exposure usually presents no hazard. Consideration must be given to the possibility of reflections as well as direct exposure to the beam.

Permissible Exposure Levels

No definitive measurements of the threshold levels for eye damage have been made. However, 10^{-6} W/cm^2 for continuous wave (CW) visible lasers and 10^{-6} J/cm^2 for non-Q-switched pulsed lasers are generally considered safe levels for the maximum intensity incident upon the cornea of the human eye [5].

Skin exposures 10^5 times as large as corneal exposure are allowable. The intensities encountered in the AVLOC experiments are far below this level so that only corneal exposure need be considered.

The maximum allowable reflectance from a diffuse surface is 0.9 J/cm^2 for a pulse and 2.5 W/cm^2 for a CW laser. Specular reflections should be considered to be the same as direct exposures.

Calculation of Beam Intensity

The average intensity of a circular laser beam is given by

$$I = \frac{\alpha E}{\pi \left(\dfrac{a + r\phi}{2}\right)^2} \qquad (121)$$

or

$$I = \frac{1.27 \, \alpha \, E}{(a + r\phi)^2} \qquad (122)$$

where

E = output power (CW) or energy (pulse) of the laser;

α = attenuation of the beam, or in the AVLOC project, the atmospheric attenuation = $e^{-\mu r}$;

a = diameter of emergent beam at transmitter (cm);

r = distance from transmitter to observer (cm);

and

ϕ = beam divergence (rad).

264

AVLOC Laser Beam Intensities

To make a worst-case hazard analysis, no atmospheric attenuation was assumed in the following calculations.

ARGON BEACON (UPLINK) LASER BEAM, 488 nm

The uplink CW argon laser was capable of a maximum power output of 1W and a minimum beam divergence of 1 μrad (results from diffraction limit of 61-cm telescope through which the laser beam is transmitted); however, the operational limits for this project were a maximum laser power of 100 mW and a minimum beam divergence of 100 μrad. The 100-μrad beam divergence resulted in a beam diameter of 2.75 m at the test aircraft at an altitude of 21.34 km (70 000 ft). From equation (121) the following beam intensities (I) are found:

$$I \text{ (at telescope)} = 34.2 \times 10^{-6} \text{ W/cm}^2$$

and

$$I \text{ (at test aircraft, 100-}\mu\text{rad beam)} = 1.8 \times 10^{-6} \text{ W/cm}^2 \quad .$$

The latter figure was still slightly above the permissible exposure level, so the Air Force flight crew was protected as described in the following paragraphs. The analysis of the hazard to private and commercial aircraft flying at intermediate altitudes is also covered as follows.

He-Ne (DOWNLINK) LASER BEAM, 632.8 nm

The airborne He-Ne laser was capable of a maximum power output of 5 mW and a minimum beam divergence of 6 μrad (results from a diffraction limit of 10.16-cm telescope through which the laser beam was transmitted); however, the operational limit for the beam divergence for this project was 50 μrad. The 50-μrad beam divergence resulted in a beam diameter of 1.15 m at the ground from an altitude of 21.34 km. From equation (121) the following beam intensity (I) is found:

$$I \text{ (at ground station, 50-}\mu\text{rad beam)} = 0.48 \times 10^{-6} \text{ W/cm}^2 \text{ .}$$

This number falls within the safety limits of permissible exposure.

PULSED ARGON LASER (GROUND BASED ACQUISITION AID), 514.5 nm

The GBAA employs a 2-W (peak power) argon pulsed laser with a 12 μsec pulse at a 1000 pulses per second repetition rate (24 mW average power). The beam divergence is 1.7 mrad (0.1 deg). The fact that the laser is repetitively pulsed requires that we consider both average power density and the energy density per pulse. The application of equation (121) gives the following results for a 21.34-km altitude:

$$E = 2.2 \times 10^{-12} \text{ J/cm}^2/\text{pulse}$$

and

$$I = 2.2 \times 10^{-9} \text{ W/cm}^2 \text{ average.}$$

Both of these are far below the safe levels. In fact, at a range of only 972 m, the energy density per pulse and average power density are only 10^{-9} J/cm^2 and 10^{-6} W/cm^2, respectively.

Assessment and Control of the Hazard

Persons exposed to the greatest hazard in the AVLOC experiments were the project personnel involved in various checkout and flight operations on the ground. However, to assure the maximum protection to the general public and to other agency personnel, certain safety precautions were taken. The following specific areas were considered in order of emphasis.

SAFETY OF PRIVATE, MILITARY, AND COMMERCIAL AIRCRAFT

To properly assess the hazard here, we must consider the maximum "time of exposure" to the laser beam, noting that a plane will fly through the small-diameter laser beam quite rapidly. Since the time of exposure will be inversely proportional to the speed of the aircraft and the magnitude of the exposure inversely proportional to its altitude, the maximum exposure will be for a slow, low-flying aircraft.[2] We take the worst case to be

Min. speed = 44.7 m/sec (100 MPH)

and

Min. altitude = 914 m (3000 ft) .

The ground station argon laser beams (the downlink He-Ne is clearly safe and need not be considered) in the tracking mode have an angular velocity of 9.1 mrad/sec) from the equation $v = \omega r$, which relates the linear velocity v to the angular velocity ω and the range r, we find that the linear velocity that the argon laser beams sweep out at 914-m range is 8.32 m/sec. Therefore, the plane will have a minimum velocity relative to the laser beam of 36.4 m/sec. The maximum exposure time, then, is 0.7 m (argon beacon laser beam diameter at 914-m altitude) divided by 36.4 m/sec (aircraft velocity relative to laser beam), or 19.2 msec.

---

2. There could be one exception to this worst case, that being in the rare event that a light aircraft would attempt to "track" the laser beam. A theoretical case does exist whereby the aircraft pilot could maneuver himself into a position where he could "track" the laser beam and, in turn, "stare" into it. From a practical point of view, however, this case is virtually impossible. In addition, this impending situation would be quite obvious to ground control personnel, and the laser would be shut down immediately until the intruder could be chased off.

Because of the short exposure time, the problem can then be considered as an exposure to a pulsed laser [6], so we determine the energy density Q integrated in the exposure time of 19.2 msec. Continuing on a worst-case basis, we use the argon beacon laser power density of 34×10^{-6} W/cm^2 (from a preceding subsection):

$$Q = 34 \times 10^{-6} \text{ J/sec/cm}^2 \ (19.2 \times 10^{-3} \text{ sec})$$

$$= 0.65 \times 10^{-6} \text{ J/cm}^2 \ .$$

Since this is below the permissible exposure level, the AVLOC experiment is deemed to be no hazard to general aviation.

SAFETY OF AIR FORCE WB-57F CREW

The flight crew presented a special problem. First of all, it should be noted that the WB-57F flight crew could readily "stare" at the uplink argon laser beams, since these beams were tracking the WB-57F aircraft during the experiment. For maximum experiment flexibility, the output power of the argon beacon laser could not be restricted to a value so low that direct viewing of the beam would not be hazardous (although this could have been done if necessary since the airborne equipment could detect a lower power density than is considered hazardous). As was shown above, the highest operational argon beacon power (i.e., mW) could result in a power density at the test aircraft slightly above the permissible exposure level.

Thus, the crew – pilot and operator – were provided protection from the beam, either by shielding so that they could not see the beam or by eye protection. Either approach could be used for the operator because there was no requirement for him to be able to see out of the plane during experiment operations; curtains are available for this purpose. The pilot must be able to see out; therefore; eye protection was called for. This was not straightforward because of the pressure suit and faceplate. Protective visors had not been developed for this type of suit, and standard goggles cannot be fitted to either the inside or the outside of the bubble. Thus, it was necessary to develop a special protective visor for this project.

It was shown above that the argon laser power density at the aircraft might be as much as a factor of two above the permissible level. It can be readily seen, then, that a special visor with an optical density of 1 (i.e., transmission of 10 percent at the 488-nm line would restrict the intensity to well within the safe limits. Special visor(s) with an optical density of > 1 were provided for this purpose.

SAFETY OF AVLOC PROJECT PERSONNEL

Because of their close proximity to the operating lasers, AVLOC project personnel were exposed to the greatest hazard. However, all persons involved were throughly familiar with lasers and the hazards they present. To assure maximum portection, however, the procedures listed as follows were disseminated and strictly enforced.

SAFETY PROCEDURES

General

1. Only authorized and protected personnel will be allowed within the posted area of an operating laser.

2. Laser warning signs will be posted on the outside of the ground station, on the telescope and transceiver package, on the underside of the aircraft, on the airborne package, on the GBAA, on the GCE, and wherever else applicable.

3. Equipment containing high-voltage supplies will be clearly identified with appropriate markings.

4. All reflecting surfaces in the observatory dome will be painted with nonreflecting coatings.

Safe Operating Procedures

1. Never permit the eye to be in the direct path of the laser beam or its specular reflection.

2. Do not look directly into the expected path of the laser beam when there is a possibility that the laser may be fired.

3. Wear protective goggles whenever possible.

4. When wearing protective goggles, never permit the eye to be in the direct path of the laser beam.

5. Keep specular reflectors out of the path of the laser beam.

6. Never view a direct laser beam with a telescope or binoculars.

7. Use matte (diffusely reflecting) surfaces to observe beam incidence, alignment, etc.

8. All laser beams should be terminated at the end of their useful beam paths; lasers with beam outputs at both ends will be covered at the end not being used.

9. Never permit an operating laser to be unattended or unsupervised.

10. When the airborne package (AOCP) is being tested in the laboratory or on the runway, care should be taken not to look directly into the exit aperture while the shutter is open.

11. When using the GCE, be sure that attenuating filters are in place before looking through telescope viewer.

12. A warning should be called out before operating laser equipment during ground checkout operations so that other personnel in the area are not taken by surprise.

13. Personal jewelry should be held to a minimum while servicing electrical equipment and while operating lasers (because of possible beam reflection into eyes).

14. Apply the usual electrical precautions when working with lasers having high-voltage power supplies.

EXPERIMENT AND EQUIPMENT VERIFICATION TESTS

Environmental Testing

QUALIFICATION APPROACH

The original philosophy of this program, relative to equipment qualification, was to buy the most economical equipment available and hope that it would survive the aircraft operating environment. This philosophy was dictated by fiscal necessity. However, after completion of design but before procurement began, there was a shift in attitude on this point, and limited funds were made available for qualification of the flight hardware. At that time a low-budget qualification effort was undertaken. The results of that effort are summarized in Table 29. The new philosophy was to purchase flight-qualified versions of items that were low cost to begin with, so that the total additional dollars would not be that great. This was done only for items in which the flight-qualified versions could be added without redesign effort. For other items, a limited amount of vibration tests would be performed for verification and assurance.

Under this approach, nearly all the supporting electronics was purchased in flight-qualified versions. The exceptions, as noted in the table, are the small power supplies and the onboard digital computer. To change power supplies would have required some packaging redesign, and no flight-qualified computers were available at that time at a cost the program could afford. Therefore, these items were subjected to limited vibration tests.

VIBRATION TESTS

The vibration environments of concern are depicted in Figure 144. Four vibration curves are given: (1) the MIL-E-5400 design specification for aircraft mounted equipment; (2) the test environment recommended by General Dynamics for equipment hard mounted in the WB-57F aircraft, (3) the composite baseline aircraft vibration environment the equipment would be subjected to during all flight regimes, including takeoffs and landings, and (4), the response of the Barry T-64 isolators to the baseline aircraft environment.

TABLE 29. AVLOC RELIABILITY DATA

	Flight Qualified	Environmental Specifications	Operating Modes	Operating Temp (°C)	Vibrations	Altitude	Equipment Location
VCO Assembly	Yes	N.S.	Data Acq.	-55 to +125	30 g 55—2000 Hz	Vacuum	Canister
AUX VCO Assembly	Yes	N.S.	Data Acq.	-55 to +125	30 g 55—2000 Hz	Vacuum	Canister
Multiplexer	Yes	N.S.	Data Acq.	-55 to +100	20 g 10—2000 Hz	Vacuum	Canister
Measurement Distributor						—	Canister
T-Bar Relay	Yes	MIL-R-5757	Data Acq.	-55 to -85	10 g 10—55 Hz	9.14	Canister
Time Code Generator	Yes	MIL-E-5400	Data Acq.	-55 to +71	5 g 5—500 Hz	9.14	Canister
5 V dc Power Supply	No	N.S.	Slave Track Data Acq.	-7 to +52	N.S.	9.14	Canister
Control Panel B						—	Cockpit Sta. 2
15 V Dual Power Supply	No	N.S.	Slave Track Data Acq.	-15 to +70	N.S.	9.14	Cockpit Sta. 2
Synchro/Linear Converter	No	Select MIL Version	Slave Tracking	-55 to +85	N.S.	9.14	Cockpit Sta. 2
Phaostron Meters	Yes	MIL-A-6752	Manual Command Data Acq.	-55 to +70	MIL A6752	9.14	Cockpit Sta. 2
Control Panel A							Cockpit Sta. 2
± 5 V dc Power Supply	No	N.S.	All	-40 to +70	N.S.	9.14	Cockpit Sta. 2
Digital Display	Yes	MIL-E-5400	Data Acq.	-54 to +71	5 g 5—500 Hz	9.14	Cockpit Sta. 2
60 Hz Inverter		150-073	All		10 g 10—500 Hz	13.7	Canister
28 V dc Supply	Yes	MIL-1-4807 MIL-1-4970 MIL-E-5272	Tracking Command (Uplink)	-40 to +85	MIL-E-5272	15.2	Canister
Power Distributor							Canister
Power Relay	Yes	MIL-R-6106	All	-70 to +120	10—1500 Hz	24.4	Canister
Circuit Breakers	Yes	MIL-E-5272	All	-54 to +120	MIL-E-5272	18.3	Canister
SPC-16 Computer	Yes	Flight Qualify	All	0 to +50	N.S.	9.14	Canister
Tape Recorder	Yes	MIL-E-5400	Data Acq.	-54 to +71	MIL-E-5400	15.2	Nose Compartment
Charge Amplifier	Yes	MIL-E-5272	Data Acq.	-40 to +85	25 g 35—2000 Hz	9.14	Canister
Triaxial Accelerometer	Yes	MIL-E-5272	Data Acq.	-40 to +85	500 g	Vacuum	On Gimbal Platform
AOCP	No	MIL-E-5400	All	15 to +32	N.S.	9.14	Experiment Enclosure
Remote Electronics Pkg.	No	MIL-E-5400	All	15 to +32	N.S.	9.14	Canister
Gimbal Platform	Yes	MIL-E-5400	All	-72 to +70	MIL-E-5400	6.1	Bomb Bay
Gimbal Electronics	Yes	MIL-E-5400	Downlink Data Acq.	-55 to +85	10—55 Hz	9.14	Canister

272
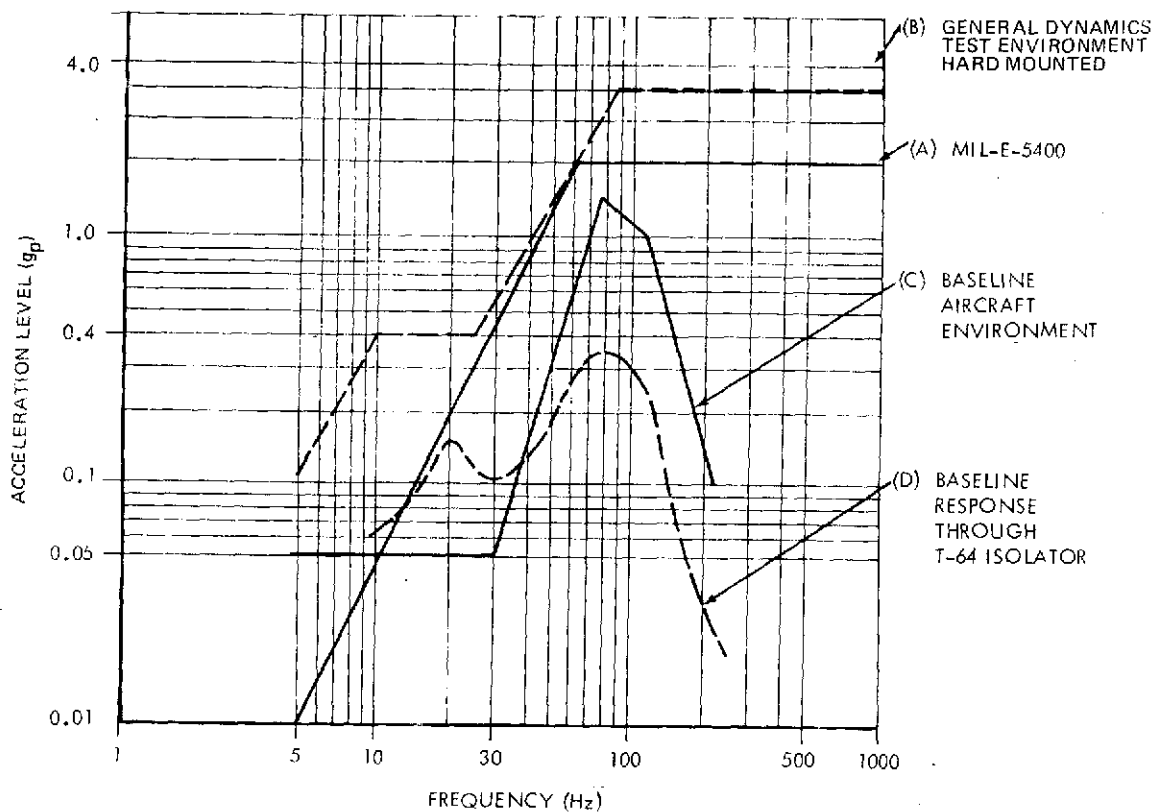
Figure 144. Vibration curves.

EXPERIMENT PLATFORM

The experiment platform was subjected to a vibration test program consisting of both sinusoidal and random vibration inputs. The specified test environment was applied to each of the three mutually perpendicular axes of the experiment platform. The experiment platform vibration testing was performed by Wyle Laboratories in Huntsville.

Test Setup

The experiment platform was suspended from the vibration test fixture by its four isolation mounts. The test fixture was mounted between two phase-controllable electrodynamic shakers. The input vibration levels were controlled by using a minimum of two accelerometers. Before testing, a fixture evaluation test was performed. The test approach was to perform a research-type

sinusoidal evaluation test in one axis; when performance was established, a low-level random test was conducted. After the performance was established in one axis, the established level was applied to each of the remaining two axes.

An important feature of the tests was that, with the exception of the fixture evaluation tests, all vibration tests were performed with the airborne tracking systems (coarse and fine) in active track of the GCE argon laser — this can be seen from the test setup photographs in Figures 145 through 150. This provided a very straightforward indication of the tracking systems performance in a vibration environment, i.e., as the vibration input became increasingly severe, "loss of lock" could be correlated immediately with specific input vibration characteristics.

Procedures and Tests

The gimbal mirror platform and AOCP were removed from the experiment platform and replaced with dummy weights. The experiment platform was then attached to a vibration test fixture which was mounted on two Ling A275 vibration exciters. Figure 150 shows the isolator mount/test fixture interface.

Twelve accelerometers were installed on the isolators and platform frame as shown in Figure 151. A series of fixture evaluation tests was performed in the vertical (Z) axis as described in Table 30.

TABLE 30. FIXTURE EVALUATION TESTS

Test No.	Test Level	Remarks
1 and 2	Sinusoidal Sweep: 200 to 5 Hz at 1 octave/min 200 to 5 Hz 0.05 g Peak	Digi-mark incorrect during Test No. 1
3, 4, and 5	Sinusoidal Sweep: 200 to 5 Hz at 1 octave/min 200 to 5 Hz	The isolator springs at accelerometer locations 1 and 3 were tightened after Tests Nos. 3 and 4. Isolators at accelerometer locations 1 and 6 hit the mechanical stops at approximately 12 Hz.
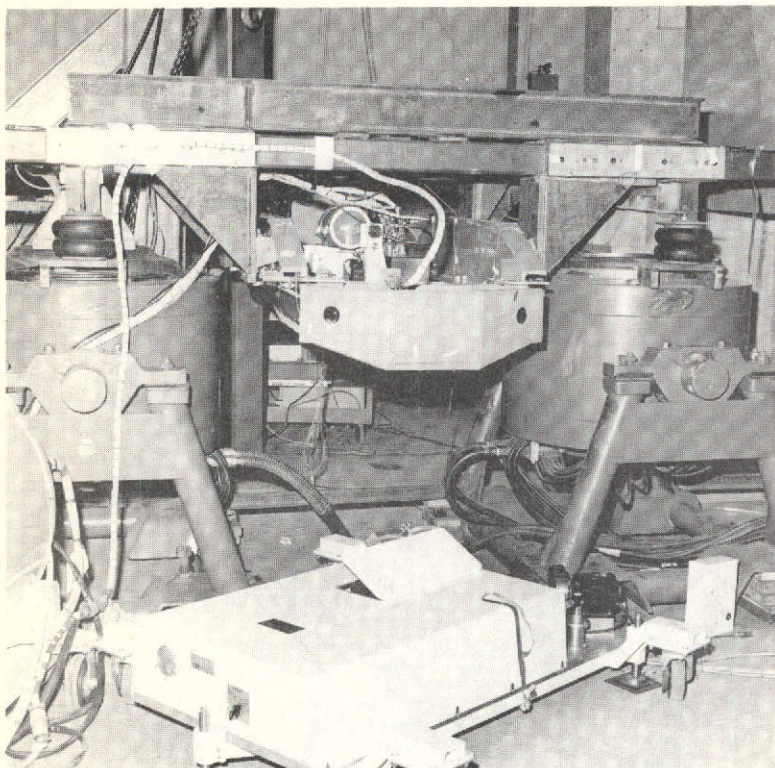
Figure 145. Vibration test setup (Z-axis), from front of experiment platform.
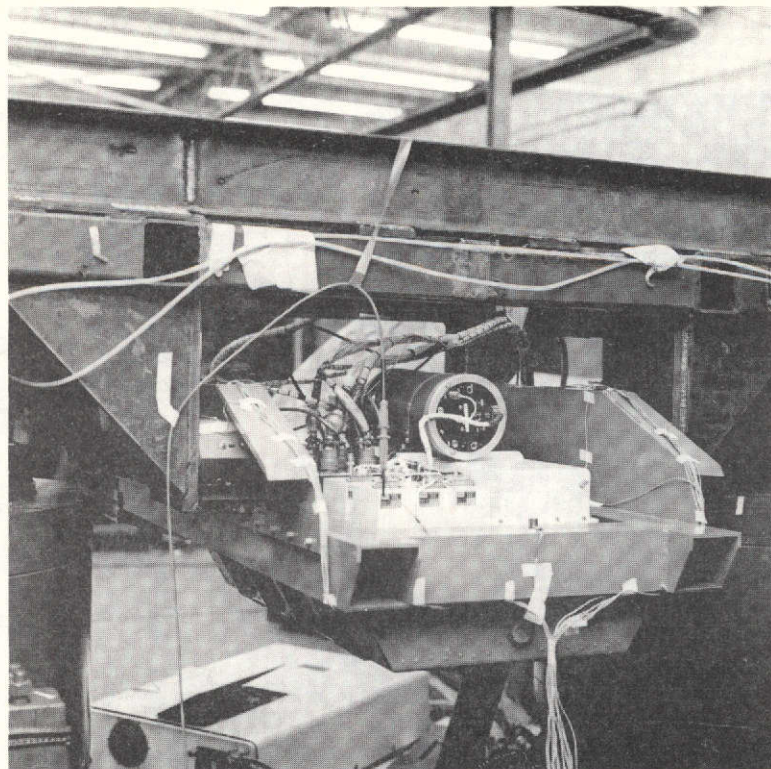
Figure 146. Vibration test setup (Z-axis), from rear of experiment platform.
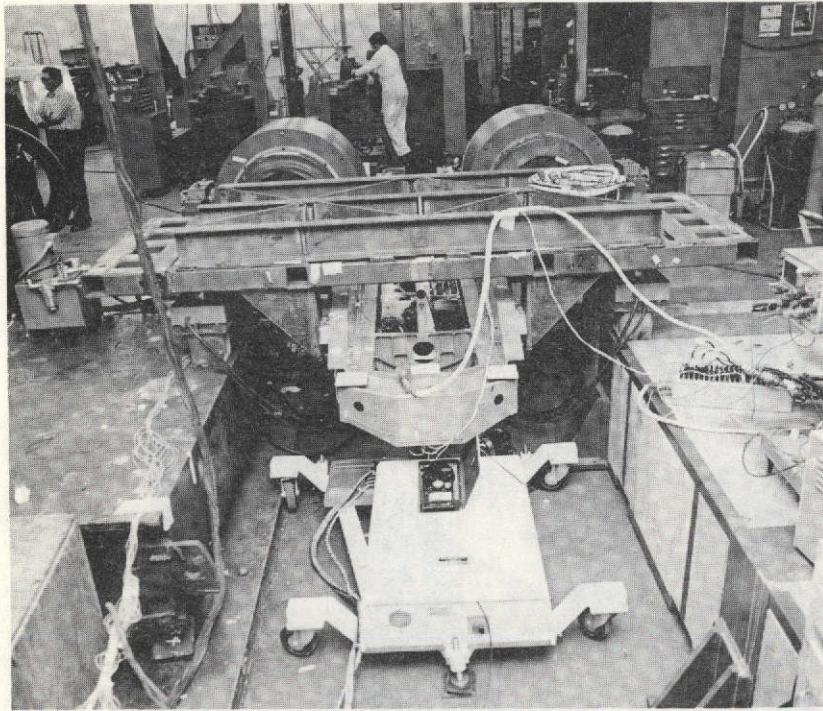
Figure 147. Vibration test setup (Y–axis).
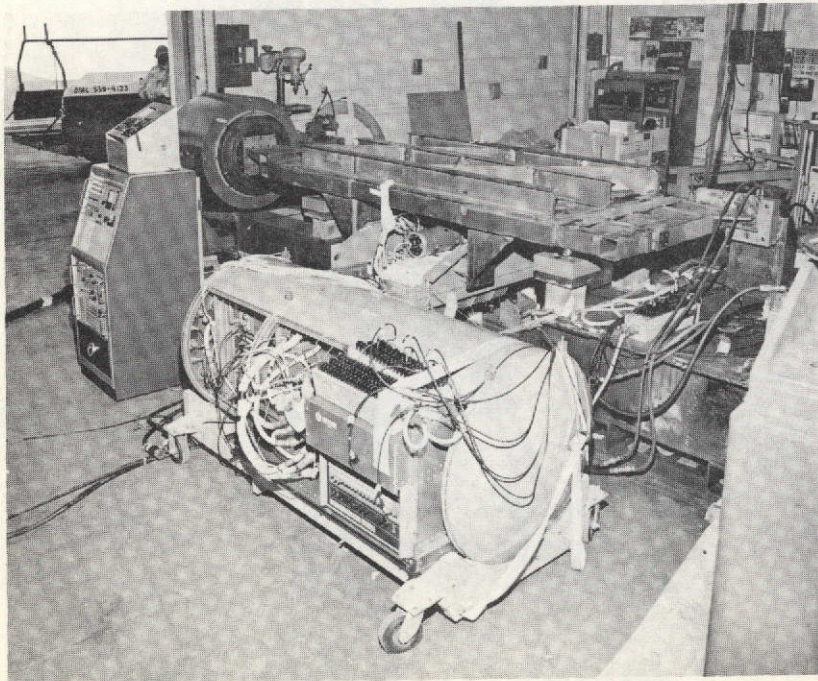
Figure 148. Vibration test setup (X–axis).
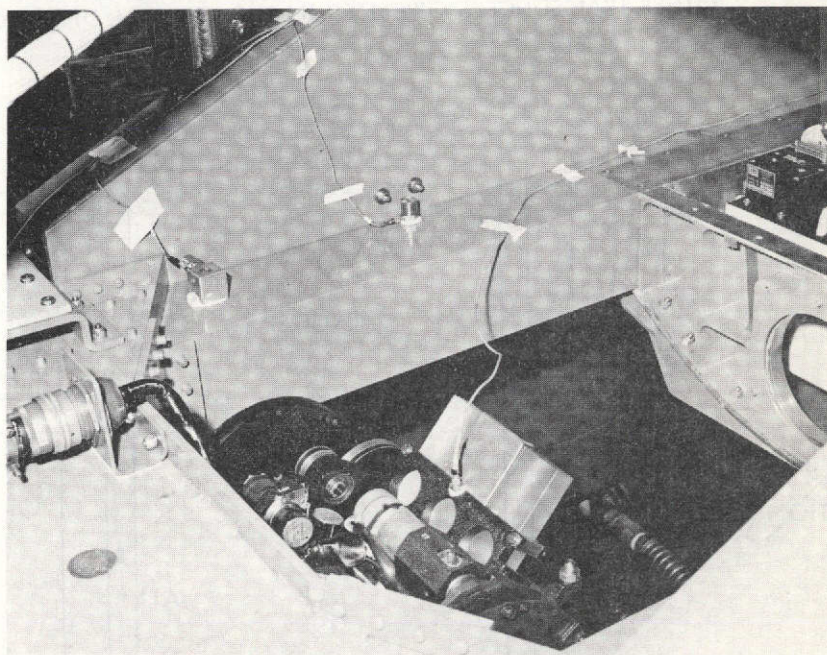
Figure 149. Accelerometer location on gimbal mirror platform.
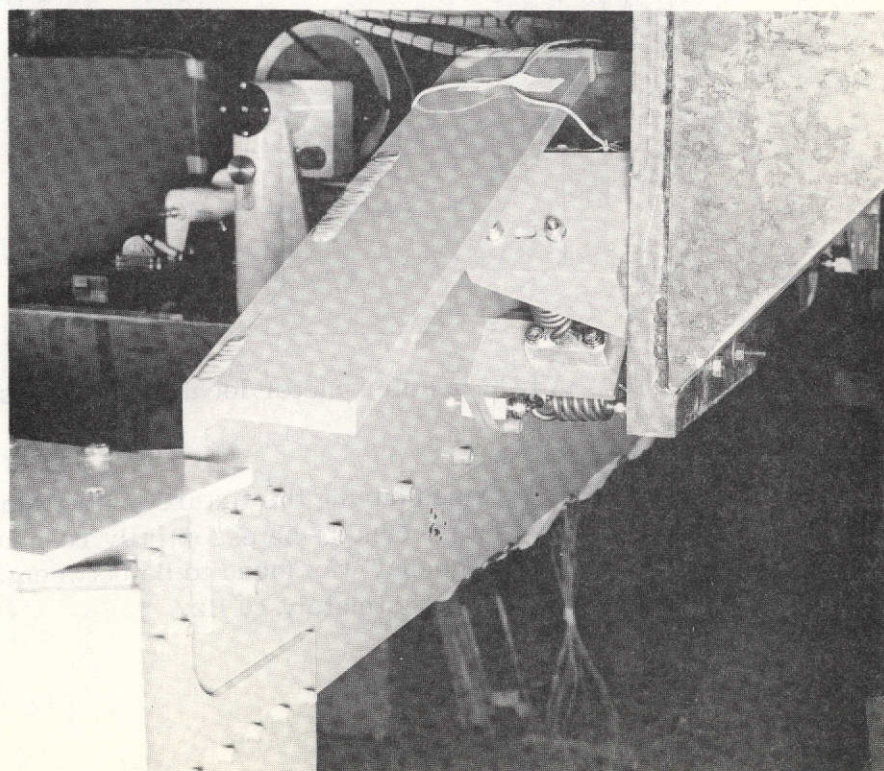
Figure 150. Isolator mount/test fixture interface.
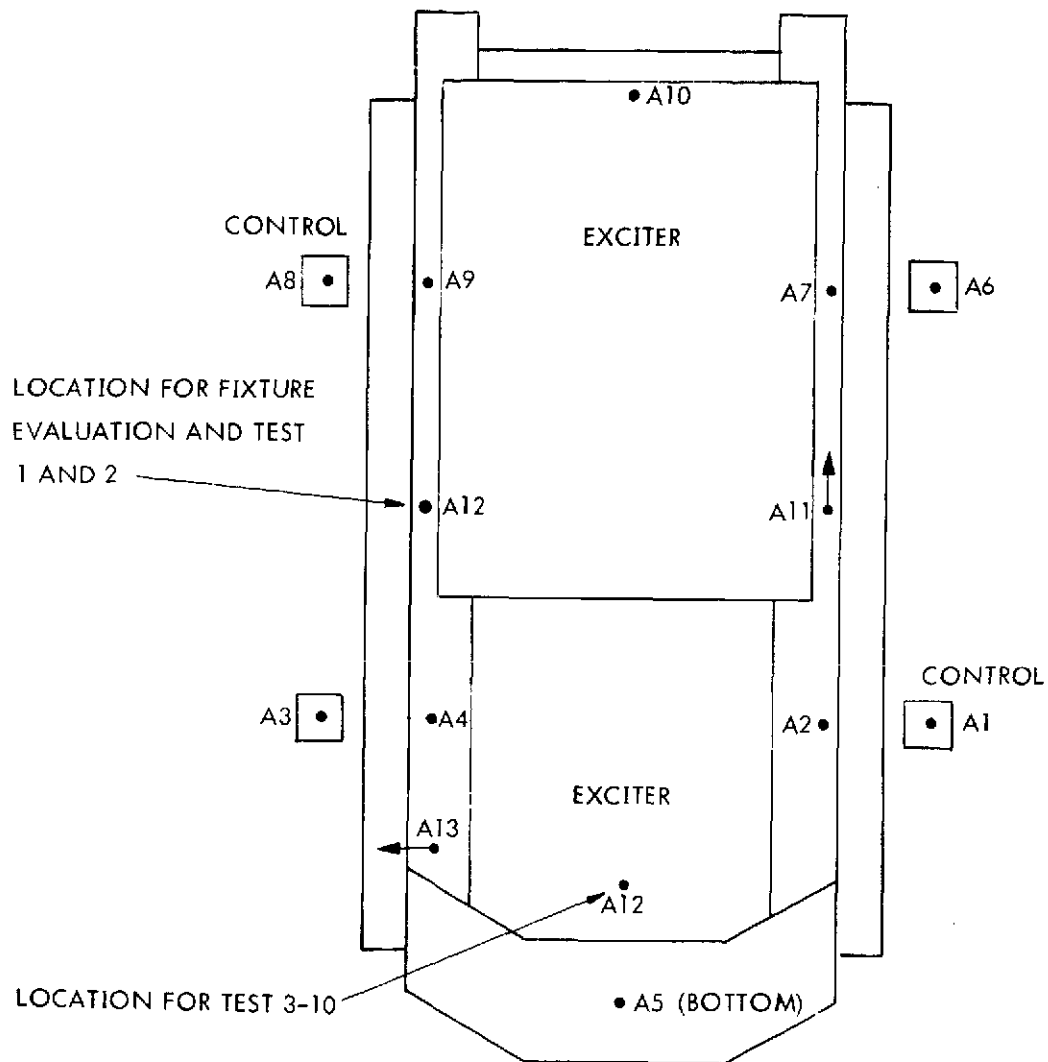
Figure 151. AVLOC accelerometer locations (Z-axis).

The oscillograph data obtained during the fixture evaluation test series were analyzed. The test fixture was found to be essentially resonant free to 200 Hz. The isolator resonant frequency was found to be between 5 and 15 Hz, with peak amplitude occurring at approximately 10 Hz.

The gimbal mirror platform and AOCP were reinstalled in the experiment platform (the platform cover was not installed). The specimen was then subjected to sinusoidal vibration test runs in the vertical (Z) axis. See Figures 145 and 146 for the Z-axis mechanical test setup and Figure 151 for the accelerometer location and orientation. The parameters of Tests Nos. 1 through 6 are given in Table 31.

The experiment platform cover was installed and the specimen subjected to sinusoidal and random vibration tests in the Z-axis. The parameters of Tests Nos. 7 through 10 are given in Table 32.

The isolator resonance was found to be between 5 and 15 Hz, with peak amplitudes occurring between 10 and 12 Hz. A pitching motion about the longitudinal axis occurred at 7 Hz but had no noticeable effect on system performance. The system remained in the fine track mode during all sinusoidal sweep tests.

At the conclusion of Test No. 10, the test setup was disassembled and oriented for testing in the longitudinal (Y) axis as shown in Figure 147. The specimen was subjected to sinusoidal and random vibration test runs in this axis. The parameters for Tests Nos. 11 through 15 are given in Table 33. Refer to Figure 152 for accelerometer location and orientation.

The isolator resonance was found to be between 5 and 15 Hz with peak amplitudes occurring at approximately 9 Hz. A pitching motion about the longitudinal axis occurred at 7 Hz but had no noticeable effect on system performance. The system remained in the fine track mode during all sinusoidal sweep tests up to and including 0.1 g peak input.

At the conclusion of Test No. 15, the test setup was disassembled and oriented for testing in the lateral (X) axis as shown in Figure 148. The specimen was subjected to sinusoidal and random vibration test runs in this axis. The parameters for Tests Nos. 16 through 19 are given in Table 34. Refer to Figure 153 for the accelerometer location and orientation.

The isolator resonance was found to be between 5 and 15 Hz, with peak amplitudes occurring at approximately 9 Hz. A pitching motion about the longitudinal axis occurred at 7 Hz but had no noticeable effect on system performance. The system remained in the fine track mode during all sinusodial sweep tests.

TABLE 31. PARAMETERS FOR TESTS NOS. 1 THROUGH 6

Test No.	Test Level	Remarks
1	200 to 5 Hz at 1 octave/min 200 to 5 Hz at 1 octave/min	
2	200 to 5 Hz 0.1-g Peak	
3 and 4	Sinusoidal Sweep: 200 to 5 Hz at 1 octave/min 200 to 5 Hz 0.05-g Peak	Accelerometer No. 12 was moved from the platform frame to the gimbal mirror platform as shown in Figure 149. Incorrect readout on digi-mark during Test No. 3. Selected accelerometer channels and eight channels of specimen operational data were recorded on oscillograph.
5	Sinusoidal Sweep: 200 to 5 Hz at 1 octave/min 200 to 5 Hz 0.1-g Peak	Oscillograph ran out of paper at 10 Hz. Test repeated from 20 to 5 Hz and recorded on oscillograph only. Beam steerers were switched on and off a number of times between. 15 - 5 Hz. The system re-acquired the beam in each instance. The AVLOC control system was also turning on and off between 15 - 5 Hz and the system was able to re-acquire the beam.
6	Sinusoidal Sweep: 200 to 5 Hz at 1 octave/min 200 to 5 Hz 0.2-g Peak	To preclude possible damage to the AVLOC system, a 0.2-g peak was established as the maximum level to which the system would be subjected.

TABLE 32. PARAMETERS FOR TESTS NOS. 7 THROUGH 10

Test No.	Test Level	Remarks
7	Sinusoidal Sweep: 200 to 5 Hz at 1 octave/min 200 to 5 Hz 0.05-g Peak	Accelerometer No. 2 moved to the top of the airborne platform cover. The video channel was inoperative during test.
8	Sinusoidal Sweep: 200 to 5 Hz at 1 octave/min	The video channel was inoperative during test.
9	Random Vibration: 20 to 1 kHz at 2 dB down from 1 g rms (flat spectrum)	Intermittent loss of fine track during test.
10	Random Vibration: 20 to 1 kHz at 9.5 dB down from 1 g rms (flat specturm)	Intermittent loss of fine track during test.

Comments on Test Results

The specimen was visually inspected upon completion of the vibration tests, with no damage or degradation noted. Peak g versus frequency plots of the accelerometer data acquired during the sinusoidal vibration tests, power spectral density plots of the accelerometer data acquired during the random vibration tests, and transmissibility plots of the isolator system for each high-level sinusoidal test in each axis are included in Reference 18.

CANISTER

The REC was vibration-tested in the MSFC environmental test facility. The test setup is illustrated in Figures 154 and 155. The accelerometer locations are shown in Figure 156. Both sine wave and random inputs were run in the X and Y axes. The vibration test data obtained were routine and are not included in this report; they are available for inspection upon request. At the conclusion of the canister vibration tests, full operation revealed no malfunctions of either the components or subsystems.

TABLE 33. PARAMETERS FOR TESTS NOS. 11 THROUGH 15

Test No.	Test Level	Remarks
11 and 12	Sinusoidal Sweep: 200 to 5 Hz at 1 octave/min 200 to 5 Hz 0.05-g Peak	The exciters were 180 deg out of phase during Test No. 11.
13	Sinusoidal Sweep: 200 to 5 Hz at 1 octave/min 200 to 5 Hz 0.1-g Peak	
14	Sinusoidal Sweep: 200 to 5 Hz 0.2-g Peak	Package hit mechanical stops at 10 Hz. Test was aborted at 9 Hz because system was unable to track properly.
15	Random Vibration 20 to 1 kHz (variable bandwidth and level) Bandwidth (Hz) 20 — 1 kHz -6.5 db (tracked properly) 20 — 1 kHz -5.5 dB (intermittent loss of track) 70 — 500 Hz -5.5 dB (tracked properly) 20 — 500 Hz -5.5 dB (tracked properly) 20 — 500 Hz -4.5 dB (intermittent loss of track) 20 — 300 Hz Full level (0.73 g rms) (tracked) properly)	

TABLE 34. PARAMETERS FOR TESTS NOS. 16 THROUGH 19

Test No.	Test Level	Remarks
16	Sinusoidal Sweep: 200 to 5 Hz at 1 octave/min 200 to 5 Hz 0.05-g Peak	Isolators intermittently hit mechanical stops between 9 and 10 Hz.
17	Sinusoidal Sweep: 200 to 5 Hz at 1 ocatve/min 200 to 5 Hz 0.1-g Peak	Isolators hit mechanical stops between 9 and 10 Hz.
18	Sinusoidal Sweep: 200 to 5 Hz at 1 octave/min 200 to 5 Hz 0.2-g Peak	Isolators firmly bottomed out against the mechanical stops at 9 Hz.
19	Random Vibration: 20 to 1 kHz (varied bandwidth and level) Bandwidth (Hz) 20 — 1 kHz 0.7 (intermittent loss of track) 20 — 1 kHz 0.66 (intermittent loss of track) 20 — 500 Hz 0.86 (intermittent loss of track) 20 — 1 kHz 0.5 (lost track two times within a period of two minutes. The AVLOC control system was turned off and the gimbal mirror moved. The system was turned on and was able to properly reacquire the beam.)	
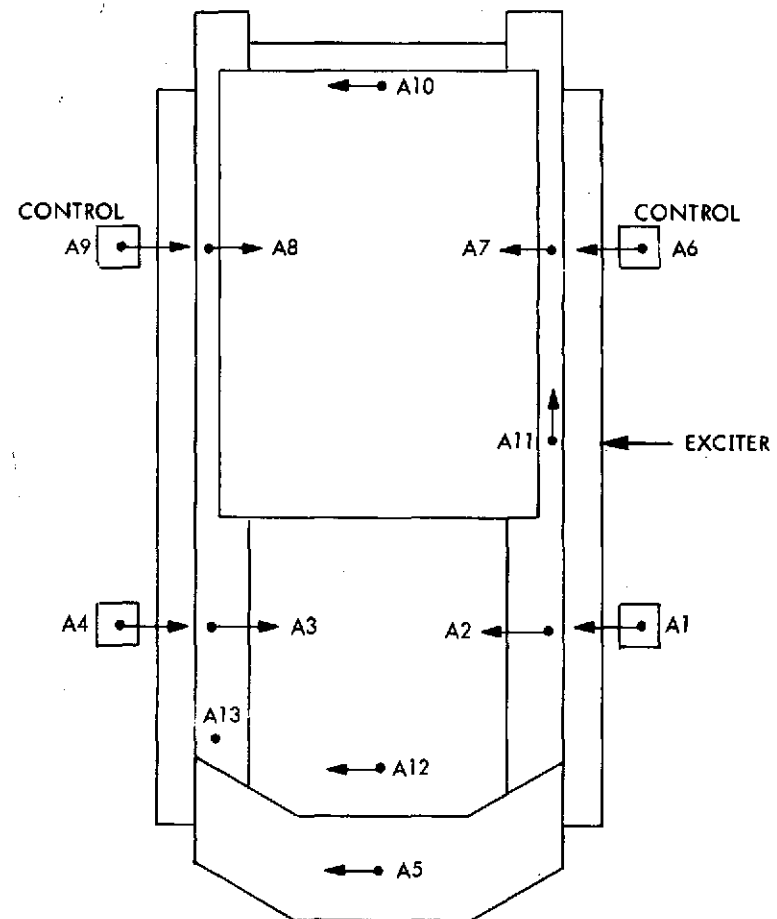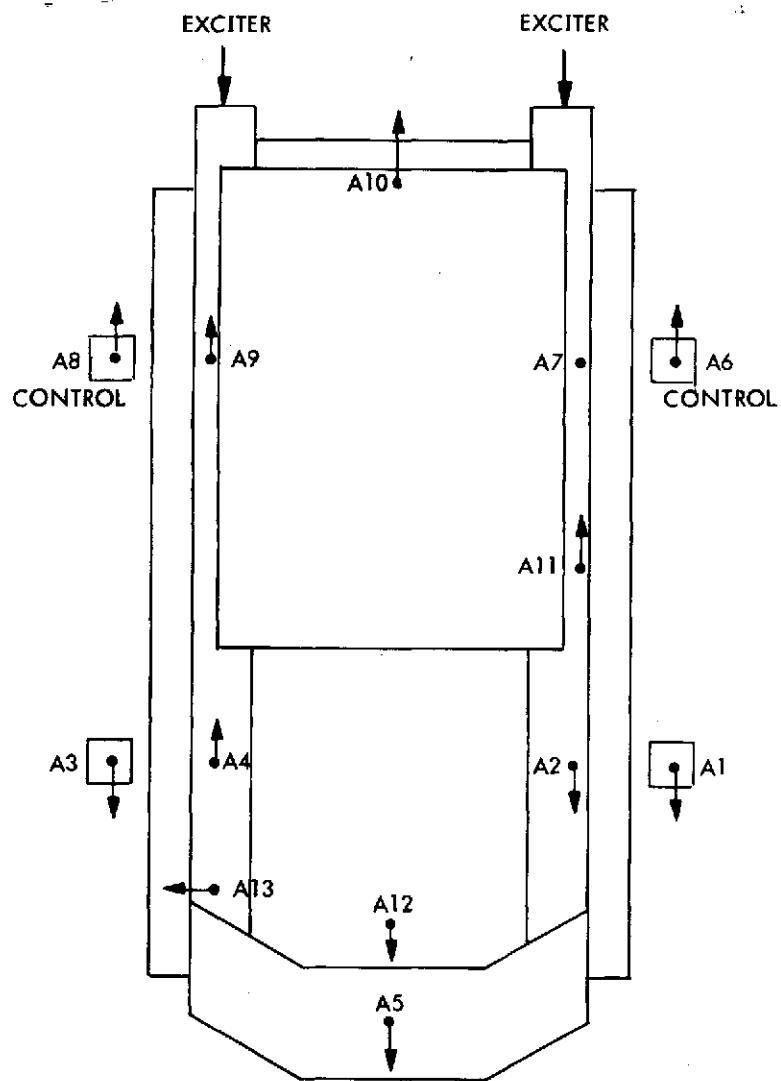
Figure 152. AVLOC accelerometer locations (Y-axis).

Figure 153. AVLOC accelerometer locations (X-axis).
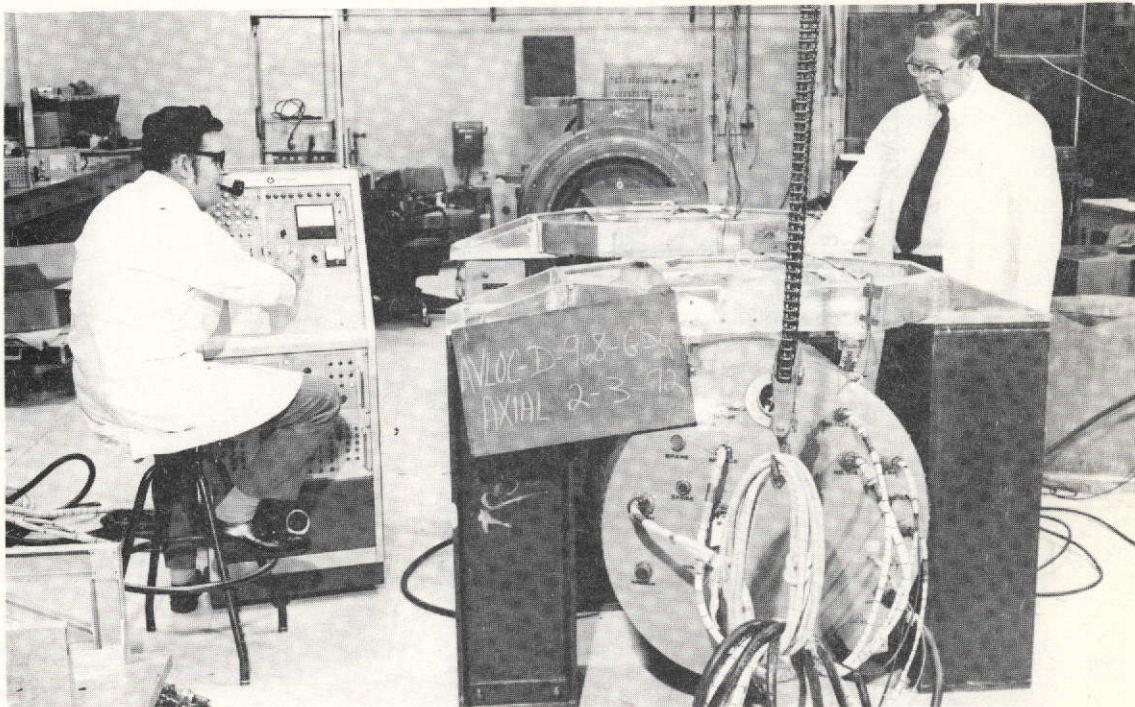
Figure 154.   Vibration test of REC, X-axis.
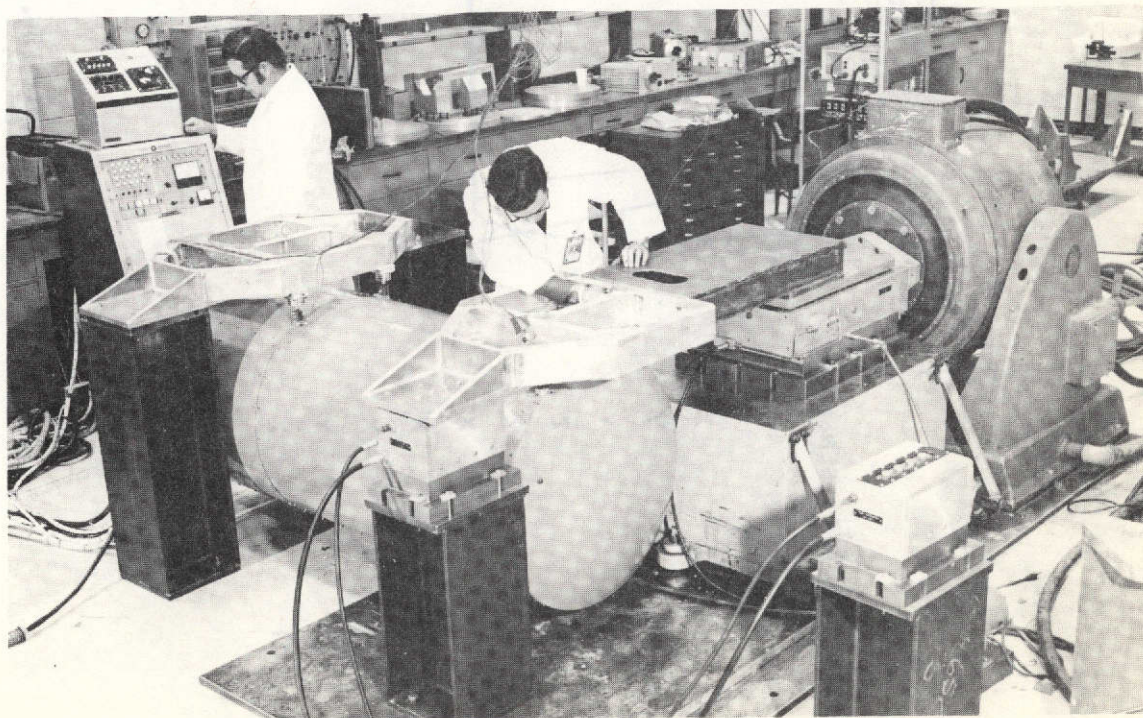
Figure 155.   Vibration test of REC, Y-axis.

ACCELEROMETER NO.	SENSITIVE AXIS
1	X
2	X
3	Y
4	Y
5	Z
6	Z
7	X
8	X
9	X
10	Y
11	Z

CONTROL Y

CONTROL X

CONNECTORS
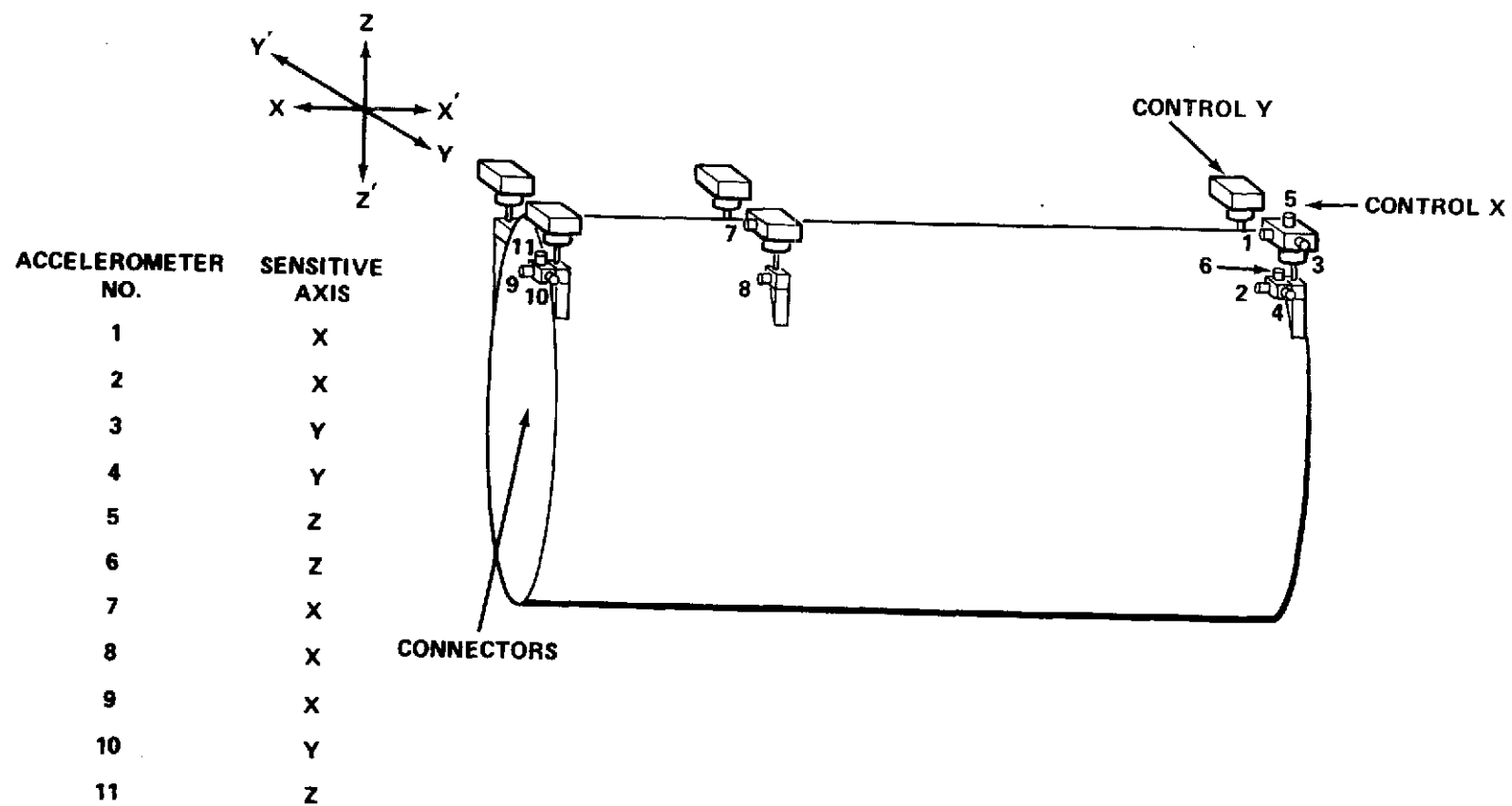
Figure 156. AVLOC REC.

PRESSURE TESTS

Because of safety considerations, it was necessary to proof-test the REC and AOCP enclosure. Test data are given in Table 35. The AOCP enclosure was tested to twice the working pressure and the canister to USAF requirements of 1.5 times the working pressure.

TABLE 35. PRESSURE TEST RESULTS

		AOCP	Canister	Remarks
Dynamic Proof Pressure Test	Design Pressure	13.76×10^4 N/m^2 (20 psi)	13.76×10^4 N/m^2	No structural deformation or failure occurred
	Working Pressure	3.44×10^4 N/m^2 (5 psi)	3.44×10^4 N/m^2	
	Test Pressure	6.88×10^4 N/m^2 (10 psi)	5.17×10^4 N/m^2 (7.5 psi)	
	Test Time	10 min	10 min	
Static Leak Test	Test Pressure	3.44×10^4 N/m^2 (5 psi)	3.44×10^4 N/m^2	O-ring seals required
	Test Time	1 min	1 min	around door mounting bolts

THERMAL/VACUUM

Because the thermal/vacuum environment that the AVLOC airborne equipment would be exposed to in the WB-57F aircraft was expected to be very mild [the AVLOC environmental control system was designed to maintain a minimum pressure of 4.03×10^4 N/m^2 (5.85 psia) and a temperature of 24°C ± 9° (75° F ± 15° F)], no thermal/vacuum tests were originally conducted. However, after being plagued by continuing failure to successfully track during the earlier flights, it was decided that the AOCP should undergo thermal/vacuum testing.

The AOCP was placed in a vacuum chamber containing an optical window so that the AOCP could track on the GCE argon laser during the tests. These tests uncovered two major problems: scintillation monitor breakdown and power monitor breakdown.

SCINTILLATION MONITOR BREAKDOWN PROBLEM

With the AOCP optically linked with the GCE and the ID tracker error, E_Y, E_Z, being monitored, the chamber pressure was slowly decreased. At approximately 6.88×10^4 N/m^2 (10 psi), large spikes began to appear on the recorded E_Y, E_Z signals (Fig. 157). This indicated severe tracking performance degradation, confirmed by simultaneous monitoring of the cruciform track scan on an oscilloscope. These spikes were caused by a high-voltage breakdown of the scintillation monitor PMT. The PMT is physically close to the ID tracker, and the voltage breakdown of the PMT caused conducted electromagnetic interference in the ID tracker, appearing as the tracker spikes just mentioned.

Another symptom of this voltage breakdown problem was that the scintillation monitor signal level (indicative of received argon laser power) rapidly decreased to zero. These symptoms were very similar to Flight No. 8 telemetry data.

This high-voltage breakdown problem was fixed by rewrapping the PMT with Mylar insulation. The associated 1500-V power supply was replaced because of possible internal damage.

POWER MONITOR BREAKDOWN PROBLEM

After the fix was made on the scintillation monitor problem, a similar high-voltage breakdown problem associated with the power monitor PMT was discovered at 2.41×10^4 N/m^2 (3.5 psi). Again, the ID tracker performance, due to RFI coupling, was severly degraded. This problem was solved by rewrapping the power monitor PMT with Mylar insulation also. The associated 1000-V power supply was replaced because of possible internal damage.

Some additonal observations from the thermal/vacuum tests are that (1) using the GCE, the boresight of the AOCP transmit/receive channels was checked and found to be unaffected and (2) the He-Ne laser output power was monitored and found to be unaffected.

288
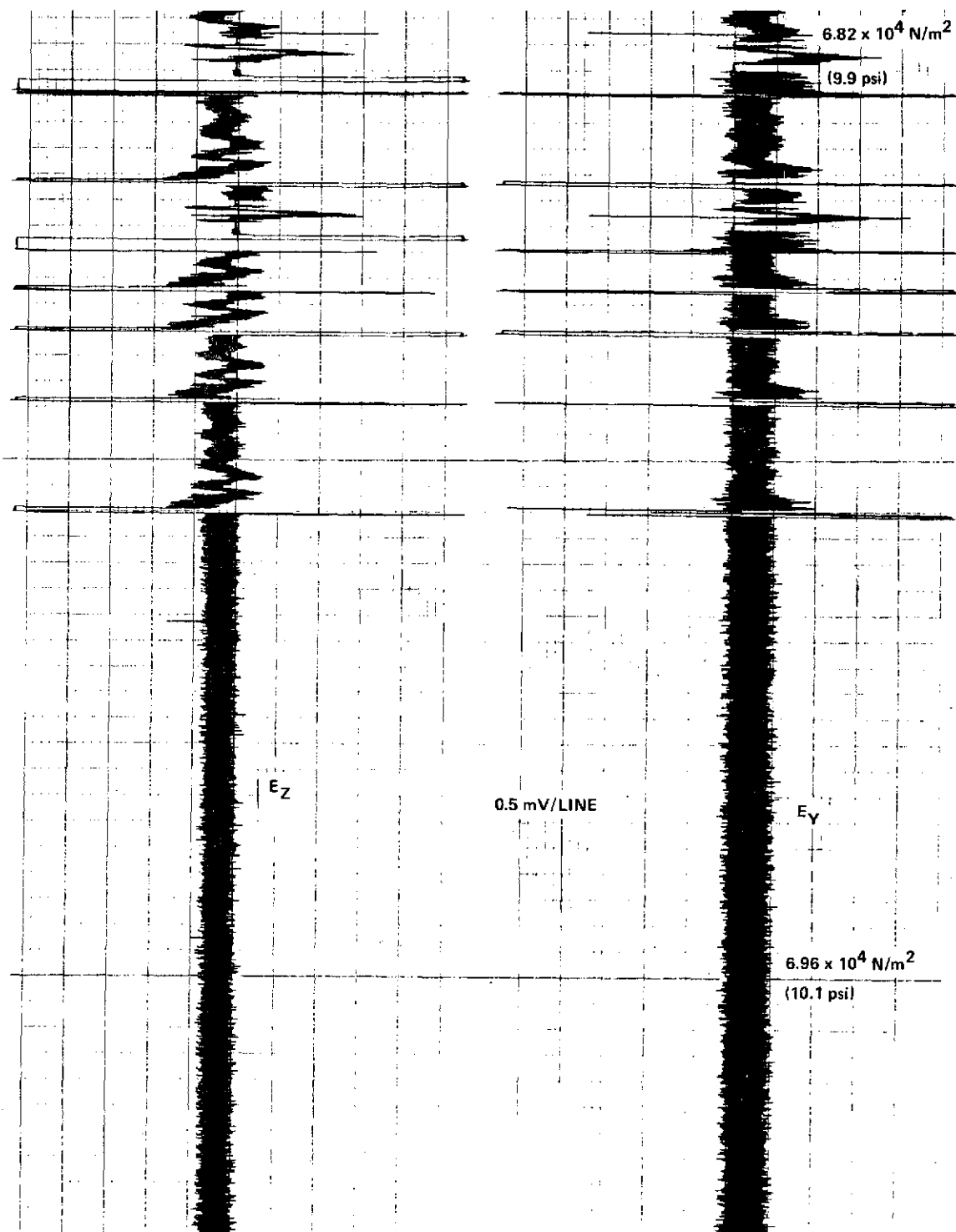
Figure 157. Tracker error signals, reduced pressure.

Static and Dynamic Tracking

FIELD TESTS

Following delivery of the airborne experiment hardware and associated checkout equipment to MSFC, extensive testing was performed on the integrated AVLOC system, i.e., tests involving linkup of the airborne system with the ground station. These tests were called Field Tests. The MSFC Field Test range, illustrated in Figure 158, was between the Astronics Laboratory (Bldg. 4487) and the Madkin Mountain tracking station.
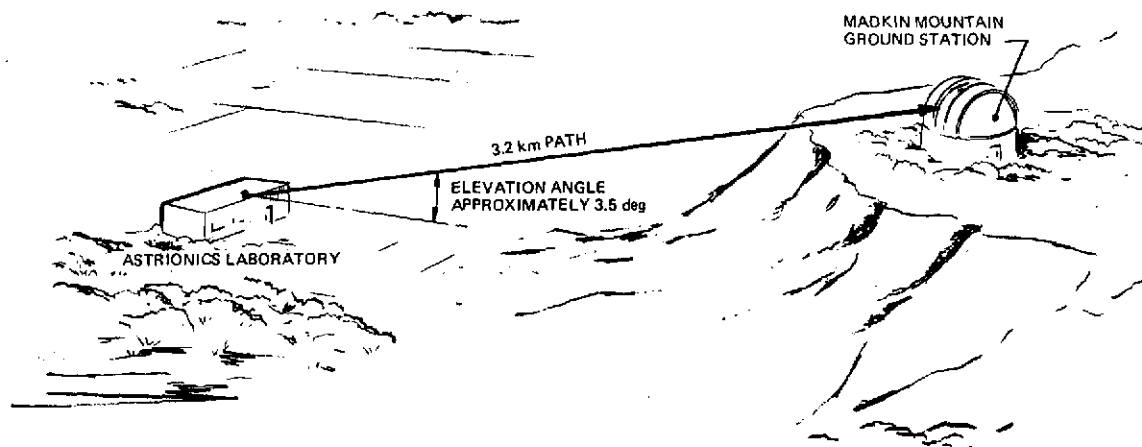
Figure 158. NASA/MSFC Field Test range.

With proper setup and orientation of the equipment, complete tests could be conducted, including coarse and fine tracking at each terminal plus communications systems checkout. The full sequence for an all-systems test was as follows. Coarse acquisition was conducted at the tracking station by the GBAA (by acquiring and tracking a retroreflector placed near the AOCP); this provided illumination of the AOCP by the beacon laser and subsequent coarse acquisition via the gimballed mirror and TV tracker. This, in turn, allowed fine tracking by the AOCP on the beacon laser and, finally, fine tracking at the ground station of the He-Ne laser from the AOCP. After the tracking loop was closed, commands were transmitted on the uplink, and the various communications modes were checked out on the downlink.

During the Field Tests, which lasted several weeks, many latent problems were discovered and resolved and many improvements made. The Field Test phase is indispensable to a program of this kind. In the following paragraphs the more significant problems encountered will be discussed.

One of the first problems discovered was failure of the ID tracker in the AOCP to properly track the beacon laser in the scintillation environment. Apparent angular modulation was experienced, which was excessive in both amplitude and frequency, making it virtually impossible to close the beam-steerer loop. This apparent angular modulation was traced to amplitude scintillation in the atmosphere causing dynamic phase changes in the ID tracker video amplifier.

Two separate problems existing in the ID tracker contributed to the tracking difficulties experienced in the initial tests. They were (1) excessive phase shift in the video signal over the input signal dynamic range, and (2) inadequate AGC bandwidth. Field modifications were performed to obtain a functional tracking system.

The phase shift problem existing in the video amplifier was a result of the gain controlling device working against the reactances of the ID PMT and the input to the 10.7-MHz communication amplifier, which is paralled across the tube at this point. The resulting phase shift over the input dynamic range was in excess of 70 deg. The design modification isolated the tube output reactance from the gain control device. This isolation amplifier converted the current output from the ID tube to a voltage. The gain controlling device (field effect transistor) was then allowed to operate against a resistive source as a voltage-controlled attenuator. The resulting phase shift over the dynamic range was less than 2.5 deg. Phase data taken with an oscilloscope are difficult to determine accurately to small phase angles.

The AGC bandwidth was approximately 10 Hz, which is below the normal frequency range of amplitude scintillation. The video amplifier low-frequency cutoff was approximately 100 Hz and limited the effective AGC bandwidth that could be incorporated. By adding additional low-frequency breaks in the video amplifier, the low-frequency cutoff was moved to 1.5 kHz. The AGC control circuit was redesigned and the AGC bandwidth increased to 120 Hz. The above modifications resulted in redesign of the video amplifier input stages, gain controlling circuits, and AGC amplifier. Further improvements and redesign are discussed in the Engineering Evaluation section of this report.

Figure 159 summarizes the performance of the AGC amplifier before and after modification. The AGC bandwidth was increased and the video bandwidth was narrowed to avoid overlap and control system instabilities. Some samples of the pointing performance are shown in Figures 160 through 162, which are strip-chart recordings of the tracker outputs. Each of these data shows a region in time during which the beam steerers were turned off. When the beam steerers were off, the tracker outputs, E_Y and E_Z, indicated the amount of angular fluctuation of the arriving beacon laser. The angular fluctuations observed were partly due to atmospheric steering and partly to system vibration (AOCP mount, gimballed mirror, etc.). The beam steerers were then manually turned on, and the input fluctuations were steered out, as indicated by the lower amplitude portions of the tracings in Figures 160 through 162. The closed-loop pointing precision at this time can be seen to be between 6.8 and 8.7 μrad peak to peak in the presence of severe turbulence, which corresponds to an rms accuracy of slightly over 1 μrad.

Figure 163 shows a correlation of the received power fluctuations (lower trace), as determined from the linear baseband scintillation monitor output, and the closed-loop pointing accuracy of the AOCP in the upper trace.

Several problems were encountered during Field Tests of the GBAA. One problem was associated with the initial configuration whereby the receiver and beam-steering assemblies were mounted on opposite sides of the laser. This resulted in rather weak signal returns as a result of the offset; therefore, to increase sensitivity, the receiver was relocated to the same side as the beam deflector assembly.

Another GBAA problem was beam-pointing instability as a function of the telescope orientation (the GBAA was hard mounted to the telescope). A single "U"-shaped channel main frame was originally used as the main packaging platform. The receiver and beam-steering assemblies were cantilever-mounted to the side of the channel main frame. To eliminate beam motion due to mechanical instability, the test bed main frame was reinforced with a box-type structure undergirding the entire U-frame channel. Additional supporting brackets were added to rigidify the transmitter input and output optics and the receiver sensor assembly. A brief description of the structural modifications is given in the following paragraphs.

The design approach was based on the fact that several units — laser, beam steerer, and receiver — were to be mounted individually on a mount system of sufficient rigidity to maintain inter-unit alignment in spite of overall system orientation throughout the tracking sequence.
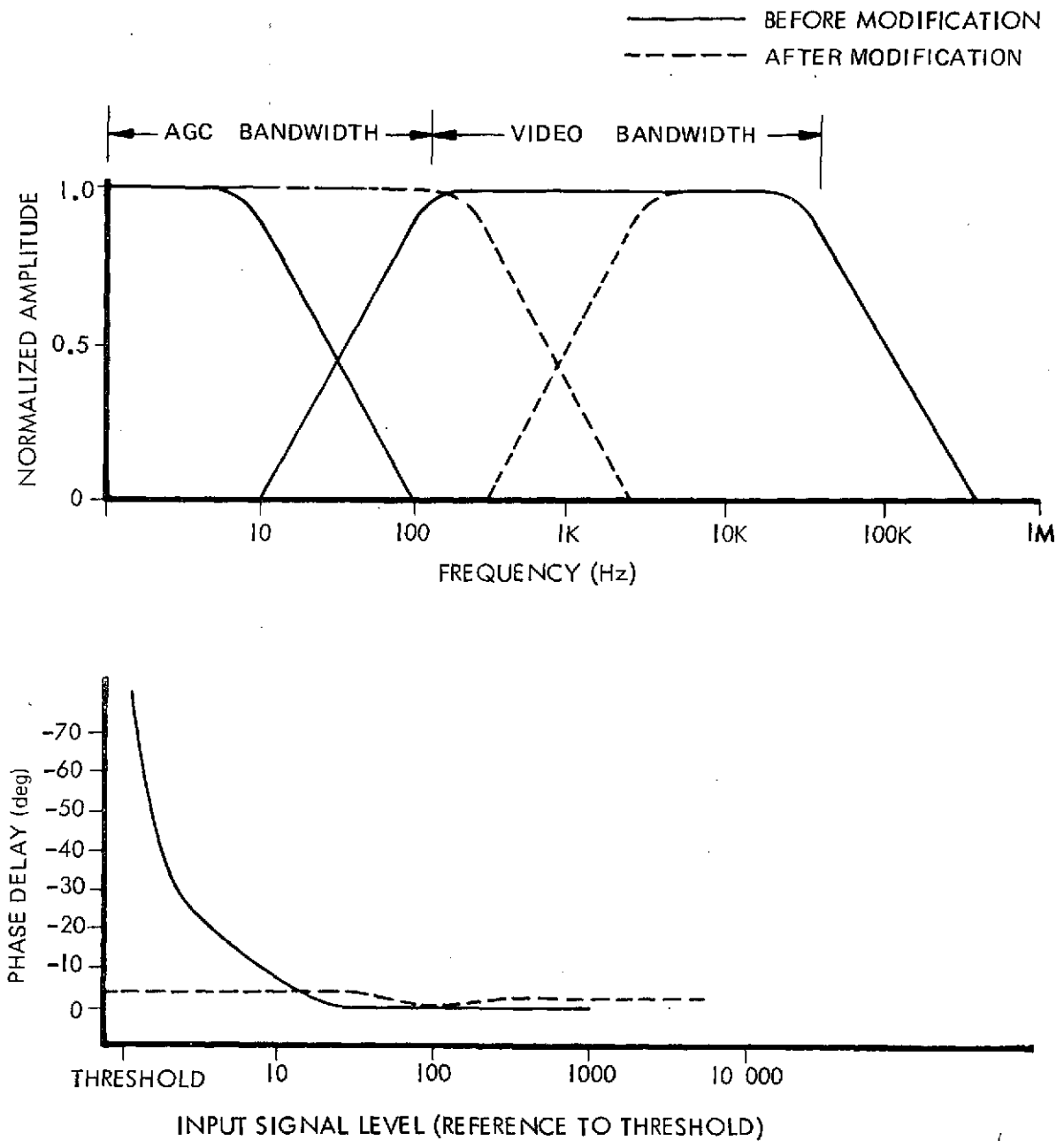
Figure 159. Tracker AGC amplifier characteristics.

Consequently, the structural mechanical mount was configured to provide rigidity with overall system deflections in the area of 0.00045 to 0.0025 cm maximum when inverting or reorientating the system in a worst-case condition.

This was accomplished with a base mount constructed as follows. The basic structure is a 22.9-cm by 15.2-cm deep by 134.6-cm long box beam containing the basic telescope mount hole pattern. The box beam is built of 0.635-cm and 0.95-cm plates with 0.635-cm shear panels as required with the top and bottom plates (0.95 cm) machined for flatness and parallelism. A second structural member, a 22.9-cm by 134.6-cm long channel machined flat, is attached to the box beam and contains the appropriate attach bracketry for mounting and alignment of the laser unit. This channel is fastened to the box beam in such a manner as to obtain an overall box beam — channel composite structure. Next, two angle bracket structural units are intertied to the box beam — channel assembly at required locations to provide the necessary beam-steerer and receiver mount surfaces. Interrelated alignment set screws and bracket-saddle-strapping are provided to stabilize the beam-steerer telescopic tube structure and the receiver container for required alignment and overall unit stiffness.

The overall structural mechanical assembly is relatively simple in concept but is of sufficient size structurally and configured mechanically to achieve the required mounting configuration and overall laser optical alignments.

In addition to the preceding instabilities, it was also discovered that a major contributing factor to the GBAA beam-pointing instability was a loose lens in the beam-steerer assembly collimating optics. This problem was easily corrected after being traced to its cause.

During routine Field Tests of the GBAA, the transmitted beam divergence was discovered to be 5.6 mrad; it was readjusted to the desired 3.8 mrad.

A major objective of the Field Tests was to perform closed-loop tracking between the ground station and the flight hardware in the configuration depicted in Figure 158. The primary problems encountered here were the buildup of an oscillation in the ground station telescope after "handover" from coarse to fine track; this was traced to a software problem in the SCC-4700 computer routine. A software problem was also found at the other end of the loop in the "gimbal mirror fine track mode". After these problems were corrected, the entire acquisition and tracking loop was successfully closed at both ends.
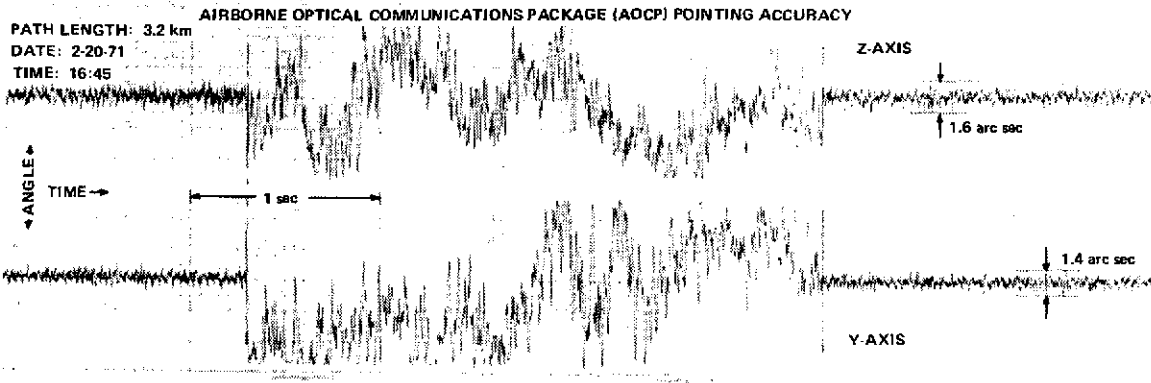
Figure 160. ID tracker pointing performance.
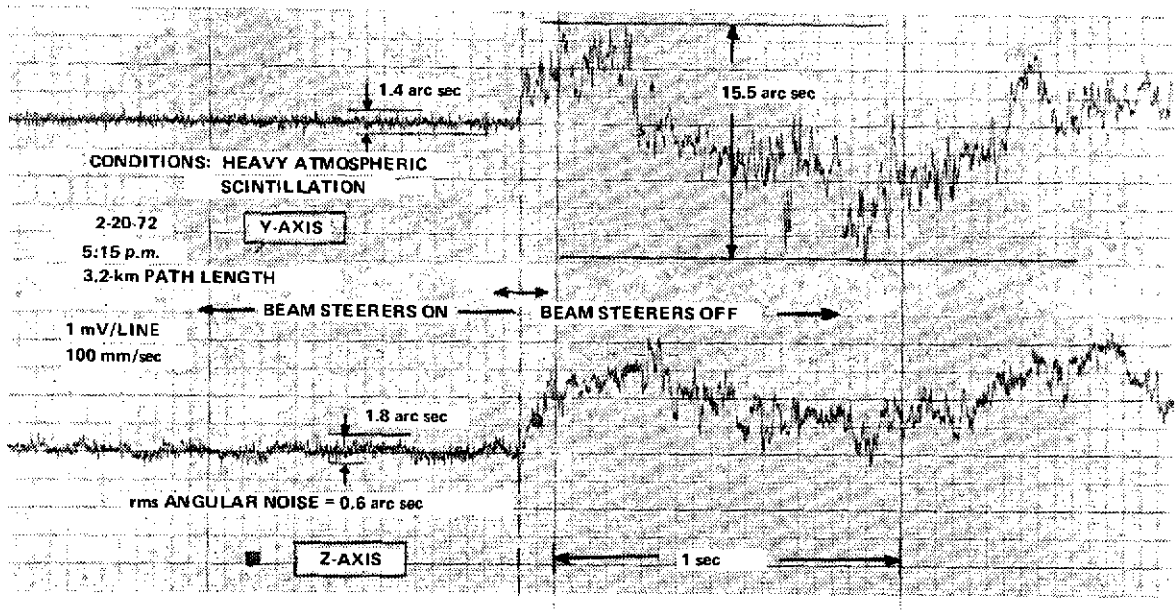
Figure 161. Data sample A, AOCP Field Test tracking and pointing.

A number of relatively minor problems were encountered in the field testing of the communications channels. These typically involved, for example, the proper selection of polarity on the PN generator in order for the ground station bit error detector to function proberly. One minor problem experienced during the Field Tests turned out to be a major difficulty during Flight Tests — this involved proper adjustment of the laser-modulator train, and, particularly, instability of the modulation over an extended period of time. This problem is discussed in detail elsewhere in this report.
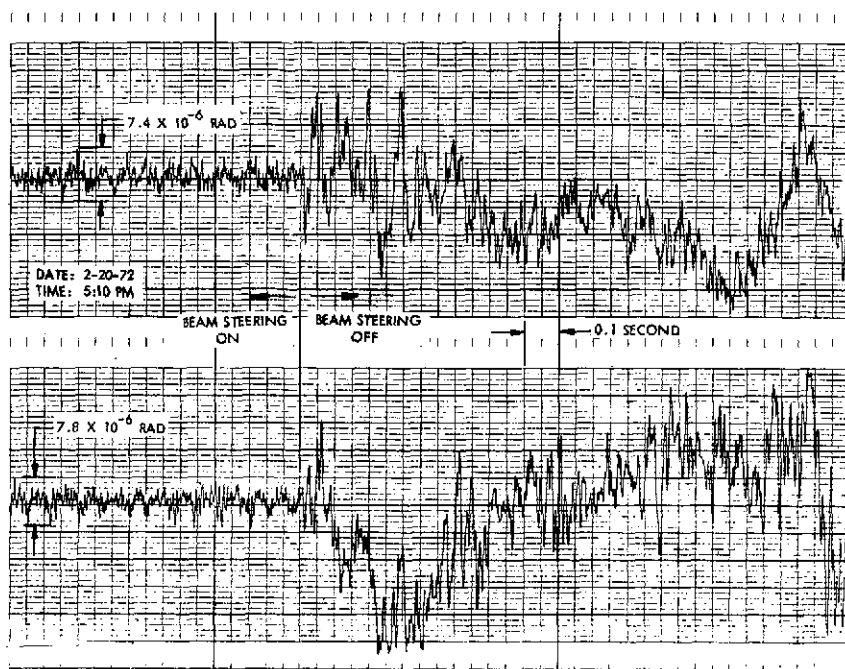
Figure 162. Data Sample B AOCP Field Test tracking and pointing.
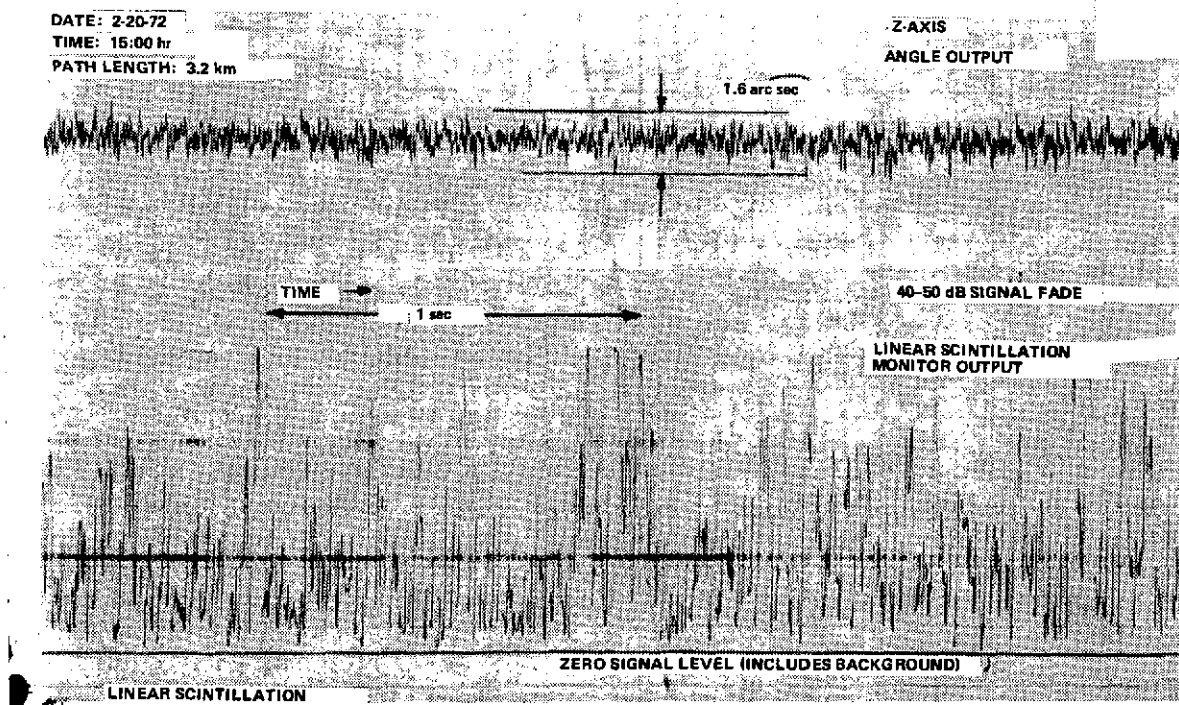
Figure 163. Field Test data sample showing scintillation monitor output
and pointing accuracy.

One of the last experiments to be performed in the Field Test phase was the acquisition and tracking of the beacon laser by the flight package under simulated aircraft range conditions. The beacon laser power was decreased to a level corresponding to the R^2 attenuation for a nominal range of 22.9 km (75 000 ft). At the same time, the beacon laser divergence control was set for maximum beam divergence. Under these simulated range conditions, the flight package did acquire and track the beacon laser successfully, including both the coarse and fine track systems. It was apparent, however, that the trackers were operating in a marginal fashion because of the resulting low power density ($\sim 10^{-10}$ W/cm^2).

After this final simulated flight test was completed, the airborne equipment was packed and shipped to Kirkland Air Force Base, Alburquerque, New Mexico, for installation into the WB-57F aircraft.

HELICOPTER TESTS

As a separate phase of the Field Tests, a number of helicopter test flights were conducted to dynamically test the GBAA — telescope control system (or coarse tracking system) and the QMP — telescope control system (or fine tracking system), as well as the "handover" from coarse to fine control.

The procedure for conducting these flights was simple but effective. A passenger riding in the helicopter would hold a retroreflector, keeping it coarsely pointed at the tracking station. Meanwhile, the telescope was manually slewed to establish the GBAA Fence scan forward of the helicopter's approach. In this way, acquisition and tracking by the GBAA system were easily established, allowing determination of the system's dynamic characteristics as well as checkout of the GBAA — telescope drive hardware and software.

Likewise, by means of a He-Ne laser boresighted to the 61-cm telescope, (632.8-nm) radiation could be retroreflected from the same retroreflector, allowing acquisition and tracking by the QMP fine tracker and checkout of the QMP — telescope drive hardware and software. Incidental to these tests was the full exercising of these pertinent subsystems. In summary, the helicopter tests were extremely beneficial, and helicopter checkout flights were often conducted on an impromtu basis as a part of the preflight aircraft test routine.

System Calibration

This section describes the calibration procedures for the various AOCP subsystems and presents calibration data acquired before shipment of the system hardware.

MODULATION INDEX

Modulation index measurements were made using the PN input to the modulator driver. The modulation sensor in the GCE provided an output (dc coupled) to an oscilloscope from which the peak and minimum of the detected modulation waveform could be measured. The modulation index was maximized by adjustment of the modulation transfer characteristic operating point using the Soleil–Babinet compensator as described earlier in the Modulator section of this report. The modulation index can be varied over a range from zero to 75 percent. The voltage transfer characteristics for the modulator are also given in the Modulator section of this report.

The AOCP modulation index can be readily and conveniently measured using the GCE and is a routine preflight procedure.

TRANSMITTED BEAM DIVERGENCE

The transmitted beam divergence was measured by projecting the beam onto a scene at a long distance and determining the beam cross-section diameter. Figure 164 illustrates the experimental setup. The beam diameter is measured at the exit aperture of the afocal telescope and at the screen at a distance of 36.58 m. The beam diameter thus determined corresponds to approximately the $1/e^2$ intensity points. The beam-divergence angle θ is given by

$$\theta \simeq \frac{\overline{B} - \overline{A}}{R} \tag{123}$$
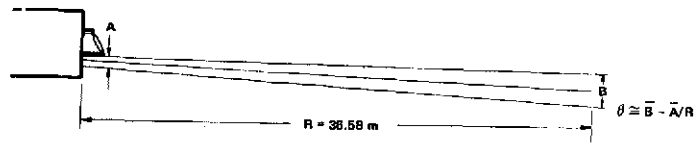
a. Beam-divergence measurement geometry.
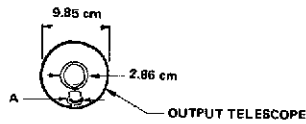
b. Transmitter aperture showing beam position.
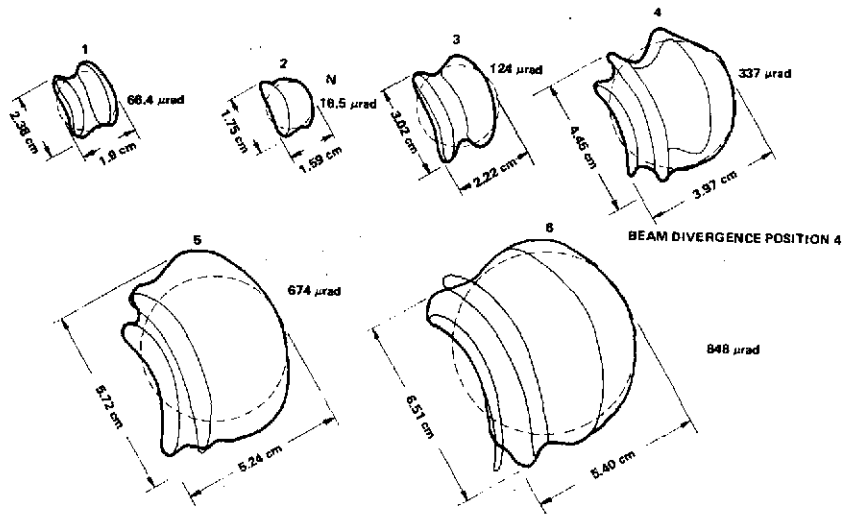
c. Beam-divergence position

Figure 164. Transmitted beam pattern at 36.58 m.

where $\overline{B}$ is the beam cross-section diameter at the scene, $\overline{A}$ is the beam diameter at the exit pupil of the afocal telescope, and R is the distance to the screen. Because of the initial poor quality of the afocal telescope corrector plate, considerable transmitted beam distortion was present, causing fringes to appear in the beam cross section. Figure 164 shows tracings of the beam profile at the screen for the various beam-divergence positions. Estimates of the effective beam diameter were made by averaging many readings taken by several observers. Table 36 summarizes the diameter averages for a given beam-divergence control position and indicates the equivalent beam-divergence angle.

TABLE 36. BEAM-DIVERGENCE CALIBRATION DATA

Stepper Motor Position	$\overline{A}$ Avg. Diameter Transmit Beam (cm)	$\overline{B}$ Avg. Diameter Beam at Distance R (cm)	θ Beamwidth (μ rad)	θ Beamwidth (Arc Sec)
1	1.91	2.16	66.4	13.7
2	1.60	1.65	16.48	3.4
3	2.29	2.74	123.6	25.5
4	3.07	4.32	337	69.5
5	2.74	5.21	674	139
6	3.00	6.10	848	175

It should be noted that the beam-divergence cam was positioned so that is was possible to move on either side of the collimation and actually converge the beam somewhat at position No. 2. The beam-divergence control was later a adjusted at MSFC, and the calibration was repeated by both ITT and NASA personnel. The revised calibrations for thest two sets of measurements are plotted in Figure 165 with the original data.

LASER POWER MONITOR

The function of the laser power monitor is to measure the average modulated power output of the AOCP He-Ne laser. The laser power was measured at the output of the AOCP afocal telescope and compared with the voltage
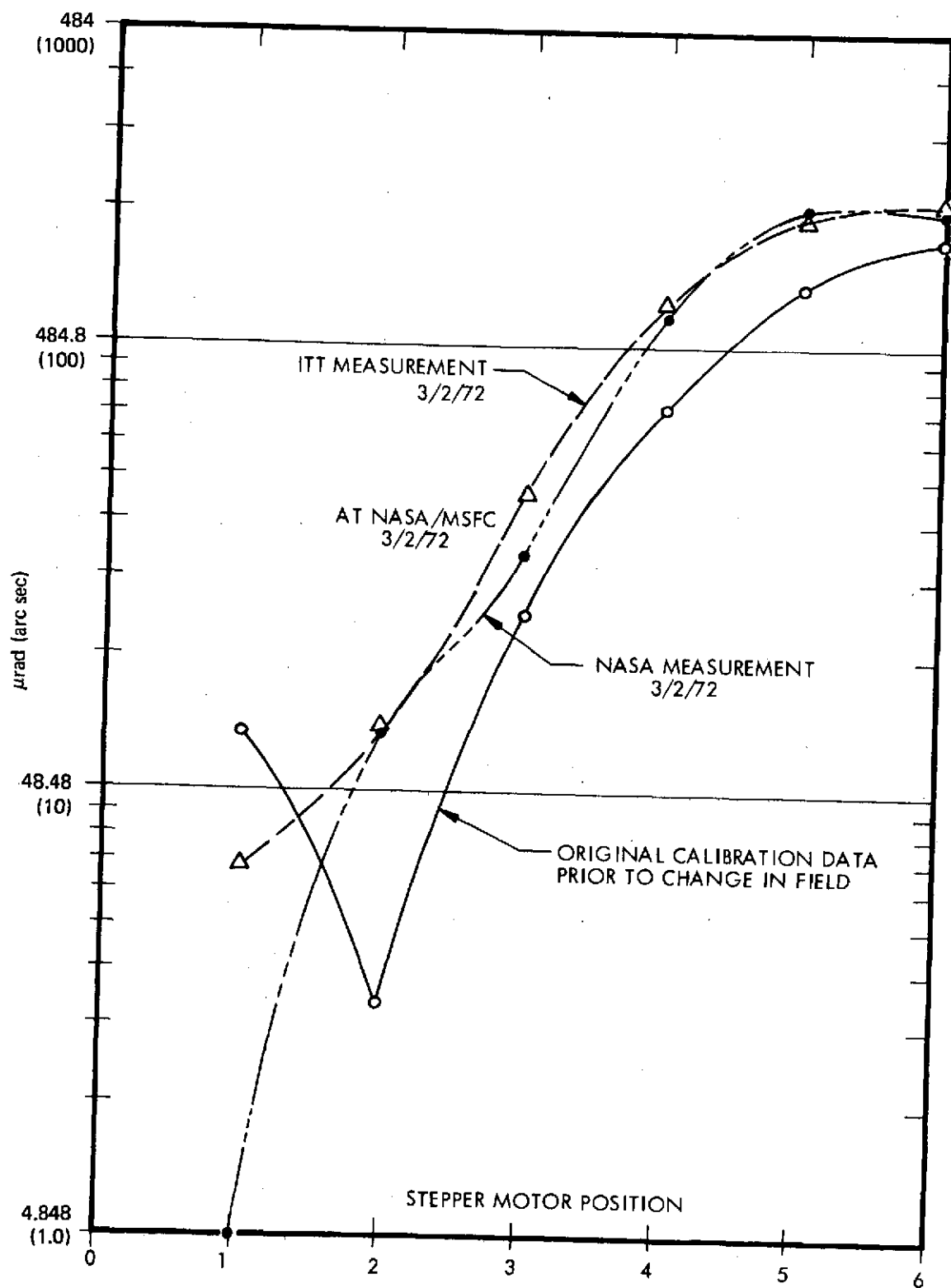
Figure 165. AOCP transmitted beam-divergence calibration.

obtained from the power monitor output. The measurement standard was a precisely calibrated photodiode power detector, and power level changes were made by inserting ND filters into the transmitter path before the laser power monitor location. Figure 166 is a plot of the laser power monitor calibration data.
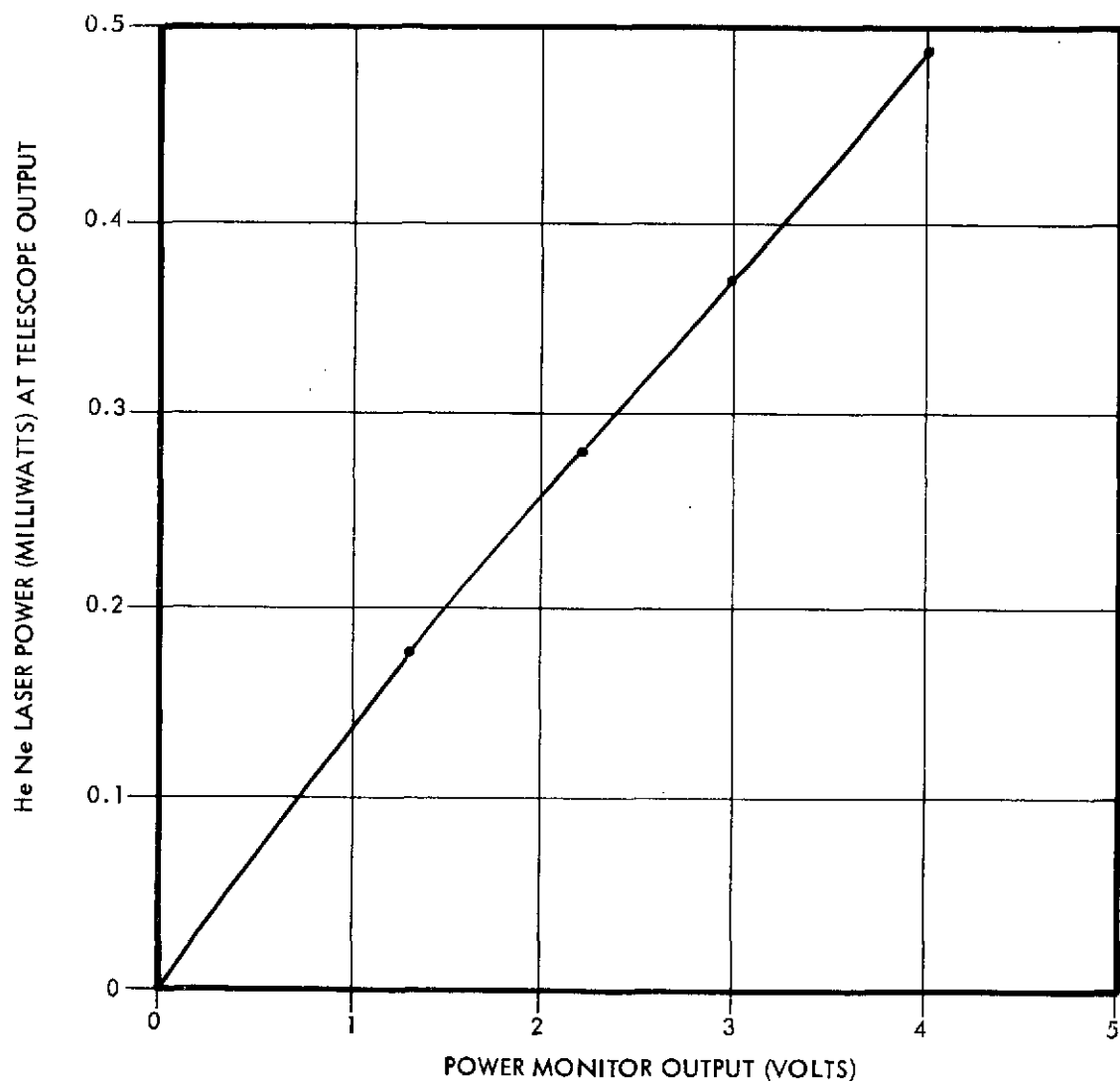
Figure 166. AOCP laser power monitor calibration

SCINTILLATION MONITOR

Calibration of the scintillation monitor subsystem utilized the GCE modulated beacon laser as a source and a National Bureau of Standards traceable vacuum photodiode standard detector. Figure 167 illustrates the photodiode radiometer construction. Because of a nonuniform beam intensity profile from the GCE, a large area collector was used which simulated the AOCP entrance pupil in size and shape, including the central obscuration. The GCE modulation index was adjusted to 70 percent, and the power transmitted was measured with the calibrated photodiode radiometer in a darkened environment. Then the beam from the GCE was permitted to impinge on the AOCP aperture, and the scintillation monitor outputs were recorded. This was repeated for various power levels to obtain a sufficient number of points for plotting. Note that the scintillation monitor outputs are related to the total power at the AOCP collection aperture rather than at the photodetector located within the AOCP. Plots of the scintillation monitor calibration for each of the three outputs are given in Figure 168a, b, and c. Outputs of the scintillation monitor can be obtained as a function of irradiance at the collection aperture for a uniformly illuminated aperture by dividing the power of the calibration curves by the collection area, as shown in Figure 168d.

TRACKER LINEARITY

The tracker subsystem transfer characteristic gain-slope and linearity was measured. The measurement procedure was to place the AOCP tracker into the fine track operation mode on the GCE beacon and precisely deflect the GCE output beam, using the GCE finely adjustable folding mirror. The beam deflection angle, as measured by the autocollimator, was recorded and plotted with the corresponding tracker output voltage. The data taken was plotted on a 1.83-m (6-ft) graph, and linearity and orthogonality were determined to be better than 0.5 percent. A summary of these data is given in Figure 169. The tracker transfer characteristic gain is determined by the slopes of the Z-axis and Y-axis plots and is indicated on the graph.

Data were taken at various light levels covering a dynamic range of greater than 30 dB in voltage. Figure 170 shows the optical image shape at the image dissector photocathode in terms of the aperture size as determined by scanning the image plane with the image dissector aperture. The plot indicates an optical image size to be very nearly the size of the aperture.
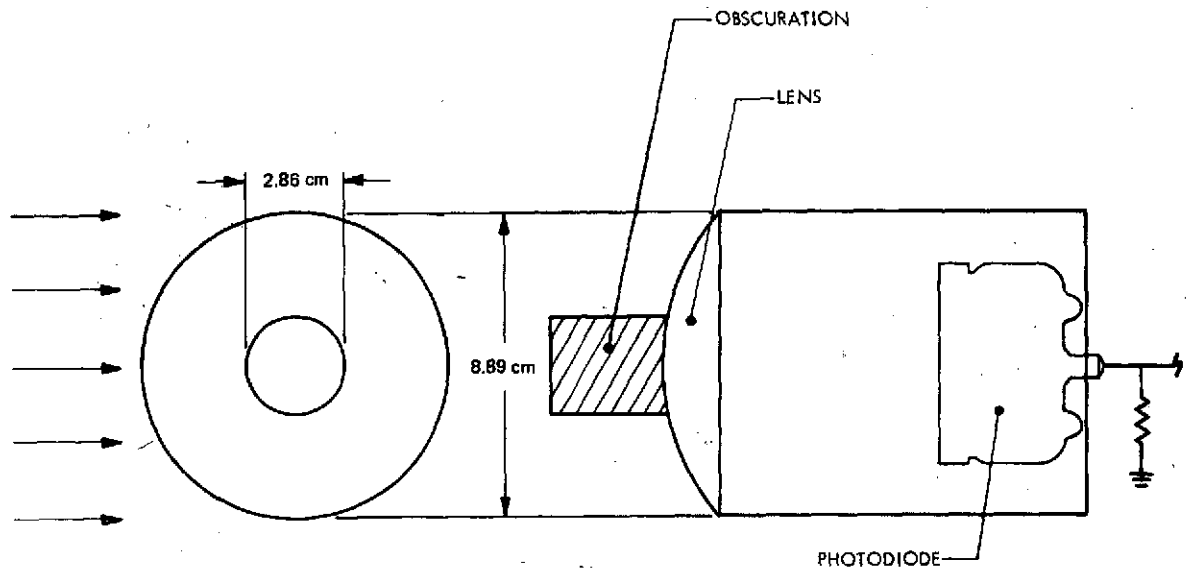
Figure 167. Scintillation monitor calibration reference.

BORESIGHT STABILITY

The AOCP transmitter/receiver boresight alignment stability was measured at reduced pressure to demonstrate the integrity of the pressurized transmitter compartment and its ability to withstand the forces produced on the compartment. Figure 171 shows the AOCP unit mounted in a vacuum test chamber that permitted the system to be operated and the output beam direction to be monitored as the pressure was reduced. The system was pumped down to 10^{-4} T and held for 8 hr. No beam wander was observed nor was the pressure in the compartment reduced as a result of this test. Beam position was continually monitored during pumpdown by observing the position of the laser beam directly from the transmitter compartment impinging on a screen at a distance of 15.24 m (50 ft).

This test also verified the integrity of the high-voltage components operating in a reduced pressure environment. Later in the flight test phase of the program, some problems occured from high-voltage breakdown at reduced pressure. This is believed to have been caused by the frequent subjection to moisture condensation resulting from faulty air conditioning during the flight tests. The problem was fixed by potting and additional high-voltage insulation in the high-voltage areas. Boresight instabilities were also experienced during the flight tests; this problem is further discussed in another section of this report.
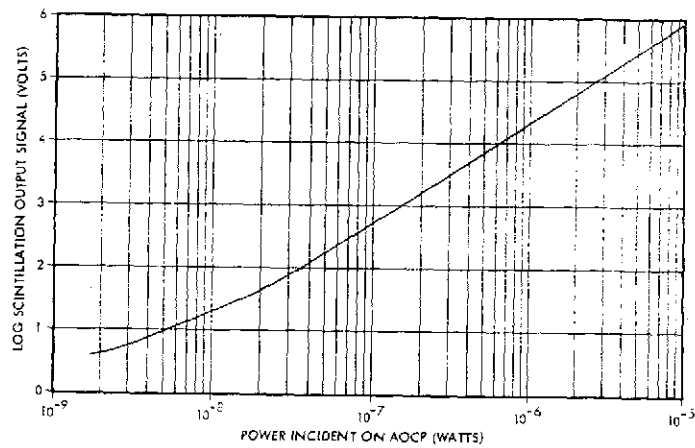
a. 10.7-MHz scintillation monitor log output calibration.
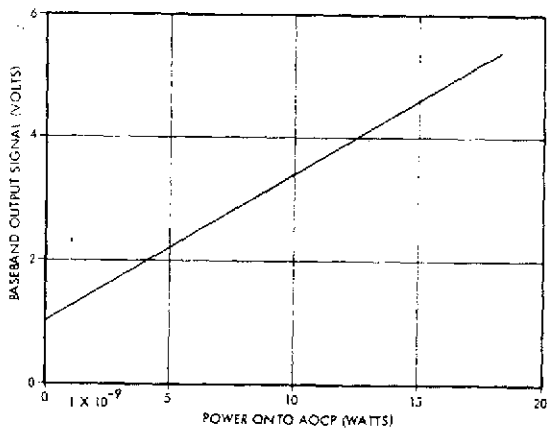
b. Baseband scintillation monitor output calibration.
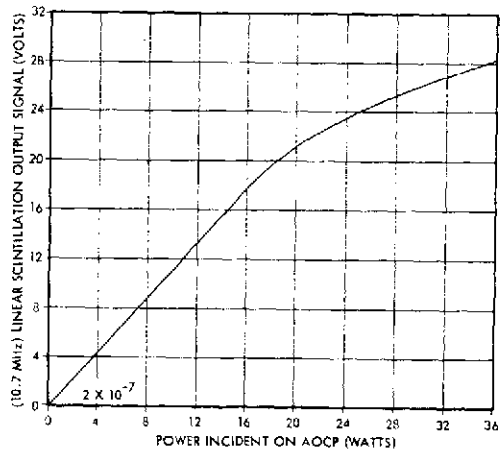
c. 10.7-MHz scintillation monitor linear output calibration.

Figure 168. Scintillation monitor calibration.
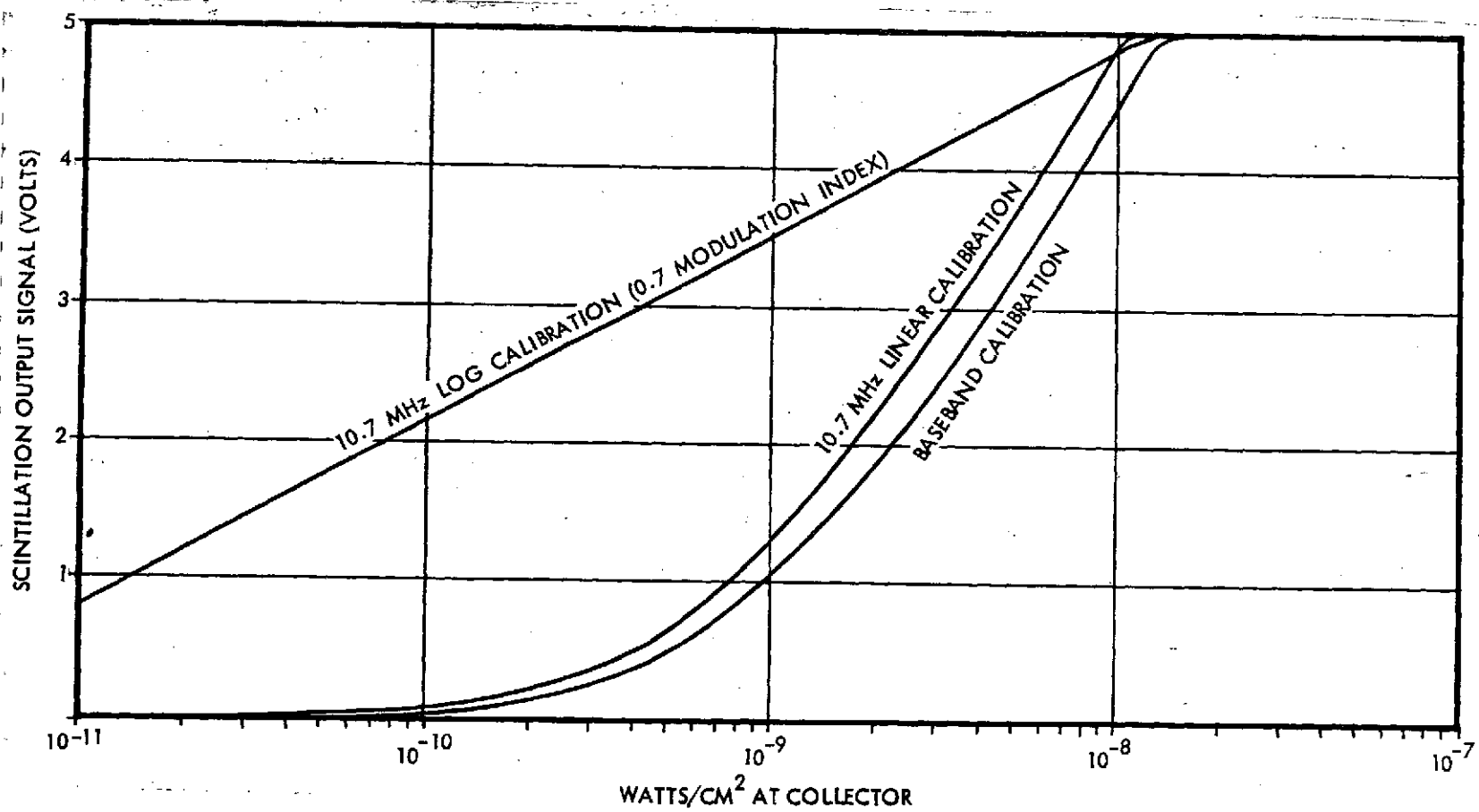
d. Scintillation monitor irradiance curves.

Figure 168. (Concluded).

AOCP TRACKER OUTPUT
TRACK MODULATION ~ 30%
INSTANTANEOUS FOV 84.8 µrad
OPTICAL POWER ON DETECTOR = 7 x 10⁻¹⁰ W
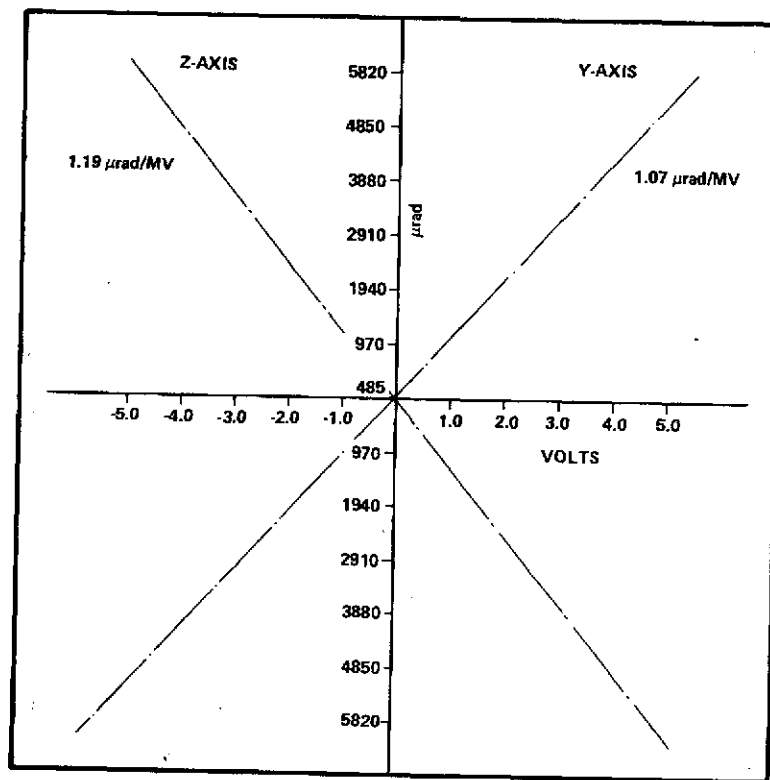
Figure 169. AOCP tracker linearity and gain calibration.
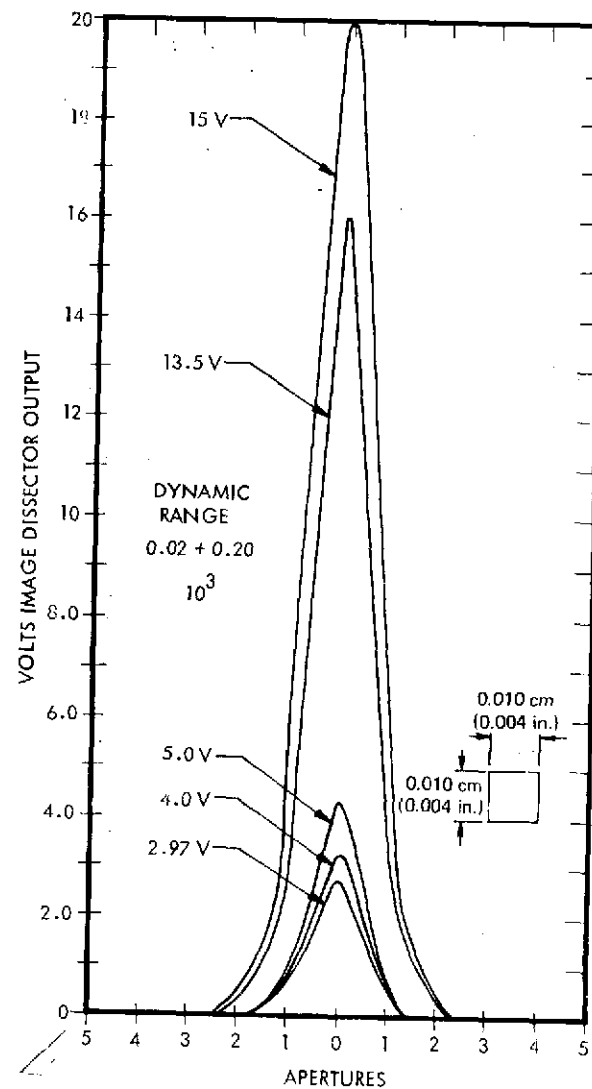
Figure 170. AOCP tracker linearity
and gain calibration.
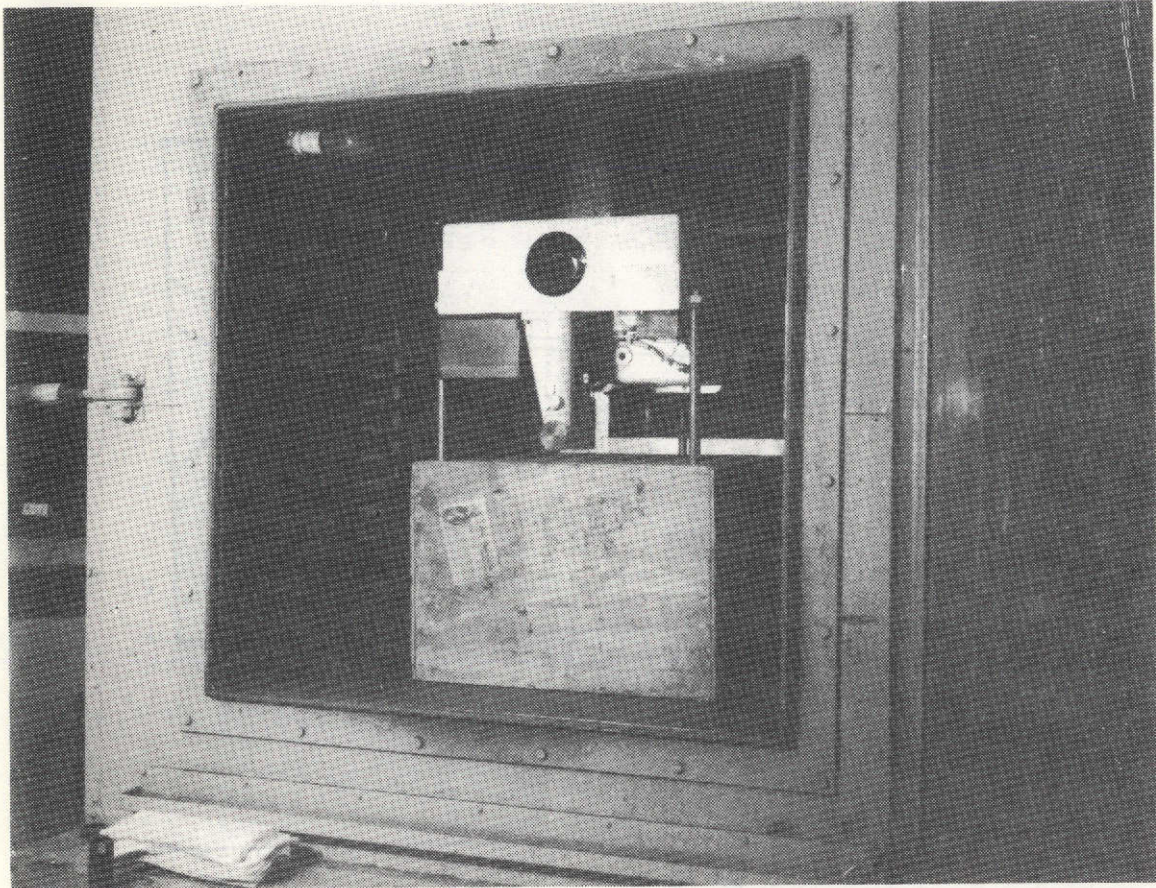
Figure 171. AOCP environmental test.

GROUND STATION

COMMUNICATIONS PHOTODETECTOR CALIBRATION

Irradiance of a 632.8-nm light source was measured using an EG & G Model 585-66 radiometer. The photodetector being calibrated was substituted for the radiometer, and the anode current was measured to determine anode radiant sensitivity. Another reading was taken with the anode and all dynodes connected together to form a photodiode. Their reading was a measure of photocathode radiant sensitivity S_d. Electron multiplier gain G was determined by dividing the first reading by the second. Dark current was measured by blocking the incident radiation when the photodetector was operating as a photo-multiplier.

Table 37 is a summary of the calibration data recorded for this particular photodetector. This is the most recent calibration data on the ground station receiver.

TABLE 37. COMMUNICATION PHOTODETECTOR CALIBRATION DATA

Photodetector . . . . RCA 8644, S/N 11-9-141

Applied voltage . . . . 1521 V

Cathode radiant sensitivity S_d . . . . 1.86 × 10^{-2} A/W

Anode radiant sensitivity . . . . 843 A/W

Electron multiplier gain G . . . . 4.53 × 10^5

Incident power for 1 μA anode current . . . . 1.2 × 10^{-9} W

Dark current . . . . 7.0 × 10^{-9} A

Two logarithmic amplifiers are associated with the communication photodetector. One is a low-pass amplifier used to monitor the average received power and provide baseband scintillation data. Figure 172 is the response curve relating the receiver power at the photocathode to the output voltage of the amplifier. The other logarithmic amplifier is tuned to a 2-MHz component of the downlink modulation. It is used as a separate scintillation monitor above baseband and is insensitive to background radiation. Figure 173 is the response curve associated with this amplifier.

UPLINK (BEACON) LASER POWER MONITOR CALIBRATION

The uplink laser power monitor was used as a relative power indicator for the 488-nm argon laser. Approximately 5 mW at the telescope Coudé focus corresponded full scale on the power monitor.
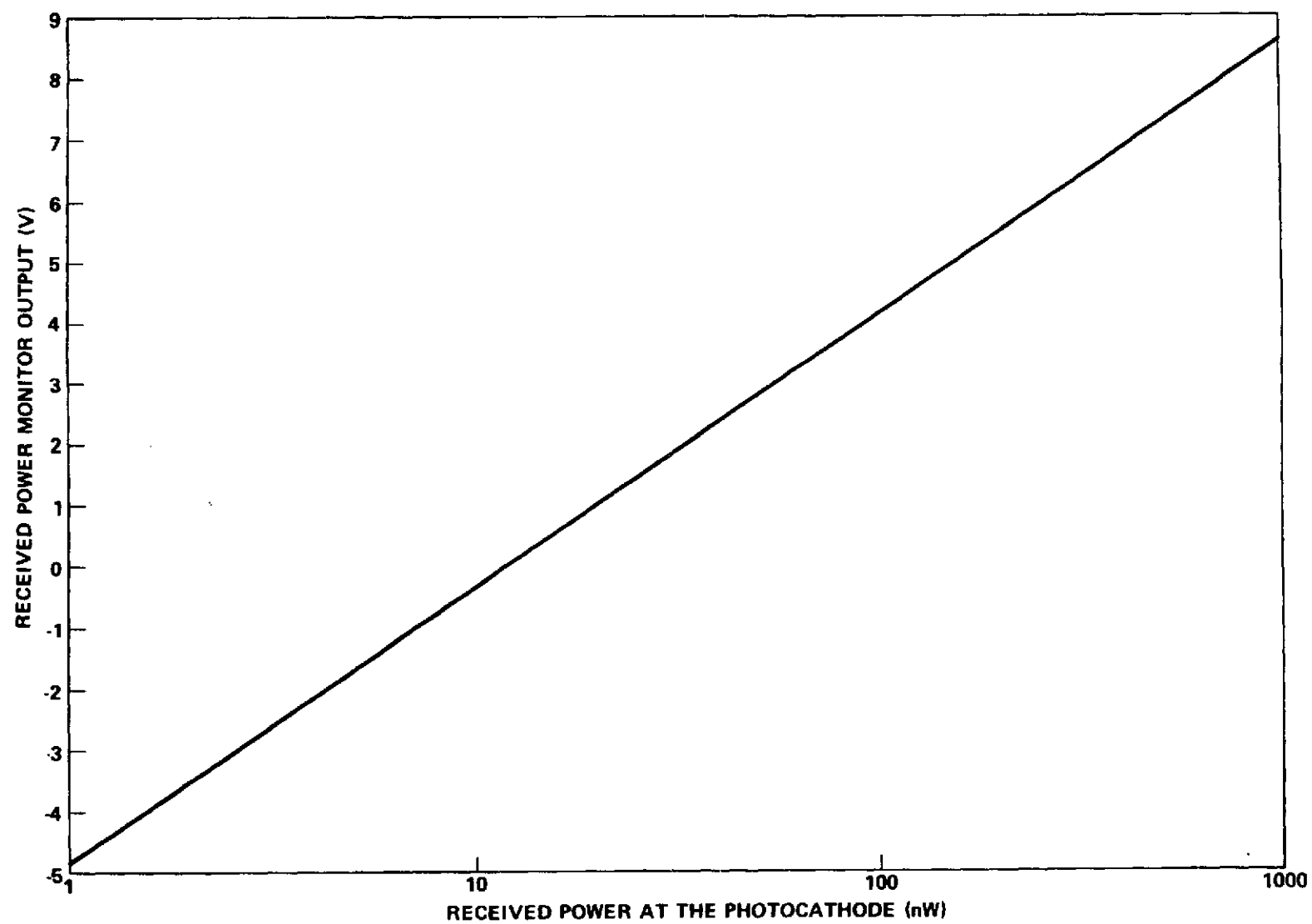
Figure 172. Received power calibration curve.
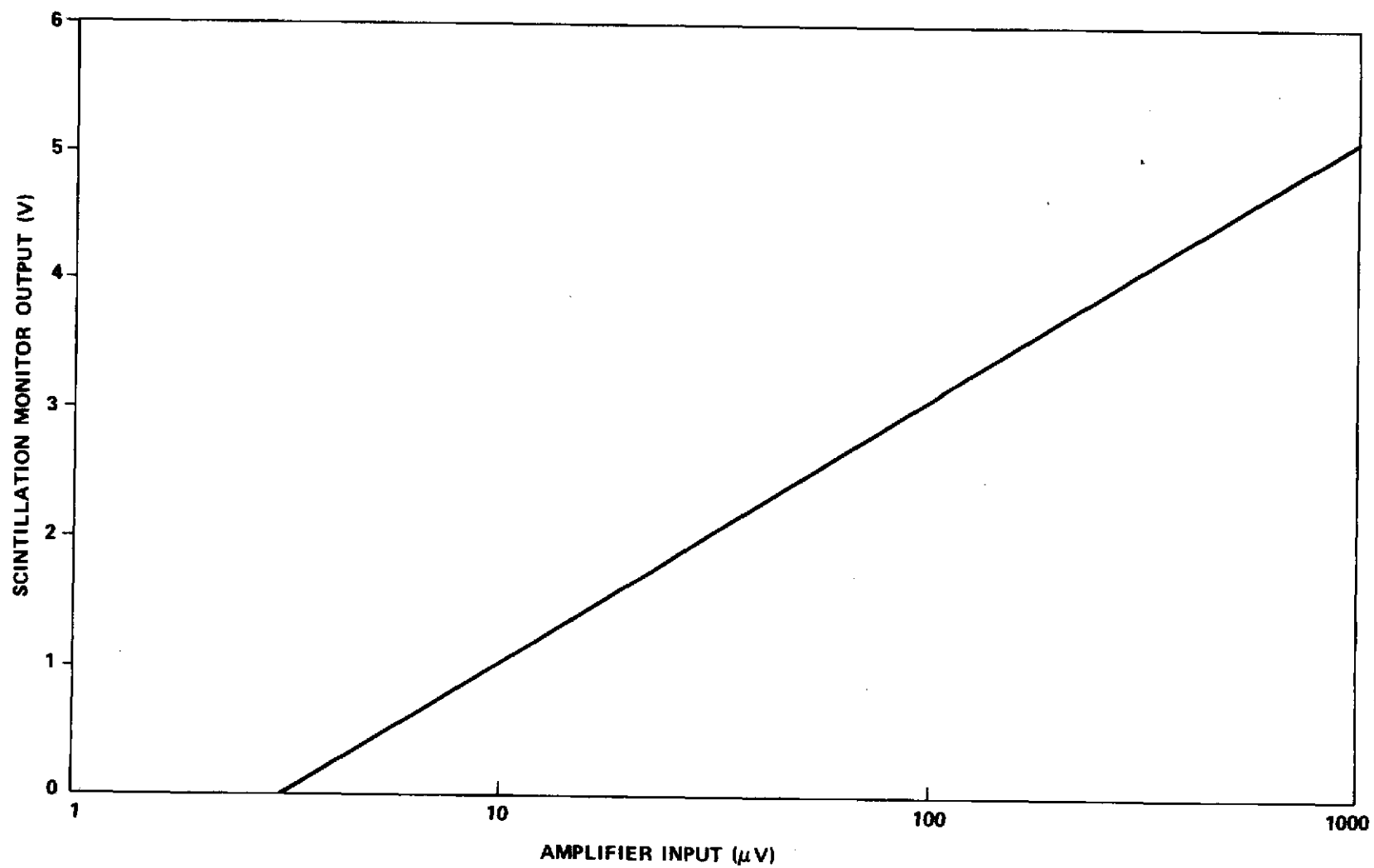
Figure 173. 2-MHz scintillation monitor calibration curve.

Absolute calibration was not possible since modulator alignment had a great influence on the actual power transmitted. Before each flight and immediately after the modulator was aligned, a reading of power in the transmit beam was taken at the Coude focus.

UPLINK BEAM-DIVERGENCE CALIBRATION

Interferometric measurements were made on the beam-divergence assembly to determine beam divergence as a function of position of the moveable optical element. Position data were recorded as resistance readings on the linear potentiometer associated with the unit. This variable resistance was used in generating an analog voltage proportional to beam divergence. A beam divergence of 0 to 436 μrad half angle was scaled to 0 to 5 V at the tape-recorder input. The scale factor is 87.2 μrad/V.

TRANSFER MIRROR CALIBRATION

The transfer mirror assembly was calibrated by driving the mirror with a known voltage and measuring the beam angle caused by the reflection from the mirror. The gain factor with the angle referred to object space of the telescope was

$$K_2 = 6.30 \times 10^{-6} \text{ rad/V} \quad . \tag{124}$$

The transfer mirror position that was recorded on tape was $10\,K_2$ or 6.30×10^{-5} V.

QUADRANT MULTIPLIER PHOTOTUBE (QMP) CALIBRATION

In a manner similar to the transfer mirror calibration, the QMP gain factor was determined. The transfer mirror was driven with a known voltage and with that axis operating open loop, the error signal was measured at the output of the summing amplifier. This voltage divided by the driving angle was the gain factor K_1.

$$K_1 = 9.36 \times 10^5 \text{ V/rad} \qquad . \qquad\qquad\qquad (125)$$

This voltage is referred to elsewhere as the tracking error signal.

RECEIVER ATTENUATION CALIBRATION

Three ND filters were arranged so that they could be remotely inserted in the received beam individually or in combinations. These filters were selected to have densities of 0.5, 1.0, and 2.0.

FLIGHT TEST PROGRAM

Operational Procedures

METEOROLOGICAL

Weather forecasts were a critical factor in the flight phase of the program and often dictated the tempo of preflight checkouts. At times the airborne equipment had to be installed in the aircraft and checked out in a matter of a few hours to take advantage of a short period of clear weather. At the other extreme, there were occasions when the equipment was checked out and ready to fly but had to wait several days for clear weather.

Usually a definite flight time was scheduled, based on a 24 to 48 hour advance weather forecast. From this point the forecast was updated with increasing frequency as the countdown neared takeoff time, with the final go/no-go decision being made approximately one hour before takeoff (approximately two hours before aircraft arrival over station).

Following this decision, a balloon-lofted radiosonde package was launched from the MSFC weather station, approximately 4 km from the tracking station. The radiosonde provided pressure, temperature, wind speed, and wind direction data versus altitude up to approximately 33 km. Atmospheric humidity was also measured up to approximately 12 km. The wind profile data were immediately relayed to JSC for flight planning purposes and to the radar site at Redstone for use in vectoring the aircraft in the circular flight path about the Madkin Mountain optical tracking station. Instrumentation was also located at the Madkin Mountain tracking station to record local temperature, humidity, and wind data.

AIRCRAFT OPERATIONS

PREFLIGHT PROCEDURES

Preflight checkout procedures are outlined as follows. Full details of these procedures can be found in Reference 7.

Preliminary Setup

Involves removal of bomb bay fairing, providing electrical power, air conditioning, etc., and installation of the experiment equipment. The experiment assembly is installed with the aid of the transport dolly discussed earlier. The REC is installed with the use of manual hoists (Fig. 108).

Power Up

Pertains to proper setting of control panel switches and automatic sequencing of flight computer.

Warmup Procedure

Regards usual inspection and cleaning of optical windows, and setup of GCE and oscillograph. Oscillograph setup includes verification of proper data being recorded on appropriate channels. O-Graph channel allocations are listed in Table 38. The channel allocations of the commutator wave train are shown in Table 39. The value of each channel is represented by a pulse height, and the channels are displayed in time sequence following the master pulse. Scale data are on channels 1 and 2.

Preliminary Equipment Status Check

Verify that the ac and dc voltages are within tolerances.

GCE/AOCP Alignment

Procedures call for optically aligning the GCE so that its argon laser is oriented to illuminate the AOCP coarse tracker and fine tracker, a picture of the equipment setup was shown in Figure 62. When proper optical alignment is achieved, charts of the E_Y and E_Z signals are obtained, using the 2-channel brush recorder. Chart recordings of E_Y, E_Z are obtained corresponding to beam steerers off and beam steerers on.

TABLE 38. O-GRAPH CHANNEL ALLOCATIONS

O-Graph Channel	Data Signal
1	Pitch Gimbal Angle ϕ
2	Roll Gimbal Angle θ
3	Beam Steerer B_Y
4	Beam Steerer B_Z
5	Computer status
6	Yaw vibration
7	Longitudinal vibration
8	Commutator wave train
9	Fine track error E_Y
10	Fine track error E_Z
11	Pitch vibration
12	Log amplitude scintillation
13	Power monitor
14	Timing wave train

TABLE 39. ALLOCATION OF PAM CHANNELS

PAM Channel	Data Signal
1	0-V Pulse
2	5-V Pulse
3	Fine Beacon Presence
4	TV Filter
5	Scintillation Aperture
6	Beam Divergence
7	Laser Shutter
8	Linear Scintillation
9	Receiver Attenuation
10	Coarse Beacon Presence
11	115 V, 60 Hz
12	115 V, 400 Hz
13	28 V, unregulated
14	28 V regulated
15	+5 V dc supply
16	+15 V dc supply
17	AOCP Temperature
18	Canister Temperature

Systems Operational Test

Data Acquisition System

Make a cursory check of TM channels with system in fine track.

Uplink Commands.

Using the Tone Generator in the GCE console, send all commands in sequence via the GCE modulator and verify their execution in the AOCP. The various command actions are listed below:

1. Track Mode Defeat
2. Aperture select
3. Receiver Attenuation
4. Beam Divergence
5. TV Filter
6. Laser Shutter Control
7. Select Video
8. Select TM
9. Select Recorder Monitor
10. Select Pseudorandom Word
11. Beam Steerer Disable

A detailed list of commands and their coding sequence is given in the Equipment Description portion of this report.

AOCP Modulation

Using the GCE photodetector, measure the modulation index of the AOCP He-Ne laser beam.

Inflight Test

Depress the In-flight TEST button on control panel A (located in cockpit) and verify the in-flight test sequence on the two-digit display. The sequence is as follows:

- 30. The in-flight test has been initiated by the computer.

- 14. The computer has verified that the He-Ne laser power level is satisfactory. (If unsatisfactory, a 15. will be displayed).

316

- 06. The computer has stepped the receiver attenuation filter wheel through its range and verified that the indications are proper. (If proper indications are not received an 07. will be displayed.)

- 41. The computer has reset all software to the initial acquisition state (received attenuation to minimum and beam divergence to maximum) and has resumed the operations in progress at the time the inflight TEST button was pushed.

Status Display Verification

Repeatedly send commands and verify that two-digit display on cockpit panel changes properly.

Pilot's Directional Indicator (PDI)

Using a variable frequency input at the GCE, verify that PDI meter deflects full scale left for a frequency of 518 Hz, is centered or zero for 560 Hz, and deflects full scale right for 602 Hz.

Dynamic Tracking Performance

Using the GCE nutating mirror, check dynamic performance of AOCP tracking systems.

Vibration Measurement

Verify vibration measurements system by tapping the triaxial accelerometer and noting the signal pulses on the appropriate O-graph channels.

Preflight Tape Calibration

With the tape recorder running, place calibration levels on tape using the GSE calibration selector.

Securing for Flight

Power Down

Set gimbal to caged position and turn power off at cockpit panel. Verify that the gimbal platform is mechanically caged.

Mechanical Securing

Clean gimbal mirror, AOCP optical window and inside of fairing window; install fairings; clean outside of fairing window; remove covers from retro-reflectors; inspect all retroreflector arrays for mechanical security.

Abort Procedures

Detailed procedures were established for delaying a scheduled flight, or aborting and then rescheduling a flight because of problems that might be encountered during AVLOC preflight checkout, or as a result of problems developing at the GS or with the aircraft itself.

IN-FLIGHT PROCEDURES

In-flight procedures are outlined as follows. Full details of these procedures can also be found in Reference 7.

Preflight Setup

Set electrical POWER switch and ACQUIRE switch to off, AUTO/MAN switch to AUTO, TAPE SPEED switch to 7 1/2-ips, and temperature control POWER switch to ON, AUTO/HOLD switch to AUTO.

Power Up at 7.6 Km (25 000 ft) Altitude

Read and record AOCP and canister temperatures. Anytime during flight that temperature exceeds 49 deg C (120 deg F), add cooling air by moving AUTO/HOLD switch to COOL position.

Using appropriate switches, turn on power to experiment equipment and tape recorder and verify that the Experiment Status Display shows the digits: 00, 99, 30, 14, 06, 22 at 2-sec intervals.

Push the tape record STOP button.

Record the gimbal elevation and azimuth angles.

After allowing the experiment equipment to warm up for 15 min, record the canister and AOCP temperatures.

Experiment Control Exercise No. 1 (During Ascent)

Place AUTO/MAN switch in MAN and verify that two-digit display remains at 22; place OFF/ACQUIRE switch in ACQUIRE and verify that two-digit display changes to 41.

Using L/R-UP/DOWN thumb switch, exercise gimbal mirror and verify its proper operation; return AUTO/MAN switch to AUTO and OFF/ACQUIRE switch to OFF.

Record AOCP and canister temperatures.

Experiment Control Exercise No. 2 (Upon Arrival at Maximum Altitude)

Depress red TEST button and verify that the two-digit display reads 30, 14, 06, 22, in sequence.

Repeat experiment control exercise no. 1.

Experiment Control Exercise No. 3 (at Maximum Altitude Just Before Reaching Birmingham)

Repeat experiment control exercise no. 2.

Radar Acquisition

Communications between the aircraft and both the Ground Station and Radar site were by VHF and UHF radio. Primary communication was on VHF at 138.25 MHz. Secondary communication was on UHF at 264.75 MHz. Back-up to radio communication was air-to-ground telephone via Autovon network.

The pilot flew directly from Houston to Birmingham, where initial radio contact was established. At Birmingham, the aircraft was flown due north towards the Huntsville airport. Radar acquisition was ordinarily achieved when the aircraft was in the Birmingham area and the aircraft was vectored on an approach path tangent to the desired circular flight path around Madkin Mountain Ground Station.

At the appropriate time, the radar controller would have the pilot initiate the bank angle to place the aircraft into its circular flight path. Using the real-time plot of the aircraft's track, the radar controller updated the pilot continuously on the bank angle required to maintain the circle. The changing bank angle was dictated by prevailing wind conditions.

On the few occasions when radar acquisition was not achieved, the pilot visually flew the best circle possible, using prominent landmarks.

Experiment Operations

The tape recorder was turned on while enroute from Birmingham to Huntsville.

The first step required was to achieve GBAA acquisition. This was accomplished by vectoring the aircraft through certain "windows" in the sky to which the GBAA had been pointed by proper orientation of the 61-cm telescope.

With the GBAA tracking the target aircraft, the beacon laser was simultaneously illuminating the aircraft because of prior boresighting of the two beams. At this point, the aircraft Scientific Equipment Operator (SEO) would attempt onboard acquisition of the beacon laser by slewing the gimbal mirror. Initially, this was done by manually slewing the mirror to the appropriate angles correlated with the GS-to-aircraft zenith angle and the aircraft bank angle. This procedure was cumbersome and rather unsuccessful. Later in the flight program software was incorporated into the on-board computer to automatically scan the mirror in a regular search pattern, effectively increasing the field of view of the coarse tracking system. This technique worked quite well. Coarse acquisition was indicated by the TV BEACON light on the control panel.

Following coarse acquisition achievement the fine track system had to acquire and track the beacon laser. This was indicated by a FINE TRACK light on the control panel. This proved to be the most difficult task in the experiment operations and this problem is fully discussed in the following sections of this report.

When fine track was attained by the airborne system, the overall tracking loop could generally be successfully closed by obtaining fine track at the Ground Station transceiver.

The last major step in the experiment operations was communications link evaluation. On the uplink, commands were transmitted and subsequently executed quite reliably. However, unreliable closed-loop tracking made downlink communications virtually impossible.

The flight crew maintained a data log book to assist in subsequent troubleshooting and data analysis.

Power Down Procedure

Power down commenced upon radio signoff from the ground station. The procedure was simply to cut off the power switches to the experiment equipment and tape recorder, observe that the two-digit display changed to 22, and verify that the gimbal angles returned to the caged position.

POSTFLIGHT PROCEDURES

Experiment Hardware Checkout

The primary purpose of the postflight checkout was to verify that the experiment hardware was functional after landing. Therefore, an abbreviated version of the preflight checkout procedures was performed. In addition, these procedures included checking that the gimbal platform was caged, replacing the covers on the retroreflectors, and removing the tape reel from the recorder.

Data Reduction

The data reduction referred to concerns the work performed at the Wave Analysis Laboratory of JSC. Immediately after the mission, the flight tape was taken to the lab for duplication and analysis. The primary purpose of this operation was for a "quick-look" analysis to allow maximum reaction time for any hardware modifications or procedural changes deemed necessary for the next flight. Oscillographs were obtained in several different formats. The signals that were generally most useful for diagnostic purposes were:

1. Coarse track beacon presence
2. Fine track beacon presence
3. Fine track error, E_Y, E_Z
4. Beam-steerer error, B_Y, B_Z
5. Computer status
6. AOCP temp
7. Canister temp
8. Vibration amplitudes
9. Time
10. Scintillation detector outputs

GROUND OPERATIONS

RADAR PROCEDURES

Communication with the pilot was by VHF radio. Communication with the ground station was on FM radio. Initial radio contact with the flight crew was established as the aircraft neared the Birmingham area.

Radar acquisition was usually achieved as the aircraft approached the Birmingham area. At Birmingham the aircraft would turn North on a heading toward the Huntsville Jetport. During this final approach phase, the aircraft was usually being tracked successfully by radar. Thus, it was during this phase that the first vectoring commands were issued by the radar operator in order to place the aircraft on an approach path tangent to the desired circular pattern centered on the ground station. The desired circle was one having a radius of 12.2 km (40 000 ft).

During the acquisition approach, the radar operator furnished the pilot with altimeter calibration data in terms of absolute altitude above the Madkin Mountain Ground Station site.

When the aircraft reached a point approximately due west of the Ground Station, the pilot was requested to bank at an angle determined by prevailing high altitude winds, to attain the desired circular pattern. From this point in the mission the radar operator continually vectored the aircraft to maintain the tightest possible circle. The radar operator's estimate of the required bank angle was based on a knowledge of the prevailing winds and the real time target track on the X-Y plotter. It was found that it was both convenient and desirable for the radar operator to control the path of the target aircraft even after GBAA acquisition.

GROUND STATION PROCEDURES

Preflight

Preflight checkout at the ground station began about 4 hours before the aircraft's expected arrival to ensure that all essential equipment was operational prior to takeoff.

GBAA

Proper laser operation was checked; laser power output and gas pressure were the primary monitoring items. The GBAA transmit/receive boresight, electronics and overall system operation were conveniently and comprehensively tested by ranging to a retroreflector several miles distant. This test was always performed as part of the preflight check. Any existing boresight error was corrected by appropriate biasing of the beam steerers.

Telescope/Computer

The telescope electromechanical system, computer hardware, servo loop and interface were tested by inserting a computer program causing the telescope to slew automatically in a predetermined fashion.

Telescope/GBAA Boresight

The boresight between the GBAA and telescope was checked and adjusted by projecting the beacon laser beam from the telescope onto a target screen several miles distant while simultaneously tracking with the GBAA on a retroreflector located immediately adjacent to the screen. The error in the separation of the two was corrected by programming the appropriate offset constants into the control computer.

Transceiver

The transceiver electronics were fully exercised. Final alignment on the laser-modulator was done only after an appropriate warmup time; even then, a compromise was required between depth of modulation, beam shape, and transmitted power. The modulation and beam characteristics also changed with time so that periodic readjustment was required. The boresight between the transmit and receive channels in the transceiver was checked internally. This boresight procedure was also cross-checked in a closed-loop fashion during the Field Test phase.

Telemetry and Tape Recorder

All TM hardware was checked and calibrated. Calibration signal levels were also placed on the various recorder channels. This calibration provided for 0, 25, 50, 75, and 100 percent amplitude calibration levels on both VCO subcarrier channels and FM tape recorder data channels.

Radio Communications Check

All radio systems — VHF, UHF, and FM — were verified operational via checkout calls between the radar site and the ground station.

Weather Data

Temperature, humidity, wind direction, and wind velocity were recorded at the ground station. A radiosonde balloon was released at the weather station about two hours before aircraft takeoff. Upper atmosphere wind conditions were later relayed to the flight crew before takeoff.

Helicopter Tests

Dynamic testing of the GBAA/Telescope/Computer loop was frequently carried out during the preflight checkout phase by tracking on a hand-held retroreflector(s) carried in a helicopter which flew an appropriate course near the ground station. The transceiver fine track system was simultaneously tested by tracking on the return He-Ne laser signal from the same retroreflector(s). The source of this laser energy was a He-Ne laser attached to and boresighted with the 61-cm telescope.

In-Flight

GBAA Acquisition and Tracking

The first step in the flight procedures was the coarse acquisition and tracking of the target aircraft with the GBAA. Continuous tracking with the GBAA involved closing the loop from the GBAA through the computer to the telescope since the GBAA was hard-mounted to the telescope. Initial acquisition was effected by establishing the GBAA fence scan at a predetermined "window" in the sky, through which the aircraft was vectored by the radar operation. When acquisition and tracking was established by the GBAA, the loop was automatically closed through the computer to the telescope. Unless clouds were encountered, this automatic GBAA tracking of the target aircraft could be maintained indefinitely and uninterrupted tracking was commonly maintained for several circles.

Beacon Laser Illumination of Aircraft

With coarse tracking of the aircraft reliably established, the airborne experiment package could be illuminated with the beacon laser. It was

324

empirically found that this was best accomplished with the joystick telescope control mode. Making use of the boresighted TV cameras attached to the 61-cm telescope, the joystick was used to achieve vernier adjustments of the telescope resulting in maximum brightness (at 488 nm) of the retroreflector array mounted nearest the experiment window. During this procedure, the beacon laser beam divergence was also varied to improve the reliability of tracking by the airborne package.

Uplink Commands

The aircraft coarse tracking system generally tracked the beacon laser beam accurately enough that sufficient energy was received by the ID detector to allow reception and execution of commands from the ground station. Using this ground-to-air optical command link, commands were reliably transmitted and executed to vary downlink beam divergence, receiver attenuation, and downlink communications mode (i.e. PN, TM, video, or recorder monitor).

Transceiver Fine Track System

When the airborne fine track system operated for any continuous period of time, the QMP tracker would track reliably on the downlink He-Ne laser beam whenever the airborne transceiver boresight was within tolerance. This sometimes required remote boresight adjustments from the cockpit. These boresight adjustments were accomplished via radio commands from the ground station with the objective of maximizing the received 633-nm laser power.

Bit Error Detector/TM/Video

Although there were numerous periods when the ground station fine track system was locked onto the 633-nm laser beam, the depth of modulation on the beam was never sufficient during these times to allow the various receivers to lock on.

Log Book

All significant occurrences during the flight were carefully recorded in a logbook and listed according to universal time.

EXPERIMENT OPERATIONS PLAN

A typical Experiment Operations Plan is given as follows.

FLIGHT NO. _____ EXPERIMENT OPERATION PLAN

I.   Objectives of Flight No. _____.

   A.   Evaluate Acquisition Performance

      1.   GBAA acquisition target at 18.3 km vs. radius

      2.   Use of video aid in establishing two-way tracking at dusk.

      3.   Establishing two-way tracking at dark without video aid.

   B.   Evaluate Tracking Performance

      1.   Determine the range of parameter values over which uplink
           and downlink tracking is satisfactory

      2.   Effect of aircraft environment on AOCP tracking

   C.   Systematically evaluate communication performance on BER
        channel

   D.   Evaluate uplink scintillation

II. Aircraft over Madkin Mountain   6:15 p.m.

III. Initial Conditions

AOCP		Ground Station	
Scintillation aperture	10 cm	Receiver attenuation	0 dB
Receiver attenuation	0 dB	Tracker attenuation	0 dB
Beam divergence	1.05 mr (219 arc sec)	Receiver aperture	60 cm
Video filter	in	Tracker detector FOV	180 arc sec 0.864 mr
Downlink modulation	none	Receiver detector FOV	180 arc sec . 0.864 mr
		Argon beam divergence	180 arc sec 0.864 mr
		Argon beacon laser power	maximum

Telescope at window no. 23.

326

IV. Acquisition Sequence

    A. Radar acquires and vectors aircraft into window no. 23

    B. GBAA acquisition

    C. With video aid, ground station computer operator establishes two-way tracking

    D. Command downlink telemetry

V. Post Acquisition Tracking Evaluation

    A. Command downlink TM

    B. Establish nominal tracking performance

        Establish nominal tracking performance at both aircraft and ground by varying the following parameters: Argon beacon divergence, AOCP tracker attenuation, AOCP beam divergence, Ground terminal tracker attenuation, Ground terminal FOV. This will be done by minimizing the peak-to-peak tracking error at both terminals.

    C. Command recorder monitor downlink modulation and verify by observing received signal on an oscilloscope and checking decommutator operation.

    D. Command TM downlink modulation

    E. Evaluate PDI operation by verbal verification with aircraft pilot and monitoring GBAA/computer display of aircraft flight path for one or more circles. (If PDI provides adequate information, radar operator will not control aircraft except in case of loss of optical tracking).

    F. Verify AOCP BER is operational

        1. Command BER and verify

        2. Command TM downlink

G.   Evaluate range of parameters which will allow adequate tracking.

1.   The parameters will be varied one at a time with all other variables set at their nominal values determined in above paragraph A.   Each parameter will be varied over its entire range or until tracking becomes marginal.   This information will be used by the PDI to establish the parameter values used during subsequent experiments on this flight.   The criteria for marginal tracking is defined in the following manner:

AOCP tracking is marginal when the ID begins to drop in and out of lock.   Ground transceiver tracking is marginal when the transceiver communication detector drops below 1μ A (1.2 nanowatts received power).

2.   The sequence and range of parameter variation will be as follows:

a.   Argon beacon divergence (full angle)

864, 576, 288, 144, 48, 24, 0 μradi

b.   Vary attenuation in AOCP

0, 0.5, 1.0, 1.5 ND

c.   AOCP beam divergence

1050, 830, 533, 274, 96, 32 μrad

d.   Ground Station Tracker FOV

864, 576, 288, 144, 48, 24 μrad

e.   Tracker attenuation on Ground Station

0, 0.5, 1, 1.5, 2, 2.5 ND

Perform a. above for nominal value of AOCP beam divergence and b. largest value of AOCP beam divergence as determined from G.2.c.

NOTE: All data in above will be recorded in 1 minute time intervals or larger if necessary.

3. Tighten the beam divergence at both ends to the minimum practicable values as determined in F.1. above. Record for one minute time interval. Attenuation will be put in each end to prevent detector saturation. During all tracking data, scintillation data are being recorded.

VI. Communication Performance Evaluation

A. Command BER on downlink

B. Set tracking dependent parameters to nominal values at determined in paragraph V.A.

C. Evaluate BER performance

Parameters will be varied one at a time with all other variables set at their nominal values as determined in pagagraph V.A. Each parameter will be varied over its entire range for until tracking becomes marginal and/or the average BER goes below 10^{-2}.

The sequence and range of parameter variation will be as follows:

a. Ground transceiver aperture diameter

61, 40, 20, 10, 5, 2.54 cm

Decrease receiver attenuation as necessary to extend range of data

b. AOCP beam divergence

1050, 830, 533, 274, 96, and 32 μrad

c. Receiver FOV (communication detector)

864, 576, 288, 144, 48, 24 μrad

> d. Argon beacon divergence
>
> 864, 576, 288, 144, 48, 24, 0 μ-rad
>
> e. AOCP tracker attenuation
>
> 0, 0.5, 1.0, 1.5 ND

NOTE: All data will be taken for 1 minute time intervals or longer if necessary.

VII. Uplink Scintillation

   A. Set tracking dependent parameters to nominal values

   B. Command Downlink TM. Verify tracking is as previously observed.

   C. Command decrease AOCP scintillation aperture. Record for one mintue.

   D. Command increase AOCP scintillation aperture

   E. Vary Argon beacon divergence over the following range:

   864, 576, 288, 144, 48, 24, 0 μ-radians

   F. Command decrease AOCP scintillation aperture

   G. Repeat E.

VIII. Repeat any of above experiments as time permits where data anomalies may exist.

FLIGHT RESULTS

A resume of the flight results is given below. A copy of individual Summary Flight Reports is filed in Appendix F.

Flight No. 1

The Flight was a successful one when GBAA acquisition and tracking was achieved on the fourth pass. GBAA acquisition and tracking was successfully performed up to 17.6 km (58 000 feet) altitude. The flight was curtailed somewhat because of a GS computer hardware problem.

Flight No. 2

The GBAA worked well again. Coarse acquisition and tracking by the flight equipment failed although the beacon laser illuminated the aircraft fairly consistently through use of the joystick. For future flights, the He-Ne laser shutter will be held open and the TV Tracker 488-nm filter will be made switchable from the cockpit.

Flight No. 3

The flight was a very limited success, with a few seconds of coarse acquisition and tracking obtained. The mission was hindered by a requirement for "recycling" of the GBAA laser and GS computer problems. It was determined that the following changes should be made prior to the next flight:

1. TV tracker sensitivity remotely controlled from cockpit

2. Install cockpit TV monitor

3. Design computer generated scan for gimbal mirror

Flight No. 4

Because of the prevailing weather conditions, there was no chance for a successful flight. During the entire time that the aircraft was over station, the weather was uniformly bad with 80-90 percent cloud cover.

Flight No. 5

The new onboard acquisition technique (computer-generated gimbal mirror scan) worked according to plan and essentially solved the acquisition problem. Acquisition by the fine track systems at both ends of the loop was accomplished numerous times during the flight, cumulative fine track time was approximately 20 sec; the received power at both the aircraft and the ground station was very low and definitely marginal for tracking. For future

flights, the initial beam divergence setting of the He-Ne laser will be reduced by one step, and stringent minimums will be set for allowable atmospheric attenuation.

Flight No. 6

Long, unbroken periods of coarse tracking with the onboard TV tracker were obtained for the first time, usually with the 488-nm TV filter switched out.

There was no success in achieving closed loop tracking with the fine track systems.

The received power at the aircraft was "indicated" by the TM data to be low.

Very low temperatures were experienced in the AOCP, reaching a low of $-20°$ C $(-5°$ F$)$. It became apparent that temperatures in the airborne equipment are a sensitive function of the thrust settings on the aircraft engines. Temperature control by insertion of orifices in the aircraft cold air duct were ineffectual.

Flight No. 7

Mission was unsuccessful because of a problem in the ground station which prevented any kind of tracking with the telescope mount. Troubleshooting of the problem was actively underway during the time that the aircraft was over station, but without successfully making a fix. The problem was later traced to the I/O hardware in the SCC-4700 computer.

Flight No. 8

Flight results were generally similar to Flight No. 6. Acquisition and coarse tracking went extremely well with very long, unbroken periods of coarse tracking taking place both onboard the aircraft and at the ground station; however, there was again a failure to achieve closed loop tracking with the fine track systems.

Since the weather was quite good and the AOCP temperature stabilized at 22° to 24° C, there apparently existed a fundamental problem in the system. As a result, the airborne equipment was removed from the aircraft and shipped to MSFC for extensive testing.

As in Flight No. 6, coarse tracking at both ends was reliable, but only very brief intermittent fine tracks were obtained. Again, TM, measurements of received laser power pointed to a marginal, or below minimum, beacon laser power level.

Flight No. 9

The flight was partially successful since many periods of fine track were experienced at both the aircraft and ground station terminals.

Closed-loop fine tracking was achieved many times during the flight, with the longest period consisting of approximately 20 consecutive seconds. Cumulatively, there were several minutes of closed loop fine tracking.

Fine track at the aircraft terminal occurred frequently throughout the flight, with the longest periods lasting 60 consecutive seconds without loss of TAR PRES signal. Cumulatively, there was over 30 min of fine track at the aircraft terminal.

For the first time, commands were transmitted from the ground station over the argon beacon laser beam and faithfully executed by the flight package.

There were several indicators that the atmospheric transmission was poor over the ground station-aircraft path and this undoubtedly lessened the chances for a fully successful flight.

Typical tracking stabilities achieved during the flight were (1) Ground Terminal: Coarse (GBAA) 0.87 mr peak-to-peak, Fine (Transfer mirror) 25 μr peak-to-peak; and (2) Aircraft Terminal: Coarse (gimbal mirror) 250 μr peak-to-peak, Fine (beam steerers) 30-40 μr peak-to-peak. Boresight problems with the He-Ne laser onboard the aircraft were revealed for the first time; while in closed-loop track, the received red laser power level was very low.

Flight No. 10

The mission failed because a circuit breaker failure in the airborne equipment prevented applying power to the AVLOC system.

Flight No. 11

The flight failed when the airborne He-Ne laser would not turn on.

Flight No. 12

      A successful flight with extended periods of closed loop tracking obtained for the first time. Coarse tracking went well at both ends from the start of the mission. About 30 min into the flight, the AOCP fine tracker began to stay locked in for extended periods, but the received red laser light at the ground station was extremely dim as a result of a boresight error (approx. 0.5 mr) in the AOCP transmit channel. After removal of a ND filter from in front of the ground station tracking detector, the tracker sensitivity was increased sufficiently to track on the very low level received red laser power. Thereafter, prolonged periods of closed loop tracking were obtained. Specifically, during the last 50 min of the mission, there were over 50 segments of extended closed loop tracking, with a cumulative closed loop time of over 15 min and individual segments as long as 180 consecutive seconds. Tracking errors (rms) of approximately 5 μrad were obtained and the beacon laser power received at the AOCP was significantly increased when the air to ground tracking loop was closed.

Boresight adjustments were remoted to the cockpit for the next flight.

Flight No. 13

      Flight failed when the airborne He-Ne laser would not turn on.

Flight No. 14

      Flight was unsuccessful because of irregularities in the airborne tracker. With considerable effort, fine track could be achieved very briefly, but not maintained. Postflight checkout traced the trouble to a bias voltage problem in one of the beam-steerer circuits.

Flight No. 15

      As in Flight No. 12, relatively long periods of closed loop tracking were obtained once again. Flight TM revealed that the AOCP tracker errors were degraded on this flight, running typically 30 arc-seconds peak-to-peak. TM data shows also that the received beacon laser power level was rather low (typically 2.0 V) throughout the flight (a beacon laser-modulator alignment for optimum power could not be obtained on this night) and this was a likely con-tributing factor to the poor tracking performance. It was noted that tracking performance appeared to be most reliable at an AOCP temperature of 13° C and that performance improved when the AOCP heaters were turned off,

indicating a power overload problem. Extended periods of closed loop tracking were also obtained with the beam steerers off, including one long segment of nearly a full orbit.

A highlight of this particular flight was the success achieved in bore-sighting the downlink He-Ne laser beam. By requesting the aircraft operator to remotely adjust the boresight, and then noting the photomultiplier tube (PMT) current increase/decrease in the GS transceiver, the received red laser power could be peaked up rather accurately and easily. It was also discovered that when the AOCP temperature varied by a few degrees, the bore-sight required readjustment. As a result of this boresight adjustment capa-bility, there was a considerably higher red laser power level available for tracking on this flight than for No. 12.

Another highlight of this flight was the successful closed-loop tracking of the target aircraft as it passed over a thin cirrus cloud; the received laser power could be seen to decrease significantly at the leading edge of the cloud and then increase again at the trailing edge.

Uplink command communications over the beacon laser beam were executed routinely, but downlink communications failed because of a low modulation index. There was just enough modulation present on the downlink to notice video pattern differences when switching from one mode to another, such as from bit error to TM.

PROPAGATION EXPERIMENTS

Introduction

The principal objectives of the AVLOC test were the engineering evalua-tion of an operational optical communications system and the scientific inves-tigation of optical propagation over vertical paths through the atmosphere. To fulfill the second objective extensive measurements of scintillation, bit error rates (BER), angle of arrival fluctuations and atmospheric attenuation were planned. Each of these quantities was to be investigated as a function of receiving and transmitting aperture, range and zenith angle, and all measure-ments except BERs were to be made on both uplink and downlink beams. Since the AVLOC tests were to extend over the period of a year it was also expected that seasonal variations in propagation characteristics and the effects of meteorological conditions could be studied.

Table 40, reproduced from the original measurements plan, lists the proposed propagation experiments.

TABLE 40. MEASUREMENTS OUTLINE

Quantity Measured	Parameters	Analysis to Yield

Scintillation (downlink)	Receiving Aperture
	Range
	Zenith Angle
		Log amplitude variance.
		Probability density function.
		Verify theoretical predictions concerning zenith angle, and range dependence.
		Aperture averaging effects:
		  a. Reduction of signal variance.
		  b. Change of probability density function.
		Difference in uplink and downlink.

Scintillation (uplink)	Receiving Aperture Range Zenith Angle Transmitter Aperture	Log amplitude variance. Probability density function. Verify theoretical prediction concerning zenith angle and range dependence. Verify no uplink aperature averaging. Effect of transmitting aperture size. Differences in uplink and downlink.
Angle of Arrival Fluctuations (downlink)	Range Range Zenith Angle Receiving Aperture	Variance. Probability density function. Aperture averaging. Dependence on range and zenith angle. angle. Differences between uplink and downlink.
Angle of arrival Fluctuations (uplink)	Range Zenith Angle	Variance. Probability density function. Dependence on range and zenith angle. Differences between uplink and downlink.
BER	Range Zenith Angle Beam Divergence Transmitter Power	Verify theoretical prediction of BER dependence on system noise and irradiance fluctuation variance.
Atmospheric Transmittance	None	Atmospheric transmittance at optical wavelengths.
Engineering Measurements		Determine ability to acquire and track. Evaluate system performance.

336

Early in the project's design phase it was realized that certain of these measurements presented greater experimental difficulties than had been anticipated. For example, accurate measurements of atmospheric transmission requires a precisely calibrated detector on the aircraft to monitor transmitted power and an exact knowledge of the beam profile. It soon became apparent that it would be very costly to implement a meaningful transmission measurement. Since funds were limited this experiment was eliminated from the measurements plan. Likewise, it was decided that meaningful measurement of the angle of arrival fluctuations would impose excessive requirements on the accuracy of the tracking system and these experiments were also eliminated. Thus at the beginning of the operational phase of the project the planned measurements consisted of uplink scintillation, downlink scintillation, BERs and a qualitative investigation of the effect of atmospheric attenuation.

Equipment problems during the early flights severely limited the amount of time available for data collection and prevented the completion of even the reduced measurements program. Useful data was collected only on flight nos. 9, 12, and 15 and during these flights the system was fully operational only part of the time. It was, therefore, impossible to conduct extensive investigation into the effect of transmitter and receiver aperture size nor could BER measurements be made. Because of the extremely low level of the downlink received power, the data amplifiers were not operating in a linear signal region. This faction led to measured data which were not suitable for extensive analysis of downlink scintillation.

In summary, reliable data has been obtained only for the uplink scintillation experiments although some qualitative information concerning atmospheric transmission is also available.

Data Collected

The following is a summary of the experimental data collected aboard the aircraft and at the ground station.

AIRCRAFT DATA

The data collected aboard the aircraft is shown in Table 41. All data was recorded on magnetic tape.

TABLE 41. AIRCRAFT DATA

Tape Channel	Quantity
1	Image Disector Error, Y component
2	Image Disector Error, Z component
3	Beam-Steerer Angle, Y component
4	Beam-Steerer Angle, Z component
5	Vibration, Pitch
6	Vibration, Yaw
7	Vibration, Longitudinal
8	Log Amplitude Scintillation
9	Linear Amplitude Scintillation
10	PAM DATA

The ID errors (channels 1 and 2) are error voltages generated in the tracking system that are proportional to the angle of arrival of the incoming beam. The beam-steerer angles (channels 3 and 4) are the voltages applied to the beam steerers. Vibration data (channels 5 through 7) were obtained from three vibration sensors mounted along mutually orthogonal axes on the airborne communications package. Linear amplitude scintillation (channel 9) is the instantaneous received power at the aircraft while log amplitude scintillation (channel 8) is the same signal after passing through a longarithmic amplifier. Channel 10 (PAM data) consists of a number of measurements that were made periodically and multiplexed onto a single channel for recording. The PAM data is listed in Table 42. A complete description of the way in which this data was obtained can be found in the system description elsewhere in this report.

Data Reduction

AIRCRAFT DATA

SELECTION OF DATA SLICES

Data was recorded on analog magnetic tape throughout the entire time that the WB-57 aircraft was over station. Oscillograms were first made from the analog tapes and inspected to determine those periods during which uninterrupted power was being received at the aircraft and the airborne tracking system was operating normally. Based on this inspection time slices were selected for further processing.

338

TABLE 42. PAM DATA

VCO Channel	Data	Quantity Recorded
3	Beacon Presence	ON/OFF
4	TV Filter	OUT/IN
5	Receiver Aperture	OUT/IN
6	Beam Divergence	Arc Seconds
7	Laser Shutter	OUT/IN
8	Tracker Attenuation	Position
9	Receiver Attenuation	OUT/IN
10	Fine Track	ON/OFF
11	60 Hz Power	Voltage
12	400 Hz Power	Voltage
13	28Vdc unregulated	Voltage
14	28Vdc regulated	Voltage
15	5Vdc	Voltage
16	15Vdc	Voltage
17	AOCP Temperature	°C
18	Canister Temperature	°C

ANALOG/DIGITAL CONVERSION

Selected data was digitized and recorded on digital magnetic tape for computer processing. A sampling rate of 2000 samples/sec was used to provide an upper frequency cutoff of 1 kHz. The quantization level of 1024 (10 bits/sample) was used to accommodate the required 60 dB dynamic range.

PROBABILITY DENSITY AND MOMENTS

The probability density function (PDF) and cumulative distribution function is computed for each channel of the selected data slices. Based on the PDF, the first four central moments, i.e., mean, variance, third moment and fourth moment are computed. Next, the skewness and kurtosis are computed from these moments. For normal (gaussian) distribution, the kurtosis will be equal to three and skewness equal to zero

TEST FOR NORMALITY OF PROBABILITY DISTRIBUTION

The fact of kurtosis being equal to three and skewness being zero is not enough to establish the normality of any distribution. At best it is only a quick check. The standard statistical test for goodness-of-fit for normality is the chi-square test. This is a one-way test giving the upper confidence limit for any prescribed level of significance. One problem in using the chi-square test is the choice of the class number and class limits for the PDF, since it is known that different choices may yield different results. A procedure for minimizing the subjectiveness has been proposed by Mann and Wald (ref. 8,9). This procedure computes the number of classes based on the number of data points used and the desired level of significance. Further, the corresponding class limits are chosen in such a way that the theoretical distribution under test in each class interval is equal. The Mann-Wald procedure is used in the present data processing.

POWER SPECTRAL DENSITY (PSD)

The fast Fourier Transform (FFT) is used for computing the PSD of the data channel of interest. The particular version for the PSD employed in this study is based on time averaging over short, modified periodograms obtained by the FFT (ref. 10). Further, use is made of the complex-conjugate relationship of the FFT for real time series, so that two real data series can be transformed simultaneously in order to cut the required computation time approximately in half (ref. 11).

CORRELATION COEFFICIENT

To determine quantitatively the degree of dependence between any two data series, the correlation coefficient is computed. It is defined as the normalized time-lagged product between the given two random time series of interest. Its value should be within ± 1.

SUMMARY OF DATA RECORDED

Useful data was obtained only on flights 9, 12, and 15. The data segments that were digitized and processed are listed in Tables 43, 44, and 45.

TABLE 43. AVLOC FLIGHT 9 AIRCRAFT DATA

Data Piece No.	A/D Time (Seconds)
2	15
3	10
4	50
5	20
6	10
7	30
8	40
9	10
10	10
11	20
12	50
13	30
14	30
15	20
16	50
Total Time	395 seconds

TABLE 44. AVLOC FLIGHT 12 AIRCRAFT DATA

Data Piece No.	A/D Time (Seconds)
1	200
2	70
3	100
4	190
5	80
6	80
7	100
8	200
9	70
10	190
11	80
12	100
13	
14	
Total	1,460 Seconds

TABLE 45. AVLOC FLIGHT 15 AIRCRAFT DATA

Data Piece No.	A/D Time (Seconds)
1	26
2	30
3	60
4	30
5	30
Total Time	176 sec

Data Analysis

UPLINK SCINTILLATION

The uplink scintillation was measured by a tracking photodetector in the AOCP which measured the instantaneous received power. The photodetector output was recorded in three modes; linear, logarithmic, and base band. The base band channel consisted of direct recording of the detector output. To avoid the effects of background radiation the uplink beacon was modulated at 10.7 MHz, and the amplitude of this frequency component recorded (linear channel). The 10.7 MHz signal was also passed through a log-amplifier before recording (logarithmic channel). Inspection of the data has shown that the amplitude scintillation was so large that the linear range of both the linear and base band channels was exceeded. The logarithmic channel was well within the dynamic range of the system. For this reason we have based all analysis on the logarithmic channel data.

The available data consist of 15 segments from flight 9, 14 segments from flight 12, and 3 segments from flight 15 as indicated in Tables 43, 44, and 45. At least one 10 second segment was selected from each data piece for analysis. The reduced flight data are available in Reference 17.

LOG NORMALCY

According to the most generally accepted theory of atmospheric turbulence, amplitude scintillation is expected to follow a log-normal probability distribution, i.e., the logarithm of the amplitude fluctuations should be a

gaussian random variable. To test this hypothesis three statistical techniques were used, the method of moments, the chi-square test, and plots of the cumulative probability of the log and linear scintillation on "probability paper." In the last method the horizontal coordinate scale is such that if the data is indeed normal the resulting plot will be a straight line. Plots for the log and linear recordings of a typical data segment are shown in Figures 174 and 175. Other data segments yielded essentially similar results.
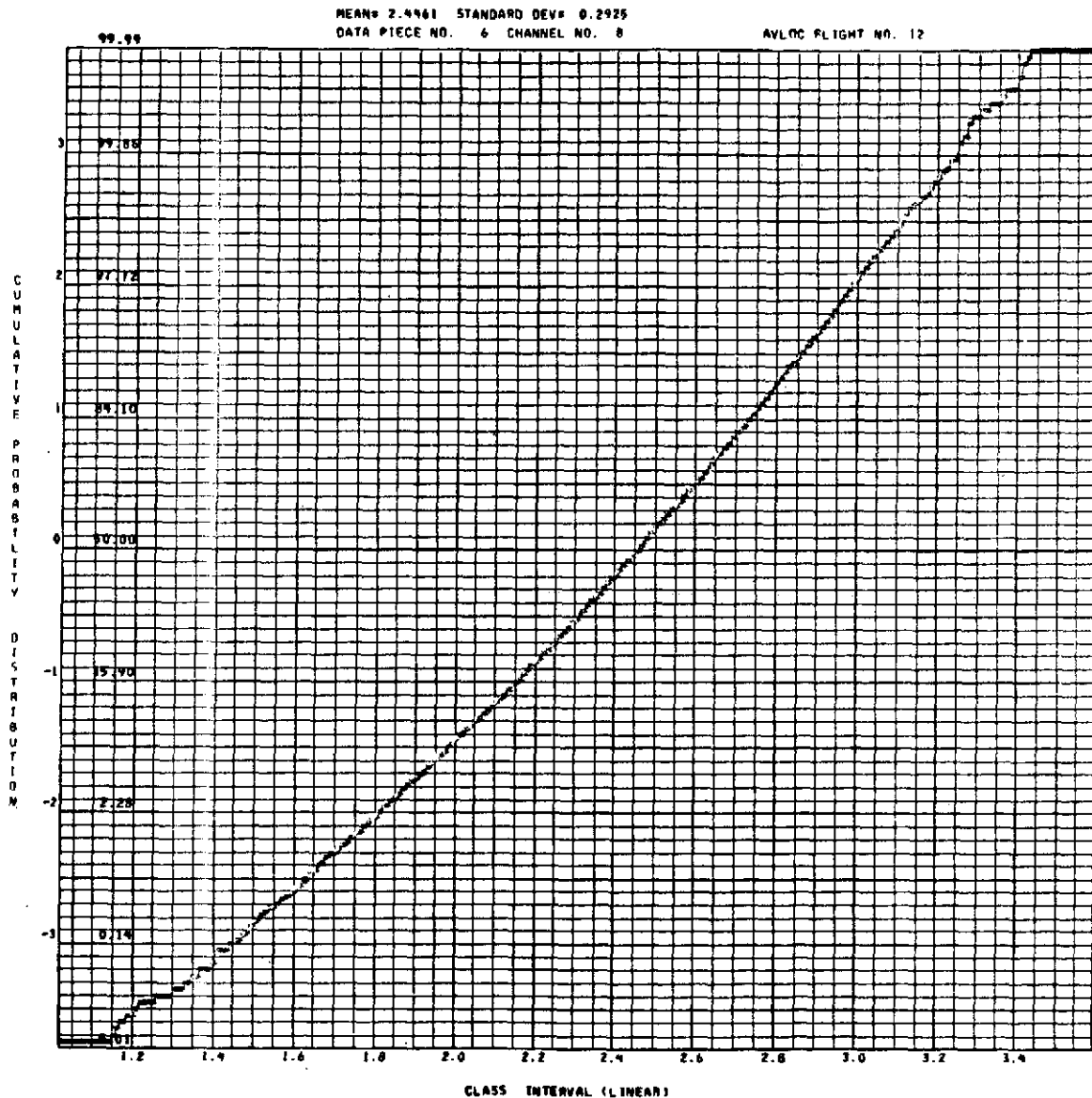
Figure 174. Cumulative probability distribution of the uplink log amplitude scintillation.
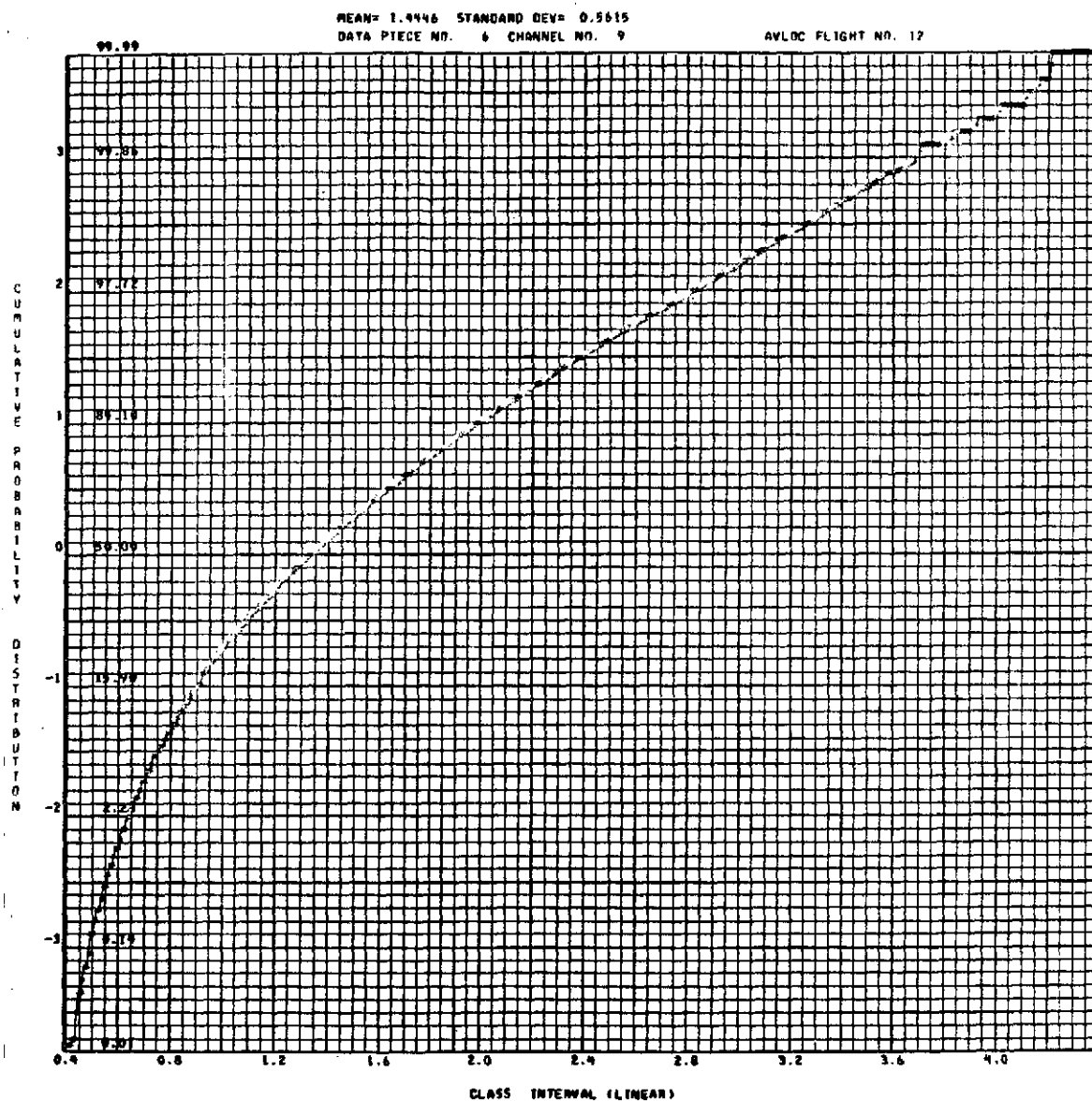
Figure 175. Cumulative probability distribution of the uplink
linear amplitude scintillation.

Inspection of the probability distribution curves and the statistical
moments indicates that in all cases the observed scintillation more nearly
approximated a log-normal distribution than a gaussian. The goodness-of-fit
to the log-normal distribution was moderately good. There was a general
trend for the fit to become worse as the amplitude variance increased. We have

344

carefully considered all possible sources of experimental error that might bias the observed probability distributions; a discussion of the possible sources of error is given in the following section. Although we have been unable to identify any single error that could be expected to cause the observed discrepancy with log-normalcy it is still possible that the effect might be due to the accumulation of errors from several sources.

In summary, the observed data shows a strong tendency toward log-normalcy. On the basis of the observed data we are unable to determine with certainty whether the observed departure from the expected distribution is due to experimental error or represents a real deviation of the propagation process from the theoretically predicted result.

AMPLITUDE VARIANCE

As previously stated the base band and linear scintillation data showed saturation effects because the dynamic range of the signal exceeded the linear range of the recording channel. For this reason we have taken the variance from the log scintillation channel only.

It is convenient to convert the variance of the logarithmic signal to intensity variance. This may be accomplished as follows. We assume that the log channel output is a voltage V which is related to the received intensity I by

$$V = \alpha \ln I + \gamma \quad . \tag{126}$$

Likewise, the output of the linear channel S is given by

$$S = \beta I \quad , \tag{127}$$

where α, β and γ are constants that depend upon the amplifier gains in the two channels. Solving equation (126) for I we have

$$I = \exp \frac{V - \gamma}{\alpha} \quad , \tag{128}$$

hence,

$$S = \beta \exp\left[\frac{V - \gamma}{\alpha}\right] \qquad (129)$$

or

$$S = \exp\left[\frac{V - \gamma}{\alpha} + \ln\beta\right] \quad . \qquad (130)$$

We may replace the quantity $- \gamma/\alpha + \ln\beta$ by a new constant δ, so

$$S = e^{\delta} \cdot e^{V/\alpha} \quad . \qquad (131)$$

Now let S_0 be the mean value of S;

$$S_0 = e^{\delta} \langle e^{\gamma/\alpha} \rangle \quad . \qquad (132)$$

The variance of S is

$$C_s = \langle (S - S_0)^2 \rangle \quad , \qquad (133)$$

$$C_s = \langle (e^{\delta} e^{V/\alpha} - e^{\delta} \langle e^{V/\alpha} \rangle)^2 \rangle \quad , \qquad (134)$$

$$C_s = e^{2\delta} \langle e^{V/\alpha} \rangle^2 \left\langle \left(\frac{e^{V/\alpha}}{\langle e^{V/\alpha} \rangle} - 1\right)^2 \right\rangle \quad . \qquad (135)$$

Now we assume that I is log normal, hence V is a gaussian random variable. For any gaussian random variable X (ref. 12),

346

$$\langle e^{ax} \rangle = \exp\left[a\langle x \rangle + \frac{a^2}{2} \langle (x - \langle x \rangle)^2 \rangle \right] \quad , \qquad (136)$$

$$\langle e^{ax} \rangle = \exp\left[a\langle x \rangle + \frac{a^2}{2} Cx \right] \qquad (137)$$

$a = $ a constant. Hence,

$$\langle e^{v/2} \rangle = \exp\left[\frac{\langle V \rangle}{\alpha} + \frac{CV}{2\alpha^2} \right] \qquad (138)$$

$$C_s = e^{2\delta} \langle e^{v/\alpha} \rangle^2 \left\langle \frac{e^{2v/\alpha}}{\langle e^{v/2} \rangle^\alpha} - 2 \frac{e^{v/\alpha}}{\langle e^{v/\alpha} \rangle} + 1 \right\rangle \qquad (139)$$

$$C_s = S_0^2 \left\langle \frac{e^{2v/\alpha}}{\langle e^{v/\alpha} \rangle^2} - 2 \frac{\langle e^{v/\alpha} \rangle}{\langle e^{v/\alpha} \rangle} + 1 \right\rangle \qquad (140)$$

$$C_s = S_0^2 \left[\frac{\langle e^{2v/\alpha} \rangle}{\langle e^{v/\alpha} \rangle^2} - 1 \right] \quad . \qquad (141)$$

Then using the above relationship

$$C_s = S_0^2 \left[\frac{\exp \frac{2\langle V \rangle}{\alpha} + \frac{2Cv}{2}}{\exp 2\frac{\langle V \rangle}{\alpha} + \frac{Cv}{2\alpha^2}} \right] - 1 \qquad (142)$$

$$C_s = S_0^2 \left[\exp\left(\frac{Cv}{\alpha^2} \right) - 1 \right] \quad , \qquad (143)$$

or introducing the standard deviations σ_s and σ_r in place of the variances

$$\sigma_s = \sqrt{C_s} \qquad \text{and} \qquad \sigma_v = \sqrt{C_v} \qquad (144)$$

we finally obtain,

$$\sigma_s/S_0 = \left[e^{(v/\alpha)^2} - 1 \right]^{1/2} . \qquad (145)$$

But since

$$\sigma_s = \beta\sigma_I \qquad (146)$$

and

$$S_0 = \beta I_0 \qquad (147)$$

$$\sigma_I/I_0 = \left[e^{(\sigma v/\alpha)^2} - 1 \right]^{1/2} \qquad (148)$$

which is the required expression for the normalized standard deviation of the intensity fluctuations.

The one remaining constant in equation (145) and (148) can be evaluated from the calibration curve of the scintillation detector. Based on post flight calibration data, α has been found to be 0.532 volts.

Table 46 gives the log variance C_v and the normalized intensity variance σ_I/I_0 for each data segment. The mean and standard deviation of (σ_I/I_0) for each flight is given in Table 47.

348

TABLE 46. MEAN AND VARIANCE FOR LOG SCINTILLATION (UPLINK)

Flight	Data Piece No. a.	Mean V_0	Standard Deviation σv	Normalized Intensity Standard Deviation σ_I/I_0
9	2	3.114	0.332	0.690
9	3	3.139	0.325	0.673
9	4A	3.185	0.320	0.660
9	4B	3.206	0.329	0.683
9	5	3.097	0.282	0.566
9	6	3.147	0.344	0.720
9	7	3.129	0.298	0.607
9	8A	3.028	0.198	0.385
9	8B	3.038	0.198	0.385
9	9	3.307	0.312	0.641
9	10	3.077	0.307	0.629
9	11	3.153	0.330	0.685
9	12A	3.140	0.326	0.675
9	12B	3.094	0.276	0.556
9	13A	3.090	0.143	0.274
9	13B	3.085	0.151	0.290
9	14	3.271	0.302	0.617
9	15	3.114	0.289	0.586
9	16	3.068	0.308	0.631
12	1	2.776	0.315	0.648
12	2	2.689	0.434	0.972
12	3		0.433	0.944
12	4	2.650	0.380	0.816
12	5	2.743	0.401	0.874
12	6	2.446	0.293	0.595
12	7	3.549	0.428	0.493
12	8	2.955	0.422	0.936
12	9	2.966	0.334	0.695
12	10	2.774	0.335	0.698
12	11	0.191	1.588	8.605 b.
12	12	Missing		
12	13	0.189	1.773	25.813 b.
12	14	3.0468	0.426	0.948
15	1	3.116	0.424	0.942
15	2	2.976	0.479	1.118
15	3	3.021	0.499	1.188
15	4	Missing		
15	5	Missing		

a. A and B indicate two 10-sec segments taken from the same data piece.
b. These data not used.

349

TABLE 47. AVERAGES FOR INDIVIDUAL FLIGHTS

	Average	Standard Deviation (SD)
Flight 9		
Mean	3.130	0.070
Normalized SD	0.576	0.134
Flight 12		
Mean	2.859	0.283
Normalized SD	0.767	0.156
Flight 15		
Mean	3.038	0.058
Normalized SD	1.083	0.103

The quantities shown in Table 47 are the mean and standard deviation (SD) of the received power and hence are proportional to the mean and SD of irradiance. The SD of power is in fact equal to the SD of irradiance because of the normalization. Most theoretical results, however, are expressed in terms of the log amplitude variance C_1. This quantity is easily obtained from the data as follows. C_1 is defined as

$$C_1 = \left\langle (1 - \overline{1}) \right\rangle^2 \tag{149}$$

where 1 is the log amplitude

$$1 = \ln(A/A_0) = 1/2 \ln(I/I_0) \quad . \tag{150}$$

Making use of equation (126) and the definition of C_V

$$C_V = \left\langle (V - \overline{V}) \right\rangle^2 \quad , \tag{151}$$

we have

$$C_v = \left\langle \left(\alpha \ln \frac{I}{\delta} - \left\langle \alpha \ln \frac{I}{\delta} \right\rangle \right)^2 \right\rangle \qquad (152)$$

which upon expanding the square and collecting terms becomes

$$C_v = \alpha^2 \left\langle \left(\ln I - \left\langle \ln I \right\rangle \right)^2 \right\rangle . \qquad (153)$$

Likewise,

$$C_i = 1/4 \left\langle \left(\ln I - \left\langle \ln I \right\rangle \right)^2 \right\rangle ; \qquad (154)$$

hence,

$$C_i = \frac{1}{4\alpha^2} C_v . \qquad (155)$$

Using this expression we may calculate the log amplitude variance and corresponding SD from the variance of the signal voltage V. The results for each flight are given in Table 48.

The observed scintillation variances are of the order of magnitude that one would expect from atmospheric propagation theory and in general agreement with other experimental data. Minott, Bufton and Fitzmaurice [1] report an average C_1 of 0.18 for data collected during the GSFC BAPE I. This is in good agreement with the AVLOC value of 0.13.

Propagation theory predicts that for an infinitely small source the log amplitude variance is given by [1]

$$C_1(0) = .56k^{7/6} \int_0^Z ds \; C_n^2(S)[(Z-S)\left(\frac{S}{Z}\right)]^{5/6} \qquad (156)$$

351

TABLE 48. LOG AMPLITUDE VARIANCE

Flight 9 $\sigma_l = .2873$ $C_l = .074$	SD $(\sigma_l) = 0.59$
Flight 12 $\sigma_l = .3819$ $C_l = .133$	SD $(\sigma_l) = 0.051$
Flight 15 $\sigma_l = .4673$ $C_l = .190$	SD $(\sigma_l) = 0.032$
Average all Flights $C_l = .132$	

where Z is the source to receiver distance measured along the propagation path, k is the propagation number and C_N^2 (s) is the index of refraction structure constant which expreses the strength of turbulence at each point along the propagation path. A model of the turbulent atmosphere proposed by Hugnagel [14] and Stanley [13] predicts that C_N^2 (h) will be given by

$$C_N^2 (h) = C_{N_0}^2 h^{-1/3} e^{-h/h_0} \tag{157}$$

where h_0 is a scale factor usually taken to be 1000 m, h is attitude, and $C_{N_0}^2$ is a constant that expresses the gross turbulence strength. Both $C_{N_0}^2$ and h_0 depend strongly upon local meteorological conditions. It is generally agreed that while equation (157) predicts the gross variation of C_N^2 with altitude, the actual turbulence structure is layered and shows strong local fluctuations not predicted by this model. These turbulence layers are associated with wind shears in the upper atmosphere and often occur near the tropopause. For these reasons a proper analysis of log amplitude variance would require a knowledge of the turbulence profile obtained independently of the optical measurement. Such data could be obtained from radiosonde-borne micro-thermal probes but was not available during the AVLOC test.

352

Equation (156) must be corrected for the finite source diameter of the laser beam and for aperture averaging effects at the receiver. Fried [15] has shown that this correction depends on the normalized source size

$$\Omega = \frac{k\alpha_0^2}{h_0} \sec \theta \qquad (158)$$

where α_0 is the real part of the complex gaussian beam parameter and θ is the zenth angle. Once Ω has been computed the required correction can be obtained from curves in the quoted reference.

Fried [16] has investigated the effects of aperture averaging and found that the signal variance is given by

$$\sigma_S^2 = 2\pi \int_0^D p dp \, K_\theta \, (\rho_1 D) \, C_I \, (\rho) \qquad (159)$$

where D is the receiver aperture diameter, C_I the intensity covariance at the receiver and K_θ the diffraction-limited optical transfer function of the receiver. From equation (158) one may compute an averaging function θ which is the ratio of the observed signal variance to the signal variance in the absence of aperture averaging. For an infinite plane wave propagating from space to earth one finds that θ depends on the turbulence strength C_1 (0) and a normalized aperture

$$D/ \sqrt{4h_0 \sec \theta /}_k \qquad (160)$$

For our test condition Fried's results indicate that θ will be greater than 0.9. This theory is not strictly applicable to the AVLOC test for these reason: There is a gaussian beam wave, not a plane wave; the propagation direction is from earth to space, and it neglects the effect of the central obscuration in the Cassegrainian receiving telescope. Nevertheless, Fried's results should provide an estimate of the magnitude of the aperture effects. Clearly this effect is small, probably less than the probable error in the data, and can be neglected.

353

Because of the lack of precise knowledge of the turbulence profile that existed during the AVLOC test and the absence of a theory of aperture averaging that is applicable without extensive modification, we have not undertaken a precise comparison of the observed log amplitude variance with those predicted by theory. However, using Hufnagel's model with the usual choice of h_0 and $C_{N_0}^2$, equation (156) predicts values of $C_1(0)$ on the order of 0.1 which is in relatively good agreement with the observed amplitude variances.

POWER SPECTRAL DENSITY

Power spectral density (PSD) is defined as the Fourier transform of the irradiance covariance function and is equivalent to the average received power per unit bandwidth at each frequency. The PSD's have been computed for each data segment. A typical PSD is shown in Figure 176. The PSD's from other data segments were essentially similar.

All PSD's showed a more or less linear decrease with increasing frequency from a few Hertz to 1000 Hz, the latter value being the maximum frequency component obtainable with the selected sampling rate. In all cases the power density decreased about one order of magnitude at 100 Hz and two orders of magnitude at 1000 Hz.

MEASUREMENT ACCURACY

Although the observed scintillation data tended strongly toward a log normal distribution the lack of strict log normalcy has caused some concern that the data may be biased by extraneous noise. All apparent sources of extraneous noise that might contribute to the observed scintillation has been considered and it has been concluded that none could reasonably be expected to account for this effect. Each of the possible sources of experimental error is discussed in the following paragraphs.

Detector Noise

The power signal to noise S/N ratio in the detector can be estimated from the PMT parameters. S/N is given by

$$S/N = \frac{(i_s)^2}{(i_{N_1})^2 + (i_{N_2})^2} , \qquad (161)$$

354

where $\left(i_s\right)^2$ is the mean square detector current due to the signal, $\left(i_{N_1}\right)^2$ is that due to the shot noise in the PMT, and $\left(i_{N_2}\right)^2$ is that due to the Johnson noise in the load resistor. As usual $\left(i_{N_2}\right)^2$ may be neglected since both the signal and shot noise terms are multiplied by the square of the tube gain and the Johnson noise term is not. Now,

$$i_S = \frac{GPe\eta}{h\nu_s} \, (2m) \, \cos \omega_m t \tag{162}$$

where

G = PM gain,

η = quantum efficiency,

e = electronic charge,

P = received signal power,

h = Plank's constant,

ν_s = signal frequency,

m = modulation index,

ω_m = modulation frequency,

and

$$\left(i_{N_1}\right)^2 = 2G^2e\left(i_c + i_d\right) \, \Delta\nu \quad , \tag{163}$$

i_c = current due to incident radiation

i_d = dark current

$\Delta \nu$ = post detection bandwidth

$$i_c = Pe\eta/h\nu_s \qquad .$$

Therefore,

$$S/N - \frac{i_c{}^2 m^2}{e(i_c + i_d) \Delta\nu} \qquad . \tag{164}$$

where a factor of 2 has been introduced from the time average of $(i_s)^2$ we we assume the following parameters:

$$\eta - 15\%$$

$$I_d - 1.2 \times 10^{-9} \text{ A},$$

$$P = 6 \times 10^{-9} \text{ W},$$

$$\nu_s = 6.16 \times 10^{14} \text{ Hz},$$

$$\Delta\nu = 5 \times 10^3 \text{ Hz},$$

$$m = .3 \qquad .$$

The values of η and I_d are typical of the RCA 8644 PMT used for scintillation detection in the AOCP, P is the average power measured on all flights, and m represents a worst case (minimum) modulation index. With these values the estimated power S/N ratio is 10^5 corresponding to a voltage S/N ratio of approximately 300.

The shot noise induced by background radiation has been neglected in the preceding calculations since all tests were conducted at night.

356

The normalized SD of intensity (σ_I / I_0) was typically on the order of 0.5. Therefore, it follows that the observed fluctuation in the output signal due to scintillation would be approximately 150 times greater than those due to detector noise.

Amplifier Noise, Recorder Characteristics, Electrical Pickup

All data channel amplifiers and recorders were designed to accomodate the expected data without introducing either excessive noise or biasing the data by reduced bandwidth or dynamic range. Throughout the flight test the data channel amplifier and data acquisition systems appeared to operate normally; we do not believe, therefore, that they represent a significant source of experimental error.

The scintillation data, along with all other data channels, did show a weak but persistent 56 Hz component which was been identified as electrical pickup from the aircraft's (nominally) 60 Hz power system. In our estimation, however, this 60 Hz pickup was not strong enough to bias the experimental data.

Pointing

One possible source of error is false scintillation caused by pointing error. Since the beam has a gaussian rather than uniform intensity profile any pointing error is time dependent it will cause irradiance fluctuations that will be indistinguishable from scintillation. The gaussian beam profile may be expressed as

$$I = I_0 e^{-\theta/\theta_0} \tag{165}$$

where θ_0 is the angular beam width. Then the intensity fluctuation ΔI caused by a pointing error $\Delta\theta$ is

$$\Delta I = I_0 - I \approx I_0 - I_0 e^{-\Delta\theta/\theta_0} \tag{166}$$

357

or

$$\Delta I/I_0 \sim 1 - e^{-\Delta\theta/\theta_0} \tag{167}$$

A reasonable criteria is that $(\Delta I/I_0)^2$ be much less than the intensity variance due to scintillation. The observed intensity variances are on the order of 1/4 hence we might require.

$$1 - e^{-\Delta\theta/\theta_0} \quad .01 \tag{168}$$

$$e^{-\Delta\theta/\theta_0} = .99 \tag{169}$$

or

$$\Delta\theta/\theta \approx .01 \tag{170}$$

That is, the pointing error should be less than 1 percent of the beam width to insure that the error in observed variance is no more than about 2 1/2 percent. On the AVLOC test the observed pointing errors were about 5 μ rad (1 arc sec) and the beam width θ_0 was about 0.87 mrad (180 arc sec). We conclude therefore that pointing error could not cause an error of more than about 2 percent in the observed intensity variance.

The preceding analysis assumes a smooth, gaussian intensity profile. If the beam contained "hot spots", the false scintillation induced by even a small pointing error could be much worse. The possibility of this having occurred cannot be eliminated with complete certainty; however, observation of the transmitted beam has indicated that the intensity profile is smooth and free from detectable "hot spots".

As a final check on the effect of pointing accuracy, we have cross correlated the instantaneous power received at the aircraft with beam steerer voltages in the transmitter. If pointing was in fact introducing appreciable false scintillation we would expect to see a strong positive correlation. No significant correlation was found.

Aircraft-Induced Turbulence

Scintillation due to the turbulence around the aircraft is not significant because of the thinness of the turbulence layer and its proximity to the receiver. Referring to equation (171) we see that the aircraft turbulence would contribute an amount:

$$\Delta C_e(0) = .56 \, k^{7/6} \int_{Z-\Delta Z}^{Z} C_N^2(AC) \, [(Z-S(\tfrac{S}{Z}))]^{5/6} \, dS \qquad (171)$$

to the observed log amplitude variance. Clearly with ΔZ small (a few meters) and the weighting function $[(Z-S)(\tfrac{S}{Z})]^{5/6}$ approximately zero $(Z \approx S)$ this term will be negligible.

Vibration

To ensure that the observed scintillation did not include vibration induced noise the vibration of the AOCP was monitored along three orthogonial axis by piezoelectro sensors. PSD's of the vibration were computed and the vibration data was cross correlated with scintillation.

The lateral vibration (yaw) showed a strong, rather sharp resonance at 10 Hz and a weaker broad resonance near 100 Hz. Above 200 Hz the vibration fell quickly to zero. The longitudinal vibration data had a single strong peak at 200 Hz. Both axes also have a number of other sharp spikes. Especially noticable are those at 55 Hz, 110 Hz, etc. which are probably related to the aircrafts 60-Hz (nominal) power frequency.

None of the features in the vibration PSD could be identified in the scintillation PSD; neither was there any significant correlation between these data. We therefore conclude that aircraft vibration has no effect on the recorded data.
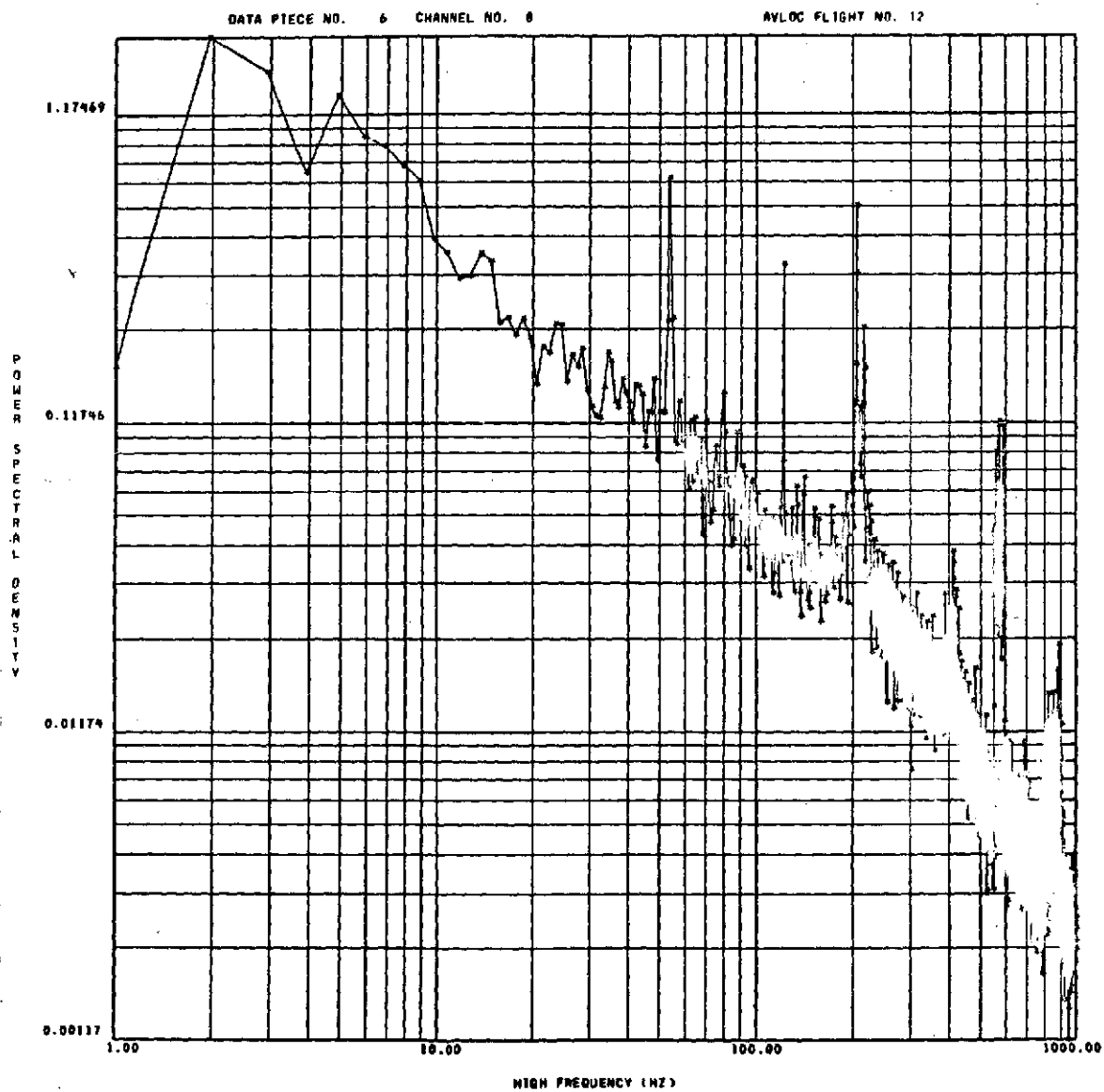
Figure 176. Power Spectral Density of Uplink Log Amplitude Scintillation.

ENGINEERING EVALUATION

Planned Measurements

In order to evaluate the system from an engineering viewpoint, both the aircraft and ground systems were instrumented to provide data in three major areas. These were: (1) Tracking systems performance, (2) Environmental and experiment conditions, and (3) Support systems conditions (power, timing, etc.). These measurements are further seen as follows:

1. Aircraft Systems

    a. tracking system performance

        (1) gimbal mirror angle Φ, Θ

        (2) beamsteerer angle By, Bz

        (3) image dissector (10) error angle Ey, Ez

    b. environmental conditions

        (1) temperatures; cannister, AOCP

        (2) vibration; yaw, pitch, longitudinal

    c. support systems

        (1) power — 60V, 400V, regulated and unregulated supplies

        (2) timing IRIG B

        (3) computer status — experiment conditions

2. Ground Systems

    a. tracking systems

        (1) coarse tracker (GBAA) error X, Y

(2) fine tracker error X, Y

(3) telescope drive error α, δ

b. experiment conditions

(1) range and ground track circle, Δ flight path geometries

(2) telescope velocities (polar and declination)

(3) tracker and receiver FOV's and aperture

The principal goal of these measurements was to provide a complete assessment of the performance of the tracking systems used in the experiment. This included measurement of the level of performance, i.e., tracking accuracies, usable signal ranges, and the overall ability of the system to meet the design requirements for proper system operation. In addition, it was necessary for these engineering measurements to provide sufficient data to allow a thorough assessment of the deficiencies, should they occur, in operation of any of the major critical subsystems. The influence of the operating environment, and its effect upon the conduct of the experiment, was considered to be of great importance. The effects of vibration, pressure, temperature, i.e., the whole of the high altitude aircraft environment and its suitability as an experiment platform, were measured.

Acquisition

GROUND SYSTEMS

During the initial design and conceptual planning of the AVLOC experiment, the initial acquisition and coarse tracking of the aircraft appeared to present the greatest degree of technical difficulty. The original concept of this system was based upon the use of a medium high power GaAs laser unit. It could be shown that this system would, in theory, have the capability to perform the required acquisition and track functions, but the margin of power available and reliability of such hardware was simply not sufficient to provide a comfortable level of confidence. Attention was then given to the investigation of pulsed argon-ion lasers as the illumination source for the system. The calculations proved that considerably greater margin of performance could be achieved with the 514.5-nm argon laser. This approach was settled upon for the final system design.

A great deal of effort was spent analyzing the optimum flight path geometries (See Appendix C) to allow the best acquisition procedure. Since the GBAA could only provide search coverage over a 10 deg × 10 deg field of view, it became necessary to direct, and ensure the flight path of the aircraft would intersect this preplanned acquisition space. At this time arrangements were made with the U.S. Army, at Redstone Arsenal, to provide assistance in tracking and providing vectoring data to the aircraft pilot. This procedure allowed the aircraft to be tracked by radar during the final 240 km (150 mi.) approach to Redstone Arsenal. The pilot was directed, by radio, to fly a prescribed flight path which would ensure the aircraft's passage through the spatial acquisition window and into the circular path over Madkin Mountain. In addition, several acquisition windows were defined to allow a quick setup for reacquisition should the pilot "miss" the window or acquisition not occur.

Contrary to preliminary assessments of this procedure, the coarse acquisition and tracking proved to be the most easily accomplished and generally most reliable procedures of the experiment. After the pilot had gained familiarity with the flight path and could correlate the acquisition windows with the flight path, several acquisitions were made without the assistance of radar vectoring.

During the early phases of activity tracking the aircraft, two problems in technique and two hardware problems arose which required immediate resolution. The problems associated with the hardware were as follows. First, during initial testing, the GBAA optical and mechanical systems were found to have a significant problem with boresite drift. There were a number of contributing factors to this situation and the problem was solved in the following manner. The pulsed argon laser was found to have a considerable angular wander of its output beam as its spatial orientation was varied. The manufacturer of the laser was consulted to provide an explanation and solution to this problem. Details of this study are presented in Appendix D. The conclusions of this effort resulted in a new suspension geometry for the laser plasma tube, and thus eliminate the problem of beam wander from the laser.

It was found at this time that there was still too great a degree of boresight change as the instrument was oriented to various attitudes. This led to an examination of the optical and mechanical mounting configuration. Two problems were discovered in this area. The stiffness of the mounting platform and optical assemblies (Beamsteerer & Image Dissector attachment brackets) was found to be insufficient. The mechanical structures were then strengthened to eliminate any significant mechanical motion between the transmit and receive channels of the GBAA. In addition, it was discovered that a lens assembly in

the beamsteerer beam-forming optics was improperly mounted and was also contributing to a shift in the pointing angle of the transmit beam. With resolution of these boresight difficulties now in hand, the operation of the acquisition system was considerably enhanced. The system was still not without its operational problems. The laser now began exhibiting a nagging problem of gas cleanup and pressure changes. It was necessary to closely monitor operation of the laser and to perform a LN_2 cooled gas cycling of the discharge tube. This procedure was eventually adopted as standard preflight procedure and thus insured reliable operation of the laser and acquisition system.

Having resolved the hardware problems with the acquisition system, a new technique in tracking operation was required. The GBAA exhibited an inherent noise level which was of the same magnitude as the required coarse pointing accuracy, approximately ± 291 μrad (± 1 arc min). A new computer software routine was written to provide a numerical filtering of the coarse pointing position data. The filtering process allowed a rapid closing during the acquisition sequence while providing a highly filtered slow response around target null. The program also allowed an updating of the boresight offset, (between GBAA and telescope boresight) during active tracking. The system would now track with the required accuracy and stability but would allow the target to be nulled and "float" slightly away from exact beacon boresight center line. A manual joystick guidance procedure was implemented as being the most practical solution to enhance the time of acquisition. Correction voltages from the manually operated joystick were summed into the computer as a high frequency response error signal, i.e., the GBAA provided a slow response average position error signal while the joystick error signals were used as fast response position corrections. This change in acquisition procedure solved the remaining operational difficulties and the procedure of acquisition, coarse tracking, and illumination of the aircraft with the ground based beacon became a reliable, routine procedure.

AIRCRAFT SYSTEMS

Although the ground station acquisition procedures became somewhat routine, the aircraft systems, designed to provide coarse tracking of the ground station, required some degree of enchancement to provide for proper operation. The primary system utilized in the aircraft coarse tracking system was a modified vidicon TV tracking system as described previously in the System Description section. During initial flights serious difficulties were encountered in attempting satisfactory coarse track performance. This difficulty led to several changes being implemented in the system. During the period of equipment checkout at MSFC in the Spring of 1972, it was discovered

that the dielectric filter used in the TV camera optical system had severely deteoriated. This deteoriation consisted of a severe shift in its optical pass-band, and only about 10 percent of its central area was of sufficient optical quality. This filter was replaced. Later the capability was added to allow the experiment operator in the aircraft to remove this filter from the optical system via a cockpit control switch. The removal of this filter allowed the system to track on both the 514.5-nm GBAA laser and the 488-nm beacon laser.

As with the ground station, there were also operational difficulties which required resolution. The TV track system provides for a 5 deg × 5 deg acquisition field. As is shown in Appendix E, this requires that the gimbal mirror be oriented properly as the aircraft's attitude changes during the flight path. Initial procedures called for the gimbal mirror to be set at a prescribed roll and pitch angle. During initial flight testing it was determined that a more flexible mode of mirror orientation was required. A joystick control was utilized to control the mirror position with the operator receiving pointing angle information from the ground operators. Even this procedure did not fully solve the long delays encountered in the coarse acquisition sequence. At this time it was decided to allow the flight computer to scan the gimbal mirror through an optimum search acquisition scan. This procedure enabled the operator to set the mirror in a rough degree of orientation and the mirror would then scan about this area until target acquisition occurred. The ability of the system to scan over large angular areas plus the capability for the system to track both 514.5-nm and 488-nm lasers enhanced operation of the system considerably. In addition, a TV monitor was installed in the operator's cockpit to allow visual monitoring and evaluation of the operation of the coarse TV tracking system. This procedure now allowed the sequence and operation of acquisition and coarse track to proceed smoothly during the final series of flights.

Aircraft Systems Performance Evaluation

This section will deal with data and degree of performance achieved with AVLOC flights series instrumentation. Information presented here was obtained primarily from flights numbered 9, 12, and 15. This and following sections will present data demonstrating performance of the system primarily from an engineering point of view.

Although no angular tracking error data were recorded from the coarse TV tracking system, its performance deserves some treatment at this point. The only information recorded from the coarse system was a status indicator

signifying when the system was in coarse track lock. It should be noted that with sufficient illumination no significant periods were found in the flight data when the coarse acquisition did not function properly. Some of the more significant parameters of interest concerning this system are boresight stability, tracking stability, and tracking sensitivity.

All of these parameters were found to indicate proper system function, and performance within the design parameter values.

FINE TRACKING SYSTEM

In discussing the aircraft's fine tracking system, several thoughts should be held in mind:

    a. The performance levels required for proper system operation

    b. Levels achieved in flight testing

    c. Difficulties encountered during flight testing

    d. Improvements made to achieve proper subsystem and system operation

The design levels of performance for the fine tracking image dissector tracker are described in detail in the Equipment Description section. Some of the more pertinent parameters bear repeating at this point:

    a. Sensitivity: 2×10^{-10} w/cm^2

    b. Tracking accuracy: 5 μ rad peak-to-peak

    c. Tracking Bandwidth: 1000 Hz

Probably the most intensive effort of this program centered upon the resolution of difficulties surrounding the operation of the fine tracking system, i.e., the image dissector tracker and beamsteerer loop. The unfortunate aspect of these problems was that all the problems associated with the fine tracking techniques were not solved until after the flight series was terminated. These difficulties were, however, fully resolved after the return of the flight hardware to MSFC in the Spring of 1973.

366

The following information outlines tracking performance achieved during the flight series under various conditions. Shown in Figure 177 is the resultant residual error being tracked by the ID. These data were taken with the beam-steerer servo loop in operation. It should be noted that these data represent the actual dynamic pointing error of the return transmitted laser beam. (Not taken into account are static and dynamic boresight errors.)
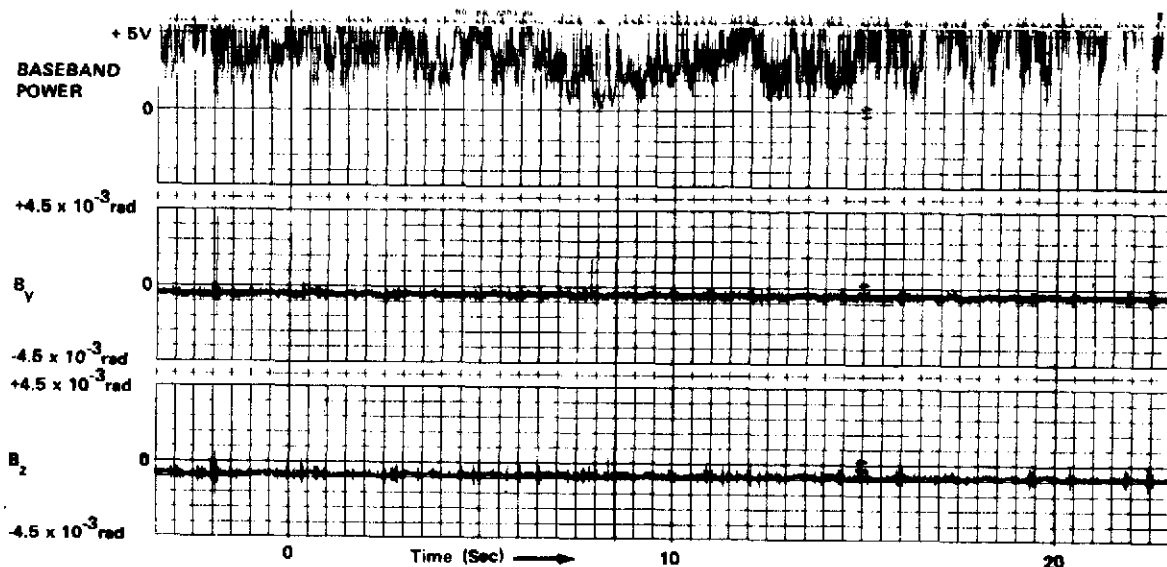

Figure 177. Beamsteerer position and received power with loop closed.

In order to appreciate the tracking environment in which the fine tracking was required to operate, probably the most informative data may be seen in Figure 178. This oscillograph section shows the fine track image motion with the beamsteerer loop turned off. The angular motion shown here consists of contributions from atmospheric disturbance, and aircraft vibration.

To determine the dynamic closing rate characteristics of the fine tracking loop (image dissector and beamsteerer) a high-speed oscillograph run was made upon the telemetry (TM) data at a point immediately after fine track lock. The data are shown in Figure 179.

These data seem to indicate a quite acceptable degree of performance of the fine tracking system. There were, however, several problems encountered with the fine track system, particularly with regard to the designed track

sensitivity and scintillation induced track instability. One problem encountered
with the fine track sensitivity was due to (as in the case of the coarse TV track-
ing system) a dielectric bandpass filter. It was determined that this filter was
actually redundant in the system and also increased the attenuation of the fine
track channel of the aircraft package. It was determined, therefore, to remove
this filter entirely and thereby enhance the systems sensitivity by approximately
a factor of two.
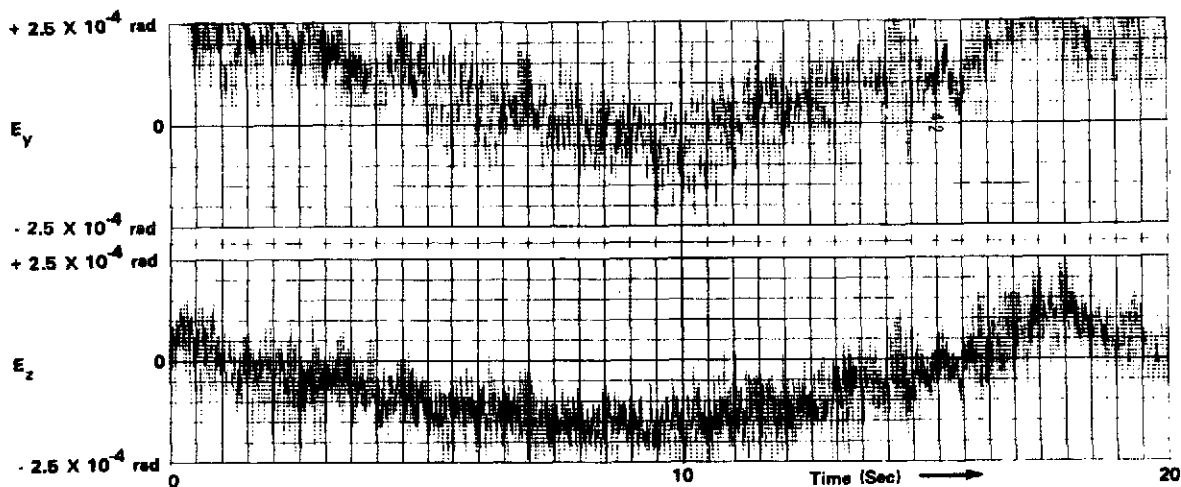
Figure 178. Image dissector error with beamsteerer loop open.
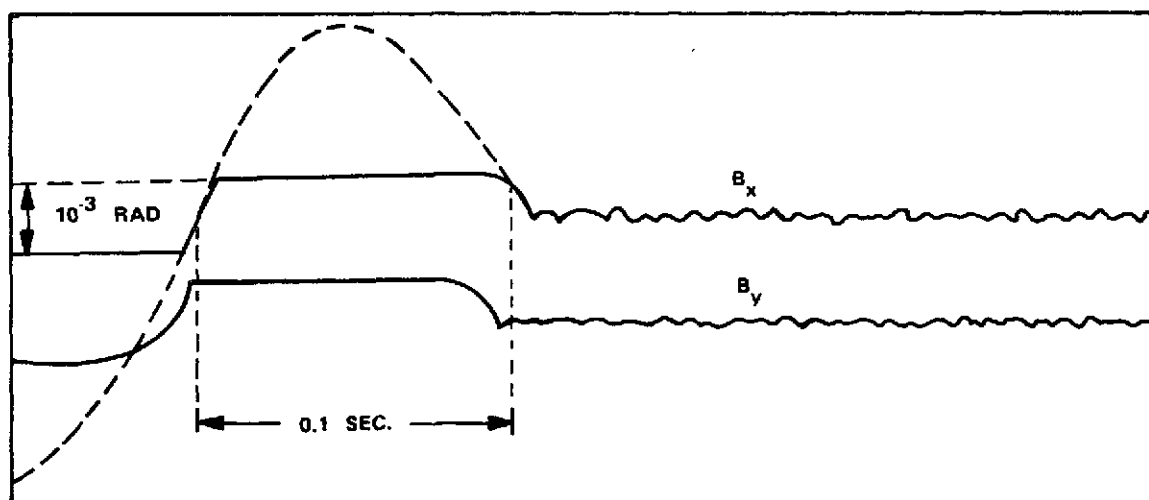
Figure 179. Beamsteerer loop settling characteristics.

One of the most severe problems associated with the fine track system was the scintillation induced tracking instability. An example of this instability is shown in Figure 180.
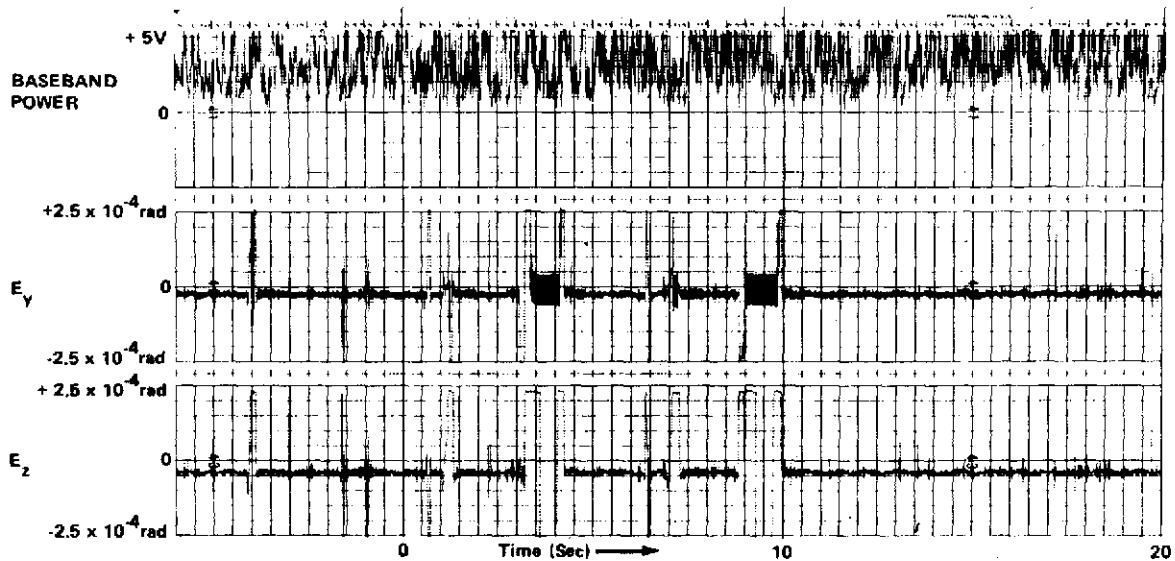
Figure 180. Image dissector error during period of scintillation dropout.

Although a more complete treatment of the solution of these problems appears later, it is considered noteworthy to mention at this point how these problems were finally solved. In short it was determined that the primary cause of the tracking instability was due to the method in which the target presence (TAR PRES) status signal was derived. When this design was changed along with a redesign of the AGC preamp, the problem of scintillation induced track instability was totally solved. It should also be noted that due to these design changes after completion of the flight series, the threshold sensitivity of the tracker was increased nearly an order of magnitude. Further flight tests should demonstrate a considerably improved level of performance with the present hardware design.

Additional data regarding the system's physical experiment conditions are shown in the following power spectral analysis performed on the aircraft TM data. Shown in Figure 181, is a typical PSD of the fine track error signals. Also shown in Figure 182 is a PSD of fine track error signals but with the beamsteerers turned off. From these two plots the relative energy

369

being tracked by the beamsteerer loop can be seen. In addition, the distribution of energy contributed by both atmosphere and aircraft environment can be seen.
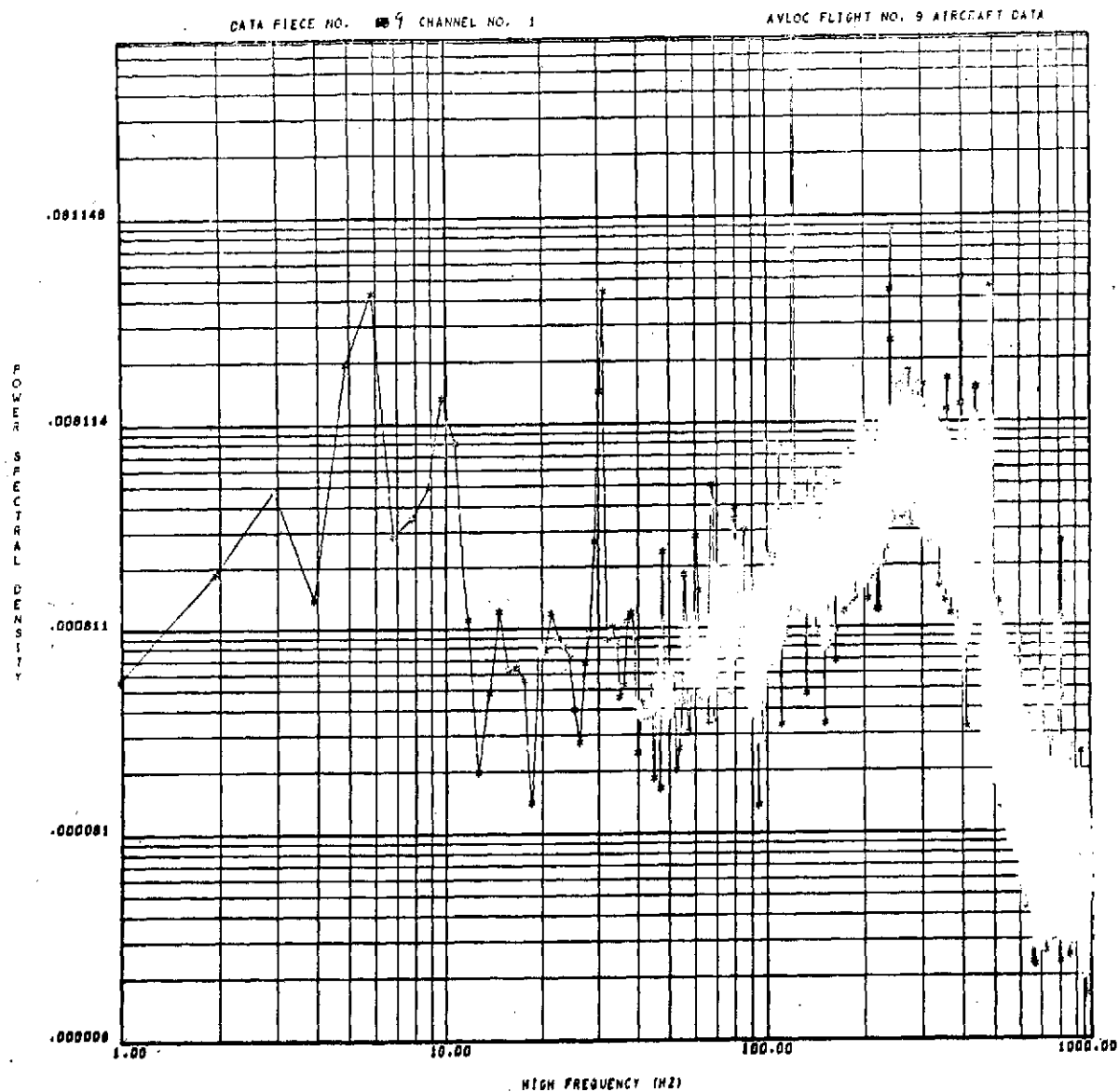

Figure 181. Image dissector error PSD with beamsteerer loop closed.

To more fully understand the aircraft environment, a treatment of the scintillation seen by the tracking system is in order. Shown in Figure 183 is

a PSD of the scintillation spectrum. This plot is typical of those seen through-
out the majority of flight data. A more complete treatment of scintillation
data is given in the Engineering Evaluation section. However, it is of interest
to note, from an engineering design standpoint, the relative distribution of
energy seen as scintillation by the tracking systems.
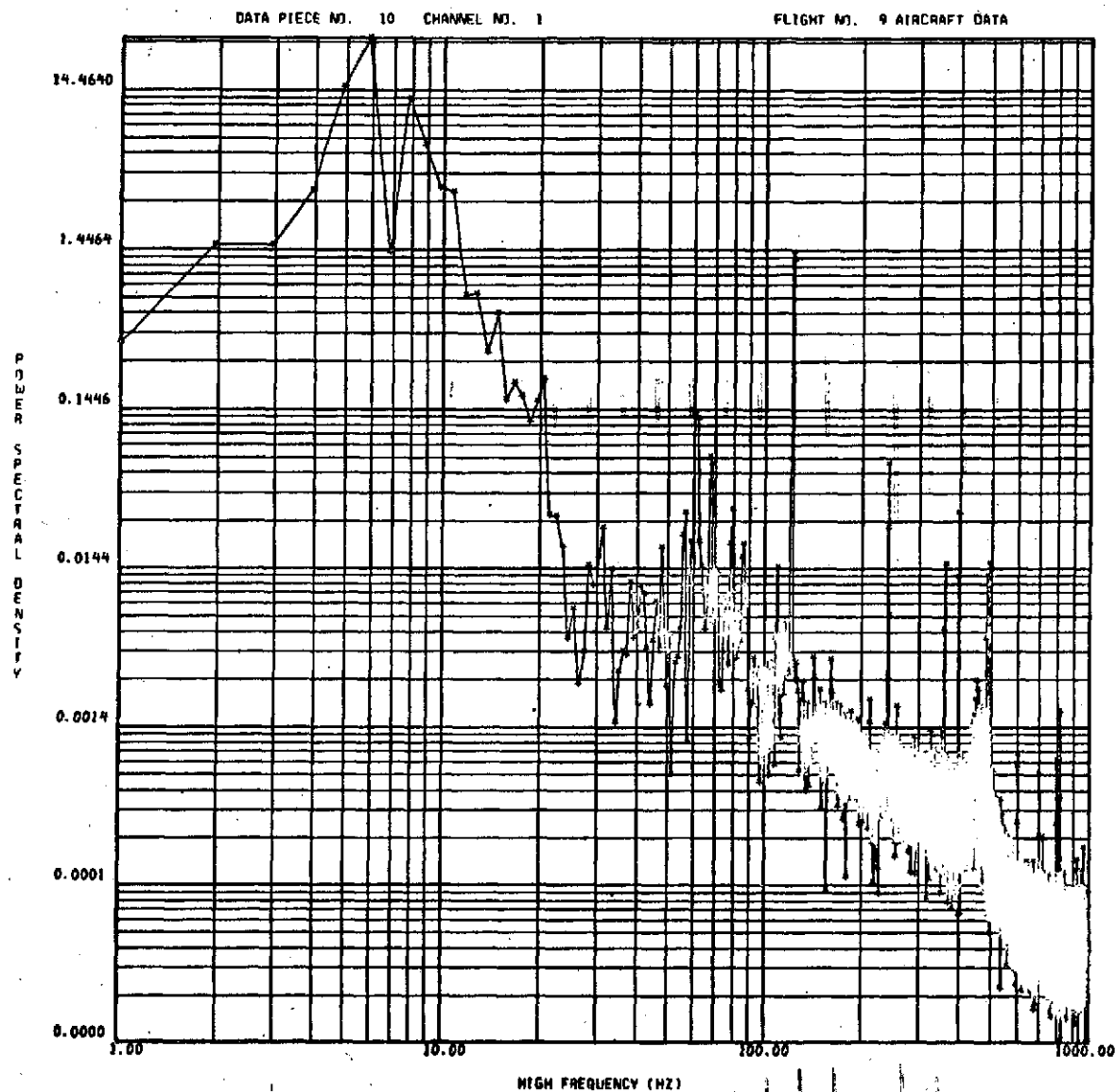
Figure 182. Image dissector error PSD with beamsteerer loop open.
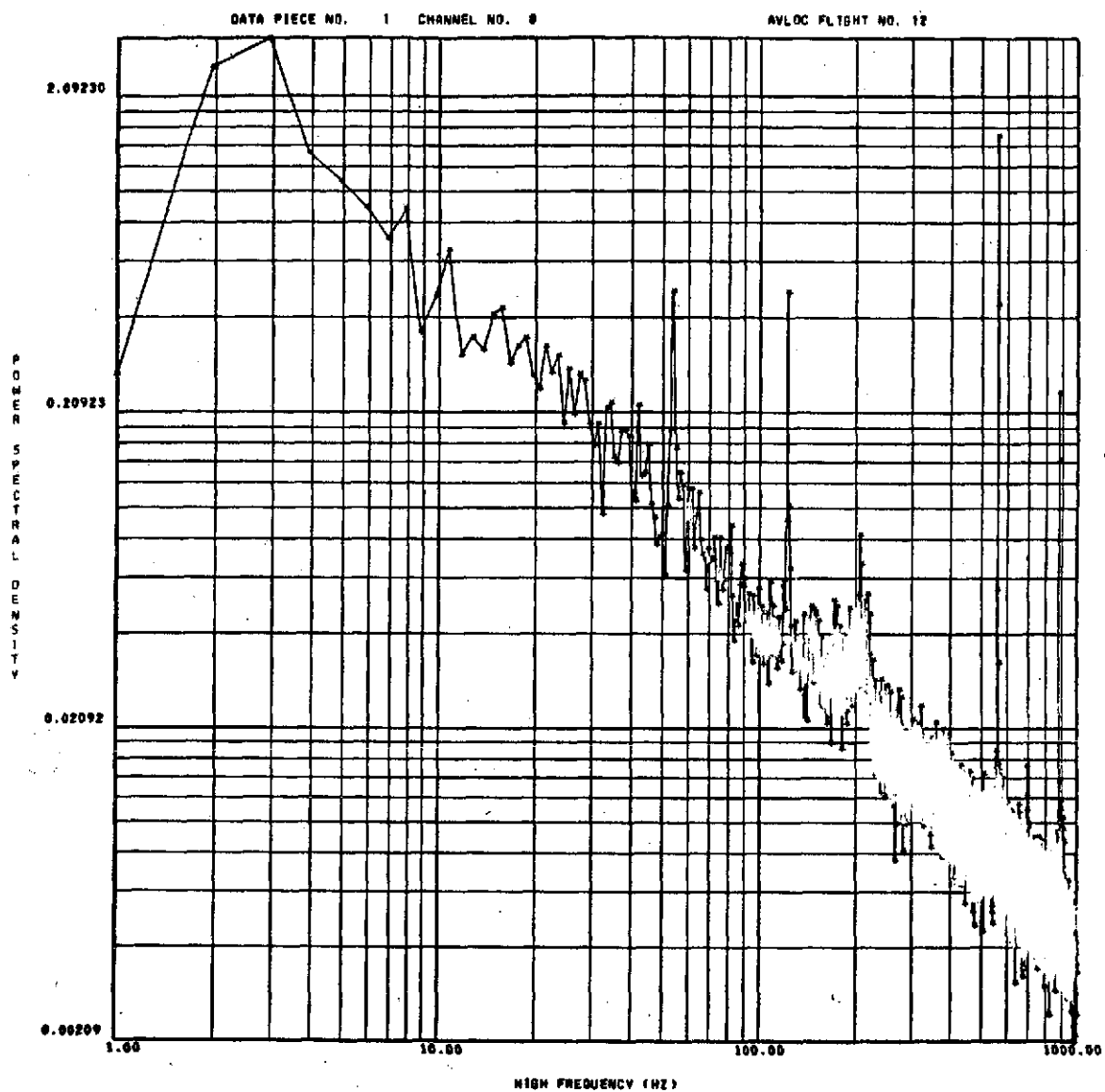
Figure 183. Uplink scintillation PSD.

BEAMSTEERER SYSTEM

As an integral section of the aircraft's fine tracking system, the beam-steerer servo system was a critical component receiving a considerable degree of effort. This system, in conjunction with the ID fine tracking system, became the subject of probably the most intensive effort of the project. This effort was directed at providing the system with sufficient performance margin to allow

372

reliable performance of the total system. Unfortunately these goals became a rather elusive factor of the project and regrettably were not completely solved until post flight modifications of the system were made at MSFC.

In this section will be presented the results of data obtained on the beamsteerer system, its performance limitations, and modifications made to the system as a result of testing performed during the flight testing and ground operations.

The design performance goals were: (1) a tracking accuracy of 5 μrad, (2) a tracking bandwidth of 100 Hz, and (3) a boresight accuracy of 25 μrad. Early in the program, the testing and performance of the beamsteerer loop indicated certain efficiencies which required a concerted effort to resolve. These problems occurred in two basic areas of operation. First, the gain bandwidth of the servo loop appeared insufficient to fully track out the angular disturbances which would be induced by the aircraft environment and the atmospheric path fluctuations. Secondly, the loop was fast enough to essentially "run away" from the fine tracker. That is, the rate at which the beamsteerers could deflect was greater than the tracking velocity capability of the tracker. This seemingly paradoxical condition was solved by a redesign of certain circuitry in the beamsteerer system and by limiting the angular rate of the beamsteerer loop during acquisition of the target. After the target was acquired this rate limitation was removed and the system was allowed to operate in a higher gain mode.

After these modifications had been implemented, the series of flight tests were begun. Shown below are data typical of results obtained during the flight series. The following data shows the angular tracking characteristics observed in flight tests along with power spectral data indicating the experiment environment in which the system operated. Figure 184 depicts the operation and angular disturbances being tracked by the beamsteerer system.

Shown in Figure 185 is a typical plot of the disturbances which the beamsteerer loop was required to track. It should be noted that for ideal operation of the system the beamsteerer loop should be tracking all angular disturbance inputs to the system, thereby producing a complete null at the ID tracker outputs. A gauge of the performance of the beamsteerer loop is, therefore, the residual error being sensed by the ID. Since by nature the frequency response of the beamsteering system is limited, in comparison to the image dissector tracker, the resultant residual errors observed in the image dissector outputs will contain energy in a spectrum above the response of the beamsteerer system. The spectra of this residual error is shown in Figure 186.
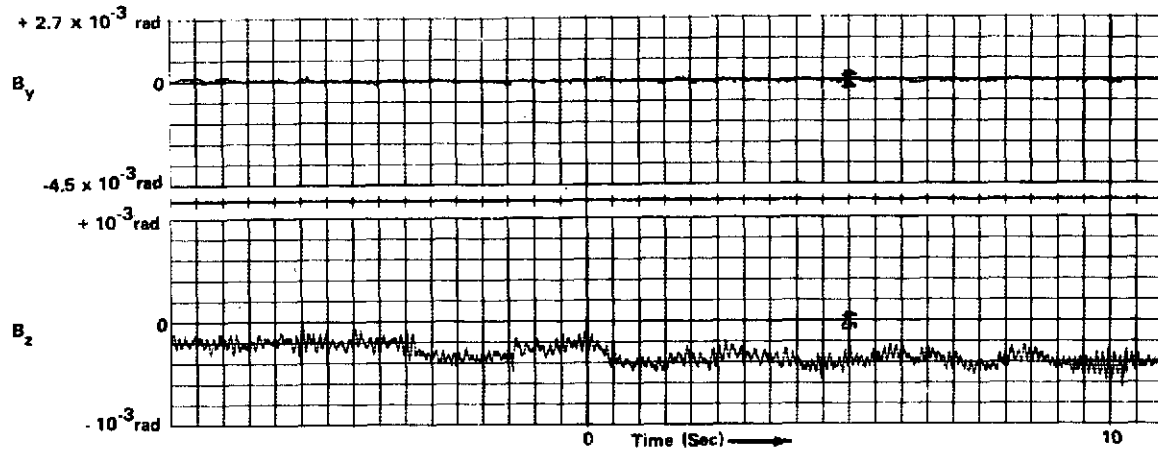
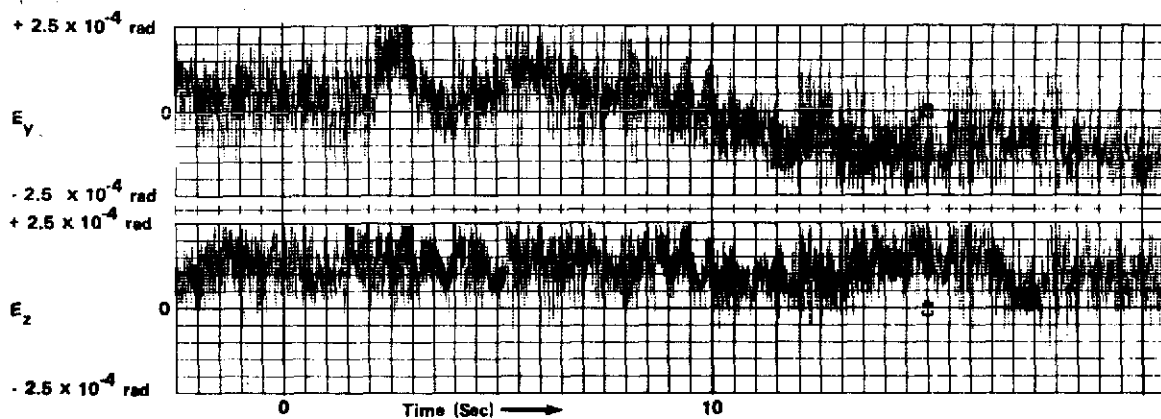Figure 184. Beamsteerer position with loop closed.

Figure 185. Image dissector error signals with beamsteerer loop open.

The foregoing data illustrate the performance of the beamsteerer tracking loop during conditions of reasonably good performance. It should be noted, however, that this degree of performance was not always achieved. Limitations and deficiencies of the hardware became evident. Perhaps the most difficult problem encountered with this hardware system was the instability of the transmitted beam boresight alignment. The boresight was checked as a standard preflight procedure and invariably indicated proper operation of the equipment. It was toward the end of the flight series, however, that provisions

374

were included in the flight hardware to allow adjustment of boresight alignment while in flight. During the final flight of the series, flight 15, it was demonstrated just how significant a change occurred in boresight alignment after preflight checks had been performed. It was also noted during this flight that significant instabilities in this alignment occurred. It was also apparent that this drift in alignment varied throughout the flight experiment time. Shown in Figure 187 is a depiction of corrections made to the boresight alignment during the flight time of flight number 15.
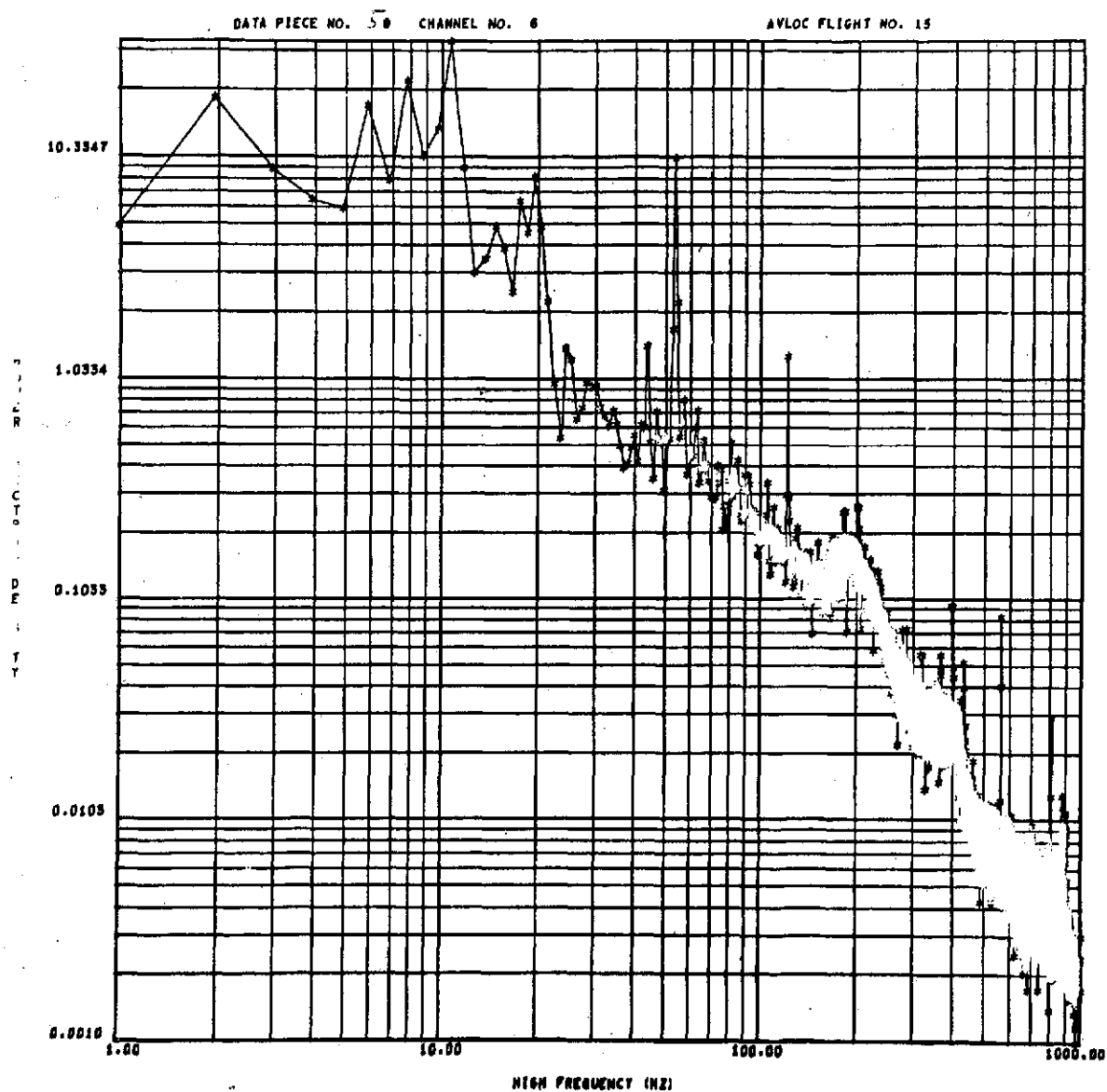
Figure 186. Image dissector signal PSD with beamsteerer loop closed.

FLIGHT No. 15

START

NUMBERS INDICATE ARCSECONDS OF MOVEMENT.

20

20

10

10

10   10

10   10

10 10

10

TIME $= t_0 + 01:35$

START

20   10

40

40

10

20

20

TIME $= t_0 + 02:11$
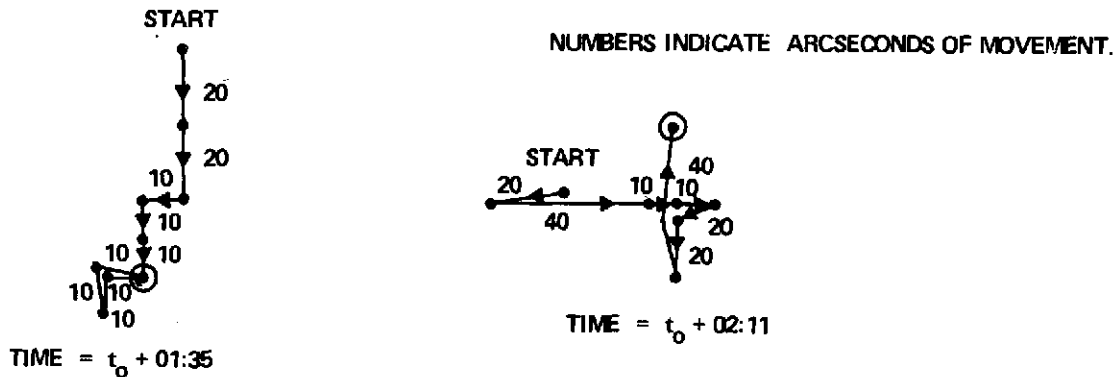
Figure 187. Boresight correction during flight no. 15.

Upon completion of these first AVLOC flight series the aircraft system was returned to MSFC. One of the prime goals in performing post-flight analysis of the equipment was the determination of precisely what could be done to better assure in the future operational performance of the beamsteerer fine-track system. These results are presented in detail in the Flight Hardware Modifications and Field Changes section, but in essence are outlined here. Perhaps the most serious problem encountered involved the power amplifiers which drove the beamsteerer motors. It is these amplifiers in conjunction with their driving circuitry which were subject to drift and instability. This characteristic greatly aggravated the boresight stability problems encountered in flight. It was also discovered that certain amplifier circuits were frequency compensated in such a manner as to severely affect their phase linearity characteristics which in turn led to complications arising in tracking instability observed at low light tracking levels. The results of redesign in this circuitry and their corresponding improvement in performance are presented in the next section.

GIMBAL MIRROR SYSTEM

The primary objectives of the gimbal mirror system were to provide a stable, low bandwidth, servo-controlled line of sight to the airborne communications package. Although this requirement sounds rather mundane, the stability of this system required serious consideration. In early testing of the completed aircraft system, a rather serious problem of resonant vibration of the mirror system was encountered. In order to alleviate the susceptibility of the system to vibration, in particular the gimbal mirror, several modifications were made to its structure.

A sketch of the unmodified gimbal platform is shown in Figure 188a. This configuration exhibits a relatively large overhung mass (roll yoke) cantilevered from the platform main frame and supported by a roll trunnion. Detail static deflection measurements were made on this platform to determine which sections were most susceptible to vibration. The results of these tests pinpointed two problem areas: (1) the roll trunnion and associated support bearings were deflecting under load and (2) the yoke (an open channel) was twisting on either side of its attach point to the roll trunnion. The modifications to overcome these problems are illustrated in Figure 188b. The modified and unmodified main frame assemblies are shown to the same scale. To minimize deflection, the roll trunnion was increased from 1.59 cm (0.625 in.) diameter to 4.76 cm (1.875 in.) diameter and the single bearing was replaced by a preloaded pair. To reduce yoke twist, the open channel was augmented by a solid rectangular bar 7.62 cm (3 in.) deep by 3.81 (1.5 in.) thick. The main frame was enlarged, of course, to accommodate the other modifications. A picture of the modified platform is shown in Figure 189.

Following these modifications, the system was again subjected to vibration testing and found to perform in the expected vibration environment quite satisfactorily. The design goals for the gimbal mirror parameters were (1) pointing accuracy of 0.5 deg, (2) bandwidth of 10 Hz, (3) pointing stability of 582 μrad (2 arc-min), and (4) operating temperature of -40° C to 50° C, (-40° F to 120°F). The only serious problem encountered in the operational aspects of this subsystem was the capability to open loop point the system for acquisition as outlined in this section. This problem was quite easily overcome, however, and the gimbal mirror system performed quite well throughout the flight series.

Shown in Figures 190 and 191 are the results of the pointing accuracy of the gimbal mirror system. The data were taken with the beamsteerers disabled so that any optical power received at the ground was determined by the pointing accuracy of the gimbal mirror. It can be seen from the data that the accuracy to which the mirror system was capable of pointing was on the order of 250 μrad.
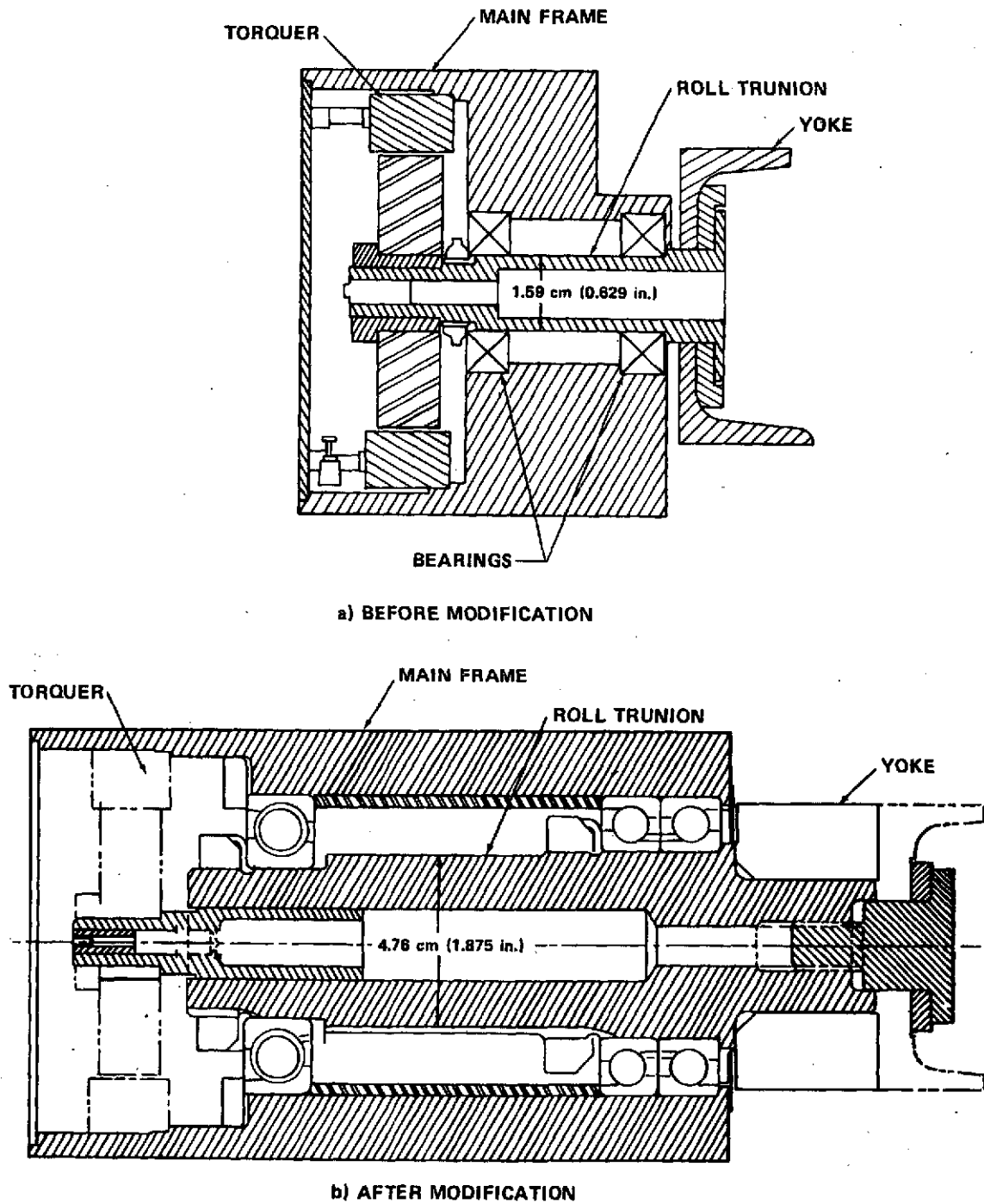
a) BEFORE MODIFICATION

b) AFTER MODIFICATION

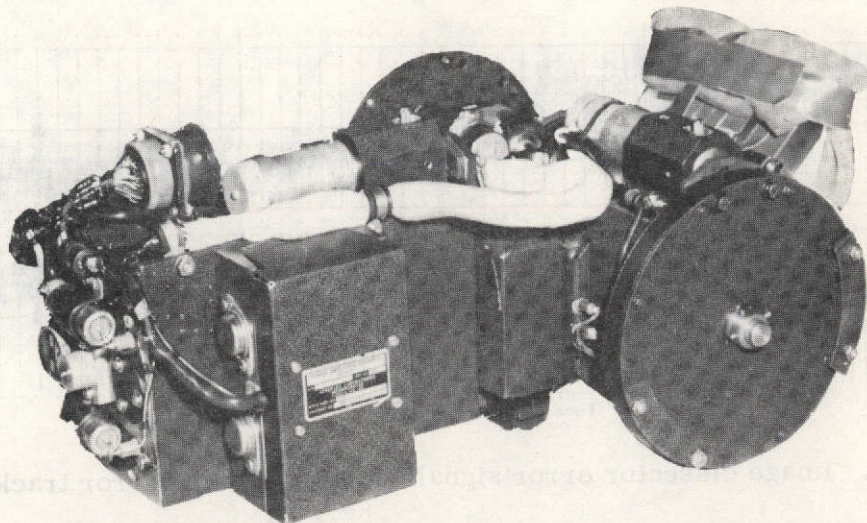Figure 188. Gimbal mirror platform main frame assembly.

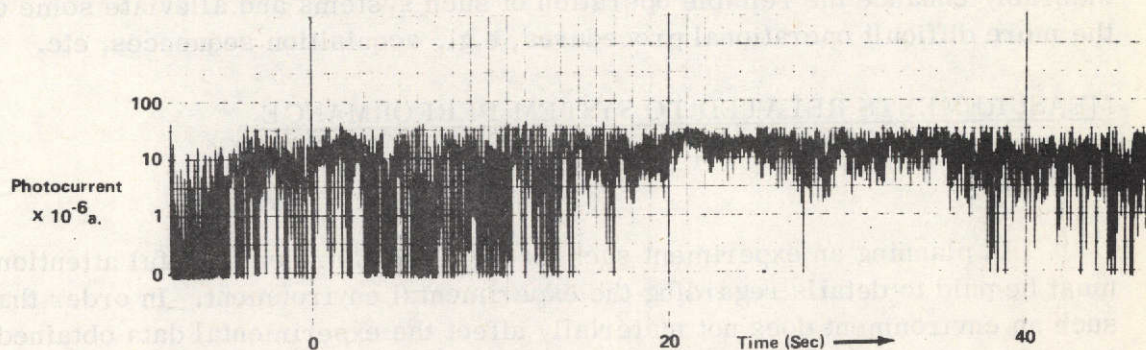Figure 189. Modified gimbal mirror platform.

Figure 190. Downlink received power during gimbal mirror tracking.

One aspect of the flight tests indicates the possibilities for a considerable degree of improvement with regard to the coarse pointing mirror subsystems. Although in these experiments the coarse mirror performed exceedingly well, a great deal of improvement could be realized in this area. In future system design the capability of refined mirror pointing systems should be utilized. By designing the capability for highly accurate pointing of such a coarse mirror system a degree of redundancy is gained in the event of failure of the fine resolution beamsteerer system.
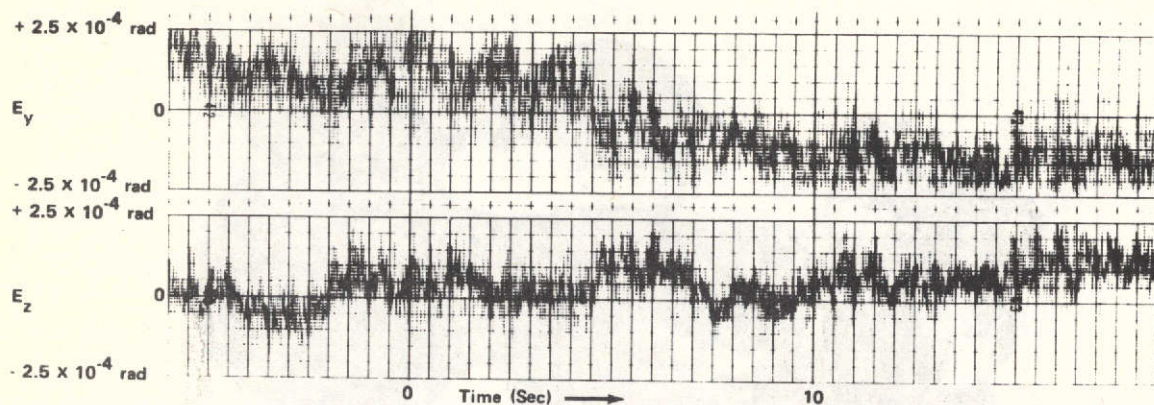
Figure 191. Image dissector error signals during gimbal mirror tracking.

Two areas which should receive attention are the inclusion of a high resolution angular readout system and the potential usage of a small, stable platform, attitude reference system. Improvements such as these could considerably enhance the reliable operation of such systems and alleviate some of the more difficult operational procedures, e.g., acquisition sequences, etc.

MEASUREMENTS RELATED TO SYSTEM PERFORMANCE

VIBRATION

In planning an experiment such as the AVLOC project careful attention must be paid to details regarding the experimental environment. In order that such an environment does not materially affect the experimental data obtained from this type of experiment, a great deal of effort must be expended to assure that the experiment is successfully isolated from unwanted environmental influences. The effects of temperature, vibration, etc., must be recognized as being relatively severe in an aircraft as contrasted to laboratory or even satellite experimentation.

Perhaps one of the more successful aspects of this program involves the degree to which this system operated successfully in the aircraft environment. The effects of vibration on measurements made by the aircraft and ground measurements, as is shown by the following data, are exceedingly small. In those instances where vibration effects were measured, their nature and characteristics were entirely predictable.

380

The first major concern over vibration effects was its influence upon the tracking data being taken by the aircraft fine tracking system. In order to determine the precise effects of vibration upon the data, a test of correlation was made between vibration measured on the experiment platform (3 axis) and the fine tracking measurement data. These correlations were performed on several sets of data and on many flights. In no case did this correlation become greater than about 10 percent. The principal frequency component of this correlation was measured to be 8 to 10 Hz. This effect was predicted, i.e., this corresponds to the fundamental resonance of the experiment platform suspension assembly. Should the aircraft tracking system be unduly affected by vibration, one would expect a corresponding influence upon scintillation as seen by the ground based receiver system. These data, too, were correlated with aircraft vibration measurements. Virtually no correlation was measured which would indicate ground measurements were being influenced by aircraft vibration effects. This degree of "no-effect" is an extremely important point which should be stressed, since vibration induced effects upon measurement could destroy that measurement's usefulness in determining other atmospherically induced phenomena.

Shown in Figure 192 is a typical sample of vibration measurements made by transducers attached to the experiment platform. This array consisted of three mutually orthogonal accelerometers aligned with the aircraft's roll, pitch and yaw axes. Shown in Figure 193 is a power spectral density plot of this vibration.
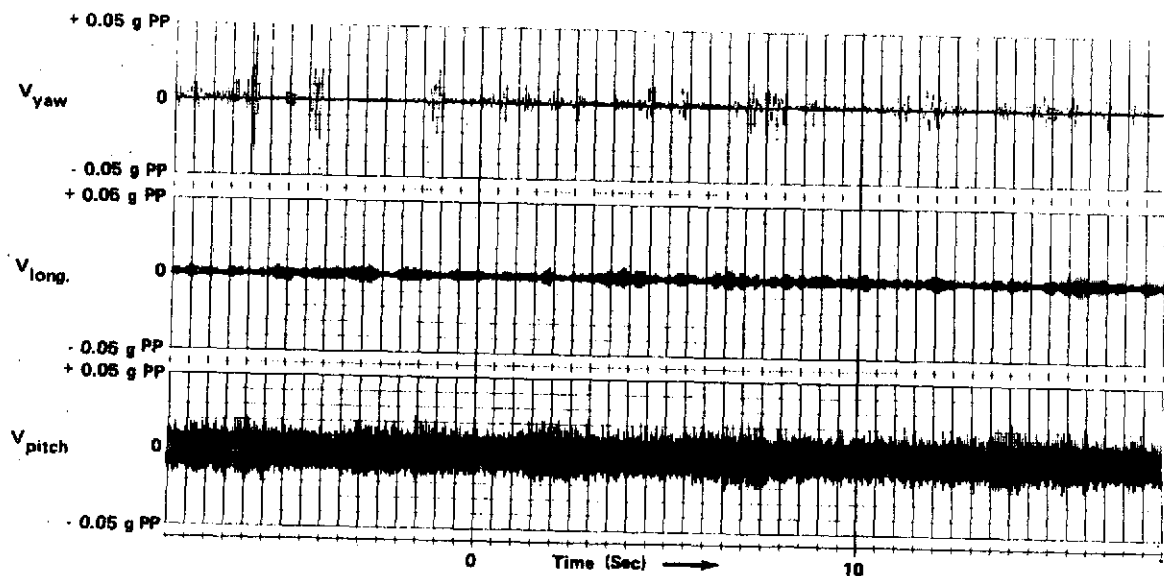

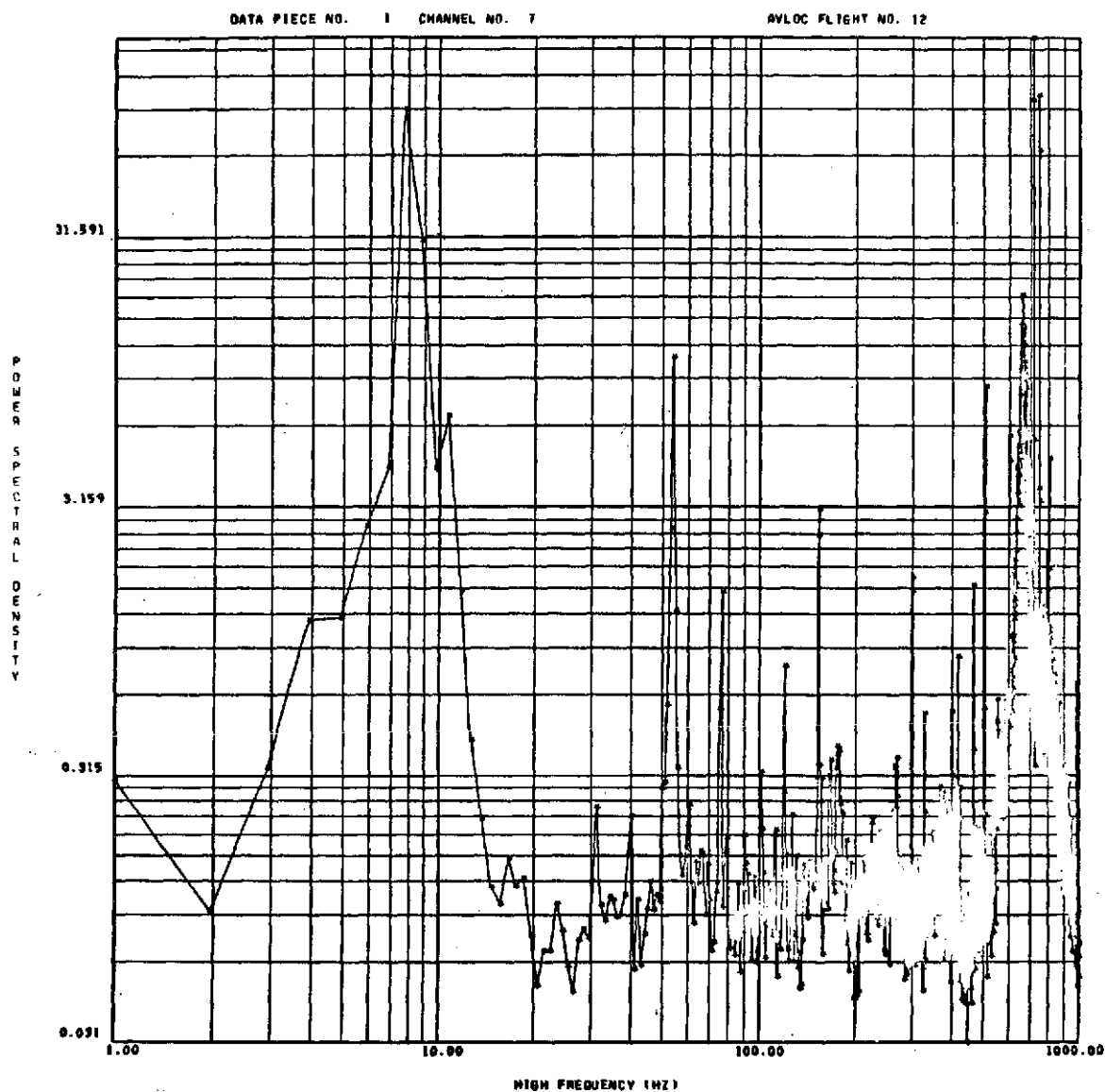Figure 192. Aircraft platform vibration.

Figure 193. Pitch vibration PSD.

The correlation data previously described are shown in Figure 194. This correlation is between the fine tracker output and the yaw component of vibration. Here we see the greatest correlation observed in the experiments. This effect, as previously stated, is less than 10 percent and at predominant frequencies of 50 and 8 Hz. Again this measurement is aircraft vibration and aircraft tracking.
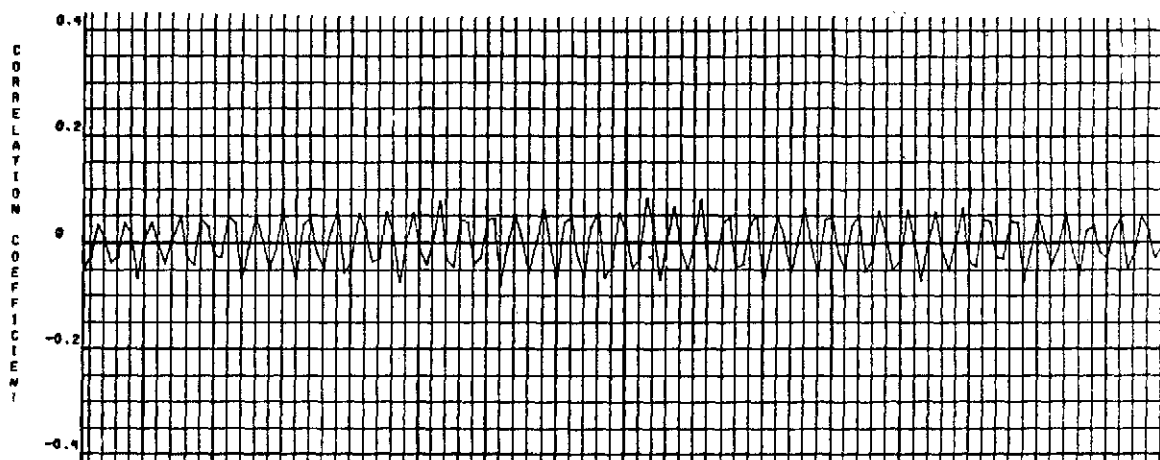
Figure 194. Correlation of yaw vibration and $\left(E_x^2 + E_y^2 \right)$.

Another measurement investigated for potential effects was the aircraft received scintillation data. Again correlations were made between the uplink received scintillation data and all three axes of vibration, for any potential vibration induced effects, As before, virtually no effects were noted, as seen in Figures 195 and 196.
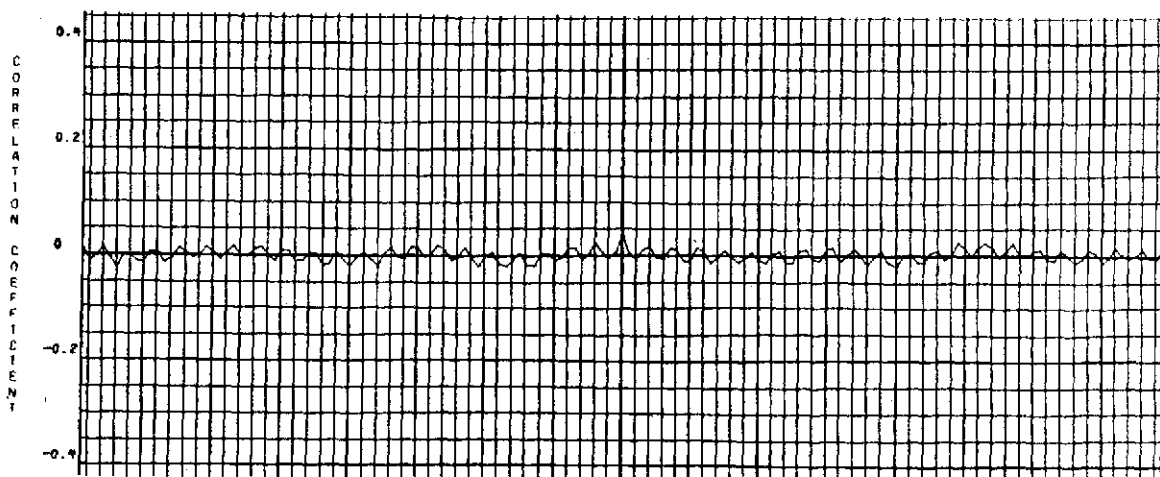

Figure 195. Correlation of pitch vibration and log scintillation.

As a final but exceedingly important test, the aircraft vibration data was correlated with received power measurements of the ground system receiver data. As can be seen from the following plots, (Figs. 197 and 198) these correlations yielded the smallest measureable effects.
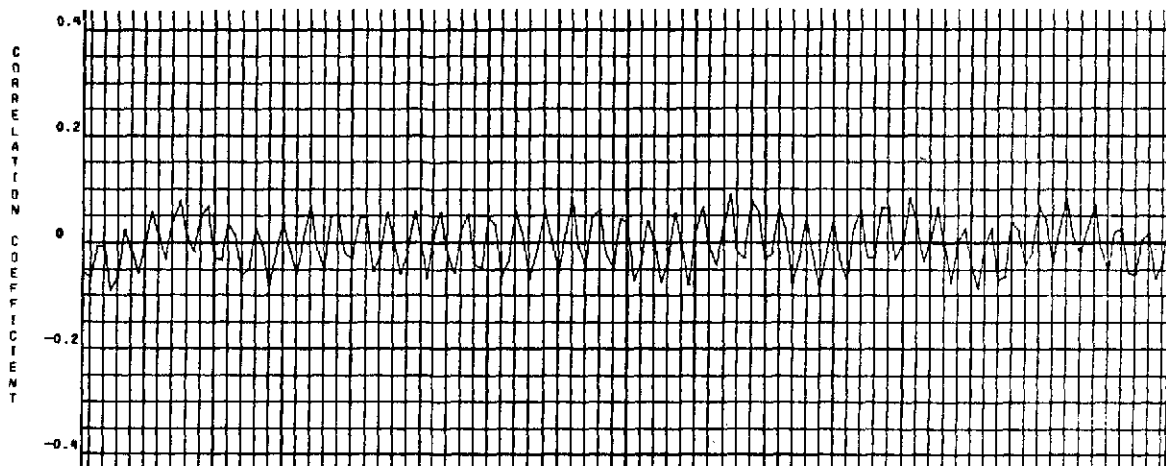
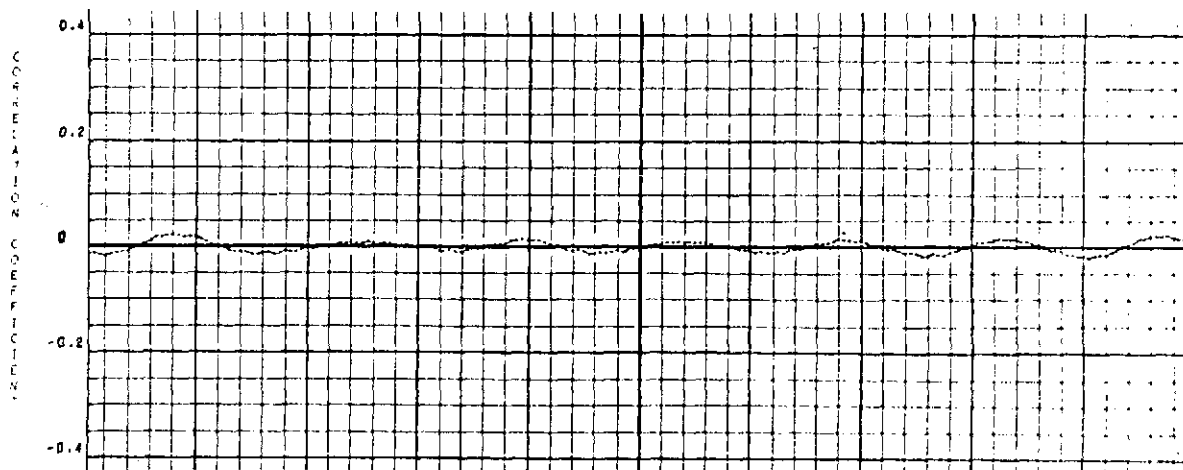Figure 196. Correlation of yaw vibration and log scintillation.

Figure 197. Correlation of pitch vibration and downlink scintillation.

The temperature control of the aircraft was originally assessed as a relatively cut and dried problem. This, however, was not the case. The original design requirements called for this system to maintain a temperature of 25° C ± 9°. Due to many problems associated with the aircraft's thermal control system, this performance was never fully achieved. This lack of reliable temperature control led to two major areas of difficulty which the system was not designed to handle.

These two problems arose in the area of boresight stability and modulator performance. Numerous other small problems arose which were attributed to lack of temperature control but none were quite as serious as these two.
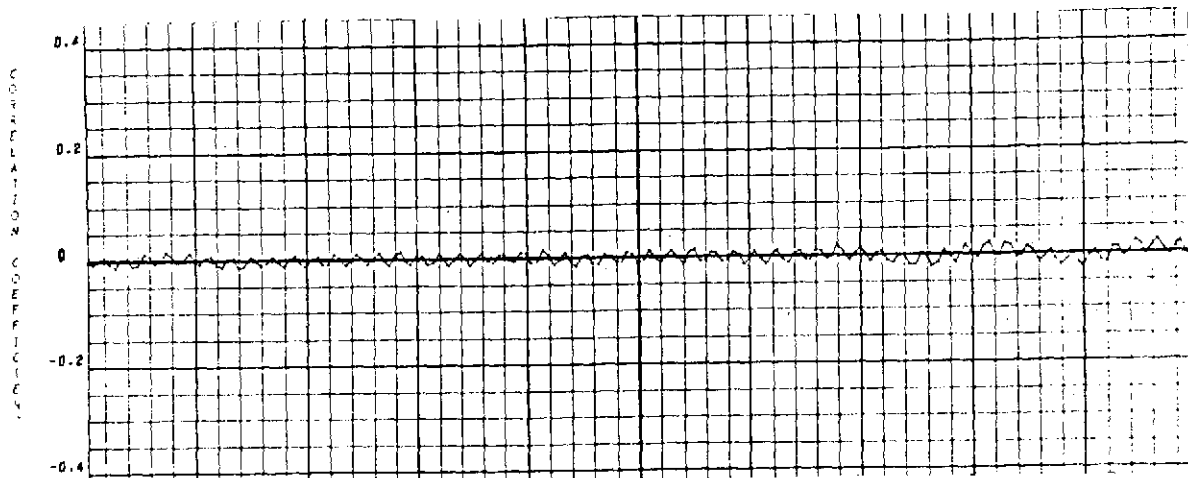
Figure 198. Correlation of pitch vibration and ground station tracker error.

Many efforts were made in an attempt to balance the temperature distribution between the AOCP and the remote equipment cannister. Although a considerable improvement was made in the final few flights of the series, a completely normal temperature profile was never fully achieved. During some of the early flights, temperatures would be measured as low as $-18°$ C in the communications package. Shown in Figure 199 is a typical temperature profile.

BORESIGHT STABILITY

As previously mentioned, the stability of the boresight requirements of the received and transmitted line of sight is of paramount importance to any cooperative tracking laser communications system. It is perhaps one of the key elements of performance which must be most accurately accomplished for successful system operation.

The required accuracy for such boresight is primarily determined by the divergence of the optical beam which one is transmitting, i.e., the error in boresight must be much less than the transmitted beam divergence. In the case of this experiment, the transmitted aircraft beam was to be varied between divergence angles of 35 μrad. and 1 mrad. It was determined through various tests that the boresight stability was being affected and was not being as accurately controlled as required for these divergence ranges.

FLIGHT NO. 15

15.5°C (60°F)

4.5°C (40°F)

-6°C (20°F)

0:0   1:00   2:00   3:00   4:00

A - AOCP TEMP.
C - EQUIPMENT CANNISTER TEMP.

FLIGHT No. 12

26.6°C (80°F)

15.5°C (60°F)

4.5°C (70°F)

-6°C (20°F)

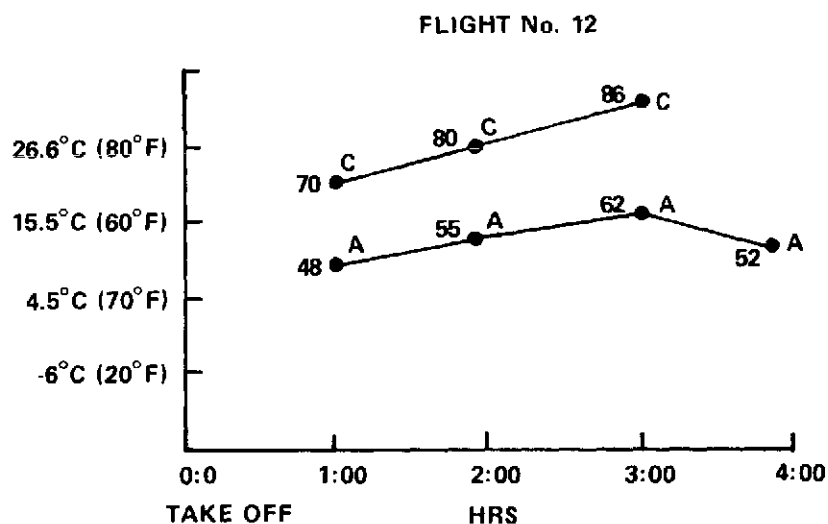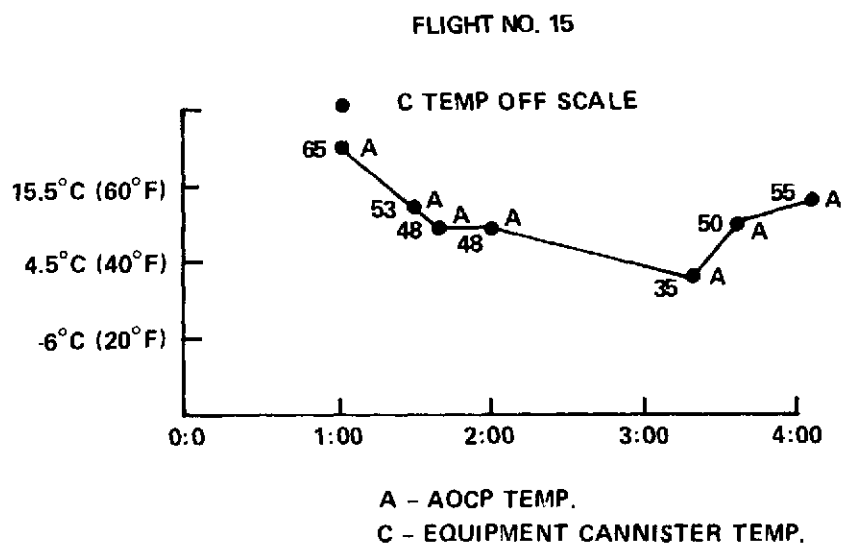0:0   1:00   2:00   3:00   4:00
TAKE OFF   HRS

Figure 199. Flight equipment temperature profile.

Although many anomalies were noted in the boresight stability throughout the flight series and traced to a number of hardware problems, perhaps the most important information derived from these tests is the imperative need for onboard active boresight correction.

It becomes virtually impossible to construct an electro-optical system which is required to operate in a semiopen loop configuration, such as the

AVLOC system, which will retain its alignment while operating in an environment such as the aircraft. It, therefore, becomes essential that the capability for active boresight correction be included in the design of any future systems such as this. Whether the system is self-aligning or remotely controlled is not of particular importance, the key point is that this capability be inherent in the system design.

A number of factors, which may not be totally obvious, have significant effect upon the boresight drift of such a system, to the extent that they may render a system totally inoperative. These are: (1) thermomechanical drift of the optical package, (2) dc drift of the beamsteering drive electronics, (3) dc drift of the tracking sensor electronics, and optical LOS deviations induced by the modulator optical system and pointing instability inherent in the laser. All of these disturbances must be compensated for and this implies the need for onboard, active boresight control.

COMMUNICATIONS COMPONENTS

Laser

The laser chosen for this experiment was selected on the basis of its availability and its ruggedness. As the series of flights continued it was shown that this unit performed quite admirably for its time in use. Although the unit and its power supply were not initially designed for flight ruggedized operation few problems were encountered with the laser until the final few flights. The problem encountered was the inability of the laser's power supply to ignite the discharge tube. The reasons for this problem were: (1) the laser had accumulated many hours of operating time, and this long operation time had gradually increased the initial ionization potential of the tube which in turn required a higher starting voltage from the power supply; and (2) the inverters which supplied the 110-V, 60-Hz power to the system were operating at the low end of their output capability. The laser power supply was not capable of, or designed to provide for operation with these two limit case requirements, i.e., low input voltage and high output starting potential.

The solution of this problem required replacement of the marginal laser head, i.e., a new tube with lower starting potential, and testing of the available power supplies on hand. The power supply which would reliably start at the lowest input voltage level was installed in the system and no further problems with the laser were encountered.

Modulator

The modulator used in the system performed, in general, quite well. No serious problems in its alignment stability were noted. The design technique of using an external variable polarization analyzer (in this case a Soleil-Babinet compensator) is somewhat in question. It was determined during field testing that the index of modulation, nominally 0.70, would occasionally drop to approximately 0.5 to 0.6. The modulation index performance could be regained by adjustment of the compensator but was still subject to drift. Probably the most perplexing problem discovered in testing was that sometimes, from one day to the next, 180 deg phase inversion of the optical modulation signal was measured at the receiver. Although no entirely satisfactory explanation of this phenomena has been given it is felt that this problem also lies in the area of the external compensation optics.

Beam Profile

As is the case with any precision optical system, an extreme amount of care and precision is required in the design and fabrication of every optical component in the optical system. Any mirror surface or lens element can have a disastrous effect upon the total system performance. In the case of this system, several design changes and remanufacture of certain elements were required. Although a great deal of effort was expended upon the optical system there were still deficiencies in the portion of the transmit optics. The overall performance of the optical system, considering the relatively low expense of the components, could be considered only somewhat better than marginal. The most profound effect of transmit beam degradation can be observed in the following far field pattern photograph, Figure 200. It was noted in ground scintillation measurements, that a very rapid and seemingly unexplainable degree of scintillation depth was observed. It is rather obvious from Figure 201 that were a receiver to be sampling the energy at various points on the edges of this energy distribution an extremely deep and unusual scintillation pattern would be observed.

Shown in Figure 202 are the scintillation data obtained from flight no. 15. In this case the boresight was corrected to place the central area of the transmitted energy over the ground station. It can be seen from the data that the deep fades prominent at the edge of the far field pattern were not observed.
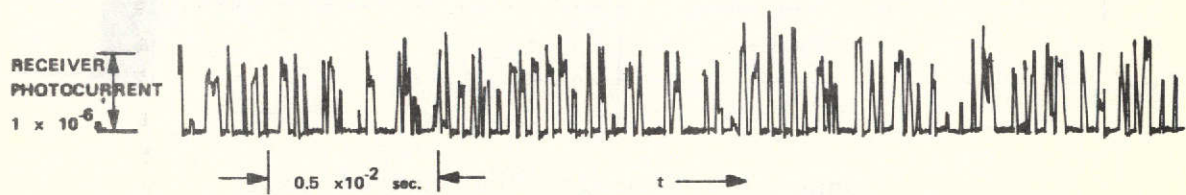
Figure 200. AOCP transmitter far field pattern.

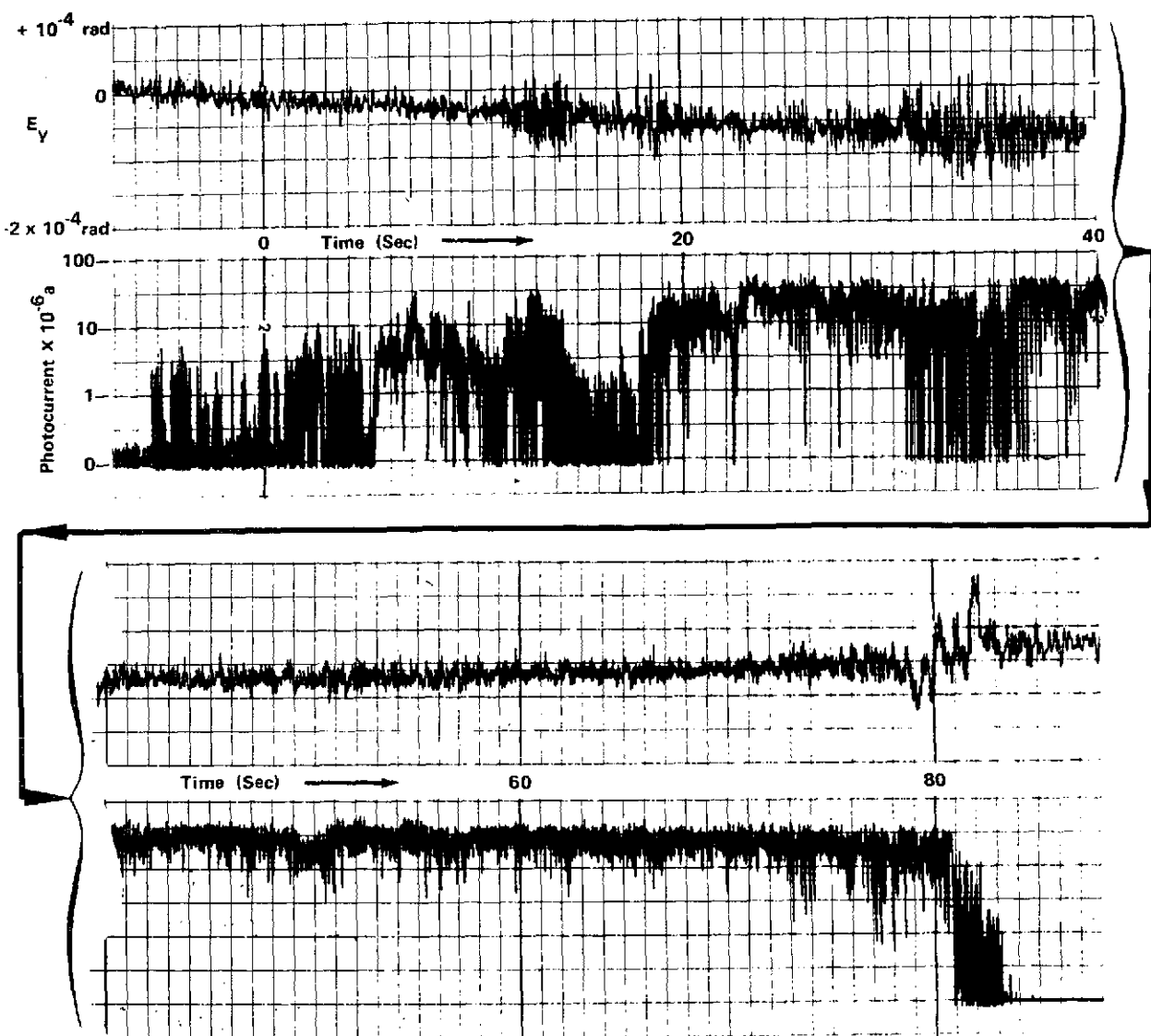Figure 201. Ground receiver scintillation.

Figure 202. Ground station received power.

Ground Station Data

In evaluating the data collected by the ground station instrumentation during the AVLOC test series, two categories of information become of interest: (1) data which lends itself to rigorous statistical analysis for comparison with atmospheric propagation theory, and (2) data which are of engineering significance to verify and evaluate the design performance of the various acquisition, tracking, communication, and control systems.

390

Due to difficulties in achieving an acceptable degree of performance by the aircraft system, i.e., periods of sustained fine track lock-on and an accurately boresighted downlink transmitted beam, no significant quantities of downlink scintillation data were collected. This is due primarily to the fact that received power levels at the ground terminal were below the required ranges for adequate communication channel performance. This power level was too low to allow the scintillation channel electronics to operate in a region of linear signal range. Therefore, a lengthly statistical analysis of the data are not of great benefit and are not presented here.

ACQUISITION AND TRACKING

Fundamental to all discussion of tracking and acquisition techniques and performance is consideration of the 61-cm (24-in.) telescope, mount and computer control system. A brief outline will be presented here to acquaint the reader with the overall problem of acquiring the target aircraft, tracking the target with the GBAA coarse acquisition and tracking system, and finally tracking the target with the fine tracking system of the ground transceiver. This overview is presented here to help the reader more fully understand the relationship between the performance levels, i.e., tracking accuracies, bandwidths, etc., of the various subsystem elements and the overall system performance.

The first point of interest is the overall software control system block diagram, Figure 203. From this the various program blocks required to point, control, and sense data from the various tracking system inputs can be seen.

Shown in Figures 204 and 205 is the servo software routine to provide for filtering and bandwidth accommodations of the coarse and fine tracking systems.

It will be noted from these diagrams that the system has to provide for 2 significantly different tracking bandwidths. This is required to accommodate the GBAA 16 samples/sec data rate and also the 100 samples/sec obtained from the fine tracking system. In addition the routine for processing data from the GBAA was implemented to provide additional filtering and averaging of the position error data to achieve the required 0.873-mrad (34-min) overall system pointing accuracy.

Figures 206 and 207 show two additional programs which were required for the overall system. The first is an acquisition window program which
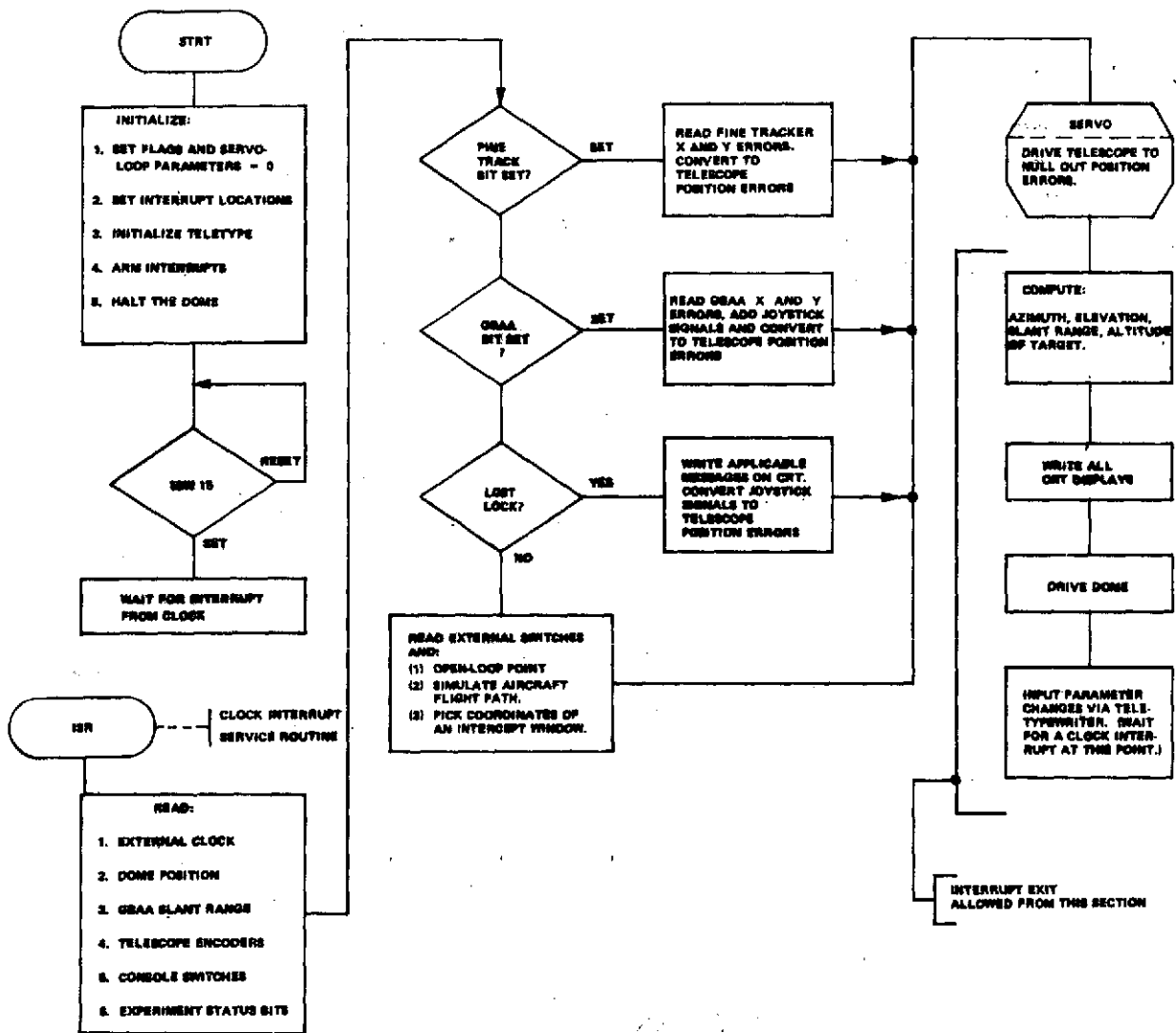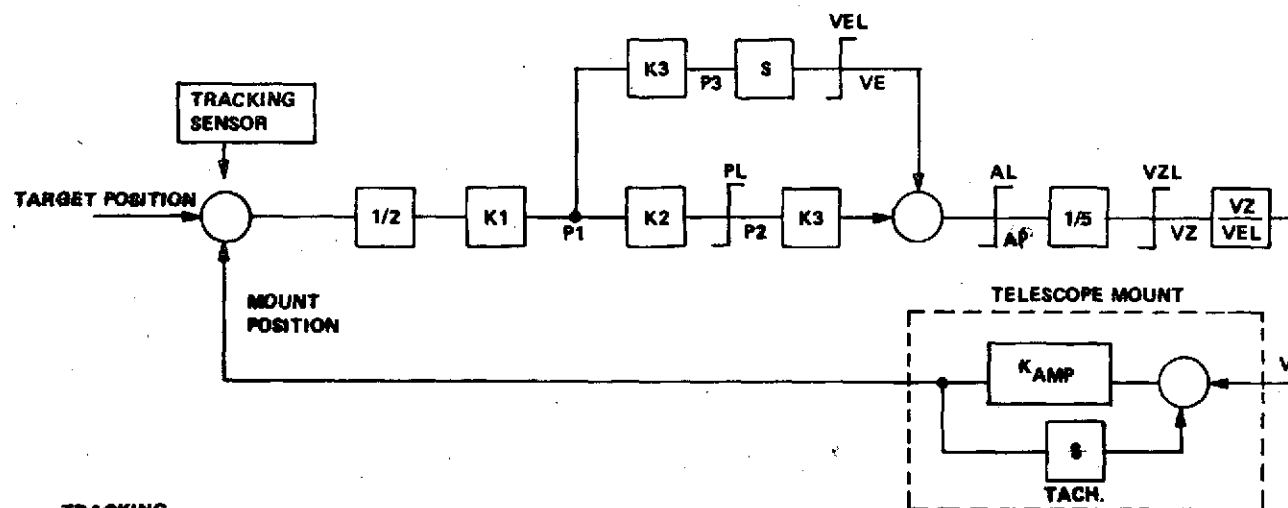
Figure 203.   Control computer software block diagram.

Figure 204. Computer servo control block diagram.

TRACKING MODE	K1	K2	K3	PL		AL	VZL
POSITION LOOP	2	.25	14	.02777	.632	.040555	.027777
COARSE TRACK	2	.25	0.7	.002777	.06555	.040555	.027777
FINE TRACK	2	.25	14	.00277	.316	.253	.027777

WHERE THE FOLLOWING CONVENTION IS USED:

ANGULAR POSITION - FRACTION OF ½ CIRCLES/SEC.
ANGULAR VELOCITY - FRACTION OF ½ CIRCLES/SEC.
ANGULAR ACCELERATION - FRACTION OF ½ CIRCLES/SEC.

GBAA

K3 = 0.7
PL = 0.27777×10^{-2}

VEL = 0.55555×10^{-1} (10 deg/sec)

AL = 0.40555×10^{-1} (7.3 deg/sec)

VZL = 0.2777×10^{-1}

FINE TRACK

K3 = 14
PL = 0.27777×10^{-2}

VEL = 0.316 (57 deg/sec)

AL = 0.253 (45.6 deg/sec)

VZL = 0.2777×10^{-1}

P1

P1	=	P1*2.0
P2	=	P1*0.25
P3	=	K3*P1
VE	=	(P3-ZP) 1/T
ZP	=	P3

/PZ/>PL — YES → PZ = PL* (SIGN P2)

NO

/VE/>VEL — YES → VE = VEL* (SIGN VE)

NO

AP = VE + (K3*PZ)

/AP/>AL — YES → AP = AL* (SIGN AP)

VZ = VA + AP*T

/VA/>VZL — YES → VZ = VZL*(SIGN VZ)
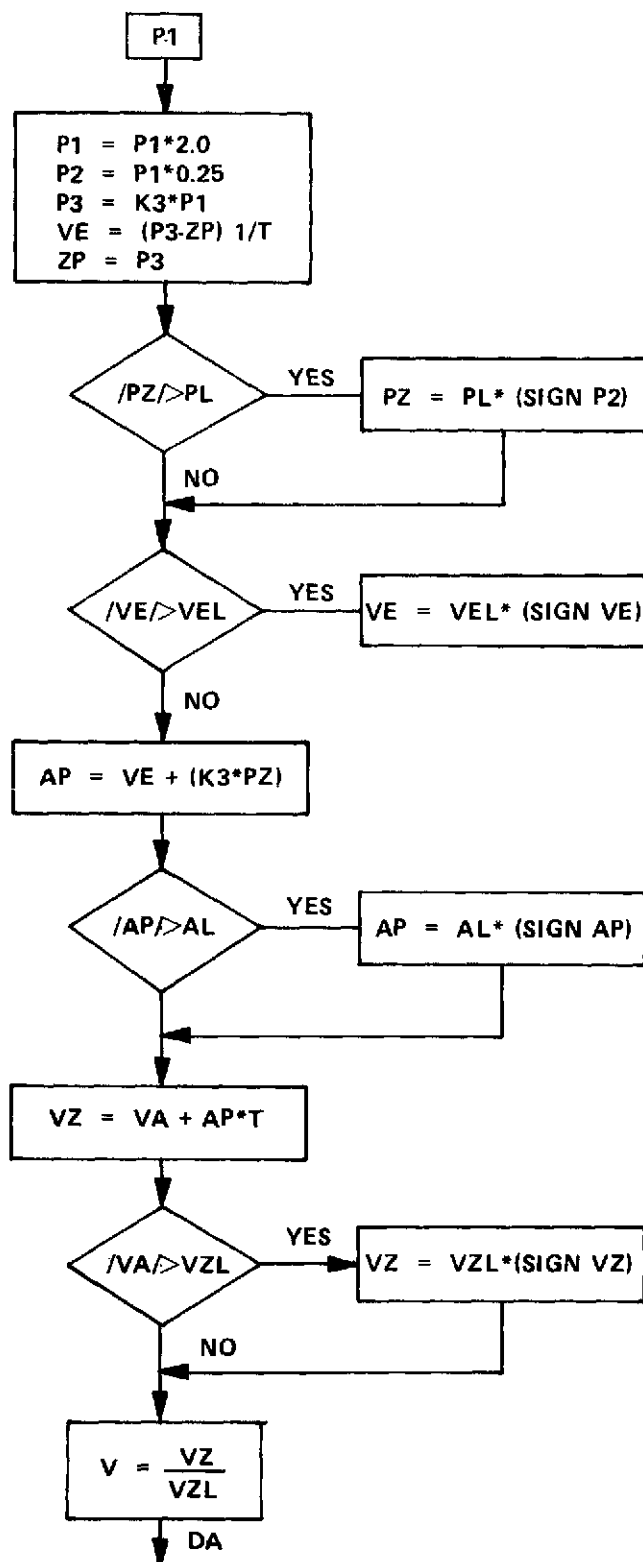
NO

V = $\dfrac{VZ}{VZL}$

DA

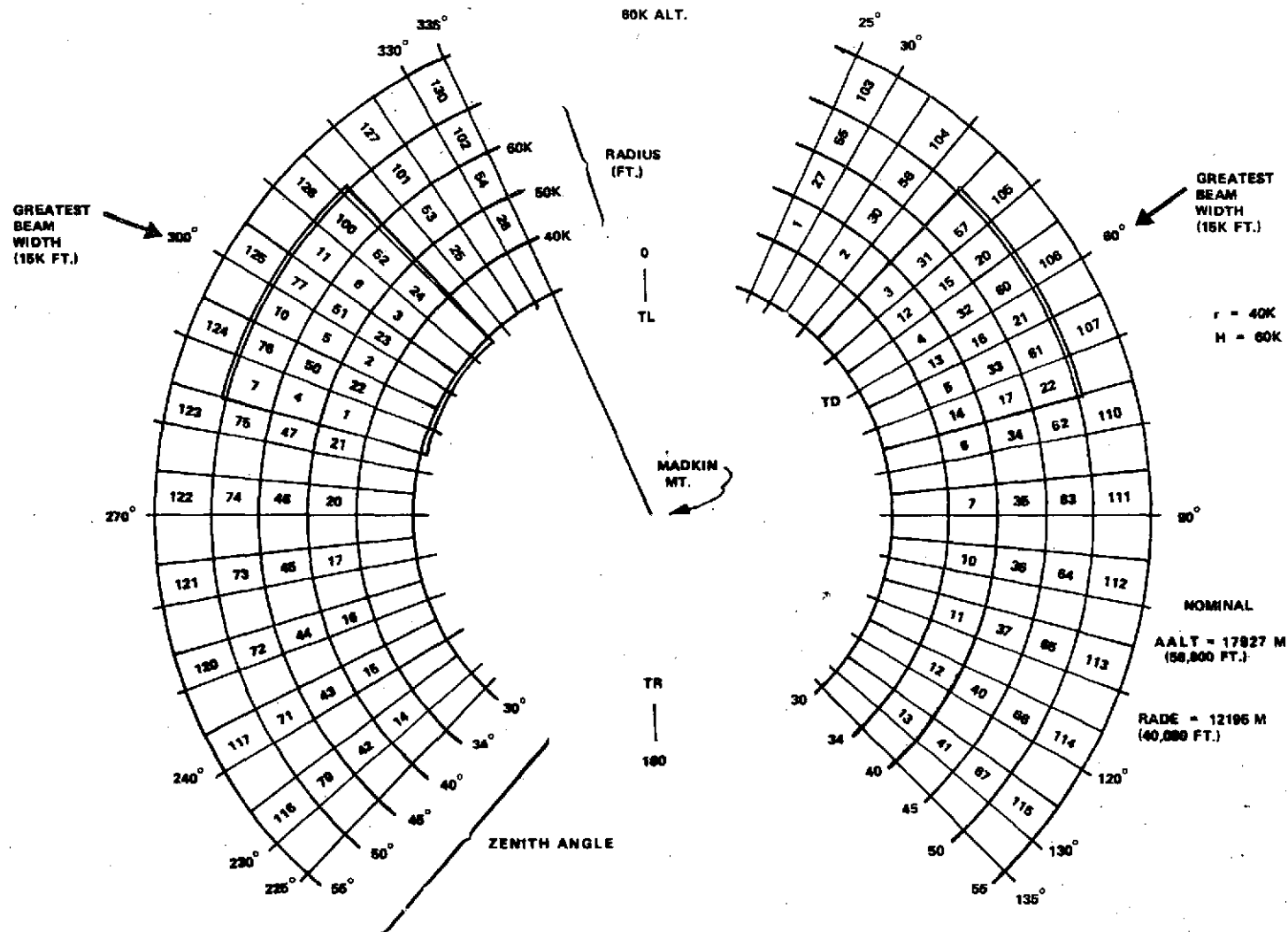Figure 205. Computer servo control flow chart.

394

Figure 206. Prepositioning window locations.

$$\cos\alpha_W = \cos\delta \, \cos\phi \, \cos\theta + \sin\delta \, \sin\theta$$

$$\cos\beta_W = \cos\delta \, \sin\phi$$

$$\cos\gamma_W = -\cos\delta \, \cos\phi \, \sin\theta + \sin\delta \, \cos\theta$$

$$T_{xe} = K_D \, \sin\delta \, \cos\phi \, \cos\theta + r \, \sin\phi \, \cos\theta - K_D \, \cos\delta \, \sin\theta + K_{xe}$$

$$T_{ye} = - K_D \, \sin\delta \, \sin\phi + r \, \cos\phi$$

$$T_{ze} = - K_D \, \sin\delta \, \cos\phi \, \sin\theta - r \, \sin\phi \, \sin\theta - K_D \, \cos\delta \, \cos\theta + K_{ze}$$

$$T = \left[T_{xe}^2 + T_{ye}^2 + T_{ze}^2 \right]^{1/2}$$

$$\cos\alpha_T = \frac{T_{xe}}{T} \, , \quad \cos\beta_T = \frac{T_{ye}}{T} \, , \quad \cos\gamma_T = \frac{T_{ze}}{T}$$

$$\cos\theta_{TW} = \cos\alpha_T \, \cos\alpha_W + \cos\beta_T + \cos\gamma_T \, \cos\gamma_W$$

$$W = - T \, \cos\theta_{TW} + \left[T^2 \, \cos^2\theta_{TW} - T^2 + R^2 \right]^{1/2}$$

$$R_y = W(-\cos\delta \, \sin\phi) + T_{ye}$$

$$R_z = W(- \cos\delta \, \cos\phi \, \sin\theta + \sin\delta \, \cos\theta) + T_{ze}$$

$$\cos\epsilon = \frac{R_z}{\left[R_y^2 + R_z^2 \right]^{1/2}}$$

ϵ is the azimuth of the dome measured clockwise from North.

$\phi = \Phi - 180°$ Φ is the polar axis encoder reading.

$\delta = 180° - \Delta$, Δ is the declination axis encoder reading.

$\theta = 34.667$ degrees,

$r = 1.33$ meters

$K_D = 15.25$ cm.

$K_{xe} = 0.889$ meters

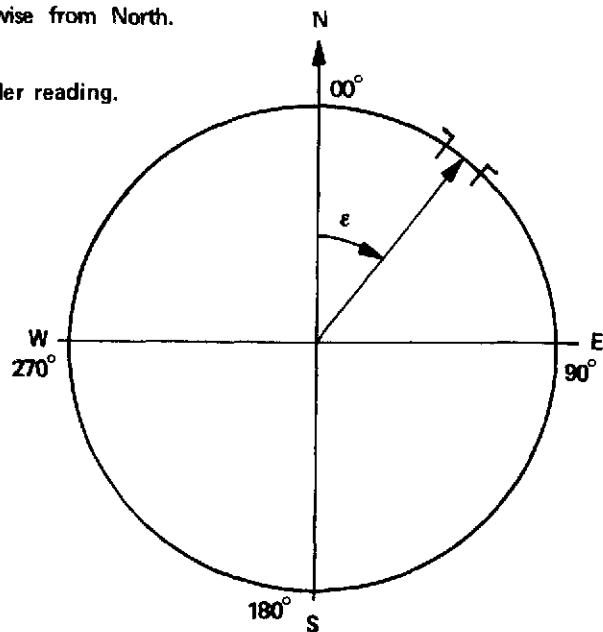$K_{ze} = 68.6$ cm.

$R = 3.81$ meters

Figure 207. Dome control equations.

would position the ground telescope to one of several predetermined acquisition window in the circular flight path. The second is a derivation of the equations required to automatically position the dome over the telescope's line of sight. The problem of dome control turned out to be an extremely complicated exercise to solve adequately. The situation was compounded by the offset geometry of the telescope installation, the necessity for maintaining an adequate viewing angle of the GBAA, and other complications. The solution of the dome control equations required, in final form, approximately half of the available computer memory storage. This is to say that the dome control program required as much programming as the rest of the control and display software combined.

A general discussion of the GBAA tracking system has been presented earlier so a lengthly discussion of its characteristics need not be presented here. Some of the designed system parameters are

(1) a tracking accuracy of ± 0.436 mrad (± 1.5 Δ min),

(2) a required tracking sensitivity of 24 7.62-cm diameter retroreflectors at a range of 18 km,

(3) an angular position data rate of 16 samples/sec, and

(4) an angular position range of ± 5 deg.

The significant points of discussion in evaluation of the GBAA's performance deal with the observed sensitivity and tracking accuracy. Early in the program some difficulties were encountered with the pulsed laser used in the GBAA. This problem was soon solved and the system worked quite reliably. The pointing position data from the GBAA to the control computer did, however, require a limited degree of numerical filtering in order to achieve the desired tracking accuracy.

Figure 208 shows the typical tracking signal obtained from the GBAA while undergoing field tests during a helicopter tracking experiment. The target range during this test was approximately 5 km.

Shown in Figure 209 is the signal obtained while tracking the WB-57F aircraft at an altitude of 18.3 km (60 000 ft). The data were taken early in the program and are somewhat degraded from the desired accuracy.
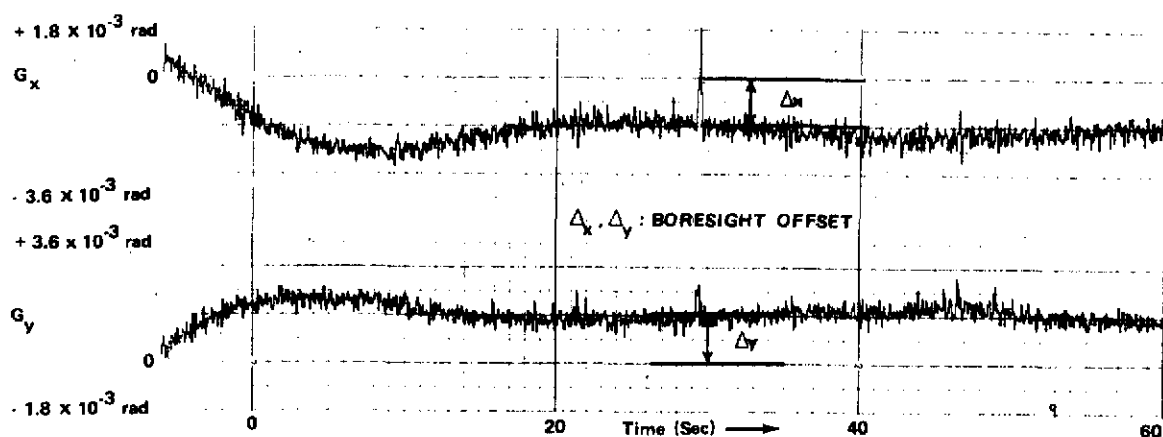
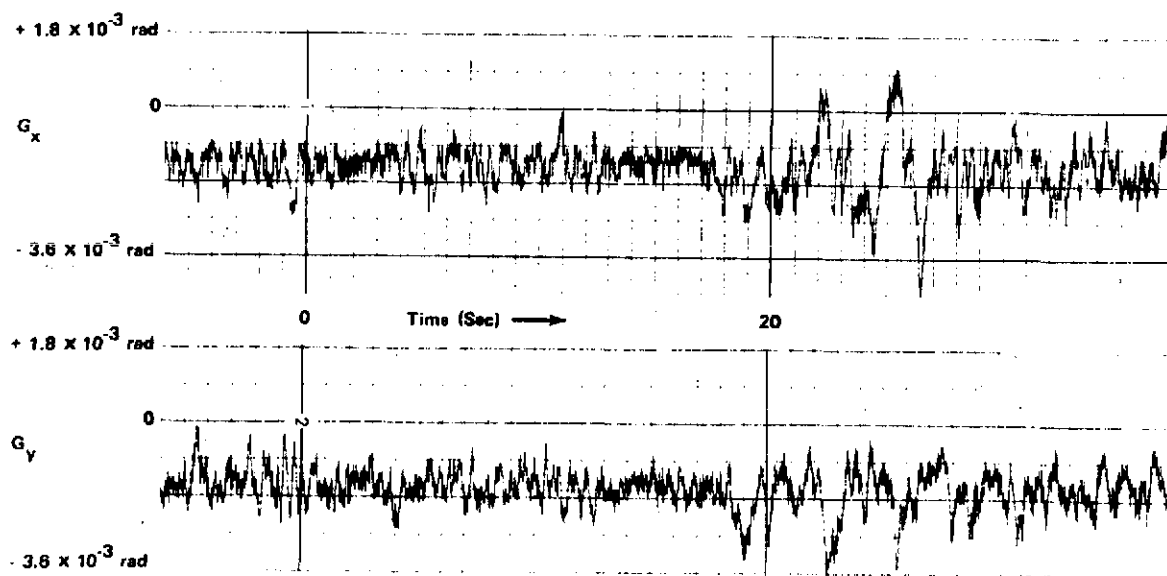Figure 208. GBAA error signals during helicopter test.

Figure 209. GBAA error signals tracking WB-57 aircraft.

Figure 210 shows the same type of data taken during a later flight.
Prior to taking the data some rework of the GBAA logic circutry had occurred
and the tracking accuracy of the system had improved noticeably. Although no
recorded data was taken to illustrate the tracking sensitivity of the GBAA, it
was an unqualified success at tracking extremely low return signal levels.
Even during periods of aircraft maneuvering which obscured certain corner
reflector arrays, the system tracked the aircraft with little or no loss of
track information. In general the system performed much more reliably and
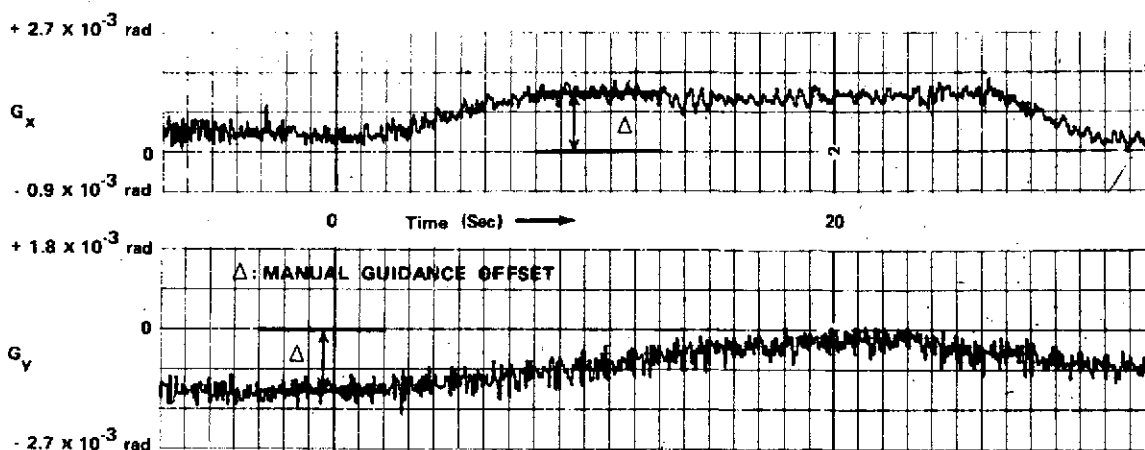to a greater degree of sensitivity than had been expected.

Figure 210. GBAA error signals tracking WB-57 aircraft, modified system.

The data taken with regard to the fine tracking system actually addresses two systems: (1) the transceiver fine tracking system, and (2) the telescope-computer closed loop. The pertinent parameters of the fine tracking system are: (1) a tracking range of ± 0.436 mrad (± 1.5 arc min), (2) a tracking accuracy of ± 5 μrad (± 1 arc sec), (3) a tracking bandwidth of 100 Hz, and (4) a sensitivity of 10^{-9} watts received. All data taken during all the flight series indicate that the complete fine tracking loop performed precisely as designed. The sensitivity of the system was shown to be more than adequate. As will be shown in a later section on 632.8-nm corner reflector tracking, a modification, during a flight test, allowed for approximately an order of magnitude increase in tracking sensitivity and allowed for experiments to be performed which had not been previously planned. One consideration which should be kept in mind, as the reader reviews the tracking data presented here, is the range of tracking velocities encountered during a typical circular path over the ground station. The typical velocities seen at the acquisition points were in the range of 0.5 deg/sec.

The control system was programmed such that closing tracking velocities were controlled and limited (during the coarse acquisition and tracking sequence) to stay within the dynamic tracking limitations of the tracking sensors. The maximum tracking velocities reached during a complete circle registered quite high values. As the target approached the polar region of the circular flight path, velocities reached values of 3 deg/sec to 5 deg/sec. The data presented in the following figures depict the tracking accuracy achieved by the pointing system of the main telescope. The tracking errors in a region of constant velocity, even at high velocities were on the order of 10 μrad. To

399

reiterate, the data were actual telescope pointing and following errors. The accuracy with which the fine tracking system was tracking the target and directing the transmitter beacon was significantly better than this value. Residual pointing errors were not recorded, but were observed on monitoring equipment and found to be significantly less than 5 μrad in all instances. The largest following errors observed in the telescope's tracking accuracy were during acceleration and deceleration at the high velocity regions around the polar area of the circular flight path (this is characteristic of equatorial telescope mounts tracking targets which traverse paths which approach a line of sight path near parallelism with an axis of rotation.)

The following data illustrate the accuracy with which the system performed. Shown in Figure 211 is a plat of typical polar and declination velocities seen during a circular flight path. On some occasions the polar velocity was observed at values somewhat larger than shown here, but these values are more typical of a controlled flight path. The data in Figure 212 were taken during field testing and verification of tracking system performance. The data were taken while tracking a helicopter moving at a constant velocity of approximately 3.5 deg/sec.

Figure 213 is representative of the tracking performance typically achieved during periods of fine track lock-on by the aircraft. At no time was the accuracy of this system even considered to be of marginal performance. The accuracy and dynamic range of the ground fine tracking system met all expected and design parameters and in some conditions (periods of high velocity tracking) actually exceeded the anticipated degree of accuracy.

BORESIGHT

The whole category of ground station transmitter beam control, intensity and profile was subject to one of the most intensive investigations of the project. The photometry of the transmitted beacon intensity has been treated elsewhere in this report and will not be reiterated here except to restate that at divergence angles of less than the full 0.873-mrad (3-arc min) FOV, the beacon intensity was entirely adequate for reliable tracking by the aircraft terminal.

Also to be considered is the necessity to maintain boresight of the fine track LOS and the transmitted beacon. Since the beam divergence is varied during a flight experiment it also is necessary that no variation exist in this boresight relationship as the transmitter beamwidth is varied.
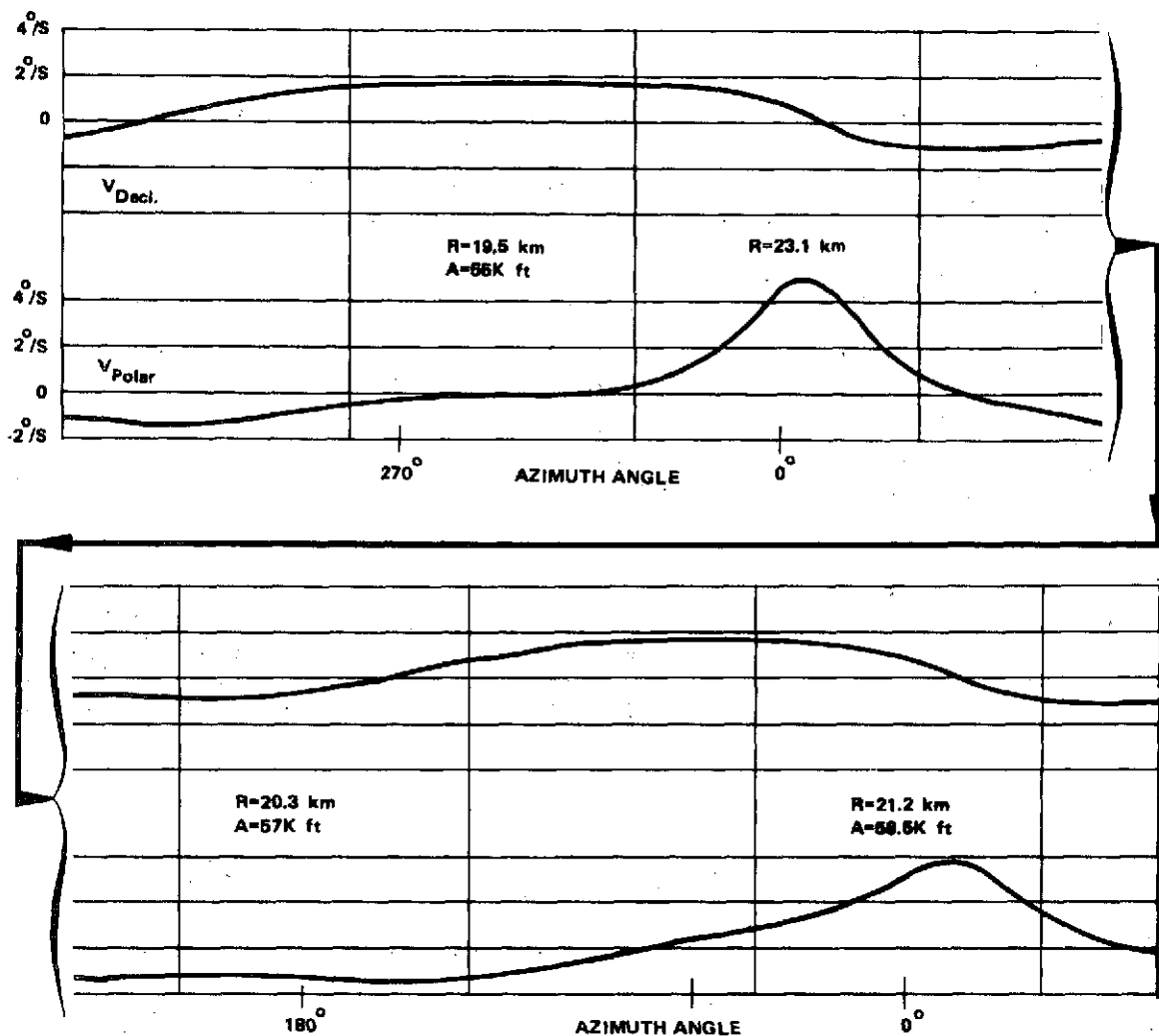
Figure 211. Polar and declination velocity versus azimuth angle.

During initial verification tests of the ground station system, a series
of experiments were performed over an 8-km (5-mi) test range at MSFC. A
632.8-nm He-Ne laser source was used to provide a fine tracking target and the
return beacon energy (488 nm) was observed at the remote test site. During
these experiments, a test was devised to measure the boresight error at the
fine track channel in the ground station transceiver. By using this technique
the system could be adjusted for minimum boresight error at the ground station.
This procedure was thoroughly verified through the series of tests over the
test range. The tests for boresight accuracy were incorporated into the
standard preflight procedures to assure an accurate boresight alignment was
maintained over the full range of divergence angles. Also, during any par-
ticular flight, this measurement was rechecked and alignment of the boresight
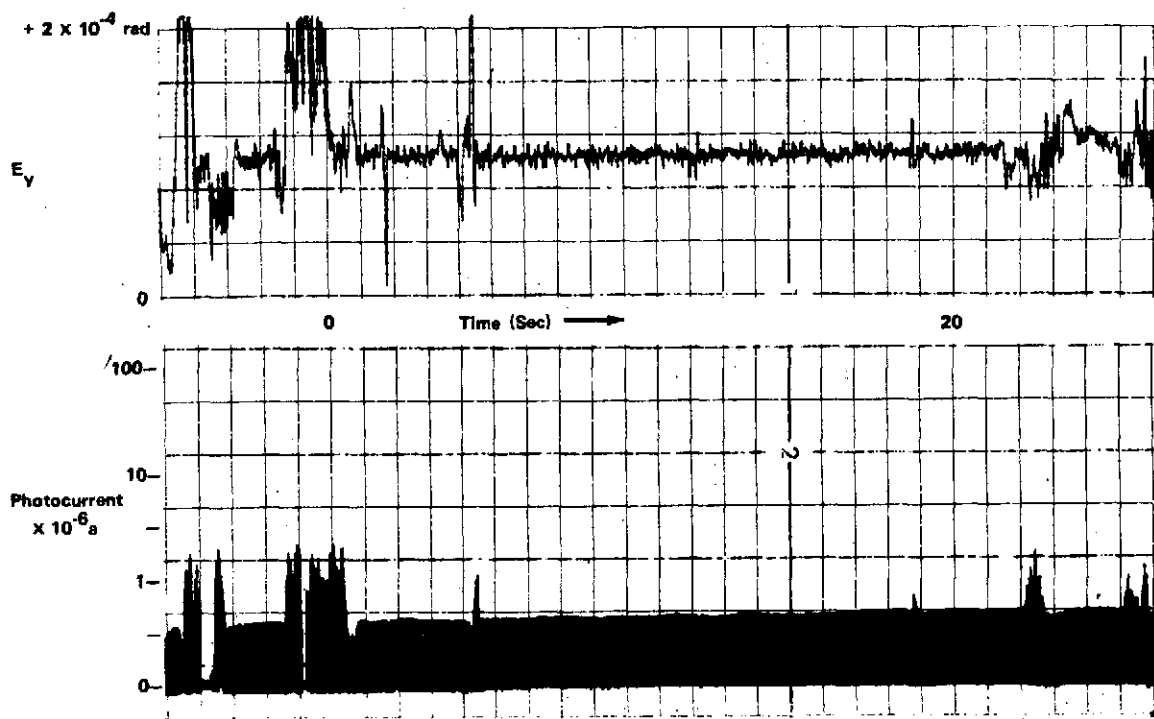was readjusted to maintain an accurate alignment.

Figure 212. Fine track signals during helicopter test.
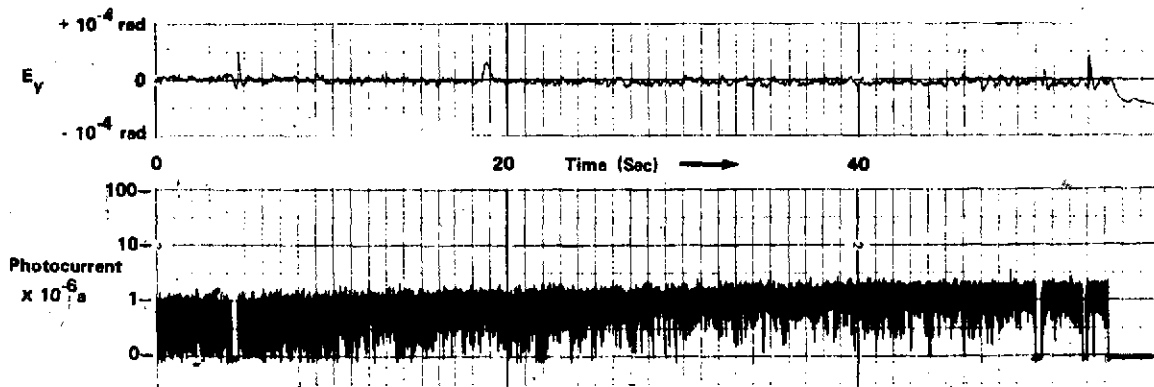
Figure 213. Fine track signals during WB-57 flight.

During long periods of operation, it was noted that drift would occur in the transmitter boresight alignment. This drift was attributed to two major causes. First was the long term thermal drift of the laser. This phenomenon was noted early in the program, and was partially solved by utilizing a controlled, constant temperature cooling system for the laser plasma tube. Although this greatly reduced the thermal angular drift of the laser output beam, a small amount of drift was still apparent.

402

Secondly, and of more significance, was drift of the optical modulator. This effect was manifest in two areas, angular drift and modulation index variation. The problems associated with the modulator will be discussed more fully later, but the significant point of relevance here is that of angular deviation and drift. Due to the power levels which were used (approximately 250 mW (it was determined that absorption and heating losses in the modulator were contributing to distortion and misalignment of the optical materials in the modulator. This in turn led to a deviation of the transmitted beam and variation in modulation index.

By careful monitoring of the system it was, however, possible to maintain an overall accurate boresight alignment of the system. Guidance of this accuracy can be seen in Figure 214. This figure shows the power received at the aircraft erminal, as the ground station 488-nm beacon divergence is varied from an angle of 0.436 mrad to a minimum angle of 20 μrad. It will be noted that a dropout of signal occurred in the range of 20 μrad divergence. This indicates a boresight accuracy of approximately 10 μrad.

Perhaps the most significant result of the problems encountered with maintaining this accurate alignment, is the obvious need for remote monitoring and alignment of the transmitter/receiver channels. Preferably this function would be implemented in an automatic system. Until the quality of lasers and modulators reach a sufficient degree of stability, the need for this alignment monitoring and adjustment capability will be inherent in any system of this type.

BEAM PROFILE

One of the most curious, and as yet not fully understood, phenomena associated with the transmitter is that of the energy profile of the transmitted beam. This distribution would ideally have followed the classical Gaussian distribution for a laser beam. This, however, was not the case. It was noted, during all attempts to measure this pattern, that the energy received, at a distant receiver, did not follow the divergence square relationship. That is, with a beam divergence of 145 μrad the energy was not four times as great as at a divergence angle of 290 μrad. This effect may have had several causes. It is generally felt, however, that the energy distribution, instead of being Gaussian, had a somewhat peaked distribution allowing a greater than normal fraction of the energy in the central portion of the beam. Measurements were made over long path ranges of different distances, and all measurements disclosed the same effect. Due to the extreme complexity of the optical system used to control the beam divergence of the transmitter, a significant portion of this effect may be attributed to wavefront deformations introduced by this system. Again, however, this phenomenon is still not fully understood at this time.
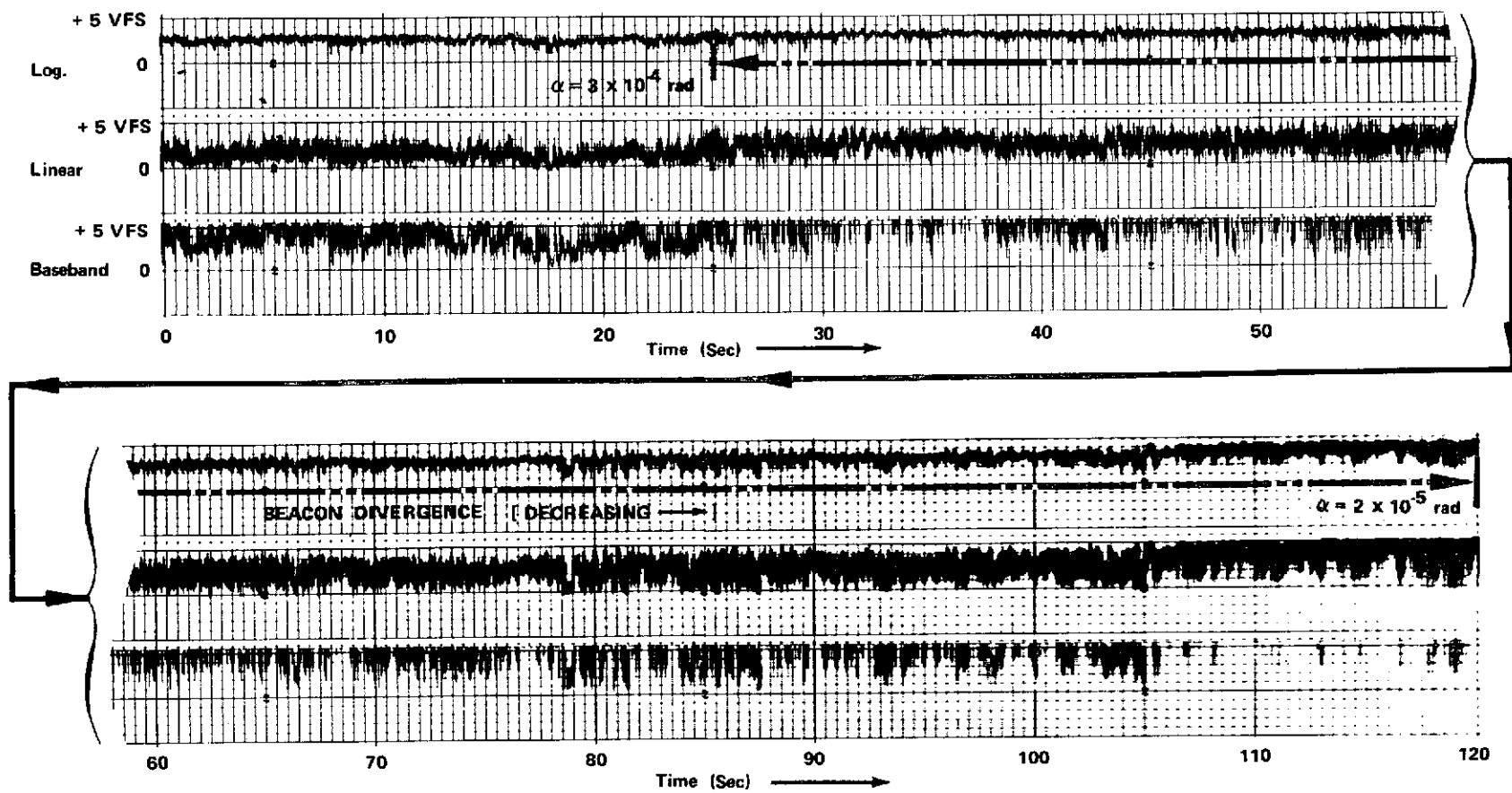
Figure 214.   AOCP received beacon power.

An additional point of note concerns the means by which one transmits a diverging beam through a Cassegrain telescope configuration to a target within the near field diffraction distance of the telescope. It was originally intended to fully fill the telescope aperture with the transmitter beam. During field testing, however, it was discovered that this technique simply will not work. As the transmitted beam diverges, the obscuration produced by the telescope secondary mirror forms a shadowed area which grows as the beam is diverged. This shadow completely voids the receiver terminal of energy. It is necessary, therefore, to offset the transmitted beacon and reduce its diameter to allow it to pass through the telescope unobstructed. This geometry is shown in Figure 215.
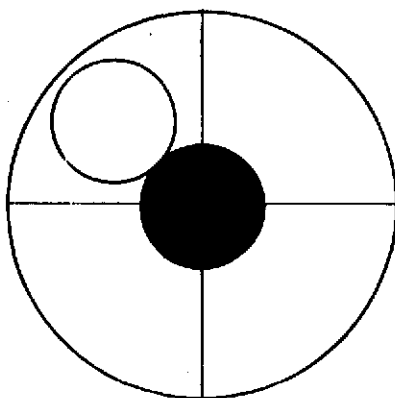
Figure 215. Beacon exit location in ground station telescope.

UPLINK COMMUNICATION SYSTEM PERFORMANCE

The function of the communication hardware at the ground terminal was to provide an information channel to the airborne experiment equipment to: (1) provide command data to the AOCP for control of various optical parameters and data channel switching, and (2) provide course deviation information to the pilot to maintain a more accurately referenced circular flight path.

After the acquisition and fine track modes of both aircraft and ground systems had been accomplished, the ground to air communication link was exercised and found to work extremely well.

As previously described, the ground-to-aircraft channel was based on utilization of 488-nm laser with a 10.7-MHz modulation carrier. This carrier was then, in turn, frequency modulated with various audio subcarriers to provide for command and PDI data.

During the final series of flights when the aircraft system could establish sustained periods of fine track lock-on, the command channel was quite extensively exercised.

All of the command functions were tested and found to function quite reliably. During the final flights quite long periods of sustained fine track were achieved. This allowed the use of the orbital track PDI to be evaluated. This system was used by the pilot and was found to function quite well. The basic concept of total dependence on this indicator to maintain an accurate circular path is somewhat questionable though, due to the problem of wind drift and the time at which correction must be applied for a proper flight path. The computation, transmission, and display of orbital deviation to the aircraft did, however, function quite well.

Perhaps the most serious problem encountered with the ground station communication link was drift of the modulator. This problem with the modulator became more evident when the index of modulation was monitored over an extended period of time. A monitoring device was implemented to allow a remote measurement of modulation index. This measurement was monitored during the duration of an aircraft flight. If the performance of the modulator was found to be degrading significantly, an operator would then readjust the alignment of the modulation channel. It was noted that a severe degradation in modulation index was also accompanied by a corresponding transmitter boresight misalignment. Typical values for the modulation depth ranged from approximately 35 percent to approximately 90 percent. For most of the experiment time this value was in the range of 70 to 80 percent. When the modulation depth had degraded to 35 to 40 percent a need for readjustment was indicated, and adjustment of the system usually returned the performance to its nominal values.

Resolution of the problems encountered with the modulator will require considerably more work in the field of electrooptic modulator technology before a great deal of confidence can be placed in their reliable operation. Changes in alignment and index changes of the materials need to be much more carefully controlled before a hands-off reliable system can be assured. If this cannot be overcome, a system of monitoring and automatic control will be required.

Observations of 632.8 nm Auxillary Tracking

In the process of establishing procedures for insuring the boresight alignment of the coarse and fine tracking systems, an auxiliary 632.8 nm laser was attached to the 61-cm telescope. This laser was then boresighted to the main telescope and used as a source to illuminate a carrier reflector array at a remote location. The alignment tests for boresight involved tracking the retroreflector array with the coarse acquisition system (514.5 nm) and simultaneously tracking the array with the fine tracking system at 632.8 nm. The angular difference measured as boresight error between the two systems was then programmed into the control computer to establish a fixed boresight offset to insure a coaligned tracking configuration while tracking the aircraft. This procedure was performed prior to all flights to insure correct boresight of the coarse and fine tracking systems.

Although the auxillary 632.8 nm laser was not originally intended for use during the flights, it was later decided to attempt tracking the aircraft corner reflectors by illuminating the aircraft with the auxiliary laser and tracking the return energy with the 61-cm telescope and fine tracking system. The laser was used without any additional beam-forming optics and transmitted a nominal 2-mrad beam. The transmitted power was approximately 5 mW. Although this experiment was attempted more or less out of curiousity, it produced somewhat surprising results. By removing one of the attenuation filters in the fine tracking channel of the ground transceiver, a sufficient level of return energy was available for tracking. Thus, the laser on the telescope (632.8 nm) could be energized and the aircraft tracked by the ground transceiver fine tracking system. This procedure was utilized several times during the final series of flights. Although a reasonable margin of return signal was available by this technique it could not be used reliably for any extended period of time. Due to the small spatial resolution of the fine tracking system, the fine tracker would effectively jump from one corner reflector array to another. This condition would eventually degenerate to a low frequency oscillation of the tracking system in jumping from array to array of the aircraft corner reflectors.

An extremely important result was concluded from this exercise. That was to validate the accuracy to which the fine tracking system, control computer, and telescope drive could track the aircraft target throughout its circular flight path. At the time of the first attempt of tracking the aircraft corner reflectors with the fine tracking system, no period of sustained fine track of the aircraft had yet been achieved. By the successful results obtained during this auxiliary experiment, the validity of the complete fine tracking loop was thus thoroughly proven. Shown in Figure 216 is a period of fine track using the auxilliary ground 632.8-nm transmitter and fine track system.
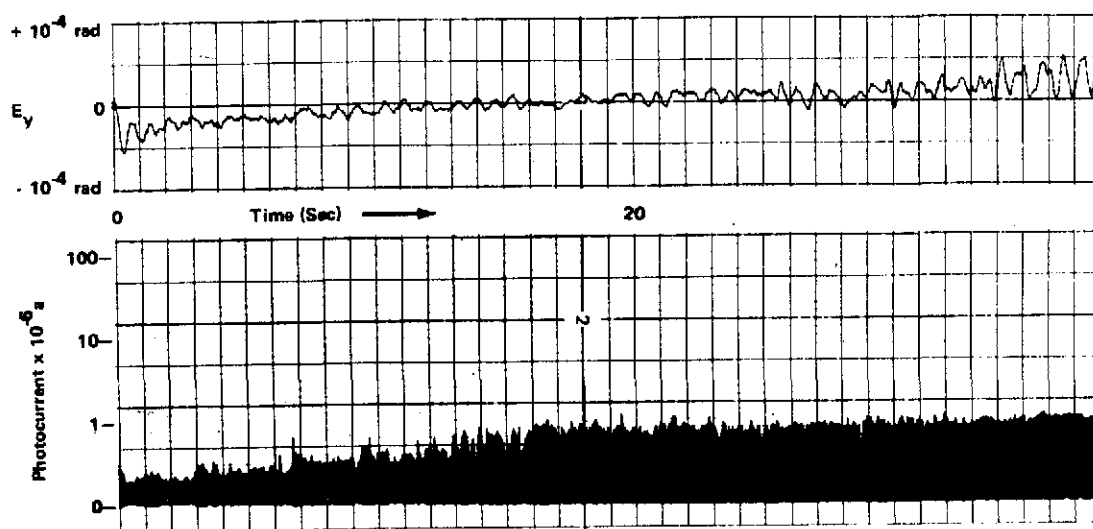
Figure 216. Fine track signals using strap-on 632.8-nm source.

FLIGHT HARDWARE MODIFICATIONS AND FIELD CHANGES

Field Changes at Ellington AFB

As a result of operational problems, several hardware changes were made in the field during the course of the flight program. More details on these changes are given in this section. These field changes are summarized in Table 49, including the reason for making a particular change. Basically, all the changes involved three areas: 1) the coarse acquisition problem; 2) the fine track problem; and 3), the temperature control problem.

The coarse acquisition problem involved the failure of the gimbal platform/coarse TV tracker to acquire the ground beacon during the first three flights. It was to solve this problem that the first four changes listed in Table 49 were made. By removing the He-Ne shutter, thereby allowing the red beam to be transmitted continuously, the ground station could determine if the gimbal platform was properly pointed for a significant part of the time. Probably the most important of these changes was the incorporation of the gimbal scan search routine in the software. The basic coarse TV tracker field of view is approximately 5 deg square. The scan routine effectively increased this to 11 deg square as shown in Figure 217. For simplicity, the search is assumed to start at $(\theta, \phi) = (0, 0)$, whereas in practice it would normally start at or close to (54 deg, -2 deg), depending on how well the pilot is holding the nominal 34-deg zenith circle and 20-deg bank angle. The starting coordinates are always given to the operator by the ground station crew.

408

TABLE 49. SUMMARY OF AVLOC FIELD CHANGES

|	Description of Change	Reason for Making Change
1.	Remove shutter from He-Ne laser in aircraft.	So that the red beam might be seen on the ground even without fine track at the aircraft.
2.	Install cockpit control for removal/insertion of TV filter.	So that for night operation, the coarse TV might track on both the green and blue lasers.
3.	Install cockpit monitor and controls for coarse TV tracker.	So the operator could optimize the TV sensitivity against a particular background and report on what the TV was actually viewing.
4.	Incorporate a search routine for gimbal platform in computer software.	To effectively "increase" the TV acquisition range from 5 deg × 5 deg to 11 × 11 deg.
5.	Restrict size of cold-air duct in ECS by 60 percent.	To increase the heat available to the AVLOC equipment and better balance the AOCP and canister temperature.
6.	Change software program to reduce initial He-Ne beam divergence from 1.06 mrad to 0.84 mrad.	To increase the received power at the ground station.
7.	Install heater in AOCP enclosure.	To raise AOCP temperature and help balance the AOCP-canister temperature.
8.	Install cockpit control for disabling beamsteerers.	To determine if the beamsteerer loop was causing fine track problem.
9.	Install cockpit display for switching out "scintillation hold" feature.	To determine if it was the "scintillation hold" relay within the beamsteerer loop that was causing the fine track problem.
10.	Relocate AOCP temperature telemetry sensor from overall enclosure to inside the modulator compartment.	To determine the operating temperature of the modulator compartment so that the boresight and modulator adjustments could be done at this temperature.
11.	Install remote boresight controls in cockpit.	To allow the operator to statically align the transmit/receiver beams, based on directions via radio from the ground station.
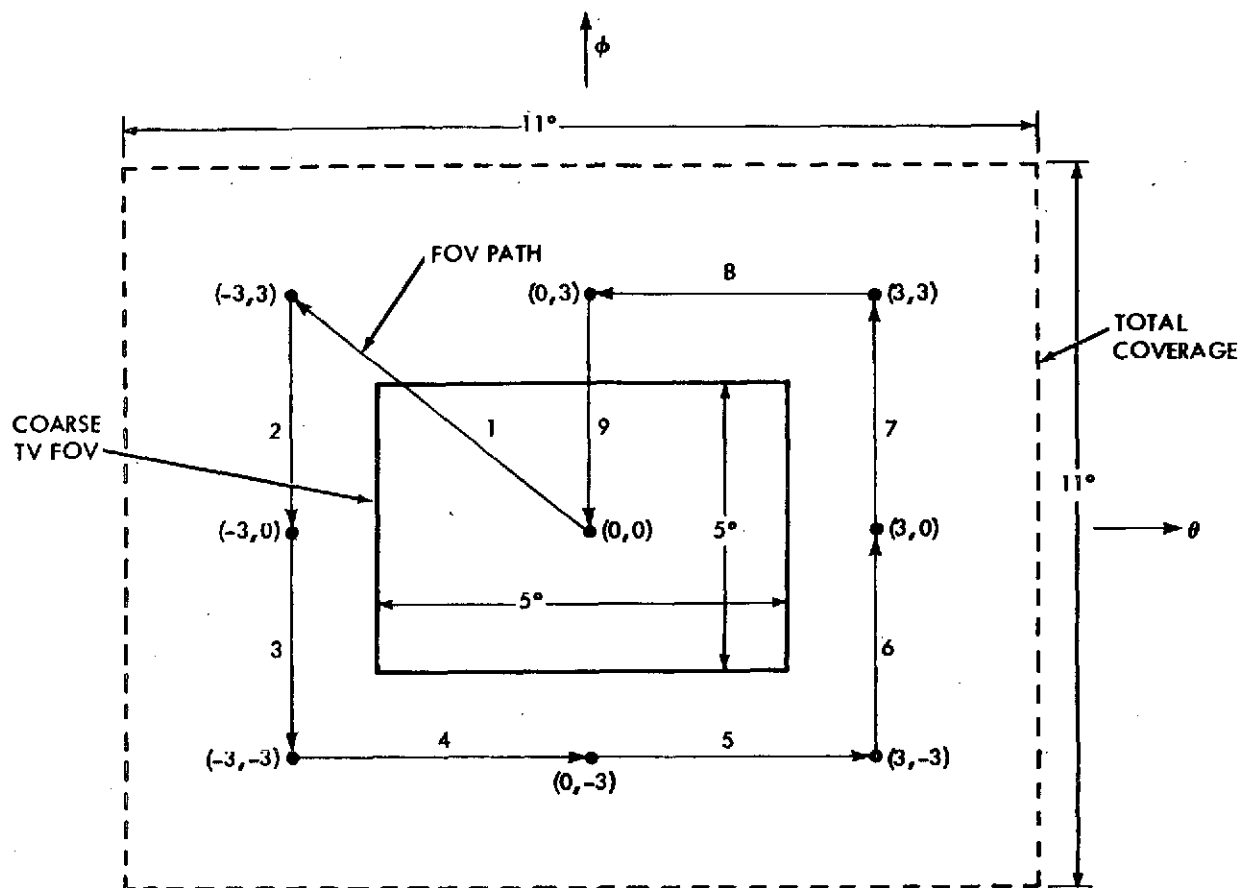
Figure 217. Gimbal search scan.

The search pattern is generated by stepping the pointing direction in 3-deg steps as shown in Figure 217. The gimbals come to a complete stop after each step, which allows the vidicon tube to integrate any received image for sufficient time to trigger its target-presence generator.

Changes 5, 7 and 10 of Table 49 relate to the overall temperature control problem.

Actually, the term problem could be misleading, since the ECS system met its minimum performance requirements. This system was designed to maintain the temperatures of both the AOCP and the canister at between $60°F$ and $90°F$ under a normal mission flight profile. A normal flight profile involves rapid ascent to maximum altitude and operation there throughout the mission until time for descent. The temperature requirements were met for this profile.

However, although the ECS system satisfied its performance specifications, it was less than satisfactory in three major respects: 1) the ECS system had marginal heat capacity, 2) the heat capacity was highly dependent on engine thrust setting, and 3) there was an inherent imbalance between the AOCP and the canister, with the canister running 20-25° F hotter.

The heat capacity of the system was such that, with the heat valve fully open and the engine thrust at a maximum, the AOCP temperature at maximum altitude never ran greater than 65-70° F. This means that any time altitude was reduced, which was a frequent requirement in order to increase the received beacon power level, the AOCP temperature would quickly drop below th 60° F design specification because of the lower engine setting.

The temperature imbalance between the AOCP and the canister was caused simply by the fact the canister dissipated more heat (1000 watts vs 160 watts). Eventually, electric heaters were added to the AOCP enclosure to increase its heat generation. A better solution, had there been time and money, would have been to redo the ECS duct work so as to place the canister and AOCP in series, with the AOCP making use of the heat from the canister.

Changes 6 and 11 of Table 49, and 10 to a certain extent, are related to the problem of maintaining two-way lock and downlink reception. The received He-Ne power at the ground station throughout the flight program never rose above the marginal level. This power was determined by the beam divergence, the boresight alignment, and the modulator alignment, which affected both boresight and modulation index (TM reception was dependent on good modulation, whereas two-way lock was dependent only on received power). Thus, the first change, a quite simple one, was to reduce the initial beam divergence from 1.06 mrad to 0.84 mrad (one step). This helped but did not solve the basic problem, that the transmit/receive paths were consistently misaligned during flight operations. Since the boresight was believed to be temperature dependent, the next step was to install a temperature sensor in the sealed modulator-laser compartment in order to measure the actual operating temperature there. The modulation index and boresight adjustment could then be set up on the ground at this operating temperature. The results showed that in flight the laser compartment remained at 65-70°F even when the AOCP temperature was much lower. This was because of the heat generated inside the sealed compartment.

Unfortunately, although it might have helped some, this approach did not solve the boresight problem (and with a boresight problem, the modulation index cannot be effectively measured). The next step was to install remote boresight controls in the cockpit. This system, which was tested only on the last flight, proved to be very successful. However, it was not possible to set the modulation index on the ground at the proper temperature. Therefore,

even for the last flight, when all the problems were believed to have been solved, TM reception on the ground was bad; and indeed it is not known for sure even yet that the modulation-index problem was completely solved.

Changes 8 and 9 of Table 49 were related to the fine track problem. This problem manifested itself as a tendency of the system to jump into and out of fine track more or less continuously. The beamsteerer loop was suspected to be the cause all along. By installing cockpit controls that allowed the beam-steerers to be disabled by the operator in flight, it was proved conclusively that this was the case. The next step was to determine which part of the beam-steerer loop was the difficulty. The scintillation-hold relay was suspected. Therefore, a cockpit switch was installed which allowed the operator to disable this relay in flight. The test results, however, proved inclusive. The fine track problem is discussed in detail in the following subsection of this report.

Laboratory Test and Modification of Airborne Fine Track System

At the conclusion of the WB-57F flight program, the AOCP fine track system was still beset with continuing failure to track reliably, despite many repeated efforts at patching up the system. The problem was an inability to get the AOCP to lock-on and track the upcoming beacon from the ground station with the AOCP beamsteerer control loop active. A reasonable amount of tracking could be accomplished with the beamsteerer loop off and only the gimbal mirror active, but this did not produce sufficient accuracy. Since the aircraft was no longer available for use, it was decided to bring the equipment back to MSFC and try to analyze the problem.

After considerable discussion, the following items were outlined as control problem areas that required investigation and possible modification to effect satisfactory operation:

1. Tracking rate — what is the limiting caused by?

2. Size of spot on the ID from GCE — how does this compare with the beacon laser projected from the GS?

3. What is the amplitude of movement of the aperture of the ID during track mode?

4. Measure the saturation voltages of Ey, Ez, By, Bz, in the beamsteerer amplifiers.

5. Verify the time constants involved in acquisition and the transient conditions during switchover to track mode.

6. Investigate noise levels for improving S/N ratio.

7. Investigate the approximately 200-Hz scintillation induced phenomenon.

After the equipment was returned and put in operation it was checked to see if operation remained as it was when installed in the aircraft. This was confirmed to be the case although a number of extraneous problems were encountered in doing so. One particular problem that appeared was in the gimbal mirror drive system which would fail to track under certain circumstances. It was decided that because of time limitations the AOCP fine track problem should be worked on first, so the gimbal mirror problem was deferred.

The AOCP was set up to track between the Madkin Mt. GS and Astrionics Lab and certain problems were observed. The beamsteerer tracking system again would not consistently lock on the ground station. In order to try and understand what was occurring a set of recordings were made of the ID output with the system in track and with the beamsteerers off. These recordings indicated signals having excursions of approximately 68 μrad peak to peak and frequencies approaching 200 Hz. It was known that angular scintillations at frequencies much above 20 Hz should be much less than those observed. This suggested that the automatic gain control on the ID must be failing to remove the amplitude variations in the signal which causes them to be interpreted as angular scintillations. Because of this, an analysis of the ITT 32-kHz video amplifier was begun.

It was observed during operation of the AOCP that the output of the 32-kHz video amplifier was very noisy and had significant amplitude variations in the output. This was true even though the input signal was as much as 20 mV at the time. An analysis of this amplifier and some of the findings are given in the next paragraph. In addition, a replacement amplifier is shown with some of the salient features described.

Figure 218 is a schematic of the original 32-kHz video amplifier. The operational amplifier in the forward path (μA 739) is a low noise wide bandwidth amplifier selected to keep the phase shift at 32 kHz near zero. The two operational amplifiers (μA 747) are used in conjunction with the 2N5245 FET's to produce a wide bandwidth AGC. Additional AGC is used in the first amplifier stage via the 2N3910 transistor and the 2N5245 FET.

During analysis of this amplifier it was discovered that there was about 60 deg of phase lag at 32 kHz. Bench tests determined that the lag was occurring in the second and third operational amplifiers. The cause was traced to the 0.01 μf capacitors between pins 11 and 12 and pins 2 and 3 of these amplifiers. These capacitors were removed and the amplifier seemed to operate

413

normally; however, the amplifier is excessively complicated and the frequency response was not high enough to be capable of removing the signal amplitude variations, therefore, another amplifier was breadboarded and used. Figure 219 is a schematic diagram of this amplifier. As can be seen by comparison with the original amplifier, this is a simpler scheme having only two AGC stages driven by a single AGC amplifier. The phase shift through this amplifier at 32 kHz is negligible and the AGC will respond to changes of 40 dB up to frequencies of 1 kHz. When tracking the Madkin Mountain laser the system has performed well, essentially eliminating the signal fades and reducing the observed angular scintillation as well.

One of the major weaknesses of the original AOCP tracking system was the tracking rate limitation of the ID sensor. Tests run on the AOCP system using the GCE revealed that target rates greater than 3 deg/sec would cause the ID to lose the target. Thus, even for small scintillations the signal was often lost. This caused the insertion of a number of components in the beamsteerer loop to reduce the rate of the beamsteerer during acquisition. (This is explained in another paragraph).

The cause of this problem is understood by an examination of the circuitry on schematics, Figures 220 and 221, which are drawings of the deflection loops of the ID. The left hand side of the drawing is the demodulator and integrator. The gain of this circuit is low because of the long time constant associated with the integrator, (e.g.,

$R_3 \times \dfrac{C_5 C_6}{C_5 + C_6} = 2 \times 10^3 \times 160 \times 10^{-6} = 0.32$ seconds). This charging time constant determines the maximum rate the signal can follow the target. By reducing the size of the capacitors C_5 and C_6 and adding some additional gain in the (μ A 741) operational amplifier on the output the demodulator gain was raised sufficiently to bring the tracking rate up to about 50 deg/sec. This greatly improved the ability of the system to track without loss of target with the beamsteerers off and in addition made the response of the ID tracker comparable to the beamsteerer. In addition, this allowed the beamsteerer electronics to be modified to eliminate the rate limiting circuitry and thus greatly simplify these electronics. The modified demodulator circuitry is shown on the modified schematics Figures 222 and 223.

The beamsteerer electronics are shown in Figures 224 and 225. A number of modifications were made to this electronics to improve operation.

One place that seemed to cause problems was the input amplifier section. The original system had a gain of about 268 in the two μ A 747 (A1-a & A1-b) operational amplifiers. This was followed by an attenuation network before being applied to the operational amplifier OP-05 which drives the beam-
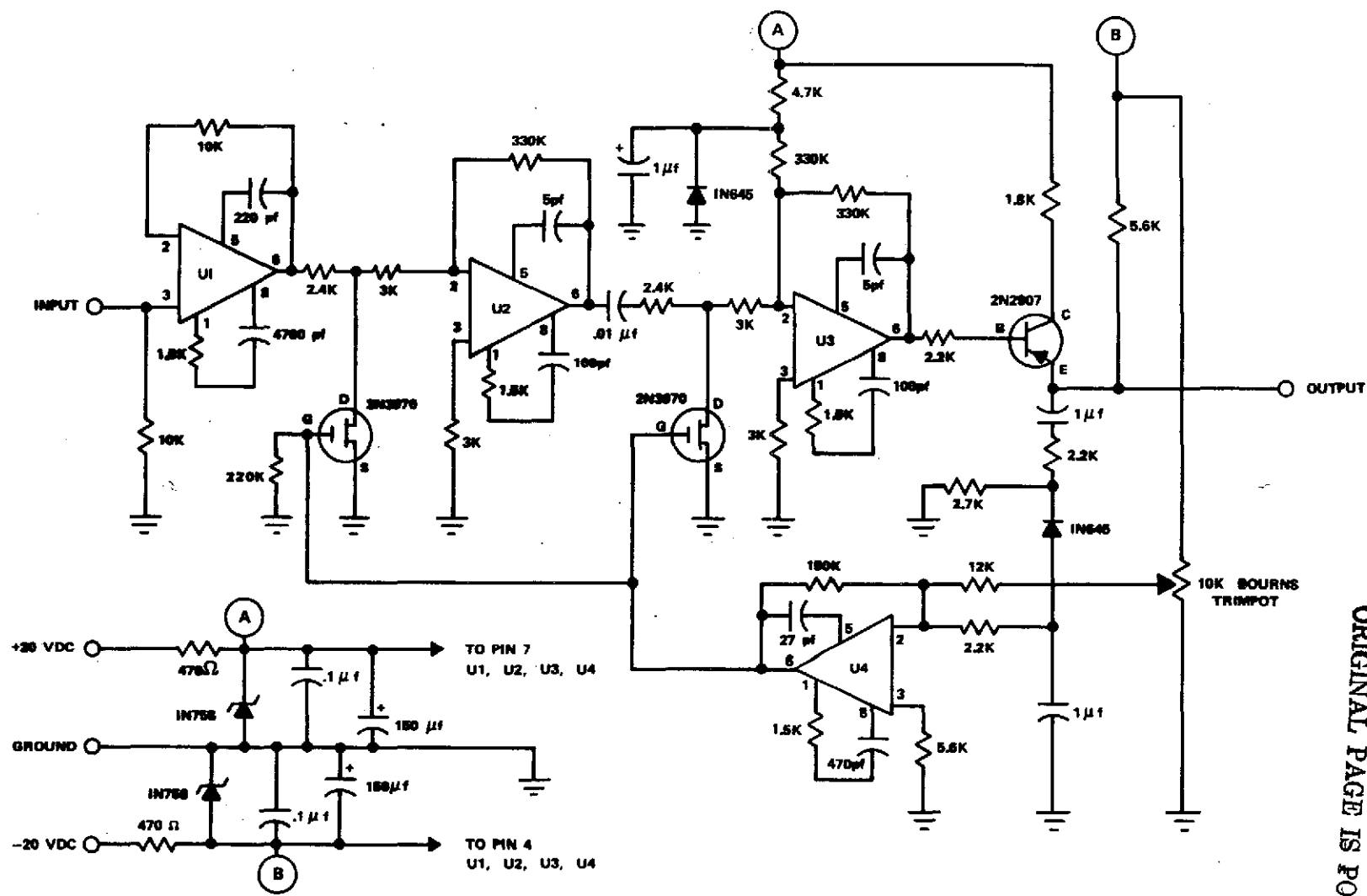
Figure 218. 32-kHz video amplifier.

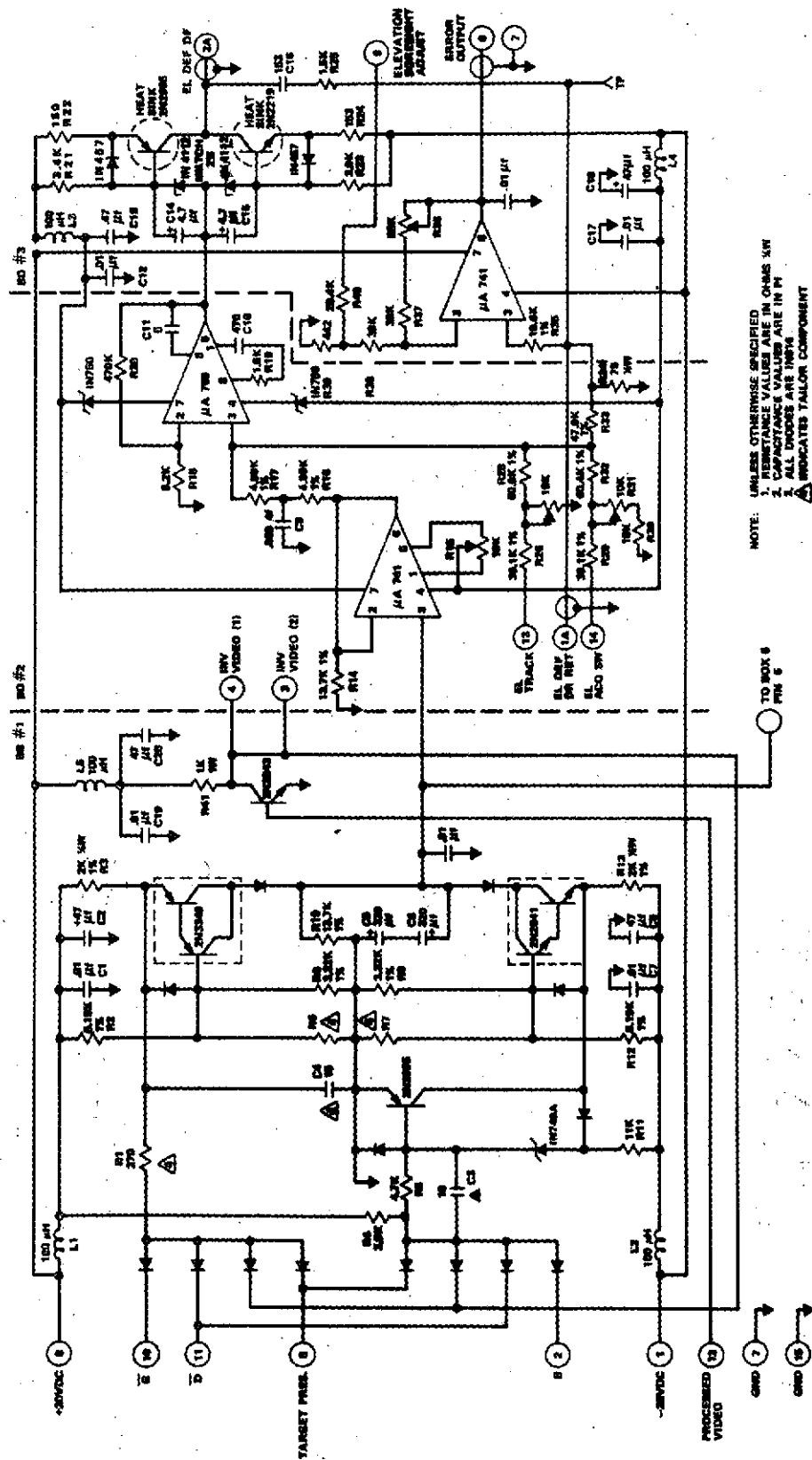NOTE: 1. U1 U1, U2, U3, U4 ARE UA709

Figure 219. 32-kHz video amplifier, modified version.

Figure 220. Elevation error generator.
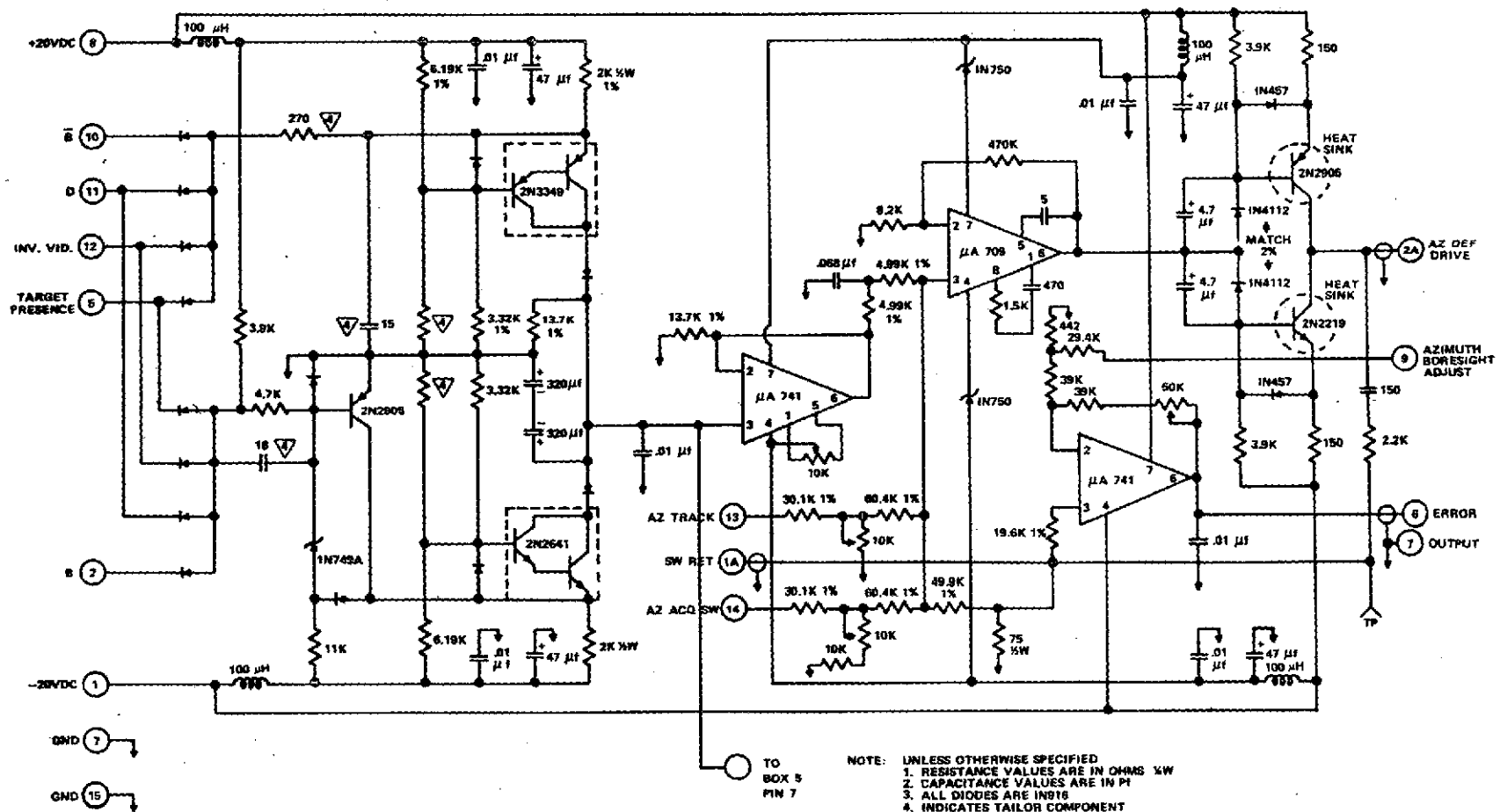
Figure 221. Azimuth error generator.
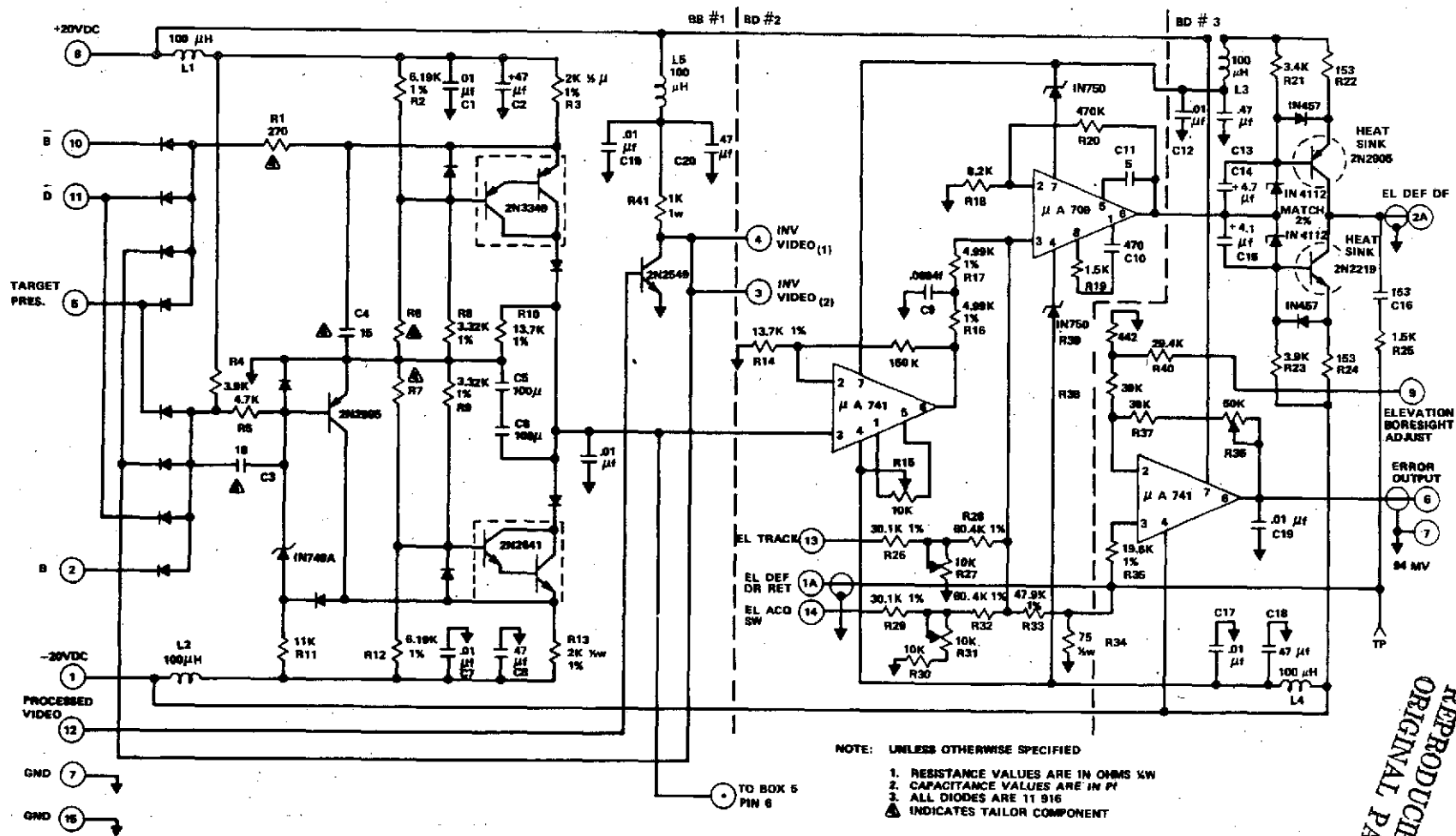
Figure 222. Elevation error generator, modified.

Figure 223.   Azimuth error generator, modified.
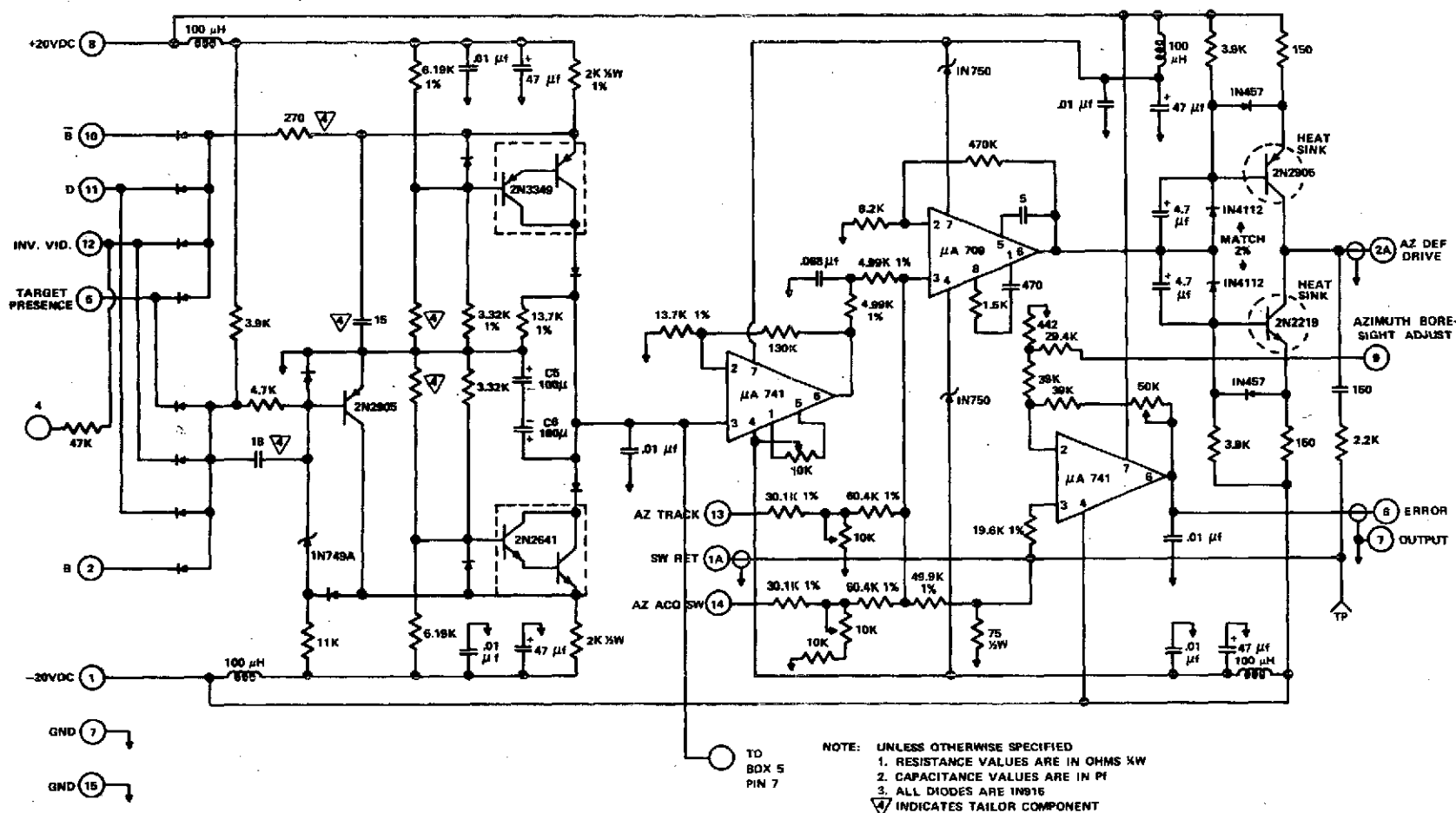
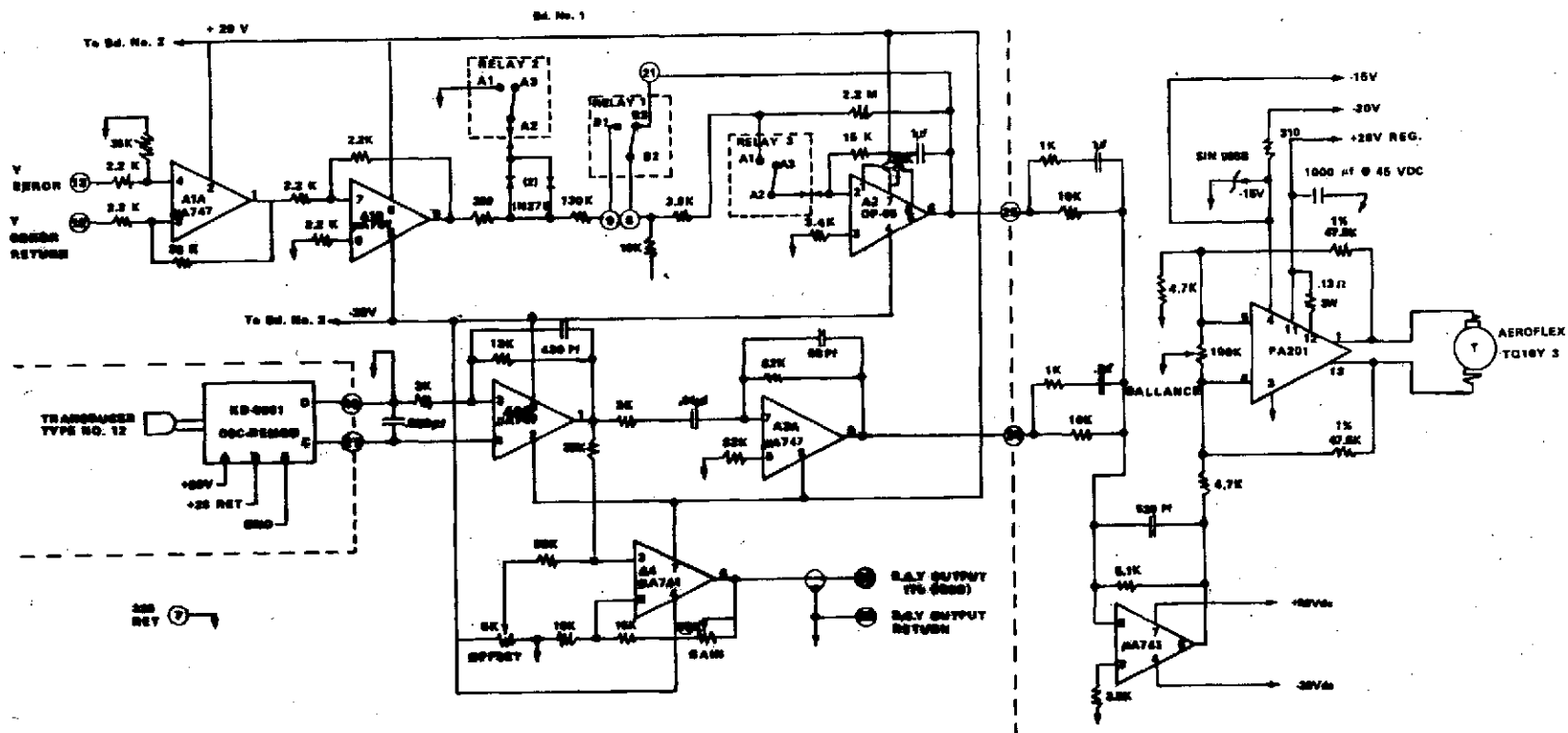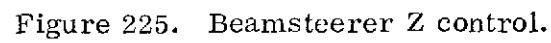Figure 224. Beamsteerer Y control.

Figure 225. Beamsteerer Z control.

steerer power amplifier. This gain of 268 allowed a signal of 70 mV or greater to saturate the second stage (Al-b). This amplitude represents an error of only 63 μ rad in the incoming target beam. Therefore, large scintillations, acquisition and numerous other distrubances caused the amplifier to saturate and create significant distortion.

The reason for this type design arose because of the necessity of rate limiting the beamsteerers to keep the ID from losing the target because of inability to track at rates above about 3 deg/sec. After this was changed as described in a previous paragraph so that rates of up to 40 to 50 deg/sec could be tracked, the necessity of rate limiting was obviated. Therefore, this circuit was changed to remove this anomaly, by reducing the input gain to unity, and also to eliminate the attenuating networks. This also eliminated the need for relay 2 which simplifies the electronics significantly. Some additional modifications to the amplifier OP-05 were made to reduce the lag there. All these modifications are shown on the enclosed drawings (Figs. 226 and 227).

One additional modification was required in the beamsteerer control. Throughout the program there have been problems with the commercial power amplifiers (PA 201 by Analog Devices of Norwood, Mass.) used and for any future flights these should be replaced. To make these work more satisfactorily in the present system it was required that the two be run from separate power supplies. There appears to be sufficient cross-coupling between the two amplifiers to cause stability problems in the present configuration.

Throughout the AVLOC program there have been questions on the quality of the AOCP optics, especially with respect to the capability to produce a focused spot sufficiently small on the photocathode of the ID (The aperture in the ID is about 0.004 in., therefore, the target image should be at least this small). Early in the program, when the AOCP was first brought to MSFC and tested, it was discovered that the telescope optics on the input were not of sufficient quality to produce the required target diameter and a new telescope was ordered and installed. Because of this background, the optics were checked and focused as well as possible.

Tests on the AOCP using the GCE still revealed that a target diameter of greater than 0.004 in. was being produced. Investigations revealed that part of this problem was in the GCE optics. A modification was made to this equipment, by installing a 0.005-in. mechanical aperture in the light path, to insure that the GCE output collimation angle was not adding to the problems of the AOCP. With this modification, the AOCP optics were focused and tests run which concluded that the target diameter was very close to the 0.004 in. required. This improved the tracking accuracy of the AOCP ID loop.
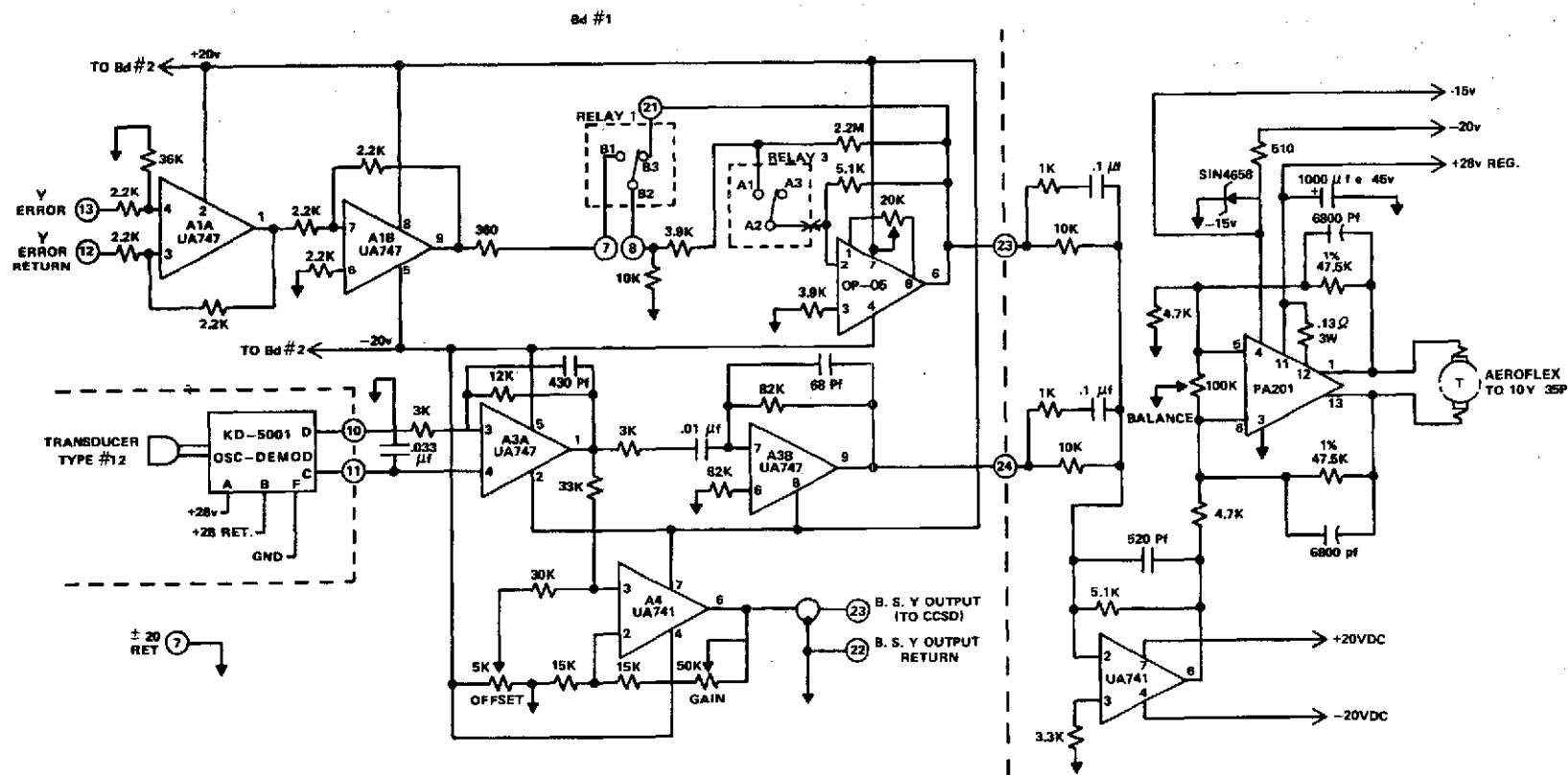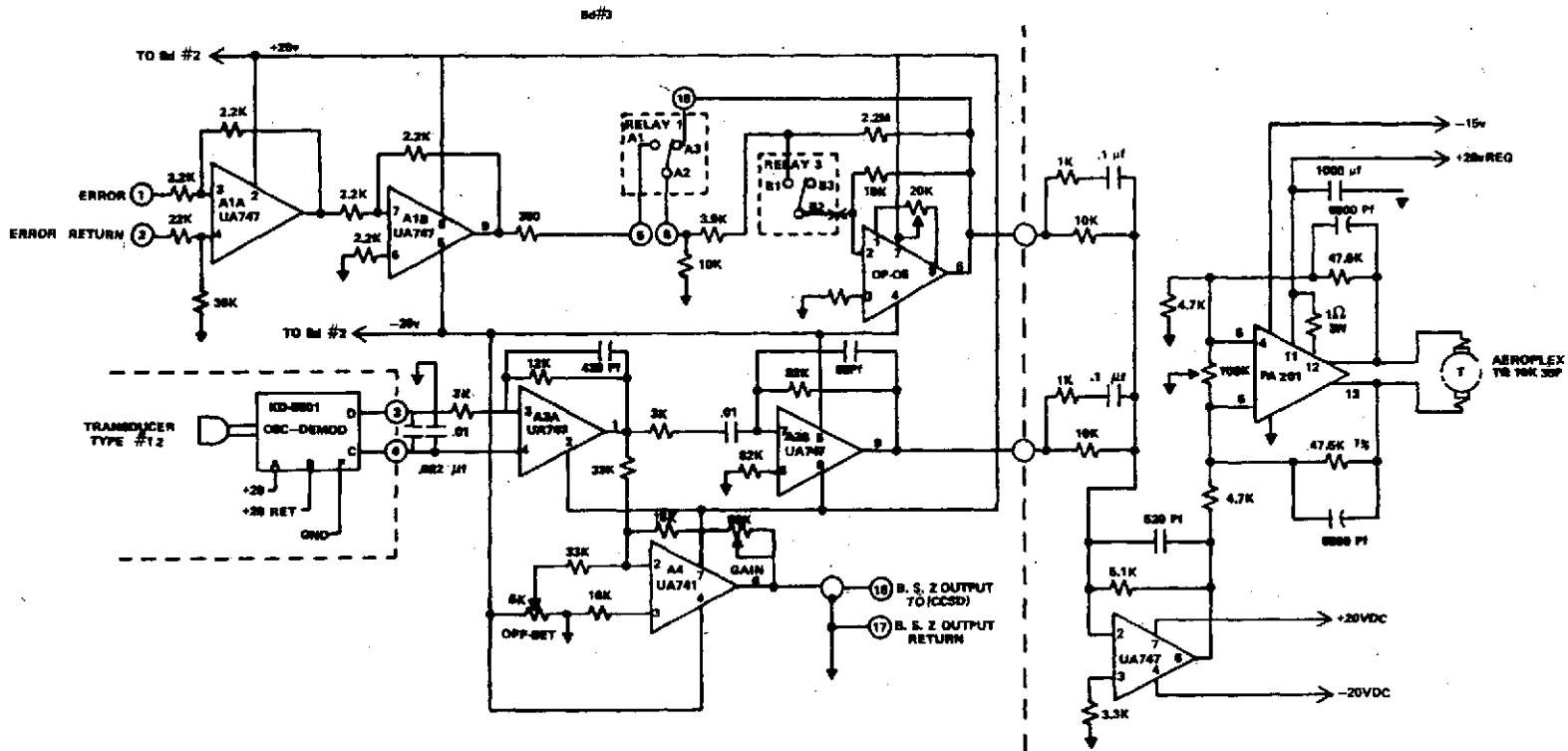
Figure 226. Beamsteerer Y control, modified.

Figure 227. Beamsteerer Z control, modified.

During subsequent testing of the AOCP it was discovered that when tracking with the beamsteerers ON and with large signal fades the beamsteerer loop would drop out but the ID would continue to track. This is a problem that has plagued the program for some time. An analysis revealed that this phenomenon could only occur if the target presence circuit driving the beam-steerer ON relay was dropping out before the actual target was lost. A check of the input to the circuit driving this relay revealed this to be the case (See Figs. 228, 229, 230). This was being caused by the target presence output from the 10.7-mHz amplifier which appears as a 32-kHz square wave and becomes a narrower pulse as the signal strength goes down. This drives into a low pass filter on the input of the driver circuit (Fig. 229) and for the narrower pulses the voltage is not sufficient to switch the input transistor.

By changing the input to this circuit from the 10.7-mHz amplifier to the output of the other target presence circuit this problem is improved. However, a better solution was found and is shown in the modified schematics (Figs. 231 and 232). On Figure 231 the input (Pin 23) was driven from the 10.7-mHz amplifier, but this was changed and is now driven by the output from the 32-kHz preamplifier. The output of this circuit (Pin 21) on this print, then drives a new circuit on Figure 232 consisting of an LM107 operational ampli-fier biased off when the target is not present and which is turned on when the target is present. The input circuit consisting of a 47K resistor and 6 μf capacitor produces a short time delay when acquisition first occurs to allow the ID output time to settle to a final value before the beamsteerers are energized.

The output of the LM 107 then drives the existing circuit which ener-gizes the beamsteerer relay and closes this loop. The two 2N2222 transistor stages could be eliminated in this circuit, but were left in the circuit for convenience.

The work described in this subsection was performed for the purpose of determining the causes of problems which had existed during the flight program. Therefore, when problems were uncovered solutions were sought which required a minimum of resources to correct. A number of the solutions are not as satisfactory as desired and additional development is needed. In particular, the present circuits associated with the beamsteerers are far from optimum. A new design, both electronic and electro-mechanical, was begun but has been dropped pending the decision of management on the continuation of this program. If the program is continued there are now very few unknowns in the pointing and tracking and a very much improved system could be readily assembled.
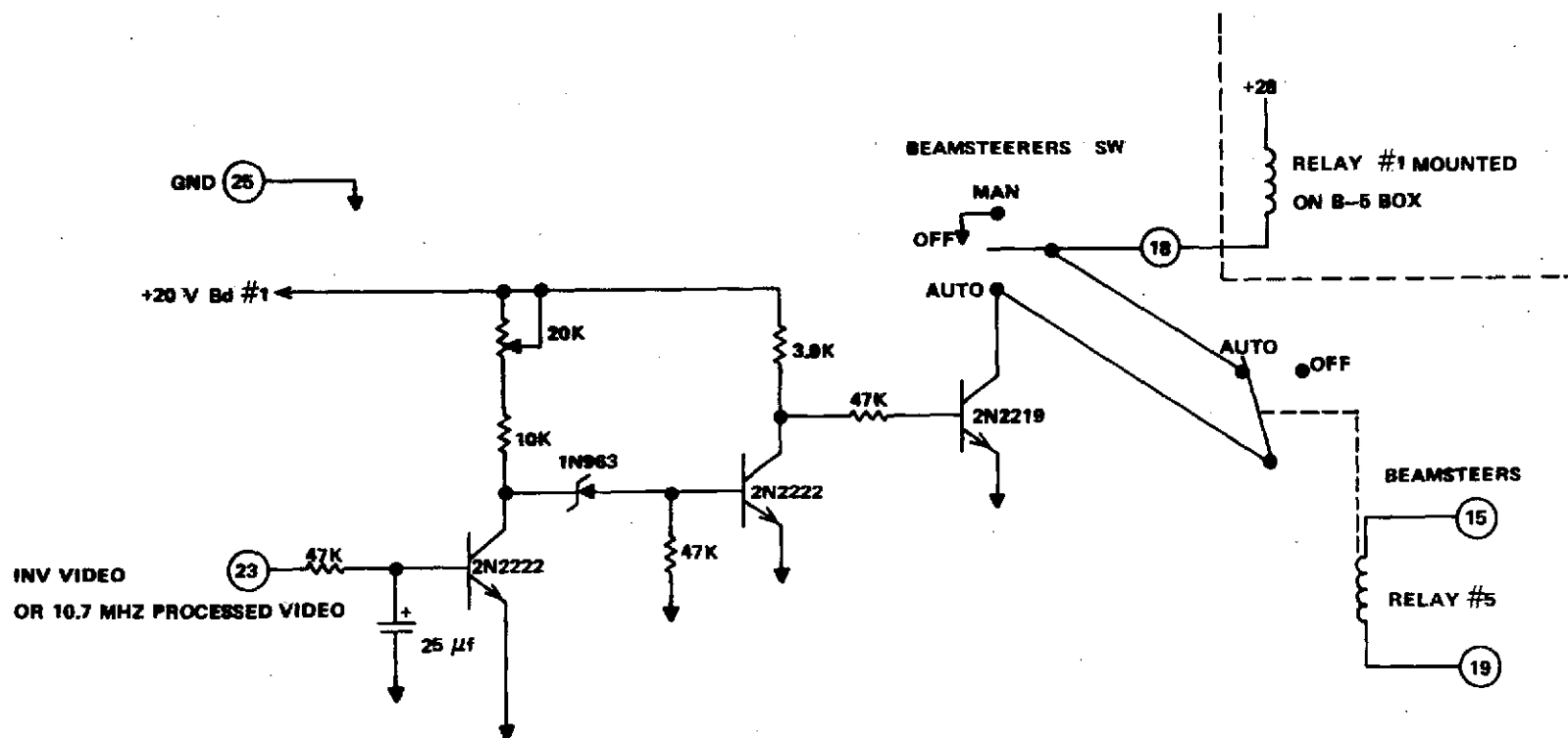
Figure 228. Target presence generator.

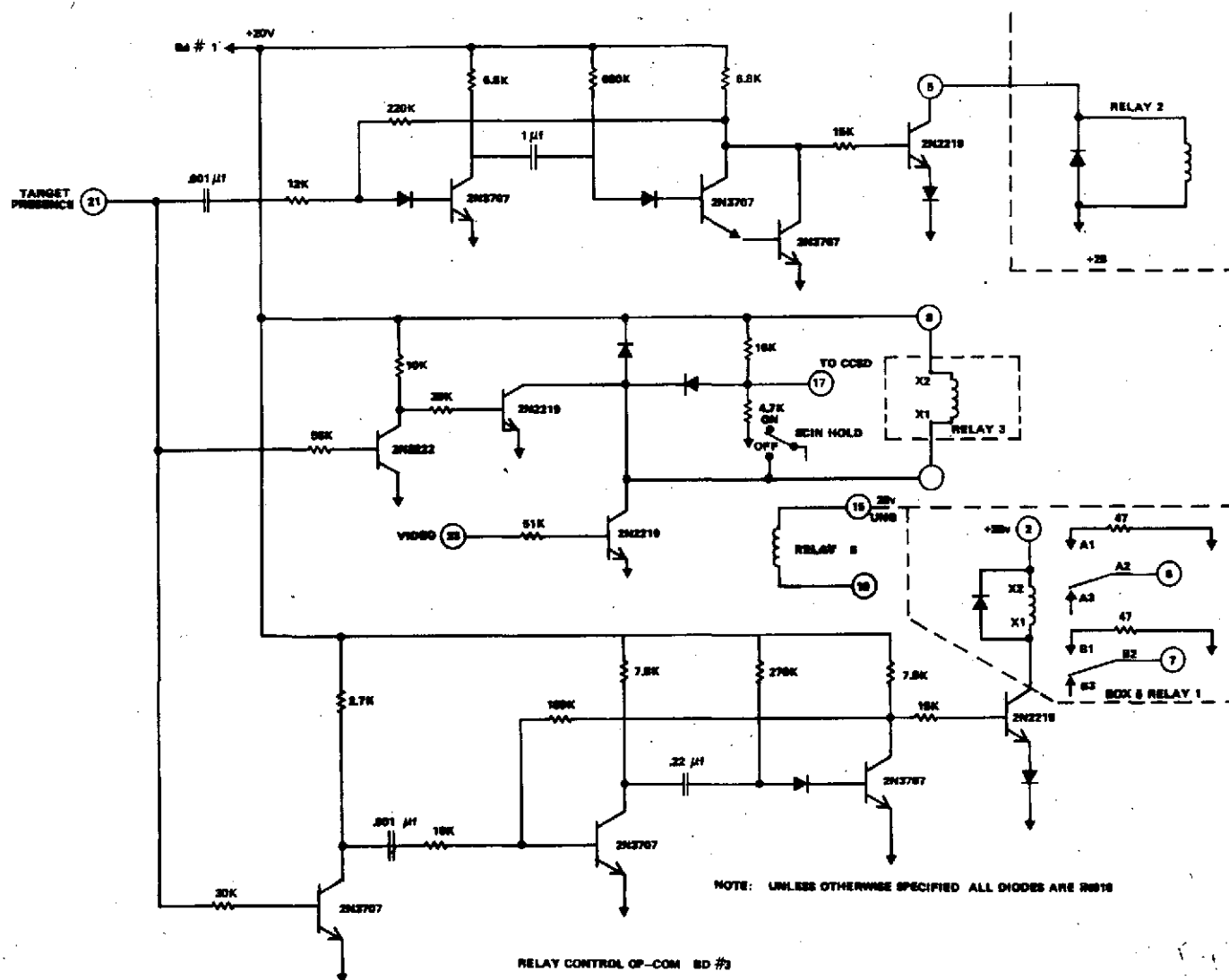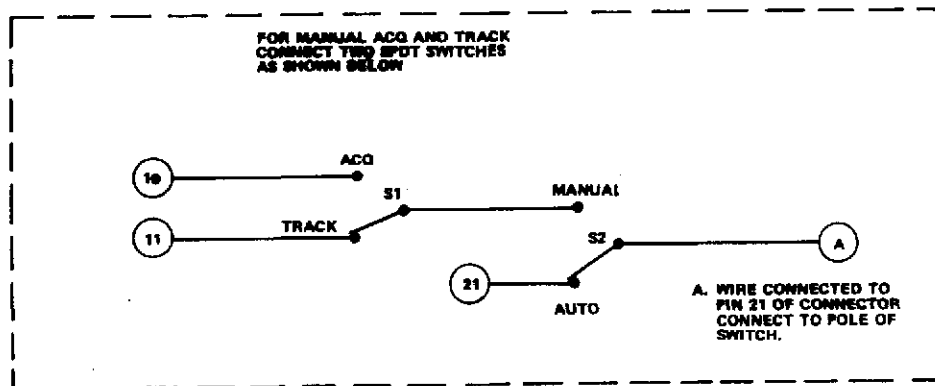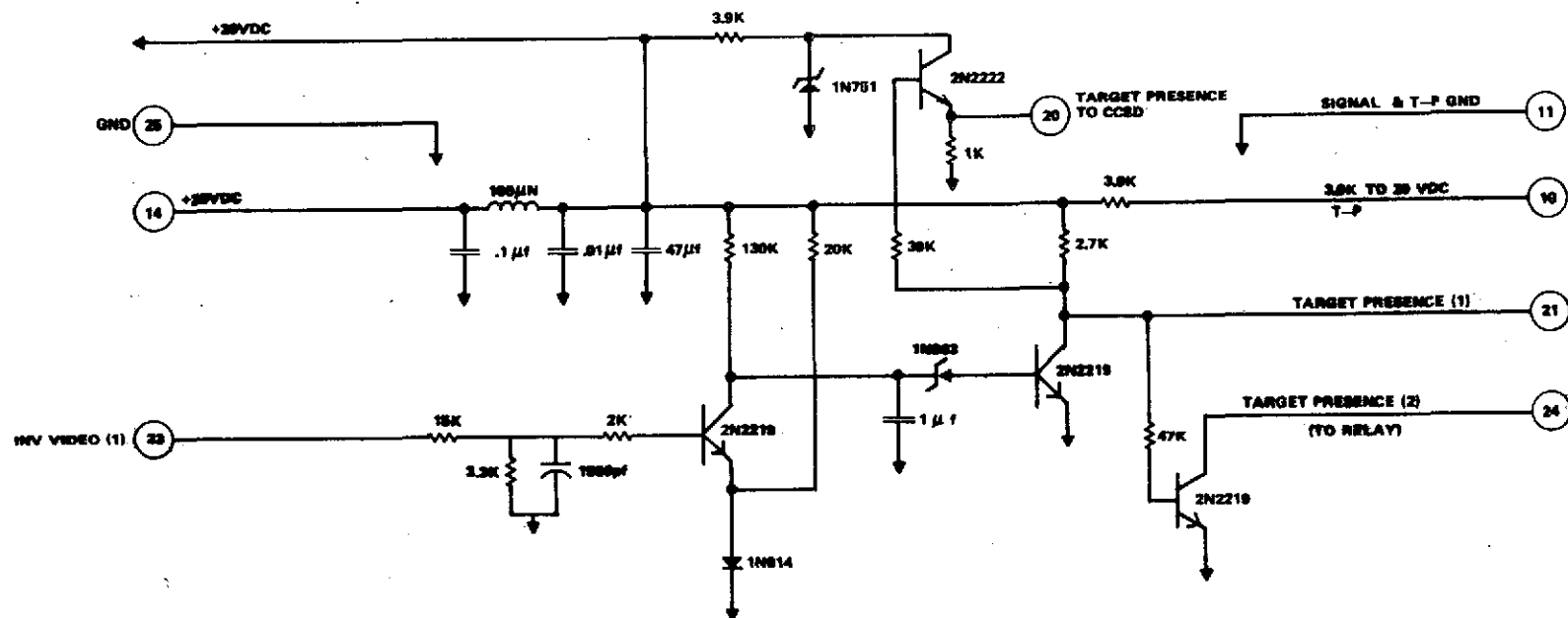Figure 229.   Beamsteerer target presence generator.

Figure 230. Relay control.

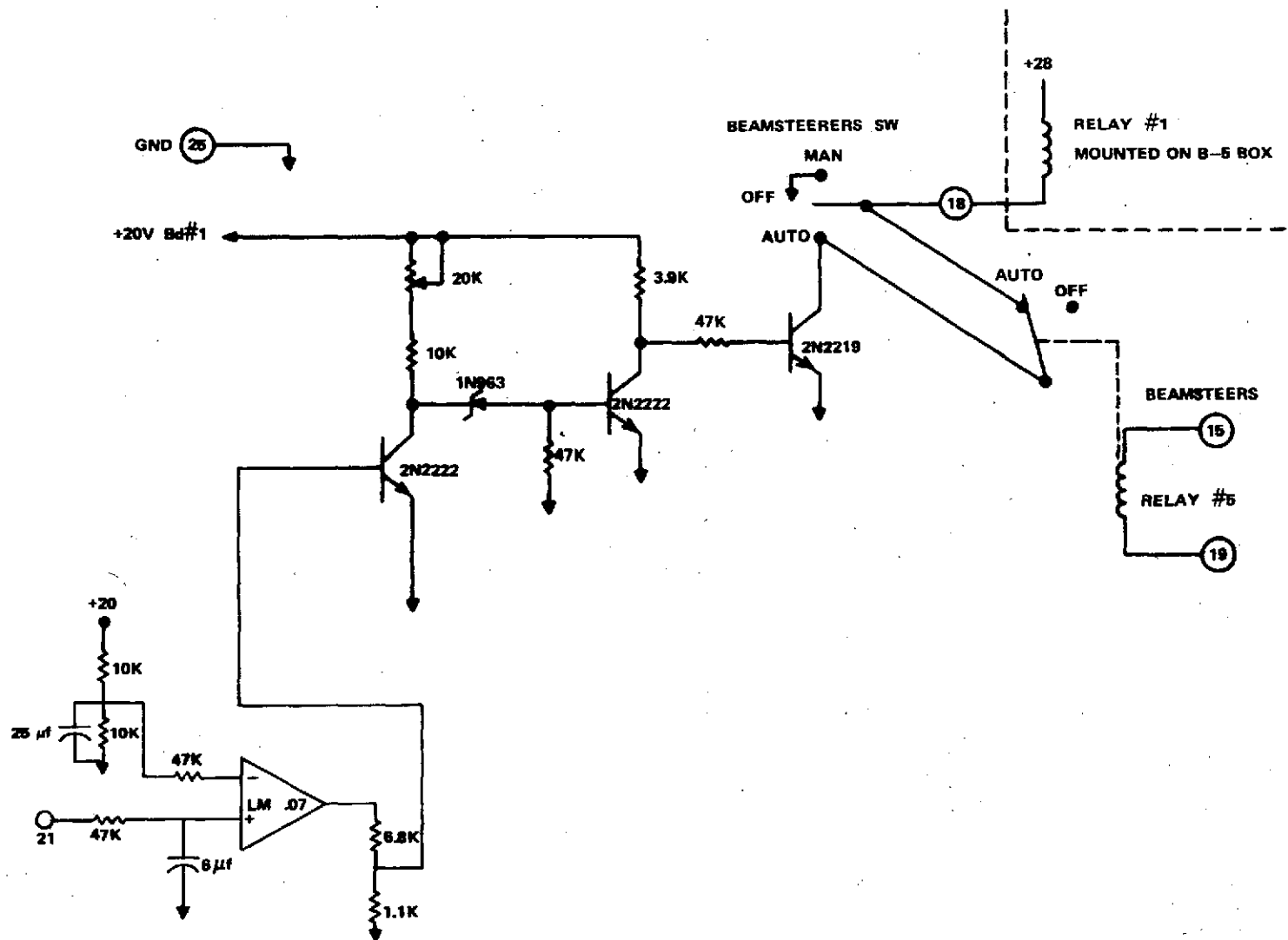Figure 231. Target presence generator, modified.

Figure 232. Beamsteerer target presence generator, modified.

The final tests run on the AOCP package, tracking between the Astrionics Laboratory and Madkin Mountain GS, were highly successful. Tracking was essentially continuous and anytime the signal was lost only momentary delays were encountered (≈ 1 second) before tracking was resumed. The tests also indicated that the sensitivity of the system had been improved although no special effort was made to increase the sensitivity of the video amplifier.

C. Recalibration of AOCP Scintillation Monitor

Calibration data on pertinent system components were given in earlier sections of this report. The calibration of the scintillation monitor was suspected to have changed in the course of the flight program. Therefore, when the AVLOC equipment was returned to MSFC upon the cessation of the flight program, a recalibration of the scintillation monitor was performed. The curves attained for the log (10.7 MHz), linear (10.7 MHz), and baseband signals, respectively, are given in Figures 233, 234, 235.

RESULTS AND CONCLUSIONS

Significant Results

The AVLOC experiment was the first full field test of two way optical communications to an airborne vehicle and was also the first demonstration of a fully operational scanning laser radar. The problems associated with a communications system operating between an aircraft, or a spacecraft, and a ground terminal are much more severe than those encountered either in the laboratory or over a fixed range. Unlike ground-to-ground communications, ground-to-aircraft communications involves acquisition and tracking functions which complicate the system and of necessity degrade communications performance. Furthermore, the aircraft-to-ground link is always subject to the uncertainties of the field environment. The AVLOC project demonstrated the ability to integrate acquisition, tracking and communications subsystems into a complete communications system capable of operation in the real world environment. This is a significant milestone in the development of space qualified optical communications.
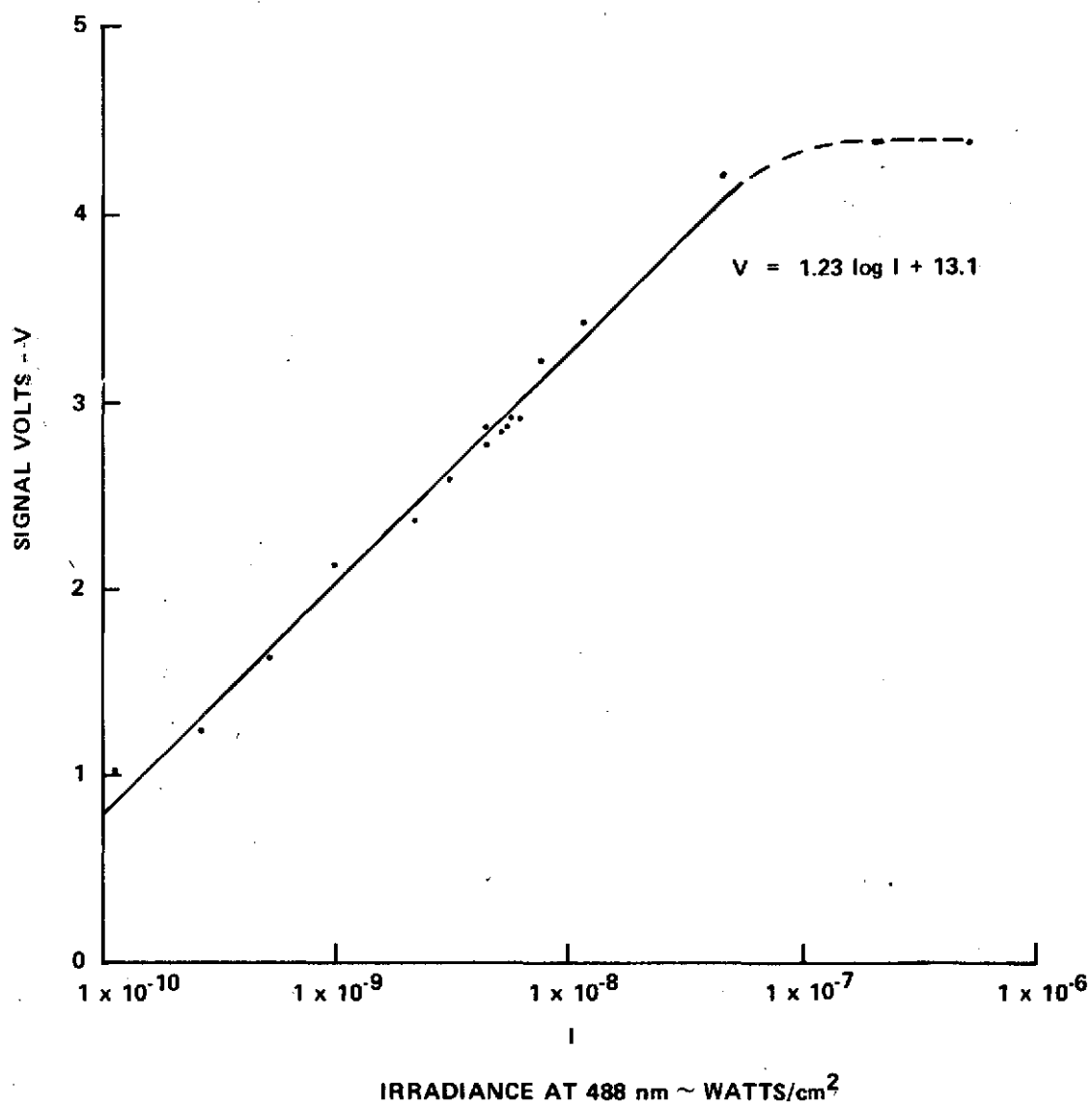
Figure 233. AOCP scintillation monitor calibration, log (10.7 MHz) signal.
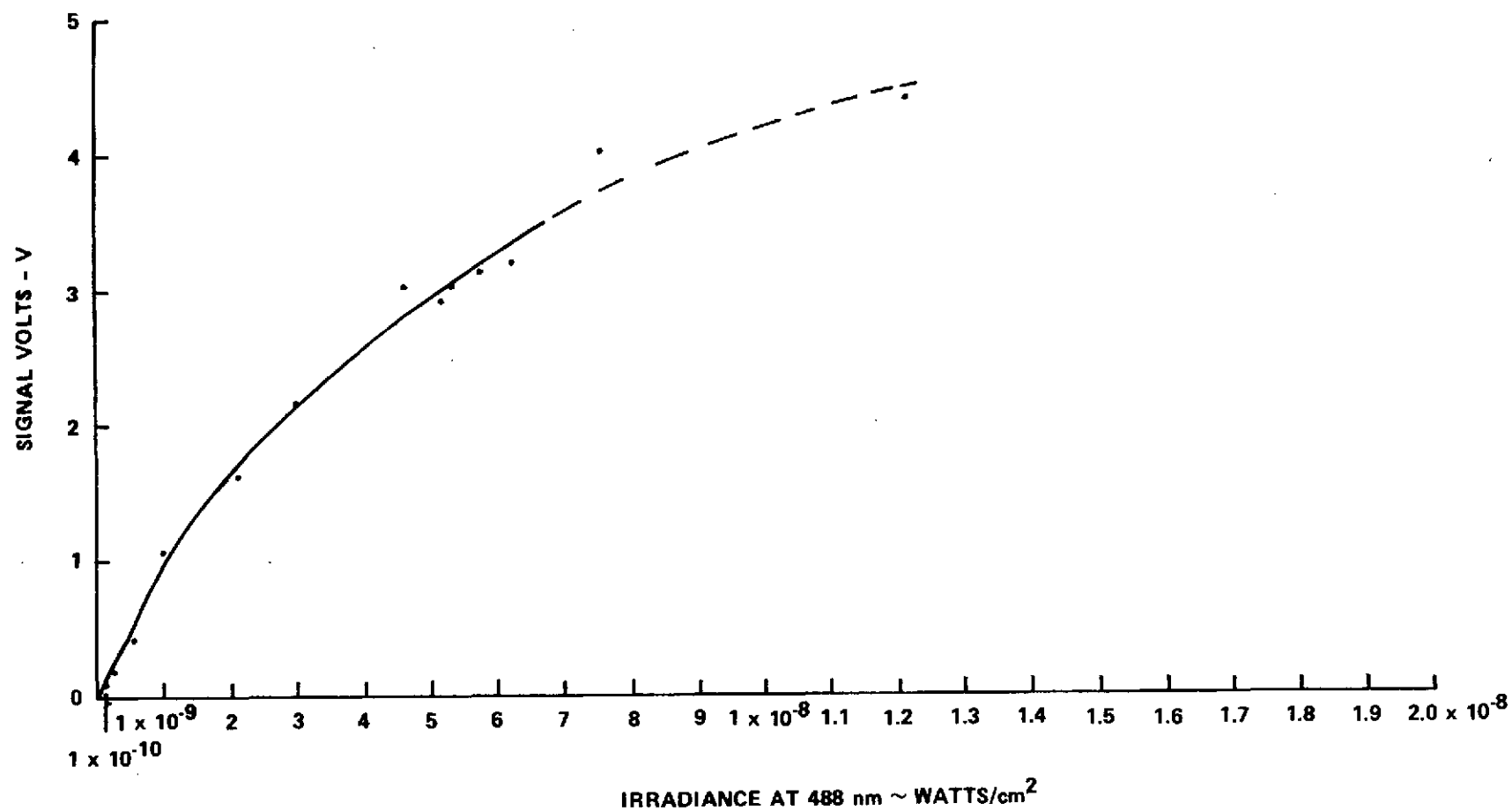
Figure 234. AOCP scintillation monitor calibration, linear (10.7 MHz) signal.

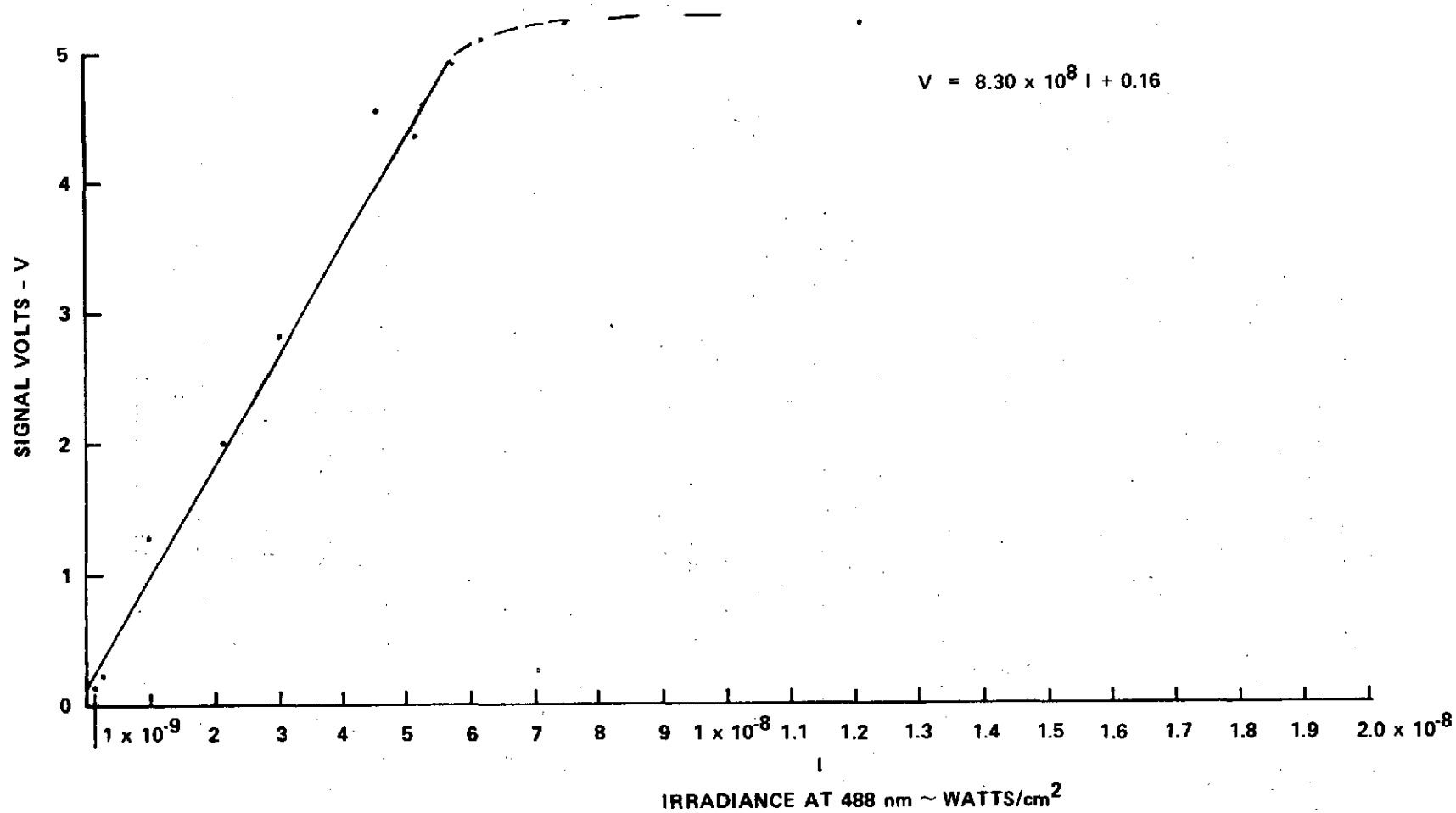$$V = 8.30 \times 10^8 \, I + 0.16$$

IRRADIANCE AT 488 nm ~ WATTS/cm^2

Figure 235. AOCP scintillation monitor calibration, baseband signal.

Even though numerous problems were encountered during the course of this project the major engineering objectives were eventually achieved. We therefore judge that from an engineering point of view the project was generally successful. The scanning laser radar (GBAA) operated reliably throughout the entire series of test and seldom failed to acquire the aircraft on the first pass. After acquisition, handoff of the tracking function to the main optical system occurred smoothly and reliably. During later flights the aircraft and ground stations were able to cooperatively track even in conditions of deep fade. While cooperatively tracking, the aircraft and ground station were able to point their transmitted beams with precisions of better than 25 and 10 μrad, respectively. Although the system never operated reliably for an extended period of time it did clearly demonstrate the ability to optically track a rapidly moving target in the presence of strong atmospheric scintillation. The conclusion, therefore, is that the acquisition and tracking techniques used on this project have been shown to be both feasible and practical.

The uplink communications channel was used to allow the ground station personnel to remotely control the operation of the AOCP. This channel operated satisfactorily during most of the test. The ground station was consistently able to transmit commands to the AOCP, the AOCP's response being verified by the experiment status indicator aboard the aircraft. Tests of the downlink channel were hindered by the failure of the tracking system to maintain two-way lock for extended periods of time. Although downlink communications were established briefly it was impossible to obtain usable data on the channel bit error rates.

Perhaps the most significant engineering result of this project was the identification of a number of problem areas that had not been anticipated prior to the flight test. These include the small aperture of the aircraft transceiver, problems with certain logic circuits associated with switching to the reacquisition mode, mechanical vibration, variations in the modulation depth, problems with maintaining boresight, and variations in the atmospheric attenuation. Most of these problems were identified early in the flight test program and many of them were corrected on later flights. Two significant problem areas, boresight alignment and modulation depth fluctuation, were diagnosed but could not be corrected before the termination of the project. Sufficient insight to the nature and cause of these difficulties has been gained to allow them to be adequately corrected on any future aircraft optical communication experiments. Each of these problem areas is further discussed in detail. The identification of these problem areas was an essential prerequisite to any successful satellite-borne optical communications experiment.

Propagation Experiments

The most useful propagation data that were obtained consisted of measurements of the uplink scintillation. In general these data agreed with the predictions of the currently accepted theory of optical propagation through the atmosphere and with the results of previous experimental measurements over vertical paths such as BAPE I and II. The probability density function of the uplink scintillation was roughly log-normal and the observed deviations from log-normalcy were within the experimental accuracy and were judged not to be statistically significant. The observed values of log amplitude variance of the scintillation fell within the range expected by theory and were of the same order of magnitude as those measured by Minott, Bufton and Fitzmaurice. Likewise the PSD of the scintillation was in agreement with the observations of these investigators.

Because of engineering and operational difficulties with the pointing and tracking system, little useful data were obtained on downlink scintillation, angular scintillation or bit error rates.

On the basis of the limited results obtained, it is concluded that the presently available theory of optical propagation through the atmosphere is adequate for predicting the magnitude of the scintillation of a beam propagating upward through the atmosphere.

Problem Areas

As previously mentioned, one of the most significant results of this project was the identification of a number of unsuspected problem areas that, had a satellite experiment been undertaken without preliminary aircraft testing, would have undoubtedly resulted in the failure of the satellite project. These problem areas are:

SMALL RECEIVING APERTURE ON THE AIRCRAFT

The power transferred from a transmitting aperture to a receiving aperture is determined not by the individual aperture diameters but by their product. Thus it is possible to compensate for a small transmitter aperture by a large receiver and vice versa. For a communications link between a mobile station and a fixed station it would seem desirable, therefore, to use a large aperture at the fixed terminal and a small one at the mobile terminal, thus economizing on size and weight in the mobile transceiver. The trade-off, however, neglects aperture averaging effects.

During this project it was found that the relatively small (10-cm) aperture of the AOCP was insufficient to provide enough aperture averaging on the uplink channel to eliminate deep fades due to scintillation. This was a design deficiency which should be corrected on any future optical communications systems by explicitly including scintillation effects in design trade-offs used to choose the aperture diameter.

IMAGE DISSECTOR LOGIC

The optical tracking system included provisions for automatically reentering the acquisition mode in the event that tracking was lost. The circuitry that governed switching from tracking to reacquisition mode contained a built-in delay that held the system in the tracking mode for a predetermined time after a loss-of-track condition occurred. This delay, referred to as "scintillation hold," was intended to allow the system to continue in the tracking mode during a momentary fade due to deep scintillation.

Although the concept of the scintillation hold seemed straightforward enough, it soon became apparent that there were fundamental difficulties involved. Throughout the flight test the scintillation hold logic caused the aircraft system to intermittently enter the reacquisition mode, resulting in the loss of a great amount of valuable data. In fact, this problem was largely responsible for the scarcity of scientific data collected during the AVLOC flights.

One of the main difficulties in correcting this problem during the flight test was the fact that it was not obvious what action should be taken to best preserve system operation during a deep scintillation fade. Since the conclusion of the flight test the question of detector logic has been addressed and a new system has been devised and tested on the Madkin Mountain range. On the basis of these tests it is believed that the improved logic, which is described in the last section, will not be susceptible to false-alarm loss-of-track as the first system was. It is therefore assumed that this problem is solved, although additional flight tests are needed to fully verify this assumption.

MECHANICAL VIBRATION

Mechanical vibration aboard the aircraft proved to be a more severe problem than was anticipated. This was due in part to the fact that the standard vibration data assumed for the original design of the AOCP did not accurately represent the enviornment aboard the WB-57F aircraft. The vibration problem

was identified early in the flight program. After extensive shaker-table tests of the AOCP and accelerometer measurement on the aircraft, the isolation mount for the AOCP was redesigned, effectively eliminating the vibration problem.

VARIATION OF MODULATION DEPTH

Unexplained changes in the modulation index of the uplink beam were periodically encountered. These changes are probably associated with thermal and mechanical instability in the ground station optical system and can be eliminated by careful mechanical design.

BORESIGHT

Considerable difficulty was encountered in maintaining boresight alignment in the optical system. Although this was not totally unexpected the severity of the problem was greater than had been anticipated. Like the modulation index variations, changes in boresight were attributed to mechanical and thermal effects in the optical system, indicating the need for better design and construction of the optical mounts.

MANUAL CONTROL OF AOCP

As originally conceived, the AOCP was to be controlled entirely from the ground with functions such as changing filters or beam divergence being commanded by signals sent to the aircraft on the uplink laser beacon. Two considerations influenced the choice of this approach. First, it was desired to simulate as nearly as possible a satellite terminal. We therefore envisioned the AOCP as a hands-off package. Secondly, it was thought that the aircraft crew, being unfamiliar with the experimental equipment and preoccupied with navigation of the aircraft, would be unable to satisfactorily operate the airborne optical transceiver. Early in the flight test it became apparent that there was a flaw in this approach; namely, that if uplink communications were not immediately established the configuration of the AOCP could not be modified. In these cases it was desirable to be able to attempt to establish communications by changing beam divergence, insertion or removal of filters, etc. Later in the program the AOCP was modified, therefore, to provide for manual control of certain critical adjustments. This procedure worked well. On several flights, the aircraft scientific experiment operator, acting on instructions from ground station personnel, was able to help establish downlink tracking and save what would otherwise have been a wasted flight.

In part this difficulty arose because of the initial assumption that the system configuration that would be most likely to achieve acquisition and communications could be predicted. This proved to be incorrect, since different configurations are needed for different atmospheric conditions. For example, strong scintillation and very clear air indicates the use of a wide transmitter beam, while weak scintillation requires the use of a narrower beam.

ATMOSPHERIC ATTENUATION

On different nights, when surface visibility, meteorological conditions and stellar brightness were similar, order of magnitude differences were observed in the atmospheric attenuation of the laser beams. These changes in attenuation were attributed to the presence of otherwise undetectable cirrus clouds. On the basis of these observations it was concluded that clear air attenuation and attenuation by very thin layers of clouds are much more significant than have been previously suspected. This presents an area in which additional study is required.

Ability to Achieve Original Program Objectives

At the conclusion of the AVLOC flight test many of the original program objectives had not been fully met; principally, downlink communications had been established only momentarily and not reliably for extended periods of time, quantitative measurements of bit error rates on the downlink channel had not been made, and a number of the scientific experiments on laser propagation through the atmosphere had not been performed. The failure to meet all of the program objectives was due largely to equipment problems that prevented the system from becoming operational until late in the flight test program. It seems that the AVLOC flight tests have, however, proved the basic feasibility of the technical approach to optical acquisition and tracking and that a follow-on project could reasonably be expected to fulfill all of the original program goals.

The optimistic predictions for the success of a follow-on aircraft communications experiment are based on the experience gained during the AVLOC program. A number of problem areas have been identified and in many instances corrected. Problems with vibration in the AOCP and temperature control aboard the aircraft, for example, were corrected by redesign of parts of the AOCP and the fixes were tested and proved adequate on subsequent

flights. Likewise the problem of the inability to change the configuration of the aircraft package before establishing uplink communications was corrected by adding manual controls. Other problems, such as the logic of the scintillation hold circuit, were identified but were not correctable before the conclusion of the flight test. Many of these problems have subsequently been addressed and the proposed remedies tested in the laboratory and on the Madkin Mountain optical range. Definitive approaches and techniques may now be proposed that will correct difficulties encountered on this project.

It is believed that the AVLOC flight tests have uncovered the major problem areas in optical communications and have indicated practical solutions to these problems. With the application of the experience gained in this project and careful design techniques confidence in the success of a follow-on program is assured.

Suitability of an Aircraft for Optical Communications Experiments

On the basis of experience during this project it is concluded that an aircraft is eminently suited both as a test bed for optical communications packages and for performing scientific experiments on optical propagation through the atmosphere.

As a test bed the aircraft allows the optical designer and communications systems engineer to verify concepts and test systems and components in an environment that realistically simulates many real world conditions that will be encountered in satellite communications systems. The following are among the advantages of an aircraft for this application:

1) Although not identical, the ground to aircraft channel closely simulates the ground to spacecraft channel. The scintillation is of the same order of magnitude in the two cases and is subject to the same diurnal variations. Likewise the attenuation is the same in both channels.

2) The aircraft environment is subject to the same 'real world' effects as the spacecraft. Both environments are subject to vibration, motion, and temperature fluctuations. In fact, in many ways the aircraft presents a more severe environment for an optical system than a spacecraft.

3) Unlike a spacecraft, the aircraft allows the engineer to test, modify, and retest a system within a short time frame, thus giving him the capability of experimentally developing system concepts and components that is unavailable in a satellite experiment.

4) The aircraft realistically simulates the angular motion of a spacecraft. In this respect an aircraft is superior to a balloon as a test bed for satellite systems.

5) An aircraft, unlike an unmanned satellite or balloon, allows for a human operator, thus increasing the available flexibility and allowing the possibility of in-flight modification of the system or the experimental procedure.

6) Finally, an aircraft experiment is inexpensive relative to a satellite experiment. In view of the lower cost as well as the flexibility provided by an aircraft it seems highly desirable that any satellite experiment be preceded by extensive system development using aircraft and by aircraft testing of the fianl system before committing it to space.

An aircraft borne system is also advantageous for conducting scientific propagation experiments. Although the aircraft-to-ground channel is not identical to the space-to-ground channel, this in no way invalidates aircraft experiments. If theory correctly predicts the results of an aircraft experiment, it should also correctly predict the results of a satellite experiment. Thus, an aircraft-borne experiment is as useful for verifying theory as is a satellite-borne experiment. Furthermore, the air-to-ground experiment is capable of measuring basic atmospheric parameters such as refractive index structure constant and attenuation. To reiterate, an aircraft, unlike a ballon, allows for a human experimenter at both terminals, thus increasing the potential experimental flexibility. Considering the flexibility and economy of aircraft experiments it seems logical that an aircraft should be considered the primary vehicle for propagation experimentation.

RECOMMENDATIONS

Experience with the AVLOC optical communications experiment has offered conclusive evidence that optical frequencies are a viable alternative to microwaves for high-data-rate space communications. But, in order to realize the potential that is inherent in optical communications, it is essential that an on-going program of laboratory research and field testing be maintained. Based on the results of the AVLOC project, the following specific recommendations are respectfully submitted for the implementation of such a program.

Next Phase AVLOC Aircraft Test

It is recommended that additional aircraft test flights be conducted using a modified version of the existing AVLOC hardware. The objectives of this program would be (1) to verify the solutions that have been proposed for overcoming the difficulties encountered on the previous series of flight tests; and (2) to fulfill the original scientific and engineering objectives established for the AVLOC project.

Many of the approaches proposed for correcting deficiencies in the existing flight hardware have been fully tested in the laboratory and on the optical range. Nevertheless, it seems essential that the proposed modifications be verified in a flight environment before proceeding to more sophisticated airborne or satellite-borne communications experiments.

With regard to the second objective of the follow-on program, it is believed that the original AVLOC program goals still represent valid scientific and engineering experiments that should be pursued.

Second Generation Aircraft Test Program

It seems essential, before committing to a satellite program, that all systems concepts and components be fully verified by both aircraft and laboratory testing. In this way any unforeseen problems can be identified and corrected with minimum delay and expense. Once a system is launched into space all chance of modifying it is irrevocably lost (at least, prior to the advent of the Space Shuttle). The risk involved in making such a commitment without exhausting every possibility for preliminary testing is too great to justify the initial savings in time and money. In keeping with this philosophy,

it is recommended that once the initial AVLOC program objectives have been obtained, a follow-on program using second-generation hardware should be initiated before proceeding to an operational satellite system.

Satellite Program

When all system concepts and components have been fully proven by aircraft test, we would recommend the construction of an operational satellite system.

Scientific Experimentation

The AVLOC tests indicate that the currently accepted theory of optical propagation through the atmosphere is adequate for the design of a workable communications system. This is not to say, however, that further investigation of propagation phenomena and refinement of atmospheric parameters are not needed. In particular, recommendation is made that fundamental research be continued in the following areas:

Measurement of atmospheric attenuation, especially investigation of the attenuation by dust and thin clouds. The goal of this research would be to determine the range of attenuations that could be expected and to estimate the statistical probability of encountering a given value of attenuation.

Investigation of the vertical profile of refractive index structure constant. Most theoretical treatments of vertical propagation paths assume the structure constant profile due to Hufnagel and Stanley. Recent experimental investigations have shown that high altitude turbulence may be greater than that predicted by this model, and that there may be important local turbulence associated with high altitude wind shears. This also requires further investigation.

SUMMARY

Introduction

In support of the overall communications program of NASA's Office of Aeronautics and Space Technology, the George C. Marshall Space Flight Center

has conducted a series of optical communication experiments between a high altitude aircraft package and a ground terminal located at MSFC on Madkin Mountain. Each communication terminal consisted of an optical tracking system with image motion compensation and a laser transmitter with a modulator. Thus, each terminal could track on the laser beam of the other end and transmit information or commands to the other via its laser beam. This project is the airborne visible laser optical communication experiment (AVLOC). The experiments were intended to perform three functions: (1) to provide engineering data needed for the evaluation of techniques of optical communications and for future systems, (2) to collect scientific data on the propagation of visible wavelength radiation through the atmosphere, and (3) to demonstrate the feasibility of optical communication and tracking techniques for aircraft-to-ground and satellite-to-ground links.

Several groups were involved in this project. The MSFC Astrionics Laboratory had overall responsibility for the project including experiment definition, integration and checkout, and construction and operation of the ground station. ITT Aerospace Corp. built the airborne optical communication package (AOCP), the ground based acquisition aid (GBAA), and the ground checkout equipment (GCE). Chrysler Corp. Space Division was responsible for the remainder of the airborne system including the flight computer and integration of the aircraft system as well as for remote operations at Kirkland AFB. Other organizations participating in this project were the MSFC meteorological group, the U.S. Army Missile Command, whose personell operated the microwave radar installation, and the U.S. Air Force, which supplied and operated the aircraft. Principal investigator on this project was J. L. Randall; company principal investigators were Estel Hoverstein, (MIT-Lincoln Lab, now with the Defense Communication Agency), Sherman Karp (NASA/Electronics Research Center, now with the Department of Transportation) and William E. Webb (University of Alabama). The project managers were Wayne Wagnon and St. John Courtenay. Peter Marrero was project engineer.

The aircraft used in this experiment was an Air Force WB-57F. The desired aircraft flight path was a circular path at 18.3-km (60 000-ft) altitude in a 12.2-km (40 000-ft) radius. The circular path was desired to obtain data at a constant slant range, which allowed for more meaningful data reduction. The modified WB-57F entered the optical acquisition area of the GBAA from the south on a line 12.2 km (40 000 ft) west of the ground terminal at an altitude of 18.3 km (60 000 ft). When the aircraft was due west of the ground terminal, it began a right turn to enter a circular path centered around the ground terminal. During the experiment the aircraft was tracked by the GBAA and microwave radar. Information from these two radar systems provided data that were used to keep the aircraft in the desired flight path.

Description of Equipment

The experimental system consisted of both the airborne package and the Madkin Mountain ground station. Both the airborne package and the ground station had transceivers so that data on both uplink and downlink propagation could be obtained. The airborne transceiver had a 5-mW He-Ne laser operating at 632.8 nm. An electro-optic modulator with a modulation index of 0.65 was used to send a 30-Mbit/s data rate. The downlink could be modulated with a 31-bit pseudorandom word (PN), a video picture or TM data. Downlink scintillation data could be collected either on baseband or on the 2-MHz component of the PN.

The ground station beacon was a 250-mW argon laser operating at 488 nm. The uplink beacon was modulated by a 10.7-MHz subcarrier frequency to send commands to the AOCP. Both baseband and the 10.7-MHz component were recorded for uplink scintillation data. The ground station had a pulsed laser radar (GBAA) that performed initial acquisition of the aircraft by tracking corner reflectors on the bottom of the aircraft. A backup visual acquisition and tracking system, consisting of three television cameras and three monitors, were also provided at the ground terminal.

The primary ground terminal receiving and transmitting optics consisted of a 61-cm (24-in.) Cassegrainian telescope with the experimental transceiver package located at its Coudé focus. The incoming 632.8-nm beam from the airborne He-Ne laser passed through a wavelength selective beam splitter to separate it from the 488-nm uplink beam. It was then directed through a system of optics to a tracking detector, a communications detector, and a background detector. The tracking detector was a quadrant photomultiplier that provided signals to a piezoelectric-driven beamsteerer for fine pointing. These signals, along with the output of the angle encoders on the telescope mount, were fed into an SCC 4700 computer which performed the necessary coordinate transformations and generated signals to drive the polar equatorial telescope mount, keeping the incoming signal in the center of the beamsteerer range. The communications detector was a photomultiplier tube whose output provided the wide bandwidth downlink communications channel. The output of the communications channel was routed to the communications electronics where it was decoded and applied to the bit error detector and to the recorder. In addition to the communications and tracking detectors, the ground terminal contained a background detector that recorded the background intensity in a narrow bandpass at 700 nm. This information was correlated to degradation of the communication performance. A command tone transmitter allowed the selection of tone sequences which were transmitted

446

to the aircraft on the uplink laser beam. These tone sequences, when received and decoded at the airborne terminal, performed control functions such as increasing or decreasing beam divergence, changing receiver attenuation, and selecting downlink modulation. The uplink laser beam was generated by an argon laser which passed through a modulator and beamsteerer and out through the telescope. The beamsteerer was driven by the computer to direct the uplink beam directly back along the incoming beam.

During the acquisition phase of the experiment, the GBAA operated in a search mode, putting up a 10-deg-wide radar fence in the direction the aircraft was to enter the acquisition area. When the aircraft entered the radar fence, reflections from retroflectors attached to the underside of the aircraft were received by the GBAA. On receiving reflections from the retroflectors, the GBAA entered a track mode and provided pointing information through the computer to the telescope mount. These pointing errors were used to refine the telescope position until the transceiver system acquired track of the downlink laser beam. Once the transceiver entered the track mode, it answered the tracking function. The GBAA continued to track the aircraft to provide range and aircraft position information. To assist the aircraft pilot in maintaining the aircraft on the desired circular flight path, the position information from the GBAA were compared to a computed desired flight path. A signal representing the difference between the desired and actual flight paths was routed to the command tone transmitter where an audio tone representing this difference was generated and used to modulate the uplink laser beam. When the tone was detected and decoded at the aircraft, it was used to generate a positive or negative dc voltage which drove a pilot's direction indicator informing the pilot of the magnitude and direction of the flight path error.

Also, rigidly attached and boresighted to the telescope were three television (TV) cameras; each has a different field of view (FOV) and its own monitor. When used with the joystick telescope control, these cameras provided a means of visually acquiring and tracking the aircraft. When displaced, the joystick applied electrical signals to the computer which influenced telescope drive rates proportional to the amount and direction of joystick displacement. By manual manipulation of the joystick, the telescope could be pointed so that the aircraft was in the FOV of a 30-deg-FOV camera. When the aircraft is centered on the 30-deg-FOV TV monitor, it will be in the FOV of a 10-deg-FOV camera; and when centered on the 10-deg-FOV monitor, it will be in the FOV of the 1-deg-FOV camera. When the aircraft is centered on the 1-deg-FOV monitor and remains centered, telescope drive rates will be adjusted to the proper value for short term tracking of the aircraft and for laser beam acquisition.

Once the GBAA had acquired the aircraft corner reflectors and was tracking, the beacon laser illuminated the aircraft. The gimballed mirror of the aircraft package was then computer scanned in the general direction of the ground terminal. This allowed the 488-nm radiation to enter the 5-deg by 5-deg deg FOV of the TV tracker which acquired and locked onto the beam. Angle error information would then be provided to the onboard computer to generate a drive signal for the gimbal mirror. This allowed the uplink radiation to enter the 0.5-deg by 0.5-deg acquisition FOV of the image dissector which acquired and locked onto the beam. All data in the aircraft were recorded on an Ampex AR1700 flight recorder but the same data could be telemetered to ground over the 30-Mbit link for analysis on the ground. A separate detector monitors uplink scintillation. The scintillation detector has an aperture control to vary the effective receiver aperture diameter.

Test Measurements

Two of the main objectives of this experiment were to collect data on the propagation of visible wavelength radiation through the atmosphere and to provide engineering data on system performance for reference on future systems.

The principal measurements to be made were: (1) Engineering measurements of pointing and tracking precision, (2) Scintillation, (3) Angle of arrival fluctuations, (4) Bit error rate, and (5) Atmospheric attenuation. In Addition, several supporting experiments were to be performed during aircraft tests.

Flight Program

Fifteen flight tests were conducted between August 1972 and March 1973. The flight tests gave an insight into the myriad problems associated with an optical tracking and communications system where the location of one of the terminals is remote and moving at high velocity.

Many of the problems encountered were resolved; some remain in question, but a wealth of knowledge was obtained which can be of direct consequence to satellite applications. Initial acquisition of the narrow beacon laser beam was mastered so that coarse tracking at each end of the link became routine. Reliable fine track proved to be more elusive but significant progress was made. During periods of reliable fine track, commands were readily transmitted on the uplink laser beam and faithfully executed at the aircraft

448

terminal. Initially, there were serious boresight problems with the downlink beam but this was solved by remoting boresight adjustments to the cockpit. Downlink communications were unsuccessful due to the poor modulation quality on the He-Ne laser beam.

The flight test program, in other words, was extremely fruitful in revealing many latent problems which would have remained undetected in a laboratory environment.

REFERENCES

1. Minott, Peter O.; Bufton, Jack L.; and Fitzmaurice, Michael W.: Results of the Balloon Atmospheric Propagation Experiment Flights of 1970 (BAPE I). Goddard Space Flight Center, Greenbelt, Md., March 1972.

2. Reference Data for Radio Engineers. Howard W. Sams, Inc., a subsidiary of ITT Corp., Indianapolis/Kansas City/New York, fifth ed., fourth printing, 1972.

3. Skolinik, M.I.: Introduction to Radar Systems. McGraw-Hill Book Co., New York, 1962, p. 267.

4. Bell, E. E.; Eisner, L.; Young, J.; and Oetjen, R. A.: Spectral Radiance of Sky and Terrain at Wavelengths Between 1 and 20 Microns. Journal of the Optical Society of America. Vol. 50, December 1960, p. 1314.

5. Control of Hazards to Health from Laser Radiation. Technical Bulletin MED 279, Departments of the Army and the Navy, Feb. 24, 1969.

6. A Guide for Uniform Industrial Hygiene Codes or Regulations for Laser Installations. American Conference of Governmental Industrial Hygienists, 1968; see Table II.

7. AVLOC Operations Plan (aircraft operations) June 1972, Chysler Corp. under contract NAS8-25418.

8. Mann H. B. and Wald A., Annuals Math. Stat. September 1942.

9. Williams, C. A. Jr., J. Am. Stat. Assoc. 45, March 1950.

10. Welch, P. E., IEEE Trans. Audio and Electroacoustics, Vol. AU-15 June 1967.

11. Bingham, C. Godfery M.D., and Turkey, J. W., IEEE Trans, Audio and Electroacoustics. Vol AU-15, June 1967.

REFERENCES (Continued)

12. Fried D. L., J. Opt. Soc. Am. 56, 1372-1379, (1966).

13. Hufnagel, R. E. and Stanley, N. R., J. Opt. Soc. Am. 54, 52-61 (1964).

14. ASTIA No. AD-476244, Perkin Elmer Corp. (1966).

15. Fried D. L., J. Opt. Soc. Am. 57, 181, (1967).

16. Fried D. L., J. Opt. Soc. Am. 57, 169, (1967).

17. Northrop report, "Measurement Program for High Altitude Aircraft Tests," Vol. I, II, III, dated July, 1973, generated under NASA Contract NAS8-29194.

18. Anon., "Vibration Test Program on AVLOC Airborne Platform," NAS 8-21908, Wyle Corp., Feb. 9, 1972.

NOTE: Appendices A through I are available on a request basis only. Requests should be directed to :

George C. Marshall Space Flight Center
Marshall Space Flight Center, Alabama   35812

Attn: Wayne Wagnon; Code EC31

APPROVAL

AIRBORNE VISIBLE LASER OPTICAL COMMUNICATIONS (AVLOC) EXPERIMENT

Electronics and Control Laboratory

The information in this report has been reviewed for security classification. Review of any information concerning Department of Defense or Atomic Energy Commission programs has been made by the MSFC Security Classification Officer. This report, in its entirety, has been determined to be unclassified.

This document has also been reviewed and approved for technical accuracy.

F. W. WAGNON
Project Manager

F. BROOKS MOORE
Director, Electronics
and Control Laboratory

DISTRIBUTION

INTERNAL

DA01	EC31
CC	Mr. Wagnon (20)
AS61 (2)	EC43
AS61 L (8)	Mr. Courtenay
AB51	EC31
Mr. Hildreth	Dr. Randall (20)
AT01 (6)	PF05
EA01	Mr. G. Emanuel
Mr. Smith	
ER01	
EC01	
Mr. Moore	

EXTERNAL

NASA Headquarters
Washington, D.C. 20546
Attn: Mr. Edward C. Buckley (10)
Code REM

Mr. Hugh Fosque
Code TA

Mr. Jack Levine
Code RG

Goddard Space Flight Center
Greenbelt, MD 20771
Attn: Dr. Henry Plotkin
Code 520

Dr. Michael W. Fitzmaurice
Code 520

Mr. Walter J. Carrion
Code 520

Hayes International Corp
HIC Building
Huntsville, AL 35807
Attn: Mr. W. T. Weissinger

Ames Research Center
Moffett Field, CA 94035
Attn: Mr. J. M. Deerwester
Code MO 202-9

Langley Research Center
Langley Station
Hampton, VA 23365
Attn: Mr. G. B. Graves, Jr.
Code 117

Mr. Lloyd W. Root, Jr.
AMSMI-RER
Bldg. 5400, Rm D-223
Redstone Arsenal, AL 35808

Mr. Gordon R. Griffith
Redstone Arsenal Airport Safety
AMSMI-KSTA, Bldg. 4809
Redstone Arsenal, AL 35808

Scientific and Technical Information
Facility (25)
P.O. Box 33
College Park, MD 20740
Attn: NASA Representative (S-AK/RKT)

Dr. Sherman Karp
Naval Electronics Lab Center
Code 2400
271 Catalina Blvd.
San Diego, Calif. 92152

Dr. Estil Hoversten
Defense Communication Agency
8th and South Courthouse Rd.
Arlington, Va. 22204

Dr. William E. Webb
Department of Engineering
University of Alabama
University, AL 35486

ITT Gilfillan
7821 Orion Ave.
P.O. Box 7713
Van Nuys, CA 91409
Attn: Mr. John Ward

Chrysler Corporation Space Division
P.O. Box 29200
New Orleans, LA 70129
Attn: Mr. Dave Buell

U.S. Army Missile Command
Attn: Mr. F. C. Bunn
Code AMSMI-RTF
Redstone Arsenal, AL 35809

Headquarters USAF
The Pentagon
Attn: AFXOOTR (Col. Onial Thomas)
Room: BF 934
Washington D.C. 20330

Headquarters USAF
The Pentagon
Attn: AFSMEB (Col. P.R. O'Malley)
Room: 4D 260
Washington D.C. 20330

CMDR 58th WRS
Code OPL, Bldg. 1017
Kirkland AFB
Albuquerque, NM 87117

CMDR 9th WRW (2 Copies)
Attn: DOQ
McClellan AFB, CA 95652

Dr. William C. Eppers
AFSC/AFAL (TEL)
Wright Patterson AFB, OH 45433

Mr. Ben E. Bunch
Box 9071
Kirkland AFB
Albuquerque, NM 87117

Mr. Grover C. Combs
Code MMH, Bldg 300
Warner Robins AFB
Warner Robins, GA 31093

Mr. Robert Hudman
Code MMHTA, Bldg 300
Warner Robins AFB
Warner Robins, GA 31093

Mr. Henry E. Midura
Chief, Air Space Branch
Air Traffic Division
P.O. Box 20636
East Point, GA 30320

Mr. Paul W. Hancock
Chief, Engineering & Services Div.
Installations & Services Office
AMSMI-OE Bldg. 7101
Redstone Arsenal, AL 35808